

Vol. 18. No 3, 2016

ISSN 1507-2711
Cena: 25 zł (w tym 5% VAT)

EKSPLOATACJA I NIEZAWODNOŚĆ

MAINTENANCE AND RELIABILITY



Polskie Naukowo Techniczne Towarzystwo Eksploatacyjne
Warszawa

Polish Maintenance Society
Warsaw

Professor Andrzej Niewczas, PhD, DSc (Eng)

*Chair of Scientific Board
President of the Board of the Polish Maintenance Society*

Professor Holm Altenbach, PhD, DSc (Eng)

Otto-von-Guericke-Universität, Magdeburg, Germany

Professor Karol Andrzejczak, PhD, DSc

Poznań University of Technology, Poznań

Professor Gintautas Bureika, PhD, DSc (Eng)

Vilnius Gediminas Technical University, Vilnius, Lithuania

Professor Zdzisław Chlopek, PhD, DSc (Eng)

Warsaw University of Technology, Warsaw

Dr Alireza Daneshkhah

*Warwick Centre for Predictive Modelling
University of Warwick, UK*

Professor Jan Dąbrowski, PhD, DSc (Eng)

Białystok Technical University, Białystok

Professor Sławczo Denczew, PhD, DSc (Eng)

The Main School of Fire Service, Warsaw

Professor Mitra Fouladirad, PhD, DSc

Troyes University of Technology, France

Dr Ilia Frenkel

Shamoon College of Engineering, Beer Sheva, Israel

Professor Olgierd Hryniewicz, PhD, DSc (Eng)

Systems Research Institute of the Polish Academy of Science, Warsaw

Professor Hong-Zhong Huang, PhD, DSc

*University of Electronic Science and Technology of China,
Chengdu, Sichuan, China*

Professor Krzysztof Kolowrocki, PhD, DSc

Gdynia Maritime University

Professor Vaclav Legat, PhD, DSc (Eng)

Czech University of Agriculture, Prague, Czech Republic

Professor Jerzy Merksiz, PhD, DSc (Eng)

Poznań University of Technology, Poznań

Professor Gilbert De Mey, PhD, DSc (Eng)

University of Ghent, Belgium

Professor Maria Francesca Milazzo, PhD, DSc, (Eng)

University of Messina, Italy

Professor Tomasz Nowakowski, PhD, DSc (Eng)

Wrocław University of Technology, Wrocław

Professor Marek Orkisz, PhD, DSc (Eng)

Rzeszów University of Technology, Rzeszów

Professor Stanisław Radkowski, PhD, DSc (Eng)

Warsaw University of Technology, Warsaw

Professor Jan Szybka, PhD, DSc (Eng)

AGH University of Science and Technology, Cracow

Professor Katsumi Tanaka, PhD, DSc (Eng)

Kyoto University, Kyoto, Japan

Professor David Vališ, PhD, DSc (Eng)

University of Defence, Brno, Czech Republic

Professor Min Xie

City University of Hong Kong, Hong Kong

Professor Irina Yatskiv, PhD, DSc (Eng)

Riga Transport and Telecommunication Institute, Latvia

Co-financed by the Minister of Science and Higher Education

The Journal is indexed and abstracted in the Journal Citation Reports (JCR Science Edition), Scopus, Science Citation Index Expanded (SciSearch®) and Index Copernicus International.

The Quarterly appears on the list of journals credited with a high impact factor by the Polish Ministry of Science and Higher Education and is indexed in the Polish Technical Journal Contents database – BAZTECH and the database of the Digital Library Federation.

All the scientific articles have received two positive reviews from independent reviewers.

Our 2015 Impact Factor is 1.248

Editorial staff:

Dariusz Mazurkiewicz, PhD, DSc (Eng), Associate Professor (Editor-in-Chief, Secretary of the Scientific Board)
Tomasz Klepka, PhD, DSc (Eng), Associate Professor (Deputy Editor-in-Chief)
Teresa Błachnio-Krolopp, MSc (Eng) (Editorial secretary)
Andrzej Koma (Typesetting and text makeup)
Krzysztof Olszewski, PhD (Eng) (Webmaster)

Publisher:

Polish Maintenance Society, Warsaw

Scientific patronage:

Polish Academy of Sciences Branch in Lublin

Address for correspondence:

“Eksploracja i Niezawodność” – Editorial Office
ul. Nadbystrzycka 36, 20-618 Lublin, Poland
e-mail: office@ein.org.pl
http://www.ein.org.pl/

Circulation:

550 copies

Science and Technology

Abstracts	III
Marek HAWRYLUK, Marcin KASZUBA, Zbigniew GRONOSTAJSKI, Przemysław SADOWSKI	
Systems of supervision and analysis of industrial forging processes Systemy nadzoru i analizy przemysłowych procesów kucia	315
Bolesław KARWAT, Marek NOCUIŃ, Ryszard MACHNIK, Jerzy NIEDŹWIEDZKI	
Modelling and study the effect of selected design features for the operating parameters of industrial electrostatic precipitators Modelowanie i badania wpływu wybranych cech konstrukcyjnych na parametry eksploatacyjne elektrofiltrów przemysłowych	325
Jacek MUCHA, Jan JAWORSKI	
The tool surface wear during the silicon steel sheets blanking process Zużycie powierzchni narzędzi podczas eksploatacji w procesie wykrawania blachy krzemowej	333
Stanisław KRUCZYŃSKI, Marcin ŚLĘZAK, Wojciech GIS, Piotr ORLIŃSKI	
Evaluation of the impact of combustion hydrogen addition on operating properties of self-ignition engine Ocena wpływu spalania dodatku wodoru na własności eksploatacyjne silnika o zapłonie samoczynnym	343
Tadeusz DZIUBAK	
The effects of dust extraction on multi-cyclone and non-woven fabric panel filter performance in the air filters used in special vehicles Wpływ odsysania pyłu na charakterystyki multicyklonu i włókninowej przegrody filtracyjnej filtru powietrza pojazdu specjalnego	348
Miroslaw KARCZEWSKI, Leszek SZCZĘCH	
Influence of the F-34 unified battlefield fuel with bio components on usable parameters of the IC engine Wpływ mieszanin jednolitego paliwa pola walki F-34 z biokomponentami na parametry użyteczne silnika	358
Gökhan GÖKDERE, Mehmet GÜRCAN	
New reliability score for component strength using kullback-leibler divergence Nowa metoda oceny niezawodności na podstawie wytrzymałości elementów z zastosowaniem dywergencji Kullbacka-Leiblera	367
Joanna RYMARZ, Andrzej NIEWCZAS, Aneta KRZYŻAK	
Comparison of operational availability of public city buses by analysis of variance Porównanie gotowości autobusów komunikacji miejskiej z zastosowaniem metody analizy wariancji	373
Hao-Wei WANG, Ke-Nan TENG	
Residual life prediction for highly reliable products with prior accelerated degradation data Prognozowanie trwałości reszkowej wysoce niezawodnych produktów na podstawie danych historycznych z przyspieszonych badań degradacji	379
Andrzej KOSUCKI, Piotr MALENTA	
The possibilities of reducing the operational load of hoisting mechanisms in case of dynamic hoisting Możliwości zmniejszenia obciążeń eksploatacyjnych mechanizmów dźwignic dla przypadku dynamicznego podnoszenia ładunku	390
Zhihua WANG, Junxing LI, Yongbo ZHANG, Huimin FU, Chengrui LIU, Sridhar KRISHNASWAMY	
A novel Wiener process model with measurement errors for degradation analysis Analiza degradacji z zastosowaniem nowego modelu procesu Wienera uwzględniającego błędy pomiarowe	396
Łukasz STAWIŃSKI	
Experimental and modeling studies of hydrostatic systems with the counterbalance valves which are used in hydraulic lifting systems with passive and active load Eksperymentalne i modelowe badania układu hydraulicznego z zaworami hamującymi typu counterbalance stosowanymi w układach dźwigowych z obciążeniem biernym i czynnym	406
Grzegorz DOMBEK, Zbigniew NADOLNY	
Liquid kind, temperature, moisture, and ageing as an operating parameters conditioning reliability of transformer cooling system Rodzaj cieczy, temperatura, zawilgocenie oraz zesterzenie jako parametry eksploatacyjne warunkujące niezawodność układu chłodzenia transformatora	413
Ji-Min LU, Fares INNAL, Xiao-Yue WU, Yiliu LIU, Mary Ann LUNDTEIGEN	
Two-terminal reliability analysis for multi-phase communication networks Analiza niezawodności par terminali w wielofazowych sieciach komunikacyjnych	418

Witold PAWLOWSKI, Lukasz KACZMAREK, Petr LOUDA

- Theoretical and experimental modal analysis of the cylinder unit filled with PUR foam**
Teoretyczna i eksperymentalna analiza modalna zespołu bębna wciągarki wypełnionego pianką poliuretanową..... 428

Andrzej ŻUCHOWSKI

- Analysis of the influence of the impact speed on the risk of injury of the driver and front passenger of a passenger car**
Ocena wpływu prędkości zderzenia na ryzyko obrażeń kierowcy i pasażera samochodu osobowego 436

Yi-Chao YIN, Hong-Zhong HUANG, Weiwen PENG, Yan-Feng LI, Jinhua MI

- An E-Bayesian method for reliability analysis of exponentially distributed products with zero-failure data**
Metoda bayesowskiej estymacji wartości oczekiwanej dla produktów o rozkładzie wykładniczym wykorzystująca dane o niezaistniałych uszkodzeniach 445

Michael MUTINGI, Charles MBOHWA, Venkata P. KOMMULA

- Multi-criteria reliability optimization for a complex system with a bridge structure in a fuzzy environment: A fuzzy multi-criteria genetic algorithm approach**
Wielokryterialna optymalizacja niezawodności złożonego systemu o strukturze mostkowej w środowisku rozmytym. Metoda rozmytego wielokryterialnego algorytmu genetycznego..... 450

Zhiao ZHAO, Jing QIU, Guanjun LIU, Yong ZHANG

- Research on time-varying characteristics of testability index based on renewal process**
Badanie zmiennych w czasie własności wskaźnika testowalności na podstawie procesu odnowy 457

Paweł OSTAPKOWICZ, Andrzej BRATEK

- Possible leakage detection level in transmission pipelines using improved simplified methods**
Weryfikacja możliwego poziomu wykrywalności wycieków w zakresie zastosowania zmodyfikowanych uproszczonych metod diagnostycznych .. 469

HAWRYLUK M, KASZUBA M, GRONOSTAJSKI Z, SADOWSKI P. **Systems of supervision and analysis of industrial forging processes.** Eksploatacja i Niezawodność – Maintenance and Reliability 2016; 18 (3): 315–324, <http://dx.doi.org/10.17531/ein.2016.3.1>.

The work presents the concept of a multifunctional automatized forging station with a supervisory system of the process and the production management, with the option of application mainly at forging shops (with somewhat outdated machines) equipped with older-generation devices and forging units. The concept of such a station, which applies the, already partially, implemented construction and technological solutions, is a result of an extensive analysis of the current needs of forging plants and it has been supported by the acquired knowledge and experience of the authors, who specialize in the construction of measurement systems and other devices for the forging industry. The systems built by the authors makes it possible to measure and archive as well as fully monitor the most important technological parameters of the process, such as: the course of the forging forces in the function of time/shift, correlated with a measurement of the temperature of the preforms and dies as well as the number of the produced forgings. The elaborated systems, owing to their inclusion in the general production management system (which plays a supervisory role over the whole process), also allow for an analysis of the occurring changes during the process, including the proceeding wear of the forging tools as well as an analysis of the parameters determined throughout a long period of time, management of the machines and equipment (the work of the machines, their breakdowns, repairs etc.), and the human resources, as well as adaptation of the production organization to the increasing market demands. The presented concept of a complex approach to the issue of automatization of the forging line is a reply to the constantly developing forging technology, caused by market competitiveness, which requires automatization of the production, with the purpose to produce forgings of a higher quality, and, at the same time, reduce the costs.

KARWAT B, NOCUN M, MACHNIK R, NIEDZWIEDZKI J. **Modelling and study the effect of selected design features for the operating parameters of industrial electrostatic precipitators.** Eksploatacja i Niezawodność – Maintenance and Reliability 2016; 18 (3): 325–332, <http://dx.doi.org/10.17531/ein.2016.3.2>.

Electrostatic precipitators are currently most commonly used in industrial processes equipment to reduce dust emissions into the atmosphere. A significant impact on the process of extraction of two-phase gas/dust medium has the shape and configuration of the discharge electrodes, affecting the shape of the electric field in the chamber electrostatic precipitator. Geometric parameters of discharge electrodes and their arrangement in the chamber electrostatic should provide uniform current density distribution at the surface of the collecting electrodes. The article presents an analysis of the impact of geometry and configuration of industrial - blade type discharge electrodes on the distribution of current density on the collecting electrode. On the basis of the measurement results mathematical model was worked out which allows simulation of the current density distribution depending on the shape of the electrodes. The model allows to specify the most appropriate parameters of distance between the emission elements of discharge electrode and the distance between the electrodes. Preferred geometric parameters and configuration of discharge electrodes was determined by analyzing power spectral density magnitude (PSD) and the mean square value (RMS) of current density. The results indicate the possibility of reducing the number of elements of emission corona electrodes without worsening of the operating parameters of electrostatic precipitator.

MUCHA J, JAWORSKI J. **The tool surface wear during the silicon steel sheets blanking process.** Eksploatacja i Niezawodność – Maintenance and Reliability 2016; 18 (3): 332–342, <http://dx.doi.org/10.17531/ein.2016.3.3>.

The surface wear mechanism of punches for the silicon sheets blanking was presented. In the studies the differences in the wear of high-speed tool (produced by casting and sintering), where observed. The influence of additional TiN coating on the punches flank degradation intensity was obtained. The strengthening zone changes of the sheared blank material close to cutting line were observed. The punch wear influence on the M530-50A silicon sheet material hardness changes was described.

KRUCZYŃSKI S, ŚLĘZAK M, GIS W, ORLIŃSKI P. **Evaluation of the impact of combustion hydrogen addition on operating properties of self-ignition engine.** Eksploatacja i Niezawodność – Maintenance and Reliability 2016; 18 (3): 343–347, <http://dx.doi.org/10.17531/ein.2016.3.4>.

The work presents the results of effect of the addition of hydrogen in an amount up to 9% of mass of diesel oil into the intake system of Perkins1104C-E44TA engine. The impact of hydrogen addition on process heat release in the combustion chamber and the concentration of CO, THC, NOX and PM in the exhaust at predetermined engine operating conditions. It was summarised that the analysis of the results does not justify the use of hydrogen as a fuel additive in self-ignition engines.

HAWRYLUK M, KASZUBA M, GRONOSTAJSKI Z, SADOWSKI P. **Systemy nadzoru i analizy przemysłowych procesów kucia.** Eksploatacja i Niezawodność – Maintenance and Reliability 2016; 18 (3): 315–324, <http://dx.doi.org/10.17531/ein.2016.3.1>.

W pracy przedstawiono koncepcję wielofunkcyjnego, zrobotyzowanego stanowiska kuźniczego wraz z systemem nadzoru procesu i zarządzania produkcją, z możliwością jego aplikacji przede wszystkim dla kuźni (z nie najnowszym parkiem maszynowym) wyposażonych w starsze urządzenia i agregaty kuźnicze. Koncepcja takiego stanowiska, wykorzystująca częściowo wdrożone już autorskie rozwiązania konstrukcyjno-technologiczne, jest wynikiem szerokiej analizy aktualnych potrzeb zakładów kuźniczych oraz poparta została zdobytą wiedzą i doświadczeniem autorów zajmujących się budową systemów pomiarowych i innych urządzeń dla przemysłu kuźniczego. Budowane przez autorów systemy pozwalają na pomiar i archiwizację oraz pełny monitoring najważniejszych parametrów technologicznych procesu, m.in.: przebiegów sił kucia w funkcji czasu/przemieszczenia, skorelowanych z pomiarem temperatury wstępników i matryc oraz ilości wyprodukowanych odkuwek. Opracowane systemy, dzięki ich włączeniu w nadrzędny system zarządzania produkcją (pełniący funkcję nadzoru nad całym procesem), pozwalają również na analizę zachodzących zmian podczas procesu, w tym postępującego zużycia narzędzi kuźniczych oraz analizę rejestrowanych parametrów w długim okresie czasu, zarządzania parkiem maszynowym i zasobami sprzętowymi (pracą maszyn, ich awariami, naprawami, itp.), zasobami ludzkimi oraz dostosowaniem organizacji produkcji do rosnących wymagań rynkowych. Przedstawiona przez autorów koncepcja kompleksowego podejścia do zagadnienia robotyzacji linii kuźniczej jest odpowiedzią na nieustanny rozwój technologii kucia, spowodowany konkurencyjnością rynku, wymuszający na kuźniach zautomatyzowanie swojej produkcji, w celu wytwarzania odkuwek o lepszej jakości przy jednoczesnym obniżeniu jej kosztów.

KARWAT B, NOCUN M, MACHNIK R, NIEDZWIEDZKI J. **Modelowanie i badania wpływu wybranych cech konstrukcyjnych na parametry eksploatacyjne elektrofiltrów przemysłowych.** Eksploatacja i Niezawodność – Maintenance and Reliability 2016; 18 (3): 325–332, <http://dx.doi.org/10.17531/ein.2016.3.2>.

Elektrofiltry są obecnie najczęściej stosowanymi, w procesach przemysłowych, urządzeniami do redukcji emisji pyłów do atmosfery. Znaczący wpływ na przebieg procesu odpylania ośrodka dwufazowego gaz/pył ma kształt oraz konfiguracja elektrod emisyjnych, wpływające na ukształtowanie pola elektrycznego w komorze elektrofiltru. Parametry geometryczne elektrod ulotowych oraz ich rozmieszczenie w komorze elektrofiltru powinny zapewniać równomierny rozkład gęstości prądu na powierzchni jego elektrod zbiorczych. W artykule przedstawiono analizę wpływu geometrii oraz konfiguracji przemysłowych elektrod ulotowych typu ostrzowego na rozkład gęstości prądu na elektrodzie zbiorczej. Na podstawie wyników pomiarów opracowano model matematyczny umożliwiający symulację rozkładu gęstości tego prądu w zależności od kształtu elektrod. Model umożliwia określenie korzystnych wartości odległości pomiędzy elementami emisyjnymi elektrody ulotowej oraz odległości pomiędzy tymi elektrodami. Korzystne parametry geometryczne i konfigurację elektrod ulotowych określano na podstawie analizy magnitud gęstości widmowej mocy (PSD) oraz wartości średniokwadratowej (RMS) gęstości prądu. Uzyskane wyniki wskazują na możliwość zmniejszenia ilości elementów emisyjnych elektrod ulotowych bez pogorszenia parametrów eksploatacyjnych elektrofiltru.

MUCHA J, JAWORSKI J. **Zużycie powierzchni narzędzi podczas eksploatacji w procesie wykrawania blachy krzemowej.** Eksploatacja i Niezawodność – Maintenance and Reliability 2016; 18 (3): 332–342, <http://dx.doi.org/10.17531/ein.2016.3.3>.

W niniejszym artykule przedstawiono opis mechanizmu zużycia powierzchni roboczych stempli wykrawających elementy z blachy krzemowej. Badania wykazały różnice w zużyciu narzędzi dla stali szybko tnącej w przypadku dwóch procesów jej wytwarzania (odlewnia i spiekania). Wykazano wpływ dodatkowej powłoki z TiN na intensywność degradacji powierzchni przyłożenia stempli wykrawających. Obserwacji poddano zmiany obszaru umocnienia materiału wykrawanego w pobliżu linii cięcia. Określono wpływ zużycia stempli na zasięg zmian twardości materiału blachy krzemowej M530-50A.

KRUCZYŃSKI S, ŚLĘZAK M, GIS W, ORLIŃSKI P. **Ocena wpływu spalania dodatku wodoru na własności eksploatacyjne silnika o zapłonie samoczynnym.** Eksploatacja i Niezawodność – Maintenance and Reliability 2016; 18 (3): 343–347, <http://dx.doi.org/10.17531/ein.2016.3.4>.

W pracy przedstawiono wyniki badań wpływu dodatku wodoru w ilości do 9% masy oleju napędowego do układu dolotowego silnika Perkins1104C-E44T. Oceniono wpływ dodatku na proces wydzielania ciepła w komorze spalania i stężenia CO, THC, NOX i PM w spalinach w ustalonych warunkach pracy silnika. W podsumowaniu stwierdzono iż analiza wyników badań nie uzasadnia stosowania wodoru jako dodatku do paliwa w silnikach o zapłonie samoczynnym.

DZIUBAK T. **The effects of dust extraction on multi-cyclone and non-woven fabric panel filter performance in the air filters used in special vehicles.** *Eksploracja i Niezawodność – Maintenance and Reliability* 2016; 18 (3): 348–357, <http://dx.doi.org/10.17531/ein.2016.3.5>.

Common impurities found in the inlet air to the internal combustion engine of motor vehicles are characterized. Dust concentrations in the air were analysed for different operating conditions of a motor vehicle. It is shown that the most common and the most harmful air impurity for the technical machinery is a mineral dust from roads. The benefits of using the inertial filter (multi-cyclone) as a first stage of air filtration, including extended engine life are presented. The methods of dust extraction from a dust collector of the air filter multi-cyclone are shown. The necessity of regular ejection dust extraction from the multi-cyclone dust collector is shown. A dust extraction rate m_0 is defined and its effects on the cyclone separation efficiency and flow resistance are shown. The test method and the test conditions for a two-stage filter in multi-cyclone - non-woven fabric filter element configuration are developed. The characteristics of the separation efficiency and flow resistance of the cyclone and the non-woven fabric filter were determined as a function of dust mass supplied with the inlet air to the two-stage filter for three different extraction rates and without dust extraction from the multi-cyclone dust collector. The separation efficiency and flow resistance were determined for a multi-cyclone and a non-woven fabric filter without dust extraction from the multi-cyclone dust collector and with or without periodical maintenance. The benefits of periodical cleaning of the dust collector were shown.

KARCZEWSKI M, SZCZĘCH L. **Influence of the F-34 unified battlefield fuel with bio components on usable parameters of the IC engine.** *Eksploracja i Niezawodność – Maintenance and Reliability* 2016; 18 (3): 358–366, <http://dx.doi.org/10.17531/ein.2016.3.6>.

The problem of the military vehicles engines fuelling increases with the growth of the amount of vehicles in the armies. At the same time, another problem with fuel supply in modern engines is the use of bio component additives, which changes characteristics (quality) of the used fuels. Therefore, it is important to take actions to adapt engines to powering with fuels coming from renewable sources. The aim of the research was to define the influence of an engine supplying fuel on work parameters and exhaust gases composition in the G9T Renault diesel engine. The tests were conducted during fuelling of the engine with six kinds of fuels: basic fuel (diesel oil), NATO code F-34 fuel, as well as fuel mixtures: F-34 and RME with different ratio. In the result of the research it was concluded that the parameters of the G9T Renault engine with the common rail fuel system in terms of F-34 and RME consumption (using) decreased in comparison to diesel oil basic fuel.

GÖKDERE G, GÜRCAN M. **New reliability score for component strength using Kullback-Leibler divergence.** *Eksploracja i Niezawodność – Maintenance and Reliability* 2016; 18 (3): 367–372, <http://dx.doi.org/10.17531/ein.2016.3.7>.

The reliability of technical systems is one of the most important research subjects in the point reached by modern science. In many recent studies, this problem is solved by evaluation the operation performance of determined one or more components operating under stress. At this point, $R=P(X<Y)$ is taken as a basis. Here, X is the stress applied on the operating component and Y is the strength of the component. In this study we aim to propose a new method by using Kullback-Leibler divergence for computing the reliability of the component under stress-strength model. The superiority of the proposed method is that when the component durability is equal to applied stress Kullback-Leibler divergence is equal to zero. In addition to that when more than one stresses exists at the same time the formed function can include all stresses at the same time. When R is used, this is not possible because of stresses are evaluated separately. As Kullback-Leibler divergence is calculated depending on time, the strength of the component is evaluated within a dynamic structure.

RYMARZ J, NIEWCZAS A, KRZYŻAK A. **Comparison of operational availability of public city buses by analysis of variance.** *Eksploracja i Niezawodność – Maintenance and Reliability* 2016; 18 (3): 373–378, <http://dx.doi.org/10.17531/ein.2016.3.8>.

This paper analyses the influence of selected factors of operational availability of public city buses from the Municipal Transport Company (MPK) in Lublin based on a case study for two makes of buses: Solaris and Mercedes-Benz. The study investigated changes in operational availability in a function of operating time with a division into two periods of operation: warranty and post-warranty. To evaluate the significance

DZIUBAK T. **Wpływ odsysania pyłu na charakterystyki multicyklonu i włókninowej przegrody filtracyjnej filtru powietrza pojazdu specjalnego.** *Eksploracja i Niezawodność – Maintenance and Reliability* 2016; 18 (3): 348–357, <http://dx.doi.org/10.17531/ein.2016.3.5>.

Scharakteryzowano przebieg czyszczenia powietrza wlotowego silnika spalinowego pojazdu mechanicznego. Przeanalizowano wartości stężenia pyłu w powietrzu dla różnych warunków eksploatacji pojazdów. Przedstawiono korzyści w postaci wydłużenia czasu eksploatacji silnika wynikające ze stosowania filtru bezwładnościowego (multicyklonu), jako pierwszego stopnia filtracji powietrza. Pokazano metody usuwania pyłu z osadnika multicyklonu filtru powietrza. Wykazano konieczność bieżącego, poprzez eekcyjne odsysanie, usuwania pyłu z osadnika multicyklonu. Zdefiniowano stopień odsysania pyłu m_0 oraz wykazano jego wpływ na skuteczność filtracji i opory przepływu cyklonów. Opracowano metodykę i warunki badań filtru dwustopniowego pracującego w układzie: multicyklon-włókninowy wkład filtracyjny. Wyznaczono charakterystyki skuteczności filtracji i oporów przepływu multicyklonu oraz włókniny filtracyjnej w zależności od masy pyłu dostarczonej wraz z powietrzem wlotowym do filtru dwustopniowego dla trzech wartości stopnia odsysania $m_0 = 5\%$, $m_0 = 10\%$, $m_0 = 20\%$ oraz bez odsysania pyłu z osadnika multicyklonu. Wyznaczono charakterystyki skuteczności filtracji i oporów przepływu multicyklonu oraz włókniny filtracyjnej bez odsysania pyłu z osadnika multicyklonu i z okresowym obsługiwaniem oraz bez obsługi. Wykazano konieczność okresowego czyszczenia osadnika pyłu.

KARCZEWSKI M, SZCZĘCH L. **Wpływ mieszanin jednolitego paliwa pola walki F-34 z biokomponentami na parametry użyteczne silnika.** *Eksploracja i Niezawodność – Maintenance and Reliability* 2016; 18 (3): 358–366, <http://dx.doi.org/10.17531/ein.2016.3.6>.

Problemy zasilania silników pojazdów wojskowych narastają wraz ze wzrostem liczby pojazdów w armiach. Silniki tłokowe i turbinowe wykorzystują paliwa różniące się zakresem temperatury destylacji. Dodatkowym problemem przy zasilaniu współczesnych silników spalinowych jest konieczność stosowania biokomponentów, które mogą zmieniać właściwości paliw podstawowych i wpływać na pogorszenie przebiegu spalania. Dlatego też konieczne jest podejmowanie działań prowadzących do zbadania wpływu paliw pochodzących ze źródeł odnawialnych na parametry pracy silników. Celem badań było ocena wpływu zastosowanego paliwa na parametry użyteczne i skład spalin tłokowego silnika o zapłonie samoczynnym Renault G9T. Badania przeprowadzono podczas zasilania silnika sześcioma rodzajami paliwa: paliwem podstawowym, jakim był olej napędowy, paliwem lotniczym o kodzie NATO F-34, mieszaninami paliw: F-34 i estrów metylowych wyższych kwasów tłuszczowych oleju rzepakowego. W wyniku przeprowadzonych badań stwierdzono, że parametry silnika Renault G9T z wysokociśnieniowym układem wtrysku, zasilanego paliwem F-34 i biokomponentami uległy pogorszeniu w stosunku do podstawowego paliwa, jakim był olej napędowy, co może mieć znaczenie przy wykorzystaniu tego rodzaju paliw w silnikach pojazdów wojskowych.

GÖKDERE G, GÜRCAN M. **Nowa metoda oceny niezawodności na podstawie wytrzymałości elementów z zastosowaniem dywergencji Kullbacka-Leiblera.** *Eksploracja i Niezawodność – Maintenance and Reliability* 2016; 18 (3): 367–372, <http://dx.doi.org/10.17531/ein.2016.3.7>.

Niezawodność systemów technicznych jest jednym z najważniejszych tematów badawczych we współczesnej nauce. Wiele z ostatnich badań, problem ten rozwiązuje poprzez ocenę wydajności pracy jednego lub większej liczby wybranych elementów działających pod wpływem obciążenia. Za punkt wyjściowy przyjmuje się $R=P(X<Y)$. X to obciążenie przyłożone do elementu roboczego, a Y to wytrzymałość elementu. W przedstawionej pracy, chcemy zaproponować nową metodę, w której do obliczania niezawodności elementu w ramach modelu typu "obciążenie-wytrzymałość" wykorzystuje się dywergencję Kullbacka-Leiblera. Proponowana metoda ma tę przewagę, że gdy wytrzymałość elementu jest równa przyłożonemu obciążeniu, dywergencja Kullbacka-Leiblera jest równa zero. Poza tym, gdy jednocześnie występuje więcej niż jeden rodzaj obciążenia, utworzona funkcja może obejmować jednocześnie wszystkie te obciążenia. Nie jest to możliwe przy zastosowaniu R , ponieważ obciążenia są oceniane oddzielnie. Ponieważ dywergencję Kullbacka-Leiblera oblicza się w funkcji czasu, wytrzymałość elementu ocenia się w strukturze dynamicznej.

RYMARZ J, NIEWCZAS A, KRZYŻAK A. **Comparison of operational availability of public city buses by analysis of variance.** *Eksploracja i Niezawodność – Maintenance and Reliability* 2016; 18 (3): 373–378, <http://dx.doi.org/10.17531/ein.2016.3.8>.

Celem pracy była analiza wpływu wybranych czynników gotowości technicznej autobusów komunikacji miejskiej na przykładzie autobusów marki Solaris i Mercedes-Benz w Miejskim Przedsiębiorstwie Komunikacyjnym (MPK) w Lublinie. Przeprowadzono badania zmian gotowości technicznej w funkcji czasu użytkowania z podziałem na dwa okresy użytkowania: gwarancyjny i pogwarancyjny. Do sprawdzenia istotności różnic średnich

of differences between average operational availability with regards to the above periods, one-way analysis of variance was applied. The results demonstrate that in the warranty period the operational availability of both makes of buses is similar, while the post-warranty period reveals a significant difference, with the operational availability being higher for Mercedes buses. As a result, this method can be of use for investment projects during purchase of new vehicles.

WANG H-W, TENG K-N. **Residual life prediction for highly reliable products with prior accelerated degradation data.** *Eksploracja i Niezawodność – Maintenance and Reliability* 2016; 18 (3): 379–389, <http://dx.doi.org/10.17531/ein.2016.3.9>.

To precisely predict the residual life for functioning products is a key of carrying out condition based maintenance. For highly reliable products, it is difficult to obtain abundant degradation data to precisely predict the residual life under normal stress levels. Thus, how to make use of historical degradation data to improve the accuracy of the residual life prediction is an interesting issue. Accelerated degradation testing, which has been widely used to evaluate the reliability of highly reliable products, can provide abundant accelerated degradation data. In this paper, a residual life prediction method based on Bayesian inference that takes accelerated degradation data as prior information was studied. A Wiener process with a time function was used to model degradation data. In order to apply the random effects of all the parameters of a Wiener process, the non-conjugate prior distributions were considered. Acceleration factors were introduced to convert the parameter estimates from accelerated stress levels to normal stress levels, so that the proper prior distribution types of the random parameters can be selected by the Anderson-Darling statistic. A Markov Chain Monte Carlo method with Gibbs sampling was used to evaluate the posterior means of the random parameters. An illustrative example of self-regulating heating cable was utilized to validate the proposed method.

KOSUCKI A, MALENTA P. **The possibilities of reducing the operational load of hoisting mechanisms in case of dynamic hoisting.** *Eksploracja i Niezawodność – Maintenance and Reliability* 2016; 18 (3): 390–395, <http://dx.doi.org/10.17531/ein.2016.3.10>.

The simulation and experimental tests of hoisting mechanism in case of dynamic lifting the payload with clearance of ropes are presented in this paper. The minimization methods of the overloading of hoisting mechanisms were described. Basing on simulation tests the method that assured minimization of dynamics overloading with a few dozen to a few percent was introduced. It was determined the impact of the level of sensitivity of forces in ropes measurement on minimization of the overloading. The examples of the method implementation used for the real hoisting mechanism were shown.

WANG Z, LI J, ZHANG Y, FU H, LIU C, KRISHNASWAMY S. **A novel Wiener process model with measurement errors for degradation analysis.** *Eksploracja i Niezawodność – Maintenance and Reliability* 2016; 18 (3): 396–405, <http://dx.doi.org/10.17531/ein.2016.3.11>.

Degradation analysis can be used to assess reliability for complex systems and highly reliable products, because few or even no failures are expected in a reasonable life test span. In order to further our study on degradation analysis, an independent increment random process method with linear mean and standard deviation functions is presented to model practical degradation procedures. It is essentially a Wiener process method. Since measurement errors are often created by imperfect instruments, procedures and environments during degradation investigation, the measurement error is incorporated into the independent increment random process. Furthermore, statistical inferences of this model are discussed, and close forms of a product's median life and percentile of the failure time distribution (FTD) are also derived. The proposed method is illustrated and verified in a comprehensive simulation study and two practice applications for storage disks and Infrared light-emitting diodes. Meanwhile, the time-transformed Wiener process model with measurement error is considered as a reference method. Comparisons show that the proposed model can provide reasonable results, even in considerably small sample size circumstance.

STAWIŃSKI Ł. **Experimental and modeling studies of hydrostatic systems with the counterbalance valves which are used in hydraulic lifting systems with passive and active load.** *Eksploracja i Niezawodność – Maintenance and Reliability* 2016; 18 (3): 406–412, <http://dx.doi.org/10.17531/ein.2016.3.12>. The article describes the structure and principle of the brake valve type counterbalance and the impact of its setup on the operating safety of hydrostatic systems with variable load, and in particular the problem of vibration and instability of operation

wartości gotowości technicznej, w zależności od marki autobusów oraz w zależności od okresów eksploatacji zastosowano jednoczynnikową analizę wariancji. Wykazano, że w okresie gwarancyjnym gotowość techniczna autobusów obu marek jest porównywalna, natomiast w okresie pogwarancyjnym jest istotnie różna, wyższa dla autobusu marki Mercedes. W rezultacie metoda ta może zostać użyta do programu inwestycyjnego podczas zakupu nowych pojazdów.

WANG H-W, TENG K-N. **Prognostowanie trwałości resztkowej wysoce niezawodnych produktów na podstawie danych historycznych z przyspieszonych badań degradacji.** *Eksploracja i Niezawodność – Maintenance and Reliability* 2016; 18 (3): 379–389, <http://dx.doi.org/10.17531/ein.2016.3.9>.

Precyzyjne przewidywanie trwałości resztkowej użytkowanego produktu stanowi klucz do prawidłowego utrzymania ruchu w oparciu o bieżący stan techniczny (condition-based maintenance). W przypadku produktów o wysokiej niezawodności, trudno jest uzyskać ilość danych degradacyjnych, która umożliwiałaby precyzyjne prognozowanie trwałości resztkowej przy normalnym poziomie obciążeń. Dlatego też bardzo ważnym zagadnieniem jest wykorzystanie historycznych danych degradacyjnych umożliwiających zwiększenie trafności prognozowania trwałości resztkowej. Przyspieszone badania degradacyjne, które powszechnie wykorzystuje się do oceny niezawodności wysoce niezawodnych produktów, mogą dostarczać bogatych danych o przyspieszonej degradacji. W przedstawionej pracy badano metodę prognozowania trwałości resztkowej opartą na wnioskowaniu bayesowskim, w którym jako uprzednie informacje wykorzystano dane z przyspieszonych badań degradacji. Dane degradacyjne modelowano za pomocą procesu Wienera z funkcją czasu. Aby móc zastosować efekty losowe wszystkich parametrów procesu Wienera, rozważano niesprężone rozkłady a priori. Wprowadzono współczynniki przyspieszenia, które pozwoliły na przekształcenie szacowanych wartości parametrów z poziomu obciążeniostosowanych w próbie przyspieszonej do poziomu obciążeń normalnych, co umożliwiło wybór odpowiednich typów parametrów losowych rozkładu a priori wykorzystaniem statystyki testowej Andersona-Darlinga. Metodę Monte Carlo opartą na łańcuchach Markowa z próbnikiem Gibbsa wykorzystano do oceny średnich a posteriori parametrów losowych. Proponowaną metodę zweryfikowano na podstawie przykładu samoregulującego przewodu grzejnego.

KOSUCKI A, MALENTA P. **Możliwości zmniejszenia obciążeń eksploatacyjnych mechanizmów dźwigni dla przypadku dynamicznego podnoszenia ładunku.** *Eksploracja i Niezawodność – Maintenance and Reliability* 2016; 18 (3): 390–395, <http://dx.doi.org/10.17531/ein.2016.3.10>.

W artykule przedstawiono badania symulacyjne i eksperymentalne mechanizmu podnoszenia dla przypadku podrywania ładunku. Opisane zostały metody zmniejszania przeciążeń układu napędowego mechanizmów podnoszenia. Wskazano w oparciu o badania symulacyjne metodę zapewniającą minimalizację przeciążeń dynamicznych w czasie podrywania ładunku z kilkudziesięciu do kilku procent. Określony został wpływ poziomu czułości pomiaru sił w linach na minimalizację przeciążeń. Zaprezentowano przykłady zastosowań metody na rzeczywistej wciągarnie bębnowej.

WANG Z, LI J, ZHANG Y, FU H, LIU C, KRISHNASWAMY S. **Analiza degradacji z zastosowaniem nowego modelu procesu Wienera uwzględniającego błędy pomiarowe.** *Eksploracja i Niezawodność – Maintenance and Reliability* 2016; 18 (3): 396–405, <http://dx.doi.org/10.17531/ein.2016.3.11>.

Analizę degradacji można stosować do oceny niezawodności wysoce niezawodnych złożonych systemów i produktów, ponieważ w ich przypadku istnieje bardzo niskie lub zerowe prawdopodobieństwo wystąpienia uszkodzenia w trakcie badania trwałości w przyjętym okresie eksploatacji. W artykule przedstawiono nowo opracowane podejście do modelowania procesu degradacji wykorzystujące metodę procesu o przyrostach niezależnych oraz pojęcia funkcji średniej liniowej i funkcji liniowego odchylenia standardowego. Zasadniczo jest to metoda oparta na procesie Wienera. Ponieważ badania degradacji często wiążą się z błędami pomiarowymi wynikającymi z niedoskonałości stosowanych narzędzi, procedur i warunków badawczych, opisujemy proces o przyrostach niezależnych uwzględniający błędy pomiaru. Ponadto, w pracy omówiono wnioski statystyczne, jakie można wyciągnąć na podstawie przedstawionego modelu oraz wyprowadzono wzory ogólne na średnią długość życia produktu oraz na percentyl rozkładu czasu do uszkodzenia. Proponowaną metodę zilustrowano i zweryfikowano na podstawie kompleksowego badania symulacyjnego oraz przykładów praktycznego zastosowania modelu w odniesieniu do dysków pamięci masowej oraz diod podczerwieni. W artykule przedstawiono także model procesu Wienera z transformowanym czasem uwzględniający błąd pomiaru, który posłużył za model referencyjny. Porównania pokazują, że proponowany model może dawać poprawne wyniki, nawet przy bardzo małej liczbie próbek.

STAWIŃSKI Ł. **Eksperymentalne i modelowe badania układu hydraulicznego z zaworami hamującymi typu counterbalance stosowanymi w układach dźwigowych z obciążeniem biernym i czynnym.** *Eksploracja i Niezawodność – Maintenance and Reliability* 2016; 18 (3): 406–412, <http://dx.doi.org/10.17531/ein.2016.3.12>.

Artykuł opisuje budowę oraz zasadę działania zaworu hamującego typu counterbalance oraz wpływ jego nastaw na bezpieczeństwo pracy układów hydrostatycznych przy

of such systems after stop and restart with the active load. Mathematical and physical models of the valve and hydrostatic system with variable load have been developed. The models have been verified on the test bench, on which it is possible to the formation of arbitrary diagrams and extortion. The static and dynamic characteristics of the valve and the key operating parameters of the hydrostatic system that affect its useful properties have been shown. The simulation studies, which identify critical design parameters of the valve, that are crucial to the behaviour of the valve, and thus, hydrostatic system, has been carried out.

DOMBEK G, NADOLNY Z. **Liquid kind, temperature, moisture, and ageing as an operating parameters conditioning reliability of transformer cooling system.** Eksploatacja i Niezawodność – Maintenance and Reliability 2016; 18 (3): 413–417, <http://dx.doi.org/10.17531/ein.2016.3.13>.

The article presents research results of thermal properties of insulating liquids used in power transformer cooling system. The authors analyzed the influence of such factors, as the kind of the liquid, temperature, moisture and ageing rate of the liquid on thermal properties of the liquids. The analyzed properties of the liquids were thermal conductivity coefficient λ , kinematic viscosity ν , density ρ , specific heat c_p , and thermal expansion factor β . These properties determine the ability of the liquid to heat transport – heat transfer factor α – what means the properties describe reliability of power transformer cooling system. The authors calculated the factor of heat transfer by the investigated insulating liquids on the basis of measured values of thermal properties.

LU J-M, INNAL F, Wu X-y, Liu Y, Lundteigen MA. **Two-terminal reliability analysis for multi-phase communication networks.** Eksploatacja i Niezawodność – Maintenance and Reliability 2016; 18 (3): 418–427, <http://dx.doi.org/10.17531/ein.2016.3.14>.

Most researches of network reliability generally assume that the system structures do not change with time. This paper presents the concept of multi-phase network systems (MPNS) to consider dynamic characteristics of networks, and analyze the reliability of MPNS. MPNS reliability is evaluated through a cross-phase binary decision diagram (BDD). The BDD-based algorithm can act as a platform to consider various components behaviors such as repair and growing pressure. Case study shows that the proposed MPNS concept is an effective description of some practical communication networks, and the cross-phase BDD model is efficient in analyzing MPNS reliability.

PAWŁOWSKI W, KACZMAREK L, LOUDA P. **Theoretical and experimental modal analysis of the cylinder unit filled with PUR foam.** Eksploatacja i Niezawodność – Maintenance and Reliability 2016; 18 (3):428–435, <http://dx.doi.org/10.17531/ein.2016.3.15>.

In the paper the dynamic properties of the cylinder unit as a part of the theatre scenography lifting mechanism have been investigated. The noise and vibration problem of the cylinder unit when lifting loads turned out to be the crucial limit in application of the whole mechanism for lifting scenography elements on a theatre stage. The construction of the mechanism was examined and the main source of noise was identified as the cylinder unit. Theoretical modal analysis confirmed that thesis. Experimental modal analyses of the hollow cylinder unit as well as the cylinder with the PUR foam filling were performed. The results showed significant improvement of the dynamic properties due to the vibration amplitude decrease for the first three vibration modes of the filled cylinder. The research method of modal analysis turned out to be highly efficient in dynamic properties determination in the industrial practice. The method of improving the dynamic properties of the mechanical construction by filling closed regions with PUR foam is of a great importance for industrial application and seems to be economically effective.

ŻUCHOWSKI A. **Analysis of the influence of the impact speed on the risk of injury of the driver and front passenger of a passenger car.** Eksploatacja i Niezawodność – Maintenance and Reliability 2016; 18 (3):436–444, <http://dx.doi.org/10.17531/ein.2016.3.16>.

The subject of the analysis was the influence of the speed, at which a personal car hit an obstacle, on the risk of injury of the driver and the passenger sitting in the front seat. With this goal in mind, several hundred of crash tests were analysed, published on the Internet by National Highway Traffic Safety Administration (USA). The analysis focuses on the cases involving a frontal impact of the car on a rigid barrier. For the purpose of assessing the forces acting on a dummy, Head Injury Criterion (HIC36) and Chest Acceleration (CAcc), were applied, calculated on the basis of the resulting acceleration of

zmieniającym się obciążeniu, a w szczególności problem drgań i niestabilności pracy takiego układu hydrostatycznego po zatrzymaniu i ponownym uruchomieniu po przejściu z obciążenia biernego na czynne. Opracowane zostały modele matematyczne i fizyczne zaworu oraz układu hydrostatycznego ze zmiennym obciążeniem, które zweryfikowano na stanowisku badawczym, na którym możliwe jest kształtowanie dowolnych przebiegów i wymuszeń. Zamieszczone zostały charakterystyki statyczne i dynamiczne zaworu oraz przebiegi kluczowych parametrów pracy układu hydrostatycznego, które mają wpływ na jego właściwości użytkowe. Przeprowadzone badania symulacyjne identyfikują krytyczne parametry konstrukcyjne zaworu, które mają kluczowe znaczenie na zachowanie się zaworu, a co za tym idzie, układu hydrostatycznego. Słowa kluczowe: bezpieczeństwo obsługi maszyn, układy hydrostatyczne, zawór hamujący, counterbalance, dźwigi koszone, żurawie.

DOMBEK G, NADOLNY Z. **Rodzaj cieczy, temperatura, zawilgocenie oraz zesterzenie jako parametry eksploatacyjne warunkujące niezawodność układu chłodzenia transformatora.** Eksploatacja i Niezawodność – Maintenance and Reliability 2016; 18 (3): 413–417, <http://dx.doi.org/10.17531/ein.2016.3.13>.

W artykule przedstawiono wyniki badań właściwości cieplnych cieczy elektroizolacyjnych, wykorzystywanych w układzie chłodzenia transformatora wysokiego napięcia. Dokonano analizy wpływu takich czynników jak rodzaj cieczy, temperatura, stopień jej zawilgocenia oraz zesterzenia na właściwości cieplne cieczy. Analizowanymi właściwościami cieczy były przewodność cieplna właściwa λ , lepkość kinematyczna ν , gęstość ρ , ciepło właściwe c_p oraz rozszerzalność cieplna β . Właściwości te określają zdolność cieczy do transportu ciepła – współczynnik przejmowania ciepła α , a tym samym warunkują niezawodność układu chłodzenia transformatora. Na podstawie zmierzonych przez autorów wartości właściwości cieplnych określony został współczynnik przejmowania ciepła badanych cieczy elektroizolacyjnych.

LU J-M, INNAL F, Wu X-y, Liu Y, Lundteigen MA. **Analiza niezawodności par terminali w wielofazowych sieciach komunikacyjnych.** Eksploatacja i Niezawodność – Maintenance and Reliability 2016; 18 (3): 418–427, <http://dx.doi.org/10.17531/ein.2016.3.14>.

Większość badań niezawodności sieci ogólnie przyjąć, że struktury systemu nie zmieniają się w czasie. W artykule przedstawiono koncepcję systemów sieciowych wielofazowych (MPNS) rozpatrywanie dynamicznych właściwości sieci i analizy niezawodności MPNS. MPNS niezawodność jest oceniany przez cross-fazowego schematu decyzyjnego binarny (BDD). Algorytm z siedzibą w BDD może działać jako platforma do rozważenia różnych komponentów zachowań, takich jak naprawy i rosnącej presji. Studium przypadku pokazuje, że proponowana koncepcja MPNS jest skutecznym opis niektórych praktycznych sieci komunikacyjnych, a cross-fazowego modelu BDD jest skuteczny w analizie MPNS niezawodność.

PAWŁOWSKI W, KACZMAREK L, LOUDA P. **Teoretyczna i eksperymentalna analiza modalna zespołu bębna wciągarki wypełnionego pianką poliuretanową.** Eksploatacja i Niezawodność – Maintenance and Reliability 2016; 18 (3):428–435, <http://dx.doi.org/10.17531/ein.2016.3.15>.

W artykule przedstawiono badania dynamicznych właściwości zespołu bębna wciągarki służącej do podnoszenia scenografii teatralnej. Problem nadmiernego hałasu i drgań wciągarki podczas podnoszenia elementów scenografii okazał się istotnym problemem użytkowym ograniczającym możliwości zastosowania urządzenia w teatrze. Przeprowadzono analizę konstrukcji mechanizmu wciągarki i wskazano zespół bębna jako źródło nadmiernego hałasu. Tę tezę potwierdzono przeprowadzając teoretyczną analizę modalną zespołu bębna. W części doświadczalnej badań przeprowadzono analizę modalną oryginalnego, pustego zespołu bębna a następnie zespołu wypełnionego pianką poliuretanową. Otrzymano wyniki badań doświadczalnych, na podstawie których dokonano obserwacji, że amplituda pierwszych trzech postaci drgań swobodnych analizowanego zespołu została znacznie obniżona, co skutkuje znaczną redukcją hałasu generowanego przez bęben wypełniony pianką poliuretanową. Analiza modalna okazała się wysoce przydatna w praktyce przemysłowej w celu określania dynamicznych właściwości urządzeń mechanicznych. Na podstawie wyników przeprowadzonych badań modalnych sformulowano wnioski, że metoda wypełniania zamkniętych obszarów konstrukcji mechanicznych pianką poliuretanową w celu poprawienia właściwości dynamicznych urządzenia może być szeroko wykorzystana w praktyce przemysłowej ze względu na wysoką skuteczność oraz ważny aspekt ekonomiczny w postaci niskiej ceny takiego rozwiązania.

ŻUCHOWSKI A. **Ocena wpływu prędkości zderzenia na ryzyko obrażeń kierowcy i pasażera samochodu osobowego.** Eksploatacja i Niezawodność – Maintenance and Reliability 2016; 18 (3):436–444, <http://dx.doi.org/10.17531/ein.2016.3.16>.

Rozważono wpływ prędkości uderzenia samochodu osobowego w przeszkodę na ryzyko obrażeń kierowcy oraz pasażera na przednim fotelu. W tym celu wykorzystano wyniki kilkuset testów zderzeniowych, udostępnionych w Internecie przez National Highway Traffic Safety Administration (USA). Uwagę skupiono na czołowe uderzenie samochodu w sztywną barierę. Podczas oceny obciążeń manekinów wykorzystano wskaźniki obrażeń głowy HIC36 oraz torsu CAcc, które oblicza się na podstawie wypadkowego przyspieszenia działającego na głowę i tors manekina. Oddzielnie rozważono obciążenia manekina reprezentującego 50-centylowego mężczyznę (M50) oraz 5-centylową kobietę

head and chest of the dummy. Separate analyses were performed for the forces acting on the dummy representing 50-centile man (M50) and 5-centile woman (F5). A statistical analysis of the results of the crash tests was performed in order to determine the typical values of HIC36 and CAcc factors, as well as the risk of severe injury of the driver and the passenger at a given collision speed. The risk of injury was calculated on the basis of provided in the research literature so-called injury risk curves. It was determined that increasing the speed at which a car hits an obstacle from 25 km/h up to 56 km/h results in the increase in the risk of severe injury (AIS4) of the driver and the passenger from 2 to 10%. Some functions were proposed, describing the relation between the risk of injury and the velocity of collision.

YIN Y-C, HUANG H-Z, PENG W, LI Y-F, MI J. **An E-Bayesian method for reliability analysis of exponentially distributed products with zero-failure data.** Eksploatacja i Niezawodność – Maintenance and Reliability 2016; 18 (3):445–449, <http://dx.doi.org/10.17531/ein.2016.3.17>.

This paper investigate an E-Bayesian estimation as a reliability analysis method for the seekers to deal with the zero-failure life testing data. Firstly, we introduce an E-Bayesian estimation for the exponential distribution, and then propose a zero-failure model with assumptions. Using the proposed model, we set up a series of life tests for the seekers, and apply the E-Bayesian estimation on the observed zero-failure data to calculate the failure rate and reliability of the seekers. Finally, the reliability estimation results of the seekers demonstrate the performance of the proposed method.

MUTINGI M, MBOHWA, KOMMULA VP. **Multi-criteria reliability optimization for a complex system with a bridge structure in a fuzzy environment: A fuzzy multi-criteria genetic algorithm approach.** Eksploatacja i Niezawodność – Maintenance and Reliability 2016; 18 (3):450–456, <http://dx.doi.org/10.17531/ein.2016.3.18>.

Optimizing system reliability in a fuzzy environment is complex due to the presence of imprecise multiple decision criteria such as maximizing system reliability and minimizing system cost. This calls for multi-criteria decision making approaches that incorporate fuzzy set theory concepts and heuristic methods. This paper presents a fuzzy multi-criteria nonlinear model, and proposes a fuzzy multi-criteria genetic algorithm (FMGA) for complex bridge system reliability design in a fuzzy environment. The algorithm uses fuzzy multi-criteria evaluation techniques to handle fuzzy goals, preferences, and constraints. The evaluation approach incorporates fuzzy preferences and expert choices of the decision maker in regards to cost and reliability goals. Fuzzy evaluation gives the algorithm flexibility and adaptability, yielding near-optimal solutions within short computation times. Results from computational experiments based on benchmark problems demonstrate that the FMGA approach is a more reliable and effective approach than best known algorithm, especially in a fuzzy multi-criteria environment.

ZHAO Z, QIUJ, LIU G, ZHANG Y. **Research on time-varying characteristics of testability index based on renewal process.** Eksploatacja i Niezawodność – Maintenance and Reliability 2016; 18 (3): 457–468, <http://dx.doi.org/10.17531/ein.2016.3.19>.

Testability indices are used in the phases of testability design and testability demonstration. This paper focuses on fault detection rate (FDR), which is the most widely used testability index. Leading hypothesis suggests that the value of FDR of a system is usually a certain value. However, few attempts have been made to research the statistical characteristics of FDR. Considering the fault occurrence process and test uncertainty, FDR is time varying and a special statistical process. Under the assumption of perfect repairs, we build a fault occurrence model based on the renewal process theory. Supposing that test uncertainty is mainly induced by test fault, the renewal process is employed to depict the occurrence process of test faults. Simultaneously, we depict the process of test state change and then construct the fault detection logic based on the digraph model. Combining the fault occurrence model and the fault detection logic, we focus on the expectation of FDR, which is one of the key statistical characteristics. By comparison, we introduce the calculation method of expectation of FDR in two cases, including without considering test uncertainty and considering test uncertainty. To validate the conclusions presented in this paper, we carry on a simulation case using an integrated controller. Based on the theoretic and simulating methods, the expectation of FDR tends to be a constant with the increase of time under the assumptions made in this paper. The statistical characteristic of FDR presented in this paper would be the basic theoretical guide to testability engineering.

(F5). Przeprowadzono statystyczną ocenę wyników testów zderzeniowych, której celem było określenie dominujących wartości wskaźników HIC36 i CAcc oraz ryzyka ciężkich obrażeń kierowcy i pasażera przy danej prędkości zderzenia. Ryzyko obrażeń obliczono na podstawie dostępnych w literaturze tzw. funkcji ryzyka obrażeń. Ustalono, że zwiększenie prędkości uderzenia samochodu w przeszkodę z 25 km/h do 56 km/h zwiększa ryzyko ciężkich obrażeń (AIS4) kierowcy i pasażera z 2 do 10%. Zaproponowano funkcje wiążące ryzyko obrażeń i prędkość zderzenia.

YIN Y-C, HUANG H-Z, PENG W, LI Y-F, MI J. **Metoda bayesowskiej estymacji wartości oczekiwanej dla produktów o rozkładzie wykładniczym wykorzystująca dane o niezaistniałych uszkodzeniach.** Eksploatacja i Niezawodność – Maintenance and Reliability 2016; 18 (3):445–449, <http://dx.doi.org/10.17531/ein.2016.3.17>.

W pracy analizowano estymację bayesowską wartości oczekiwanej jako metodę analizy niezawodności urządzeń naprawdzających w przypadkach, gdy dane z badań trwałości są danymi o uszkodzeniach niezaistniałych (zerowych). W pierwszej części pracy opisano E-estymację bayesowską dla rozkładu wykładniczego, a następnie zaproponowano model uszkodzeń niezaistniałych oraz opisano jego założenia. Wykorzystując zaproponowany model, zaprojektowano i zrealizowano serię badań trwałości urządzeń naprawdzających jak również zastosowano E-estymację bayesowską w celu obliczenia intensywności uszkodzeń oraz niezawodności badanych urządzeń. Wyniki oceny niezawodności urządzeń naprawdzających potwierdzają przydatność proponowanej metody.

MUTINGI M, MBOHWA, KOMMULA VP. **Wielokryterialna optymalizacja niezawodności złożonego systemu o strukturze mostkowej w środowisku rozmytym. Metoda rozmytego wielokryterialnego algorytmu genetycznego.** Eksploatacja i Niezawodność – Maintenance and Reliability 2016; 18 (3):450–456, <http://dx.doi.org/10.17531/ein.2016.3.18>.

Optymalizacja niezawodności systemu w środowisku rozmytym to problem złożony ze względu na konieczność wzięcia pod uwagę wielu niedokładnie określonych kryteriów decyzyjnych, takich jak maksymalizacja niezawodności systemu i minimalizacja kosztów. Wymaga ona zastosowania wielokryterialnych metod podejmowania decyzji, które łączą pojęcia z zakresu teorii zbiorów rozmytych oraz metody heurystyczne. W niniejszej pracy przedstawiono rozmyty wielokryterialny model nieliniowy (FMGA) oraz zaproponowano rozmyty wielokryterialny algorytm genetyczny do projektowania niezawodności złożonych systemów mostkowych w środowisku rozmytym. Algorytm wykorzystuje techniki rozmytej oceny wielokryterialnej do określania rozmytych celów, preferencji oraz ograniczeń. Metoda oceny uwzględnia rozmyte preferencje i eksperckie wybory decydeny dotyczące kosztów oraz celów niezawodnościowych. Ocena rozmyta nadaje algorytmowi cechy elastyczności oraz adaptacyjności, pozwalając na otrzymanie niemal optymalnych rozwiązań w krótkim czasie obliczeniowym. Wyniki eksperymentów obliczeniowych opartych na problemach wzorcowych pokazują, że podejście z zastosowaniem FMGA jest bardziej niezawodne i wydajne niż najbardziej znany algorytm, zwłaszcza w rozmytym środowisku wielokryterialnym.

ZHAO Z, QIUJ, LIU G, ZHANG Y. **Badanie zmiennych w czasie własności wskaźnika testowalności na podstawie procesu odnowy.** Eksploatacja i Niezawodność – Maintenance and Reliability 2016; 18 (3): 457–468, <http://dx.doi.org/10.17531/ein.2016.3.19>.

Wskaźniki testowalności wykorzystuje się w fazach projektowania oraz potwierdzania testowalności. Przedstawiony artykuł poświęcony jest wskaźnikowi wykrywalności błędów (fault detection rate, FDR), który jest najczęściej stosowanym wskaźnikiem testowalności. Wiodąca hipoteza sugeruje, że wartość FDR dla danego systemu jest zwykle wartością pewną. Istnieje jednak niewiele badań na temat statystycznych własności FDR. Biorąc pod uwagę proces występowania błędów oraz niepewność pomiarów, współczynnik FDR można opisać jako zmienny w czasie specjalny proces statystyczny. Przy założeniu naprawy doskonałej, zbudowaliśmy model występowania błędów w oparciu o teorię procesu odnowy. Przyjmując, że niepewność testową wywołują głównie błędy testowe, wykorzystaliśmy proces odnowy do zobrazowania procesu występowania błędów testowych. Jednocześnie przedstawiliśmy proces zmiany stanu testu, a następnie zbudowaliśmy logikę wykrywania błędów w oparciu o model grafu skierowanego. Łącząc model występowania błędów z logiką wykrywania błędów, opracowaliśmy metodę obliczania wartości oczekiwanej FDR, która jest jedną z najważniejszych własności statystycznych tego wskaźnika. Dla porównania, metodę obliczania wartości oczekiwanej FDR zastosowaliśmy w dwóch przypadkach, z uwzględnieniem i bez uwzględnienia niepewności testowej. Aby zweryfikować wnioski przedstawione w niniejszej pracy, przeprowadziliśmy symulację z wykorzystaniem zintegrowanego kontrolera. Obliczenia teoretyczne i symulacja pokazują, że wartość oczekiwana FDR wraz z upływem czasu staje się wartością stałą w warunkach założonych w niniejszej pracy. Przedstawiona w artykule charakterystyka statystyczna FDR stanowi jedną z podstaw teoretycznych inżynierii testowej.

OSTAPKOWICZ P, BRATEK A. **Possible leakage detection level in transmission pipelines using improved simplified methods.** Eksploatacja i Niezawodność – Maintenance and Reliability 2016; 18 (3): 469–480, <http://dx.doi.org/10.17531/ein.2016.3.20>.

This paper deals with issues of detecting leaks in liquid transmission pipelines. It presents an overall comparison of three improved simplified methods, i.e. correlation analysis of pressure and flow rate, pressure monitoring and volume balance. Besides the well-known solutions, the authors also propose a detection algorithm with a new process variable structure and with two options of a resulting function. These methods do not require a complicated mathematical model and highly specialist measuring hardware. Their application and maintenance are easy and low cost. The interest of this paper is to determine the leakage detection level, when these methods are used for diagnosing single leakages under steady-state operating pipeline's conditions. The assessment, carried out on a laboratory water pipeline, was based on two performance indexes, i.e. a magnitude of a minimal leakage, which can be detected and the response time, i.e. time between the moment of beginning (occurrence) of leakage and the moment when it has been detected. The obtained results proved a high efficiency of proposed techniques in detection of leaks.

OSTAPKOWICZ P, BRATEK A. **Weryfikacja możliwego poziomu wykrywalności wycieków w zakresie zastosowania zmodyfikowanych uproszczonych metod diagnostycznych.** Eksploatacja i Niezawodność – Maintenance and Reliability 2016; 18 (3): 469–480, <http://dx.doi.org/10.17531/ein.2016.3.20>.

Artykuł dotyczy zagadnień diagnozowania wycieków z rurociągów przesyłowych cieczy z wykorzystaniem metod, które bazują na pomiarach wewnętrznych parametrów przepływu (zmiennych procesowych), tj.: strumienia i ciśnienia. Artykuł prezentuje porównanie trzech zmodyfikowanych uproszczonych technik, tj.: analizy korelacyjnej sygnałów ciśnienia i przepływu, monitorowania zmian ciśnienia i bilansu strumieni. Oprócz uprzednio znanych rozwiązań autorzy proponują również rozwiązanie algorytmu detekcyjnego o nowej strukturze zmiennych i o dwóch wariantach funkcji wynikowych. Metody nie wymagają zastosowania skomplikowanych modeli rurociągu, cechuje je niski koszt w sensie wymagań dotyczących urządzeń pomiarowych oraz łatwa realizacja i obsługa. Obszarem zainteresowania niniejszego artykułu jest określenie dla proponowanych metod wskaźników jakościowych, w przypadku diagnozowania pojedynczych wycieków w stanach ustalonych. Taka ocena dotyczy w szczególności ustalenia możliwego poziomu wykrywalności wycieku, tj. minimalnej wielkości wycieku, który może być wykryty. Innym określanym parametrem jest tzw. czas odpowiedzi, tj. czas od momentu wystąpienia wycieku do jego wykrycia. Podstawę weryfikacji stanowiły badania eksperymentalne przeprowadzone na stanowisku z modelem fizycznym rurociągu. Uzyskane wyniki potwierdziły wysoką skuteczność proponowanych technik wykrywania wycieków.

Article citation info:

HAWRYLUK M, KASZUBA M, GRONOSTAJSKI Z, SADOWSKI P. Systems of supervision and analysis of industrial forging processes. *Eksplotacja i Niezawodność – Maintenance and Reliability* 2016; 18 (3): 315–324, <http://dx.doi.org/10.17531/ein.2016.3.1>.

Marek HAWRYLUK
Marcin KASZUBA
Zbigniew GRONOSTAJSKI
Przemysław SADOWSKI

SYSTEMS OF SUPERVISION AND ANALYSIS OF INDUSTRIAL FORGING PROCESSES

SYSTEMY NADZORU I ANALIZY PRZEMYSŁOWYCH PROCESÓW KUCIA*

The work presents the concept of a multifunctional automatized forging station with a supervisory system of the process and the production management, with the option of application mainly at forging shops (with somewhat outdated machines) equipped with older-generation devices and forging units. The concept of such a station, which applies the, already partially, implemented construction and technological solutions, is a result of an extensive analysis of the current needs of forging plants and it has been supported by the acquired knowledge and experience of the authors, who specialize in the construction of measurement systems and other devices for the forging industry. The systems built by the authors makes it possible to measure and archive as well as fully monitor the most important technological parameters of the process, such as: the course of the forging forces in the function of time/shift, correlated with a measurement of the temperature of the preforms and dies as well as the number of the produced forgings. The elaborated systems, owing to their inclusion in the general production management system (which plays a supervisory role over the whole process), also allow for an analysis of the occurring changes during the process, including the proceeding wear of the forging tools as well as an analysis of the parameters determined throughout a long period of time, management of the machines and equipment (the work of the machines, their breakdowns, repairs etc.), and the human resources, as well as adaptation of the production organization to the increasing market demands. The presented concept of a complex approach to the issue of automatization of the forging line is a reply to the constantly developing forging technology, caused by market competitiveness, which requires automatization of the production, with the purpose to produce forgings of a higher quality, and, at the same time, reduce the costs.

Keywords: supervisory systems, industrial forging process, measurement & control systems.

W pracy przedstawiono koncepcję wielofunkcyjnego, zrobotyzowanego stanowiska kuźniczego wraz z systemem nadzoru procesu i zarządzania produkcją, z możliwością jego aplikacji przede wszystkim dla kuźni (z nie najnowszym parkiem maszynowym) wyposażonych w starsze urządzenia i agregaty kuźnicze. Koncepcja takiego stanowiska, wykorzystująca częściowo wdrożone już autorskie rozwiązania konstrukcyjno-technologiczne, jest wynikiem szerokiej analizy aktualnych potrzeb zakładów kuźniczych oraz poparta została zdobytą wiedzą i doświadczeniem autorów zajmujących się budową systemów pomiarowych i innych urządzeń dla przemysłu kuźniczego. Budowane przez autorów systemy pozwalają na pomiar i archiwizację oraz pełny monitoring najważniejszych parametrów technologicznych procesu, m.in.: przebiegów sił kucia w funkcji czasu/przemieszczenia, skorelowanych z pomiarem temperatury wstępniaków i matryc oraz ilości wyprodukowanych odlewów. Opracowane systemy, dzięki ich włączeniu w nadrzędny system zarządzania produkcją (pełniący funkcję nadzoru nad całym procesem), pozwalają również na analizę zachodzących zmian podczas procesu, w tym postępującego zużycia narzędzi kuźniczych oraz analizę rejestrowanych parametrów w długim okresie czasu, zarządzania parkiem maszynowym i zasobami sprzętowymi (pracą maszyn, ich awariami, naprawami, itp.), zasobami ludzkimi oraz dostosowaniem organizacji produkcji do rosnących wymagań rynkowych. Przedstawiona przez autorów koncepcja kompleksowego podejścia do zagadnienia robotyzacji linii kuźniczej jest odpowiedzią na nieustanny rozwój technologii kucia, spowodowany konkurencyjnością rynku, wymuszający na kuźniach zautomatyzowanie swojej produkcji, w celu wytwarzania odlewów o lepszej jakości przy jednoczesnym obniżeniu jej kosztów.

Słowa kluczowe: systemy nadzoru i kontroli, przemysłowy proces kucia, systemy pomiarowo-kontrolne.

Introduction

The industrial processes of die forging (depending on the production scale and the forging mass), are realized on machines with high forming forces, most often on presses and hammers, and also, possibly,

upsetting machines. The performed analyses of the level of technological solutions in the die forging processes show that, in a great majority of processes, the die forging production takes place in the traditional non-automatized way, on separated forging unit stations, where all the

(*) Tekst artykułu w polskiej wersji językowej dostępny w elektronicznym wydaniu kwartalnika na stronie www.ein.org.pl

working actions, including: removing the charge from the heater and placing it in the die impression, relocating the formed forging on the successive impressions, are performed manually. A consequence of the level of the applied traditional die forging technologies are problems resulting from the low repeatability of the performed actions as well as the significant effect of the human factor on both the production process itself and the conditions of machine work, which significantly affects the activity of the enterprises and the speed of development of this branch of industry [12, 13, 14, 15, 16, 17, 21].

At present, forging shops, to manufacture a given product, often use old machines, without monitoring systems of the working parameters, which, due to their age, easily fail, and the wear of the cooperating movable elements, as well as the clearances, cause big problems in stabilizing the production process. Additionally, one should consider the character of the forging process and the relatively low life of the forging tools, connected with their wear, due to big temperature changes and high pressures. For financial reasons, forging plants rarely decide to purchase a new device dedicated to a specific production line. The commonly applied forging machines and devices are usually equipped with simple control and measurement systems, which merely allow for the control of: the maximal forging force, the machine's work speed, the number of forgings and the initial temperatures of the preforms [6, 9, 18, 22, 23]. Such measurement and control systems, which monitor the whole process, have been successfully applied in factories (so-called, assembly shops, involving the process of joining, bonding, welding, painting and others) as well as in automatized stamping presses. On the other hand, in the case of industrial forging processes, these systems are only beginning their development.

The changes observed on global forging markets, the high competition and the constant technological progress create demand for products of increasingly high quality and reduced costs from the forging producers [20]. They consist mainly of matching production to the requirements associated with changes in materials and technological products and to increase production flexibility while maintaining its competitiveness [33]. Frequent changes of produced assortment and conducting production using fixed assets machine requires the use of complex systems of measurement and control, which will allow for rapid diagnosis process, in order to adapt and optimize and, thanks to constant analysis, ensure the safety of machinery, low failure, and finally the profitability of production. Using the existing machine park, whose work is monitored by the relevant systems provides greater the universality of machines, allows for quick start production and significantly reduces implementation costs of the new product [15, 25, 29].

This also directly affects the development of the die forging technology, in respect of the currently constructed and installed measurement and control systems (which only slightly affect the production management), as well as automatization and robotization of the production line.

1. Supervisory measurement and control systems

A measurement system can be defined as a set of functional units which form an organizational whole included in the common regulation for the realization of a specific metrological purpose. The system regulation is usually realized by means of a superior functional unit called the controller, which works according to a programmed algorithm. Most measuring systems characterize in algorithmization of the measuring processes and integration of equipment and software. Depending on the general application, measuring systems can be divided into: research systems, measurement and control systems and measurement and diagnostic systems. In industrial applications, the measurement and control systems have found their special application. These systems use large numbers of sensors installed all over the controlled object, owing to which they are universal and allow for a measurement, control and analysis of nearly all the quantities.

Such systems provide the possibility of continuous monitoring of the technological process parameters and the work of the participating machines during the implementation of the industrial production processes (measurement, archiving and advanced analysis of the correlated quantities).

The measurement and control systems, known as ICS (Industrial Control Systems) of extended functionality, which include SCADA (Supervisory Control And Data Acquisition Systems), DCS (Distributed Control Systems) as well as less technologically advanced systems realized with the use of PLC controllers, allow for a fast flow of information concerning the production process, the appropriate process parameters and the machine work, an analysis of the production history and the effect of the particular factors on the process, as well as a conscious technological development supported by the measurement results and a reduction of the production costs. Their basic purpose, in the case of forging processes, is the measurement and detailed analysis of the forces, temperature field distribution of the tools and preforms, the acoustic emission events, the forging tool life, as well as analysis of the state of machines, movable element lubrication, vibrations of the rotators which store the energy, aiming at improving the operation of the forging units [2, 4, 5, 8, 9, 24].

It should be noted that the most extensive and developed area of application of such systems are industrial processes of sheet forming as well as in factories assembling parts and subassemblies, mainly for the automotive industry, which is partly due to the extreme conditions that prevail in the industrial processes of forging hot. For example, the work [29] presents a system of monitoring and control of the pressing process through feedback, allowing for the reduction of defects and the number of corrections as well as a better quality of the end products in the form of collar drawpieces. As regards the die forging processes, such systems are still beginning to develop, which is partly caused by the extreme conditions of the industrial process of hot die forging. A description of the systems dedicated strictly to forging processes and their applications can be found in [7, 9, 18, 19, 23, 30]. For example, the work [30] develops a real time control system of placing the forgings in the consecutive dies by a manipulator, which allows for very fast changes in the introduced algorithm. The work [33], in turn, performs an analysis of the forging quality by way of applying visual measurement and control systems, especially visual systems. The literature extensively discusses the application of the measurement and control systems in the analysis of the state of the forging tools [4, 5, 8, 24, 30]. For example, the work [8] analyzes and points to (mainly based on the numerical calculations) the most crucial points, for different types of presses, where the highest stress concentrations occur, as well as the areas where one should expect failure. The measurement and control systems can also be used for controlling, measuring and analyzing selected parameters on semi-industrial stations testing the abrasive wear of the forging tools in the case of high pressures [19].

Obviously, such systems, after the verification of their work under industrial conditions and modification of their application, can constitute not only specialized measurement and control tools used, for example, for an advanced analysis of the tool life, but also specific systems of supervision over the work of the forging tools as well as analysis of the industrial forging process in respect of monitoring the parameters of the process itself, the work efficiency of the machines, monitoring the efficiency of the forging plant, the machine shutdowns and breakdowns as well as the machine operation schedules and the management of the machine maintenance costs. What is more, IT applications dedicated for specific industrial plants, especially forging shops, allow for on-line monitoring of each machine and forging unit, provide a whole spectrum of information on the current production, orders and duties, as well as deficiencies, shutdowns, and scheduled machine inspections and repairs. The increasing market requirements concerning the efficiency and quality of production, also at forging

shops, enforce the introduction of new solutions to optimize the whole production process. An important part of these solutions are the popular Andon (Japanese for 'light signals') systems, which are part of the, mentioned earlier, larger systems: SCADA and DCS. Fig. 1 shows exemplary schematics of how such a system operates.

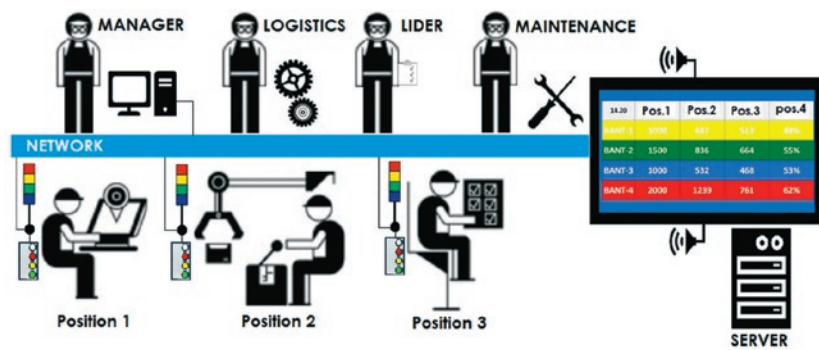


Fig. 1. Schematics of an application of the Andon system for the optimization of the whole production process

Such systems, being part of the concept of 'lean production', provide the possibility to increase the control over the production process, improve the quality, discipline the workers as well as record and analyze the events. At present, the classic Andon systems resemble a board with the numbers of zones of the operator's work or the names of the machines. When a problem occurs, the worker, by pushing the appropriate button, signals the occurrence of a non-standard situation at his work station and his need of assistance in its elimination. More advanced systems based on the original Andon concept, beside the information on non-standard situations, also use signals from the measurement and control systems, owing to which the non-standard course of the process, resulting e.g. from the technological parameters of the process, the work of the machines, the selection of the product etc., is signalized much sooner.

2. The concept of a multi-functional robotized forging station with a process supervising system

The development of the forging branch directly affects the development of the used devices and the applied technologies. The continuous technological progress enforces increasing the production elasticity, as well as increasing its competitiveness and product quality. An improvement of competitiveness can be achieved by way of production automatization. A popular way of automatizing the forging processes is the application of transfer presses. Automatization of this type is offered by press producers such as Schuler, Komatsu, AIDA, MEER and ThyssenKrup. At present, for the big lot production of medium and large forgings, there are three available systems, i.e. press lines, transfer presses with 3-axis transfer devices and transfer presses with a cross transfer system. This technology is, however, significantly limited to the specific type of press and assortment of the forged elements. This solution is dedicated to the automatization of big lot processes and it significantly limits the possibility of changing the forging assortment. Most of the companies which offer their solutions for automatizing the forging processes limit their offer only to the technological lines with relatively new machines and devices, which are usually equipped with sets of sensors, drivers and systems, allowing for mutual communication as well as communication with the superior systems. Applications of the companies specializing in automatization of the forging processes are mostly based on using the existing robots and manipulators of such global potentates as: FANUC, KUKA, ABB, Kawasaki and Comau [1, 3, 10, 11, 26, 28, 31, 32]. They are mostly ready, advanced, units with many levels of tolerance and a construction allowing for universal applications,

mainly on assembly lines of sheet elements and, sporadically, robots working under hard forging conditions (high temperatures, vibrations, dustiness). There are also a few small companies specializing in the construction of robots for the operation of presses, e.g. Copren [11] which offers ROBOCOP with three axes, or Oriimec [31], which offers

a simple three-axial robot G-50 with the PTP-type control, designed for the operation of presses of low tonnage. This robot can be mounted on rails with the purpose to be moved between presses. In Whirpool plants in the USA, between October 2004 and June 2005, on three press lines, 21 five-axis robots SP80X by Motoman were applied [28]. The presses are used for door elements, frames and casings made of sheets of different sizes. Robotization of these presses has increased the capacity by 50 % and improved the quality of the drawpieces. In Europe, Jaguar Cars, Great Britain, is the most robotized factory [27] – it uses over 400 robots at different stages of the production process, e.g. in the press section, where aluminium elements of the luxurious Jaguar XJ car are pressed.

Application of such type of devices requires a large financial investment, due to the price of the robot itself, the advanced control system and the following operation and maintenance costs. Also, solutions proposed by those companies, despite being universal in character, concern only a specific part of the technological process. Integrator companies focus mainly on the manipulator arm together with the grabbing unit, which transports the material to the heater, as well as the consecutive forging operations, followed by cutting and assigning the detail to the following operation. Installation of such devices only rarely includes other important aspects which determine the whole forging process, such as the life of the forging instrumentation, connected with the tribological conditions. For example, ABB reports that, in 2001, in Great Britain, it assembled 18 production robots and 80 different elements [1]. This robotized line is a whole complex including automatic tool replacement, security control, diagnostics, visualization of the course of the production process, inspection of selected operations, collecting information on daily production, elaborating reports and analyses, device and system diagnostics, tracking of the process history etc. All this is, however, only a selected fragment of the whole technology, focusing mainly on the area of operation of the robot itself, or the manipulator arm, while the whole investment exceeded 12 mln euro (the cost of one robot is about 350 thousand Euro).

Based on the performed research concerning elaboration and construction of measurement and control systems for the analysis and control of industrial process of die forging [18], the authors developed a concept of an innovative, integrated, multi-functional die forging station. Beside the option of application in modern technological lines, the station is mainly dedicated to forging shops equipped with older machines and devices. One of the main assumptions of the station is modernization of the currently used machines in the existing technological line in order to adapt them to automatization. Modernization in respect of adaptation to automatization is undoubtedly innovative and is especially attractive to companies whose financial situation does not allow for big investments, such as a purchase of new forging units. This certainly constitutes an advantage of the proposed concept in respect of the very expensive free market solutions. The elaborated concept assumes that the station will be synchronized with the work of the forging unit, equipped with a dedicated measurement and control system. Additionally, the whole station will be connected with a superior production management system.

In the proposed innovative solution, constituting a complex approach to the issue of automatization and robotization of the forging line, the key (component) elements will be the following (Fig.2):

- a manipulator arm with a grabbing unit, transporting the charge material from the heater to the die impression,
- a cooling and lubricating device assuring a constant dose of the lubricant and implementing the assumed process of ‘maintaining’ long life of the forging tools,
- a measurement and control system installed on the forging unit, synchronized with a simultaneous, separated, work of the arm and the cooling and lubricating device,
- a superior production management system, which will play a supervisory role over the whole process.

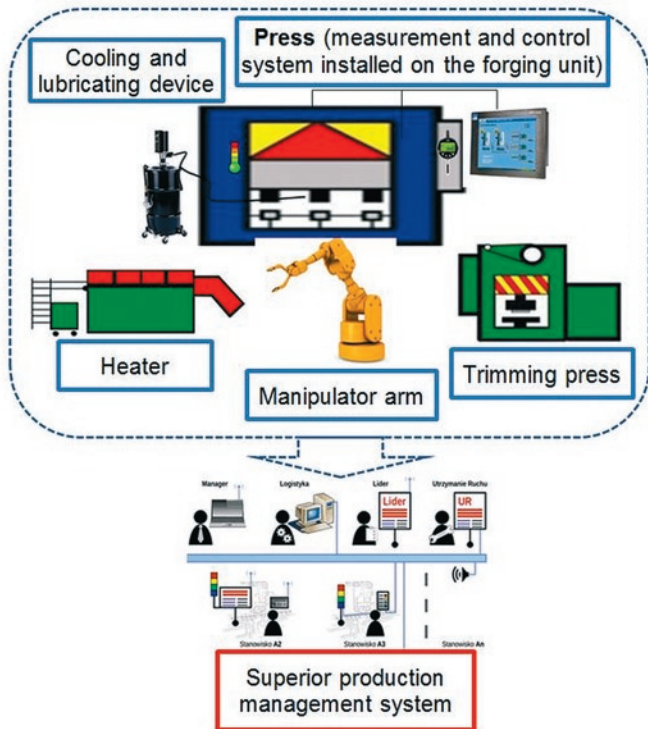


Fig. 2. Schematics of an integrated, automatized die forging station

In the opinion of the authors, the proposed solution thoroughly covers the whole process, considering all the existing factors. Each part of the station needs to be designed in such a way which will guarantee its autonomous, proper, functionality and cooperation with the rest of the system. The idea of the authors is combining the particular elements, taking advantage of the synergy effect, which will bring much more measurable benefits, in both the scientific and the financial aspect. Presented below is the innovativeness of the key elements of the station in respect of the currently applied solutions.

2.1. Manipulator arm with grabbing unit

A key element of the developed position is simple keypad with the least number of degrees of freedom, allowing for completing the tasks related to the forging processes which are currently performed by man. The use of a simple, and thus inexpensive, construction- and operation-wise, robot is possible owing to the complex approach of the authors to automatization. One of the basic conditions for applying a simple manipulator is elimination of the possibility of the forging's being jammed in the impression and assurance of a precisely repeatable position of the preform and the forging. The industrial robot market is separated into the sector of ready units of many levels of tolerance, of a construction which assures universal applications, and the manipulator market allowing for the implementation of similar tasks when the number of the tolerance levels and the universality of application are limited. A manipulator, used for removing the material

from the heater and placing it in the press, must face the environmental conditions of the production hall. That is why the producers of advanced and complicated robots offer various solutions to this problem, from protective covers, to compressed air blowthrough, to paint covering for the protection against dust and humidity. Beside the low price, another advantage of the proposed manipulator will be, owing to its simplicity, the lack of elements which are especially sensitive to the proximity of heat sources, and so, protection of this type will not be necessary. The main rotation axis mounted on the foundation will assure the required rigidity of the manipulator, which will allow for a dynamic movement, with the loads of up to 5 kg. The main executive elements, i.e. pneumatic actuators, will be used to drive the arm and assure the work of the holder. The applied actuators, equipped with high temperature seals, and high temperature and splinter resistant conduits will increase the system's strength against the environmental conditions. In the forging process with the use of the discussed manipulator, it is very important to assure the appropriate positioning of the treated material at each stage of the process (upsetting, blocking, final forging), which allows for grabbing and transporting of the forgings. And so, an important element of the manipulator is the grabbing unit, which must be adapted to the shapes of the products of the given plant. This will be a gripping device connected with the universal arm of the manipulator. The gripper, made of inconel, in the form of the "C" system, with mobile arms, will guarantee the appropriate gripping ability, which has been confirmed by many laboratorial tests. The currently applied industrial robots perform such tasks properly; however, their price significantly exceeds the financial capabilities of the companies [32].

2.2. Cooling and lubricating devices

The authors are planning to use the elaborated and implemented, proprietary, cooling and lubricating system [12]. At present, one of the devices being part of the system is already working in a Polish forging shop, and others are being tested at other plants from the forging branch. The elaborated lubricating and cooling device, constructed as a low-pressure one, is safer than the commonly applied devices of this type with pressure vessels. Assuring the optimal work and lubrication temperature of the forging tools is very important from the point of view of the optimization of their life and the quality of the forgings. In

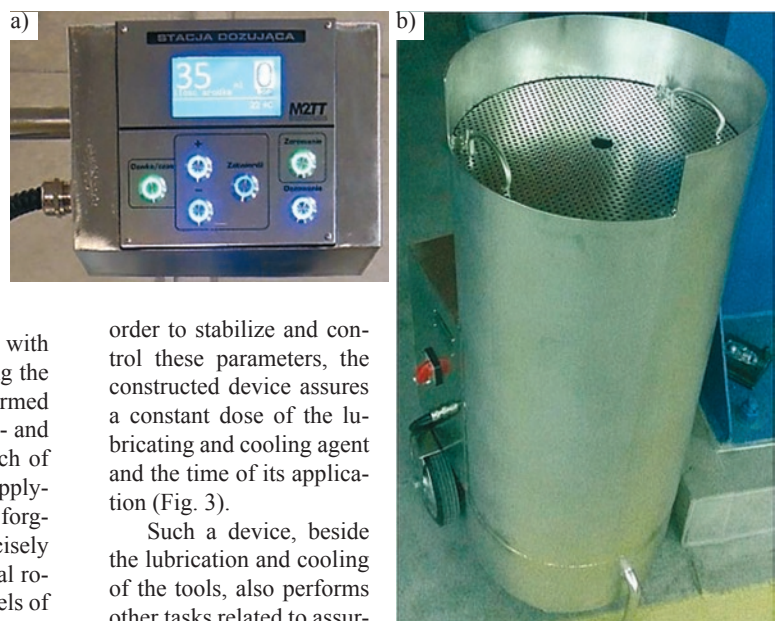


Fig. 3. A dosing and lubrication device controlling the amount of the lubricating and cooling agent: a) view of the controlling panel, b) view of the container [12]

ing the optimal working conditions of the tools, such as additional drying off of the accumulator water, which can cause the formation of 'pockets', which, in turn, may result in incomplete filling of the impression and non-uniform cooling of the tool surface. This device allows for adapting, depending on the need, the dose of the fluid ejected on the upper and lower tools as well as the time of its supply. The basic functional elements assuring repeatability of the lubrication cycles are: a peristaltic pump driven by a stepper motor, which precisely controls the fluid dose, a set of valves controlling the flow of the air which atomizes and pushes the fluid, cleaning the fluid distribution system, and a head spraying the applied liquid agent on the surface of the dies. The change of the supply time allows for controlling the water content in a volume unit of the ejected air-water-graphite mixture. Longer supply times allow for more effective cooling of the surface layer of the tools and leave it dry after the cycle completion. A properly selected time of the lubricating agent ejection favours the appropriate atomization of the fluid, thus hindering the process of graphite accumulation in the bends of the dies and the process of water accumulation on their surface. The regulation of the content of the liquid phase in the lubricating and cooling mixture consists in changing the opening time of the spraying valve and the rate of the liquid's flow to the spraying head. The device is also equipped with an anti-depositional mixer, which allows for maintaining uniformity of the graphite suspension in the water, which, in turn, assures a constant amount of the lubricating agent. It is crucial to select the appropriate moment of atomizing the agent. At present, in a majority of cases, it consists in activating the spray shower after a given forging operation, which causes the risk of spraying the hot forging before it leaves the die impression. Such a situation results in a part of the scale being left in the impression and the impression being insufficiently cooled (lubricated). The authors have elaborated special pyroelectric sensors with a regulated threshold of operation, set in such a way so that the path of removing the forging can cross the sensor beam, which guarantees elimination of the problem (Fig. 4). Additionally, this system will make it possible to count the number of the forged products. At present, most forging shops which do not own control systems perform this task by approximation, i.e. by determining the number of forgings by weight or by counting the mean number from a particular shift (8 hrs). Also, counters of the number of press cycles are often used, which is justified only in the case when each work cycle finishes with manufacturing a product (instead of e.g. testing the movement of the press or positioning the tools).

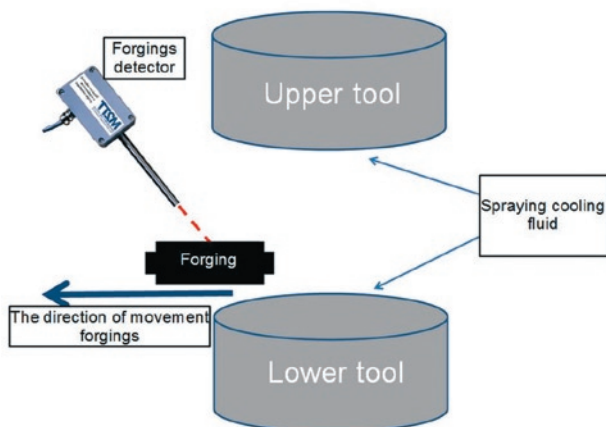


Fig. 4. Schematics of the elaborated tool lubricating system, which also assures removing of the scale and drying of the tools

2.3. Measurement and control system

Within the frames of the performed long-term research, the authors have elaborated and constructed measurement and control systems for the analysis and control of industrial die forging processes, which have been used e.g. in the process of forging of catches used to move concrete blocks on an eccentric press in the TR device (INOP, Poznań), and in the process of hot forging of a CV joint casing on a crank press in closed dies (GKN Driveline Oleśnica) [18]. The elaborated systems are built of an industrial computer (a real time controller, a fast multi-channel measurement card, an operational memory chip, high capacity hard disks, a set of amplifiers and converters) and appropriate measurement sensors (of the force, shift, pyrometers, thermocouples, encoders, accelerators, piezoelectric sensors etc.). Fig. 5 shows a fragment of the recording of the force from four operations

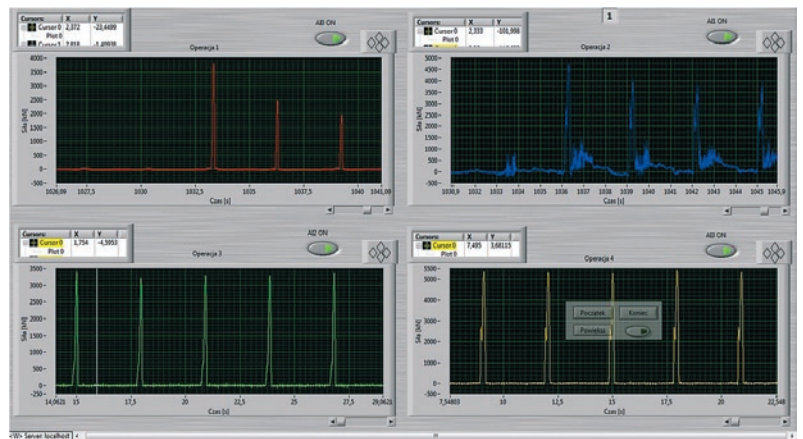


Fig. 5. Panel with displays of forces for four operations of forging a CV joint casing

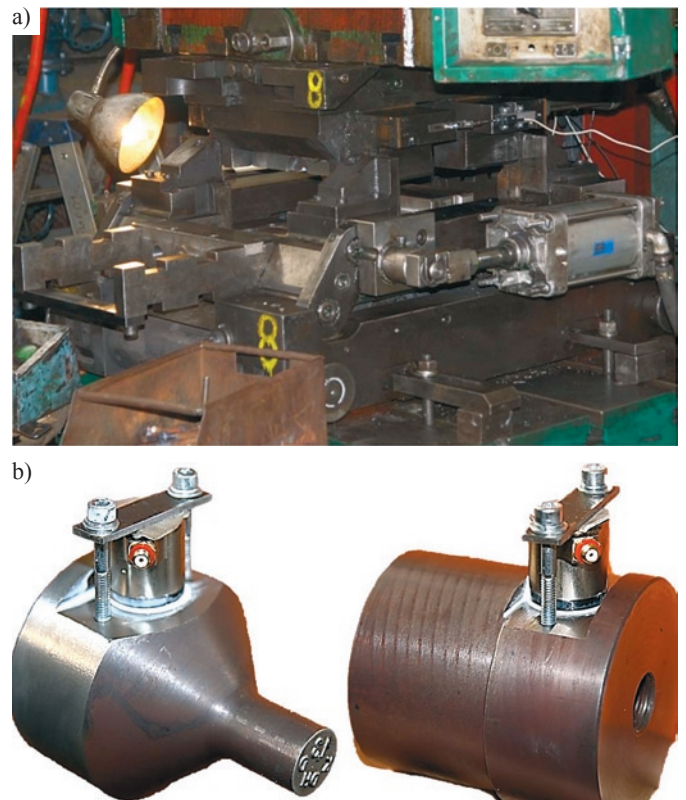


Fig. 6. a) View of the TR device b) punches for 2nd and 3rd operation with an AE sensor

obtained by the system built to monitor and archive the force in the process of forging a CV joint casing.

Also, tests with the use of the elaborated measurement system for the analysis of the acoustic emission (AE) signal were performed. The tests included the process of forging a catch for moving concrete blocks, realized on an eccentric press in the TR device in INOP, Poznań (Fig. 6a). The system was used for the pioneering research of the acoustic emission signal, which allowed for the determination of the wear of the tools used in the second and third operation of forging the catch. The tools were equipped with AE sensors (Fig. 6b).

The sensor mounted on the surface of the punch receives elastic waves, which originate from other parts of the machine as well as from the treated material. Next, the acoustic emission events are plotted on the force diagram corresponding to the analyzed forging operation (Fig. 7).

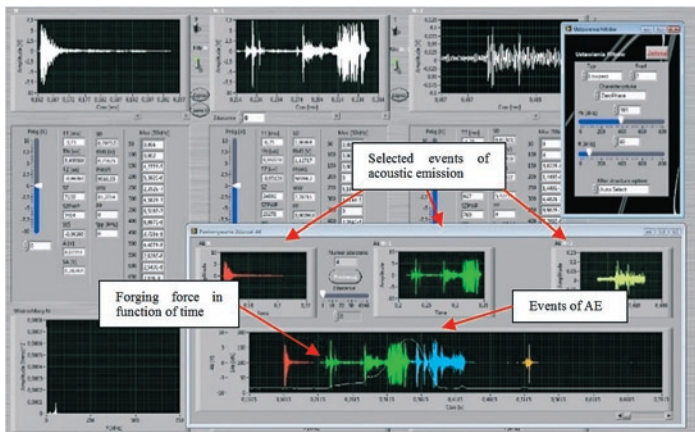


Fig. 7. View of the main panel for the analysis and selection of acoustic emission events [18]

After the verification of most of the acoustic emission events, it will be possible to search the signal and recognize the new occurring events and next replace the broad band sensor with a resonance one. The narrowing of the signal frequency will increase the signal sensitivity, thus detecting the events responsible for the microcracks of the punch material or its wear.

The concept of a measurement system within the frames of a multifunctional, robotized, forging station, beside the component elements of the systems constructed by the authors, which were mentioned before, also assumes installation of a rotational speed converter on the flywheel shaft of the press crank, which allows for an energy analysis of the machine and correlation of the results with the results of the

force measurements. Such a system will provide the possibility to measure the physical quantities, such as the forging forces, the tool temperature, the mobile element location etc. It is crucial to properly distribute the measurement sensors, as well as determine of their dynamics and fault tolerance. What is especially important is the possibility of calibration, which guarantees accuracy in the whole range of the measured values (Fig. 8). A significant part of the system is constituted by a system for measuring the tool temperature. The latter is crucial from the point of view of the production process itself, as well as the life of the tools. Owing to a common data server, such information can be used to control the cooling intensity and the amount of the lubricant, which are regulated by a device designed to cool and lubricate the tools.

The calibration process, which has been the subject of a few years of research, is fully recognized and it guarantees obtaining accurate measurement results. The commonly applied calibration methods assume calibration with the use of hydraulic actuators, which stretch the body of the frame, or forging metal cylinders of the appropriate size. These methods, while justified, do not provide good results, mostly because they are performed under static conditions and they require completing additional actions. The force measurements are made directly by means of tensometric strain gauges, extensometers glued to the press columns as well as sensors based on the piezoelectric phenomenon and the systems integrating the charge (Fig. 9).

All the signals, after conditioning in the measurement area, which guarantees resistance to interferences caused by the presence of drivers and the induction heater, as well as the interferences coupled on the supply network, will be transmitted to the measuring server, which, in turn, will send them to the main server, at the same time determining the parameters for the control system of the machine and the production process, constituting the superior (IT) system of production management.

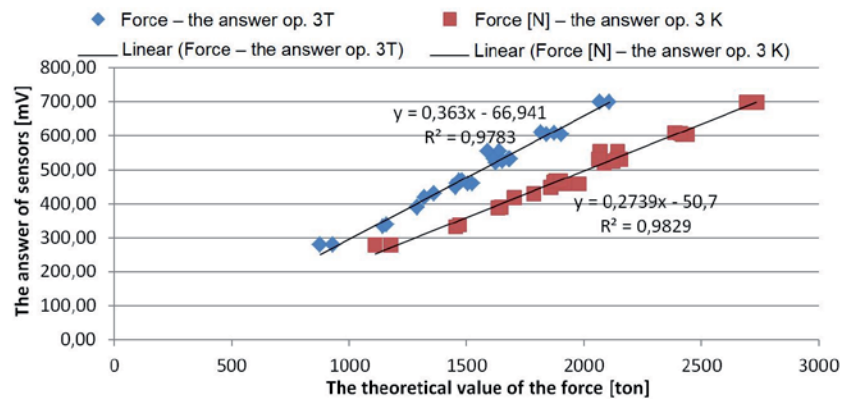


Fig. 9. Results of measurement system calibration for tensometric gauges and piezoelectric sensors

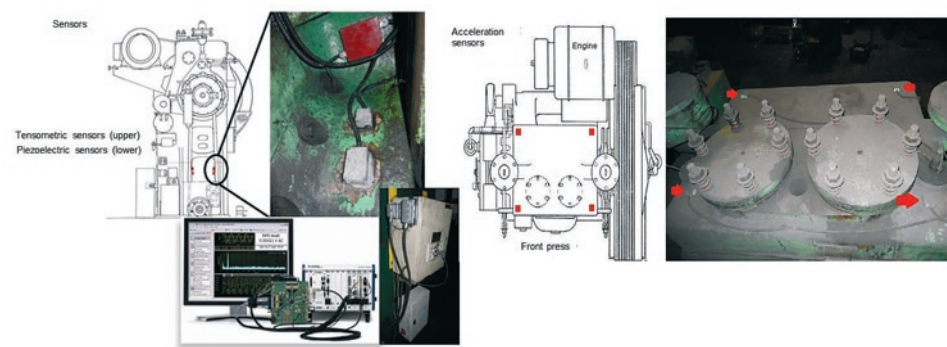


Fig. 8. Measurement and control system with an example of sensor distribution

By using high-performance computing machines, Real Time's systems, many parameters and analysis will be made on the spot measurements. This will ensure the independent operation of each of the subsystems, some functionality and make it independent subsystems of failure of other components of the position.

2.4. Superior production management system

The authors are also planning to elaborate an IT system which will play a supervisory role over the whole process. Monitoring systems, such as ANDON or similar solutions, are commonly available, being implemented by many companies. On the other hand, it is difficult to find such operation compatibility of the measuring system mounted on the unit and the system monitoring the breakdowns and contributing to the production schedule. The reason for this is the lack of specialized solutions adapted to the needs of the particular production processes implemented by companies with a high understanding of the problem and the values of the given process indicators. Integration of all the production stages and the supervision of the production machines in one superior system elaborated by a consortium specializing in forging and measuring technologies. The elaborated superior system will also allow for an analysis of the recorded parameters throughout a long period of time, which provide the possibility of development, in the area of the applied technology, of the management of the equipment resources (machine work, breakdowns, repairs etc.) and the human resources, as well as adaptation of the production organization to the increasing market demands. This will also allow for the construction of a complete and universal tool for the supervision of the process and the development of the forging technology.

Fig. 10 shows a practical implementation of the tool work supervision system and the analysis of the industrial process by the system developed by the authors.

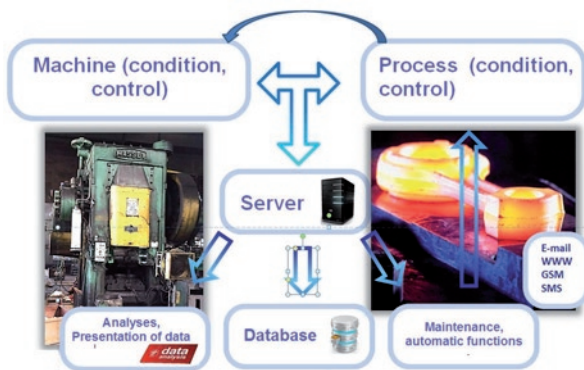


Fig. 10. Schematics of a practical implementation of the tool work supervision system and the industrial forging process analysis. The application working on a dedicated data server performs real time monitoring of the conditions of the production process (right) and the work of the machines taking part in the production.

Such a system is constructed of few modules, which communicate with each other, owing to which each event occurring in the forging process carries information causing a specific reaction in the whole system. The whole is connected by means of a special IT system, which plays a supervisory role over the process. What is innovative about this solution is the integration of the measurement and control system with the system of monitoring breakdowns as well as production and machine efficiency, which will allow for breakdown prevention and will help with scheduling technological breaks and the necessary repairs. The system will also make it possible to automatically assign temporary work parameters to the given event in the form of a breakdown or manufacturing defect and to improve the technology.

Owing to the application of efficient calculation machines and Real Time systems, many parameters and analyses will be performed in the area of the measurement. This

will assure an independent work of each subsystems and high functionality, and will prevent the subsystems from being affected by the breakdowns of other component parts of the station.

One of the modules of the elaborated solution is a module which integrates the production and the movement maintenance, making it possible to record and analyze a very large number of production parameters. Fig. 11 shows an exemplary 'screenshot' of how this mod-

Fig. 11. Application panel with the major production schedule parameters

ule works, where one can see the current production plans, with the (reference) codes of the forgings, the applied instrumentation, its life and other parameters.

The planner, while defining the production for the given machine (or machines), assigns a set of tools and human resources, and enters the data on the production itself. Fig. 12 shows selected technological parameters referring to the forging force in time and in the function of the angular position of the shaft.

View of the panel of the data analysis from the sensors monitoring one production process. The system analyzes, in a continuous mode, the values of the forces and the temperature of the tools, the forging and the preforms. It counts the elements at each production stage and recognizes the operation number in the multi-operational forging process. At the same time, it enters the analysis results into the data base, so that they can be used later for the analysis of the technology, identification of the breakdown causes or breakdown prevention.

It is also possible to perform a complex analysis of the current production, with respect to its efficiency, shutdown times, number of manufactured forgings, defects etc. (Fig. 13a). Often, such information can be found in a few screens located in the central part of the forging shop. (Fig. 13b).



Fig. 12. Application panel with the major technological parameters of the selected forging process

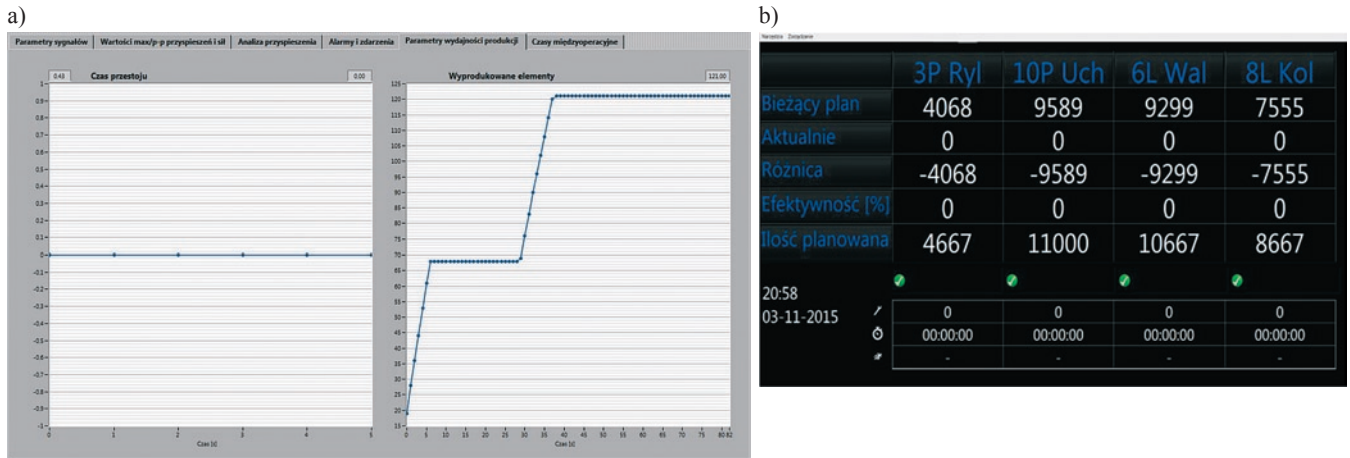


Fig. 13. a) Application panel with the major technological parameters of the selected forging process, b) information monitor/board

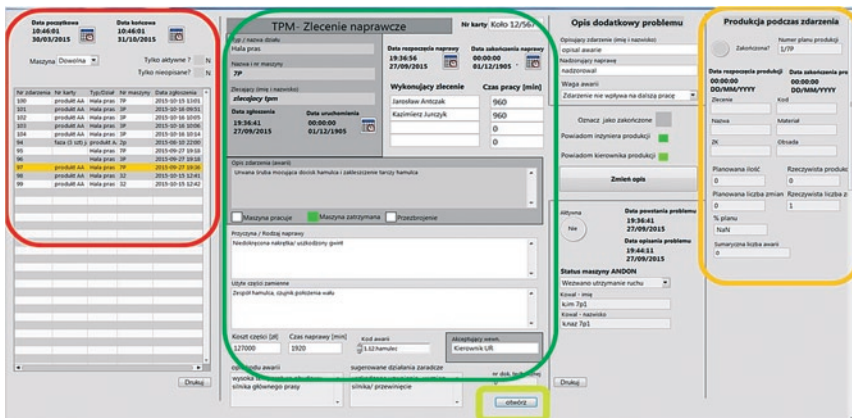


Fig. 14 'Screen shot' from the breakdown monitoring system application

Fig. 14 shows a 'screenshot' of an application of the breakdown monitoring system, where one can see: the time of occurrence of such a breakdown event, the location, the production parameters during the event etc.

The breakdown monitoring system allows for an immediate action (based on a special procedure algorithm), e.g. repair order, review of the repair documentation of the given breakdown based on the previous events or the documentation prepared beforehand, which significantly shortens the time of solving the problem and resuming the production process.

Achieving the highest global standards of production quality and competitiveness requires improving the forms and methods of production management. Undoubtedly, nowadays, this is connected with the use of IT technologies, which include: advanced measurement systems, electronic devices, communication technologies and other peripheral devices for collecting, processing, analyzing and transmitting information. All this as a whole favours the improvement of production management and its structural elements.

The implementation of an integrated, multi-functional die forging station into the production process will also contribute to stabilizing the current production, increase the efficiency and productivity of forging units and significantly broaden the production capabilities of the whole company. The authors are also planning to introduce such an integrated, multi-functional die forging station to other forging units – presses as well as hammers. The scheduled, very high, functionality level of the station assumes the option of its reconfiguration and elastic adaptation in respect of the changing machines and production schedule of the given company. The station elaborated by the authors will constitute a unique solution, as similar solutions encountered in

forging shops both in Poland and the world are usually dedicated to one machine or process, and their modernization is impossible or unprofitable. It will increase the control and automatization of the currently realized forging processes, and the given forging shop will benefit e.g. in the form of robotization and automatization of the production process.

What is more, owing to its innovativeness, it will significantly affect the fulfillment of the increasing needs of the clients and thus increase the competitive level of the company, as it will characterize in the following elements:

- Extended control and stability of the current production.
- Increased production efficiency, owing to the applied manipulator transporting the forgings.
- Robotization and elaboration of universal forging and trimming technologies in the selected work center with the consideration of the series of types of the forging group.
- Significant increase of the life of the applied forging tools, owing to the integrated lubricating and cooling device (constant and directed lubricant dose).
- Process mapping at all production stages.
- Fast analysis of the effect of the applied changes in any location of the applied technology on the whole process and the machine (verification of the possibility of press overload due to a die shape change), which will accelerate the technology development and lower the implementation costs.

3. Conclusions

The measurement and control systems elaborated and constructed by the authors allow for continuous monitoring (measurement, archiving and analysis) of the most important industrial forging parameters, such as: the forging forces in the function of time/shift and the tool temperature. The performed verification of the work of such systems under industrial conditions and their appropriate software and equipment development makes them a unique system of supervision over the work of the forging tools and analysis of the industrial forging processes in respect of monitoring the parameters of the whole manufacturing process. Additionally, through the elaborated dedicated IT applications for specific industrial/forging plant, they allow for an on-line monitoring of each machine, device and unit (scheduled inspections and performed repairs), and of the work efficiency of the particular plant sections or stages of the production process, thus providing a broad information spectrum on the current load and the state of

the machines, as well as the current production, orders, deficiencies, shutdowns, and in this way, providing the possibility of production management. Another aspect of applying such type of systems is the option of verifying the simultaneously performed numerical modeling of the processes, with a special consideration of the tool life.

The continuous development of the forging technology makes the forging plants automatize their production in order to meet the demands of the market. This leads to the introduction of new construction and technology solutions. An answer to this state of affairs is the presented concept of an innovative solution, which constitutes a complex approach to the issue of automatization and robotization of the forging line. The concept assumes the construction of an integrated, multi-functional die forging station, whose key elements will be:

- a manipulator arm with a set of grippers, which transports the charge material from the heater to the die impression,
- a proprietary (already constructed) cooling and lubricating device which assures a constant dose of the lubricant and realizes a complex process of ‘maintaining’ long life of the forging tools,

- a measurement and control system elaborated by the authors and installed on the forging unit, synchronized with a simultaneous and independent work of the arm and the cooling and lubricating device,
- a superior system of production management (partially built), which will play a supervisory role over the whole process.

The intention of the authors is, however, combining the particular elements and taking advantage of the synergy effect, which will provide much more benefit, of both scientific and financial kind. This solution will contribute to an even better and more thorough control over the forging processes. Introducing an integrated, multi-functional die forging station into the production process will stabilize the current production, improve the conditions of operation and productivity of the forging units as well as significantly increase the production capabilities of the whole company. At present, the benefits of a synergy of the particular elements of the elaborated, integrated, multi-functional station are difficult to determine. Such assessment will be possible only when the station is practically implemented.

References

1. ABB, www.abb.com/robotics.
2. Amada Oceania Pty Ltd., www.amada.com.au.
3. Bilsing Automation. www.bilsing-automation.com.
4. Cechura M, Hlavac J, Kubec J, Functions and features monitoring of forming machines, research report V-10-091, VSCVTT, 2010.
5. Cechura M, Housa J, Energy analysis of forming machines and further proposals for decreasing of energy consumption, research report V-11-037, VSCVTT, 2011.
6. Cechura M, Chval Z, Convectional versus multiple operating press, Brno 2013; 67-70.
7. Grosse C.U., Ohtsu M., eds. Acoustic emission testing - basics for research - applications in civil engineering. Springer. (2008).
8. Chval Z, Effect of heat load to the forming machines, MM Science Journal, 2013; 418-421
9. Chval Z, Cechura M, Monitoring extremely stressed points on stands of forging presses, Procedia Engineering 2015; (100): 841 – 846, <http://dx.doi.org/10.1016/j.proeng.2015.01.439>.
10. Comau. www.comau.com.
11. Copren. www.copren.com.
12. Gronostajski Z., Hawryluk M., Jakubik J., Kaszuba M., Misun G., Sadowski P.: Solution examples of selected issues related to die forging, Archives of Metallurgy and Materials 2015; 60(4): 2767-2775.
13. Gronostajski Z. Kaszuba M., Hawryluk M., Zwierzchowski M., Niechajowicz A., Polak S.: Die profile optimization for forging constant velocity joint casings, Archives of Metallurgy and Materials 2011; 56(2): 551-558, <http://dx.doi.org/10.2478/v10172-011-0059-z>.
14. Gronostajski Z., Kaszuba M., Hawryluk M., Zwierzchowski M.: A review of the degradation mechanisms of the hot forging tools. Archives of Civil and Mechanical Engineering 2014; 14(4): 528-539, <http://dx.doi.org/10.1016/j.acme.2014.07.002>.
15. Gronostajski Z., Hawryluk M., Kaszuba M., Marciniak M., Niechajowicz A., Polak S., Zwierzchowski M., Adrian A., Mrzyglód B., Durak J.: The expert system supporting the assessment of the durability of forging tools, International Journal of Advanced Manufacturing Technology 2016; 82: 1973–1991, <http://dx.doi.org/10.1007/s00170-015-7522-3>.
16. Gronostajski Z., Hawryluk M.: The main aspects of precision forging. Archives of Civil and Mechanical Engineering 2008; 8(2): 39-57, [http://dx.doi.org/10.1016/S1644-9665\(12\)60192-7](http://dx.doi.org/10.1016/S1644-9665(12)60192-7).
17. Gronostajski Z., Hawryluk M., Kaszuba M., Zwierzchowski M.: Analysis of forging process of constant velocity joint body. Steel Research International 2008; 1: 547-554.
18. Gronostajski Z., Hawryluk M., Kaszuba M., Sadowski P.: Measuring & control systems in industrial die forging processes. Eksploatacja i Niezawodność - Maintenance and Reliability 2011; 3: 62-69.
19. Hawryluk M., Marciniak M., Misun G.: Possibilities of investigating abrasive wear in conditions close to those prevailing in industrial forging processes. Eksploatacja i Niezawodność - Maintenance and Reliability 2014; 16(4): 600-607.
20. Hawryluk M., Jakubik J.: Analysis of forging defects for selected industrial die forging processes, Engineering Failure Analysis 2016; 59: 396–409, <http://dx.doi.org/10.1016/j.engfailanal.2015.11.008>.
21. Hawryluk M., Zwierzchowski M.: Structural analysis of hot forging dies with regard to their life. Eksploatacja i Niezawodność - Maintenance and Reliability 2009; 2(42): 31-41.
22. Hlavac J., M. Cechura, V. Kubec, Technologia, Boundary conditions setting questions for virtual simulation of mechanical presses, 2009; 61, ISBN 978-80-227-3135-5.
23. Islam El-galy, Bernd-Arno Behrens Online monitoring of hot die forging processes using acoustic emission (part i), J. Acoustic Emission 2008; 26: 208-218.
24. Karamyshev A.P.: The production of a machine designed for the cold radial cyclic forging of solid and tube billets, WIT Transactions on Ecology and the Environment, 2014; 169-177, ISSN: 17433541.
25. Katalog zrobotyzowanych stanowisk w przemyśle polskim. Wydawnictwo Przemysłu Maszynowego, Warszawa 1987.
26. KUKA Robot Group. www.kuka.com.

27. Mortimer J.: Mix of robots used for Jaguar's aluminium- bodied XJ luxury car. *Industrial Robot*, 2003; 2: 145–151, <http://dx.doi.org/10.1108/01439910310464168>.
28. Motoman, www.motoman.com
29. Neugebauer R, Bräunlich H, Scheffler S, Process monitoring and closed loop controlled process. *Archives of Civil and Mechanical Engineering* 2009; 2(9): 105-126, [http://dx.doi.org/10.1016/S1644-9665\(12\)60063-6](http://dx.doi.org/10.1016/S1644-9665(12)60063-6).
30. Nye T.J., Elbadan A.M, Bone G.M, Real-time process characterization of open die forging for adaptive control, *Journal of Engineering Material Technology* 2000; 123(4): 511-516, <http://dx.doi.org/10.1115/1.1396350>.
31. Oriimec, www.oriimec.com
32. World Robotics 2004. *Statistic, Market Analysis, Forecasts, Case Studies and Profitability of Robot Investment*. United Nations, New York, Geneva 2004.
33. Zhenyuan J, Bangguo W, Wei L, Yuwen S, An improved image acquiring method for machine vision measurement of hot formed parts, *Journal of Materials Processing Technology* 2010; 210: 267–271, <http://dx.doi.org/10.1016/j.jmatprotec.2009.09.009>.

Marek HAWRYLUK

Marcin KASZUBA

Zbigniew GRONOSTAJSKI

Wrocław Technical University of Technology,
ul. Łukasiewicza 5, 50-371 Wrocław, Poland

Przemysław SADOWSKI

Measurement and Medical Technologies Transfer
ul. Piękna 64C/2, 50-506 Wrocław, Poland

E-mails: marek.hawryluk@pwr.edu.pl, marcin.kaszuba@pwr.edu.pl,
zbigniew.gronostajski@pwr.edu.pl, m2tt@m2tt.com

Bolesław KARWAT
Marek NOCŮN
Ryszard MACHNIK
Jerzy NIEDŹWIEDZKI

MODELLING AND STUDY THE EFFECT OF SELECTED DESIGN FEATURES FOR THE OPERATING PARAMETERS OF INDUSTRIAL ELECTROSTATIC PRECIPITATORS

MODELOWANIE I BADANIA WPŁYWU WYBRANYCH CECH KONSTRUKCYJNYCH NA PARAMETRY EKSPLOATACYJNE ELEKTROFILTRÓW PRZEMYSŁOWYCH*

Electrostatic precipitators are currently most commonly used in industrial processes equipment to reduce dust emissions into the atmosphere. A significant impact on the process of extraction of two-phase gas/dust medium has the shape and configuration of the discharge electrodes, affecting the shape of the electric field in the chamber electrostatic precipitator. Geometric parameters of discharge electrodes and their arrangement in the chamber electrostatic should provide uniform current density distribution at the surface of the collecting electrodes. The article presents an analysis of the impact of geometry and configuration of industrial - blade type discharge electrodes on the distribution of current density on the collecting electrode. On the basis of the measurement results mathematical model was worked out which allows simulation of the current density distribution depending on the shape of the electrodes. The model allows to specify the most appropriate parameters of distance between the emission elements of discharge electrode and the distance between the electrodes. Preferred geometric parameters and configuration of discharge electrodes was determined by analyzing power spectral density magnitude (PSD) and the mean square value (RMS) of current density. The results indicate the possibility of reducing the number of elements of emission corona electrodes without worsening of the operating parameters of electrostatic precipitator.

Keywords: electrostatic precipitator, operation, corona electrodes, modeling, simulation, sigmoidal function.

Elektrofiltry są obecnie najczęściej stosowanymi, w procesach przemysłowych, urządzeniami do redukcji emisji pyłów do atmosfery. Znaczący wpływ na przebieg procesu odpylania ośrodka dwufazowego gaz/pył ma kształt oraz konfiguracja elektrod emisyjnych, wpływające na ukształtowanie pola elektrycznego w komorze elektrofiltru. Parametry geometryczne elektrod ulotowych oraz ich rozmieszczenie w komorze elektrofiltru powinny zapewniać równomierny rozkład gęstości prądu na powierzchni jego elektrod zbiorczych. W artykule przedstawiono analizę wpływu geometrii oraz konfiguracji przemysłowych elektrod ulotowych typu ostrzowego na rozkład gęstości prądu na elektrodzie zbiorczej. Na podstawie wyników pomiarów opracowano model matematyczny umożliwiający symulację rozkładu gęstości tego prądu w zależności od kształtu elektrod. Model umożliwia określenie korzystnych wartości odległości pomiędzy elementami emisyjnymi elektrody ulotowej oraz odległości pomiędzy tymi elektrodami. Korzystne parametry geometryczne i konfigurację elektrod ulotowych określano na podstawie analizy magnitud gęstości widmowej mocy (PSD) oraz wartości średniokwadratowej (RMS) gęstości prądu. Uzyskane wyniki wskazują na możliwość zmniejszenia ilości elementów emisyjnych elektrod ulotowych bez pogorszenia parametrów eksploatacyjnych elektrofiltru.

Słowa kluczowe: elektrofiltr, eksploatacja, elektrody ulotowe, modelowanie, symulacja, funkcja sigmoidalna.

1. Introduction

Electrostatic method of purifying of exhaust gases is widely used in heating energy, metallurgy, chemical, cement and paper industry [20]. However the main sector of the economy, which use of electrostatic dust removal equipment, is energy production industry using electrostatic processes for cleaning gases generated by the combustion of different types of fuels [17]. Combustion gases contain significant amounts of dust. In power industry, the only reasonable solution from the economic point of view is to use precipitators with horizontal plate structure due to the amount of exhaust gases generated during energy production.

Electrostatic precipitators are structures suitable for use in the well-defined power plant installation. Selection of precipitator design, type of corona and collecting electrodes used [1, 2] and power supply

system are determined by the type of boiler and type of boiler fuel burned in it, and consequently by the properties of dusts which will be separated. At the stage of design the base exploitation parameters are defined i.e. guaranteed parameters and limiting parameters values defined by:

- fuel (including elemental composition, sulfur content, calorific value, ash content)
- combustion gases (minimum and maximum flow rate, humidity, temperature, dew point temperature, the content of CO₂ and O₂),
- dust (nominal and maximum concentration, the maximum content of flammable particles).

The main task of electrostatic precipitator is separation dust phase from the combustion gases, therefore the most important parameter is

(*) Tekst artykułu w polskiej wersji językowej dostępny w elektronicznym wydaniu kwartalnika na stronie www.ein.org.pl

the value of the dust emission at its output. For newly constructed facilities, depending on the fuel, concentration level of pollutants at the output of an electrostatic precipitator do not exceeds: for coal or lignite $5\div 15 \text{ mg/m}^3$, and for biomass and peat 5 to 20 mg/m^3 of dry combustion gases in the contractual conditions (content of water vapor is not larger than 5 g/kg of combustion gas in the reference conditions of $\text{O}_2 = 6\%$). This means, that for example, the concentration of dust in the exhaust gases from the combustion of coal $d_C = 26 \text{ g/m}^3$ dust collection efficiency of the electrostatic precipitator must be 99.96% .

Fuel characteristics, exhaust gas properties and the amount of dust in them determine the choice of construction solution of electrostatic precipitator:

- size, number of sections and zones of extraction, the active height and length of the electric field, the number of power supplies and independently powered electrostatic fields, etc.,
- the nominal gas flow rate (approx. 1 m/s),
- a decrease in temperature and pressure of the gas in the electrostatic precipitator (respectively: $5\div 10^\circ\text{C}$, $120\div 150 \text{ Pa}$),
- the layout, type and number of discharge and collecting electrodes,
- type and number of employed rappers of collecting and corona electrodes.

During the operation in the stable condition the basic operating parameters of electrostatic precipitator are electrical parameters resulting from the type of the high-voltage power supplies, i.e. voltage and nominal current. Currently are in use power supplies with the following output parameters; current / voltage, $400\div 2000 \text{ mA}$, $80\div 135 \text{ kV}$, respectively. The significant influence to meet the requirements on the dust emissions output of electrostatic precipitator have:

- voltage supply of corona electrodes,
- tuning of the high voltage supply control unit (operation mode),
- the frequency of the shake off the dust being deposited on the collecting and corona electrodes.

Significant impact on the course of the dust deposition process on collecting electrodes has the shape and configuration of the discharge electrodes affecting the shape of the density distribution of the electric field in the chamber electrostatic precipitator. The current density on the surface of the collecting electrode affects the mechanical properties of the deposited dust layer on the surface of the collecting electrode. The value of current density at the surface of the collecting electrode is affected by the emissivity of the electrode and the conductance two-phase medium present in the interelectrode space in case of particular electrode configuration. In the operating process of an electrostatic precipitator, both of these parameters are determined by the selection of the supply voltage of the corona electrodes and operation parameters of high voltage power supplies, at a level that prevents the phenomenon of migration of dust grains detached from the surface of collecting electrode further into the electrostatic precipitator.

In the past 20 years there have been significant changes in the structure of the discharge electrodes of electrostatic precipitators. Due to the low durability wire and tape electrode were abandoned. An important advantage of this type of electrode was uniform and relatively easy to calculate distribution an electrostatic field produced by them. Currently, there are mast type electrodes equipped with point emission elements in the form of spikes. Complex distribution of electric field around such electrodes prevents the use in theoretical analysis, mathematical models developed for the wire electrodes.

The development of information technology has enabled the use of numerical methods for modeling the phenomena occurring in the interelectrode space of electrostatic precipitator [3, 4, 5, 9, 11, 12, 23]. The next step in the development of computer simulation of the dust separation process in the electrostatic precipitators were attempts to

develop alternative models of discharge electrodes [7, 21]. Of great importance for the quantitative determination of the phenomena occurring during the discharge in the environment of gases (the degree of ionization to be calculated from the functions of the energy distribution of electrons) and the speed of propagation of the corona are the results of work in the field of plasma physics [10]. Computer simulation of the electric field parameters and its impact on the process of dust separation, is facing difficulties due to the complex geometry of the currently used corona electrodes. There are still experimental research conducted, on the basis of which it can be concluded about the process of two-phase medium dedusting, which are the combustion gases [13, 14].

This paper presents the results of research carried out on industrial spike type corona electrode. An example of construction of this type electrode is shown in Fig. 1.

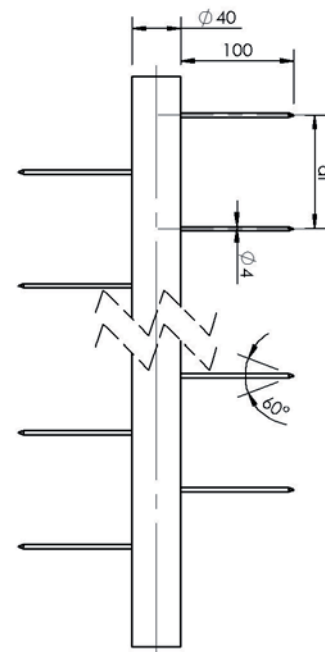


Fig. 1. Mast type spike corona electrode

Mast spike electrode consists of a carrier mast having a diameter of about 40 mm and the emission elements, which are steel bars with a diameter of 4 mm and length 100 mm , welded to the mast at the opposite sides at appropriate intervals. Emission elements are terminated with cone tip.

2. Research Methodology

Measurements of the electrical parameters of discharge electrodes was performed on the test stand shown in Figure 2 [16]. Depending on the configuration, current-voltage characteristics of the electrodes and the current density on the surface of the collecting electrode can be determined. High of the active part of the collecting electrodes is $h = 1.0 \text{ m}$ and maximum division of the collecting electrodes is $H_z = 0.6 \text{ m}$ so the measuring stand allows industrial research corona electrode of a length of 0.8 m to be tested. It consists of a support frame (1), to which the collecting electrodes with a total area of 4 m^2 (2) are fixed. The tested discharge electrode is attached to the insulated inner carrier frame (3) and supplied with a DC high voltage power supply. Measurement signals from the sensors (4) are transmitted through the connector (5) to the measurement and data acquisition systems. Measurement of the current density distribution at the surface of the collecting electrode is performed using sixteen measuring fields (4) equally distributed along the length of the collecting electrode. The

currents flowing between each of the measurement fields and the ground are sequentially selected by the 1 of 16 multiplexer and send to one of the measuring amplifier. Data acquisition and multiplexer control are made using specially prepared software based on LabView package. Registered voltage value is obtained by averaging the 2000 samples for each of the measurement fields. Data are recorded five times in the cycle, which means that the measured value of the current corresponding to the value of the current flowing through each of the measurement fields, is the mean value of 10 000 measurements.

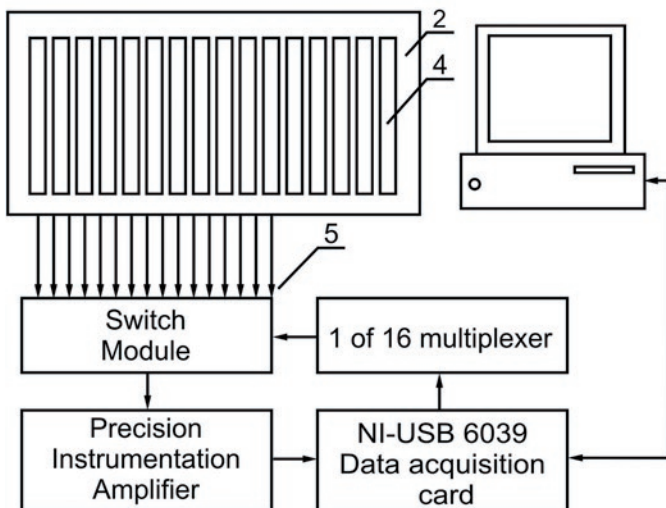
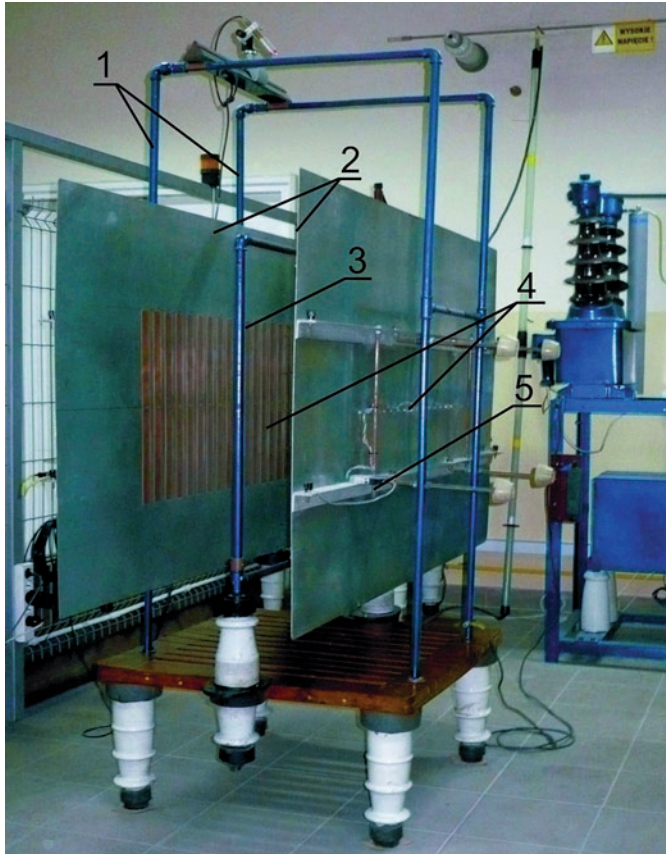


Fig. 2. The measuring stand used to determine the parameters of the corona electrode 1 – supporting frame, 2 – collecting electrodes, 3 – corona electrode support frame, 4 – sensors, 5 – electrical connectors

The analysis of measured electric parameters of the electrodes was carried out using tools developed for time series analysis. The use of statistical methods of time series analysis simplifies the analy-

sis of the results obtained in the measurement of electrical parameters of studied electrodes. It also provides information about the tested object, which cannot be obtained by other methods. For the analysis of the current distribution on the surface of the collecting electrode research methodology based on the formalism of statistical time series model was applied [6]. Analysis of the current density distribution on the surface of the collecting electrode was performed using developed for this purpose software with advanced statistical functions, serving for time series analysis *TSA (Time Series Analysis)*, a component of LabView software [24]. This program, after initial processing of the measured data allows their smoothing and calculation of the following parameters:

- the average value after elimination of extreme values,
- the mean square value *RMS (Root Mean Square)*,
- magnitude of the power spectrum *PS (Power Spectrum)* to be calculated using the algorithm of fast Fourier transform *FFT (Fast Fourier Transform)* of the current density on the surface of the collecting electrode in the form of the squares of the *RMS* values,
- power spectral density *PSD (Power Spectrum Density) FFT* of the time series X_t (in the form of squares of the *RMS* values per unit of the x-axis of collecting electrode).

For the calculation of the power spectrum and power spectral density the procedures contained in the libraries of functions built in LabView program were used.

The simplified algorithm of the program to analyze the measured data with the LabView procedures is shown in Figure 3.

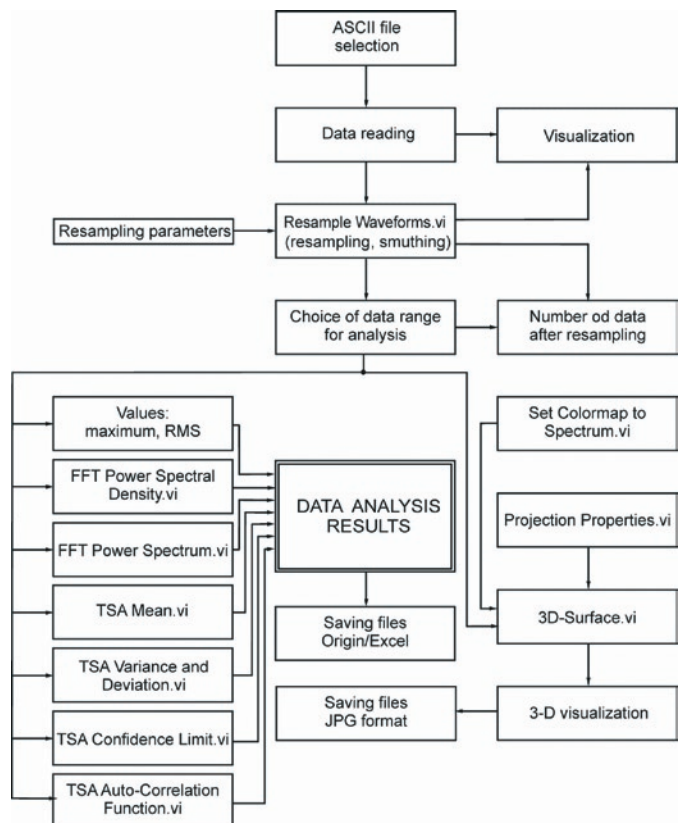


Fig. 3. Algorithm of the program to analyze the current density distribution measurements on the surface of the collecting electrode

Research on the dust separation process using industrial corona electrodes and electrodes with modified geometry was carried out in the laboratory electrostatic precipitator (Fig. 4) with the following parameters:

- the active length of the chamber: 2 m,
- the height of chamber: 1 m,



Fig. 4. View of laboratory electrostatic precipitator with removed collecting electrode. 1 – the dust feed system, 2 – diffuser, 3 – frame of discharge electrodes, 4 – discharge electrode, 5 – confuser; 6 – collecting electrode

- the inter-pitch: 400 mm or 500 mm,
- collecting electrodes: flat,
- corona electrodes: replaceable, matched to specific measurements,
- gas flow rate: 0.1 m/s to 0.8 m/s,
- a source of dust: fluidized bed chamber fed from a source of compressed air,
- administration of dust: a system of nozzles arranged vertically in the area of the inlet of the electrostatic precipitator.

Electrostatic corona electrodes are powered by a DC power supply with high voltage enables a smooth adjustment of the voltage from 0 to 75 kV.

The air flow through the electrostatic precipitator chamber was obtained through the use of suction fan powered by a frequency converter. The motor speed changes influence the performance of the fan, and thus the speed of air flow through the chamber electrostatic precipitator.

3. Results

3.1. The results of measurements of the electrical parameters of discharge electrodes

Studies of electrical parameters of discharge electrodes are made under the following conditions: temperature $t = 21\text{ }^{\circ}\text{C}$, the relative air humidity $a_h = 52\%$, barometric pressure $p = 991.9\text{ hPa}$.

Examples of current density distribution at the surface of collecting electrode for assembly of two spike electrodes for the variable distance between electrodes H is shown in Figure 5.

Figure 6 shows the cumulative results of the relationship between magnitude of power spectral density PSD and the RMS value as a function of distance between charging electrodes H and spike distance dI .

The results showed that increase the distance between the emission elements of the electrode, increases the current density J . Maximum value of the current occurs at a $dI = 250\text{ mm}$. At the same time increase, the distance between the corona electrodes causes a decrease in the value of the current density on the surface of the collecting electrode.

Analysis magnitude of power spectral density PSD and of RMS value as a function of the distance between corona electrodes H and

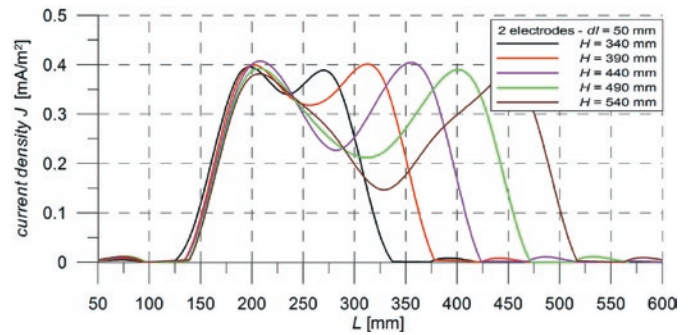


Fig. 5. Current density distribution of on the surface of the collecting electrode as a function of corona electrode space H . The distance between spikes $dI = 50\text{ mm}$ and distance between collecting electrodes $H_z = 400\text{ mm}$

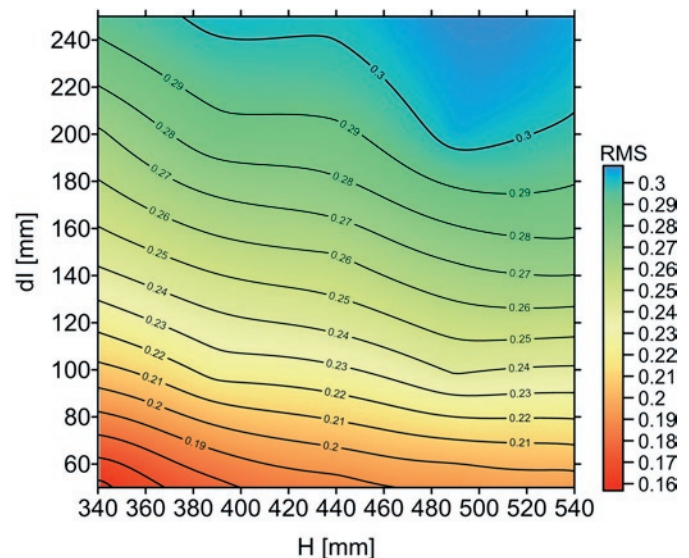
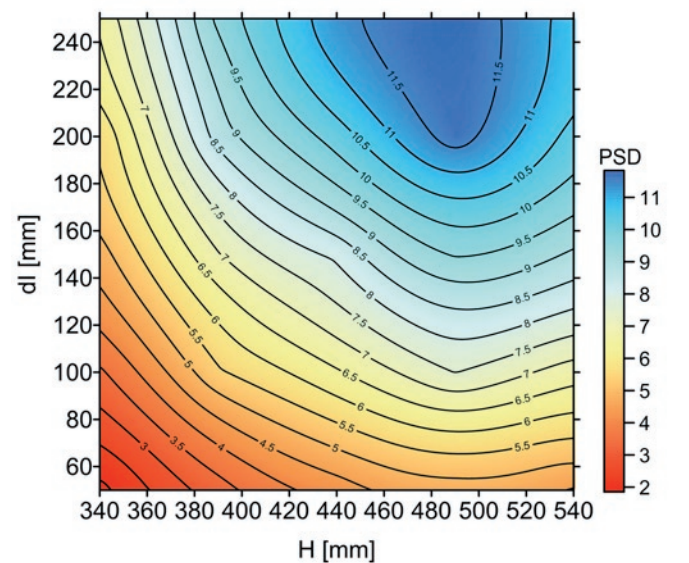


Fig. 6. The magnitude of power spectral density PSD and the RMS value of the current density J as a function of distance between charging electrodes H and spike distance dI .

emission elements of the charging electrode dI indicate that both the increase in the distance between corona electrode and the distance between the emission electrodes result in an increase both the power spectral density and the RMS current density for the tested electrodes. Areas with the highest values of the PSD and RMS indicate in blue

color – Fig. 6. The results indicate that with increasing distance between the corona electrodes maximum PSD value of the current density distribution at the surface of the charging electrode corresponds to the $H = 490$ mm.

3.2. Mathematical formula describing the distribution of the electric field in the space between electrodes in the electrostatic precipitator

Based on the measurement results a mathematical model of the current density distribution on the surface of the collecting electrode was developed. The measurement data of the current density distribution at the surface of collecting electrode J , depending on the H parameter and dI parameter (dI is the distance between emission elements) were preliminary processed. The results of the measurements were subjected to statistical analysis to eliminate the extreme values and smoothing. To negative values of the current density J zero value was assigned as zero value has no physical meaning. Then analyzed data J were converted, depending on the geometric coordinates of L , i.e. position along the collecting electrode, in such a way as to be symmetrical with respect to y axis. If the chart does not exhibit symmetry, the right site was replaced with the mirror image of the left. Figure 7 shows the result of the transformation of data in accordance with the accepted method of statistical analysis.

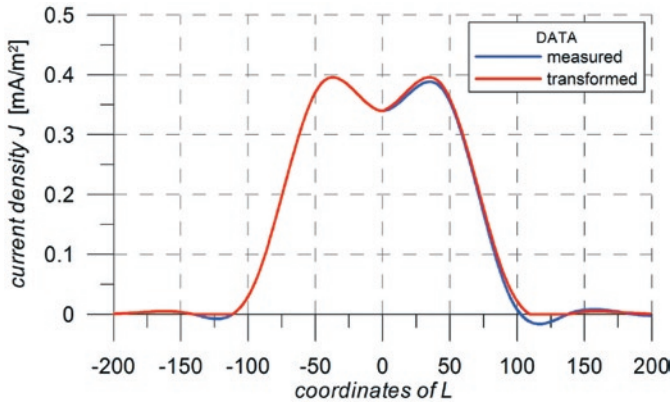


Fig. 7. Distribution of current density on the surface of collecting electrode. a) the data obtained from measurements, b) data after processing

The curve shown in Fig. 7 is the sum of two peaks with a distinct asymmetry. This pattern can be described by adding at least four symmetrical peaks with variable ratio Gauss/Lorentz [15]. However, for a general description of each peak number of parameters, such as half-width, amplitude ratio H/L need to be introduced and jet linking them to the spatial distribution of the electrodes is essential. The number of parameters can be limited by using sigmoid function [19] for the description of the outlined curve. Therefore, to approximate the current density distribution at the surface of the collecting electrode composition of asymmetric sigmoid function was applied, resulting in an ability to model asymmetric waveform. The sigmoidal form of the equation is (1):

$$y = y_0 + A[1/(1 + \exp(-x + xc/w))] \quad (1)$$

where:

- A – amplitude,
- w, xc – function parameters,
- y_0 – shift of the function value on the y axis.

Changing of w parameter changes the slope of the curve, while the parameter xc designate a point of inflection of the curve and allows to move the curve along the x axis.

Superposition of two sigmoidal functions allow asymmetric spectra to be obtain if the $w2$ and $w3$ parameters will have different values. The superposition of the two sigmoidal function can be written (2):

$$y = y_0 + A[1/(1 + \exp((-x + xc - w1/2)/w2))] \cdot [1 - 1/(1 + \exp((-x + xc - w1/2)/w3))] \quad (2)$$

where:

$xc, w1, w2, w3, xc$ – function parameters.

Parameter $w1$ modifies the value of the parameter xc and allows to change the half-width of the peak.

In case of two corona electrode assembly, the distribution of current density J on the surface of collecting electrode (Fig. 7), can be described by the sum of two asymmetric functions (3):

$$J = J_0 + A1[1/(1 + \exp((-x + xc1 - w11/2)/w21))] \cdot [1 - 1/(1 + \exp((-x + xc1 - w11/2)/w31))] + A2[1/(1 + \exp((-x + xc2 - w12/2)/w22))] \cdot [1 - 1/(1 + \exp((-x + xc2 - w12/2)/w32))] \quad (3)$$

where:

- $A1, A2$ – amplitude,
- $w11, w12, w21, w22, w31, w32$ – parameters of the function,
- $xc1, xc2$ – position of the peak's maximum on the x -axis,

$xc1$ parameter defines the position of the maximum of the first peak on the x axis and can be selected arbitrarily.

As corona electrodes have, the same geometric design features so the two peaks of the spectra should be symmetrical with respect to an axis passing through the center of the curve (Fig. 7.). Any variations in the current density distribution at the collecting electrode are due to inaccuracies of electrode manufacturing. On the basis of experimental data analysis and the symmetry condition it was assumed that the coefficients $A1 = A2 = A, y_0 = 0, w11 = w12 = w1, w21 = w32$ and $w31 = w22$. These factors are functions of the following parameters: distance between the corona electrodes H , and the distance between the emission elements dI .

The assumption of fixed numerical values for the $w1, w21$, and $w22$ coefficients, gives rise to slight discrepancies between the actual values obtained from the measurements and the values calculated using a mathematical model but this leads to a significant simplification of the model and reduce the number of variables.

Analysis of the measured data showed that in the case of $H_Z = 400$ mm, the influence of the dI distance and corona electrodes distance H on the parameters: $w21$ and $w22$ are small and neglectable. In order to reduce the number of coefficients, the following simplifying assumptions have been made: $w21 = w32 = w31 = 1.5$ and at $w22 = 2.6$.

After substituting these values to the function (3) it simplifies to the form (4):

$$J(x, H, dI) = A[1/(1 + \exp(-x + xc1 - (w1/2)/1.5))] \cdot [1 - 1/(1 + \exp(-x + xc1 - (w1/2)/2.6))] + A[1/(1 + \exp(-x + xc2 - (w1/2)/2.6))] \cdot [1 - 1/(1 + \exp(-x + xc2 - (w1/2)/1.5))] \quad (4)$$

As a result of adopted assumptions, to describe the distribution of current density J at the surface of the collecting electrode three variables depending on the scale parameter H and the scale, dI i.e. function coefficients (4): $A, xc2$, and $w11$ must be determine.

According to equation (3) changing $xc1$ parameter affects the position of the curve with respect to the x axis. The value $xc1$ was assumed arbitrarily $xc1 = 20$. This allows a comparison of the current density distribution J on the surface of the collecting electrode obtained from measurements with the results determined according to the mathematical model.

Figure 8 shows a measured data of current density distribution J approximated with the function (4) in case of spike-type electrode.

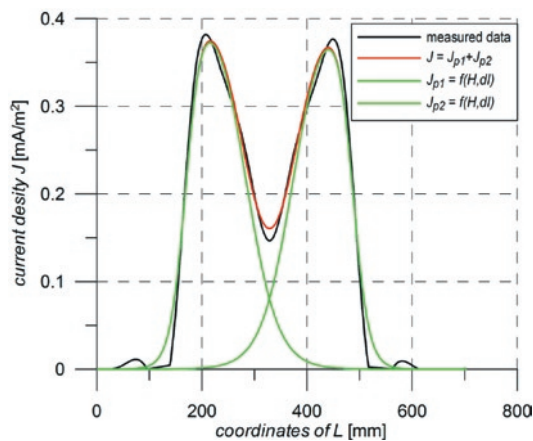


Fig. 8. Approximation using function (4) measured data of current density J for the spike corona type electrodes

Table 1 shows the coefficients of the function describing the current density distribution J on the collecting electrode.

Table 1. Function coefficients $J = f(x, H, dl)$ for the spike electrodes

Function coefficient	Value/Function
w21	1.5
w31	2.6
xc2	$xc1 - 10.634 + 0.0565 \cdot H + 0.0073 \cdot dl - 4.2857e-5 \cdot dl^2$
A	$-0.717 + 0.00485 \cdot H - 5.0655e-6 \cdot H^2 + 1.21e-3 \cdot dl$
w1	$14.0434 - 0.0415 \cdot H + 0.003 \cdot dl - 2.0e-5 \cdot dl^2$

The mathematical model that describes the distribution of current density J at the collecting electrode was verified by comparing the measurement results with the results obtained by theoretical simulation. Simulations were performed assuming variable coefficients of function (4) shown in Table 1. The simulated spectra of the current density and the recorded spectra were analyzed seeking to establish their convergence. This allowed to say what impact have simplifying assumptions in the model adopted on the real physical phenomena occurring in the space of electrostatic precipitator.

Figure 9 shows an example of a comparison of the distribution of measured current density J at the collecting electrode with the simulated one.

Black curve shows the measurement results obtained by means of approximation of the measured data using the least-squares Marquardt-Levenberger algorithm [18]. The curve marked red shows the progress generated by the simulation using the model described by equation (4), for the assembly of spike corona electrodes at the two extremes of the H scales.

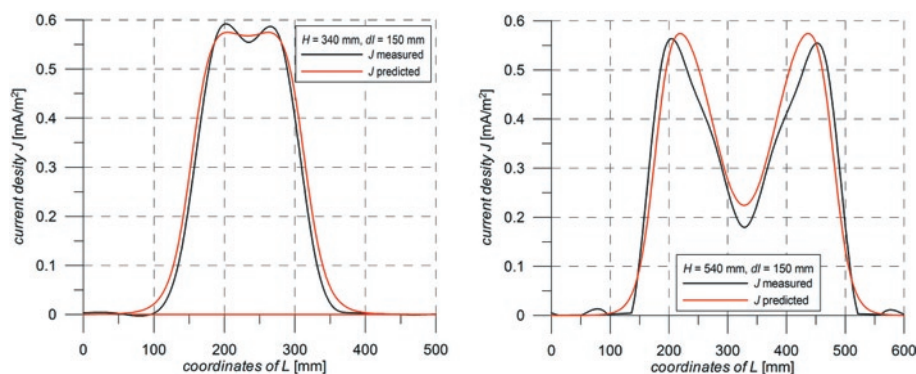


Fig. 9. Comparison of measured current density distribution data at the electrode with the spectra predicted by mathematical model

The assessment of coincidence of the model with measured data, was performed by comparing the mean square value RMS , the value I of the area (5) delimited by the current density J distribution curve of and the x-axis, of the data derived from measurements with the current density distribution J values obtained by simulation.

$$I_{H,dl} = \int_0^L J_{H,dl}(x) dx, \quad (5)$$

$$0 < L \leq 70.$$

The calculations were performed using the procedure of integration and calculation of the RMS values using mathematical procedures from the libraries of National Instruments LabView software. Comparison of the current density distribution J on the surface of the collecting electrode obtained by simulation using a mathematical model with the measurement data obtained in the laboratory showed that the differences between the measured data and simulated one for most of the analyzed geometry and configuration are less than 10% (table 2).

Table 2. Comparison of measured data with simulated one

H, dl values (mm)	$I_{H,dl}$ value (measured data)	$I_{H,dl}$ value (simulation)	Differences (%)
H=340, dl=150	6.227	5.961	4.46
H=340, dl=200	6.650	6.494	2.40
H=390, dl=150	7.082	6.986	1.39
H=390, dl=200	7.817	7.541	3.66
H=440, dl=150	7.715	8.054	4.20
H=440, dl=200	8.470	8.665	2.25
H=490, dl=150	8.676	9.136	5.04
H=490, dl=200	9.710	9.839	1.31
H=540, dl=150	9.287	10.129	8.31
H=540, dl=200	9.993	10.960	8.82

Assessing the compatibility of the mathematical model with the measurement results one should have in mind that the measurements were carried out on industrial corona electrodes. Some of these electrodes have a geometry errors resulting from the production technology. Taking into account that the developed mathematical model is used to assist in the designing of industrial electrostatic precipitators, where the geometry errors of corona electrode are quite high (manufacturing and/or assembly) the differences between the measurement results and obtained due to simulation are acceptable.

4. Results

Conducted laboratory studies have shown that the most important geometric parameter determining the electric field intensity produced by the spike corona electrode is the distance between emission elements (spikes) dl . Another important parameter is the distance between the emission electrodes H .

The current density distribution at the collecting electrode in case of mast type electrodes is depends on the value of spike distance dl and collecting electrode distance H . Most optimal ranges of these scales are determined by calculating the spectral density PS changes as a function of dl and H . Based on measurements and simulation studies, it was found that the range

of the preferred spike distances dI and collecting electrode distance H in case of spike discharge electrodes are $200 \div 250$ mm and $440 \div 550$ mm respectively. Predicted values are higher than those currently used in industrial electrostatic precipitators.

Worked out model of current density distribution on the surface of collecting electrode enables rapid determination of the electrical parameters of the spike type electrode. The results of simulation studies and carried out measurements of parameters of industrial spike electrodes showed that their geometry does not provide achievable current density. By changing the distance between the emission electrodes currently used (with spike distance $dI = 200$ mm) it is possible to obtain increase in the magnitude of power spectral density PSD of the current on the surface of the collecting electrode by 10%.

Study of the electrodes with modified geometry was carried out in the laboratory for the electrostatic precipitator using fly ash from coal combustion at concentrations of 3.4 g/m^3 and 7.2 g/m^3 . Measurements carried out have shown that for the supply voltage $U_S = 65 \text{ kV}$ average corona current value was $I_E = 0.46 \text{ mA}$. Comparison of the electrostatic precipitator performance equipped with currently used industrial electrodes, with the electrodes of the revised geometry showed no significant differences (in each case dusting efficiency approx. 99%). The reason for this are both a small length and height of active part of laboratory precipitator. It should be recognized, however, that the increase in current density on the surface of collecting electrode providing an increase in the intensity of the electric field in the chamber electrostatic will result in the improvement in the dust separation. This means that for the corresponding parameters of power supply elimination of re-detachment of dust deposited on the collecting electrode due to loss of electrical charge or reduction the impact of this phenomenon on the process of extraction will take place. One may also believe that

the above-described phenomena will allow to shorten the length of the electrostatic precipitator while maintaining the required removal efficiency.

The introduction of the proposed changes to the geometry of the discharge electrodes will not increase the efficiency of extraction of dust with diameter less than 2.5 microns ($PM_{2.5}$). Effective separation in the electrostatic precipitator of this grain fractions requires special technologies (agglomerators) [8, 22].

Summary

The results of measurements of the electrical parameters of discharge electrodes and a computer simulation of the current density distribution at the collecting electrode in case of electrostatic precipitator with flat system of collecting electrode showed that:

- Increasing the pitch (distance between electrodes): the inter-row H and inter-blades dI of discharge electrodes, compared to the currently applied pitch, increases the amplitude of the current density,
- In the case of mast type electrodes one can obtained electric field, required for optimum extraction process, reducing the number of emission elements (blades) of the corona electrode,
- Increasing inter-row scale H leads to reduction of the number of corona electrodes mounted in the chamber of electrostatic precipitator,
- The use of specified geometry and configuration of discharge electrodes will result in lower investment and operating costs of electrostatic precipitator in the range of energy consumption of the electrostatic precipitator.

Acknowledgement

The work was financed by the statutory activities of the AGH University of Science and Technology in Krakow, Faculty of Mechanical Engineering and Robotics, contract No. 11.11.130.957.

References

1. Adamiec-Wójcik I, Nowak A, Wojciech S. Application of the finite strip method to modeling of vibrations of collecting electrodes. International Journal of Structural Stability and Dynamics 2013; 13(7): 1–19, <http://dx.doi.org/10.1142/S0219455413400014>.
2. Adamiec-Wójcik I, Nowak A, Wojciech S. Comparison of Methods for Modelling Vibrations of Collecting Electrodes in Dry Electrostatic Precipitators. Archive of Mechanical Engineering 2013; 60: 431–449, <http://dx.doi.org/10.2478/meceng-2013-0027>.
3. Akishev Y, Goossens O, Callebaut T, Leys C, Napartovich A, Trushkin N. The influence of electrode geometry and gas flow on corona-to-glow and glow-to-spark threshold currents in air. Journal of Physics D: Applied Physics 2001; 34: 2875–2882, <http://dx.doi.org/10.1088/0022-3727/34/18/322>.
4. Atten A, Adamiak K, Khaddoura B, Coulomb J-L. Simulation of corona discharge in configurations with a sharp electrode. Journal of Optoelectronics and Advanced Materials 2004; 6(3): 1023–1028.
5. Batmunkh S, Battogtokh Z. Modeling an electrostatic precipitator (ESP) with ESPVI 4.0W. Second International Forum on Strategic Technology IFOST 2007: 650–653.
6. Box G E P, Jenkins G M. Time Series Analysis. San Francisco: Holden Day, 1976.
7. Brocilo D, Podlinski J., Chang J S, Mizeraczyk J, Findlay R D. Electrode geometry effects on the collection efficiency of submicron and ultra-fine dust particles in spike-plate electrostatic precipitators. Journal of Physics 2008; 142: 1–6, <http://dx.doi.org/10.1088/1742-6596/142/1/012032>.
8. Chang Q, Zheng C, Gao X, Chiang P, Fang M, Luo Z, Cen K. Systematic Approach to Optimization of Submicron Particle Agglomeration Using Ionic-Wind-Assisted Pre-Charger. Aerosol and Air Quality Research, 2015, 2709–2719, <http://dx.doi.org/10.4209/aaqr.2015.06.0418>.
9. Chung L, Chang C.-L, Bai H. Effects of Some Geometric Parameters on the Electrostatic Precipitator Efficiency at Different Operation Indexes. Aerosol Science and Technology 2000; 33(3): 228–238.
10. Dubois D, Merbahi N, Eichwald O, Yousfi M, Benhenni M. Electrical analysis of positive corona discharge in air and N₂, O₂, and CO₂ mixtures. Journal of Applied Physics 2007; 101: 053304-2-053304-9.
11. Fujishima H, Ueda Y, Tomimatsu K, Yamamoto T. Electrohydrodynamics of spiked electrode electrostatic precipitators. Journal of Electrostatics 2004; 62: 291–308, <http://dx.doi.org/10.1016/j.elstat.2004.05.006>.
12. Gooch J P, Francis N L. A Theoretically Based Mathematical Model for Calculation of Electrostatic Precipitator Performance. Journal of Air Pollution Control Association 1975; 25(2): 108–113, <http://dx.doi.org/10.1080/00022470.1975.10470054>.
13. Jędrusik M, Świerczok A. The correlation between corona current distribution and collection of fine particles in a laboratory-scale electrostatic precipitator. Journal of Electrostatics 2013; 71(3): 199–203, <http://dx.doi.org/10.1016/j.elstat.2013.01.002>.

14. Jędrusik M, Świerczok A, Teisseyre R. Experimental study of fly ash precipitation in a model electrostatic precipitator with discharge electrodes of different design. *Powder Technology* 2003; 135–136: 295–301, <http://dx.doi.org/10.1016/j.powtec.2003.08.021>.
15. Kojima I, Kurahashi M. Application of asymmetrical Gaussian/Lorentzian mixed function for X-ray photoelectron curve synthesis. *Journal of Electron Spectroscopy and Related Phenomena* 1987; 42(2): 177–181. [http://dx.doi.org/10.1016/0368-2048\(87\)85018-1](http://dx.doi.org/10.1016/0368-2048(87)85018-1)
16. Machnik R., Nocuń M. Effect of anti-corrosion coatings of corona electrodes on selected operating parameters of industrial electrostatic precipitators. *Eksplatacja i Niezawodność – Maintenance and Reliability* 2014; 16(1): 56–60.
17. Machnik R., Karwat B., Nocuń M., Niedźwiedzki J. Wpływ fizykochemicznych właściwości popiołów lotnych ze spalania węgla na proces elektrostatycznego odpylania spalin. *Przemysł Chemiczny* 2015; 94(9): 1530–1533.
18. Marquardt D, W. An Algorithm for Least-Squares Estimation of Nonlinear Parameters. *Journal of the Society for Industrial and Applied Mathematics* 1963; 11(2): 431–441, <http://dx.doi.org/10.1137/0111030>.
19. Ohishi K, Okamura H, Dohi T. Gompertz software reliability model: estimation algorithm and empirical validation. *Journal of Systems and Software* 2009; 82(3): 535–543, <http://dx.doi.org/10.1016/j.jss.2008.11.840>.
20. Parker K. *Electrical operation of electrostatic precipitators.*, London: The Institution of Electrical Engineers, 2003.
21. Suleman M, Saleem M, Siebenhofer M. Characterization of brush type discharge electrodes and impact of enhanced corona discharge on operation of electrostatic precipitators. *Journal of Electrostatics* 2012; 70: 144–148, <http://dx.doi.org/10.1016/j.elstat.2011.11.008>.
22. Truce R, Wilkins J, Crynack R, Harrison W. The Indigo agglomerator a proven technology for reducing visible emission from electrostatic precipitators. *Energetyka* 2005, 11 (617) 751–757.
23. Zhao L, Adamiak K. Numerical Simulation of the Effect of EHD Flow on Corona Discharge in Compressed Air. *IEEE Trans. on Industry Applications* 2013; 49(1): 298–304, <http://dx.doi.org/10.1109/TIA.2012.2228832>.
24. National Instruments, *LabView Advanced Signal Processing, Time Series Analysis Tools User Manual* 2005.

Bolesław KARWAT

Ryszard MACHNIK

Jerzy NIEDŹWIEDZKI

AGH University of Science and Technology
Faculty of Mechanical Engineering and Robotics
al. Mickiewicza 30, 30-059 Kraków, Poland

Marek NOCUN

AGH University of Science and Technology
Faculty of Materials Science and Ceramics
al. Mickiewicza 30, 30-059 Kraków, Poland

E-mails: karwat@agh.edu.pl, machnik@agh.edu.pl, jniedz@agh.edu.pl
nocun@agh.edu.pl

Jacek MUCHA
Jan JAWORSKI

THE TOOL SURFACE WEAR DURING THE SILICON STEEL SHEETS BLANKING PROCESS

ZUŻYCIE POWIERZCHNI NARZĘDZI PODCZAS EKSPLOATACJI W PROCESIE WYKRAWANIA BLACHY KRZEMOWEJ*

The surface wear mechanism of punches for the silicon sheets blanking was presented. In the studies the differences in the wear of high-speed tool (produced by casting and sintering), where observed. The influence of additional TiN coating on the punches flank degradation intensity was obtained. The strengthening zone changes of the sheared blank material close to cutting line were observed. The punch wear influence on the M530-50A silicon sheet material hardness changes was described.

Keywords: tool wear; high-speed steel, blanking process, silicon steel sheets.

W niniejszym artykule przedstawiono opis mechanizmu zużycia powierzchni roboczych stempli wykrawających elementy z blachy krzemowej. Badania wykazały różnice w zużyciu narzędzi dla stali szybko tnącej w przypadku dwóch procesów jej wytwarzania (odlewnia i spiekania). Wykazano wpływ dodatkowej powłoki z TiN na intensywność degradacji powierzchni przyłożenia stempli wykrawających. Obserwacji poddano zmiany obszaru umocnienia materiału wykrawanego w pobliżu linii cięcia. Określono wpływ zużycia stempli na zasięg zmian twardości materiału blachy krzemowej M530-50A.

Słowa kluczowe: zużycie narzędzi, stale szybko tnące, wykrawanie, blachy krzemowe.

1. Introduction

Production of the sheared blank elements, with a certain quality, requires an optimal process parameters selection [4, 6, 11, 30]. Gréban et al. in their work [6] presented the effects of copper alloy elements blanking process. Tekiner et al. [30] described the result of experimental analysis of the aluminum alloy element blanking process. Hernández and other authors [11] presented the influence of the punch cutting edge geometry changes on the cut surface quality. They described the influence of the blanking process clearance and punch diameter. The study concerned the acid resistant steel sheet (AISI 304). There is some dependence between the burr height changes and the punch wear during the blanking process. Study of the high-steel punch wear, for punches with front edge sloped, was presented by Cheung et al. [4]. Blanking process causes the sheet material structure changes. The case of aluminum element blanking process was analyzed by Ravela et al. [28]. The tool surface wear during the blanking process causes changes of the cut surface quality [8, 9, 14, 17–19]. The value of the cutting edge radius significantly affects on the blanking process energy consumption [16]. Tool wear, geometry and clearance influence on the burr height. The bur height can be reduced by using an appropriate tool arrangement.

Electrical steel sheets used in electrical machines have a relatively high induction, permittivity and good punchability. The sheet material magnetic properties are determined in the production process [31]. For the evaluation of the sheet punchability many criterions can be used, and the most important are:

- sheared blank part deformation resistance,
- the burr height,
- coating damage resistant during blanking process,
- material strengthening close to the cut surface,
- geometrical quality of the sheared blank sheet material,

- cutting tools durability,
- intersection surface quality of the sheared blank parts.

The excessive tool wear during the blanking process causes significant changes of the size and zone of plastic deformation concentration in sheared blank element close to the intersection surface [23, 24]. In the deformed silicon steel sheet the undesirable magnetic residue appears, which impairs the sheet magnetic properties – including the increase of the electrical current required for the sheet grains over-magnetization during the voltage transformation [31]. The phenomenon of eddy currents abnormal flow is useful in other situations and is commonly used in the surface quality measurements and in an analysis of the internal defects in element after their operation [13]. In the electrical machine case, it is not preferred to increasing of the magnetic lossiness especially in the sheets used for rotors and stators of the asynchronous motors [24]. One of the manufacturing methods, that reduce the magnetic lossiness is laser cutting process, but it is expensive and has a relatively low productivity [27]. Thus, the blanking process is still used for the rotor and stator plates manufacturing. Many studies are related with the analysis of the magnetic lossiness and magnetic disturbance in the sheets produced by various techniques [5, 15, 20, 27, 32]. Typical materials used for blanking tools are high-speed steels such as: M2, K945, M35, M42, ASP23, ASP30, ASP60 (ASP-Asea Stora Process).

In the paper the tools wear during the blanking process of the silicon steel sheets was presented. Observation was made at the micro and macro level. The mechanism of the punch surface wear was described. The influence of the punch edge wear on the medium stress distribution in sheared blank material, by using FEM, was presented.

(*) Tekst artykułu w polskiej wersji językowej dostępny w elektronicznym wydaniu kwartalnika na stronie www.ein.org.pl

2. Sheet and tools material characteristic

The silicon steel sheets M530-50A (M 45 according to AISI) (PN-EN 10106:2016-01) [26], with thickness $g=0,5 \pm 0,02$ mm were used in experiments. Sheets used in blanking process of electrical machine parts are produced by cold rolling. The M530-50A sheet material has got 1.54 T induction at 2500 A/m electrical current

Table 1. Mechanical properties of M530-50A silicon steel sheets material

$R_{0,2}$ [MPa]	R_m [MPa]	Z [%]	A5 [%]	So [mm ²]	HV5	E [MPa]
245	417	33	61	10	126	2,2e+5

Table 2. Chemical composition of M530-50A silicon sheet material (%)

P	C	Si	S	Mn	Cr	Ni	Cu	Al	Fe
0,01	0,01	1,43	0,007	0,365	<0,01	<0,01	0,05	0,335	reszta

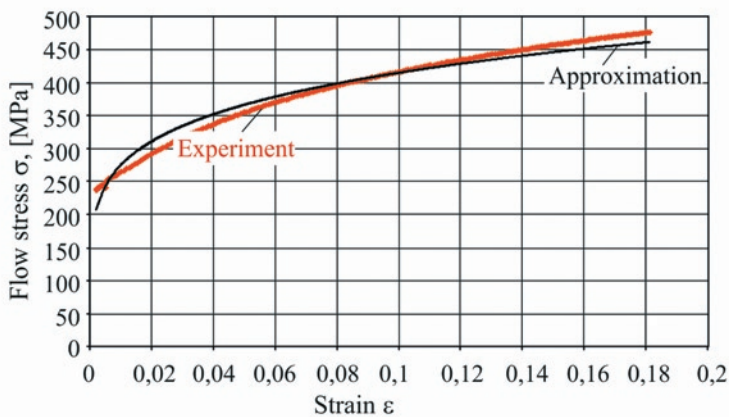


Fig. 1. Experimental hardening curve (thick line) and Hollomon equation approximation (thin line; correlation coefficient: 0,968)

and 5,3 W/kg electrical lossiness at 1.5 T induction. The main mechanical properties and chemical compositions were presented in Table 1 and Table 2. The sheet has a C6 insulating coating (according to AISI ASTM A976 [1]) of thickness $\sim 7 \pm 1,5$ μ m on each side.

Materials used on cutting tools have different mechanical properties, which determine the tool surfaces wearing out during the blanking process [2]. For experimental analysis the punches were made of: M2, M3:2 materials (Fig. 2), and M2+TiN, M3:2+TiN materials with coatings. The chemical compositions of punch materials were presented in Table 3. The M3:2 (ASP 23 Vanadis, Powder Metallurgically Produced High Speed Steel) steel is a

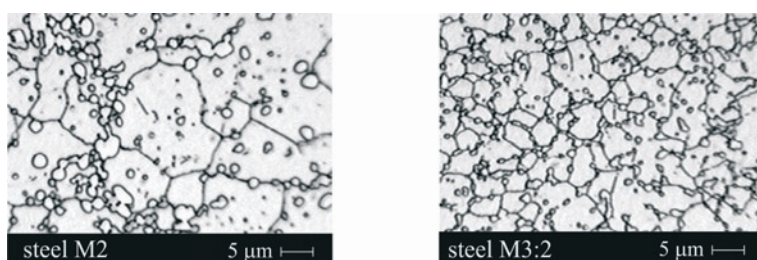


Fig. 2. An example of hardened punch material structure

Table 3. Chemical composition of punch materials [%]

Materiał	Dodatki pierwiastków									Fe
	C	Mn max	Si max	P max	S max	Cr	W	Mo	V	
M2 (SW7M)	0,82-0,92	0,4	0,5	0,03	0,03	3,5-4,5	6,0-7,0	4,5-5,5	1,7-2,1	reszta
M3:2 (ASP 23)	1,19-1,21	-	-	-	-	4,11-4,13	6,33-6,37	4,6-4,8	3,1-3,2	reszta

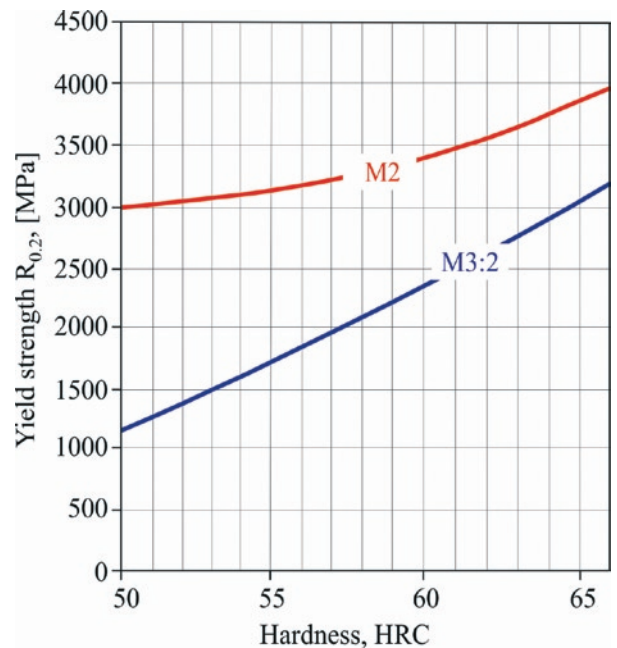


Fig. 3. Influence of the punch hardening on the material yield strength

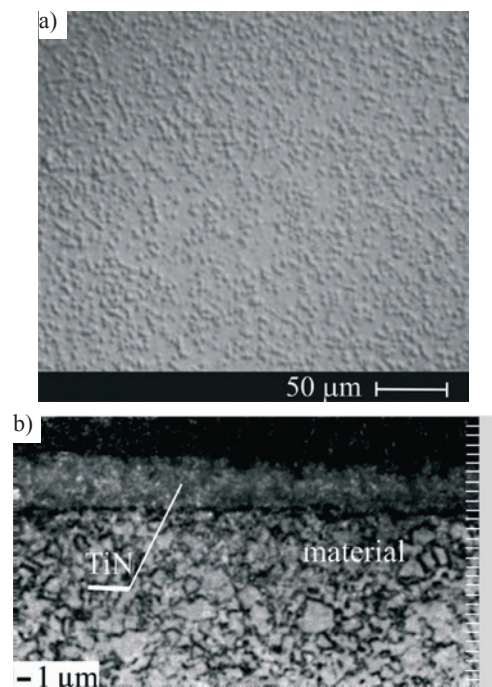


Fig. 4. An example of TiN coating structural characteristic: a) on surface, b) in cross-section. Sheet material: M3:2

material with 7980 kg/m³ average density and 66 HRC after toughening, and M2 material has an 7750 kg/m³ average density and 63 HRC. The punch materials structure after hardening was shown in Figure 2, and the influence of the materials hardness on the yield strength was presented in Figure 3. The inserts in the bottom part of blanking die were made of G40 sintered carbide material.

Punch coatings were made by using PVD method (*Physical Vapour Deposition*). The titanium nitride coatings on the tool surface was applied at 10⁻³÷10⁻² Pa working pressure. Applied TiN coating had a yield color, 2300 HV5 hardness and 3,5 ÷ 4 mm thickness. The microstructure of the punch surface with TiN coating was presented in Figure 4a, and in Figure 4b the cross-section of the TiN layer on the punch was shown.

3. Blanking punch operating conditions

The blanking process was carried out at the press and blanking die in industrial conditions. The wear tests were carried out during the blanking process of the rotor and stator plates (Fig. 5), for low power asynchronous motor.

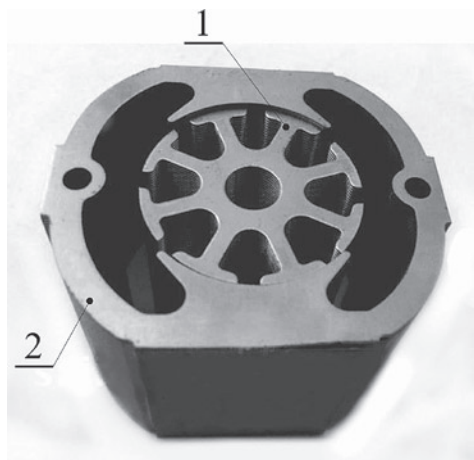


Fig. 5. Sheet packets of the rotor (1) and stator (2), M530-50A silicon steel sheet material

The use of different values of punch-die clearances and various blanking tools materials helped explain the tool wear mechanism during blanking process of the silicon steel sheet. Research conducted with this issue provide the basis for M530-50A sheets punchability analysis. The punch-die clearance 0% and 8% was defined by:

$$Lz = \frac{s}{g} \cdot 100[\%]$$

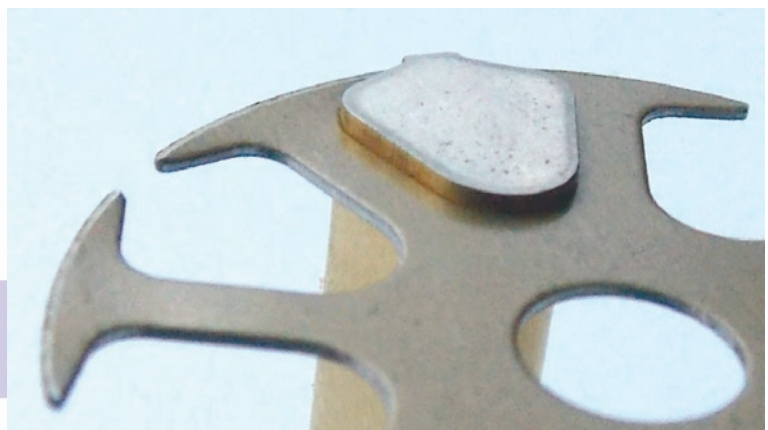
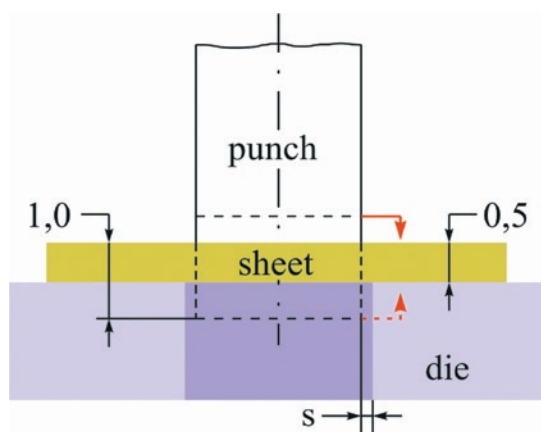


Fig. 6. Characteristic of tool and sheared blank sheets arrangement a) scheme, b) punch maximum bottom position

where:

- g- sheet thickness,
- s- punch-die blanking clearance.

The relative blanking clearance has an impact on the sheet material process separation, and determines the cut surface quality [12]. The punch-die clearance is especially important during the blanking process of very small elements [10]. The blanking speed was constant, and its value was as in typical industrial process of silicon steel sheets blanking (200 cuts/min). The blanking speed is one of the blanking process technological parameters. It has an impact on the cut surface quality and the value of the blanking force [29]. The process of sheets blanking was carried out up to 800 000 cuts. After the 800 thousand cuts the tools were resharpened to eliminate the cutting edge degradation and flank surface wear.

4. Tool surface structure changes observation

The punches during the blanking process were unleashed to flank surface wear on the surface corresponding to the sheets thickness and value of the distance necessary to forcing through the sheared blank from the separation zone. On the punch made of M2 material after 500 000 cuts some signs of wear on flank surface appeared. The scratches and grooves on the analyzed surface were occurred in different extent. The deep grooves and scratches are the material loss on the punch cutting surfaces. The products of an abrasive wear, like abraded and crushed small hard particles, during the blanking process were presented in Figure 7a. This particles under pressure adhered to the tool surface. This is adhesive wear of tool surfaces. Hard particles adhered to the punch affect on the flank surface defecting during the blanking process. For the M3:2 material the particles adhered boundary is clearly visible (Fig. 7b). The adhered particles concentration was observed on the ends of contact line between material and punch. On the surface between cutting edge and end of material-punch line contact the scratches were observed.

When the punch and sheets friction surfaces are closing to each other at distance of molecular force acting, they are tacking (Fig. 8). "Adhesions" formed in this way are tearing during the punch movement. Thus, there is new adhered particles formation and grooving on the punch movement direction. During the pressure contact of two surfaces the most common wear is an abrasive wear. This wear can proceed in two ways: contact of three bodies (Fig. 9a) and contact of two bodies (Fig. 9b). In both case in micro scale, the abrasive process between harder particles and lower hardness material is observed. When separated particles are very large and hard they can force in the material with lower hardness and make the grooves during the punch movement. Intensification of tool abrasive wear and other degradation mechanism will occur in the case of accumulation of the abrasion-induced microparticles.

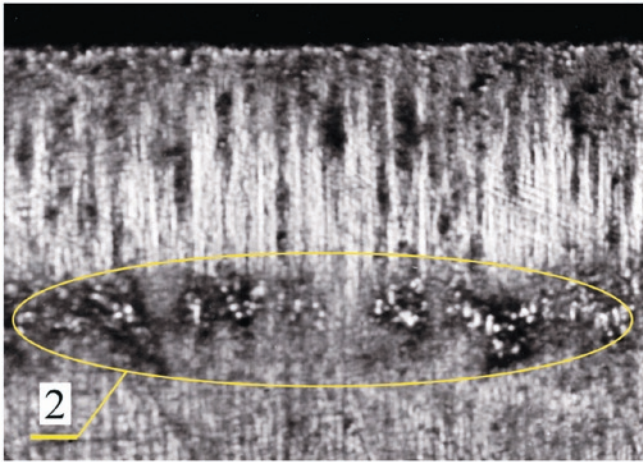
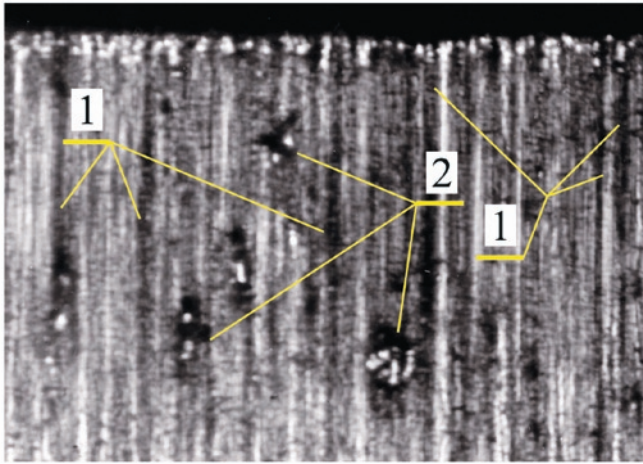


Fig. 7. Punch flank surface after 500 000 sheared blanks: a) M2; x80 zoom, b) M3:2; x160 zoom

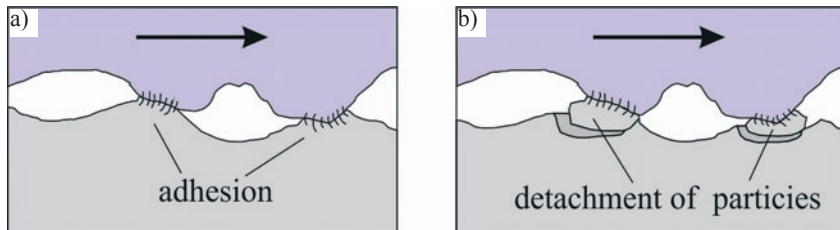


Fig. 8. Scheme of the adhesive wear: a) adhesion, b) detachment of particles

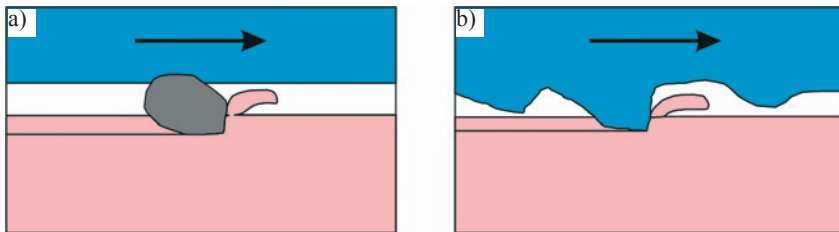


Fig. 9. Abrasive wear scheme for the contact of: a) three bodies, b) two surfaces

Initially, on whole punch circumference the contact with the unleashed silicon steel sheets caused abrasive wear mechanism (Fig. 10). On Figure 10 the punch flank surface after a several thousand cuts was presented. The dark band around the punch circumference shows the changes in the TiN coating structure. The structure changes intensity was observed by using optical equipment after a larger number of cuts.

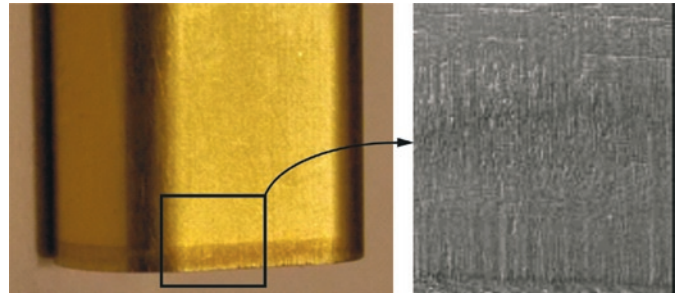


Fig. 10. Punch flank surface after a several thousand cuts ($L_z = 0\%$, M3:2+TiN)

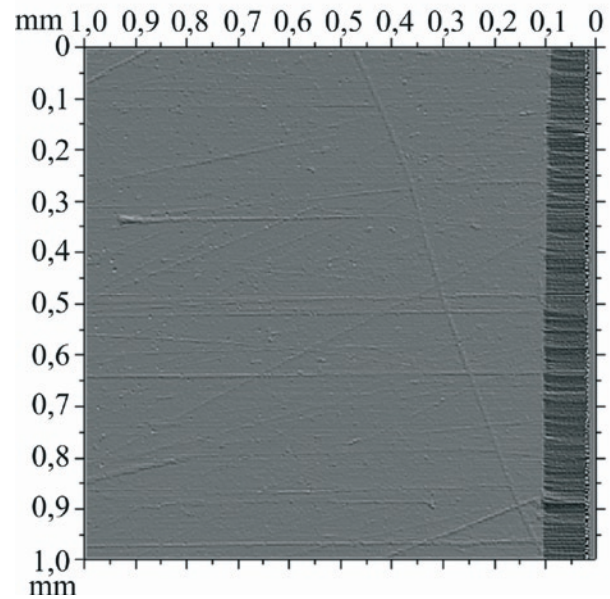


Fig. 11. The image of the punch flank surface close to cutting edge after 500 000 cuts with 8% blanking clearance (M3:2+TiN material)

The M3:2 steel produced by powder sintering technology has a slightly different structure than M2 (Fig. 2). The structure of sintered steel is close-grained structure and homogeneous (right side in Fig. 2). These two materials differ in dependence between yield stress and HRC hardness function (Fig. 3). The steel sintering technology ensures obtaining the austenite fine grain and uniform distribution of carbides in sheet structure, which is impossible to achieve by conventional methods. The M2 steel has a higher ductility, so therefore is more susceptible on grooving damaging. Reduction of this phenomena intensity can be obtained by using titanium nitride coatings. For tools made of M3:2 steel due to the structure refinement abrasive wear and micro-spallings close to cutting edge, which deeply scratch the punch flank surface, were observed (Fig. 11).

The solid inclusion of silicon steel sheet material resulted in punch surface pressure (Fig. 12). After unleashing the silicon steel sheet the contact of hard inclusions in silicon steel sheet with inclusion in punch material was obtained. As a result of cyclical repetition

of this process the gradual degradation of the tools surface with a mixes destruction mechanism occurred (grooving and spalling). The spalling forming scheme was presented in Figure 12. In the case of tools with TiN coatings in certain regions of the tools the microdamages of hard TiN layer were observed (Fig. 13).

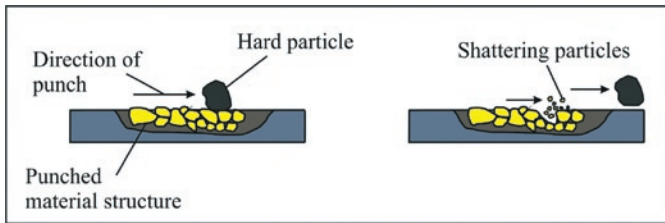


Fig. 12. Contact of the hard inclusion of the punch and sheets, and spalling mechanism

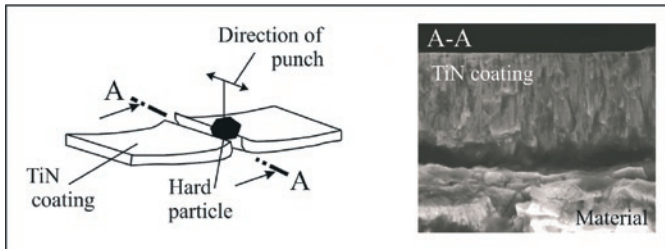


Fig. 13. Delamination between coating and surface caused by the hard inclusion in the sheared blank material

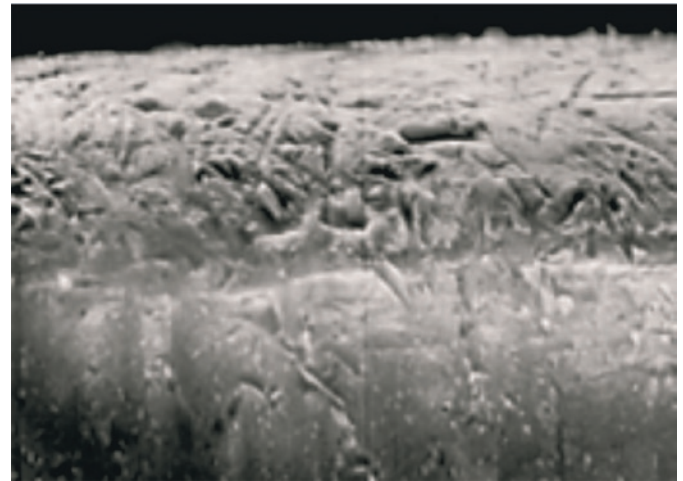


Fig. 15. Cutting edge from the flank side (M2+TiN after 500 000 cuts; x500 zoom; $L_z=8\%$)

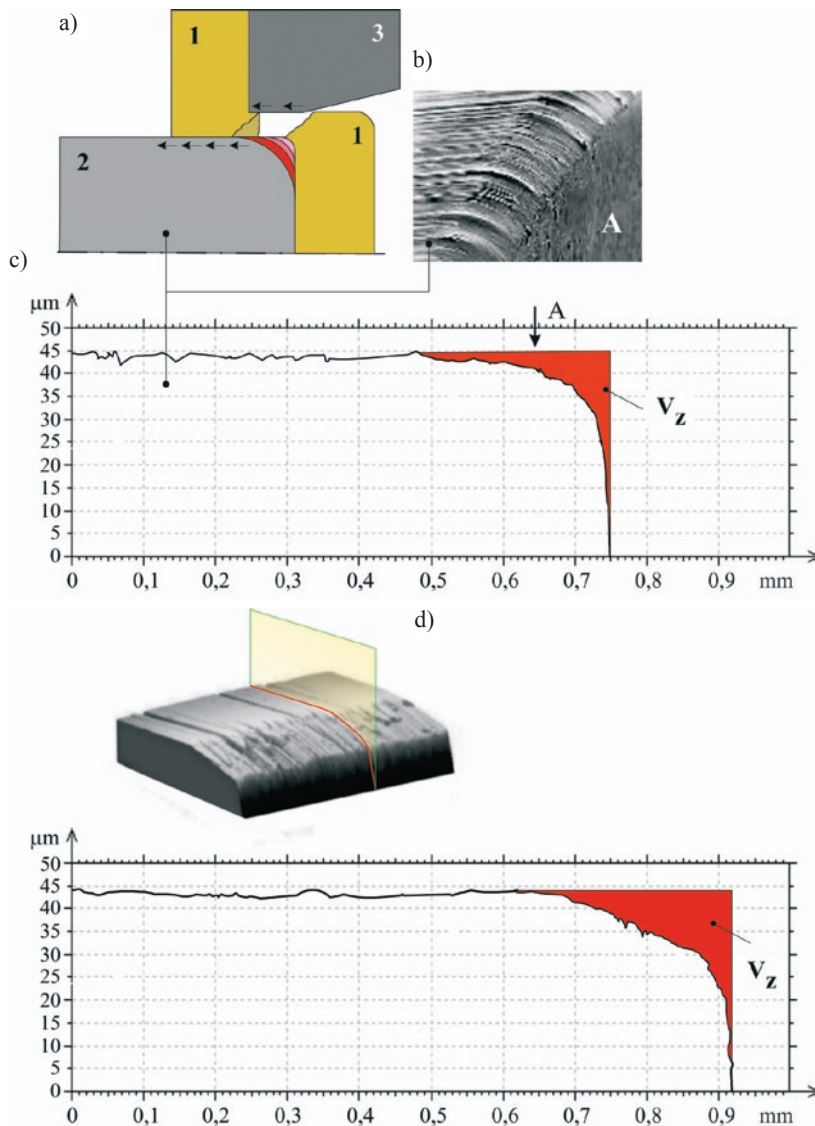


Fig. 14. Tool cutting edge changes after 800 000 cuts: a) conventional wear process (1-sheet, 2-punch, 3-shearing die), b) structure of degradation, c) punch profile for the $L_z=8\%$ clearance; d) punch profile for the $L_z=0\%$ clearance

The tool wear is depended on the blanking process parameters, sheared blanks materials and tools materials. It also depends on the tools protective coatings and the technology of coating manufacturing [21]. All these issues have an influence on the blanking process energy consumption and on the cutting tool wear [3]. For the 800 000 cuts the greatest wear was obtained for the 0% punch-die clearance (Fig. 14). With increasing number of cuts the abrasion product are adhered and moved with the punch movement. In the case of a strong adhesion of coating and adhered particles the TiN layer degradation and punch material unleashing can be obtained (Fig. 15).

The cutting tools topographic zones were scanned by using Taylor Hobson Ltd scanning head. On Figure 16 and 17 some examples of tool surface scanned by 3D scanning head and observed on the scanning microscope were presented.

The sintered steel (M3:2+TiN) was more resistant to wear than the cast steel (M2+TiN). In the case of blanking with the 8% clearance small flank surface wear occurred, the coating was undamaged except a few long grooves. The hard incisions in blanking materials scratched the punch surfaces until the grooves occurred. There were coating spalling, in small zones, which caused the punch material unleashing along the grooves line from the cutting edge (Fig. 17b). The punches made of M3:2 material with the TiN coating had a lower wear than punches made of M2 with coating. After 800 000 cuts on the M3:2+TiN punch flank surface the scratches were observed (Fig. 17b). At the blanking process beginning the TiN layer separation on the cutting edge side may have occurred. For the punches with that damages the wear process is advancing faster and the coating layer loss is increasing. From the front the flank face has wear less than in the case of the 0% blanking clearance. For the blanking process with 0% clearance the front faces wear is greater than the face wear (Fig. 14d). When the blanking process clearance is set to 8% the sheared blanks are deflecting and moving along the punch face. Thus the punch face wear is more intensively (Fig. 14c) and the value of the punch edge radius is increasing. The surface degradation for punch made of M3:2+TiN steel (Fig. 17b) is different than in the case of punch made of M2+TiN steel (Fig. 16b). Similarly case is for the punches made of M3:2(+TiN) with 0% blanking clearance (Fig. 17a). High-speed steel (cast steel) is less

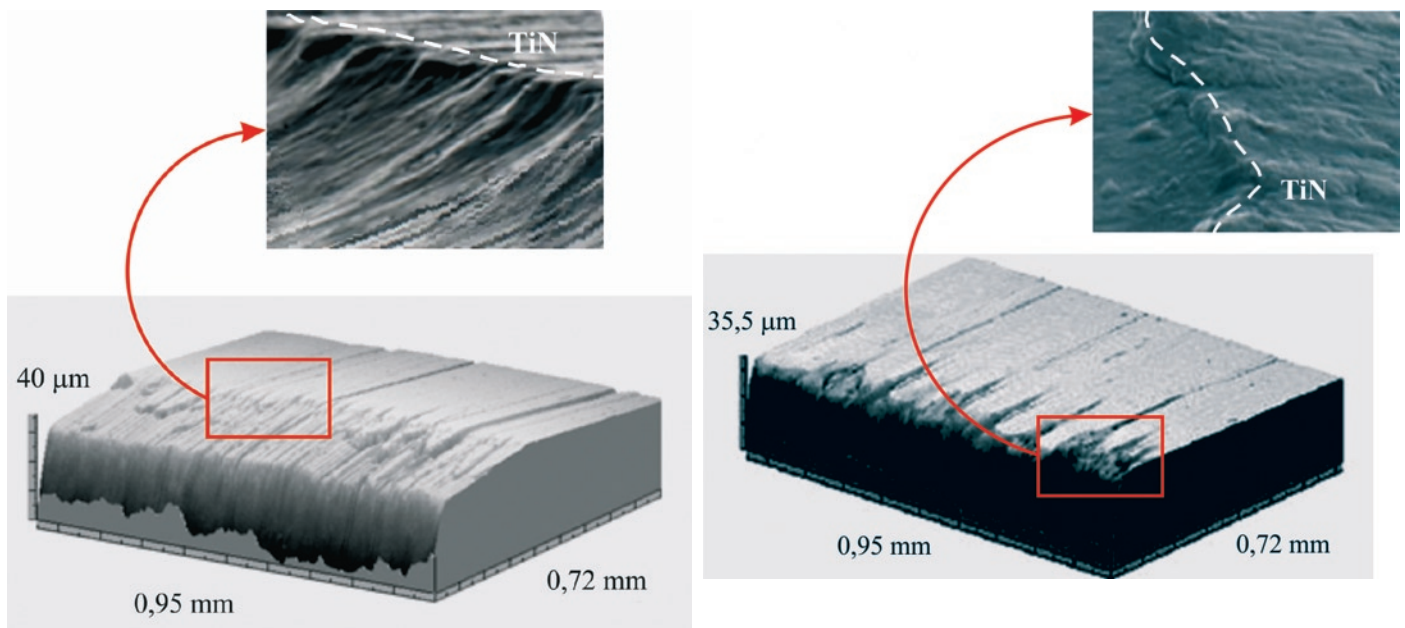


Fig. 16. M2+TiN punch flank surface after 800 000 cuts with blanking clearance: a) 0%, b) 8%

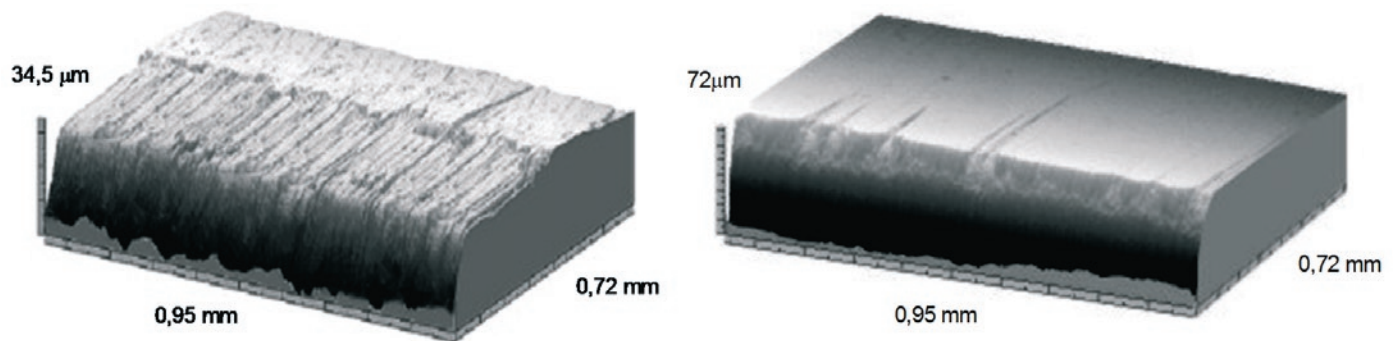


Fig. 17. M3:2+TiN punch flank surface after 800 000 cuts with blanking clearance: a) 0%, b) 8%

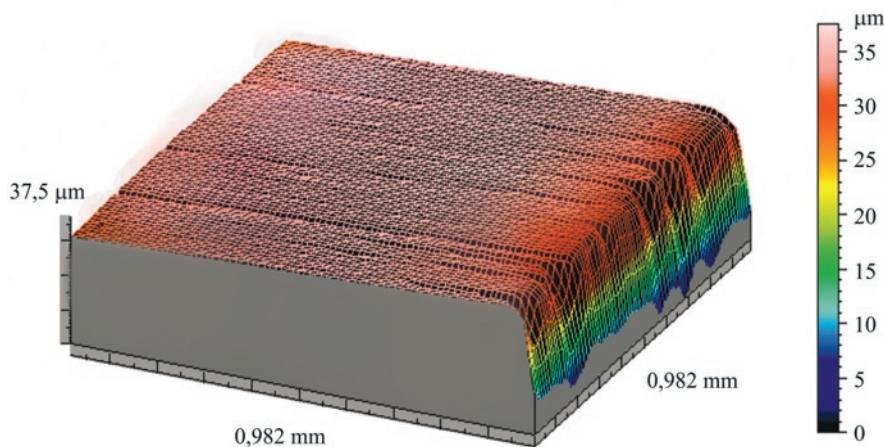


Fig. 18. Cutting edge and punch flank surface after 800 000 cuts with blanking clearance 8% (M2+TiN punch material)

resistant to ridging. After a certain time the coating layer in zones of strong ridging is spalling (Fig. 16 and Fig. 17). The sintered steel with TiN coating is more resistant to the degradation mechanism.

Applying the coating layer on the tool inhibit the surface wear, but the friction process of the unleashed sheet material and punch surfaces caused the TiN layer spalling and unleashing the punch material. Thus, the coating boundary on the punch surface was changing (Fig. 16b). This coating boundary does not have a linear characteristic and it is not a product of TiN wear but it is caused by lower wear resistance of punch material. Unfortunately, the exploitation of punches with coating losses increases the coating destruction process.

The 3,5 mm thickness surface punch, made of the M2 with TiN coating, after 800 000 cuts was presented in Figure 18. Close to the cutting edge on the flank surface the increased wear was observed (in figure the pink-white color: $36 \div 37 \mu\text{m}$). With increasing the distance from the cutting edge the red color becomes more saturated (value of $28 \div 29 \mu\text{m}$). The wear size changes on that surface are a few micrometers. This proves the TiN coating wearing out.

5. Cutting tools geometry influence on the deformation in sheet material

5.1. Microhardness distribution

During the blanking process there was no spalling or tearing of the C6 class coating despite the sheet material deformation. On both straight line (left in Fig. 19) and curved line of intersection (right in Fig. 19) the coating had a structure coherent with the tool natural material.

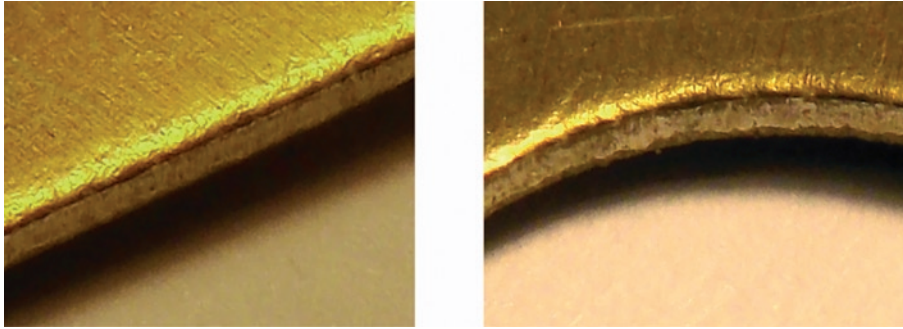


Fig. 19. Silicon steel sheet coating close to the separation surface

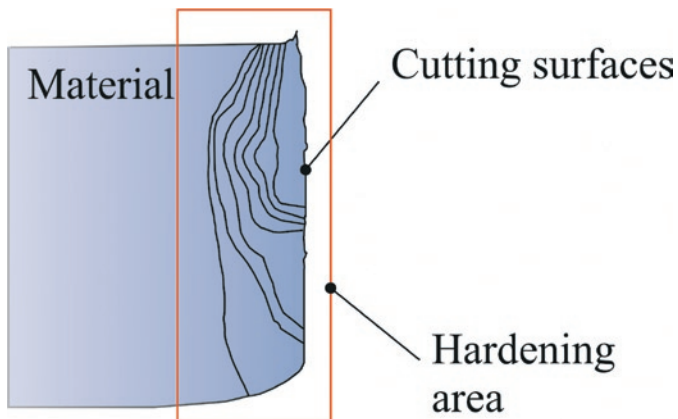


Fig. 20. Test zone of the plastic strain concentration close to the separation surface on the product cross-section

The blanking process with using excessive wear tools is influencing on the size of deformation area in the vicinity of cutting edge. Using indirect method (hardness measurement) the zone of material changes was specified. The hardness was measured by using Matsuzawa Microhardness equipment. Pyramid with 136° apex angle was used as a penetrator. The measurement were carried out at load of 0,1 kg (HV0.1) with the penetration time set up to 10 s. Initial hardness before sheet blanking process was 145 HV0.1 (average from 5 measurements). The distance between measuring point was determined on 0,05 mm. In Figure 20 the location of altered microstructure close to the separation surface, as a result of strong punch wear, was presented. During the blanking process the punch cutting edge and flank surface are wear. Thus, the punch-die clearance is increasing, the shear stress directions are changing in accordance with the theoretical separation surface. The tools geometry changes influence on

the value and size of microhardness changes of the sheet material in vicinity of the cutting line. The hardened layer thickness is related with plastic deformation phase. As the value of plastic deformation is increasing the thickness and hardness increase of strengthened layer is greater.

The maximum increase of material hardness was observed close to the cutting line and more accurately, in the vicinity of the crack initiation (Fig. 21). In all analyzed cross-sections ($1 \div 6$) the deformed sheets microhardness is about 250 HV0.1. Thus, it is 1,72 times greater than the average hardness of undeformed sheets (145 HV0.1). This

hardness increase is determined by large plastic deformations. The material strengthening is so high that the plastic cutting phase is end, and appearing microcracks begin the fracture phase. The microhardness distribution in the vicinity of intersection surface was different for blanking process with 0% and 8% of punch-die clearance. The intensity of punch surface wear influences on the value and zone of the microhardness changes. For clearance close to 0% the zone deformation changes is relatively small (Fig. 21 - 1). It increases with the tool wear (Fig. 21 - 2 and 3). Tool wear during the blanking process significantly increases the zone of plastic strain, and deteriorates the product magnetic properties. In blanking process with 8%

punch-die clearance the zone of plastic deformation (Fig. 21 - 4, 5, 6) is greater than in case with 0% clearance. The vertical dimension of the microhardness changing zone is greater for greater number of sheared blanks. Tool wear changes the punch-die clearance and thus the material fracture zone is increasing. As the punch-die clearance increased the zone of microhardness changes has also increased. The change of clearance form 0% to 8% resulted in almost double enlargement of the hardness changes zone. In the fracture zone a significant hardness increase can be observed, so the volume of material with altered magnetic properties increased.

In the electric motors assembly process it is important that the rotor and stator should be produced as most "packed" block with as small material loss. The burr height is an important issue and it should be relatively small (Fig. 22a). In blanking process with large clearance the elements are produced with larger material loss (Fig. 22b). The material rounding is also high. The strengthening zone and mate-

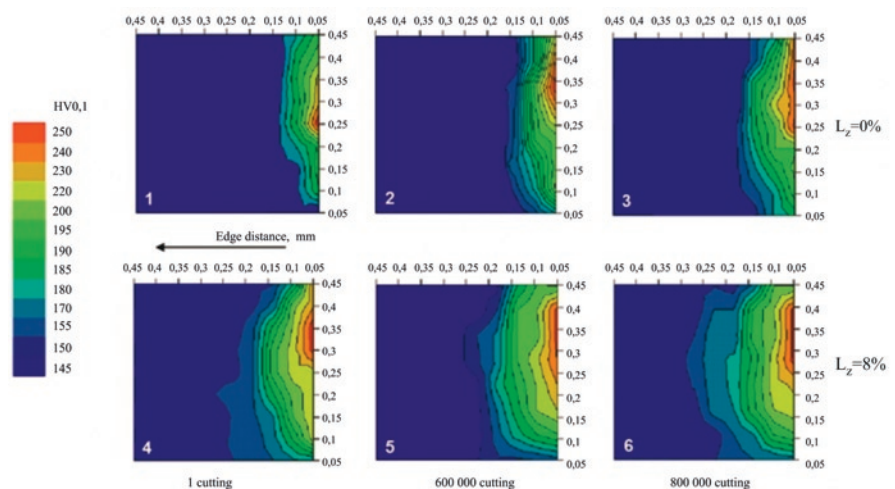


Fig. 21. Microhardness distribution on the part cross-section in vicinity of separation surface for blanking process with $L_z=0\%$ and 8% punch-die clearance after specified number of cuts

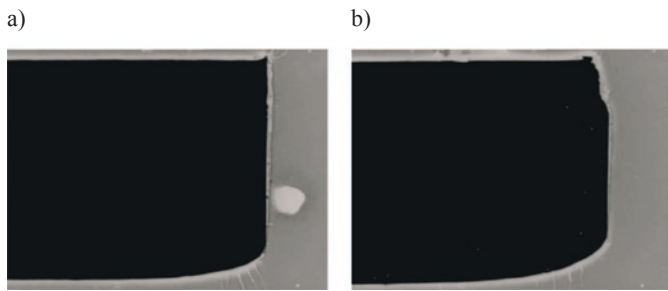


Fig. 22. Part cross-section for initial cuts with blanking clearance a) 0% and b) 8%

rial loss in vicinity of the separation surface deteriorate the magnetic properties of the rotor and stator [15, 20, 25, 31÷33].

5.2. Stress distribution

The FEM analysis of blanking process was made to obtain the influence of the tool geometry changes, as a tool wear results, on the stress distribution at the time of initial material fracturing. The punch displacement was determined in experimental research (Fig. 23) [22]. In simulations the medium stress distributions, which determining the place of fracture initiation, were obtained ($L_z=0\% \rightarrow h_s=0,41$; $L_z=8\% \rightarrow h_s=0,33$).

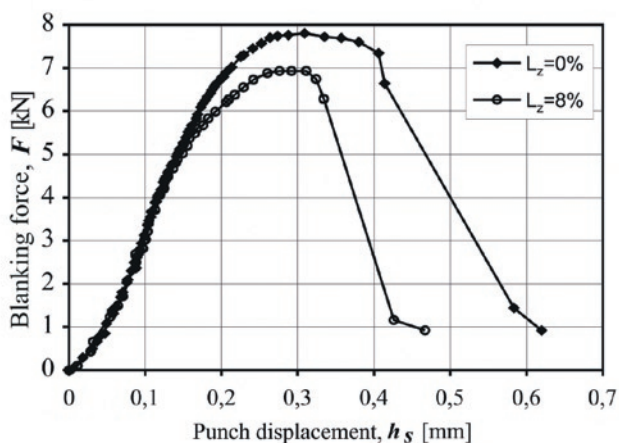


Fig. 23. Force-displacement punch curves during blanking process with different clearance

The blanking process was modeled in MSC. Marc 2010 numerical software. The tool geometry was determined based on the punch wear cutting edge (Fig. 14 and Fig. 24a). The material model was set up as elastic-plastic with non-linear strengthening with parameters: $C = 627$ MPa and $n = 0,18$ (Fig. 1). Other parameters used in numerical simulations were presented in Table 1. The friction coefficient was determined at 0,15. In axial-symmetric model the boundary conditions for the blanking process were defined. The blanking tools were defined as rigid body and the sheet plates as deformable material (Fig. 24b).

The results from the numerical analysis were the same as result from experiment. Due to the blanking tools geometry changes and punch-die clearance changes the stress state and the height of punch penetration before the strengthened material fracture starts are chang-

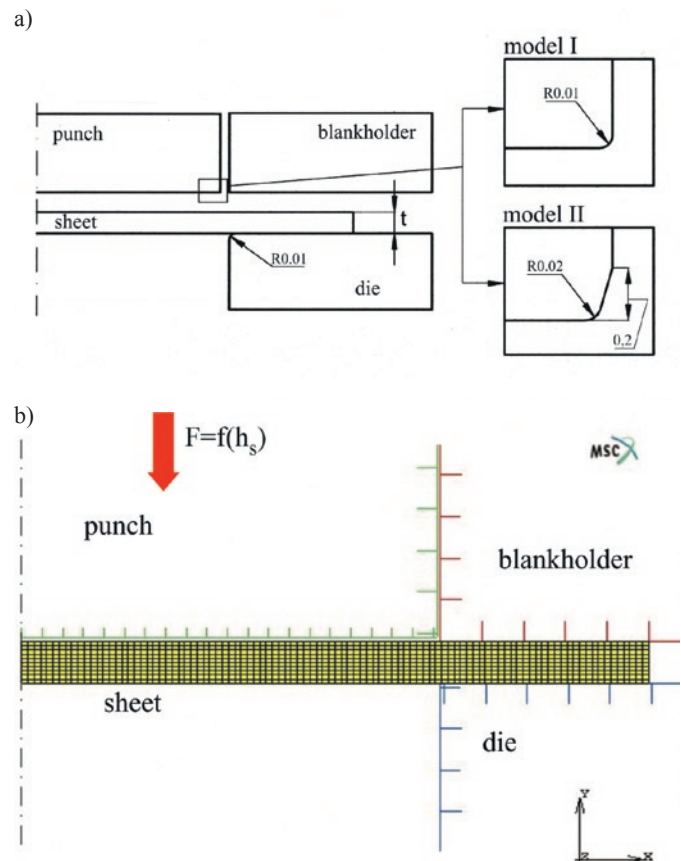


Fig. 24. FEM model assumption: a) punch model variants, b) parts definition

ing (Fig. 25, 26). In the case of sharp-edged tools the stress concentration appeared in the vicinity of punch edge and shearing die (Fig. 25). In simulation of blanking process with using wear punch (model II) the stress concentration with higher value was obtained close to the shearing die edge (Fig. 26). The stress values in the vicinity of punch edge were lower than stress values close to the shearing die edge. Due to the change of the distance between the punch cutting edge and shearing die edge the stress state on the principal directions is changing, so the average stress values are also changing.

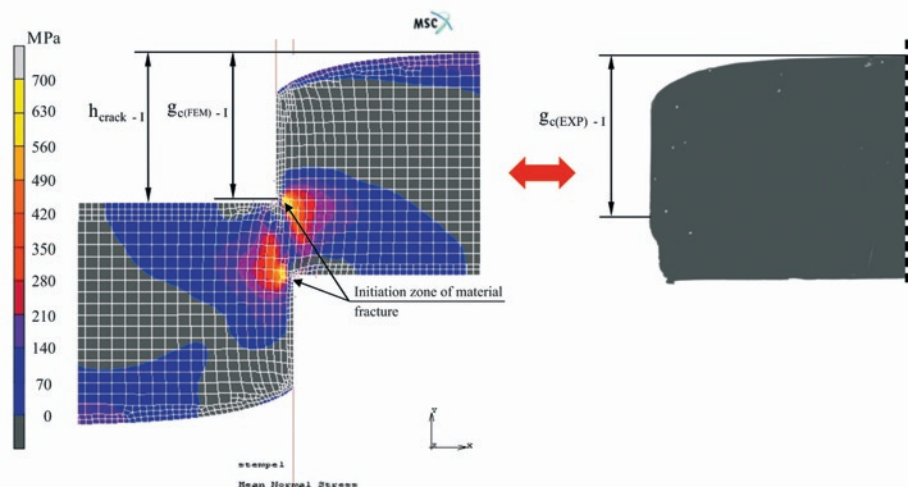


Fig. 25. Average stress distribution at the sheet material fracture phase beginning(a) and the rotor plate cross-section close to the separation surface (b) - ($r_s, r_m = 0,01$ mm, $L_z = 8\%$, at the first cuts; model I)

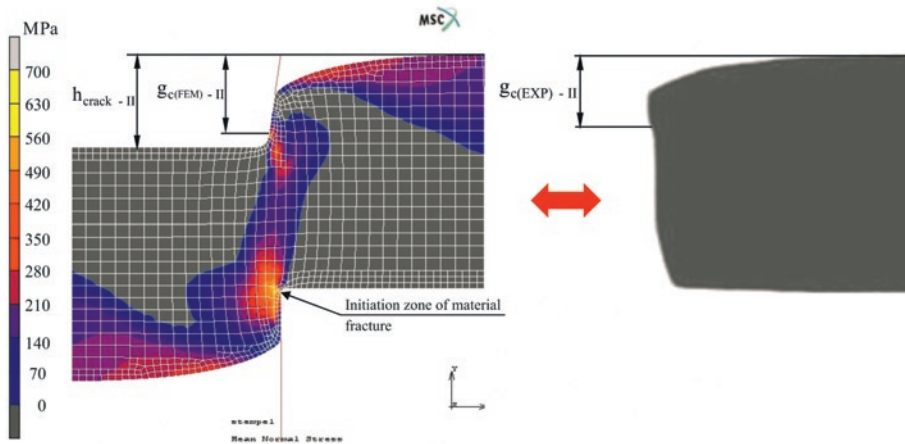


Fig. 26. Average stress distribution at the sheet material fracture phase beginning during the blanking process by punch with determined wear (a) and the rotor plate cross-section close to the separation surface (b) - ($L_z = 0\%$, after 800 000 cuts; II model)

The material and magnetic degradation on the electrical silicon steel sheets edges can not be neglected in the design process of electrical machines. Although, the sheet material magnetic properties changes are less significant for the transformers, but for the electrical machines with rotating magnetic field can result in the greater level of core losses [25, 30].

References

1. ASTM A976 – 13. Standard Classification of Insulating Coatings for Electrical Steels by Composition, Relative Insulating Ability and Application. ASTM International, 2013, pages 5.
2. Bač S., Jaworski J., Stachowicz F.: Durability dependence on cutting tool material in blanking process of generator sheet metal. In: Proceedings Conference Technology' 99, Bratislava, Slovak-Republic, 452, 1999.
3. Chumrum P., Koga N., Premanond V.: Experimental investigation of energy and punch wear in piercing of advanced high-strength steel sheet. International Journal of Advanced Manufacturing Technology, 2015: 79: 1035-1042, <http://dx.doi.org/10.1007/s00170-015-6902-z>.
4. Cheung C.F., Lee W.B., Chiu W.M.: An investigation of tool wear in the dam-bar cutting of integrated circuit packages. Wear, 2000: 237: 274-282, [http://dx.doi.org/10.1016/S0043-1648\(99\)00350-6](http://dx.doi.org/10.1016/S0043-1648(99)00350-6).
5. Emura M., Landgraf F. J. G., Ross W., Barreta J. R.: The influence of cutting technique on the magnetic properties of electrical steels. Journal of Magnetism and Magnetic Materials, 2003: 254-255: 358-360, [http://dx.doi.org/10.1016/S0304-8853\(02\)00856-9](http://dx.doi.org/10.1016/S0304-8853(02)00856-9).
6. Gréban F., Monteil G., Roizard X.: Influence of the structure of blanked materials upon the blanking quality of copper alloys. Journal Materials Processing Technology, 2007: 186: 27-32, <http://dx.doi.org/10.1016/j.jmatprotec.2006.11.226>.
7. Golovashchenko S.: A Study on Trimming of Aluminum Autobody Sheet and Development of a New Robust Process Eliminating Burrs and Slivers. International Journal of Mechanical Sciences, 2006: 48: 1384-1400, <http://dx.doi.org/10.1016/j.ijmecsci.2006.07.007>.
8. Golovashchenko S. F.: Analysis of Trimming of Aluminum Closure Panels. Journal of Materials Engineering and Performance. 2007: 16: 213-219, <http://dx.doi.org/10.1007/s11665-007-9034-2>.
9. Golovashchenko S. F.: Quality of Trimming and its Effect on Stretch Flanging of Automotive Panels. Journal of Materials Engineering and Performance, 2008: 17: 316-325, <http://dx.doi.org/10.1007/s11665-008-9220-x>.
10. Guo W., Tam H.-Y.: Effects of extended punching on wear of the WC/Co micropunch and the punched microholes. International Journal of Advanced Manufacturing Technology, 2012: 9: 955-960, <http://dx.doi.org/10.1007/s00170-011-3567-0>.
11. Hernández J.J., Franco P., Estrems M., Faura F.: Modelling and experimental analysis of the effects of tool wear on form errors in stainless steel blanking. Journal Materials Processing Technology, 2006: 180: 143-150, <http://dx.doi.org/10.1016/j.jmatprotec.2006.05.015>.
12. Hu D.-Ch., Chen M.-H., Ouyang J.-D., Yin L.-M.: Finite element analysis of the thermal effect in high-speed blanking of thick sheet metal. International Journal of Advanced Manufacturing Technology, 2015: 80: 1481-1487, <http://dx.doi.org/10.1007/s00170-015-6954-0>.
13. Jasiński W., Zawada P.: The investigation of discreteness in material of catalytic pipes by the eddy current method. Eksploatacja i Niezawodność - Maintenance and Reliability, 2003: 2: 28-30.
14. Jeong H., Ha J., Hwang J., Lee H., Kim D., Kim N.: A study on the shearing process and the burr formation of zircaloy-4 sheet by using GTN model. International Journal of Precision Engineering and Manufacturing, 2014: 15: 2167-2175, <http://dx.doi.org/10.1007/s12541-014-0578-4>.
15. Kedous-Lebouc A., Cornut B., Perrier J. C., Manfè P., Chevalier T.: Punching influence on magnetic properties of the stator teeth of an induction motor. Journal of Magnetism and Magnetic Materials, 2003: 254-255: 124-126, [http://dx.doi.org/10.1016/S0304-8853\(02\)00803-X](http://dx.doi.org/10.1016/S0304-8853(02)00803-X).
16. Klingenberg W., de Boer T.W.: Condition-based maintenance in punching/blanking of sheet metal. International Journal of Machine Tools and Manufacture, 2008: 48: 589-598, <http://dx.doi.org/10.1016/j.ijmachtools.2007.08.013>.
17. Levy B. S., Van Tyne C. J.: Review of the Shearing Process for Sheet Steels and Its Effect on Sheared-Edge Stretching. Journal of Materials Engineering and Performance, 2012: 21: 1205-1213, <http://dx.doi.org/10.1007/s11665-011-9997-x>.

6. Conclusions

The tools with TiN coating applications in generator sheet blanking process resulted in a significant increasing of the tools durability. It also reduced the zone of the sheet strengthening. The size of punch-die clearance clearly affects the cutting edges wear intensity and the quality of sheared blanks.

- For the $L_z=0\%$ clearance the cutting edge wear is advancing faster, the zone of plastic deformation is reduced and the cutting zone is increased.
- Blanking process with $L_z=8\%$ clearance results in less wear of the punch, but the quality of the separation surface is reduced and the plastic deformation zone is increased.
- The tool wear mechanism depends on the punch-die clearance. For the M530-50A steel sheet in blanking process with 8% clearance the cutting edge rounding was significant increased. And for the 0% clearance the cutting edge rounding was increasing, but also the material losses on the tool flank surface were obtained.
- TiN coating applying on the punch made by M2 and M3:2 steel resulted in increasing of the punch durability during the blanking process with $L_z=0\%$ clearance.

18. Lo S-P, Chang D-Y, Lin Y-Y.: Quality prediction model of the sheet blanking process for thin phosphorous bronze. *Journal of Materials Processing Technology*, 2007: 194: 126-133, <http://dx.doi.org/10.1016/j.jmatprotec.2007.04.110>.
19. Makich H., Carpentier L., Monteil G., Roizard X., Chambert J., Picart P.: Metrology of the burr amount - correlation with blanking operation parameters (blanked material – wear of the punch). *International Journal of Material Forming*, 2008: 1: 1243-1246, <http://dx.doi.org/10.1007/s12289-008-0167-0>.
20. Moses A. J., Derebasi N., Loisos G., Schoppa A.: Aspects of the cut-edge effect stress on the power loss and flux density distribution in electrical steel sheets. *Journal of Magnetism and Magnetic Materials*, 2000: 215-216: 690-692, [http://dx.doi.org/10.1016/S0304-8853\(00\)00260-2](http://dx.doi.org/10.1016/S0304-8853(00)00260-2).
21. Mubarak A., Akhter P., Hamzah E., Radzi M., Toff M.R.H.J.M., Qazi I. A.: Effect of coating thickness on the properties of tin coatings deposited on tool steels using cathodic arc pvd technique. *Surface Review and Letters*, 2008: 4: 401-410, <http://dx.doi.org/10.1142/S0218625X08011524>.
22. Mucha J., Stachowicz F.: Effect of clearance of blanking of generator sheets - experimental investigation and numerical simulation. *Acta Mechanica Slovaca*, 2004: 8: 301-306.
23. Mucha J.: An effect of selected parameters on shearability of the EP-530-50A. *Rudy i Metale Nieżelazne*, 2004: 1: 23-26 (in Polish).
24. Mucha J.: The analysis of selected material suitability for tools used for blanking the commutator motor elements. In: *Proceedings 9th International Scientific Conference, Applied Mechanics*, Ostrawa, VŠB—Technical University of Ostrawa, Czech Republic, 171–172, 2007.
25. Oka M., Kawano M., Shimada K., Kai T., Enokizono M.: Evaluation of the Magnetic Properties of the Rotating Machines for the Building Factor Clarification. *Przegląd Elektrotechniczny*, 2011: 9b: 43-46.
26. PN-EN 10106:2016-01. Taśmy i blachy stalowe elektrotechniczne o ziarnie niezorientowanym walcowane na zimno, dostarczane w stanie w pełni przetworzonym. PKN, 2016, stron 24.
27. Ponnaluri S.V., Cherukuri R., Molian P. A.: Core loss reduction in grain-oriented silicon steels by excimer laser scribing. Part I: experimental work. *Journal of Materials Processing Technology*, 2001: 112: 199-204, [http://dx.doi.org/10.1016/S0924-0136\(01\)00573-8](http://dx.doi.org/10.1016/S0924-0136(01)00573-8).
28. Raulea LV, Goijaerts AM, Govaert LE, Baaijens FPT (2001) Size effects in the processing of thin metal sheets. *J Mater Process Technol* 115:44–48, [http://dx.doi.org/10.1016/S0924-0136\(01\)00770-1](http://dx.doi.org/10.1016/S0924-0136(01)00770-1).
29. Slavic J., Bolka S., Bratus V., Boltezar M.: A novel laboratory blanking apparatus for the experimental identification of blanking parameters. *Journal of Materials Processing Technology*, 2014: 214: 507-513. <http://dx.doi.org/10.1016/j.jmatprotec.2013.10.006>
30. Tekiner Z., Nalbant M., Gürün H.: An experimental study for the effect of different clearances on burr, smooth-sheared and blanking force on aluminium sheet metal. *Materials and Design*, 2006: 27: 1134-1138, <http://dx.doi.org/10.1016/j.matdes.2005.03.013>.
31. Wilczyński W.: Influence of magnetic circuit production for their magnetic properties. *Journal of Materials Science*, 2003: 38: 4905-4910, <http://dx.doi.org/10.1023/B:JMSC.0000004412.94057.47>.
32. Yashiki H., Kaneko T.: Effect of alloying elements on response of nonoriented electrical steels to stamping operations. *Journal of Materials Engineering and Performance*, 1992: 1: 29-34, <http://dx.doi.org/10.1007/BF02650029>.
33. Żurek Z. H., Kurzydłowski K. J., KUKLA D., BARON D., Material Edge Conditions of Electromagnetic Silicon Steel Sheets. *Przegląd Elektrotechniczny*, 2013: 2b: 112-115.

Jacek MUCHA

Rzeszow University of Technology
Department of Mechanical Engineering
al. Powstańców Warszawy 8
35-959 Rzeszów, Poland

Jan JAWORSKI

Rzeszow University of Technology
Department of Manufacturing Processes and Production Engineering
al. Powstańców Warszawy 8
35-959 Rzeszów, Poland

E-mails: j_mucha@prz.edu.pl, jjktmiop@prz.edu.pl

Stanisław KRUCZYŃSKI
Marcin ŚLĘZAK
Wojciech GIS
Piotr ORLIŃSKI

EVALUATION OF THE IMPACT OF COMBUSTION HYDROGEN ADDITION ON OPERATING PROPERTIES OF SELF-IGNITION ENGINE

OCENA WPŁYWU SPALANIA DODATKU WODORU NA WŁASNOŚCI EKSPLOATACYJNE SILNIKA O ZAPŁONIE SAMOCZYNNYM*

The work presents the results of effect of the addition of hydrogen in an amount up to 9% of mass of diesel oil into the intake system of Perkins1104C-E44TA engine. The impact of hydrogen addition on process heat release in the combustion chamber and the concentration of CO, THC, NOX and PM in the exhaust at predetermined engine operating conditions. It was summarised that the analysis of the results does not justify the use of hydrogen as a fuel additive in self-ignition engines.

Keywords: IC engines, hydrogen, diesel, heat emission.

W pracy przedstawiono wyniki badań wpływu dodatku wodoru w ilości do 9% masy oleju napędowego do układu dolotowego silnika Perkins1104C-E44T. Oceniono wpływ dodatku na proces wydzielania ciepła w komorze spalania i stężenia CO, THC, NOX i PM w spalinach w ustalonych warunkach pracy silnika. W podsumowaniu stwierdzono iż analiza wyników badań nie uzasadnia stosowania wodoru jako dodatku do paliwa w silnikach o zapłonie samoczynnym.

Słowa kluczowe: silniki spalinowe, wodór, olej napędowy, wydzielanie się ciepła.

1. Introduction

Fuelling hydrogen internal combustion engines (HYICE) with hydrogen is presently the subject matter of numerous research & development works. According to paper [5] it is a temporary solution before projected fuel cells are implemented, which aims to prepare for and put into operation hydrogen storage and distribution infrastructure. Mainly spark-ignition engines are adapted for hydrogen fuelling but it is also possible to adjust self-ignition engines for hydrogen fuelling.

Hydrogen supply IC engine fuel should be considered depending on the type of diesel cycle:

1. The use of hydrogen alone or as an addition to gasoline or LPG and methane in spark-ignition engines;
2. The use of hydrogen as an addition to diesel oil in self-ignition engines.

1.1. Hydrogen in spark-ignition engines.

An analysis of the impact of hydrogen used as basic fuel [3, 4] proved that:

- it is possible to achieve efficiency at a level similar or higher than in case of a conventional engine fuelled with gasoline with limited engine power;
- high emission of nitrogen oxides in exhaust (fuel contains no carbon compounds producing toxic substances).

An analysis of impact of use of hydrogen as an addition to hydrocarbon fuel [1, 8, 13, 15] proved that:

- it is possible to achieve efficiency similar to that of a conventional engine fuelled with gasoline with slightly limited engine power,
- CO and HC emissions decrease, whereas the emission of NO_x increases and thermal efficiency grows when poor mixtures are used.

Hydrogen IC engines are based on the technology of spark ignition piston engines and after some modifications may be used fuelled both with conventional fuels as well as with hydrogen [5].

In the papers [3, 4], authors refer to pre-ignition hydrogen as one of the main problems in applying hydrogen in piston engines with spark ignition.

According to the authors the basic causes for pre-ignition include:

- low energy of hydrogen ignition (0,02 mJ),
- wide range of combustion limits 4%–75% v/v,
- small critical distance for flame propagation.

As regards the effects of pre-ignition the authors point to:

- lower efficiency of engine,
- engine roughness work,
- possibility that flame moves to the inlet duct.

Because small gasoline engines operate with a slightly richer mixture and do not have a catalytic reactor, their fuel consumption and emissions are very high. When gasoline engines are fuelled with hydrogen only, emission of NO_x increases and the flame often retreats to the inlet system [8].

(*) Tekst artykułu w polskiej wersji językowej dostępny w elektronicznym wydaniu kwartalnika na stronie www.ein.org.pl

Paper [1] presents results of studies of a 6-cylinder, spark-ignition engine type MAN E2876 LE302 intended for a power generator and as a standard fuelled with natural gas and hydrogen alternatively. The studies were carried out at a fixed rotational speed of 1500 rotations per minute and variable engine load. Those conditions correspond to the work of the engine in a power-generator. Parameters of the engine that had to be adjusted to hydrogen fuelling included in particular the angle of ignition advance and air fuel ratio.

Compared to natural gas fuelling, when fuelling engine with hydrogen the concentration of carbon oxide and hydrocarbons was minor and resulted mainly from the combustion of lubricating oil. However, a small increase concentration of nitrogen oxides was recorded only in conditions of load close to maximum. In both cases general engine efficiency is high and when fuelled with natural gas its maximum value is approx. 42%, whereas when fuelled with hydrogen it came to c.a. 37%.

In paper [15] the study addressed the impact of hydrogen addition to gasoline on the value of average effective pressure, engine work efficiency, efficiency filling of cylinders and emission characteristics. The results of the studies proved that fuel consumption and average effective pressure had been decreased through of hydrogen addition. The results of studies also showed that thermal efficiency of the engine was greater than in case of gasoline combustion. Furthermore, HC and CO emissions dropped owing to the use of hydrogen addition.

The results of studies presented in the paper [13] regarding impact of combusting hydrogen addition to gasoline compared to the combustion of gasoline in spark-ignition engines lead to the following conclusions:

- the engine was found working stably on poor mixtures,
- with the hydrogen addition the engine power increased,
- the unit consumption of fuel decreased and the level of HC and CO emissions lowered,
- higher level of NO_x emission was observed, especially when combusting mixtures within the range of $\lambda = 1 - 1,4$,
- with quality adjustment of the engine power, the emission of NO_x can be lowered.

Paper [10] addresses the possibility of combusting poor mixtures by adding hydrogen to a spark-ignition engine fuelled with methane. The following hydrogen additions of 10%, 30% and 50% of methane's volume were used. The results of the study show that the limit of combustion of poor mixtures may be moved towards poor mixtures by adding hydrogen, in particular in greater engine load. The impact of engine's rotational speed on the said limits is much lower. The angle of ignition advance also has impact on the limits of combustion of poor mixtures but both excessive delays as well as ignition lead is not recommended.

Paper [12] presents the results of studies conducted in ENEA laboratories, which aimed to identify potential possibilities of using mixtures of natural gas and hydrogen (known as HCNG or Hythane) in the used motor vehicles. The Iveco Daily CNG delivery van was tested, adapted to spark ignition and stoichiometric fuelling of engine with methane in ECE15 cycle, comparing levels of emission when fuelling the engine with methane with the results achieved when fuelling the engine with hydrogen and methane mixtures when combusting mixtures both stoichiometric and poor.

It was found that optimal conditions of HCNG combustion can be achieved by applying – depending on the conditions of engine's operation – both the combustion of poor mixtures in order to reduce fuel consumption and the combustion of stoichiometric mixtures in order to reduce emission of harmful substances. Effective combustion of poor mixtures requires – however – optimisation of compression ratio and charging of the engine, the angle of ignition advance and the share of hydrogen in the mixture mainly because of decreased engine

power due to lower content of energy in the volume of HCNG mixture (11% in case of a mixture with 15% of hydrogen in its volume).

Summarising, the analysis of results of studies justifies the use of hydrogen as a fuel addition in spark-ignition engines provided that significant changes in the engine construction are introduced, mainly by using hydrogen injection to the combustion chamber while at the same time combusting poor mixtures at low engine load and stoichiometric mixtures with full engine load. It is necessary to introduce a system eliminating NO_x in combustion gases, e.g. SCR system.

1.2. Hydrogen in self-ignition engines.

Hydrogen in a self-ignition engine may be used only as an addition to diesel oil or biodiesel [8] as it has poor self-ignition properties and as such cannot be used alone in this type of engine. Studies conducted at the Poznań University of Technology in the Institute of IC Engines and Transport [2] show that hydrogen addition of 5% ÷ 7% m/m to the combustion chamber has no greater impact on engine performance but it does result in increased CO and PM emissions.

According to a study conducted in Vilnius Gediminas Technical University (VGTU) stated that smokiness decreases with the additional deployment of hydrogen. Other indicators of the exhaust gas using the hydrogen in case of the rig tests are worse [7]. Similar opinions contained in [6, 11, 14].

Because of its properties hydrogen is better predisposed to fuelling of spark-ignition engines than self-ignition engines. However, because of high calorific value, the possibility of limiting the emission of toxic substances, attempts were made to fuelling of self-ignition engines with hydrogen [17]. Those studies focused on hydrogen added to fuel because hydrogen has poor self-ignition properties and as such cannot in this type of engine be used as the only fuel. Table 1 presents a comparison of chosen properties of diesel oil and hydrogen.

Table 1. Comparison of properties of diesel oil and hydrogen [9]

Property	Unit	ON	Hydrogen
Density	kg/m ³	840	0,0824 ÷ 0,0838
Lower calorific value	MJ/kg	42,49	119,81
Flame ratio	m/s	0,3	1,85 ÷ 1,9
Cetane number	-	45 ÷ 55	-
Self-ignition temperature in air	°C	280	585
Carbonisation residue	-	0,1	0,0

The impact of hydrogen on the combustion process in self-ignition engines is similar as the impact described earlier on spark-ignition engines (low calorific value vs volume, decrease in the emission of toxic carbon compounds, high flame speed).

Current studies [9] show that depending on the quantity of the added hydrogen thermal efficiency of the engine drops, increases the delay of self-ignition and promptness in increasing pressure in the cylinder (self-ignition of the mixture occurs later while the combustion of the mixture is faster). Increased temperature leads to increase in the concentration of nitrogen oxides, but noticeable is considerable drop in the emission of carbon compounds.

The subject of the paper [2] comprised an analysis of the possibility of improving environmental friendly indicators in self-ignition engine AVL 5804 bi-fuelled with diesel oil with hydrogen addition). Bi-fuelling provided hydrogen to the inlet channel and a self-ignition dose of the diesel oil was used, each time defined for a particular load and rotational speed as a source of ignition of the hydrogen air mixture.

Fuelling the engine with diesel oil with hydrogen addition delivered to the inlet duct caused an apparent change in thermo-dynamic and ecological indicators, i.e.:

- maximum reduction of the speed in pressure growth $dp/d\alpha$ by approx. 5% and the value of the maximum pressure in the combustion chamber by approx. 6%,
- increase in the concentration of carbon oxide by approx. 150%,
- decrease in the concentration of nitrogen oxides by approx. 25%,
- decrease in the concentration of non-combusted hydrocarbons by approx. 300%,
- increase in the concentration of particles by approx. 150%.

The aim of this work was to evaluate – through tests – the impact of hydrogen addition in diesel oil on the process of heat release and concentration of harmful substances in self-ignition engines.

2. Test stand

Tests were carried out on Perkins 1104C-E44T engine with eddy current brakes Schenck WM 400 controlled with controller Schenck X-ACT. The apparatus for measuring indicated pressure and analysing thermal emission consisted of AVL INDISMAST system for engine indication and a position sensor for crankshaft AVL 365C01. Data had been sent to a PC in real time. With IndiCom software it was possible to view incoming data (also in real time), to record a cycle of 50 measurements and to save the files together with parameters of the tested engine.

Thereafter, the resulting data had been subject to processing with the use of AVL Concoerto. The said programme averaged changes of pressure in the cylinder and calculated the rate heat release without taking into account heat loss to cylinder walls (net heat emission). Moreover, during the tests CO, THC and NO_x concentration were recorded with the use of AVL CEB2 combustion gases analyser, equipped with PROVIT 5600 control panel. Measurements of the concentration PM had been estimated with AVL 415. The engine was fuelled with diesel oil (PKN Orlen) and hydrogen addition under pressure 150 bar in cylinder.

Diesel oil consumption was measured with a volume method, whereas the quantity of hydrogen after the reduction of its pressure was gauged with a specially marked rotameter. Hydrogen was delivered before the turbine to the engine's inlet system. Technical data of the engine are presented in table 2 and the test stand overview is shown (Fig. 1).

Table 2. Technical parameters of Perkins 1104C-E44T engine

Parameter	Unit	Value
Effective power	kW	74,5
Compression ratio	[-]	18,2
Cylinder diameter	mm	105
Piston stroke	mm	127
Engine displacement	dm ³	4,4
Number and cylinders, system	[-]	4, stroke
Fuelling system	[-]	Direct injection
Recharge	[-]	Yes; turbocharger

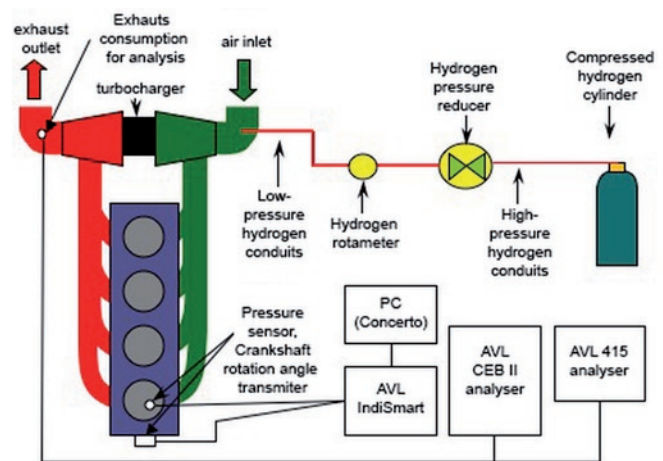


Fig. 1. Diagram of bench with diagram of engine Perkins 1104C-E44TA

3. Results of studies

The studies were conducted with a fixed rotational engine speed of $n = 1100$ rotations per minute and diesel oil in a quantity equal to torque developed by the engine at the level of $M = 165$ Nm. Hydrogen was equal to 8.9% of the mass of diesel oil by decreasing the quantity of diesel oil gradually together with the increase of hydrogen addition in order to achieve torque of approx. 165 Nm. The results of pressure measurement in the combustion chamber and the results of calculations of rate of heat release in an engine fuelled with diesel oil only and diesel oil and a hydrogen addition of 5.5% and 8.9% are presented (Fig. 2, Fig. 3) respectively.

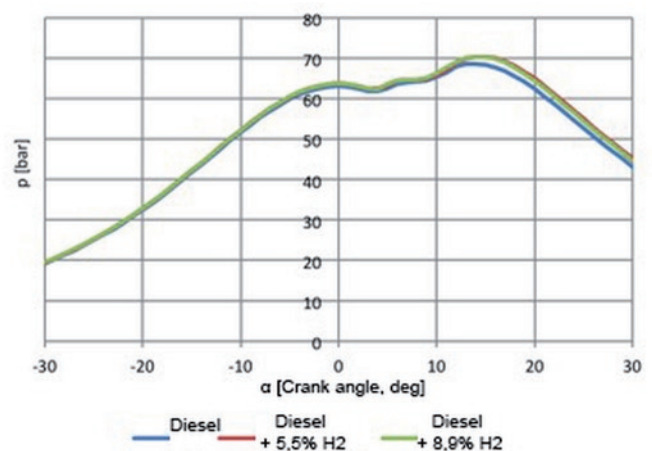


Fig. 2. An indicator diagram $p = f(\alpha)$ with the engine in the conditions of $n = 1100$ r/min, $M = 164$ Nm powered diesel and diesel with the addition of 5.5% H₂ and 8.9% H₂

Then again, the results of measurements of CO concentration using method NDIR, THC with FID method and NO_x with CL method and PM mass concentration with the filter method in an engine fuelled with diesel oil and diesel oil with hydrogen addition are presented below (Fig. 4, Fig. 5).

4. Analysis of results of tests and conclusions

Hydrogen addition did not influence definitely essential differences in the combustion process. A slight change in the character of pressure curves in the combustion chamber was noted (increase of maximum combustion pressure by approx. 2%). The curves of rate of heat release show a classic kinetic and diffusion phase depending on fuel type. The kinetic phase remained almost identical, whereas

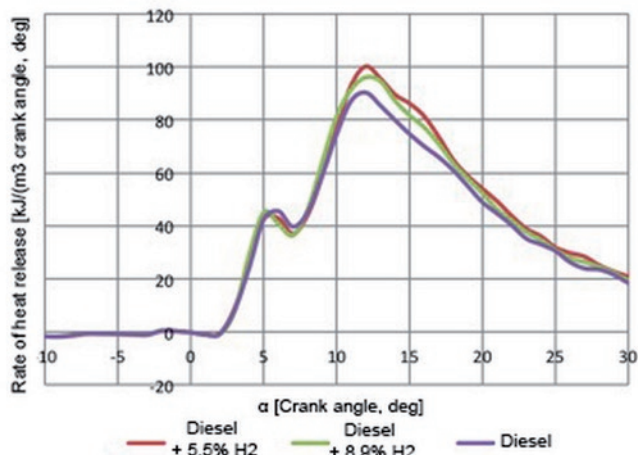


Fig 3. The rate of heat release as a function of crank angle with engine operating conditions of $n = 1100 \text{ r/min}$, $M = 164 \text{ Nm}$ powered diesel and diesel with the addition of 5.5% H_2 and 8.9% H_2

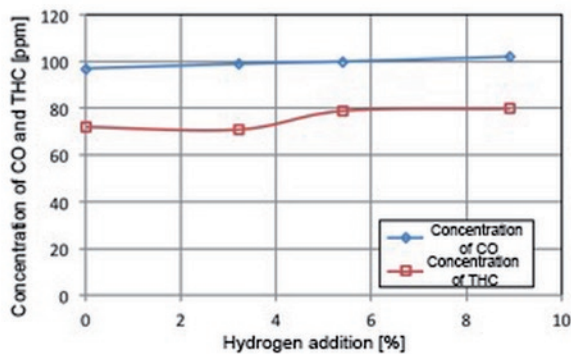


Fig 4. The results of the measurement of concentrations of CO and THC depending on the hydrogen addition with the engine supplied with diesel oil with additions of hydrogen

during the diffusion phase of rate of heat release increased by approx. 10%, most likely due to hydrogen combustion. Key parameters of the combustion process (self-ignition knock, character of respective combustion phases) remained unchanged after hydrogen addition was applied.

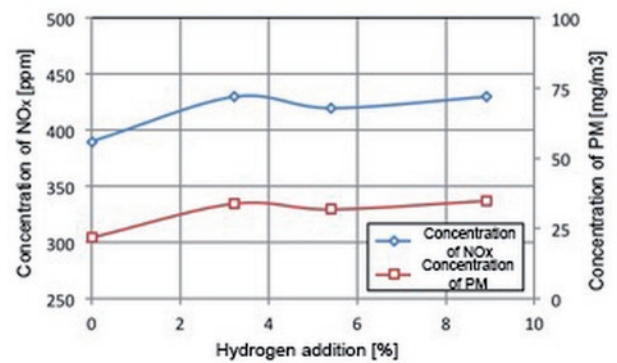


Fig 5. The results of measurements of concentrations of NO_x and PM depending on the compactness of hydrogen addition measured when the engine supplied with diesel oil with additions of hydrogen.

The results of measurements of concentration of toxic substances did not prove theories regarding the improvement of those indicators. The analysis of the impact of hydrogen addition in the inlet system of a self-ignition engine proved slight increase in the levels of all analysed constituents of exhaust (i.e. carbon oxide, hydrocarbons, nitrogen oxides and PM). Increase in CO and THC levels may stem from high reactivity of hydrogen inhibiting the oxidation of hydrocarbons as a result of which THC and PM levels increase. The increase in NO_x levels may result from increased temperature in the combustion chamber due to hydrogen addition.

The basic importance to sensible operation of technical object is the knowledge of its failures. Failure, understood as a limiting state of object can be dangerous for human life or/and does financial losses [16]. The ability of object to fulfil required function is called dependability. It covers some features of object as follows: availability, reliability, maintainability, safety, service and durability. The durability is an important tie in dependability chain [16].

Durability prediction of engine is done for example of piston rings for hydrogen fuelling engine [16]. According to [16] for hydrogen fuelling engine it can be expected faster wearing of piston rings than for petrol. The importance of fuel effect on engine durability belongs to calorific value and elementary composition of fuel first of all [16], in diesel engines too.

Summarising, the analysis of results of the studies does not justify the use of hydrogen as a fuel addition in self-ignition engines.

References

1. Brzeżański M, Mareczek M, Marek W, Papuga T. Określenie parametrów ekologicznych stacjonarnego silnika spalinowego zasilanego różnymi paliwami. Zeszyty Naukowe Instytutu Pojazdów 2014; 1(97): 101-108.
2. Daszkiewicz P. Badania możliwości poprawy wskaźników ekologicznych silników o zapłonie samoczynnym zasilanych paliwami konwencjonalnymi z domieszką wodoru. Praca doktorska 2014; 1-123.
3. Deczyński J, Żółtowski B. Wodór jako paliwo alternatywne do zasilania silników ze spalaniem wewnętrznym. Studies & Proceedings of Polish Association 2014; (69): 19-31.
4. Doppler M. Rozwój i przyszłość napędu hybrydowo-wodorowego dla samochodów. Akademia Górniczo-Hutnicza 2005; 1-7.
5. HYICE Result in Brief 2015; 1-4.
6. Jarunthammachote S, Chuepeng S, Chaisermatwan P. Effect of hydrogen addition on diesel engine operation and NOX emission: A thermodynamic study. Am. J. Applied Sci. 2012; (9): 1472-1478.
7. Keršys A, Kilinskas D, Pukalaskas S, Vilkauskas A, Keršys R, Makaras R. Investigation of the Influence of Hydrogen Used in Internal Combustion Engines on Exhaust Emission. Eksploatacja i Niezawodność – Maintenance and Reliability 2013; 15 (4): 384-389.
8. Kosar M, Ozdalyan B, Celik M B. The Usage of Hydrogen for Improving Emissions and Fuel Consumption in a Small Gasoline Engine. Journal of Thermal Science and Technology 2011; 31(2): 101-108.
9. Lejda K. Wodór w aplikacjach do środków napędu w transporcie drogowym, Wydawnictwo KORAW 2013; 1-169.
10. Ma F, Wang Y. Study on the extension of lean operation limit through hydrogen enrichment in a natural gas spark ignition engine. International Journal of Hydrogen Energy 2008; (33): 1416-1424, <http://dx.doi.org/10.1016/j.ijhydene.2007.12.040>.
11. Miyamoto T, Hasegawa H, Mikami M, Kojima N, Kabashima H. Effect of hydrogen addition to intake gas on combustion and exhaust

- emission characteristics of diesel engine. International Journal of Hydrogen Energy 2011; (36): 13138-13149, <http://dx.doi.org/10.1016/j.ijhydene.2011.06.144>.
12. Ortezi F, Chiesa M, Conigli F. Experimental Tests of Blends of Hydrogen and Natural Gas in Light Duty Vehicles. HYSYDAYS - 2nd World Energy Systems 2007; 1-11.
 13. Rusu E, Pana C, Negurescu N. Experimental Study of a Spark Ignition Engine Fueled with Gasoline and Hydrogen in Addition. U.P.B. Sci. Bull., Series D 2013; 75(4): 127-136.
 14. Saravanan N, Nagarajan G. Performance and emission studies on port injection of hydrogen with varied flow rates with Diesel as an ignition source. Applied Energy 2010; (87): 2218-2229, <http://dx.doi.org/10.1016/j.apenergy.2010.01.014>.
 15. Shivaprasad K V, Raviteja S, Chitrakar P, Kumar G N: Experimental Investigation of the Effect of Hydrogen Addition on Combustion Performance and Emissions Characteristics of a Spark Ignition High Speed Gasoline Engine. Procedia Technology 2014; (14): 141-148.
 16. Sroka Z. Durability of engine components due to alternative fuels. Eksploatacja i Niezawodność - Maintenance and Reliability 2007; (4): 9-15.
 17. Strykała J. Wodór jako paliwo, Wydawnictwa Naukowo-Techniczne 2008; 1-177.

Stanisław KRUCZYŃSKI

Marcin ŚLĘZAK

Wojciech GIS

Motor Transport Institute

ul. Jagiellońska 80, 03-301 Warsaw, Poland

Piotr ORLIŃSKI

Institute of Vehicles of the Warsaw University of Technology

ul. Narbutta 84, 02-524 Warsaw, Poland

E-mails: stanislaw.kruczynski@its.waw.pl, marcin.slezak@its.waw.pl,
wojciech.gis@its.waw.pl, p.orlinski@simr.pw.edu.pl

Tadeusz DZIUBAK

THE EFFECTS OF DUST EXTRACTION ON MULTI-CYCLONE AND NON-WOVEN FABRIC PANEL FILTER PERFORMANCE IN THE AIR FILTERS USED IN SPECIAL VEHICLES

WPŁYW ODSYSANIA PYŁU NA CHARAKTERYSTYKI MULTICYKLONU I WŁÓKNINOWEJ PRZEGRODY FILTRACYJNEJ FILTRU POWIETRZA POJAZDU SPECJALNEGO*

Common impurities found in the inlet air to the internal combustion engine of motor vehicles are characterized. Dust concentrations in the air were analysed for different operating conditions of a motor vehicle. It is shown that the most common and the most harmful air impurity for the technical machinery is a mineral dust from roads. The benefits of using the inertial filter (multi-cyclone) as a first stage of air filtration, including extended engine life are presented. The methods of dust extraction from a dust collector of the air filter multi-cyclone are shown. The necessity of regular ejection dust extraction from the multi-cyclone dust collector is shown. A dust extraction rate m_0 is defined and its effects on the cyclone separation efficiency and flow resistance are shown. The test method and the test conditions for a two-stage filter in multi-cyclone - non-woven fabric filter element configuration are developed. The characteristics of the separation efficiency and flow resistance of the cyclone and the non-woven fabric filter were determined as a function of dust mass supplied with the inlet air to the two-stage filter for three different extraction rates and without dust extraction from the multi-cyclone dust collector. The separation efficiency and flow resistance were determined for a multi-cyclone and a non-woven fabric filter without dust extraction from the multi-cyclone dust collector and with or without periodical maintenance. The benefits of periodical cleaning of the dust collector were shown.

Keywords: engines, performance, air cleanness, non-woven fabric filter, separation efficiency, separation performance, surface wear, filter life.

Scharakteryzowano zanieczyszczenia powietrza wlotowego silnika spalinowego pojazdu mechanicznego. Przeanalizowano wartości stężenia pyłu w powietrzu dla różnych warunków eksploatacji pojazdów. Przedstawiono korzyści w postaci wydłużenia czasu eksploatacji silnika wynikające ze stosowania filtru bezwładnościowego (multicyklonu), jako pierwszego stopnia filtracji powietrza. Pokazano metody usuwania pyłu z osadnika multicyklonu filtru powietrza. Wykazano konieczność bieżącego, poprzez efektywne odsysanie, usuwania pyłu z osadnika multicyklonu. Zdefiniowano stopień odsysania pyłu m_0 oraz wykazano jego wpływ na skuteczność filtracji i opory przepływu cyklonów. Opracowano metodykę i warunki badań filtru dwustopniowego pracującego w układzie: multicyklon-włókninowy wkład filtracyjny. Wyznaczono charakterystyki skuteczności filtracji i oporów przepływu multicyklonu oraz włókniny filtracyjnej w zależności od masy pyłu dostarczonej wraz z powietrzem wlotowym do filtru dwustopniowego dla trzech wartości stopnia odsysania $m_0 = 5\%$, $m_0 = 10\%$, $m_0 = 20\%$ oraz bez odsysania pyłu z osadnika multicyklonu. Wyznaczono charakterystyki skuteczności filtracji i oporów przepływu multicyklonu oraz włókniny filtracyjnej bez odsysania pyłu z osadnika multicyklonu i z okresowym obsługiwaniem oraz bez obsługiwania. Wykazano konieczność okresowego czyszczenia osadnika pyłu.

Słowa kluczowe: silniki, eksploatacja, czystość powietrza, włóknina filtracyjna, skuteczność i dokładność filtracji, zużycie powierzchni, trwałość filtru.

1. Foreword

Providing a dust-free inlet air to the internal combustion engines of motor vehicles and machines, and thus reducing wear and improving component life, always was and still is a major operational and design issue, in particular for vehicles operating in heavy-duty terrain and high dust concentration conditions (about 1 g/m^3) [2, 10, 12, 18, 20, 30]. It generally applies to special vehicles, including military vehicles with high-power diesel engines with a maximum air demand Q_{Sil} over 1 kg/s , e.g.: $Q_{Sil} = 1.21 \text{ kg/s}$, ($3,400 \text{ m}^3/\text{h}$) for T-72 tank engine and $Q_{Sil} = 2.15 \text{ kg/s}$ ($6,000 \text{ m}^3/\text{h}$) for Leopard 2 tank engine. At dust concentration level $s = 1 \text{ g/m}^3$, specific to the vehicles used on

testing grounds, the engines of those tanks draw in a stream of dust at 0.94 g/s and 1.67 g/s , respectively.

Two-stage air filters in a multi-cyclone - porous panel filter configuration (usually made of paper filter element or non-woven fabric filter element) are used to remove the dust mass, with particle size $< 100 \mu\text{m}$ [2, 4, 10], from the inlet air stream. The concept of using two-stage filters consists in initial separation of large dust particles in an inertial filter (multi-cyclone) and leaving small dust particles ($d_z < 15\text{--}30 \mu\text{m}$) in the air stream and separating small air particles (above $d_z = 2\text{--}5 \mu\text{m}$) in the panel air filter – Fig. 1.

The time in which the air filtration system reaches permissible air filter flow resistance Δp_{fdop} ($5\text{--}8 \text{ kPa}$) is significantly longer compared

(*) Tekst artykułu w polskiej wersji językowej dostępny w elektronicznym wydaniu kwartalnika na stronie www.ein.org.pl

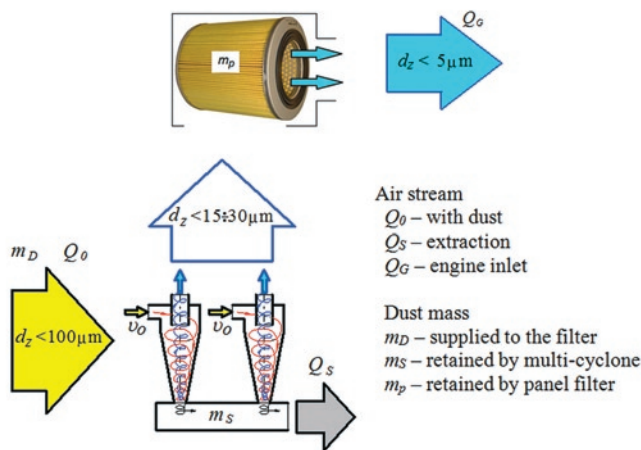


Fig. 1. Air filtration process in the two-stage filter in a 'multi-cyclone - porous panel filter' configuration.

to the panel filter under the same dustiness conditions (Fig. 2). Single filter element with an average separation efficiency of $\varphi_w = 99.95\%$ reached a flow resistance of $\Delta p_w = 9.4$ kPa after drawing in $m_D = 56$ g of dust with air. Similar filter element in a 'cyclone - filter element' configuration reached a similar flow resistance of $\Delta p_w = 9.65$ kPa after drawing in $m_D = 254$ g of dust with air, i.e. five times more.

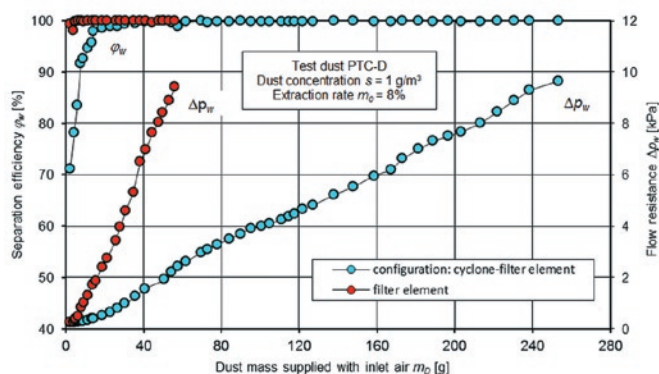


Fig. 2. Change in flow resistance $\Delta p_w = f(m_D)$ and separation efficiency $\varphi_w = f(m_D)$ of paper filter element in a single configuration and in a cyclone - filter element configuration as a function of dust mass m_D supplied with inlet air [12]

A multi-cyclone is a unit including up to several hundred cyclones arranged side-by-side in parallel on the common tube plates (top and bottom). Internal diameter of the cyclones used in the inlet air filters of motor vehicles does not exceed $D = 40$ mm. As opposed to the industrial cyclones, featuring internal diameters of $D = 250 \div 3.000$ mm), the cyclones used in air filters are often referred to as mini-cyclones.

The cyclones used in motor vehicles reach up to 96% separation efficiency [2, 4, 14]. During the 8-hour operation of T-72 tank engine in testing ground conditions, the air filter multi-cyclone may retain over 25 kg of dust. The separated dust is collected in a dust collector common for all the cyclones. The dust mass collected in the dust collector depends on the air stream, dust concentration in air and cyclone efficiency.

Storing a large volume of dust in the dust collector is not recommended due to:

- need to use high capacity dust collector, increasing overall filter dimensions and making the installation difficult,

- secondary dust aspiration due to vehicle vibrations and sudden changes in air stream direction due to changes in engine speed,
- filling up the dust collector and as a result capturing dust and reducing multi-cyclone efficiency,
- unnecessary filter structure load due to the additional weight.

In the multi-cyclones of the air filters of vehicles, in particular vehicles used in high-dust conditions, systematic (continuous) dust extraction from the dust collector using an air stream - extraction stream (ejection effect) is used.

In a multi-cyclone including a large number (50÷100 and more) of cyclones and a common dust collector, usually one or two ports are used for the dust extraction from the dust collector. The distances between the outlet ports of the streams extracted from each cyclone from the extraction system port may differ, creating problems with the dust extraction from the extreme individual cyclones. It further reduces the cyclone efficiency, and thus reduces the separation efficiency and performance of the entire multi-cyclone. The dust mass supplied to the second filtration stage is larger and further reduces the filter life (vehicle mileage) until the permissible flow resistance is reached.

The cyclone performance is usually validated by numerical tests using CFD (Computational Fluid Dynamics) software [1, 3, 7, 8, 15, 17, 21, 22, 26, 28, 32]. CFD software provides a detailed analysis of any issues related with the fluid flows, and eliminates time-consuming and expensive experiments in the design and retrofitting stage. The software provides relevant flow data (velocity field distribution, pressure field), heat transfer (temperature field) and mass transfer by numerical solving of the equations describing the changes in momentum, energy and mass balance.

There are scarce studies concerned with numerical [29] and experimental [4, 10, 11, 19] evaluation of the performance of dust extraction systems used in the multi-cyclone dust collectors.

Thus, assuming that the experimental tests are the most reliable research method, an experimental evaluation of the performance and the effects of the dust extraction from the dust collector of the motor vehicle air filter on the filtration process in the porous panel filter is presented in the study.

2. Impurities in inlet air of internal combustion engines

Atmospheric air drawn in by the internal combustion engines of motor vehicles contains large quantities of impurities, which can be classified as gaseous impurities (organic and inorganic) and particulate impurities [2, 4, 5, 6]. Dust is a dispersed phase of a two-phase system including particulate matter suspended in a gaseous dispersion phase, i.e. mixture of solid particles suspended in air.

The sources of dust emission are both natural phenomena and human activity. The dust emissions from natural sources are prevalent on a global scale. The most common natural dust emission sources are: volcanoes, deposits, marine aerosols, animal and plant materials, and forest fires [5].

In high-intensity industrial areas, the major dust emission sources are anthropogenic sources, including all production and fuel combustion processes, mostly solid fuels. Large dust volumes are generated by the power industry, chemical industry, mining industry, metallurgical industry and construction industry, in particular cement production [6].

The particulate matter can be classified by particle dimensions [5]:

- total particulate matter – mixture of small solid particles (suspended in air); conventional dimension $< 300 \mu\text{m}$,
- suspended particulate matter PM10 – conventional dimensions $< 10 \mu\text{m}$,

- fine particulate matter PM_{2.5} – conventional dimensions <2.5 μm ,
- nano particulate matter PM₁ – conventional dimensions <1 μm .

All particulate matter < 1 μm may cause premature wear of machine components and must be removed from the engine inlet air by the air filters.

The particulate matter (PM₁₀ and PM_{2.5}) emission from anthropogenic sources is mainly related to a road transport due to the large-scale character of motor vehicle use. It contributes to approx. 15% of both size fractions of the particulate matter [5, 27]. The particulate matter from motor transport (road transport) have the following sources [2, 5, 9]:

- mineral dust (road dust, with silicon dioxide as a main component) lifted from the road surface due to the movement of motor vehicles or wind,
- exhaust gases from motor vehicle engines (dust, carbon black, lead compounds, heavy hydrocarbons, particulate matter and gases),
- particulate matter from sliding pairs of motor vehicles, i.e. wear of friction linings of brakes and clutch plates [4],
- dust from tyre and surface wear due to interaction of wheels and road surface [4].

The most common impurity present in air, which is also harmful to any technical equipment is a road dust, lifted from the surface due to the traffic or wind, and supplied with inlet air to the motor cylinders.

The road dust is a polydisperse dust characterized by diversified physical and chemical properties, with basic components including grains of hard minerals: silicone dioxide (silica) and aluminium trioxide (corundum), which contribute to 60÷95% of dust content [2]. The hardness of silica particles, determined in a ten-degree Mohs scale is 7, whereas for corundum it is 9, i.e. more than for structural materials used for the construction of internal combustion engines. The dust particles are solids with irregular shape and sharp edges.

One of the characteristic properties of air is the dust concentration, measured as a dust mass (in grams or milligrams) in 1 m³ of atmospheric air. Dust concentration in air is a variable and depends on many factors. Dust concentration in air may vary depending on the operating conditions of a motor vehicle.

The lowest dust concentration in air, approx. 0.001 g/m³ [2, 4, 11] can be observed on hard surfaces and roads, and <0.001 g/m³ in residential areas. The highest dust concentration up to 3.8÷7 g/m³ [2, 9, 13, 18, 20], can be observed for a convoy of tracked vehicles on the testing ground with dry surfaces. Dust concentration in air at the air intake during helicopter take-off and landing may reach up to 3 g/m³. Dust concentration in air may reach 10 g/m³ during a sandstorm [20]. It is over 1000 times higher compared to the dust concentration on the city roads with motor vehicle traffic.



Fig. 3. Visibility limited due to the operation of: a) infantry fighting vehicle, b) tanks [18]

The dust suspended in air also reduces visibility (Fig. 3) and thus affects road safety. Dust concentration in air of 0.7 g/m³ significantly reduces the visibility and at 1.5 g/m³ the visibility is practically reduced to zero [10].

Part of the impurities supplied to the engine cylinders via the air supply system is combusted, and some are removed with the exhaust gases. Only 10÷20% of dust introduced to the engine via its inlet system is deposited on the cylinder sleeve walls. This dust forms an abrasive paste with oil, which in contact with a sliding pair piston-piston rings-cylinder (P-PR-C) results in a premature wear of cylinder sleeve, piston rings and ring grooves. The clearance between the (P-PR-C) increases, resulting in the reduction of the combustion chamber leak-tightness.

It results in a decrease in compression pressure and engine power [16], an increase in blow-by to the crankcase [24], further increasing the engine oil degradation. The engine performance and start-up capabilities of a cold engine are also affected. Fuel and engine oil consumption, as well as the emission of toxic compounds are also increased [25].

As a result of piston movement in the direction of the bottom dead centre, the piston rings remove the oil with any impurities from the cylinder bearing surface to the oil sump. The impurities are distributed in the lubrication system via the oil system to the friction areas which require oil lubrication, i.e. the following pairs: crankshaft neck-bushing, camshaft neck-bushing, valve guide-valve stem, resulting in premature wear.

The friction wear takes place where any hard solids are trapped between two mating surfaces, deform and cut micro-volumes of the surface layer of mating elements at different depths.

The authors studying the effects of impurities present in the operational fluids on the wear of piston engine components claim, that the most extensive wear is due to the dust particles with dimensions d_z corresponding to the minimum thickness h_{min} of oil film required to form an oil wedge between the mating surfaces [16].

3. Methods of dust removal from dust collector of air filter multi-cyclone

Removing the dust from a dust collector of an air filter multi-cyclone in legacy solutions was carried out by the driver as part of



Fig. 4. Dust extraction methods for inertia filters: a) manual (Jelcz 317 filter), b) rubber drain cone (Mann+Hummel filter), c) rubber drain cone d) ejection (T-72 tank filter)

the daily maintenance (Fig. 4a). In modern air filter solutions, dust is extracted from the dust collector using automatic methods:

- by opening rubber drain cones after each engine stop (Fig. 4b),
- in continuous mode by generating an air stream flow Q_s - extraction stream (ejection effect) (Fig. 4c).

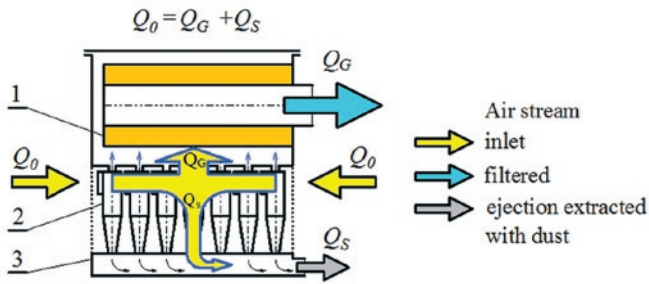


Fig. 5. Distribution of the inlet air stream in the filter with ejection dust extraction from the dust collector: 1 – panel filter, 2 – multi-cyclone, 3 – dust collector

The dust is extracted by an air stream Q_S , a part of an inlet air stream (with dust) Q_0 to the multi-cyclone (Fig. 5):

$$Q_0 = Q_G + Q_S, \quad (1)$$

where: Q_G – filter outlet air stream (clean) – engine inlet air.

Special fans and blowers are commonly used to generate the extraction stream. A major drawback of the solution is that it requires a drive, i.e. electric motor or mechanical gear coupled with the engine crankshaft. The fan performance depends directly on the engine speed, and as a result on its operating range. The fan location within the engine compartment is also pre-determined and is not necessarily optimal in relation to the filter position. Continuous fan operation also entails high requirements regarding the motor durability. The electric drive is a significant load on the system generating electrical energy for the vehicle subsystems. A fan with electric drive is used to extract dust from the air filter dust collector in Leopard 2 tanks.

To generate the extraction stream in many air filters, ejectors utilizing the energy of a compressed air stream [4] or an exhaust gas from the vehicle's exhaust system [2, 11] are used.

The extraction stream Q_S flowing through the dust collector chamber captures the dust particles and is discharged via conduits outside the vehicle.

The purpose of the ejector is to force and intensify the extraction stream flow between two spaces, usually two open thermodynamic

systems. The characteristic feature of the ejector are two streams, between which there is a transfer of momentum. The active stream has a higher momentum vector value, and its sense is strictly determined. The vector sense of the second stream (passive) is usually identical. Due to the different methods of stream delivery: active and passive, different ejector configurations are available (Fig. 6).

From the configurations shown in Fig. 6, the more practical and more commonly used in the exhaust system is the configuration shown in Fig. 6b. It is significantly easier to manufacture and has a lower weight, which in case of a vibrating exhaust system is of crucial importance. The ejector configuration is used in the ejection dust extraction from the dust collector of the T-72 and PT-91 tank air filter and special vehicles using the same suspension.

The ejector has a simple design, small number of components and no movable parts. It requires very little maintenance apart from periodical visual inspection of the technical condition and integrity of the conduit connecting the ejector with the dust collector of the inertial filter. However, the ejector requires additional energy to provide dust extraction capabilities.

The measure of an intensity of dust extraction from the multi-cyclone (cyclone) dust collector is the extraction rate m_0 defined as a quotient of air stream flow rate Q_S in the extraction system and the multi-cyclone (cyclone) outlet stream flow rate, and if the multi-cyclone is used as the first stage of air filtration in the air filter – to the

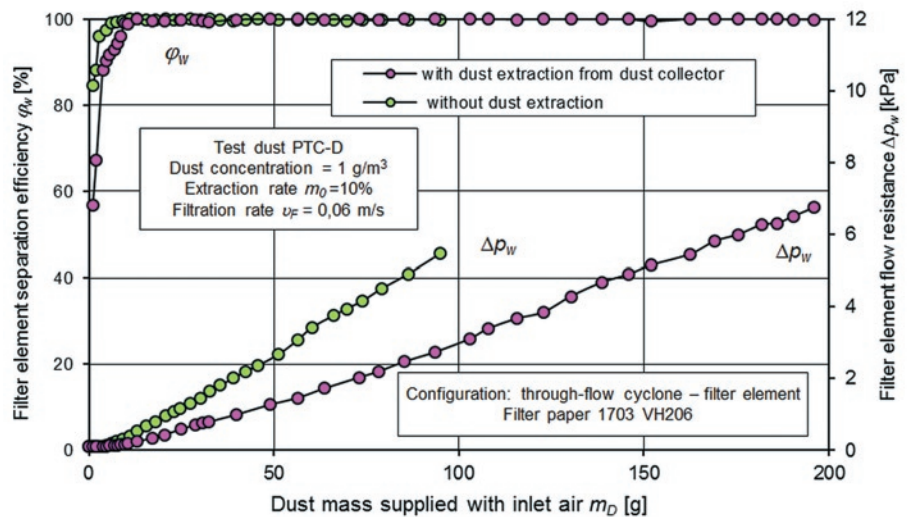


Fig. 7. Characteristics of the paper filter element downstream of the through-flow cyclone with and without dust extraction from the cyclone dust collector [12]

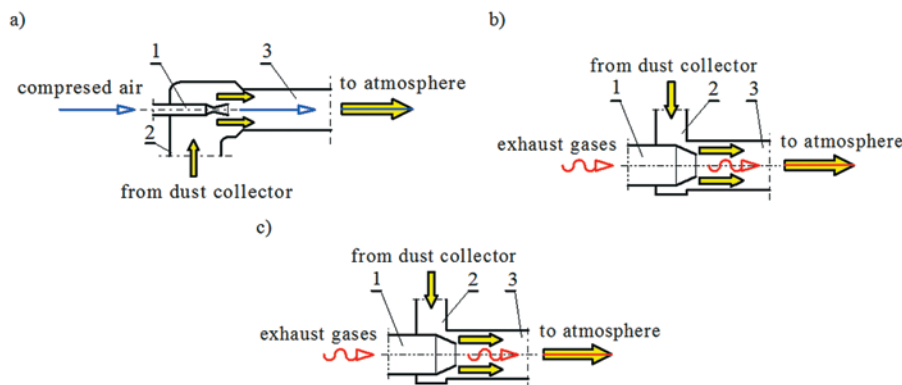


Fig. 6. Ejector configuration in the extraction system for forced ejection stream: a) compressed air, b) and c) exhaust gases: 1 – active stream inlet channel, 2 – passive stream inlet channel, 3 – mixing chamber [10]

air filter outlet stream flow rate Q_G (engine inlet air) [10, 19, 23, 31]:

$$m_0 = \frac{Q_S}{Q_G} 100\% \quad (2)$$

Removing (by extraction) the dust separated by the cyclones from the multi-cyclone dust collector results in a significant increase in separation efficiency, and thus extends the air filter life by a limited determined permissible flow resistance Δp_{fdop} . The characteristics can be verified by the flow resistance $\Delta p_w = f(m_D)$ and separation efficiency $\varphi_w = f(m_D)$ characteristics of a paper panel filter as a function of dust mass m_D

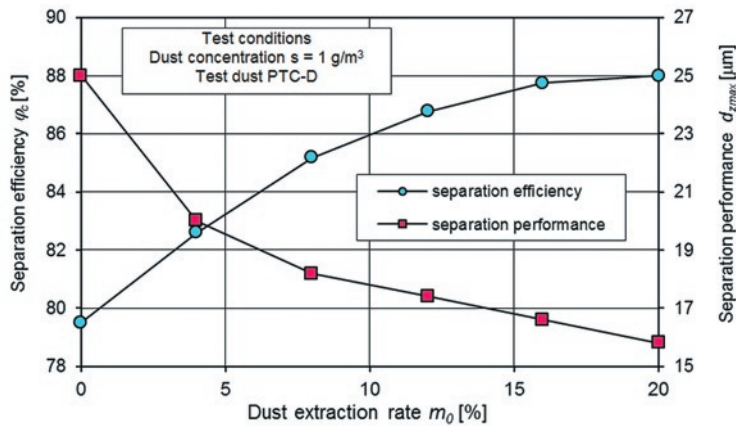


Fig. 8. Effects of the extraction rate m_0 on cyclone separation efficiency and flow resistance [14]

supplied with inlet air in serial 'cyclone - filter element' configuration (Fig. 7).

The studies on the effects of dust extraction on separation efficiency in cyclones, however scarce show that the increase in extraction rate m_0 results in a significant increase in cyclone efficiency ϕ_c , up to a certain point (Fig. 8 and 9). For through-flow cyclone (Fig. 8) the limit value is $m_{0g} = 10 \div 15\%$ [14].

An increase in the extraction rate m_0 results in an increase in cyclone flow resistance due to the increase in stream volume Q_0 and air flow rate.

There is a specific range of optimal extraction rate, which if exceeded may affect cyclone performance and increase energy losses. In the existing cyclone and multi-cyclone designs, the extraction rate m_0 is usually within $m_0 = 8 \div 15\%$, although it may sometimes reach $m_0 = 20\%$ [10, 19, 23, 31].

4. Test purpose, methods and conditions

The study aimed to determine the causes of the decrease in multi-cyclone separation efficiency depending on the mass of dust supplied to the two-stage filter and the effects of those changes on the perfor-

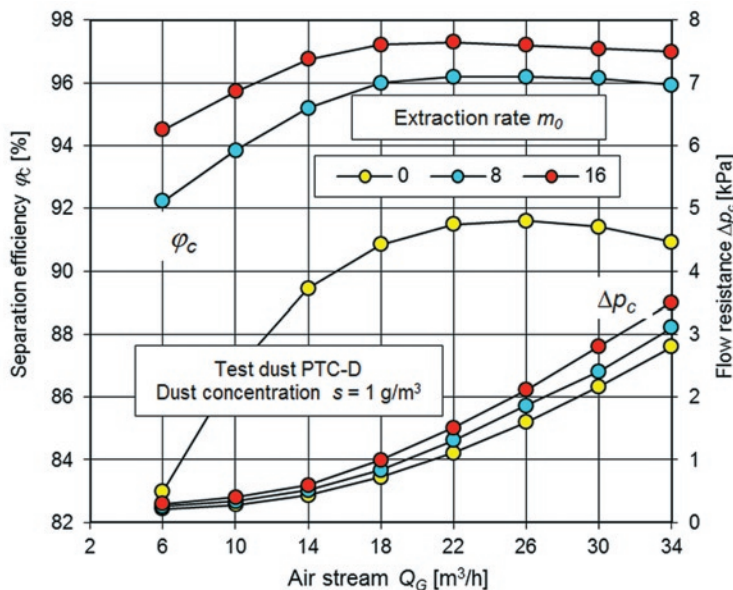


Fig. 9. Effects of the extraction rate m_0 on characteristics: separation efficiency $\phi_c = f(Q_G)$ and flow resistance $\Delta p_c = f(Q_G)$ of a return-flow cyclone with tangential inlet D-40 [12]

mance of a non-woven fabric filter used in the two-stage filtration system downstream of the multi-cyclone.

The purpose of the study was to determine the performance characteristics of a non-woven fabric filter in a two-stage filtration system and a multi-cyclone at a pre-determined air stream flow rate Q_G and ejection dust extraction rate from the multi-cyclone dust collector. The characteristics were determined for three different ejection dust extraction rates $m_0 = 5\%$, $m_0 = 10\%$, $m_0 = 20\%$ and without extraction, as well as without extraction with periodical removal of the dust from the dust collector. The ejection dust extraction rates m_0 used are based on the range of the extraction rates recorded in the existing and operating multi-cyclone designs.

The following characteristics were determined:

- filter element separation efficiency $\phi_w = f(m_D)$,
- filter element flow resistance $\Delta p_w = f(m_D)$,
- multi-cyclone separation efficiency $\phi_M = f(m_D)$.

Table 1. AC-301 non-woven fabric filter parameters by Korea Filtration Technologies Co.

Parametr	Unit	Value
Weight per unit area	(g/m ²)	210±10%
Thickness	(mm)	2.34±2.86
Air permeability	(dm ³ /m ² /s)	800÷1100 at 120 Pa
Tensile strength	(N/50 mm)	> 98
Bending strength	(N/30 mm)	1.47±2.94

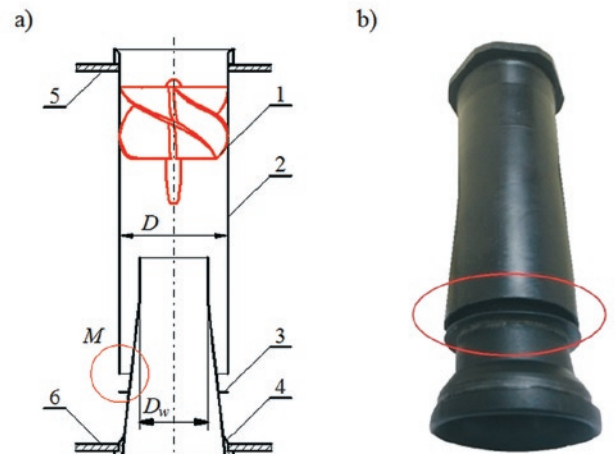


Fig. 10. Through-flow cyclone of the tested multi-cyclone: a) functional diagram, b) general view: 1 – swirl vanes, 2 – body, 3 – abutment, 4 – outlet tube, 5 – multi-cyclone top plate, 6 – multi-cyclone bottom plate, D – cyclone body internal diameter, D_w – outlet tube internal diameter; M – extracted dust outlet gap

The tests covered a filter element made of two-layer non-woven fabric AC-301 (Table 1) with a filtration surface area $F_w = 2 m^2$ and a multi-cyclone including through-flow cyclones (Fig. 10) arranged parallel in relation to each other in three columns, six cyclones per column – Fig. 11.

The main stream value was $Q_G = 600 m^3/h$. The dust was extracted from the dust collector of the multi-cyclone using ejection extraction with the air stream Q_S .

The extraction stream flow rate Q_S was determined from the following relationship for the extraction rates used $m_0 = 5\%$, $m_0 = 10\%$, $m_0 = 20\%$:

$$Q_S = Q_G \cdot m_0 \quad (3)$$

The tests were performed at a constant air stream flow through the filter $Q_G = 600 \text{ m}^3/\text{h}$ (separation rate $v_{Flop} = 0.08 \text{ m/s}$) and extraction stream flow rates $Q_s = 30 \text{ m}^3/\text{h}$, $Q_s = 60 \text{ m}^3/\text{h}$, $Q_s = 120 \text{ m}^3/\text{h}$, at dust concentration in the air at multi-cyclone inlet $s = 1 \text{ g/m}^3$, using PTC-D type test dust, locally available equivalent to AC-Fine test dust, with size distribution and chemical composition as specified in [13].

The separation efficiency φ_w of tested non-woven textile filter and multi-cyclone was determined using a mass method in subsequent j measuring cycles, with the duration (uniform test dust dispensing and distribution time) of $t_{1pom} = 3 \text{ min}$ in the initial separation period and $t_{2pom} = 15 \text{ min}$ in the subsequent period.

The following were determined after each j -th cycle:

- filter element separation efficiency φ_w from the following equation:

$$\varphi_{wj} = \frac{m_{wj}}{m_{Dwj}} \cdot 100\% \quad (4)$$

where: m_{wj} – dust mass retained by filter element, m_{Dwj} – dust mass supplied to the filter element (downstream of the multi-cyclone) during the measurement cycle.

- multi-cyclone separation efficiency φ_M from the following equation:

$$\varphi_{Mj} = \frac{m_{Mj}}{m_{Dj}} \cdot 100\% \quad (5)$$

where: m_{Mj} – dust mass retained by multi-cyclone, m_{Dj} – dust mass supplied to the multi-cyclone (filter) in the measurement cycle.

- filter element flow resistance from the following equation:

$$\Delta p_{wj} = \frac{\Delta h_{wj}}{1000} (\rho_m - \rho_H) g \text{ [kPa]}, \quad (6)$$

where: Δh_w – static pressure drop as read (in mm H_2O) from the water manometer (U-tube), ρ_m – manometer liquid density (H_2O) at measurement temperature t_H , ρ_H – atmospheric air density in kg/m^3 , g – local gravitational acceleration.

- dust concentrations in the air from the following equation:

$$s_j = \frac{m_{Dj} \cdot 60}{(Q_G + Q_s) \cdot \tau_{jpm}} \text{ [g/m}^3\text{]}, \quad (7)$$

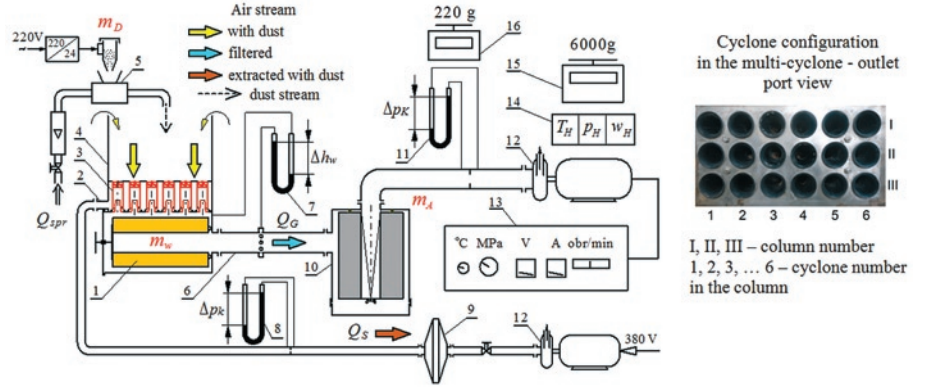


Fig. 11. Test stand diagram: 1 – filter element, 2 – dust collector, 3 – multi-cyclone, 4 – dust chamber, 5 – dust dispenser, 6 – flow resistance measuring line, 7 – filter element static pressure drop gauge, 8 – orifice differential pressure gauge (Q_s – volumetric flow rate), 9 – dust extraction line absolute filter, 10 – main line absolute filter, 11 – orifice differential pressure gauge (Q_G – stream), 12 – suction fans, 13 – engine and fan control panel, 14 – pressure, temperature and relative humidity measuring unit, 15, 16 – analytic scale

where: m_{Dj} – mass of dust supplied to the multi-cyclone (filter) in the measurement cycle.

The mass of dust retained by the filter element and the absolute filter was determined using an analytical balance with 6000 g capacity and 0.01 g readability. The mass of dust supplied to the multi-cyclone (filter) to determine the dust concentration in the air was determined using an analytical balance with 220 g capacity and 0.0001 g readability.

Q_G stream values in the main duct were determined using a 200÷1500 m^3/h measuring orifice plate, and Q_s stream values were determined using a float rotameter RIN-60 with 6÷130 m^3/h range and 2.5 accuracy class.

The tests ended after reaching a flow resistance of 6 kPa at the filter element, which is a common permissible flow resistance for motor vehicles.

Filter element tests were performed on the test stand (Fig. 11) allowing determination of basic separation efficiency and flow resistance characteristics for the air stream flow rates up to 1500 m^3/h , at the ejection extraction rate up to 20% and dust concentration up to 3 g/m^3 .

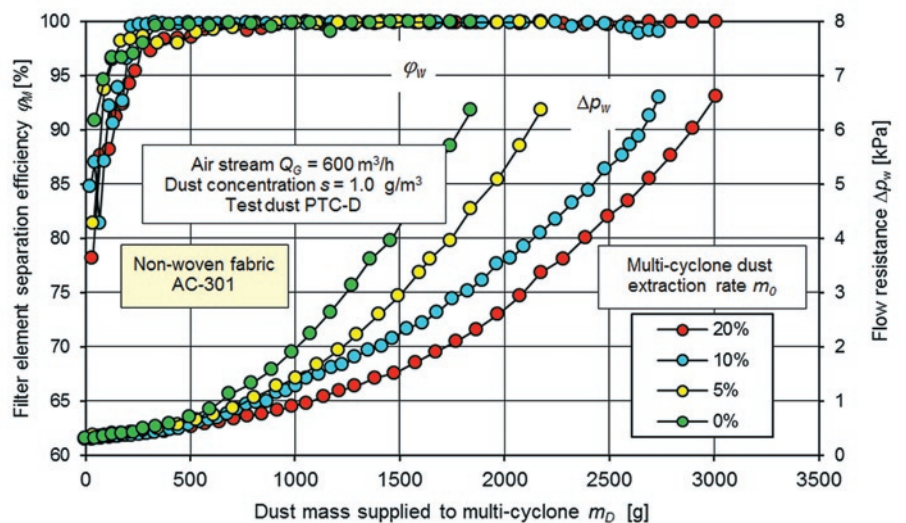


Fig. 12. Separation efficiency and flow resistance of the filter element (AC-301 non-woven fabric) used as a second filtration stage downstream of the multi-cyclone for different rates of m_0 ejection dust extraction from the dust collector

5. Test result analysis

Fig. 12 shows the separation efficiency φ_w and flow resistance Δp_w characteristics for non-woven fabric filter AC-301 in two-stage filtration configuration (downstream of the multi-cyclone) as a function of dust mass m_D supplied with inlet air to the filter. The filter element life can be divided into two periods due to the achieved separation efficiency. First (initial) period is characterized by a low separation efficiency, which systematically and rapidly increases with the volume of dust supplied to the filter. The initial period lasts from the beginning of the separation process until the non-woven fabric reaches the separation efficiency of 99.5% [8]. Main filtration period is characterized by a high (over 99.5%) and slowly but gradually increasing separation efficiency. Following the initial measurement cycles, AC-301 non-woven fabric filter efficiency was $\varphi_w = 78.8 \div 88.3\%$ (Fig. 12). The initial period (separation efficiency $\varphi_w = 99.5\%$) for the tested non-woven fabric ends after approx. 450 g of dust is supplied to the filter.

The flow resistance Δp_w of the filter element increases with the increase in the dust mass supplied to the filter, and the increase rate is higher the lower the dust extraction rate m_0 . Determined flow resistance $\Delta p_w = 6$ kPa is achieved by the filter element, after a specific dust mass is supplied to the filter. The operation of the multi-cyclone at the extraction rate of $m_0 = 20\%$ means, that the filter element achieves the flow resistance of $\Delta p_w = 6$ kPa after supplying $m_D = 2.9$ kg of dust to the system. For the extraction rate $m_0 = 10\%$ the value is $m_D = 2.7$ kg, whereas for $m_0 = 5\%$ it is $m_D = 2.1$ kg. The operation of the multi cyclone without dust extraction from the dust collector means that the filter element achieves a flow resistance of $\Delta p_w = 6$ kPa after supplying to the system $m_D = 1.8$ kg of dust, which corresponds to less than 40% compared to the multi-cyclone operation with dust extraction $m_0 = 20\%$. Time the air filtration system requires to reach a permissible air filter flow resistance Δp_{flop} is significantly shorter compared to the configuration with the dust extraction from the dust collector.

The effect is due to the reduced separation efficiency of the multi-cyclone at a reduced rate of dust extraction from the dust collector and reduced multi-cyclone separation efficiency in time - increased mass of dust supplied to the system (Fig. 13).

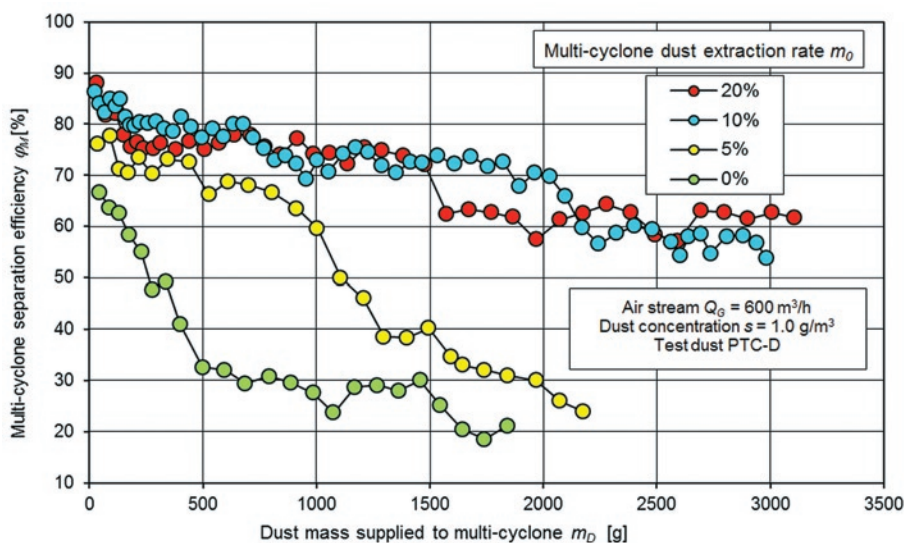


Fig. 13. Separation efficiency of the multi-cyclone at different rates m_0 of ejection extraction from the dust collector

With the increase in dust mass supplied to the filter with inlet air, the separation efficiency of multi-cyclone gradually decreases, however the lower the dust extraction rate m_0 the higher the efficiency reduction rate. The moment the multi-cyclone begins operation at the dust extraction rate $m_0 = 20\%$, its efficiency is $\varphi_M = 86.25\%$, and after supplying over 3 kg of dust, the efficiency is reduced to $\varphi_M = 61.72\%$. For multi-cyclone operation at dust extraction rate of $m_0 = 5\%$, the respective values are: initial $\varphi_M = 76.2\%$ and after delivering $m_D = 2.17$ kg of dust – $\varphi_M = 24.2\%$. The multi-cyclone separation efficiency in this case is reduced threefold. The reduction in multi-cyclone separation efficiency means that the larger dust mass is delivered to the filter element, resulting in rapid filling of the filter medium pores, and thus progressively increasing the flow rate v between the fibres. It results in a significant increase in the flow resistance (Fig. 12) as a function of $\Delta p = f(v^2)$.

If the dust collector is common for many cyclones, and the dust is extracted via one or two ports, as in tested configuration, the following can be observed [8, 9, 16]:

- extraction stream values differ for individual cyclones,
- whirling streams from individual cyclones entering the common dust collector interact with each other,
- backflow to the cyclones at the multi-cyclone periphery may occur.

Those effects may not only results in a multi-cyclone efficiency lower than resulting from the extraction rate for individual cyclones, but also in the reduction of multi-cyclone separation efficiency with the increase in dust mass delivered with air to the filter. It will thus result in:

- 1) Permanent deposition of dust on internal surfaces of the inlet components of the cyclone forming a gap, through which the extracted dust is discharged – Fig. 14. The mass of dust

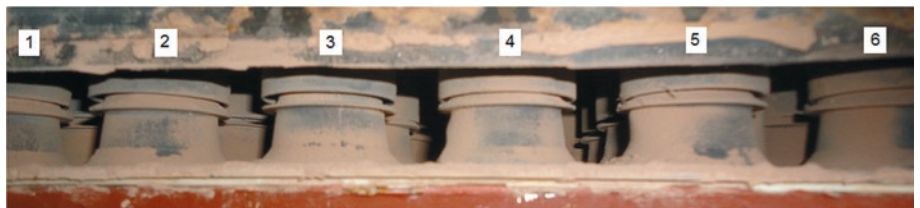


Fig. 14. Cyclone outlet gaps after supplying 500 g of dust at dust extraction rate of $m_0 = 5\%$ – view from the dust extraction manifold: 1, 2, 3, ..., 6 – consecutive cyclone number in the column

deposits in the gap increases with time, and as a result affects the extraction stream flow from the cyclone and thus may render it completely ineffective – Fig. 15.

2) Permanent deposition of dust in the corners and at the rim of the dust collector housing (Fig. 15), where the extraction is less effective compared to the cyclones closer to the extraction duct. The dust accumulated and deposited on the bottom of the dust collector affects the flow at the cyclone outlet of both the extracted dust and the clean air. As a result, the air flow through the cyclone is gradually reduced, and thus reduces its separation efficiency. The mass of dust deposited on the bottom of the dust collector and the rim increases with time, and as a result may clog the cyclone outlets and thus render it completely ineffective (Fig. 15).

The rate with which those effects, reducing the multi-cyclone separation efficiency with the

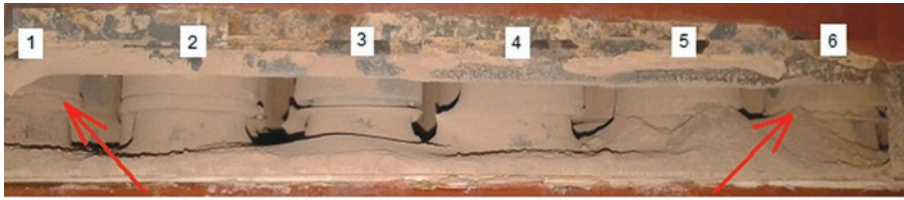


Fig. 15. Cyclone outlet gaps after supplying 2150 g of dust at dust extraction rate of $m_0 = 5\%$ – view from the dust extraction manifold: 1, 2, 3, ..., 6 – consecutive number of the cyclone in the column (arrow indicates the cyclones with gaps clogged with dust)



Fig. 16. Cyclone outlet gaps after maintenance – view from the dust extraction manifold: 1, 2, 3, ..., 6 – consecutive cyclone number in the column

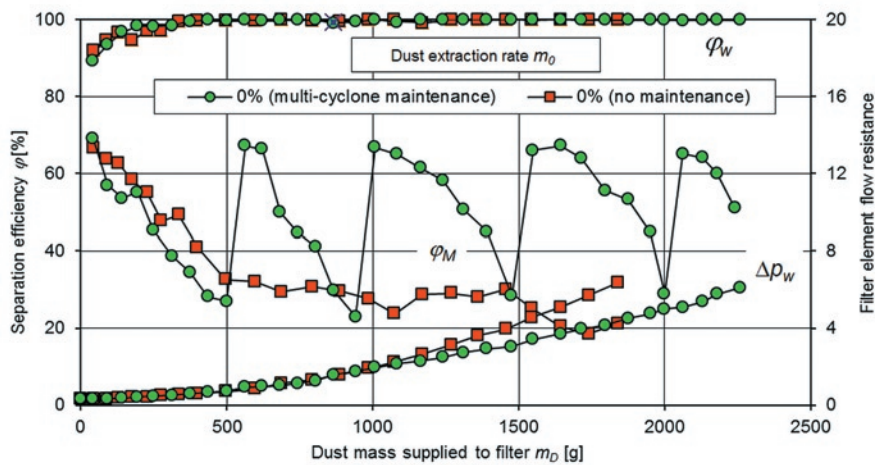


Fig. 17. Effects of periodical dust extraction from the dust collector on separation efficiency and flow resistance of the filter element (non-woven fabric AC-301) and multi-cyclone separation efficiency without ejection dust extraction from the dust collector.

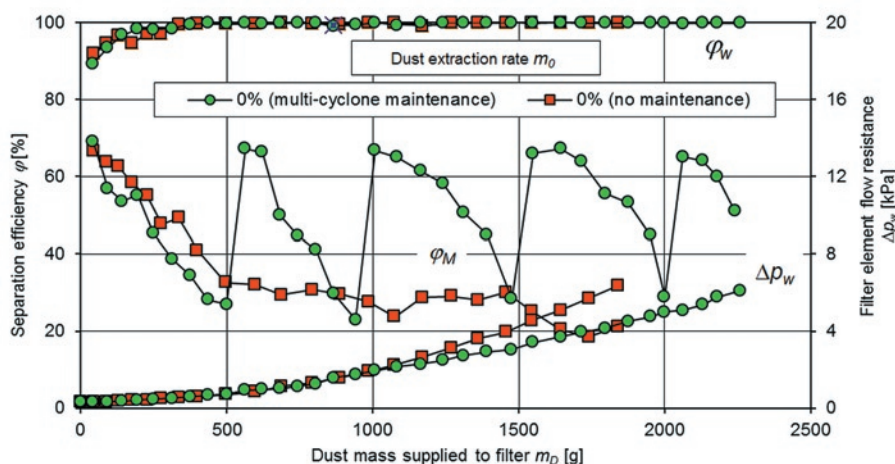


Fig. 18. Effects of dust mass supplied on the separation efficiency of multi-cyclone, filter element (AC-301 non-woven fabric) and complete filter at the ejection extraction rate of $m_0 = 10\%$

increase in mass of dust supplied to the filter, occur is higher the lower the dust extraction rate from the dust collector.

A decrease in multi-cyclone separation efficiency during operation may be prevented by periodical cleaning of the dust collector. Fig. 17

shows changes in the multi-cyclone separation efficiency with the mass of dust supplied to the filter without extraction and with periodical dust extraction (every 500 g of supplied dust) from the dust collector. At the beginning, the multi-cyclone separation efficiency was $\phi_M = 69.1\%$, and after supplying 500 g of dust, the efficiency was reduced to $\phi_M = 26.9\%$, which is similar to the value achieved by the multi-cyclone without maintenance. After the maintenance (Fig. 16) involving dust removal with compressed air, the multi-cyclone separation efficiency has increased to $\phi_M = 66.8\%$, which is similar to the initial value, and was further reduced in subsequent operation. The multi-cyclone maintenance cycle was repeated three times with a similar result – Fig. 17.

Separation efficiency of a complete two-stage air filter is determined both by the multi-cyclone and the filter element. In the initial stage, when the filter element achieves low efficiency within $\phi_w = 81.4 \div 96.6\%$, its efficiency is determined by the multi-cyclone, providing maximum separation efficiency of $\phi_M = 86.3 \div 81.4\%$ (Fig. 18). The reduction in multi-cyclone separation efficiency with the mass of dust supplied with the inlet air (vehicle mileage) does not affect separation efficiency of the complete filter.

For multi-stage filters, where the filtration stages are arranged in series, the separation efficiency is usually determined using the following equation [20]:

$$\varphi_f = 1 - \prod_{i=1}^n (1 - \varphi_{fi}), \quad (8)$$

where: n – number of filtration stages, φ_{fi} – i -th stage separation efficiency.

For the tested two-stage filter, where the first filtration stage (multi-cyclone) is characterized by the initial separation efficiency of $\phi_{M1} = 86.25\%$, and the second stage (filter element) $\phi_{w1} = 84.78\%$ (Fig. 18), the separation efficiency is:

$$\varphi_{f1} = 1 - \prod_{i=1}^n (1 - \varphi_i)$$

$$\varphi_{f1} = 1 - (1 - \varphi_{M1}) \cdot (1 - \varphi_{w1})$$

$$\varphi_{f1} = 1 - (1 - 0.8625) \cdot (1 - 0.8478)$$

$$\varphi_{f1} = 97.91\%.$$

Experimental initial separation efficiency of the filter is $\varphi_{fE1} = 97.908\%$.

After supplying $m_D = 2028.6$ g of dust (measuring cycle no. 44 Fig. 18), experimental separation efficiency of the two-stage filter is $\varphi_{fE44} = 99.97\%$, whereas the separation efficiency determined using a relationship ($\phi_{M44} = 67.73\%$, $\phi_{w44} = 99.9\%$) is similar

$\varphi_{f4} = 99.967\%$. Very high agreement of the experimental and calculation results of the separation efficiency of the two-stage filter indicates that the selected test method is accurate.

5. Summary

Two-stage (multi-cyclone - porous panel filter) filtration systems with ejection dust extraction from the dust collector are used in the filtration systems at the air inlets of the motor vehicles operating in high dust concentration conditions ($s = 1 \text{ g/m}^3$ and more).

The studies and analyses show, that the ejection dust extraction from the dust collector of the multi-cyclone used in the two-stage filter system performs its task, however it is not perfect, due to the decreasing separation efficiency of the multi-cyclone and more intensive increase in flow resistance of the filter element.

With the increase in dust mass supplied to the filter with inlet air, the separation efficiency of multi-cyclone gradually decreases, however the lower the dust extraction rate m_0 the higher the efficiency reduction rate (Fig. 13). It is due to the specific design of the multi-cyclone and imperfections of the dust extraction system. If the dust collector is common for many cyclones, and the dust is extracted via one or two ports, the extraction streams for individual cyclones vary and the backflow in the cyclones located at the perimeter of the multi-cyclone may occur.

It may result in a permanent deposition of dust in the corners and at the rim of the dust collector housing, where the extraction is less effective compared to the cyclones closer to the extraction duct. The dust accumulated and deposited on the bottom of the dust collector affects the flow at the cyclone outlet of both the extracted dust and the clean air, which, in effect, may clog the cyclone outlets and thus render them completely ineffective. The rate of these effects is higher

at lower extraction rate or multi-cyclone operation without the dust extraction from the dust collector.

In the operating conditions, it can be compensated by periodical, systematic cleaning of the dust collector and cyclone outlet slots. The multi-cyclone separation efficiency restored to its initial value has been shown (Fig. 17), however it is a difficult task, since it requires the filter to be removed from the vehicle.

The air filters in special vehicles are characterized by large dimensions and weight, and usually does not allow disassembly of the dust collector.

The settling of the dust both in the corners and on the edges of the dust collector housing and in the slots of the cyclones at the multi-cyclone circumference may be prevented with a suitable design of the inner space of the dust collector chamber. One of the methods is to divide the dust collector chamber of the multi-cyclone into individual segments and suction ducts, with assigned corresponding groups of individual cyclones. The design may provide uniform flow rates for all cyclones and prevent permanent settling of the dust in the corners and on the edges of the dust collector housing.

A segmented dust collector is also easier to design, since the basic tests are limited to individual segments, and thus easier and more cost effective.

The intensity of the increase in flow resistance Δp_w of the filter element used as a second filtration stage (downstream of the multi-cyclone) is higher, the lower the separation efficiency of the multi-cyclone. As a result, more dust is supplied to the filter element in a unit of time. Thus, in normal operation at constant permissible flow resistance Δp_{flop} , the mean time between maintenance is reduced and the operational costs are increased.

References

1. Azadi M, Azadi M. An analytical study of the effect of inlet velocity on the cyclone performance using mathematical models. *Powder Technology* 2012; 217: 121-127, <http://dx.doi.org/10.1016/j.powtec.2011.10.017>.
2. Baczewski K, Hebda M. *Filtracja płynów eksploatacyjnych*. Radom: MCNEMT, 1991/92.
3. Cernecky J, Plandorova K. The effect of the introduction of an exit tube on the separation efficiency in a cyclone. *Brazilian Journal of Chemical Engineering* 2013; 30 (3): 627-641, <http://dx.doi.org/10.1590/S0104-66322013000300020>.
4. Centisep Air Cleaner.: *Materiały informacyjne firmy PALL Corporation, USA* 2004.
5. Chłopek Z. Testing of hazards to the environment caused by particulate matter during use of vehicles. *Eksplotacja i Niezawodność – Maintenance and Reliability* 2012; 2: 160-170.
6. Chłopek Z, Jakubowski A. A study of the particulate matter emission from the braking systems of motor vehicles. *Eksplotacja i Niezawodność – Maintenance and Reliability* 2009; 4: 45-52.
7. Chu K W, Wang B, Xu D L, Chen Y X, Yu A B. CFD-DEM simulation of the gas-solid flow in a cyclone separator. *Chemical Engineering Science* 2011; 66: 834-847, <http://dx.doi.org/10.1016/j.ces.2010.11.026>.
8. Chuah L A, Gimbin J, Choong T S Y, Fakhru'l-Razi A. A CFD analysis on the effect of vortex finder and cylindrical length on cyclone hydrodynamics and centrifugal forces. *Journal - The Institution of Engineers, Malaysia* 2009; 71 (2): 51-58.
9. Durst M, Klein G, Moser N. *Filtration in Fahrzeugen*. *Materiały informacyjne firmy Mann+Hummel GMBH*. Ludwigsburg, Niemcy 2005.
10. Dziubak T. The assessment of the possibilities of improvement of the extraction evenness, in multicyclone dedusters fitted in special vehicles. *Combustion Engines* 2012; 4 (151): 34-42.
11. Dziubak T.: A study on the improvement of uniformity of dust extraction from multicyclone dust collectors. *Combustion Engines* 2011; 4(147): 69-78.
12. Dziubak T.: The research of air filtration process on paper partition in the Cyclone-porous partition" system. *Journal of KONES Powertrain and Transport* 2007; 2(14): 115-124.
13. Dziubak T., Szwedkiewicz S.: Operating properties of non-woven fabric panel filters for internal combustion engine inlet air in single and two-stage filtration systems. *Eksplotacja i Niezawodność – Maintenance and Reliability* 2015; 17(4): 519-527, <http://dx.doi.org/10.17531/ein.2015.4.6>.
14. Dziubak T, Szwedkiewicz S. Experimental research on filtering fibers in a cyclone-porous barrier system. *Combustion Engines* 2014; 3(158): 45-55.
15. Elsayed K. Optimization of the cyclone separator geometry for minimum pressure drop using Co-Kriging. *Powder Technology* 2015; 269: 409-424, <http://dx.doi.org/10.1016/j.powtec.2014.09.038>.
16. Fitch J. Clean Oil Reduces Engine Fuel Consumption. *Practicing Oil Analysis Magazine* 2002; 11-12.
17. Gawali S S, Bhambere M B. Computational fluid dynamics approach for prediction of cyclone separator pressure drop. *International Journal of Mechanical Engineering and Robotics Research* 2015; 4 (1): 374-377.

18. Grafe T, Gogins M, Barris M, Schaefer J, Canepa R. Nanofibers in Filtration Applications in Transportation. Filtration International Conference and Exposition, Chicago – Illinois, December 3-5, 2001.
19. Greenfield R. R. The Use of Cyclones for Control of Solids Emission from Fluidised Bed Boilers. Filtration & Separation 1986; 22 (1): 38-39.
20. Jaroszczyk T. Air Filtration in Heavy-Duty Motor Vehicle Applications. Proc. Dust Symposium III Vicksburg MS, 15-17 September 1987.
21. Jiao J, Zheng Y, Sun G, Wang J. Study of the separation efficiency and the flow field of a dynamic cyclone. Separation and Purification Technology 2006; 49: 157-166, <http://dx.doi.org/10.1016/j.seppur.2005.09.011>.
22. Karagoz I, Avci A, Surmen A, Sendogan O. Design and performance valuation of a new cyclone separator. Journal of Aerosol Science 2013; 59: 57-64, <http://dx.doi.org/10.1016/j.jaerosci.2013.01.010>.
23. Kim H T, Zhu Y, Hinds W C, Lee K W. Experimental study of small virtual cyclones as particle concentrators. Journal of Aerosol Science 2002; 5(33): 721-733, [http://dx.doi.org/10.1016/S0021-8502\(01\)00212-9](http://dx.doi.org/10.1016/S0021-8502(01)00212-9).
24. Koszałka G, Suchecki A. Changes in performance and wear of small diesel engine during durability test. Combustion Engines 2015; 3(162): 34-40.
25. Koszałka G. Model of operational changes in the combustion chamber tightness of a diesel engine. Eksploatacja i Niezawodność – Maintenance and Reliability 2014; 1: 133-139.
26. Ma L, Ingham D. B, Wen X. Numerical modelling of the fluid and particle penetration through small sampling cyclones. Journal of Aerosol Science 2000; 9(31): 1097-1119, [http://dx.doi.org/10.1016/S0021-8502\(00\)00016-1](http://dx.doi.org/10.1016/S0021-8502(00)00016-1).
27. Pui D Y H, Chen S Ch, Zuo Z. PM_{2.5} in China: Measurements, sources, visibility and health effects, and mitigation, Particuology 2014; 13: 1-26, <http://dx.doi.org/10.1016/j.partic.2013.11.001>.
28. Qian F, Zhang J, Zhang M. Effects of the prolonged vertical tube on the separation performance of a cyclone. Journal of Hazardous Materials 2006; 136: 822-829, <http://dx.doi.org/10.1016/j.jhazmat.2006.01.028>.
29. Reddy G C, Kuppuraj U. Numerical study of flue gas flow in a multi cyclone separator. Int. Journal of Engineering Research and Applications 2015; 5(1): 48-53.
30. Rybak P. Operating loads of impulse nature acting on the special equipment of the combat vehicles. Eksploatacja i Niezawodność – Maintenance and Reliability 2014; 3: 347-353.
31. Sage P W, Wright M A. The Use of Bleeds to Enhance Cyclone Performance. Filtration & Separation 1986; 1(23): 32-36.
32. Wang B, Xu D L, Chu K W, Yu A B. Numerical study of gas–solid flow in a cyclone separator. Applied Mathematical Modelling 2006; 30: 1326-1342, <http://dx.doi.org/10.1016/j.apm.2006.03.011>.

Tadeusz DZIUBAK

Military University of Technology

Faculty of Mechanical Engineering

ul. Gen. Sylwestra Kaliskiego 2, 00-908 Warsaw, Poland

E-mail: tadeusz.dziubak@wat.edu.pl

Mirosław KARCZEWSKI
Leszek SZCZĘCH

INFLUENCE OF THE F-34 UNIFIED BATTLEFIELD FUEL WITH BIO COMPONENTS ON USABLE PARAMETERS OF THE IC ENGINE

WPŁYW MIESZANIN JEDNOLITEGO PALIWA POLA WALKI F-34 Z BIOKOMPONENTAMI NA PARAMETRY UŻYTECZNE SILNIKA*

The problem of the military vehicles engines fuelling increases with the growth of the amount of vehicles in the armies. At the same time, another problem with fuel supply in modern engines is the use of bio component additives, which changes characteristics (quality) of the used fuels. Therefore, it is important to take actions to adapt engines to powering with fuels coming from renewable sources. The aim of the research was to define the influence of an engine supplying fuel on work parameters and exhaust gases composition in the G9T Renault diesel engine. The tests were conducted during fuelling of the engine with six kinds of fuels: basic fuel (diesel oil), NATO code F-34 fuel, as well as fuel mixtures: F-34 and RME with different ratio. In the result of the research it was concluded that the parameters of the G9T Renault engine with the common rail fuel system in terms of F-34 and RME consumption (using) decreased in comparison to diesel oil basic fuel.

Keywords: IC engine, fuel supply system, F-34 fuel, RME- Rapeseed Methyl Esters.

Problemy zasilania silników pojazdów wojskowych narastają wraz ze wzrostem liczby pojazdów w armiach. Silniki tłokowe i turbinowe wykorzystują paliwa różniące się zakresem temperatury destylacji. Dodatkowym problemem przy zasilaniu współczesnych silników spalinowych jest konieczność stosowania biokomponentów, które mogą zmieniać właściwości paliw podstawowych i wpływać na pogorszenie przebiegu spalania. Dlatego też konieczne jest podejmowanie działań prowadzących do zbadania wpływu paliw pochodzących ze źródeł odnawialnych na parametry pracy silników. Celem badań było ocena wpływu zastosowanego paliwa na parametry użyteczne i skład spalin tłokowego silnika o zapłonie samoczynnym Renault G9T. Badania przeprowadzono podczas zasilania silnika sześcioma rodzajami paliwa: paliwem podstawowym, jakim był olej napędowy, paliwem lotniczym o kodzie NATO F-34, mieszaninami paliw: F-34 i estrów metylowych wyższych kwasów tłuszczowych oleju rzepakowego. W wyniku przeprowadzonych badań stwierdzono, że parametry silnika Renault G9T z wysokociśnieniowym układem wtrysku, zasilanego paliwem F-34 i biokomponentami uległy pogorszeniu w stosunku do podstawowego paliwa, jakim był olej napędowy, co może mieć znaczenie przy wykorzystaniu tego rodzaju paliw w silnikach pojazdów wojskowych.

Słowa kluczowe: silnik spalinowy, układ zasilania, paliwo F-34, RME – estry metylowe kwasów oleju rzepakowego.

1. Introduction

Liquid fuels are the most important source of energy on modern battlefield. Availability of fuels decides about mobility of the army, effectiveness of weapons or other support equipment and delivery of needed amount of supplies. Realisation of increasing requirements of fighting troops in fuels or lubrication oils is one of the most important problems of logistic supplying of a battlefield. It is calculated, that mean use of fuel and lubrication oil may reach 30 kg per one soldier per day [4, 11]. The delivery of such a big quantity of supplies to the army, in terms of enemy interaction on communication systems and supplying infrastructure is an enormous sophisticated problem. It is why there is a trend to standardize all sorts of fuels in the army. For instance NATO introduced F-34 unified fuel for battlefield. As the effect it was decided to unify fuels for reciprocating and turbine internal combustion engines used in land vehicles and on land operating planes. Fuels known as F-34/35 were introduced. It has the same base components as plane fuel JP8 (JET-A1). It's final quality is the effect of using additive components added to the base fuel before final distribution of fuel to a vehicle's tank.

Nowadays the F-34/35 fuel is taken as unified battlefield fuel for all diesel engines of NATO nations. At the end of 20th century the

F-34 fuel was taken under investigation, which focused mainly about elder generation engines completed with in-line and rotation injection pumps [2], without engines with high pressure Common rail systems. From the time of introduction that fuel the injection equipment has changed. In-line injection pumps with plungers and barrels injection units are used very rarely. Common Rail and unit injection systems are used instead. In that system injection pressure reaches $140 \div 200$ MPa. It has a significant change on fuel quantity during injection [7, 8, 10, 13, 14]. Terms condition of fuel before injection to combustion chamber are changed relevantly, and temperature is much higher in comparison to classical in-line injection pump.

The Common Rail systems are commonly used in engines of cars, low duty and heavy duty trucks, locomotives and vessels as well as combat vehicles, for instance the MTU engines of MT 880 series. In these engines in-line pumps used in earlier version were replaced by CR systems. That systems are widely used in heavy duty trucks, which are in possession of Polish Army (MAN, IVECO).

Using raw F-34 fuel to fuel engine equipped with Common Rail system may cause serious change of work parameters. Own investigation of the G9T engine equipped with CR fuelling system led in Military University of Technology [10, 11] shows important diminish of

(*) Tekst artykułu w polskiej wersji językowej dostępny w elektronicznym wydaniu kwartalnika na stronie www.ein.org.pl

maximum torque and NO_x in exhaust gases and increasing of specific fuel consumption.

Table 1. Chosen characteristics of fuels used during investigation [3, 11]

Quantity	Unit	ON IZ-40 fuel	RME fuel	F-34 fuel
Density in temp. 15°C	g/cm ³	0,831	0,881	0,804
Heat value	MJ/kg	43,2	38,3	42,8
Temperature of ignition	°C	66	177	57
Temp. of cold filter block	°C	-31	-9	-54
Kinematic viscosity in 40°C	mm ² /s	2,35	4,60	1,27
Sulphur ratio	mg/kg	350	19	3 000
Cetane number	-	50	43	45

The F-34/35 fuels in compare to diesel oil are characterised by better characteristic in low temperature, less viscosity, less cetan number, less heat value. Technical advantage of unified fuel is: compatibility to aircraft fuel (JET-A1), less sensibility on biological contamination, availability on airports all over the world, better low-temperature characteristic, less possibility of flare/self-ignition in comparison to wide fraction hydrocarbons fuels, less emission of toxic components. Logistic advantages are supplying only one sort of fuel in the whole army, simplification of supply chain and unification of storehouses and storing facilities.

Disadvantages of the unified fuel are increasing needs and demands for fuels based on kerosene and diminish of demands for other fuels. It may cause increasing of a fuel price, diminish of an engine power connected with less heat value of kerosene, needs for modernization of currently used equipment and using fuel additives.

Using of fuels which consist of renewable components such as rapeseed methyl esters (RME) may cause shortening of supply chains. The reason is using local source of a rapeseed from nearby grain elevators which are spread on over the country. The only demand is to introduce an installation for rapeseed oil pressing and for it esterification in the army. Then the vulnerability of the army for fluctuation of supply smoothness in case of a military conflict.

"Ester" fuels are fundamentally different form hydrocarbon fuels by physicochemical characteristics. That is why in case of mixing it the final product parameters are changed. Changing of physicochemical characteristic is also connected to change of an engine work parameters [15]. Presented in different publications results of RME application in a pure form and as a mixture with diesel oil for compression ignition (CI) engines feeding are mainly similar, but the results of investigation where a mixture of RME and F-34 is used are not published. Investigation led on different engines with different combustion systems and an effective power and speed of rotation shows that bio component additive in diesel fuel influences on engine effective powers causing 5 ÷ 15% diminish of rotational speed in all range, and significant, ca. 15%, increase of fuel consumption [1, 4, 5, 9, 14].

Fuel which consists of RME has a little bit different characteristics then hydrocarbons fuels. It depends on different composition, because in molecule structure apart from a carbon and a hydrogen there is a quite big dose of an oxygen (ca.12%). An oxygen ratio and unsaturated bindings conducted to auto ignition and complete combustion. An oxygen contained in fuel has more reactivity then an oxygen consisted in the air, it increase of a cetan number of that fuel. Changing of combustion process has positive influence concentration of toxic components and diminishes a smoke emission. Disadvantage of RME is large amount of water and aggressive influence on rubber parts and film-coating lacquer. [6, 9, 12]. That fuel has more density and viscos-

ity, that its addition to standard F-34 fuel should cause the approach of the F-34 fuel attributes to diesel oil characteristic.

2. Aim and range of work

Current fuel situation in the world and predicted diminishing of natural sources of oil compel to searching for new kinds of fuels. It concerns fuels used to feed of military vehicles as well. Despite that the F-34 fuel was taken by NATO nations as basic fuel, there is very seriously considered the situation that will force to renew this fuel with other, even bio products. In the same time it is noticeable that increasing number of vehicles in military units which are powered by diesel engines equipped with the Common Rail systems and pump injection systems. Regardless of the method of high pressure injection of fuel the basic problems are the phenomena which occur during injection with high pressure of fuel and a fuel mixture creation and combustion processes.

The aim of presented results of investigation was the empiric evaluation of the F-34 fuel and its mixtures with bio rapeseed methyl esters components (RME) influence on parameters of a diesel engine equipped with high pressure injection system on example of Common Rail (CR) system.

3. Object, methodises and range of investigation

The object of investigation was a four cylinder Reanault G9T diesel engine with 95 kW effective power with rotational speed $n=2500$ rpm and 280 N*m torque with rotational speed $n=1750$ rpm, used in propulsion systems of light duty vehicles (LDV) of different producers. This is an engine with direct injection system equipped with a high pressure CR injection system. The engine is turbocharged and equipped with charged air cooling system (intercooler).

The engine was equipped by producer (in factory) with CR fueling system by Bosch, which consists of following components:

- the EDC 15A53 controller (for service),
- the CR/CP1S3/L70/10-1S high pressure fuel pump,
- the BX CRI 1 electromagnetic injectors.

The range of investigation consisted of the engine effective parameters, parameters of combustion process and composition of exhaust gases measure. The investigation was led for all the engine work field (speed characteristic and series of load characteristics in all range of rotational speed of the engine). The investigation of load characteristics was led as a method of passive experiment in steady state of the engine work with rotational speed: 1500 rpm, 2000 rpm, 2500 rpm, 3000 rpm and 3500 rpm. The external speed characteristic was done as well in range of 1000 ÷ 3750 rpm with 250 rpm step. The load characteristics were done by changing load in range from minimum (the idle speed) to maximum (on the external speed characteristic) with 30 N*m step. During investigation the same quantities of load was set. It created the possibility to compare effective parameters of the engine in the same measuring points.

During investigation effective parameters of the engine, temperature (cooling liquid, lubrication oil, exhaust gases before and after turbocharger), concentration of: carbon dioxide, oxygen, carbon monoxide, hydrocarbons, nitrogen oxides, and smoke measured as extinction of radiation absorbed by exhaust gases.

The investigation was led on a standard dynamometer stand. The engine was load by the Schenck W-230 dynamometer with 230 kW maximum power. Torque produced by dynamometer was measured with tensometric transducer. Rotational speed was measured with pulse transducer in cooperation with toothed wheel which was on a dynamometer flange. Measuring of fuel consumption was led with AVL Fuel Balance weightmeter every 5 s. Air flow by intercooler was done by two electric fans. Temperature of cooling liquid was controlled on the level 85 ÷ 90°C with use of an external heat exchanger.

Table 2. List of investigation equipment used during investigation

No.	Name of device / measured quantity	Type	Range	Accuracy
1.	Eddy current brake torque – M_o , rotated speed – n	Eddy current, Schenck W 230	$M_o = (0 \div 700) \text{ N*m}$, $n = (0 \div 4000) \text{ rpm}$	$\pm 0,1 \text{ N*m}$, $\pm 1 \text{ rpm}$,
2.	Fuel weight-meter, fuel consumption – G_e	AVL 7335 Fuel Balance	$(0 \div 200) \text{ kg/h}$	$\pm 0.005 \text{ kg/h}$
3.	Exhaust analyser – measuring of toxic elements concentration in exhaust gases carbon dioxide (CO_2), hydrocarbons (HC), carbon monoxide (CO), nitrogen oxides (NO_x), oxygen (O_2).	AVL CEBII	$\text{CO}_2 (0,01 \div 23)\%$ $\text{HC } (1,0 \div 2200) \text{ ppm}$, $\text{CO } (1,0 \div 11000) \text{ ppm}$, $\text{NO}_x (1,0 \div 6000) \text{ ppm}$ $\text{O}_2 (0,1 \div 21)\%$	$\pm 0,1\%$ measured quantity
4.	Smoke concentration – extinction coefficient of light radiation – k .	AVL Opacimeter 4390	$(0.001 \div 10.0) \text{ m}^{-1}$	$\pm 0.002 \text{ m}^{-1}$
5.	Thermocouple – measuring of exhaust temperature – T	NiCr – NiAl (K)	$(-50 \div 1100)^\circ\text{C}$	$\pm 1^\circ\text{C}$

Results of engine parameters measuring were gathered during all experiment. The purpose was current observation of a technical state or reveal of the engine possible malfunction circumstances and observation of next steps of investigation. The results of the engine effective parameters measuring were calculated back to normal atmospheric condition according to PN-ISO 15550:2009 standard.

During the investigation the engine was fuelled with fuels:

- diesel oil IZ-40 – in the paper it is signed as ON,
- F-34/35 fuel – in the paper it is signed as F-34,

- mixtures of the F-34/35 fuel and RME – in the paper it is signed as B-20, B-40, B-60 and B-80 where the number following letter B stands for a weight ratio of RME in the mixture.

4. Results of investigation

4.1. The external characteristic of the engine

The analysis of investigation results lets to evaluate the different kinds of fuels influence on the engine effective parameters, indi-

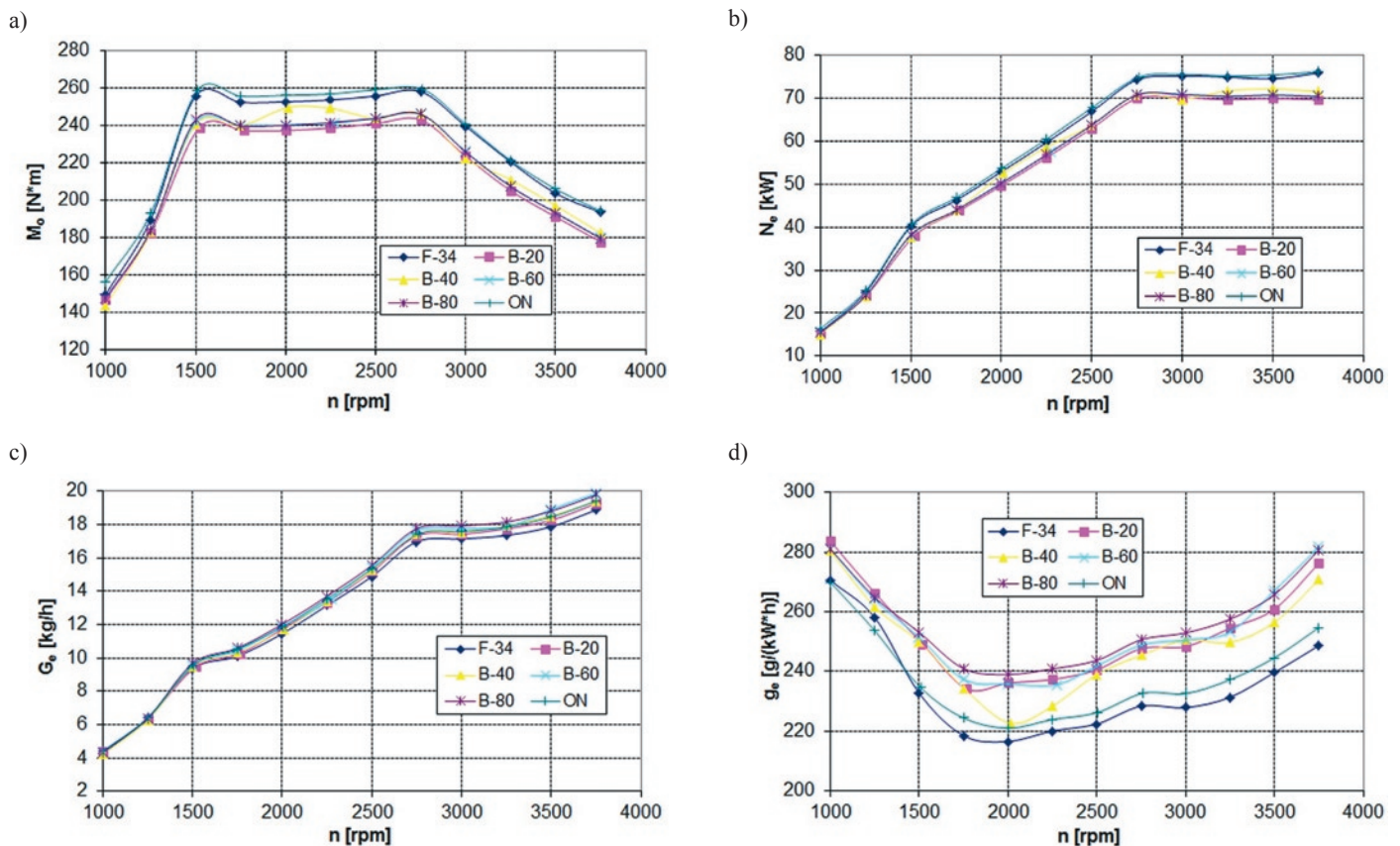


Fig. 1. External characteristic of the engine: a) torque, b) effective power, c) fuel consumption, d) specific fuel consumption.

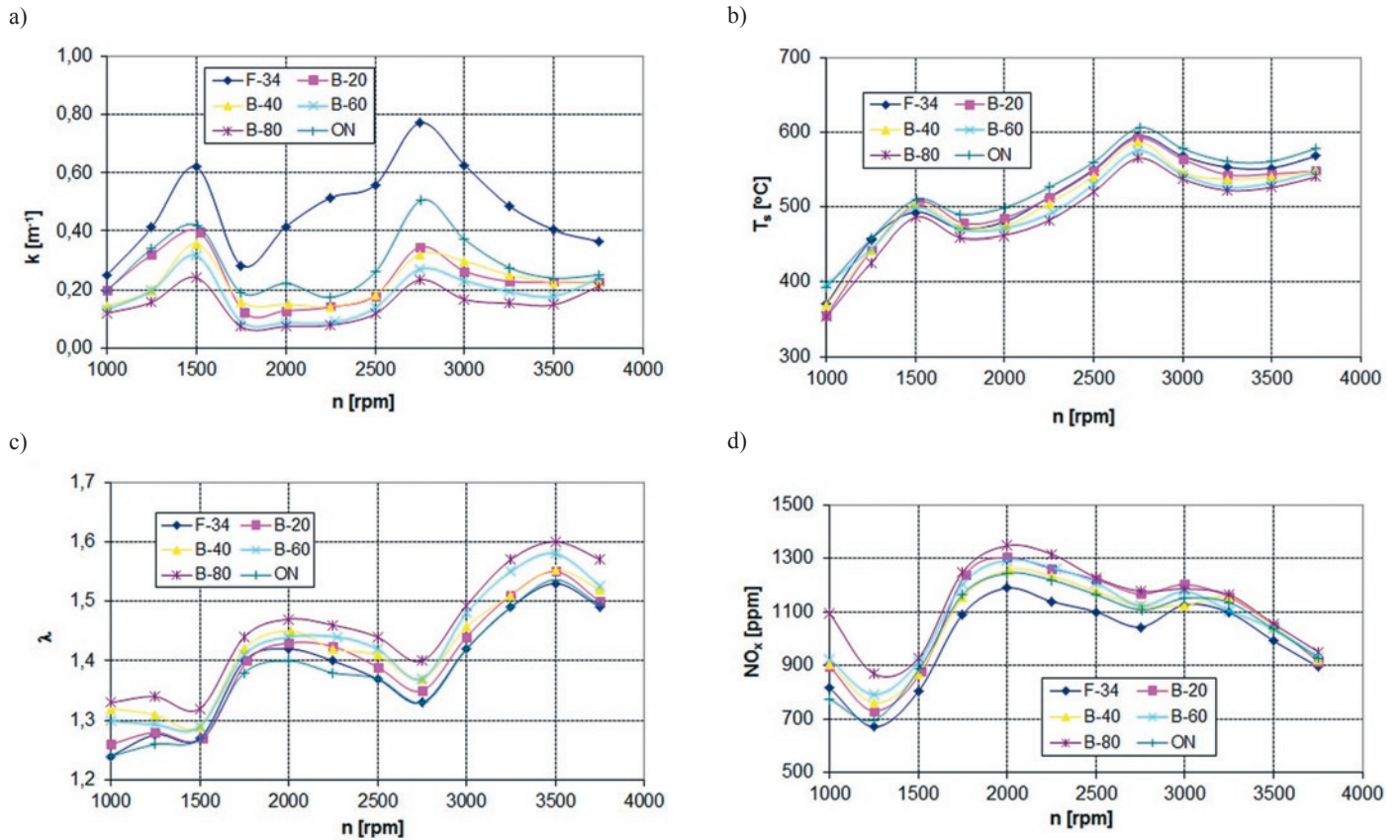


Fig. 2. External characteristic of the engine: a) extinction coefficient of absorbed radiation, b) temperature of exhaust gases, c) air/fuel ratio coefficient, d) concentration of nitrogen oxides in exhaust

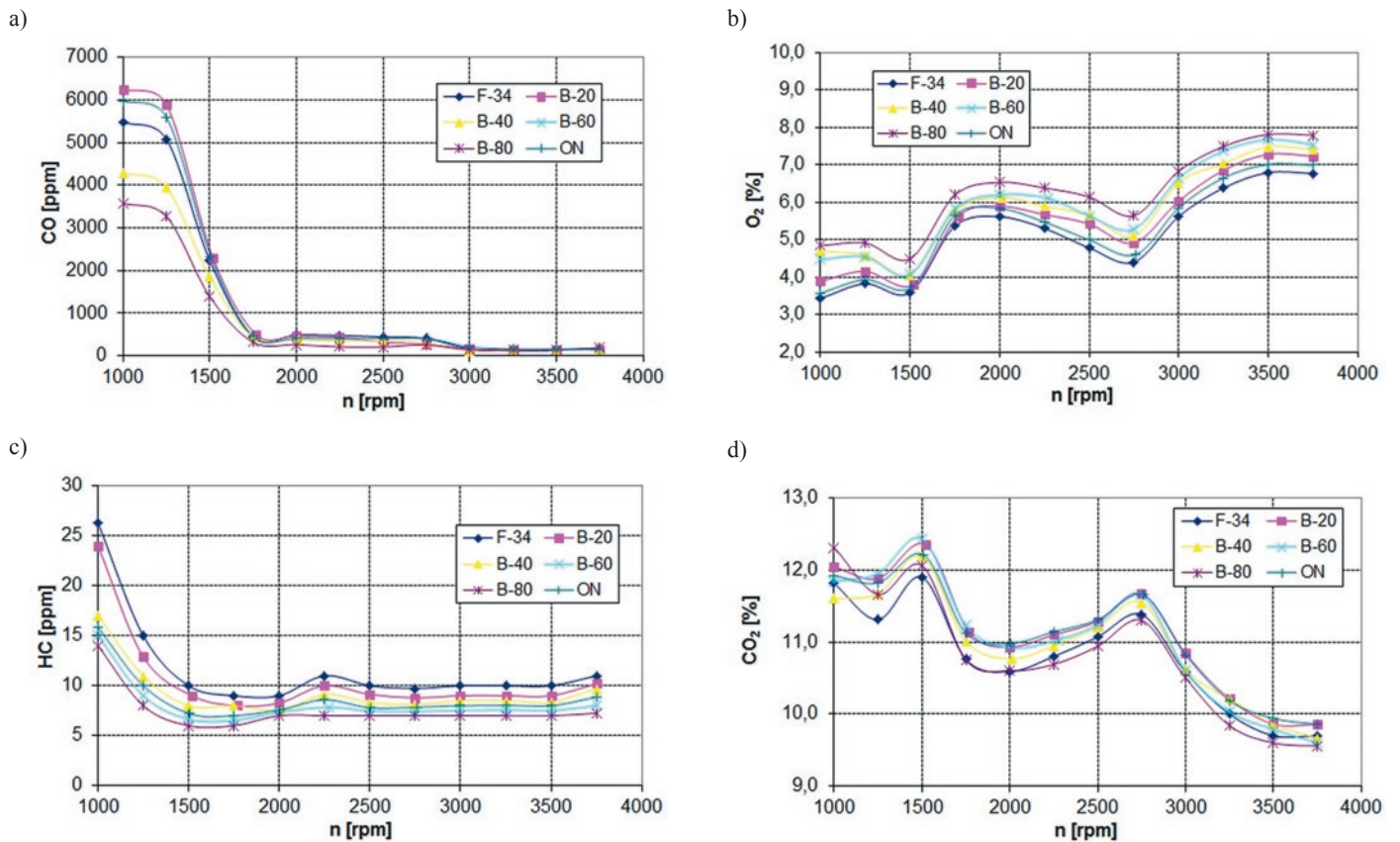


Fig. 3. External characteristic of the engine: a) concentration of carbon monoxide in exhaust, b) concentration of oxygen in exhaust, c) concentration of hydrocarbons in exhaust, d) concentration of carbon dioxide in exhaust

cated parameters, concentration of toxic components and smoke in exhaust gases.

Based on the analysis of measured external characteristics of the G9T engine fuelled with different kind of fuels it has to be said, that the biggest effective power of the engine is reached when it is fuelled with basic fuel (ON) (fig. 1a and 1b). The Usage of the F-34 fuel caused a little diminish of effective power (N_e) ca. $(1 \div 2)\%$. The RME addition to the F-34 fuel caused next diminish of effective power ca. $(7 \div 8)\%$, depending on F-34/RME mixture ratio (percent ratio of ester). The reason of it is increasing of F-34/RME mixture density and diminishing of a heat value. Differences in effective power increase due to rotated speed of the engine.

The least fuel consumption is reached for diesel oil (fig. 1.c), which is the basic fuel, although values for F-34 fuel are very similar. Using RME in fuel mixtures caused increasing of fuel consumption (G_e) ca. $(3 \div 5)\%$ depending on F-34/RME ratio and rotated speed of the engine. It is caused by lesser heat value of the mixture and necessity of delivering more fuel to the cylinder to reach the same effective power.

The least specific fuel consumption value was observed for the F-34 fuel (similar values for ON) (fig. 1.d), which are 233 g/(kW*h) and 236 g/(kW*h) respectively with rotational speed $n=1500$ rpm. Higher specific fuel consumption is caused by smaller heat value and bigger viscosity of RME. Bigger viscosity influenced on worse spraying and bigger heterogeneity of fuel stream. It caused incomplete combustion of air/fuel mixture.

The positive effect of F-34/RME mixtures' influence on emission of smoke was observed (fig. 2.a). The biggest amount of smoke was observed when the engine was fuelled with F-34 (similar values was for ON), although with mixtures with of increased ratio of esters smoke is almost 2...3 times lesser. This trend is observed in whole range of the engine rotational speed. A little later beginning of injection caused strong growth of smoke emission when the engine is fuelled with diesel oil. Diminish of smoke emission is caused by lesser effective power as well.

Temperature of exhaust gases on outlet tube is the highest when the engine is fuelled with ON and reaches 620°C with $n=1500$ rpm (fig. 2b). The lowest temperature ca. 592°C of exhaust gases was observed with mixture B-80 with $n=1500$ rpm, it can be observed diminish of temperature of more than 45°C . There is observed that with increasing RME ratio in fuel mixture temperature of exhaust is lower.

The lowest value of air/fuel ratio coefficient λ is observed when fuelling with F-34 fuel (fig. 2.c). Esters additives evidently increases λ coefficient. In case of B-80 mixture it increases ca. 25%. This is caused by bigger amount of oxygen in RME molecule and lesser need for oxygen during combustion.

Concentration of nitrogen oxides in exhaust gases is the lowest for F-34 and ON fuels in all range of rotational speed (fig. 2.d). During fuelling with RME fuel mixtures it is observed that nitrogen oxides emission is increasing ca. $(10 \div 15)\%$. It is caused by bigger amount of oxygen in RME molecule. Additionally that fuel has bigger aptitude to autoignition (bigger cetan value). It causes change in combustion process. Local temperature inside cylinder increases and causes increasing of nitrogen oxides emission. Concentration of nitrogen oxides is the lowest for F-34 and ON in all range of rotational speed of the engine. During fuelling with F-34/RME mixtures increasing of this component concentration ca. $(10 \div 15)\%$ is observed

While rotational speed is low big concentration of carbon monoxide is observed. Increasing speed causes significant diminish of carbon monoxide concentration. The biggest concentration is observed during fuelling the engine with F-34. Mixture with RME caused diminish of its concentration in range of high speed of the engine ca. $(10 \div 15)\%$ (fig. 3.a). Lower concentration of carbon monoxide in exhaust during fuelling of the engine with F-34/RME mixture testifies about changing of combustion process in compare to pure F-34 and ON. RME additives positively influenced on carbon monoxide

concentration in range of low speed of the engine. When rotational speed is above 1500 rpm it is on the same level, without regard on used kind of fuel.

Concentration of oxygen is very similar as λ coefficient. The lowest value is seen during fuelling with F-34 and ON. The biggest during fuelling with B-80 - increasing reach ca. $(20 \div 25)\%$ (fig. 3.b).

Concentration of hydrocarbons in exhaust gases is about 50% lower when fuelling with B-80 mixture for all range of the engine speed (fig. 3.c). Lower concentration of hydrocarbons in exhaust is a result of higher concentration of oxygen in air/fuel mixture as it was in case of carbon monoxide. It can be seen on fig. 4. Concentration of carbon dioxide is opposite to oxygen concentration. The lowest value is observed for F-34 fuel and the highest (ca. $(6 \div 10)\%$ for F-34/RME mixtures (fig. 3.d).

4.2. Load characteristics

Load characteristics were done in range speed $1500 \div 3000$ rpm with 500 rpm step. In the paper there characteristics with rotated speed $n=1500$ rpm (range of maximum torque speed M_{omax}) and $n=2500$ rpm (range of maximum effective power N_{emax}) are discussed. In this example there was evaluated influence of used fuel and its ecological characteristics. Range of changes is different for all parameters.

The lowest specific fuel consumption is observed during fuelling the engine with F-34 and ON fuels. In range of $n=1500$ rpm it is equal ca. 225 g/(kW*h) (227 g/(kW*h) with ON) with load

$M_o=180$ N*m. Addition of RME to F-34 fuel caused increasing of specific fuel consumption. In dependency of F-34/RME ratio this change is equal $(6 \div 16)\%$ (fig. 4.a). It is caused by lower heat value and higher density of RME. During investigation with lower load value of specific fuel consumption was lower with F-34 and ON then with RME mixtures. It was probably caused by lower temperature in combustion chamber of the engine and worse condition to fuel evaporation. Opposite situation is observed with high load of the engine when combustion intensity is increased because of addition of oxygen from RME molecules.

Having fuel consumption changes analysed it can be said that the lowest values were observed for F-34 and ON fuels. It was 3,66 kg/h and 3,76 kg/h (for $n=1500$ rpm) as well as 7,77 kg/h and 8,00 kg/h (for $n=2500$ rpm). Fuel consumption increasing ca. $(10 \div 12)\%$ (fig. 4b) going after increasing of RME ratio in fuel mixture. It is caused by diminish of mixtures heat value and compensation by increasing mass of fuel used for keeping the same level of load and speed of the engine. Increasing of fuel consumption may be caused by increasing of viscosity and worse spraying, vaporizing and burning of fuel in the engine.

Addition of RME to F-34 fuel caused significant diminish of smoke emission. It influenced on ecological properties of the engine significantly. When $n=1500$ rpm smoke emission is 2 times lower (fig. 5.a) with fuelling of B80 fuel.

Air/fuel coefficient λ is the lowest when load is maximum with $n=1500$ rpm as well as $n=2500$ rpm. Lower values were observed with fuelling by F-34 and ON and the highest with fuelling of B80 mixture (increasing reach ca. 5%). This is caused by highest concentration of oxygen in RME and lower need for oxygen during combustion in the engine chamber.

The lowest concentration of nitrogen oxides in exhaust gases is observed for F-34 and ON fuels in all range of load (fig. 5.d). During fuelling with F-34/RME mixtures nitrogen oxides concentration increasing ca. $(10 \div 15)\%$. It is caused by presence of oxygen in RME. Moreover this fuel has higher tendency for autoignition (bigger cetan number). It influence on combustion process by increasing the temperature inside cylinder and increasing of nitrogen oxides concentration.

High concentration of carbon monoxide is observed with low and medium load of the engine, for speed $n=1500$ rpm and $n=2500$ rpm

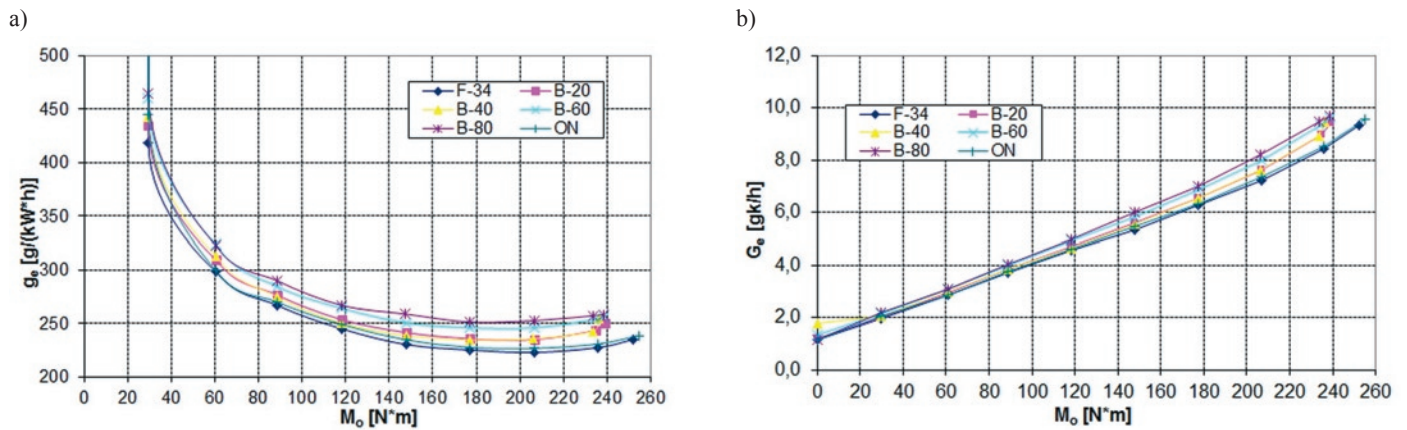


Fig. 4. Load characteristic of the engine, $n = 1500$ rpm: a) specific fuel consumption, b) fuel consumption

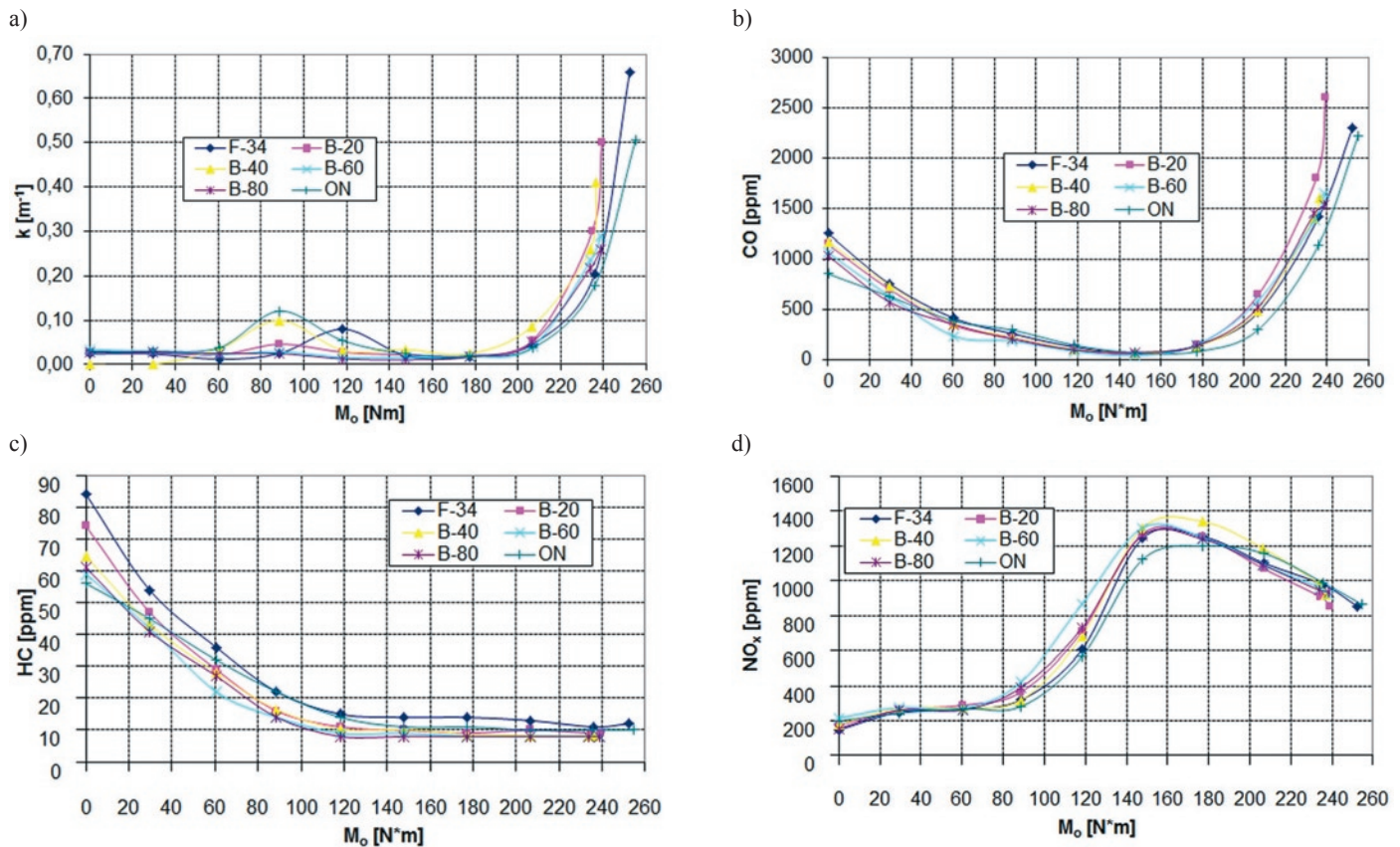


Fig. 5. Load characteristic of the engine, $n = 1500$ rpm: a) extinction coefficient of absorbed radiation, b) concentration of carbon monoxides in exhaust, c) concentration of hydrocarbons in exhaust, d) concentration of nitrogen oxides in exhaust

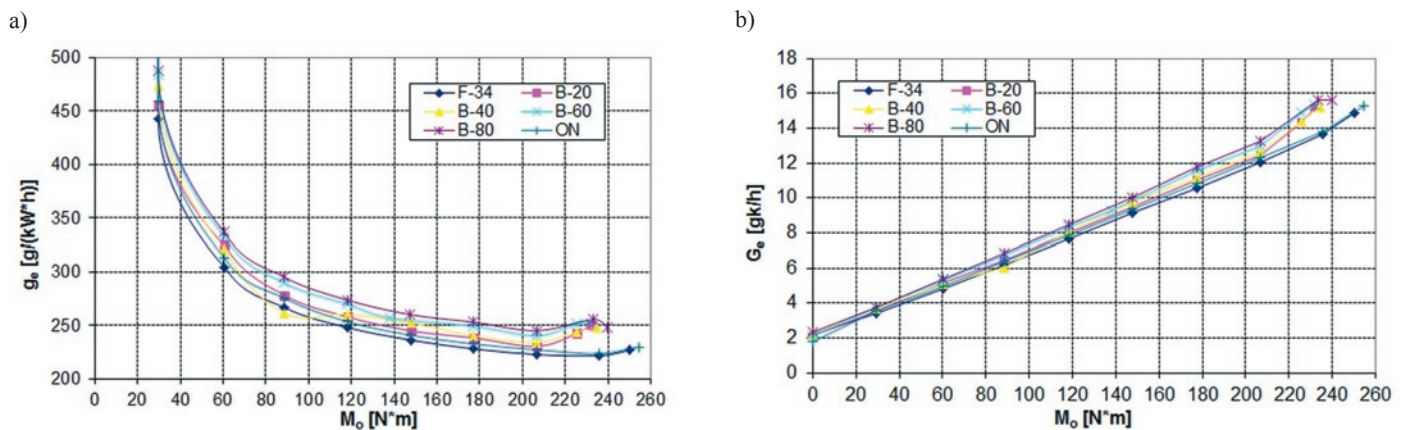


Fig. 6. Load characteristic of the engine, $n = 2500$ rpm: a) specific fuel consumption, b) fuel consumption

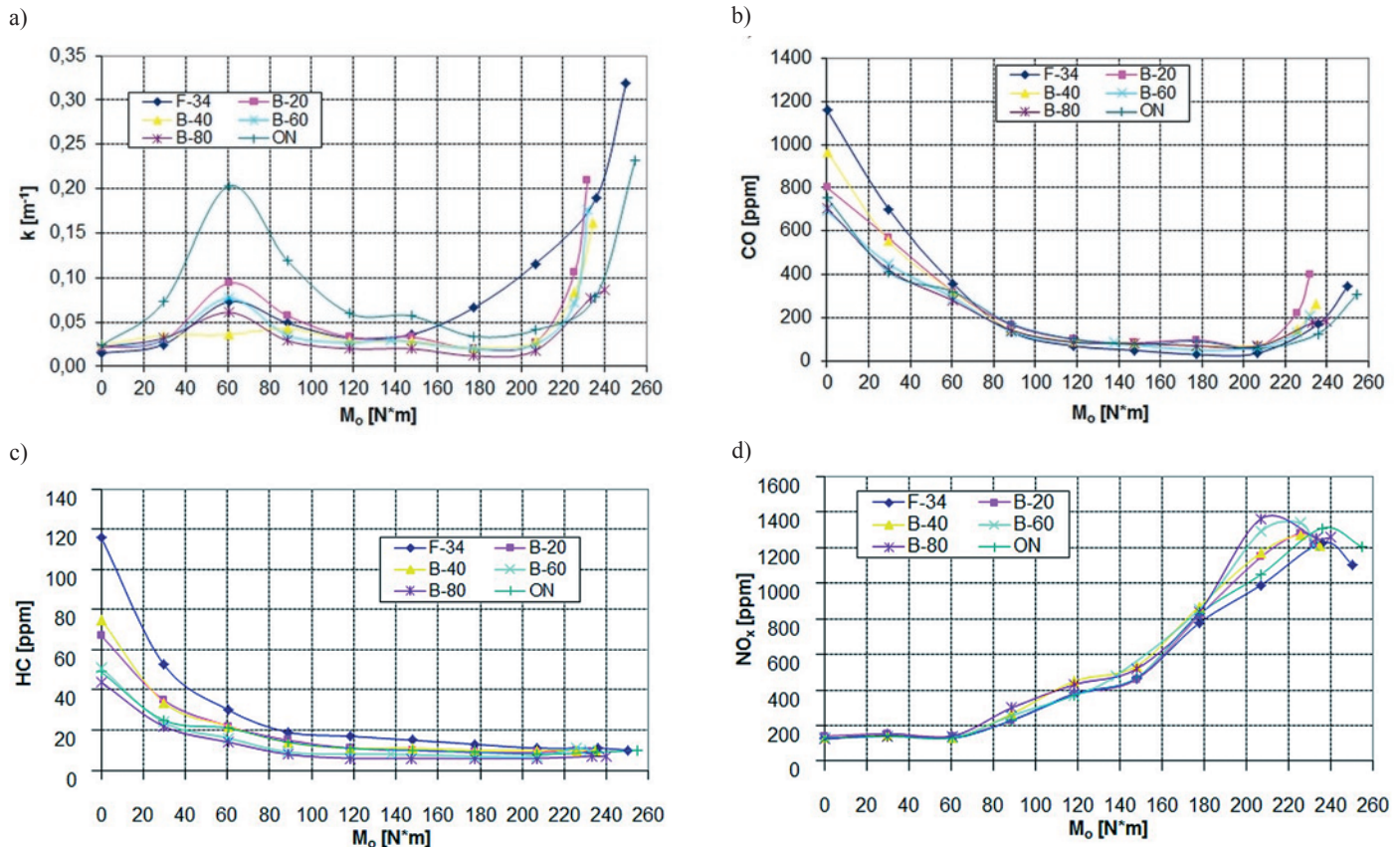


Fig. 7. Load characteristic of the engine, $n = 2500$ rpm: a) extinction coefficient of absorbed radiation, b) concentration of carbon monoxides in exhaust, c) concentration of hydrocarbons in exhaust, d) concentration of nitrogen oxides in exhaust,

as well. In range of medium value of torque concentration of carbon monoxide is persisting on low level. The highest concentration of carbon monoxide occurs during fuelling with F-34 and ON fuels. Ester additives to basic fuels persisted ca. 2 times less concentration of carbon monoxide in exhaust with speed $n=1500$ rpm (fig. 5.b). Lower concentration of carbon monoxide during fuelling the engine with mixture of basic fuel and bio component evidences about better combustion in compare to basic fuels F-34 and ON.

Concentration of hydrocarbons in exhaust gases is lower ca. (50÷60)% during fuelling with RME mixture than with F-34 fuel (with speed $n=1500$ rpm and $n=2500$ rpm) in all range of load. In the same way as carbon monoxide lower concentration of hydrocarbons with ester additives in exhaust gases is a result of its better combustion.

4.3. Influence of F-34 and RME mixture on working parameters of the engine

Analysis of combustion process in the G9T engine combustion chamber was carried on the basis of the engine working cycles investigation. During investigation several dozen of combustion processes cycles were saved, and next 10 of them were statistically recalculated and characteristic parameters of combustion process were found. The maximum value of pressure and angle of auto-ignition delay are shown on graphs. The angle of auto-ignition delay is appointed as a difference between start of an injector needle lift and start of an active combustion in the engine chamber.

Significant differences are seen on line of maximum pressure in the combustion chamber. The highest values of pressure were measured on F-34 and ON fuels. This values are similar but a little bit

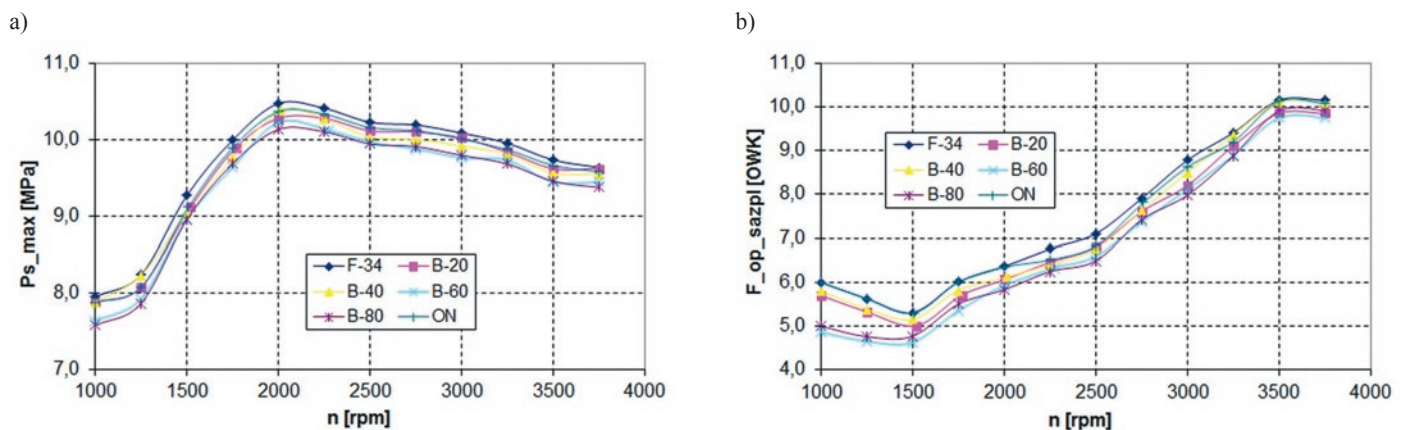


Fig. 8. External characteristic of the engine: a) maximum combustion pressure, b) angle of auto-ignition delay

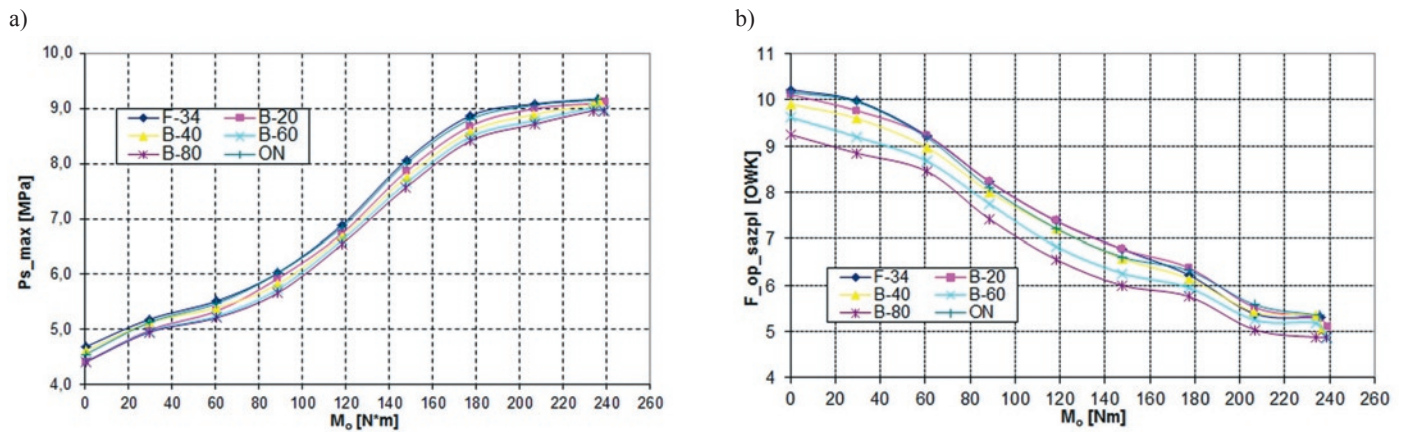


Fig. 9. Load characteristic of the engine, $n = 1500$ rpm: a) maximum combustion pressure, b) angle of auto-ignition delay

higher in case of F-34 fuelling. This difference is no higher than 0.1 MPa (fig. 8.a). When mass ratio of RME increasing in a fuel mixture the diminish of maximum pressure value in the chamber is observed. The lowest values were observed for B80 mixture. Differences between maximum value for F-34 and ON fuels and minimum value for B80 mixture were ca. 0.4 MPa in almost all range of rotational speed of the engine. The reason of such high decrease of pressure value is the lower dose of energy (lower heat value of fuel mixtures) consisted in fuel dose injected to the combustion chamber as well as longer time of injection. It causes slower heat transfer and diminish of peak values of combustion pressure.

After analysing the influence of RME ratio in F-34 fuel on the angle of auto-ignition delay (fig. 8.b) it is seen, that increasing of RME ratio causes shortening of angle of auto-ignition delay. The lowest values of angle of auto-ignition delay were observed for B80 mixture, and the highest were for F-34 fuel. For rotational speed $n=1000$ rpm difference is ca. 1° of crank shaft rotation (CSR) and it decreases with the increase of rotational speed. For speed $n=3500$ rpm is equal 0.2° CSR. Shortening of angle of auto-ignition delay for B80 fuel mixture is caused by lower temperature of auto-ignition as well as oxygen ratio in RME, which influence on speeding up of fuel oxidation.

Similar coincidences may be observed during analysis of load characteristics of the engine. While increasing of ester mass ratio in F-34/RME mixtures the diminish of maximum pressure value in the combustion chamber is observed. The lowest values were measured for B80 fuel mixture. Differences between maximum value for F-34 fuel and minimum value for B80 mixture were ca. 0.4 MPa in all range of the engine load. The reason for that decreasing of maximum pressure value is the longest time of injection of the single dose of fuel needed for creation the adequate torque [8, 11].

The opposite phenomenon may be observed during the analysis of load influence on the angle of auto-ignition delay. The highest differences are observed for the lowest load of the engine (fig. 9.b) and it reaches ca. 1° CSR. With the increase of load that angle diminishes to the level of ca. 0.5° CSR. It is caused by increasing of injection pressure [5, 8, 11]. Fuel injection pressure increase causes better spraying of fuel, the increase of fuel string range and improve homogeneity of air /fuel mixture. It shortens the angle of auto-ignition delay as well.

5. Conclusion

The usage of unconventional fuels for fuelling of military vehicle engines nowadays is a wide disputed problem. The numerous investigations about adaptation of renewable fuels for fuelling of self-ignited engines (diesels) are lead. The best matches for fuelling diesel engines are methyl esters of fatty acids. In Poland they are acquired with processing of rapeseed oil (RME). It is a method to diminish the oil

import. Using fuels based on RME is also beneficial for agricultural development.

The paper contains the results of investigation showing the influence of F-34/RME mixtures on a diesel engine work. The engine was equipped with the Common Rail fuelling system. As results of investigation there were ascertained, that with increasing of RME ratio in F-34 fuel diminish concentration of carbon monoxide and hydrocarbons in exhaust is observed. It is caused by the increasing of oxygen ratio in F-34/RME mixture (oxygen from ester molecule). On the other hand the concentration of nitrogen oxides and oxygen in exhaust increased. This change is proportional to RME ratio in F-34 fuel. This phenomenon is caused by increasing of density and viscosity of fuel mixture. It is connected to slower fuel flow by tubes and injector holes in fuelling system in compare to pure F-34 or ON flow.

As the result of investigation it was ascertained that the G9T Renault engine parameters equipped with the Common Rail system fuelled with F-34/RME mixtures changed in comparison to standard F-34 or ON fuels.

On the basis of the research it is to be said that:

- the diminish of the engine effective power reaches 15% (depending of the engine work condition or used fuel mixture), during fuelling with F-34/RME mixtures,
- in comparison to F-34 and ON fuels, lower effective power of the engine is connected with lower heat value of RME,
- specific fuel consumption is 15% higher for F-34/RME mixtures especially in ranges of high speed and load of the engine,
- RME addition to F-34 beneficially influences on smoke (soot) and particulate matters (PM) emissions; smoke emission may be up to 3 times lower in comparison to the engine fuelled with diesel oil (ON),
- using RME as additives for F-34 fuel causes the diminish of carbon monoxide concentration up to 15% especially in range of low values of rotational speed and load of the engine,
- increasing of oxygen ratio in exhaust gases of ca. 25% is caused by presence of oxygen in RME molecule,
- hydrocarbons concentration in exhaust gases is lower up to 50% during fuelling the engine F-34/RME mixture.

The investigation about unconventional fuels application contributes to its introduction to mass production. Leading that investigation is crucial because it lets us to evaluate the influence of fuel composition on engine's work in different load and speed condition.

References

1. Ambrozik A, Kruczyński S, Jakubiec J, Orliński S. Wpływ zasilania silnika spalinowego o zapłonie samoczynnym paliwem mineralnym i roślinnym na proces wtrysku oraz rozpad strugi paliwa. *Journal of KONES Powertrain and Transport* 2006; 3(13): 21-28.
2. Baczewski K, Kałdoński T, Walentynowicz J. Sprawozdanie z realizacji pracy naukowo-badawczej. Opracowanie koncepcji wdrożenia jednolitego paliwa do lotniczych silników turbinowych i silników wysokoprężnych. Warszawa: Wojskowa Akademia Techniczna, 2001.
3. Baczewski K, Kałdoński T. Paliwa do silników o zapłonie samoczynnym. Warszawa: WKŁ; 2004.
4. Brzozowski K, Nowakowski J. Toxicity of exhaust gases of compression ignition engine under conditions of variable load for different values of engine control parameters. *Eksplatacja i Niezawodność - Maintenance and Reliability* 2011; 4(52): 56-62.
5. Chong Ch. T, Hochgreb S. Spray flame structure of rapeseed biodiesel and Jet-A1 fuel. *Fuel* 2014; 115: 551-558, <http://dx.doi.org/10.1016/j.fuel.2013.07.059>.
6. Daisuke K, Hajime I, Yuichi G, Akira N, Yuzo A. Application of Biodiesel Fuel to Modern Diesel Engine. *SAE Technical Papers*; 2006-01-0233.
7. Dagaut P, Gaïl S. Chemical Kinetic Study of the Effect of a Biofuel Additive on Jet-A1 Combustion. *JOURNAL OF PHYSICAL CHEMISTRY A*, 2007, 111 (19): 3992-4000, <http://dx.doi.org/10.1021/jp067525j>.
8. Hileman J. I, Donohoo Pearl E, Stratton R. W. Energy Content and Alternative Jet Fuel Viability. *Journal of Propulsion and Power* 2010; 26 (6): 1184-1196.
9. Horn U, Egnell R, Johansson B, Andersson O. Detailed Heat Release Analyses With Regard To Combustion of RME and Oxygenated Fuels in an HSDI Diesel Engine. *SAE Technical Papers*; 2007-01-0627.
10. Karczewski M, Wilk M. Assessment of dynamic qualities of the G9T engine with common rail system, fed with battlefield-use fuel blends with a biocomponent. *Journal of KONES Powertrain and Transport* 2011; 1 (18): 243-252.
11. Karczewski M, Walentynowicz J, Szczęch L, Rajewski M, Pszczółkowski J. Sprawozdanie z realizacji pracy naukowo-badawczej. Określenie wpływu jednolitego paliwa F34/35 z biokomponentami na pracę wysokociśnieniowego układu zasilania typu Common Rail". Warszawa: Wojskowa Akademia Techniczna 2010.
12. Mayer A, Czerwiński J, Wyser M, Mattrel P, Heitzer A. Impact of RME/diesel blends on particle formation, particle filtration, and PAH emissions. *SAE Technical Paper* 2005-01-1728.
13. Osipowicz T, Abramek K. Catalytic treatment in Diesel engine injectors. *Eksplatacja i Niezawodność - Maintenance and Reliability* 2014; 16(1): 22-28.
14. Szlachta Z. Zasilanie silników wysokoprężnych paliwami rzepakowymi. Warszawa: WKŁ, 2002.
15. Zając G, Węgrzyn A. Analysis of work parameters changes of diesel engine powered with diesel fuel and FAEE blends. *Eksplatacja i Niezawodność - Maintenance and Reliability* 2008; 3: 17-24.

Mirosław KARCZEWSKI

Leszek SZCZĘCH

Institute of Motor Vehicles and Transportation

Faculty of Mechanical Engineering

Military University of Technology

ul. Gen. Sylwestra Kaliskiego 2, 00-908 Warszawa

E-mails: miroslaw.karczewski@wat.edu.pl, leszek.szczech@wat.edu.pl

Gökhan GÖKDERE
Mehmet GÜRCAN

NEW RELIABILITY SCORE FOR COMPONENT STRENGTH USING KULLBACK-LEIBLER DIVERGENCE

NOWA METODA OCENY NIEZAWODNOŚCI NA PODSTAWIE WYTRZYMAŁOŚCI ELEMENTÓW Z ZASTOSOWANIEM DYWERCENCJI KULLBACKA-LEIBLERA

The reliability of technical systems is one of the most important research subjects in the point reached by modern science. In many recent studies, this problem is solved by evaluation the operation performance of determined one or more components operating under stress. At this point, $R=P(X<Y)$ is taken as a basis. Here, X is the stress applied on the operating component and Y is the strength of the component. In this study we aim to propose a new method by using Kullback-Leibler divergence for computing the reliability of the component under stress-strength model. The superiority of the proposed method is that when the component durability is equal to applied stress Kullback-Leibler divergence is equal to zero. In addition to that when more than one stresses exists at the same time the formed function can include all stresses at the same time. When R is used, this is not possible because of stresses are evaluated separately. As Kullback-Leibler divergence is calculated depending on time, the strength of the component is evaluated within a dynamic structure.

Keywords: reliability, stress-strength model, multistate system model, Kullback-Leibler divergence.

Niezawodność systemów technicznych jest jednym z najważniejszych tematów badawczych we współczesnej nauce. Wiele z ostatnich badań, problem ten rozwiązuje poprzez ocenę wydajności pracy jednego lub większej liczby wybranych elementów działających pod wpływem obciążenia. Za punkt wyjściowy przyjmuje się $R=P(X<Y)$. X to obciążenie przyłożone do elementu roboczego, a Y to wytrzymałość elementu. W przedstawionej pracy, chcemy zaproponować nową metodę, w której do obliczania niezawodności elementu w ramach modelu typu "obciążenie-wytrzymałość" wykorzystuje się dywergencję Kullbacka-Leiblera. Proponowana metoda ma tę przewagę, że gdy wytrzymałość elementu jest równa przyłożonemu obciążeniu, dywergencja Kullbacka-Leiblera jest równa zeru. Poza tym, gdy jednocześnie występuje więcej niż jeden rodzaj obciążenia, utworzona funkcja może obejmować jednocześnie wszystkie te obciążenia. Nie jest to możliwe przy zastosowaniu R , ponieważ obciążenia są oceniane oddzielnie. Ponieważ dywergencję Kullbacka-Leiblera oblicza się w funkcji czasu, wytrzymałość elementu ocenia się w strukturze dynamicznej.

Słowa kluczowe: niezawodność, model typu obciążenie-wytrzymałość, model systemu wielostanowego, dywergencja Kullbacka-Leiblera.

1. Introduction

All technical systems have been designed to perform their intended tasks in a specific ambient. Some systems can perform their tasks in a variety of distinctive levels. A system that can have a finite number of performance rates is called a multi-state system. Generally multi-state system is consisted of components that they also can be multi-state. The performance rates of components can also vary as a result of their deterioration or in consequence of variable environmental conditions. Components failure can lead to the degradation of the entire multi-state system performance.

The performance rates of the components can range from perfect functioning up to complete failure. The quality of the system is completely determined by components.

In some cases, the status of the system depends on the effect of several stresses which cause degradation. The system may not fail fully, but can degrade and there may exist several states of the system. This situation corresponds to multistate systems. For an excellent review of multistate system we refer to Andrzejczak [1]. Indeed, a binary system is the simplest case of a multi-state system having two distinguished states; perfect functioning and completely failure. In a binary system, the definition domains of the states of the system and its components are $\{0,1\}$.

Multi-state systems have been found to be more flexible tool than binary systems for modeling engineering systems. In literature, much attention has been paid to multi-state system modeling. El-Newehi et al. [14] provided axioms extending the standard notion of a coherent system to the new notion of a multistate coherent system. For such systems they obtained deterministic and probabilistic properties for system performance which are analogous to well-known results for coherent system reliability. Hudson and Kapur [19] presented some models and their applications, in terms of reliability analyses, to situations where the system and all its components have a multiple states. Ebrahimi [11] proposed two types of multistate coherent system and presented various properties related to them. Brunella and Kapur [7] studied a series of reliability measures and expanded their definitions to be consisted with binary, multistate and continuum models. Kuo and Zuo [22] focused on multistate system reliability models and introduced several special multistate system reliability models. Eryılmaz [15] studied mean residual and mean past lifetime concepts for multistate systems. Also, for more details about multi-state system model one can see Andrzejczak [2] and [3].

For reliability analysis, stress-strength models are of special importance. In the simplest terms, stress-strength model can be described as an assessment of the reliability of the component in terms of X and Y random variables where X is the random "stress" experienced by the

component and Y is the random “strength” of the component available to overcome the stress. From this simplified explanation, the reliability of the component is the probability that the component is strong enough to overcome the stress applied on it. Then the reliability of the system is defined as:

$$P(X < Y) = \int_0^{\infty} F(x) dG(x), \quad (1)$$

where $F(x)$ and $G(x)$ are distribution functions of X and Y , respectively. Also, for $x < 0$, $F(x) = G(x) = 0$.

Extensive works have been done for the reliability of the component and its estimation under different choices for stress and strength distributions. Chandra and Owen [8] studied the estimation of the reliability of a component where component is subject to several stresses whereas its strength is a single random variable. Awad and Gharraf [4] used a simulation study which compares minimum variance unbiased estimator, the maximum likelihood estimator and bayes estimator for R when X and Y are two independent but not identically distributed Burr random variables. Kotz et al. [20] presented comprehensive information about all methods and results on the stress-strength model. Nadarajah and Kotz [24] calculated R when X and Y are independent random variables from six flexible families of bivariate exponential distributions. Eryılmaz and İçioğlu [16] studied multi-state systems in a stress-strength setup.

Traditionally, stress and strength random variables are considered to be both static when available data on X and Y are considered not to involve the time of system operation. But in real-life reliability studies, the status of a stress-strength system clearly changes dynamically with time. In many important applications, it is very necessary that we estimate the reliability of the system without waiting to observe the system failure. This problem may be achieved by modeling at least one of the stress or strength quantities as time-dependent. To pay attention this problem, Basu and Ebrahimi [5] defined the random lifetime T , of the system as:

$$T = \inf \{t : t \geq 0, Y(t) \leq X(t)\}, \quad (2)$$

where $X(t)$ and $Y(t)$ denote the stress that the system is experiencing at time t and strength at time t , respectively. For a specific time period $(0, t_0)$, the reliability of a stress-strength system, $R(t_0)$, which is defined as the probability of surviving at time t_0 , follows from (2) that:

$$R(t_0) = P(T > t_0)$$

Reliability of a stress-strength system is a function of time. This function has been studied in several papers. Ebrahimi [12] investigated this dynamic model on condition that the strength of the system $Y(t)$ is decreasing in time. Whitmore [28], Ebrahimi and Ramalingam [13], Basu and Lingham [6] considered the problem of estimating the reliability of a system when both $X(t)$ and $Y(t)$ are assumed to be independent Brownian motion processes.

In this paper, inspired by the idea of Kullback-Leibler (KL) divergence, we aim to propose a new method for computing the reliability of the component under stress-strength model. The proposed method provides a simple way for determining the component operation performance under more than one stresses depending on time.

The rest of this paper is organized as four sections. Section 2 gives some information and properties about KL divergence. In Section 3, we explain the proposed method for evaluation of the component's performance under the stress-strength model. Section 4 contains some examples to show the usefulness of the proposed method for different

marginal lifetime distributions of the stress and strength random variables. In Section 5, we summarize what we have done in the article and give some conclusions.

2. KL divergence and properties

The KL divergence (or relative entropy) which introduced by Kullback and Leibler [21], measures the distance between the distributions of random variables. If the densities $p(x)$ and $q(x)$ of P and Q , respectively, exist with respect to Lebesgue measure, the KL divergence $D_{KL}(P \parallel Q)$ of Q from P is defined as:

$$D_{KL}(P \parallel Q) = \int_S p(x) \log \frac{p(x)}{q(x)} dx, \quad (3)$$

where S is the support set of $p(x)$. Note that, $D_{KL}(P \parallel Q)$ is finite only if P is absolutely continuous with respect to Q , and $+\infty$ otherwise. Importantly, the KL divergence remains non-negative and is known as Gibbs' inequality and is zero if and only if $P=Q$, i.e., for any two distributions P and Q :

$$D_{KL}(P \parallel Q) \geq 0.$$

Note that it is not a symmetrical quantity, that is to say:

$$D_{KL}(P \parallel Q) \neq D_{KL}(Q \parallel P).$$

In information theory, machine learning and statistics, the KL divergence plays an important role. The applications of its can be found in many areas. In literature, much attention has been paid to it. Hall [18] examined Discrimination Information or KL loss in the context of nonparametric kernel density estimation. Also, he showed that its asymptotic properties are profoundly influenced by tail properties of the kernel and of the unknown density. Dahlhaus [9] calculated the asymptotic KL information divergence of two locally stationary sequences and the limit of the Fisher information matrix. Do [10] proposed a fast algorithm to approximate the KL distance between two hidden Markov models. Rached et al. [25] provided an explicit computable expression for the KL divergence rate between two arbitrary time-invariant finite-alphabet Markov sources. Wang et al. [27] proposed a universal divergence estimator for absolutely continuous distributions P and Q based on independent and identically distributed samples generated from each source. In Markov-switching regression models, Smith et al. [26] used KL divergence between the true and candidate models to select the number of states and variables simultaneously. Lee and Park [23] considered estimation of the KL divergence between the true density and a selected parametric model.

3. Proposed method

In this section, we introduce a new approach for determining the component operation performance where component is subject to $X_1(t), X_2(t), \dots, X_n(t)$ stresses, whereas its strength, $Y(t)$, is a single random process. Let us initially assume that the stresses are independent random processes having continuous cumulative distribution functions $F_{\xi}^t(x) = P\{X_{\xi}(t) \leq x\}$, $\xi=1, 2, \dots, n$ and the strength has the marginal distribution function $G^t(x) = P\{Y(t) \leq x\}$.

In our method, we first form the KL divergence $D_{KL}(Y(t) \parallel X_{\xi}(t)) = D_{KL}^{(t)}(\xi)$ of $X_{\xi}(t)$ from $Y(t)$ by using (3) for $\xi=1, 2, \dots, n$. After this, we calculate the $D_{KL}^{(t)}(\xi)$, for selected values of the parameters of marginal lifetime distributions of the stress and

strength random variables. Using these values the operation level of the component, depending on the number of stresses, can be defined as follows:

$$\text{The level of the component} = \begin{cases} n, & t < t_n \\ n-1, & t_n \leq t < t_{n-1} \\ n-2, & t_{n-1} \leq t < t_{n-2} \\ \vdots & \vdots \\ 2, & t_3 \leq t < t_2 \\ 1, & t_2 \leq t < t_1 \\ 0, & t_1 \leq t \end{cases}$$

where t_ξ denotes the time when $D_{KL(\xi)}^{(t)}$ is equal to zero, $\xi=1,2,\dots,n$.

Also using $D_{KL(\xi)}^{(t)}$ and t_ξ values we can define the following equations:

$$\zeta_t^v = \begin{cases} D_{KL(v)}^{(t)}, & t_{v+1} < t \leq t_v \\ 0, & \text{otherwise} \end{cases},$$

where $v=1,2,\dots,n-1$ and:

$$\zeta_t^n = \begin{cases} D_{KL(n)}^{(t)}, & t \leq t_n \\ 0, & \text{otherwise} \end{cases}.$$

Now with the help of the above equations, the new reliability score $Y(t)$ for the component can be expressed as follows:

$$Y(t) = \sum_{j=1}^n \chi_t^j \left(j - 1 + \frac{\zeta_t^j}{u_j} \right) \quad (4)$$

where:

$$\chi_t^j = \begin{cases} 1, & \zeta_t^j > 0 \\ 0, & \zeta_t^j = 0 \end{cases},$$

and $u_j = \sup D_{KL(j)}^{(t)}$.

In probabilistic design it is common to use parametric statistical models to compute the reliability obtained from stress-strength interference theory. In the following section we apply our method to a Weibull distributional example.

4. A Weibull distributional example

In this section, we apply the proposed method to find the component operation performance. Assume that the component is subject to $X_1(t)$, $X_2(t)$ and $X_3(t)$ stresses, which remain fixed over time, whereas its strength, $Y(t)$, is a single random variable, which is stochastically decreasing in time.

A Weibull process is a useful model for events that are changing over time. Here, let G be a Weibull cumulative distribution function and its shape parameter $\beta > 0$ is constant with aging time, while its scale parameter $\alpha(t)$ decreases over time.

Then, its cumulative distribution function can be written as:

$$G^t(x) = 1 - \exp \left\{ - \left(\frac{x}{\alpha(t)} \right)^\beta \right\}, x > 0. \quad (5)$$

Similarly, assume that X_1 , X_2 and X_3 are Weibull random variables with cumulative distribution functions:

$$F_l(x) = 1 - \exp \left\{ - \left(\frac{x}{\theta_l} \right)^\beta \right\}, x > 0, \quad (6)$$

where $\beta > 0$ is the shape parameter, $\theta_l > 0$ is the scale parameter of the distributions and $l=1,2,3$. Also both β and θ_l are constant with aging time.

For computing the operation performance of a component at first we must form KL divergence $D_{KL(l)}^{(t)}$ of X_l from $Y(t)$ for $l=1,2,3$. The KL divergence (3) can also be written for X_l ($l=1,2,3$) and $Y(t)$ as:

$$D_{KL(l)}^{(t)} = H(y, x_l) - H(y) \quad (7)$$

where:

$$H(y, x_l) = \int g_t(x) \log \frac{1}{f_l(x)} dx \quad (8)$$

and:

$$H(y) = \int g_t(x) \log \frac{1}{g_t(x)} dx \quad (9)$$

Here, $H(y)$ is the differential entropy of a continuous random variable $Y(t)$ with density $g_t(x)$. Let $Y(t)$, X_1 , X_2 and X_3 are independent. Now, using probability density functions of (5) and (6) in (8), we have:

$$\begin{aligned} H(y, x_l) &= - \int_0^\infty \frac{\beta}{[\alpha(t)]^\beta} x^{\beta-1} e^{-\left(\frac{x}{\alpha(t)}\right)^\beta} \log \left(\frac{\beta}{(\theta_l)^\beta} x^{\beta-1} e^{-\left(\frac{x}{\theta_l}\right)^\beta} \right) dx \\ &= - \log \frac{\beta}{(\theta_l)^\beta} - \frac{\beta(\beta-1)}{[\alpha(t)]^\beta} \int_0^\infty x^{\beta-1} e^{-\left(\frac{x}{\alpha(t)}\right)^\beta} \log x dx + \frac{\beta}{[\alpha(t)]^\beta (\theta_l)^\beta} \int_0^\infty x^{2\beta-1} e^{-\left(\frac{x}{\alpha(t)}\right)^\beta} dx \end{aligned} \quad (10)$$

By making the substitution $u = \left(\frac{x}{\alpha(t)} \right)^\beta$ in (10) and then using following integral:

$$\int_0^\infty e^{-t} \log t dt = -C, \quad (11)$$

where $C \approx 0.577215$ is the Euler's constant (Eq. 8.367.4 in Gradshteyn and Ryzhik, [17]), $H(y, x_l)$ can be obtained as:

$$H(y, x_l) = -\log \frac{\beta}{(\theta_l)^\beta} + (\beta - 1) \left(\frac{C}{\beta} - \log \alpha(t) \right) + \left(\frac{\alpha(t)}{\theta_l} \right)^\beta. \quad (12)$$

Similarly, using probability density function of (5) in (9), we have:

$$H(y) = -\log \frac{\beta}{[\alpha(t)]^\beta} + (\beta - 1) \left(\frac{C}{\beta} - \log \alpha(t) \right) + 1 \quad (13)$$

where suitable transformations and simplifications have been applied and also (11) used.

Table 1. Numerical values obtained from Equation (15) for $\beta=0.9$, $\theta_1=0.01$, $\theta_2=0.02$ and $\theta_3=0.05$

t	$D_{KL(1)}^{(t)}$	$D_{KL(2)}^{(t)}$	$D_{KL(3)}^{(t)}$
5	11.126	4.870	1.234
10	4.870	1.808	0.242
15	2.807	0.871	0.036
20	1.808	0.456	0.
25	1.234	0.242	0.018
30	0.871	0.123	0.059
35	0.627	0.057	0.107
40	0.456	0.021	0.159
45	0.333	0.004	0.211
50	0.242	0.	0.263
55	0.174	0.003	0.312
60	0.123	0.012	0.360
65	0.085	0.025	0.406
70	0.057	0.041	0.451
75	0.036	0.059	0.493
80	0.021	0.078	0.534
85	0.011	0.097	0.574
90	0.004	0.118	0.611
95	0.001	0.138	0.648
100	0.	0.159	0.683

Now using (12) and (13) in (7) we have:

$$D_{KL(l)}^{(t)} = \log \left(\frac{\theta_l}{\alpha(t)} \right)^\beta + \left(\frac{\alpha(t)}{\theta_l} \right)^\beta - 1. \quad (14)$$

Because of $\alpha(t)$ decreases over time, in (14), let $\alpha(t)=1/t$ then we have:

$$D_{KL(l)}^{(t)} = \log(t\theta_l)^\beta + \left(\frac{1}{t\theta_l} \right)^\beta - 1, \quad (15)$$

where $l=1,2,3$.

Clearly, when values in Table 1 used, we have:

$$\text{The level of the component} = \begin{cases} 3, & t < t_3 \\ 2, & t_3 \leq t < t_2 \\ 1, & t_2 \leq t < t_1 \\ 0, & t_1 \leq t \end{cases}$$

where $t_1=100$, $t_2=50$ and $t_3=20$. Then, for $n=3$ in (4), we have:

$$Y(t) = \chi_l^1 \left(\frac{\zeta_l^1}{u_1} \right) + \chi_l^2 \left(1 + \frac{\zeta_l^2}{u_2} \right) + \chi_l^3 \left(2 + \frac{\zeta_l^3}{u_3} \right), \quad (16)$$

where $u_l = \sup D_{KL(l)}^{(t)}; l=1,2,3$,

$$\zeta_l^1 = \begin{cases} D_{KL(1)}^{(t)}, & 50 < t \leq 100 \\ 0, & \text{otherwise} \end{cases}; \zeta_l^2 = \begin{cases} D_{KL(2)}^{(t)}, & 20 < t \leq 50 \\ 0, & \text{otherwise} \end{cases}; \zeta_l^3 = \begin{cases} D_{KL(3)}^{(t)}, & t \leq 20 \\ 0, & \text{otherwise} \end{cases},$$

and:

$$\chi_l^1 = \begin{cases} 1, & \zeta_l^1 > 0 \\ 0, & \zeta_l^1 = 0 \end{cases}; \chi_l^2 = \begin{cases} 1, & \zeta_l^2 > 0 \\ 0, & \zeta_l^2 = 0 \end{cases}; \chi_l^3 = \begin{cases} 1, & \zeta_l^3 > 0 \\ 0, & \zeta_l^3 = 0 \end{cases}.$$

Finally, using (16) for $t=5,10,...,100$ we can obtain the new reliability score presented in Table 2 for the component under stress-strength setup.

It can be observed from numerical values in Table 1 how stresses affect the performance of the component that operates under different parameters. When the component starts working, its strength is greater than all stresses. However, because the component's strength is decreasing depending on the selected time, as the uptime increases at first the KL divergence $D_{KL(3)}^{(t)}$ decreases to near zero. In this period, the strength of the component will begin to move to the good position declined from a perfect position. From the moment that $D_{KL(3)}^{(t)}=0$, the component will pass to the good working period from a perfect working period, the KL divergence $D_{KL(3)}^{(t)}$ is not considered and instead of the KL divergence $D_{KL(2)}^{(t)}$ is taken into account. The KL divergence $D_{KL(2)}^{(t)}$ will be reduced again depending on the time. From the moment it is equal to zero, the component will pass to the average working period from a good working period, the KL divergence $D_{KL(2)}^{(t)}$ is not considered and instead of the KL divergence $D_{KL(1)}^{(t)}$ is taken into account. The KL divergence $D_{KL(1)}^{(t)}$ will be reduced again depending on the time. From the moment it is equal to zero, the operation of the component will end and because the component's durability remains weak in three stresses the component will be impaired.

In stress-strength model which is designed as a theoretically, when the component's strength remains weak in three stresses the component is fail. Let us consider all stresses, by using (1), a joint reliability is not calculated but instead the reliability is calculated separately according to the stresses.

Table 2. New reliability score for the component when $\beta=0.9$, $\theta_1=0.01$, $\theta_2=0.02$ and $\theta_3=0.05$

t	$Y(t)$	t	$Y(t)$
5	3.	55	0.0156
10	2.1961	60	0.0110
15	2.0291	65	0.0076
20	2.	70	0.0051
25	1.0496	75	0.0032
30	1.0252	80	0.0018
35	1.0117	85	0.0009
40	1.0043	90	0.0003
45	1.0008	95	0.00008
50	1.	100	0.

5. Conclusion

In the study, it is theoretically assumed that a component operates under n different stresses and when the component's strength remains weak in all stresses the component is fail. Here, for reliability evaluation we provide a new approach for obtaining the component operation performance. The proposed method described here is a simple and can clearly show the chance of component operation performance depending on time while under all stresses. The evaluation of the component operation performance naturally depends on the probability distributions of stresses and selection of probability distribution of component strength. The method used in the study does not originally depend on probability distribution. Reliability function is a parametric method, but the reliability score proposed from this aspect is nonparametric method for the component. When different effect functions are used instead of probability functions of stress and strength, the recommended method can be easily used.

References

1. Andrzejczak K. Some properties of multistate BW-systems. *Serdica Bulgaricae Mathematicae Publicationes* 1987; 13: 341-346.
2. Andrzejczak K. Deterministic properties of the multistate systems. *Proceedings of the Fifth Anniversary International Conference RELCOMEX'89*, Poland, Książ Castle, September. 1989; 25-32.
3. Andrzejczak K. Structure analysis of multistate coherent systems. *Optimization* 1992; 25: 301-316, <http://dx.doi.org/10.1080/02331939208843826>.
4. Awad A M, Gharraf M K. Estimating of $P(Y < X)$ in the Burr case: A comparative study. *Commun. Statist. Simul. Computat.* 1986; 15:189-403, <http://dx.doi.org/10.1080/03610918608812514>.
5. Basu A P, Ebrahimi N. On the reliability of stochastic systems. *Statist. Probab. Lett.* 1983; 1: 265-267, [http://dx.doi.org/10.1016/0167-7152\(83\)90042-1](http://dx.doi.org/10.1016/0167-7152(83)90042-1).
6. Basu S, Lingham R T. Bayesian estimation of system reliability in Brownian stress-strength models. *Ann. Inst. Statist. Math.* 2003; 55: 7-19, <http://dx.doi.org/10.1007/BF02530482>.
7. Brunelle R D, Kapur K C. Review and classification of reliability measures for multistate and continuum models. *IIE Transactions* 1999; 31: 1171-1180, <http://dx.doi.org/10.1080/07408179908969917>.
8. Chandra S, Owen D B. On estimating the reliability of a component subject to several different stresses (strengths). *Naval Res. Log. Quart.* 1975; 22: 31-40, <http://dx.doi.org/10.1002/nav.3800220104>.
9. Dahlhaus R. On Kullback-Leibler information divergence of locally stationary processes. *Stoch. Process. Appl.* 1996; 62: 139-168, [http://dx.doi.org/10.1016/0304-4149\(95\)00090-9](http://dx.doi.org/10.1016/0304-4149(95)00090-9).
10. Do M N. Fast approximation of Kullback-Leibler distance for dependence trees and hidden Markov models. *IEEE Signal Processing Lett.* 2003; 10: 115-118, <http://dx.doi.org/10.1109/LSP.2003.809034>.
11. Ebrahimi N. Multistate reliability models. *Naval Research Logistics Quarterly* 1984; 31: 671-680, <http://dx.doi.org/10.1002/nav.3800310415>.
12. Ebrahimi N. Two suggestions of how to define a stochastic stress-strength system. *Statist. Probab. Lett.* 1985; 3: 295-297, [http://dx.doi.org/10.1016/0167-7152\(85\)90058-6](http://dx.doi.org/10.1016/0167-7152(85)90058-6).
13. Ebrahimi N, Ramalingam T. Estimation of system reliability in Brownian stress-strength models based on sample paths. *Ann. Inst. Statist. Math.* 1993; 45: 9-19, <http://dx.doi.org/10.1007/BF00773665>.
14. El-Newehi E, Proschan F, Sethuraman J. Multi-state coherent system. *Journal of Applied Probability* 1978; 15: 675-688, <http://dx.doi.org/10.2307/3213425>.
15. Eryilmaz S. Mean Residual and Mean Past Lifetime of Multi-State Systems With Identical Components. *IEEE Trans. Reliab.* 2010; 59: 644-649, <http://dx.doi.org/10.1109/TR.2010.2054173>.
16. Eryilmaz S, İşçioglu F. Reliability evaluation for a multi-state system under stress-strength setup. *Commun. Statist. Theor. Meth.* 2011; 40: 547-558, <http://dx.doi.org/10.1080/03610920903411242>.
17. Gradshteyn I S, Ryzhik I M. *Table of Integrals, Series and Products*. 6th ed. California: Academic Press, 2000.
18. Hall P. On Kullback-Leibler loss and density estimation. *Ann. Statist.* 1987; 15: 1491-1519, <http://dx.doi.org/10.1214/aos/1176350606>.
19. Hudson J C, Kapur K C. Reliability analysis for multistate systems with multistate components. *IIE Transactions* 1983; 15: 127-135, <http://dx.doi.org/10.1080/05695558308974623>.
20. Kotz S, Lumelskii Y, Pensky M. *The Stress-Strength Model and its Generalizations. Theory and Applications*. Singapore: World Scientific, 2003, <http://dx.doi.org/10.1142/9789812564511>.
21. Kullback S, Leibler R A. On information and sufficiency. *Ann. Math. Statist.* 1951; 22: 79-86, <http://dx.doi.org/10.1214/aoms/1177729694>.
22. Kuo W, Zuo M J. *Optimal Reliability Modeling, Principles and Applications*. New York: John Wiley & Sons, 2003. 23, Lee Y K, Park B U. Estimation of Kullback-Leibler divergence by local likelihood. *Ann. Inst. Statist. Math.* 2006; 58: 327-340.
23. Lee Y K, Park B U. Estimation of Kullback-Leibler divergence by local likelihood. *Ann. Inst. Statist. Math.* 2006; 58: 327-340.
24. Nadarajah S, Kotz S. Reliability for some bivariate exponential distributions. *Mathematical Problems in Engineering* 2006; 2006: 1-14, <http://dx.doi.org/10.1155/mpe/2006/41652>.
25. Rached Z, Alajaji F, Lorne Campbell L. The Kullback-Leibler Divergence Rate Between Markov Sources. *IEEE Trans. Inform. Theory*

- 2004; 50: 917-921, <http://dx.doi.org/10.1109/TIT.2004.826687>.
26. Smith A, Naik P A, Tsai C L. Markov-switching model selection using Kullback-Leibler divergence. *Journal of Econometrics* 2006; 134: 553-577, <http://dx.doi.org/10.1016/j.jeconom.2005.07.005>.
27. Wang Q, Kulkarni S, Verdú S. Divergence Estimation of Continuous Distribution based on data-dependent Partitions. *IEEE Trans. Inform. Theory* 2005; 51: 3064-3074, <http://dx.doi.org/10.1109/TIT.2005.853314>.
28. Whitmore G A. On the reliability of stochastic systems: a comment. *Statist. Probab. Lett.* 1990; 10: 65-67, [http://dx.doi.org/10.1016/0167-7152\(90\)90113-L](http://dx.doi.org/10.1016/0167-7152(90)90113-L).

Gökhan GÖKDERE**Mehmet GÜRCAN**

Department of Statistics, Faculty of Science

Fırat University, TR-23119 Elazığ, Turkey

E-mails: g.g.gokdere@gmail.com, mehmetgurcan2000@yahoo.com

Joanna RYMARZ
Andrzej NIEWCZAS
Aneta KRZYŻAK

COMPARISON OF OPERATIONAL AVAILABILITY OF PUBLIC CITY BUSES BY ANALYSIS OF VARIANCE

PORÓWNANIE GOTOWOŚCI AUTOBUSÓW KOMUNIKACJI MIEJSKIEJ Z ZASTOSOWANIEM METODY ANALIZY WARIANCJI*

This paper analyses the influence of selected factors of operational availability of public city buses from the Municipal Transport Company (MPK) in Lublin based on a case study for two makes of buses: Solaris and Mercedes-Benz. The study investigated changes in operational availability in a function of operating time with a division into two periods of operation: warranty and post-warranty. To evaluate the significance of differences between average operational availability with regards to the above periods, one-way analysis of variance was applied. The results demonstrate that in the warranty period the operational availability of both makes of buses is similar; while the post-warranty period reveals a significant difference, with the operational availability being higher for Mercedes buses. As a result, this method can be of use for investment projects during purchase of new vehicles.

Keywords: public city buses, analysis of variance, ANOVA, operational availability.

Celem pracy była analiza wpływu wybranych czynników gotowości technicznej autobusów komunikacji miejskiej na przykładzie autobusów marki Solaris i Mercedes-Benz w Miejskim Przedsiębiorstwie Komunikacyjnym (MPK) w Lublinie. Przeprowadzono badania zmian gotowości technicznej w funkcji czasu użytkowania z podziałem na dwa okresy użytkowania: gwarancyjny i pogwarancyjny. Do sprawdzenia istotności różnic średnich wartości gotowości technicznej, w zależności od marki autobusów oraz w zależności od okresów eksploatacji zastosowano jednoczynnikową analizę wariancji. Wykazano, że w okresie gwarancyjnym gotowość techniczna autobusów obu marek jest porównywalna, natomiast w okresie pogwarancyjnym jest istotnie różna, wyższa dla autobusu marki Mercedes. W rezultacie metoda ta może zostać użyta do programu inwestycyjnego podczas zakupu nowych pojazdów.

Słowa kluczowe: autobusy komunikacji miejskiej, analiza wariancji, ANOVA, gotowość techniczna.

1. Introduction

There are numerous works on availability studies, among others. In [3] a general overview of main strategies and technical steps which should be taken when designing an optimum public transportation system. Operational availability as a characteristic of transportation systems is used for analysis of so-called fast reaction systems in random moments of operations (t), for example air force, emergency medical services, fire brigades or public transportation systems [5]. Analysis of availability of different systems has been researched into by many studies in recent years. Nowadays it is applied in many sectors of the industry, including aircraft and defense sectors as well as power engineering and transportation. In [5] the authors present the possibilities of application of the RAM (Reliability, Availability and Maintainability) model in industry to identify unreliable devices with respect to operation-related frequent failures or requirements.

In [23] the authors investigate the dependencies between availability and maintainability of transportation modes and the costs of unplanned breaks and vehicle operation. The authors developed an economically-optimum model of implementation for inspection and technical services that was based on current data on vehicle damage. The study [19] examined several scenarios regarding the reliability of buses and repair service employees' shift system in a transport company to increase the vehicle's availability and reduce costs of the

whole system regarding its disturbance at vehicle failure. In [18] and [28] the authors present an optimization model of public transportation considering the design of transit routes, selection of modes of transportation and timetables. The study [24] presents a method of designing the availability of technological objects, and in [10] a theory pertaining to semi-Markov processes was used based on the authentic municipal transport system. In [2] the authors identified the object's aptitude condition, and thus optimal control processes of operation and service of particular objects on the example of public transportation bus engines.

In [27] the authors present different methods applied to estimate a functional form between overall quality of service and explanatory variables, including questionnaire items related to satisfaction accessibility (availability, information, time characteristics of service, customer service, comfort, safety, infrastructure and environment).

The operational availability index was mainly used for bus schedule reliability and current monitoring of transportation systems, especially vehicle punctuality [3, 4, 26] however, it was not often used to control quality management systems and maintenance of a given make of a vehicle.

The municipal transport company should assure a continuous monitoring on maintenance process in terms of current availability of used fleet. Resting on this assumption, the authors of the paper conducted studies on operational availability of buses of the selected makes from

(*) Tekst artykułu w polskiej wersji językowej dostępny w elektronicznym wydaniu kwartalnika na stronie www.ein.org.pl

the Municipal Transport Company (MPK) in Lublin during 6 years of their operation. This paper includes the findings of previous studies presented in [16] and [17] which are related to operational availability and reliability of buses. Also, the paper [12] presented some aspects of operation of the municipal transport system in the city of Lublin. In the present paper, the study period of the sample is extended and analysis by the one-way ANOVA method is conducted.

2. Theoretical aspects of operational availability of public buses and ANOVA analysis

The availability of a technical object is defined as the probability of an object's usability [13]. It is interpreted as the probability of an object's ability to undertake work in a defined time [9, 20]. When a system is in standby, this means that the system is neither out of operation due to preventive maintenance service nor useless due to failure. Thus, the object's availability depends not only on maintenance-related breaks, but also on the probability of the system's not performing its assigned functions (failure effect) [21]. The aim of effective maintenance is to reduce the time of unplanned system breaks (Mean Down Time MDT) and related costs [29]. Based on the literature [3, 13, 20, 24, 25] and data collected from MPK in Lublin, it has been assumed that the operational availability will be defined in this study according to the following formula:

$$K_g(t) = \frac{N_z - N_n}{N_z} \times 100 \quad (1)$$

where:

N_z – is the number of technical objects available for use in a given operating period in a given transport system;
 N_n – is the number of technical objects unavailable for use in a given operating period in a given transport system.

The aim of evaluating operational availability of buses is usually to predict if a given technical object will be available in the future and if a transport task can be executed.

This paper applies the analysis of variance to availability of a technical system. The analysis of variance (ANOVA) was formulated by Fisher in the 1920s [11, 22]. The method allows us to evaluate the influence of independent classifying factor x_j ($j=1, \dots, m$) on distribution of the dependent variable y . The analysis enables verifying if average values of the variable y for many samples are comparable. The analysis of variance was used by many authors such as [1, 7, 15] usually as a complementary analysis.

Based on the results of calculations, a zero hypothesis has to be verified with respect to equality of average values of the dependent variable for all k levels of the classifying factor:

$$H_0: \bar{y}_1 = \bar{y}_2 = \dots = \bar{y}_k \quad (2)$$

where:

\bar{y}_i ($i=1, \dots, k$), refers to an average value of the discussed variable for the k -th level of factor.

An alternative hypothesis H_1 is that at least two from the averages y_1, \dots, y_k are different, thus:

$$\bar{y}_i (i=1, \dots, k) \quad (3)$$

The one-factor ANOVA is used to check the statistical significance between independent groups based on differences in variance between the groups or within them. In the paper, the analysis of vari-

ance between groups MS Effect was applied according to the following sum of square equations [25]:

$$SS_{all} = \sum_{i=1}^p \sum_{j=1}^n (y_{ij} - \bar{y})^2 \quad (4)$$

$$SS_{between} = n \sum_{i=1}^p (\bar{y}_i - \bar{y})^2 \quad (5)$$

$$SS_{within} = \sum_{i=1}^p \sum_{j=1}^n (y_{ij} - \bar{y}_i)^2 \quad (6)$$

The degree of freedom DF between the groups is equal to the number of groups reduced by one. Inside the groups it is equal to the number of observations minus the number of groups. The MS variance is equal to the quotient of the sum of squares of freedom degrees. At the same time, the variance test is based on designation of the statistics $F = SS_{between} / SS_{within}$. The higher the F statistic is, the greater influence it has.

Assumptions that are fundamental for the analysis of variance include:

- measurability of dependent variables on a quantitative scale;
- independence of random variables in the analysed groups;
- normality of distribution of the dependent variable for each factor;
- homogeneity of variance for each factor.

In order to verify the thesis about normal distribution of the dependent variable, one of the following statistic tests can be used: χ^2 , Shapiro-Wilk's, Lilliefors' or a similar one using the quantile curve [8]. In order to verify the thesis about homogeneity of variance, the following tests can be applied: Levene's, Barlett's, Cochran's. Levene's test is the most resistant to deviations from normal probability distribution of the results, however Barlett's test works better when the criterion of normal distribution of the results is met.

3. Details of the study

The study was performed on 22 Mercedes-Benz 628 Conecto LF buses and 20 Solaris Urbino 12 buses. All buses were observed from the first day of their operation. The initial maintenance mileage was low and comparable for both makes of vehicles. The studies were conducted under natural conditions over 6 years of operation (2008-2014). The operational availability of the buses was recorded over calendar time from the first to the seventy-second month of operation. This corresponded to a total maintenance mileage equal to 7.73 million km for all 20 Solaris buses and 7.29 million km for all 22 Mercedes buses, respectively. An average monthly mileage from the last 72 months of operation was 6096 km for Solaris buses and 6464 km for Mercedes buses.

4. Empirical results

The operational availability factor of Solaris and Mercedes-Benz buses with regards to calendar time as a function of monthly operating time is presented in Figure 1. In the first period of operation (warranty), thus up till approx. the twentieth month of operation, the availability of Solaris buses was 0.897 on average. Afterwards, the factor started to decrease, reaching in the sixty-second month of operation the lowest value – 0.700. An average operational availability for the whole study period was 0.870 for Solaris buses and 0.908 for Mercedes buses, respectively. The average availability of Mercedes buses was higher only by 3.8% and was equal to 0.909 at a standard deviation of 0.059. The paper [6] analyzes the factors related to maintenance costs of buses, including the costs of fluids, repair and maintenance services.

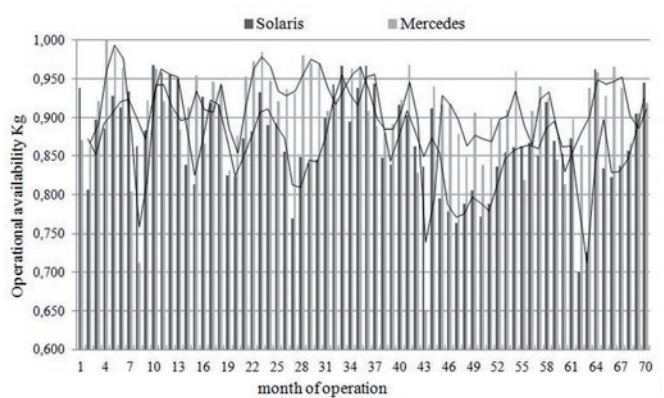


Fig. 1. Operational availability Kg of buses versus operating time (months)

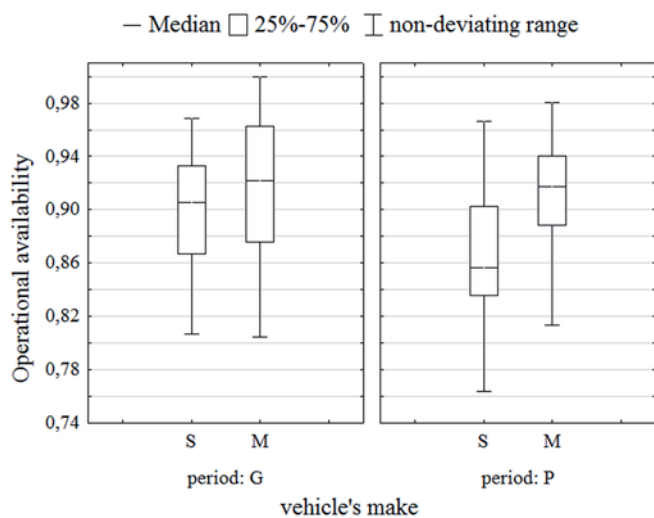


Fig. 2. Box plot of dependent variable – availability of uses (S-Solaris, M-Mercedes) in warranty (G) and post-warranty (P) periods

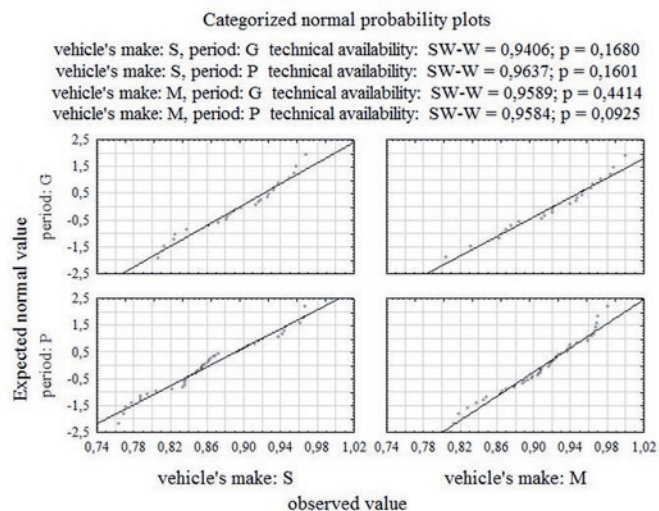


Fig. 3. Categorized normal probability plots in warranty (G) and post-warranty (P) periods

The outliers in specific periods of vehicle use were verified and excluded from further calculations. The results of operational availability divided into two groups: warranty (1-24 months) and post-warranty (25-72 months), are presented in Figure 2. In order to verify the significance of differences in average operational availability of both makes of buses, a one-way analysis of variance was conducted.

Table 1. Results of Levene's test for warranty and post-warranty periods

Operating period	Variable	Effect	Levene's test of variance homogeneity Marked effects are significant with $p < 0.05000$			
			MS Effect	MS Error	F	p
warranty	operational availability	vehicle's make	0.00003	0.00077	0.04228	0.83801
post-warranty			0.00188	0.00088	2.12498	0.14836

Table 2. Results of Hartley, Bartlett and Cochran tests for warranty and post-warranty periods

Operating period	Variable	Effect	Test of variance homogeneity				
			Hartley	Cochran	Bartlett	DF	p
warranty	operational availability	vehicle's make	1.1540	0.5357	0.1129	1	0.7369
post-warranty			1.6325	0.6201	2.6802	1	0.1016

The analysed variables are measurable and independent, therefore, the two first assumptions of variance analysis are met. Factors such as a make of a bus and warranty and post-warranty periods are independent. The Kg factor is measurable. The normal probability of distribution (third fundamental assumption) in the studied groups of data was evaluated, creating categorized normal probability plots for each group (a make of a bus). Given that according to Shapiro-Wilk's test the significance level in all four cases is higher, $p > \alpha = 0.05$, there are no grounds for rejecting the zero hypothesis (H_0) on the normal probability of distribution of operational availability of vehicles (Fig. 3).

Next, the fourth assumption on variance homogeneity was verified. Tables 1 and 2 show the probability results with respect to effect (a make of a bus) and type of operating period: warranty and post-warranty. Analyzing the obtained data by means of two normal probability tests, there are no grounds for rejection of the zero hypothesis in both operating periods of the analysed vehicles. Therefore, it can be concluded that the assumption on homogeneity of variance is met in all four cases.

The one-way variance analysis was conducted to examine the influence of a make of a bus on the vehicle's operational availability in two operating periods: warranty and post-warranty. It can be concluded from Table 3 that the significance level p for the vehicle's make in the warranty period is higher than 0.05, thus $p = 0.0929$, therefore there

Table 3. Results of one-way analysis of variance in warranty and post-warranty operating periods

Operating period	Effect	Univariate significance tests for the dependent variable: technical availability				
		SS	DF	MS	F	p
warranty	free term	38.805	1	38.805	15498.3	0.0000
	vehicle's make	0.007	1	0.007	2.95	0.0929
	error	0.113	45	0.0025	-	-
post-warranty	free term	73.22	1	73.22	30934	0.0000
	vehicle's make	0.053	1	0.053	22.58	0.0000
	error	0.215	91	0.002	-	-

Vehicle's make; warranty operating period
Current effect: $F(1, 45)=2,9475$, $p=0,09289$

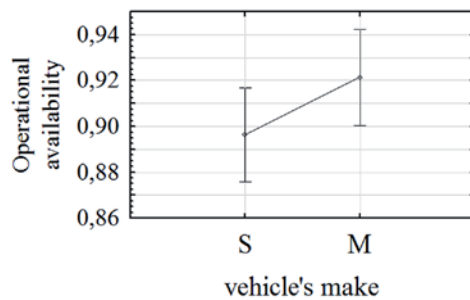


Fig. 4. Operational availability interaction curve in the operating warranty periods for Mercedes (M) and Solaris (S) buses

Operating period for Solaris buses;
Current effect: $F(1, 68)=6,2560$, $p=0,01479$

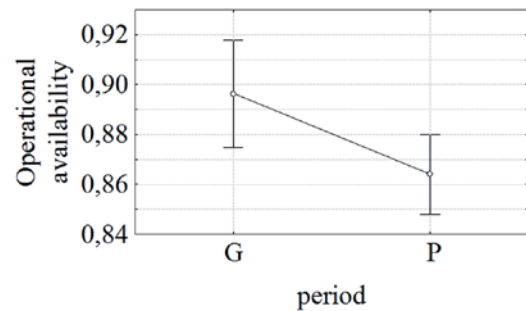


Fig. 6. Operational availability interaction curve for "operating periods": Solaris buses in warranty and post-warranty periods

Vehicle's make; post-warranty operating period
Current effect: $F(1, 91)=22,580$, $p=0,00001$

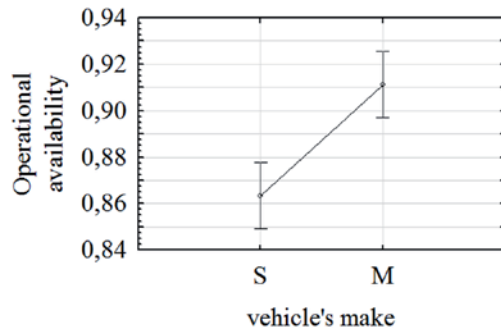


Fig. 5. Operational availability interaction curve in the operating post-warranty periods for Mercedes (M) and Solaris (S) buses

Operating period for Mercedes buses;
Current effect: $F(1, 68)=0,74797$, $p=0,39016$

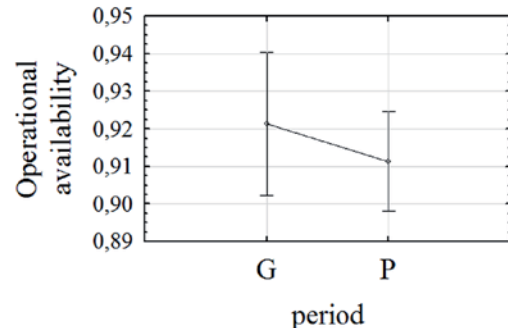


Fig. 7. Operational availability interaction curve for "operating periods": Mercedes buses in warranty and post-warranty periods

Table 4. Results of Levene's test for operating period

Operating period	Variable	Effect	Levene's test of variance homogeneity Marked effects are significant with $p < 0.05000$			
			MS Effect	MS Error	F	p
Solaris	operational availability	warranty and post-warranty period	0.0001	0.0009	0.0941	0.7600
Mercedes			0.0011	0.0007	1.4371	0.2348

Table 5. Results of Hartley, Bartlett and Cochran tests for "operating period"

Operating period	Variable	Effect	Test of variance homogeneity				
			Hartley	Cochran	Bartlett	DF	p
Solaris	operational availability	warranty and post-warranty period	1.2641	0.5583	0.3999	1	0.5271
Mercedes			1.4903	0.5984	1.2134	1	0.2707

are no grounds for rejection of the zero hypothesis (H_0). This indicates that the average operational availability in the warranty period for buses of both analysed makes does not differ significantly. The probability that $F = 22.58$ in the post-warranty period equals $p = 0.0000$. It means that with the test statistics assumed to be $p = 0.05$, the zero hypothesis (H_0) should be rejected and an alternative hypothesis (H_1) should be adopted on statistically significant difference of averages in individual groups in the post-warranty period. It can therefore be concluded that for the post-warranty period the value of operational availability differs significantly for both analysed makes of buses.

The test results of variance analysis are confirmed by interaction curve (Figs. 4 and 5). The curve illustrates the confidence intervals of 95% and average availability for the analysed operating periods. The average availability of Mercedes buses in the warranty and post-warranty periods is higher than that of Solaris buses, and a relative difference is 2.5% and 4.8% for the given operating period.

The following stage of variance analysis was conducted for the investigated operating periods, i.e. warranty and post-warranty. The normal probability test results were confirmed as per Fig. 3. Tables 4 and 5 list the probability values of tests of homogeneity assumptions of variance for classifying the effect of "operating period". Analyzing the obtained results by means of two normal probability tests, there are no grounds for rejection of the zero hypothesis that

$p > 0.05$. The assumption of homogeneity of variance is therefore met in all four cases.

A one-way analysis of variance was conducted to investigate the influence of "operating period" on operational availability of Solaris and Mercedes buses. It can be concluded from Table 6 that the significance level p for Solaris buses is lower than expected, as it equals $p = 0.0148$, therefore the zero hypothesis on equal averages should be rejected. This demonstrates a significant difference in operational availability of Solaris buses in the warranty and post-warranty periods.

Table 6. Results of one-way analysis of variance for "operating period"

Operating period	Effect	Univariate significance tests for the dependent variable: operational availability				
		SS	DF	MS	F	p
Solaris	free term	48.84	1	48.84	17853.6	0.000
	warranty and post-warranty period	0.0171	1	0.0171	6.26	0.0148
	error	0.1860	68	0.0027	-	-
Mercedes	free term	51.87	1	51.87	24829.5	0.0000
	warranty and post-warranty period	0.0016	1	0.0016	0.75	0.3902
	error	0.1421	68	0.0021	-	-

For Mercedes buses p is higher than expected, $p=0.3902$, therefore there are no grounds for rejecting the zero hypothesis. The average operational availability of Mercedes in the warranty and post-warranty periods does not differ significantly. The test results of variance analysis are also confirmed by the interaction curve (Figs. 6 and 7).

5. Conclusions

Based on the conducted studies, the following conclusions have been formulated:

1. The average operational availability of a Mercedes bus in the warranty and post-warranty periods does not differ significantly, whereas the average operational availability of a Solaris bus differ significantly for the analysed period.
2. Under warranty period, the average operational availability of Solaris vehicles was 0.896, while that of Mercedes vehicles was 0.913. A relative difference was 1.7%. The results of Hartley's, Bartlett's, Cochran's and Levene's tests demonstrate that the difference is statistically insignificant.
3. In the post-warranty period, the average operational availability of Solaris buses was 0.857, while that of Mercedes buses was 0.906. A relative difference was 4.9%. The results of Hartley's, Bartlett's, Cochran's and Levene's test demonstrate that the difference is statistically significant.
4. Such an analysis taking account of warranty and post-warranty periods allows us to use operational availability index when evaluating the usefulness of maintenance quality of buses. This is important with respect to investment when making a choice of a bus make to purchase.

References

1. Caro, E., Arévalo, I., García-Martosa, C., Conejoc, A.J.: Power system observability via optimization. *Electric Power Systems Research* 2013; 104: 207–215, <http://dx.doi.org/10.1016/j.epsr.2013.06.019>.
2. Grądzki, R., Lindstedt, P.: Method of assessment of technical object aptitude in environment of exploitation and service conditions. *Eksploracja i Niezawodność – Maintenance and Reliability* 2015; 17(1): 54–63, <http://dx.doi.org/10.17531/ein.2015.1.8>.
3. Guihaire, V., Hao, J.K.H.: Transit network design and scheduling: A global review. *Transportation Research Part A*. 2008; 42: 1251–1273, <http://dx.doi.org/10.1016/j.tra.2008.03.011>.
4. Guihaire, V., Hao, J.K.H.: Transit network timetabling and vehicle assignment for regulating authorities. *Computers & Industrial Engineering* 2010; 59: 16–23, <http://dx.doi.org/10.1016/j.cie.2010.02.005>.
5. Herder, P.M., van Luijk, J.A., Bruijnooghe, J.: Industrial application of RAM modeling development and implementation of a RAM simulation model for the Luxan plant at GE Industrial. *Reliability Engineering & System Safety* 2008; 93: 501–508, <http://dx.doi.org/10.1016/j.res.2006.10.019>.
6. Ignaciuk, P., Rymarz, J., Niewczas, A.: Effectiveness of the failure rate on maintenance costs of the city buses. *Journal of KONBiN* 2015; 3(35): 99–108.
7. Kadiyala, A., Kumar, A.: Development and application of a methodology to identify and rank the important factors affecting in-vehicle particulate matter. *Journal of Hazardous Materials* 2013; 213–214: 140–146, <http://dx.doi.org/10.1016/j.jhazmat.2012.01.072>.
8. Koronacki, J., Mielniczuk, J.: *Statystyka dla studentów kierunków technicznych i przyrodniczych*. Warszawa: Wydawnictwa Naukowo - Techniczne, 2001.
9. Legutko, S.: *Podstawy eksploatacji maszyn i urządzeń*. Warszawa: Wydawnictwo Szkolne i Pedagogiczne, 2004.
10. Migawa, K.: Semi-Markov model of the availability of the means of municipal transport system. *Scientific Problems of Machines Operation and Maintenance* 2009; 3(159): 25–34.
11. Misra, K.B. Red. *Handbook of Reliability Engineering*. London: Springer Verlag, 2008.
12. Niewczas, A., Koszałka, G., Wrona, J., Pieniak, D.: Chosen aspects of municipal transport operation on the example of the city of Lublin. *Transport* 2008; 23(1): 88–90, <http://dx.doi.org/10.3846/1648-4142.2008.23.88-90>.
13. Pham, H. *Handbook of Reliability Engineering*. London: Springer Verlag, 2003, <http://dx.doi.org/10.1007/b97414>.
14. Piasecki, S.: *Zagadnienia użytkowania maszyn i środków transportowych*. Lublin: Lubelskie Towarzystwo Naukowe, 1995.
15. Portela, S.B., Queiroga, R.M., Constantini, A., Zannin, H.T.P.: Annoyance evaluation and the effect of noise on the health of bus drivers. *Noise Health* 2013; 15(66): 301–306, <http://dx.doi.org/10.4103/1463-1741.116561>.
16. Rymarz, J., Niewczas, A., Pieniak, D.: Reliability analysis of the selected brands of city buses at municipal transport company. *J. Konbin* 2013; 26(1): 111–122, <http://dx.doi.org/10.2478/jok-2013-0087>.
17. Rymarz, J., Niewczas, A.: Ocena gotowości technicznej autobusów komunikacji miejskiej na przykładzie Miejskiego Przedsiębiorstwa Komunikacyjnego w Lublinie. *Czasopismo Techniczne* 2013; 9(109): 195–200.
18. Sanchez, S.A.: Optimizing performance-based mechanisms in road management: An agency theory approach. *European Journal of Transport and Infrastructure Research* 2015; 15(4): 465–481.
19. Savsar, M.: Modeling and simulation of maintenance operations at Kuwait public transport company. *Kuwait Journal of Science* 2013; 40(2): 115–129.

20. Stapelberg, R.F. Red. Handbook of reliability, availability, maintainability and safety in engineering design. London: Springer Verlag, 2009.
21. Szkoda, M.: Assessment of Reliability, Availability and Maintainability of Rail Gauge Change Systems. *Eksploatacja i Niezawodność – Maintenance and Reliability* 2014; 16(3): 422–432.
22. Walesiak, M., Gatnar, E. Statystyczna analiza danych z wykorzystaniem programu R. Warszawa: Wydawnictwo Naukowe PWN, 2009.
23. Wolde, M., Ghobbar, A.A.: Optimizing inspection intervals - Reliability and availability in terms of a cost model: A case study on railway carriers. *Reliability Engineering & System Safety* 2013; 114: 137–147, <http://dx.doi.org/10.1016/j.ress.2012.12.013>.
24. Woropay, M., Szubartowski, M., Migawa, K. Model oceny i kształtowania gotowości operacyjnej podsystemu wykonawczego w systemie transportowym. Radom: Wydawnictwo i Zakład Poligrafii Instytutu Technologii Eksploatacji, 2013.
25. Woropay, M., Żurek, J., Migawa, K. Model oceny i kształtowania gotowości operacyjnej podsystemu utrzymania ruchu w systemie transportowym. Radom: Wydawnictwo i Zakład Poligrafii Instytutu Technologii Eksploatacji, 2003.
26. Xuan, Y., Argote, J., Daganzo, C. F.: Dynamic bus holding strategies for schedule reliability: Optimal linear control and performance analysis. *Transport Research Part B* 2011; 45: 1831–1845, <http://dx.doi.org/10.1016/j.trb.2011.07.009>.
27. Yatskiv, I., Pticina, I., Savrasovs, M.: Urban public transport system's reliability estimation using microscopic simulation. *Transport Telecommunication* 2012; 13(3): 219–228, <http://dx.doi.org/10.2478/v10244-012-0018-4>.
28. Zhao, F., Zeng, X.: Optimization of transit route network, vehicle headways and timetables for large-scale transit networks. *European Journal of Operational Research* 2008; 186: 841–855, <http://dx.doi.org/10.1016/j.ejor.2007.02.005>.
29. Zio, E.: Reliability engineering: Old problems and new challenges. *Reliability Engineering and System Safety* 2009; 94(2): 125–141, <http://dx.doi.org/10.1016/j.ress.2008.06.002>.

Joanna RYMARZ

Lublin University of Technology
ul. Nadbystrzycka 36, 20-816 Lublin, Poland

Andrzej NIEWCZAS

Motor Transport Institute
ul. Jagiellońska 80, 03-301 Warsaw, Poland

Aneta KRZYŻAK

Polish Air Force Academy
ul. Dywizjonu 303 35, 08-521 Dęblin, Poland

E-mails: j.rymarz@pollub.pl, andrzej.niewczas@its.waw.pl,
a.krzyzak@wsosp.pl

Hao-Wei Wang
Ke-Nan Teng

RESIDUAL LIFE PREDICTION FOR HIGHLY RELIABLE PRODUCTS WITH PRIOR ACCELERATED DEGRADATION DATA

PROGNOZOWANIE TRWAŁOŚCI RESZTKOWEJ WYSOCE NIEZAWODNYCH PRODUKTÓW NA PODSTAWIE DANYCH HISTORYCZNYCH Z PRZYSPIESZONYCH BADAŃ DEGRADACJI

To precisely predict the residual life for functioning products is a key of carrying out condition based maintenance. For highly reliable products, it is difficult to obtain abundant degradation data to precisely predict the residual life under normal stress levels. Thus, how to make use of historical degradation data to improve the accuracy of the residual life prediction is an interesting issue. Accelerated degradation testing, which has been widely used to evaluate the reliability of highly reliable products, can provide abundant accelerated degradation data. In this paper, a residual life prediction method based on Bayesian inference that takes accelerated degradation data as prior information was studied. A Wiener process with a time function was used to model degradation data. In order to apply the random effects of all the parameters of a Wiener process, the non-conjugate prior distributions were considered. Acceleration factors were introduced to convert the parameter estimates from accelerated stress levels to normal stress levels, so that the proper prior distribution types of the random parameters can be selected by the Anderson-Darling statistic. A Markov Chain Monte Carlo method with Gibbs sampling was used to evaluate the posterior means of the random parameters. An illustrative example of self-regulating heating cable was utilized to validate the proposed method.

Keywords: Residual life; Bayesian inference; random parameters; Wiener process; acceleration factor.

Precyzyjne przewidywanie trwałości resztkowej użytkowanego produktu stanowi klucz do prawidłowego utrzymania ruchu w oparciu o bieżący stan techniczny (condition-based maintenance). W przypadku produktów o wysokiej niezawodności, trudno jest uzyskać ilość danych degradacyjnych, która umożliwiałaby precyzyjne prognozowanie trwałości resztkowej przy normalnym poziomie obciążeń. Dlatego też bardzo ważnym zagadnieniem jest wykorzystanie historycznych danych degradacyjnych umożliwiających zwiększenie trafności prognozowania trwałości resztkowej. Przyspieszone badania degradacyjne, które powszechnie wykorzystuje się do oceny niezawodności wysoce niezawodnych produktów, mogą dostarczać bogatych danych o przyspieszonej degradacji. W przedstawionej pracy badano metodę prognozowania trwałości resztkowej opartą na wnioskowaniu bayesowskim, w którym jako uprzednie informacje wykorzystano dane z przyspieszonych badań degradacji. Dane degradacyjne modelowano za pomocą procesu Wienera z funkcją czasu. Aby móc zastosować efekty losowe wszystkich parametrów procesu Wienera, rozważano niesprężone rozkłady a priori. Wprowadzono współczynniki przyspieszenia, które pozwoliły na przekształcenie szacowanych wartości parametrów z poziomu obciążeniowego w próbie przyspieszonej do poziomu obciążeń normalnych, co umożliwiło wybór odpowiednich typów parametrów losowych rozkładu a priori z wykorzystaniem statystyki testowej Andersona-Darlinga. Metodę Monte Carlo opartą na łańcuchach Markowa z próbnikiem Gibbsa wykorzystano do oceny średnich a posteriori parametrów losowych. Proponowaną metodę zweryfikowano na podstawie przykładu samoregulującego przewodu grzejnego.

Słowa kluczowe: trwałość resztkowa; wnioskowanie bayesowskie; parametry losowe; proces Wienera; współczynnik przyspieszenia.

1. Introduction

Recently, more and more highly reliable products have emerged in military and aerospace fields. However, it is very time-consuming to obtain enough failure data to evaluate the reliability of highly reliable products under normal stress levels. To resolve this problem, accelerated life test (ALT) is widely adopted to obtain product failure data in an acceptable time period. But for highly reliable products, even accelerated life test is not effective because little failure data can be obtained within limited time and budget. For some highly reliable product, their certain performance indexes will degrade over time. If the performance degradation can be observed, product lifetime information is likely to be extrapolated. Therefore, accelerated degradation test (ADT), under which products are put into accelerated stress levels to accelerate degradation process, has become a popular approach to

the lifetime prediction for highly reliable products [13, 21, 26, 32, 33]. However, the aim of ADT is to extrapolate the lifetime information for the population rather than the residual life for an individual.

The residual life of a product is defined as the length from the current time to the failure time, and precisely predicting the residual life is important to carry out condition based maintenance (CBM), and prognostics and health management [1, 22]. For an individual with high reliability, the degradation data observed under normal stress levels cannot show a distinct degradation trend, therefore it is difficult to precisely predict the residual life. In order to precisely predict the residual life for an individual with limited real-time degradation data, the prediction methods based on Bayesian inference have been popularly studied [3, 7, 8]. Gebraeel *et al* [5] developed an exponential degradation model with random parameters to model bearing degradation signals. They assumed the random parameters to obey conjugate prior

distributions for mathematical tractability, and obtained the prior distributions of random parameters using the historical degradation data of the population of devices, then predicted the residual life for an individual with the real-time degradation data. Chakraborty *et al* [2] also studied the exponential degradation model with random parameters, but they assumed the random parameters to obey non-conjugate prior distributions, and adopted the Metropolis-Hasting algorithm to estimate the posterior means of random parameters. Gebraeel *et al* [6] proposed a Bayesian method, which takes the failure time data as historical information while takes the real-time degradation data of an individual as filed information, to predict the residual life distribution for a rotating machinery. Karandikar *et al* [10] developed a Bayesian method, which applied Monte Carlo simulations to evaluate the posterior means of random parameters, to predict the residual life for an aircraft fuselage panel. Baraldi *et al* [1] also developed a Bayesian method, which combines the degradation data of historical equipment and the real-time observing degradation data, to predict the residual life for nuclear power plants. Jin *et al* [9] presented a Bayesian framework based on a Wiener process with random parameters. The framework utilizes off-line population degradation data and on-line individual degradation data to predict residual life. Wang *et al* [28] also studied the Bayesian method based on Wiener degradation processes.

From the above analysis, it can be concluded that the residual life prediction methods based on Bayesian inference usually take the historical degradation data or failure data under normal stress levels as prior information. However, there is a lack of research on how to use accelerated degradation data as prior information. For some high reliable products, the accelerated degradation data is the only prior information source. Thus, how to make full use of historical accelerated degradation data to predict residual life is an interesting and significant issue. In the paper, we proposed a Bayesian method, which takes accelerated degradation data as prior information while considers the real-time degradation data observed under normal stress level as field information, to improve the prediction accuracy of the residual life for a highly reliable product.

The rest of the paper is organized as follows: Section 2 describes the residual life prediction model based on a Wiener process with random parameters. Section 3 discusses how to evaluate the prior distributions of the random parameters from accelerated degradation data. We deduced the expression of the acceleration factor based on Wiener degradation process, and converted parameter estimates from accelerated stress levels to normal stress level through acceleration factors. Section 4 develops simulation tests to validate the proposed method of converting parameter estimates. Section 5 provides a case study of self-regulating heating cable to investigate the effectiveness of the proposed Bayesian method. Section 6 draws some conclusions.

2. Residual life prediction model

It is well known that the main characteristic of degradation process is uncertain over time, therefore stochastic process models, such as Wiener process, Gamma process, Poisson process, *et al*, are naturally appropriate to model the evolution of degradation process. Wiener process can characterize both monotonic and non-monotonic degradation data, and describe unit-to-unit variance of products if random parameters are considered. Hence, Wiener process has been widely applied to model stochastic degradation process, see Whitmore and Schenkelberg [31], Wang [29], Peng and Tseng [19], Wang *et al* [30], Huang *et al* [4].

In mathematics, a Wiener process $\{X(t) = \mu \cdot \Lambda(t) + \sigma \cdot B(\Lambda(t))\}$ has independent increments $\Delta X(t) = X(t + \Delta t) - X(t)$ that follow a normal distribution as:

$$\Delta X(t) \sim N(\mu \Delta \Lambda(t), \sigma^2 \Delta \Lambda(t)) \quad (1)$$

where μ is a drift parameter, $\sigma (\sigma > 0)$ is a diffusion parameter, $\Lambda(t)$ is a monotone increasing function of time t with $\Lambda(0) = 0$, $\Delta \Lambda(t) = \Lambda(t + \Delta t) - \Lambda(t)$ denotes a time increment and $B(\cdot)$ denotes a standard brown motion.

Let a constant value l represent the failure threshold, the failure time ξ can be considered to be the time when $X(t)$ firstly reaches l . So the failure time ξ can be described as:

$$\xi = \inf \{t : X(t) \geq l\} \quad (2)$$

For a Wiener process, it is well known that the failure time ξ follows an inverse Gaussian distribution. So the probability density function (PDF) of ξ can be expressed as:

$$f_{\xi}(t) = \frac{l}{\sqrt{2\pi\sigma^2\Lambda^3(t)}} \exp\left[-\frac{(l - \mu\Lambda(t))^2}{2\sigma^2\Lambda(t)}\right] \frac{d\Lambda(t)}{dt} \quad (3)$$

Given that the degradation $X(t_i)$ at time t_i does not reaches l , the residual life RL_{t_i} at t_i can be defined as $RL_{t_i} = \inf \{t : X(t_i + t) \geq l \mid X(t_i) < l\}$ [7,24]. Therefore, the PDF of RL can be written as:

$$f_{RL}(t) = \frac{l'}{\sqrt{2\pi\sigma^2(\Lambda(t))^3}} \exp\left[-\frac{(l' - \mu\Lambda(t))^2}{2\sigma^2\Lambda(t)}\right] \frac{d\Lambda(t)}{dt} \quad (4)$$

where $l' = l - X(t)$. Furthermore, the expectation of RL can be deduced from:

$$\overline{RL} = E(RL) = \int_0^{+\infty} t \cdot f_{RL}(t) dt \quad (5)$$

where $\Lambda^{-1}(\cdot)$ denotes the inverse function of $\Lambda(\cdot)$. In order to obtain better flexibility and tractability, the form of $\Lambda(\cdot)$ was specified as

$\Lambda(t) = t^r$. If $r = 1$, it is appropriate to model linear degradation processes. If $r > 1$, it is able to model convex degradation processes. If $r < 1$, it is capable of modeling concave degradation processes.

Thus, the RL can be evaluated once the estimates of μ, σ, r are obtained. However, the real-time degradation data of highly reliable product is commonly so little not to be straightforward used to obtain credible estimates $\hat{\mu}, \hat{\sigma}, \hat{r}$. To resolve the problem, we adopted a Bayesian method to obtain more credible posterior estimates of $\hat{\mu}, \hat{\sigma}, \hat{r}$ by making full use of historical accelerated degradation data. Although the application of Wiener processes in Bayesian inference has been widely studied in literature, most works assume that the random parameters of a Wiener process obey the following conjugate prior distributions: $\sigma^2 \sim \text{IG}(a, b)$, $\mu \mid \sigma^2 \sim N(c, d \cdot \sigma^2)$, where $\text{IG}(\cdot)$ represents an Inverse Gamma distribution, and a, b, c, d are hyper parameters. The above assumption has two limitations. First, the random effect of r can not be taken into account; Second, μ, σ are limited to

obey the above specified distributions, which may not be applicable to some cases. In this paper, the non-conjugate prior distributions of μ, σ, r are alternatively used in Bayesian inference, and μ, σ, r are assumed to be mutually independent. Let $\pi(\mu, \sigma^2, r)$ represent the joint prior PDF, $\pi(\mu)$, $\pi(\sigma^2)$, $\pi(r)$ be the corresponding PDF of μ, σ, r , respectively, then $\pi(\mu, \sigma^2, r) = \pi(\mu) \cdot \pi(\sigma^2) \cdot \pi(r)$.

Suppose that $\mathbf{X} = [X_1(t_1), X_2(t_2), \dots, X_{n+1}(t_{n+1})]$ is the real-time degradation data of an individual under normal stress level and $L(\Delta\mathbf{X} | \mu, \sigma^2, r)$ is a likelihood function, then the joint posterior PDF $\pi(\mu, \sigma^2, r | \Delta\mathbf{X})$ can be deduced according to the Bayesian theory [25, 34].

$$\pi(\mu, \sigma^2, r | \Delta\mathbf{X}) = \frac{L(\Delta\mathbf{X} | \mu, \sigma^2, r) \cdot \pi(\mu, \sigma^2, r)}{\int_{-\infty}^{+\infty} \int_0^{+\infty} \int_{-\infty}^{+\infty} L(\Delta\mathbf{X} | \mu, \sigma^2, r) \cdot \pi(\mu, \sigma^2, r) d\mu d\sigma^2 dr} \quad (6)$$

The marginal density functions of $\mu | \Delta\mathbf{X}$, $\sigma^2 | \Delta\mathbf{X}$, $r | \Delta\mathbf{X}$ can be expressed as:

$$\pi(\mu | \Delta\mathbf{X}) = \int_{-\infty}^{+\infty} \int_0^{+\infty} \pi(\mu, \sigma^2, r | \Delta\mathbf{X}) d\sigma^2 dr \quad (7)$$

$$\pi(\sigma^2 | \Delta\mathbf{X}) = \int_{-\infty}^{+\infty} \int_0^{+\infty} \pi(\mu, \sigma^2, r | \Delta\mathbf{X}) d\mu dr \quad (8)$$

$$\pi(r | \Delta\mathbf{X}) = \int_0^{+\infty} \int_{-\infty}^{+\infty} \pi(\mu, \sigma^2, r | \Delta\mathbf{X}) d\mu d\sigma^2 \quad (9)$$

Furthermore, the expectations of $\mu | \Delta\mathbf{X}$, $\sigma^2 | \Delta\mathbf{X}$ and $r | \Delta\mathbf{X}$ can be calculated as:

$$E(\mu | \Delta\mathbf{X}) = \int_{-\infty}^{+\infty} \mu \cdot \pi(\mu | \Delta\mathbf{X}) d\mu \quad (10)$$

$$E(\sigma^2 | \Delta\mathbf{X}) = \int_0^{+\infty} \sigma^2 \pi(\sigma^2 | \Delta\mathbf{X}) d\sigma^2 \quad (11)$$

$$E(r | \Delta\mathbf{X}) = \int_0^{+\infty} r \cdot \pi(r | \Delta\mathbf{X}) dr \quad (12)$$

Generally, it is difficult to evaluate $E(\mu | \Delta\mathbf{X})$, $E(\sigma^2 | \Delta\mathbf{X})$ and $E(r | \Delta\mathbf{X})$ through direct mathematical calculation. One alternative method is using Markov Chain Monte Carlo (MCMC) simulation with Gibbs sampling [16, 20], we implemented the method in WinBUGS.

Replace μ, σ, Λ with $E(\mu | \Delta\mathbf{X})$, $E(\sigma^2 | \Delta\mathbf{X})$ and $E(r | \Delta\mathbf{X})$ in Eq. (4) and Eq. (5), the posterior PDF of RL and the posterior expectation of RL can be obtained. There will be more field degradation data available as the individual product works over time. Once new degradation data is available, $E(\mu | \Delta\mathbf{X})$, $E(\sigma^2 | \Delta\mathbf{X})$ and $E(r | \Delta\mathbf{X})$ are immediately updated. So the RL of an individual can be real-time predicted.

3. Evaluate the prior distributions of random parameters

Before predicting RL using Bayesian method, the joint prior PDF $\pi(\mu, \sigma^2, r)$ need be evaluated from historical accelerated degradation data. In this section, we discussed the method of evaluating

$\pi(\mu, \sigma^2, r)$ from historical accelerated degradation data. Firstly, a Wiener process with 3 random parameters were used to model accelerated degradation data. Then, the acceleration factor constant principle was introduced to deduce the corresponding expression of acceleration factor for a Wiener process, and the parameter estimates were converted from accelerated stress levels to normal stress level through acceleration factors. Lastly, the Anderson-Darling goodness-of-fit method was utilized to select the proper distribution types for 3 random parameters.

3.1. Estimate parameters from accelerated degradation data

A constant stress accelerated degradation test was conducted to obtain the lifetime information of the population for a kind of highly reliable product. Suppose that S_0 denotes the normal stress level, S_k denotes the k th accelerated stress level, X_{ijk} denotes the i th degradation data of the j th product under S_k , t_{ijk} represents the corresponding observing time, $\Delta X_{ijk} = X_{ijk} - X_{(i-1)jk}$ represents the degradation data increment, and $\Lambda(t_{ijk}) = t_{ijk}^{\Lambda}$ represents the time increment, where $i = 1, 2, \dots, n_1$; $j = 1, 2, \dots, n_2$; $k = 1, 2, \dots, n_3$. According to the Wiener process features, ΔX_{ijk} follows a Normal distribution as:

$$\Delta X_{ijk} \sim N(\mu_{jk} \Delta \Lambda(t_{ijk}), \sigma_{jk}^2 \Delta \Lambda(t_{ijk})) \quad (13)$$

To obtain maximum likelihood estimates (MLEs) $\hat{\mu}_{jk}$, $\hat{\sigma}_{jk}^2$, \hat{r}_{jk} for each product, the likelihood function can be established as:

$$L(\mu_{jk}, \sigma_{jk}^2, r_{jk}) = \prod_{i=1}^{n_1} \frac{1}{\sqrt{2\pi\sigma_{jk}^2 \left(t_{ijk}^{r_{jk}} - t_{(i-1)jk}^{r_{jk}} \right)}} \exp \left[-\frac{\left(\Delta X_{ijk} - \mu_{jk} \left(t_{ijk}^{r_{jk}} - t_{(i-1)jk}^{r_{jk}} \right) \right)^2}{2\sigma_{jk}^2 \left(t_{ijk}^{r_{jk}} - t_{(i-1)jk}^{r_{jk}} \right)} \right] \quad (14)$$

3.2. Convert parameter estimates from accelerated stress levels to normal stress level

Suppose $F_k(t_k)$, $F_0(t_0)$ represents the accumulative distribution function (CDF) under S_k , S_0 , respectively, if $F_k(t_k) = F_0(t_0)$, then the acceleration factor of S_k relative to S_0 can be defined as:

$$AF_{k,0} = t_0 / t_k \quad (15)$$

In practice, Eq. (15) is rarely applied to evaluate $AF_{k,0}$ since t_0 and t_k are difficult to accurately obtained. For a Wiener process, a widely adopted assumption is that μ should change with accelerated stress level varying while σ should be invariable, see Padgett and Tomlinson [17], Park and Padgett [18], Liao and Tseng [11], Lim and

Yum [14], et al. Based on the above assumption, the expression of $AF_{k,0}$ can be expressed as $AF_{k,0} = \mu_k / \mu_0$. However, there are different assumption that both μ and σ will change with accelerated stress level varying, see Whitmore and Schenkelberg[31], Liao and Elsayed[12]. Thus, the expression of acceleration factor for a Wiener process needs further research. In this paper, we applied the acceleration factor constant principle to deduce the expression of acceleration factor for a Wiener process.

Zhou et al [35] first pointed out the acceleration factor constant principle that $AF_{k,0}$ should be a constant which does not change with time t_0, t_k and depends only on S_k, S_0 under an effective accelerated test. Moreover, to guarantee that $AF_{k,0}$ is a constant, the failure mechanism of products must remain consistent under S_k, S_0 . According to the accelerated factor constant principle, for any $t_0, t_k > 0$, the following expression is always identical:

$$F_k(t_k) = F_0(AF_{k,0}t_k) \quad (16)$$

From Eq. (16), the following identical equation can be deduced:

$$f_k(t_k) = AF_{k,0} \cdot f_0(t_0). \quad (17)$$

The deducing process was illustrated as:

$$\begin{aligned} f_k(t_k) &= \frac{dF_k(t_k)}{dt_k} = AF_{k,0} \frac{dF_0(AF_{k,0} \cdot t_k)}{d(AF_{k,0} \cdot t_k)} \\ &= AF_{k,0} \frac{dF_0(t_0)}{dt_0} = AF_{k,0} \cdot f_0(t_0) \end{aligned}$$

Substitute Eq. (3) into Eq. (17), and specify $\Lambda(t) = t$, then:

$$\begin{aligned} AF_{k,0} = \frac{f_k(t_k)}{f_0(t_0)} &= \frac{\sigma_0 AF_{k,0}^{3/2}}{\sigma_k} \exp \left[\left(\frac{l \cdot \mu_0}{\sigma_0^2} - \frac{l \cdot \mu_k}{\sigma_k^2} \right) \right. \\ &\quad \left. + \frac{1}{t_k} \left(\frac{l^2}{2\sigma_0^2 AF_{k,0}} - \frac{l^2}{2\sigma_k^2} \right) + t_k \left(\frac{\mu_0^2 AF_{k,0}}{2\sigma_0^2} - \frac{\mu_k^2}{2\sigma_k^2} \right) \right] \end{aligned} \quad (18)$$

To ensure $AF_{k,0}$ is a constant which does not change with t_k , the following relationships must be satisfied:

$$\begin{cases} \frac{l^2}{2\sigma_0^2 AF_{k,0}} - \frac{l^2}{2\sigma_k^2} = 0 \\ \frac{\mu_0^2 AF_{k,0}}{2\sigma_0^2} - \frac{\mu_k^2}{2\sigma_k^2} = 0 \end{cases} \quad (19)$$

So the following equation can be deduced:

$$AF_{k,0} = \mu_k / \mu_0 = \sigma_k^2 / \sigma_0^2 \quad (20)$$

Eq. (20) indicates that both μ and σ should change with accelerated stress level varying. When we specify $\Lambda(t) = t^r$, the following equation can be deduced:

$$AF_{k,0} = (\mu_k / \mu_0)^{1/r} = (\sigma_k^2 / \sigma_0^2)^{1/r}, \quad r_k = r_0 = r \quad (21)$$

Eq. (21) indicates that both μ and σ should change with accelerated stress level varying while r should remain invariable. The mathematical relationships between μ, σ and accelerated stresses can be modeled by reaction rate models [15]. Assume that temperature T is a stress variable and the Arrhenius relationship is correspondingly selected as the reaction rate model. According to Eq. (21), μ, σ^2 and r can be expressed as:

$$\mu_k = \exp(\lambda_1 - \lambda_2 / T_k), \quad \sigma_k^2 = \exp(\lambda_3 - \lambda_2 / T_k), \quad r_k = \lambda_4 \quad (22)$$

where $\lambda_1, \lambda_2, \lambda_3, \lambda_4$ are coefficients.

To obtain the MLEs of $\lambda_1, \lambda_2, \lambda_3, \lambda_4$, a likelihood function that incorporates all the accelerated degradation data was constructed:

$$L(\lambda_1, \lambda_2, \lambda_3, \lambda_4) = \prod_{i=1}^{n_1} \prod_{j=1}^{n_2} \prod_{k=1}^{n_3} \frac{1}{\sqrt{2\pi \exp(\lambda_3 - \lambda_2 / T_k) (t_{ijk}^{\lambda_4} - t_{(i-1)jk}^{\lambda_4})}} \exp \left[-\frac{(\Delta x_{ijk} - \exp(\lambda_1 - \lambda_2 / T_k) (t_{ijk}^{\lambda_4} - t_{(i-1)jk}^{\lambda_4}))^2}{2 \exp(\lambda_3 - \lambda_2 / T_k) (t_{ijk}^{\lambda_4} - t_{(i-1)jk}^{\lambda_4})} \right] \quad (23)$$

With $\hat{\lambda}_2$ and $\hat{\lambda}_2$, $AF_{k,0}$ was evaluated by:

$$AF_{k,0} = \exp(\hat{\lambda}_4 \cdot \hat{\lambda}_2 (1/T_0 - 1/T_k)) \quad (24)$$

To simply the computation, $(AF_{k,0})^{\hat{\lambda}_4}$ was represented by $Z_{k,0}$.

Thus, the $\hat{\mu}_{jk}, \hat{\sigma}_{jk}^2, \hat{r}_{jk}^2$ under T_k can be transformed into the corresponding values under T_0 by:

$$\hat{\mu}_{j(k0)} = \hat{\mu}_{jk} / Z_{k,0}, \quad \hat{\sigma}_{j(k0)}^2 = \sigma_{jk}^2 / Z_{k,0}, \quad r_{j(k0)} = r_{jk} \quad (25)$$

For the denotation convenience, $\hat{\mu}_{j(k0)}, \hat{\sigma}_{j(k0)}^2$ and $\hat{r}_{j(k0)}$ were replaced with $\hat{\mu}_m, \hat{\sigma}_m^2$ and \hat{r}_m , respectively, where $m=1,2,\dots,M$ and M denotes the total number of products under the accelerated test.

3.3. Select the best fitting distribution types and estimate hyper parameters

We utilized the Anderson-Darling goodness-of-fit test to select the best fitting distribution types for $\hat{\mu}_m$, $\hat{\sigma}_m^2$ and \hat{r}_m . Since the Exponential, Normal, Lognormal, Weibull and Gamma distribution have good statistical characteristics and can cover the majority of parameter distribution, they were selected to be candidates for the best fitting distribution type. The one with the smallest AD is considered to be the best fitting distribution type [24]. In addition, the Anderson-Darling statistic can also be used for hypothesis test. The null hypothesis is defined as H_0 : data follow the specified distribution type. The significance level is specified as 0.05, if the p value of Anderson-Darling is greater than 0.05, the null hypothesis is accepted.

Suppose that $\hat{\mu}_m \sim \text{Wbl}(\eta, \delta)$, $\hat{\sigma}_m^2 \sim \text{Ga}(\alpha, \beta)$ and $\hat{r}_m \sim \text{N}(a, b)$, where $\text{Wbl}(\cdot)$ denotes a Weibull distribution and η, δ is the scale parameter and shape parameter, $\text{Ga}(\cdot)$ denotes a Gamma distribution and α, β is the shape parameter and scale parameter, $\text{N}(\cdot)$ denotes a Normal distribution and a, b is the mean and variance. In order to estimate the hyper parameters, the following likelihood functions can be established:

$$L(\hat{\mu}_m; \eta, \delta) = \prod_{m=1}^M \delta \cdot \eta^{-\delta} (\hat{\mu}_m)^{\delta-1} \exp \left[- \left(\frac{\hat{\mu}_m}{\eta} \right)^{\delta} \right] \quad (26)$$

$$L(\hat{\sigma}_m^2; \alpha, \beta) = \prod_{m=1}^M \frac{\beta^{\alpha}}{\Gamma(\alpha)} (\hat{\sigma}_m^2)^{\alpha-1} \exp(-\beta \hat{\sigma}_m^2) \quad (27)$$

$$L(\hat{r}_m; a, b) = \prod_{m=1}^M \frac{1}{\sqrt{2\pi} \cdot b} \exp \left(- \frac{(\hat{r}_m - a)^2}{2 \cdot b} \right) \quad (28)$$

The prior distributions of random parameters μ, σ^2, r can be obtained as $\mu \sim \text{Wbl}(\hat{\eta}, \hat{\delta})$, $\sigma^2 \sim \text{Ga}(\hat{\alpha}, \hat{\beta})$, $r \sim \text{N}(\hat{a}, \hat{b})$.

4. Validation test

A simulation test was developed to validate the conversion method illustrated in section 3.2. The simulated degradation increment $\Delta x_{i0}, \Delta \Lambda(t_{i0})$ under S_0 was generated from a conditional Wiener process [27,28], that is:

$$\omega_0 \sim \text{Ga}(a, b), \quad \mu_0 | \omega_0 \sim \text{N}(c, d / \omega_0) \\ \Delta x_{i0} | (\mu_0, \omega_0) \sim \text{N}(\mu_0 \Delta \Lambda(t_{i0}), \omega_0^{-1} \Delta \Lambda(t_{i0})) \quad (29)$$

where $\omega_0 = \sigma_0^{-2}$ and $\Lambda(t) = t^r$. The parameters of the above model were specified as $(a, b, c, d) = (4, 2, 3, 1)$; $i = 1, 2, \dots, 10$; $h = 1, 2, \dots, 5$; $t_{i0} = 10, 20, \dots, 100$; $\Lambda(t_{i0}) = t_{i0}^r$; $r = 0.5, 1, 2$. The validation steps

were described as the following. First, the estimates $\hat{\mu}_0, \hat{\sigma}_0^2, \hat{r}_0$ were obtained from $\Delta x_{i0}, \Delta \Lambda(t_{i0})$. Then, specify the acceleration factor $AF_{k,0}$ to be 0.4, 4, respectively, and calculate the converted degradation data $\Delta x_{ik}, \Delta \Lambda(t_{ik})$ under S_k , where $x_{ik} = x_{i0}$, $t_{ik} = t_{i0} / AF_{k,0}$. Next, the estimates $\hat{\mu}_k, \hat{\sigma}_k^2, \hat{r}_k$ were obtained from $\Delta x_{ik}, \Delta \Lambda(t_{ik})$. Last, $\hat{\mu}_k / \hat{\mu}_0$, $\hat{\sigma}_k^2 / \hat{\sigma}_0^2$ and \hat{r}_k / \hat{r}_0 were computed. Table 1 shows that \hat{r}_k / \hat{r}_0 is nearly equal to 1 and both $\hat{\mu}_k / \hat{\mu}_0$ and $\hat{\sigma}_k^2 / \hat{\sigma}_0^2$ are nearly equal to $(AF_{k,h})^r$, so the result is consistent with Eq. (21).

Table 1. The results of simulation test

r	$AF_{k,h} = 0.4$			$AF_{k,h} = 4$		
	$\frac{\hat{\mu}_k}{\hat{\mu}_0}$	$\frac{\hat{\sigma}_k^2}{\hat{\sigma}_0^2}$	$\frac{\hat{r}_k}{\hat{r}_0}$	$\frac{\hat{\mu}_k}{\hat{\mu}_0}$	$\frac{\hat{\sigma}_k^2}{\hat{\sigma}_0^2}$	$\frac{\hat{r}_k}{\hat{r}_0}$
0.5	0.6325	0.6324	1.0002	2.0000	2.0002	1.0001
1	0.4000	0.4000	1.0000	4.0001	4.0001	1.0000
2	0.1600	0.1600	0.9999	15.9999	16.0002	1.0000

5. Numerical case

5.1. Modeling degradation data

The historical accelerated degradation data of self-regulating heating cable [31] was listed in Table 2. Because the type of heating cable experienced a cure process at the beginning of the degradation test, only the degradation data after the cure process were considered. There were 15 products that were averagely allocated to 3 accelerated temperature levels under a constant-stress ADT. It was assumed that the normal temperature level was $T_0 = 448.15\text{K}$. Degradation was measured as the natural logarithm of resistance, and the failure threshold l was specified as $l = \ln(2)$.

However, there was no field degradation data available under T_0 . We simulated the field degradation data which are listed in Table 3.

5.2. Determining prior distribution

Eq. (14) was used to obtain the MLEs of parameters for each product, and the estimates were listed in Table 4. For a Wiener degradation process, the independent degradation increments Δx_{ijk} of each product follows a Normal distribution, written as $\Delta x_{ijk} \sim \text{N}(\hat{\mu}_{jk} \Delta \hat{\Lambda}_{jk}(t_{ijk}), \hat{\sigma}_{jk}^2 \Delta \hat{\Lambda}_{jk}(t_{ijk}))$, where $\hat{\mu}_{jk}$, $\hat{\sigma}_{jk}^2$, \hat{r}_{jk} are the estimates of the j th product under the k th accelerated temperature level T_k . The above Normal distribution can be converted to the following standard Normal distribution:

$(\Delta x_{ijk} - \hat{\mu}_{jk} \Delta \hat{\Lambda}_{jk}(t_{ijk})) / \sqrt{\hat{\sigma}_{jk}^2 \Delta \hat{\Lambda}_{jk}(t_{ijk})} \sim \text{N}(0, 1)$. If the above relationship holds, the null hypothesis that the degradation process of the j th product under T_k obeys a Wiener process is accepted. An Anderson-Darling test with significance level $\alpha = 0.05$ validates that the degradation processes of all products obey Wiener processes.

Table 2. Historical accelerated degradation data of heating cables

Measured time ($\times 10^3$ h)	Item				
	1	2	3	4	5
(a) $T_1 = 473.15\text{K}$					
0.496	-0.120682	-0.118779	-0.123600	-0.126501	-0.124359
0.688	-0.112403	-0.109853	-0.115186	-0.118941	-0.111966
0.856	-0.103608	-0.101593	-0.105657	-0.110288	-0.107869
1.024	-0.096047	-0.094567	-0.098569	-0.103419	-0.100304
1.192	-0.085673	-0.084698	-0.088613	-0.095465	-0.085916
1.360	-0.077677	-0.076070	-0.079332	-0.084769	-0.077947
2.008	-0.045218	-0.040623	-0.045835	-0.052268	-0.045597
2.992	0.000526	0.004237	0.000533	-0.008265	0.000524
4.456	0.059261	0.063742	0.061032	0.051139	0.059544
5.608	0.093394	0.095117	0.093612	0.082414	0.084912
(b) $T_2 = 513.15\text{K}$					
0.160	-0.005152	-0.019888	-0.045961	-0.023188	-0.044267
0.328	0.056930	0.046278	0.015198	0.040737	0.018173
0.496	0.112631	0.101628	0.067119	0.095504	0.072214
0.688	0.173202	0.162705	0.128670	0.156129	0.131555
0.856	0.214266	0.202604	0.168271	0.196349	0.171394
1.024	0.272668	0.257563	0.221611	0.250900	0.225281
1.192	0.311422	0.297875	0.260910	0.291937	0.266314
1.360	0.351988	0.338902	0.302126	0.332887	0.306105
2.008	0.489847	0.461855	0.440738	0.473130	0.443941
2.992	0.656780	0.629991	0.606275	0.638651	0.611724
4.456	0.851985	0.798431	0.834114	0.798457	-
(c) $T_3 = 533.15\text{K}$					
0.160	0.123360	0.127605	0.120759	0.105206	0.120115
0.328	0.251084	0.254944	0.247156	0.232389	0.247949
0.496	0.393107	0.394496	0.391516	0.375789	0.388406
0.688	0.517137	0.518485	0.513872	0.500556	0.511850
0.856	0.598797	0.599265	0.595704	0.583362	0.595220
1.024	0.693925	0.694445	0.688930	0.679117	0.690324
1.192	0.774347	0.774428	0.770313	0.758314	0.770782

* A period denotes a missing value.

Table 3. The simulated field degradation data for an individual heating cable at T_0

Time /h	1000	2000	3000	4000	5000
Degradation	-0.2209	-0.1984	-0.1815	-0.1651	-0.1555
Time /h	6000	7000	8000	9000	
Degradation	-0.1443	-0.1323	-0.1231	-0.1128	

With Eq. (23), we obtained the MLEs of coefficients as $\hat{\lambda}_1 = 16.950$, $\hat{\lambda}_2 = 9158.226$, $\hat{\lambda}_3 = 10.317$, $\hat{\lambda}_4 = 0.612$. According to the Eq. (23), conversion coefficients were calculated as $Z_{1,0} = 2.944$, $Z_{2,0} = 13.311$, $Z_{3,0} = 25.999$. Furthermore, we converted the MLEs

Table 4. MLEs of parameters for each product

	Item				
	1	2	3	4	5
(a) T_1					
$\hat{\mu}$	0.067029	0.070533	0.070463	0.064605	0.083435
$\hat{\sigma}^2$	0.000026	0.000039	0.000035	0.000039	0.000120
\hat{r}	0.770668	0.74692	0.754380	0.776351	0.662973
(b) T_2					
$\hat{\mu}$	0.402341	0.425767	0.367615	0.427607	0.369066
$\hat{\sigma}^2$	0.000442	0.000523	0.000230	0.000753	0.000214
\hat{r}	0.602857	0.553023	0.662489	0.552906	0.665158
(c) T_3					
$\hat{\mu}$	0.788653	0.781201	0.788428	0.791756	0.784433
$\hat{\sigma}^2$	0.00117	0.001096	0.001283	0.001255	0.001017
\hat{r}	0.661216	0.664650	0.659024	0.660437	0.666665

of parameters under T_k to the corresponding values $\hat{\mu}_m$, $\hat{\sigma}_m^2$, \hat{r}_m under T_0 , respectively, as listed in Table 5.

Anderson-Darling statistic was applied to determining the best fitting distribution. Table 6 shows the values of AD . Since $\hat{\sigma}_m^2$ should be always large than zero, the Normal distribution is excluded. From Table 6, it was concluded that the Weibull distribution was the best fitting distribution type for both $\hat{\mu}_m$ and $\hat{\sigma}_m^2$, and the Normal distribu-

Table 5. The converted values $\hat{\mu}_m, \hat{\sigma}_m^2, \hat{r}_m$

	Item				
	1	2	3	4	5
(a) $T_1 \rightarrow T_0$					
$\hat{\mu}_m$	2.277E-2	2.396E-2	2.393E-2	2.194E-2	2.834E-2
$\hat{\sigma}_m^2$	8.832E-6	1.325E-5	1.189E-5	1.325E-5	4.076E-5
\hat{r}_m	0.771	0.747	0.754	0.776	0.663
(b) $T_2 \rightarrow T_0$					
$\hat{\mu}_m$	3.023E-2	3.199E-2	2.762E-2	3.213E-2	2.773E-2
$\hat{\sigma}_m^2$	3.321E-5	3.929E-5	1.728E-5	5.657E-5	1.608E-5
\hat{r}_m	0.603	0.553	0.662	0.553	0.665
(c) $T_3 \rightarrow T_0$					
$\hat{\mu}_m$	3.033E-2	3.005E-2	3.033E-2	3.045E-2	3.017E-2
$\hat{\sigma}_m^2$	4.500E-5	4.216E-5	4.935E-5	4.827E-5	3.912E-5
\hat{r}_m	0.661	0.665	0.659	0.660	0.667

Table 6. The values of AD

	Exponential	Normal	LogNorm	Gamma	Weibull
$\hat{\mu}_m$	5.449	0.905	1.016	1.032	0.806
$\hat{\sigma}_m^2$	1.733	--	0.985	0.980	0.952
\hat{r}_m	5.682	0.878	0.894	0.914	0.982

Table 7. The posterior means of random parameters after the 5th field degradation data was got

Parameter	Posterior mean	Standard deviation	MC error	Samples
μ	0.02930	0.00299	2.86E-5	9000
σ^2	4.149E-5	1.568E-5	1.59E-7	9000
r	0.6124	0.0601	6.391E-4	9000

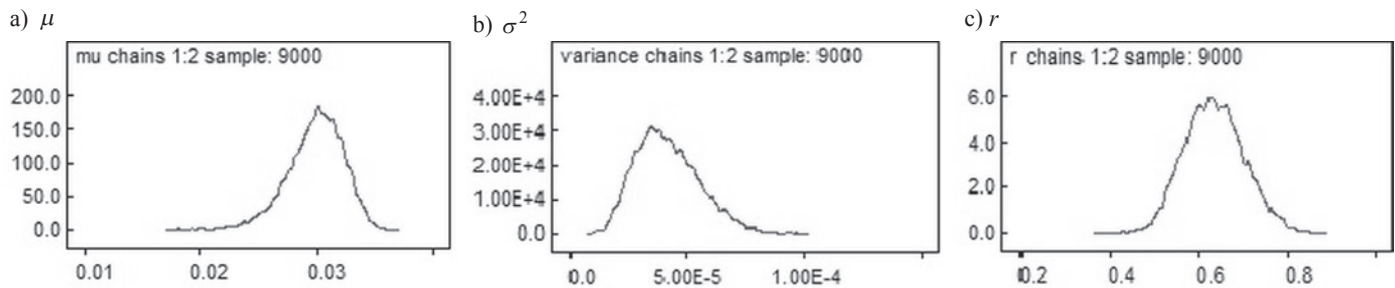
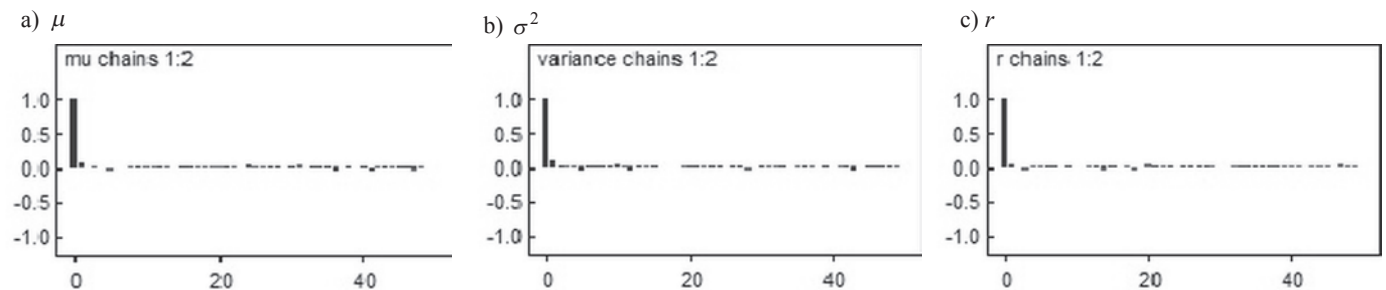
Fig. 1. The fitted posterior distributions of μ, σ^2, r 

Fig. 2. The values of autocorrelation function in the iterative processes

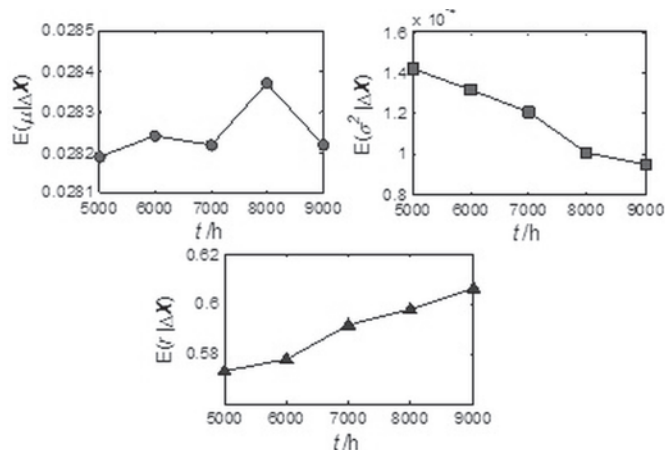
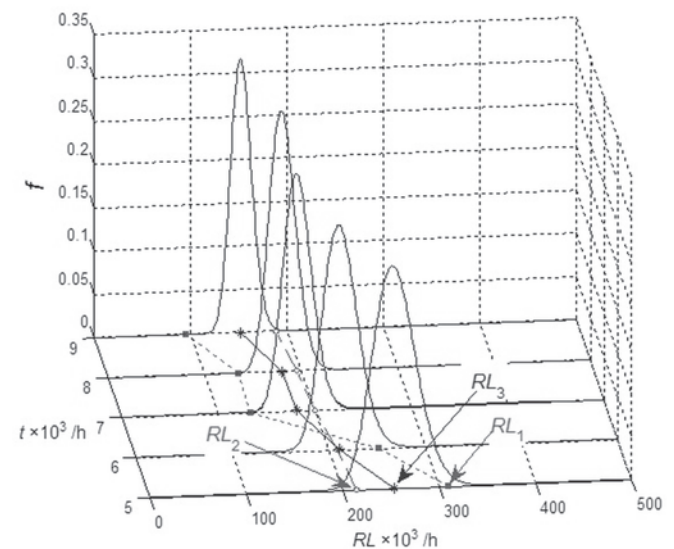


Fig. 3. The changing curves of the posterior means of random parameters

tion was the best fitting distribution type for \hat{r}_m . The MLEs of hyper parameters were obtained according to Eq. (26) and Eq. (27). So the prior distributions of 3 random parameters were evaluated from historical accelerated degradation data, they are $\mu \sim \text{Wbl}(2.952\text{E-}2, 11.464)$, $\sigma^2 \sim \text{Wbl}(3.580\text{E-}5, 2.150)$, $r \sim \text{N}(0.671, 4.774\text{E-}3)$.

After the field degradation data was obtained, the MCMC method with Gibbs sampling was used to fit the posterior distributions of random parameters in WinBUGS software. After the 5th field degradation data was got, the fitted posterior distributions were shown in figure 1. From figure 2, it can be seen that all the iterative processes are convergent since the autocorrelation functions quickly tend to 0. The

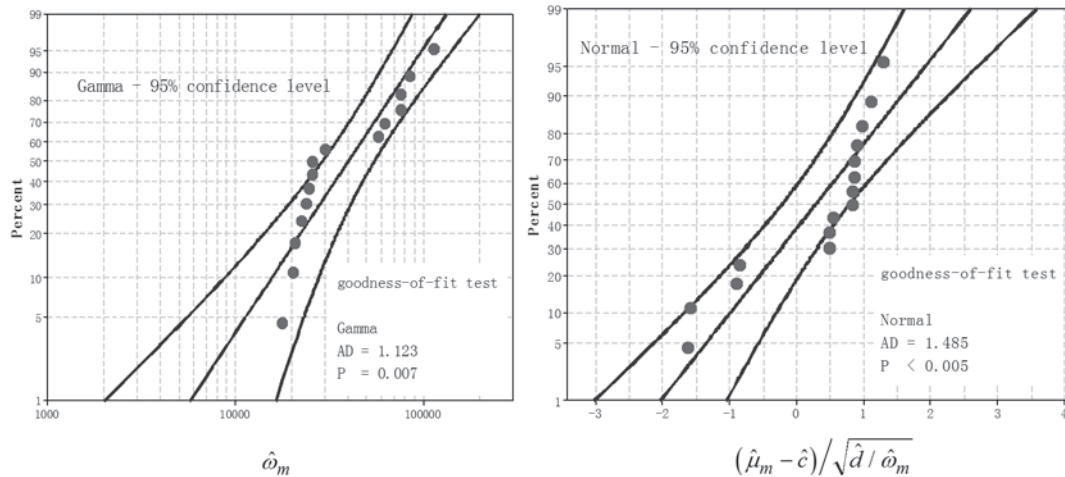
Fig. 4. The changing curves of \overline{RL}_1 , \overline{RL}_2 , \overline{RL}_3 and the PDF of RL_3

posterior means $E(\mu | \Delta \mathbf{X})$, $E(\sigma^2 | \Delta \mathbf{X})$ and $E(r | \Delta \mathbf{X})$ were evaluated in WinBUGS, as listed in table 7. Furthermore, with new field degradation data was available, $E(\mu | \Delta \mathbf{X})$, $E(\sigma^2 | \Delta \mathbf{X})$ and $E(r | \Delta \mathbf{X})$ were corresponding updated, and their changing curves were shown in Figure 3.

Let \overline{RL}_1 denote the predictions that were evaluated from only the field degradation data of an individual, \overline{RL}_2 denote the predic-

Table 8. The predictions of residual life ($RL \times 10^5$ /h)

	Measuring time /h				
	5000	6000	7000	8000	9000
\overline{RL}_1	3.089 [1.885, 5.301]	2.513 [1.211, 4.018]	1.332 [0.978, 3.890]	1.341 [1.012, 3.805]	0.939 [0.762, 2.981]
\overline{RL}_2	2.145 [1.421, 2.876]	2.081 [1.450, 2.772]	2.004 [1.498, 2.624]	1.949 [1.519, 2.468]	1.874 [1.466, 2.303]
\overline{RL}_3	2.536 [1.758, 3.212]	2.116 [1.449, 2.801]	1.816 [1.209, 2.488]	1.802 [1.233, 2.317]	1.518 [1.087, 1.955]

Fig. 5. The goodness-of-fit tests for $\hat{\omega}_m$ and $\hat{\mu}_m | \hat{\omega}_m$

tions that were evaluated by the Bayesian method with conjugate prior distributions of random parameters, \overline{RL}_3 denote the predictions that were evaluated by the method proposed in this paper, the residual life predictions and the confidence intervals of the predictions at several measuring time points were summarized in table 8. The confidence intervals were obtained with 95% confidence level by Bootstrap sampling method. The prediction method for \overline{RL}_2 was detailed demonstrated in appendix. Figure 4 shows the changing curves of \overline{RL}_1 , \overline{RL}_2 , \overline{RL}_3 and the PDF of RL_3 .

5.4. Analysis and Conclusion

In table 7, the confidence intervals of \overline{RL}_2 and \overline{RL}_3 at each measuring point are obviously smaller than those of \overline{RL}_1 . It is concluded that the prediction method taking accelerated degradation data as prior information improves the prediction precision of the residual life.

As more field degradation data was available, all the confidence intervals of $\overline{RL}_1, \overline{RL}_2, \overline{RL}_3$ became smaller. It suggests that the prediction precision was gradually improved, and the width of the PDF curve in figure 4 became narrower over time also supports the conclusion.

Compared with \overline{RL}_2 and \overline{RL}_3 , the curve of \overline{RL}_1 was not smooth and presented comparatively big changes. The reason is that the field degradation data was short and had a nonlinear change. Thus, newly obtained degradation data may significantly changes the former estimates of the parameters, which led to the poor regularity of residual life predictions. In comparison, the prediction methods for \overline{RL}_2 and \overline{RL}_3 reduced the impact of the abrupt change of the field degradation and improved the reliability of the prediction results. Com-

pared with \overline{RL}_3 , the curve of \overline{RL}_2 was more smooth and had smaller changes, because the prediction method for \overline{RL}_2 didn't consider the random effects of r . The estimates of r obtained from the prior information was used to the prediction model of \overline{RL}_2 . Thus, \overline{RL}_2 was more conservative and greatly influenced by the prior information. In contrast, the prediction method for \overline{RL}_3 took the random effects of 3 parameters into account, which let \overline{RL}_3 more sensitively reflect the variation of the field degradation data.

In addition, the prediction method for \overline{RL}_2 requires $\hat{\mu}_z$ and $\hat{\sigma}_z^2$ to follow the conjugate prior distributions as

$$\hat{\omega}_m = \hat{\sigma}_m^{-2} \sim \text{Ga}(\hat{a}, \hat{b}),$$

$$\hat{\mu}_m | \hat{\omega}_m \sim N(\hat{c}, \hat{d} / \hat{\omega}_m),$$

where $\hat{a}, \hat{b}, \hat{c}, \hat{d}$ are estimates of hyper parameters and $z = 1, 2, \dots, 15$. The Anderson-Darling statistic was used to validate the null hypothesis

that both $\hat{\mu}_m$ and $\hat{\sigma}_m^2$ to follow the conjugate prior distributions.

$$\hat{\mu}_m | \hat{\omega}_m \sim N(\hat{c}, \hat{d} / \hat{\omega}_m) \text{ was converted to } (\hat{\mu}_m - \hat{c}) / \sqrt{\hat{d} / \hat{\omega}_m} \sim N(0, 1)$$

according to the characteristics of Normal distribution. The significance level was specified as 0.5, and the information of the goodness-of-fit test was shown in figure 5. The null hypothesis was rejected since the values of p were less than 0.05. It would cause the misspecification of distribution types of random parameters if the prediction method for \overline{RL}_2 was adopted in the case study. Therefore, it was appropriate and reliable to adopt the prediction method for \overline{RL}_3 in the case study.

6. Conclusions

In this paper, a residual life prediction method for degradation product based on Bayesian inference was proposed. A Wiener process with a time function was used to model degradation data.

Our proposed method made two potential novel contributions. a). Acceleration factor was introduced to transform the test data from accelerated stresses to normal use stress, so that accelerated degradation data can be considered as prior information. b). The non-conjugate prior distributions of random parameters were applied to Bayesian inference, which not only can consider the random effects of all the parameters but also can avoid the potential misspecifications of the parameter distributions when conjugate prior distributions were adopted.

Besides, there are several meaningful workings and conclusions about the study of the paper.

- 1) The residual life prediction method based on Bayesian inference that integrated the field degradation data and accelerated

degradation data can improve the prediction accuracy and real-time updating for the residual life.

- 2) The acceleration factor constant principle was used to deduce the relationships that the parameters of the Wiener process with a time function should satisfy. It offered a feasible approach to constructing the acceleration models for the parameters of the Wiener process.

Appendix

With $\hat{\mu}_m, \hat{\omega}_m$ the prior estimates of hyper parameters a, b, c, d can be obtained from:

$$L(\hat{\omega}_m; a, b) = \prod_{m=1}^M \frac{b^a}{\Gamma(a)} \hat{\omega}_m^{a-1} \exp(-b\hat{\omega}_m) \quad (\text{A.1})$$

$$L(\hat{\mu}_m | \hat{\omega}_m; c, d) = \prod_{m=1}^M \frac{\hat{\omega}_m^{0.5}}{\sqrt{2\pi d}} \exp\left(-\frac{\hat{\omega}_m(\hat{\mu}_m - c)^2}{2d}\right) \quad (\text{A.2})$$

From the field degradation data $\mathbf{X} = [X_1(t_1), X_2(t_2), \dots, X_{n+1}(t_{n+1})]$, the posterior estimates of hyper parameters can be deduced according to the Bayesian formula:

$$\pi(\mu, \omega | \Delta \mathbf{X}) = \frac{L(\Delta \mathbf{X} | \mu, \omega) \cdot \pi(\mu, \omega)}{\int_0^{+\infty} \int_{-\infty}^{+\infty} L(\Delta \mathbf{X} | \mu, \omega) \cdot \pi(\mu, \omega) d\mu d\omega} \quad (\text{A.3})$$

where $L(\Delta \mathbf{X} | \mu, \omega)$ is a likelihood function $\pi(\mu, \omega)$ is the joint prior PDF of μ and ω , denoted as $\pi(\mu, \omega) = \pi(\mu | \omega) \cdot \pi(\omega)$ and $\pi(\mu, \omega | \Delta \mathbf{X})$ is the joint posterior PDF.

Substitute:

$$\begin{aligned} \pi(\mu, \omega) &= \frac{\omega^{1/2}}{\sqrt{2\pi\hat{d}}} \exp\left(-\frac{\omega(\mu - \hat{d})^2}{2\hat{d}}\right) \cdot \frac{\hat{b}^{\hat{a}}}{\Gamma(\hat{a})} \omega^{\hat{a}-1} \exp(-\hat{b}\omega) \end{aligned}$$

and:

$$\begin{aligned} L(\Delta \mathbf{X} | \mu, \omega) &= \prod_{j=1}^n \frac{\omega^{1/2}}{\sqrt{2\pi\Delta\Lambda(t_j)}} \exp\left(-\frac{\omega(\Delta X_j - \mu \cdot \Delta\Lambda(t_j))^2}{2\Delta\Lambda(t_j)}\right) \end{aligned}$$

into (A.3), then:

$$\begin{aligned} \pi(\mu, \omega | \Delta \mathbf{X}) &\propto L(\Delta \mathbf{X} | \mu, \omega) \cdot \pi(\mu, \omega) \\ &\propto \omega^{(n+1)/2 + \hat{a} - 1} \exp\left\{-\frac{\omega}{2} \left(\mu^2 \sum_{j=1}^n \Delta\Lambda(t_j) - 2\mu \sum_{j=1}^n \Delta X_j + \sum_{j=1}^n \frac{\Delta X_j^2}{\Delta\Lambda(t_j)} \right) - \frac{\omega}{2} \left(\frac{(\mu - \hat{d})^2}{\hat{d}} \right) - \hat{b}\omega \right\} \\ &\propto \omega^{n/2 + \hat{a} - 1} \exp\left\{-\omega \left(\hat{b} + \frac{\hat{c}^2}{2\hat{d}} - \frac{\left(\hat{d} \sum_{j=1}^n \Delta X_j + \hat{c} \right)^2}{2 \left(\hat{d}^2 \sum_{j=1}^n \Delta\Lambda(t_j) + \hat{d} \right)} + \sum_{j=1}^n \frac{\Delta X_j^2}{2\Delta\Lambda(t_j)} \right)\right\} \omega^{1/2} \cdot \exp\left\{-\frac{\omega}{2} \left(\frac{\left(\mu - \frac{\hat{d} \sum_{j=1}^n \Delta X_j + \hat{d}}{\hat{d} \sum_{j=1}^n \Delta\Lambda(t_j) + 1} \right)^2}{\frac{\hat{d}}{\hat{d} \sum_{j=1}^n \Delta\Lambda(t_j) + 1}} \right)\right\} \end{aligned}$$

- 3) The prediction method that adopts non-conjugate prior distributions can be applied to more cases, since it does not require parameters to follow the specified distribution types. Moreover, the assumption that parameters are mutually independent facilitates the engineering application of the method.

The posterior estimates of hyper parameters can be obtained as:

$$\begin{aligned} \hat{a} | \Delta \mathbf{X} &= \frac{n}{2} + \hat{a}, \\ \hat{b} | \Delta \mathbf{X} &= \hat{b} + \frac{\hat{c}^2}{2\hat{d}} - \frac{\left(\hat{d} \sum_{j=1}^n \Delta X_j + \hat{c} \right)^2}{2 \left(\hat{d}^2 \sum_{j=1}^n \Delta\Lambda(t_j) + \hat{d} \right)} + \sum_{j=1}^n \frac{\Delta X_j^2}{2\Delta\Lambda(t_j)} \\ \hat{c} | \Delta \mathbf{X} &= \frac{\hat{d} \sum_{j=1}^n \Delta X_j + \hat{c}}{\hat{d} \sum_{j=1}^n \Delta\Lambda(t_j) + 1}, \quad \hat{d} | \Delta \mathbf{X} = \frac{\hat{d}}{\hat{d} \sum_{j=1}^n \Delta\Lambda(t_j) + 1} \end{aligned}$$

The form of $\Lambda(t)$ was specified as $\Lambda(t) = t^{\hat{r}}$, where \hat{r} was estimated from the accelerated degradation data. Furthermore, the posterior means $E(\mu | \Delta \mathbf{X})$, $E(\omega | \Delta \mathbf{X})$ of μ, ω were evaluated. Substitute $E(\mu | \Delta \mathbf{X})$, $E(\omega | \Delta \mathbf{X})$ and $\Lambda(t) = t^{\hat{r}}$ into Eq.(4) and (5), \overline{RL}_2 can be evaluated.

References

- 1 Baraldi P, Mangili F, Zio E. A prognostics approach to nuclear component degradation modeling based on Gaussian process regression. *Progress in Nuclear Energy* 2015; 78: 141-154, <http://dx.doi.org/10.1016/j.pnucene.2014.08.006>.
- 2 Chakraborty S, Gebraeel N, Lawley M, et al. Residual-life estimation for components with non-symmetric priors. *IIE Transactions* 2009; 41(4): 372-387, <http://dx.doi.org/10.1080/07408170802369409>.
- 3 Chiachio J, Chiachio M, Saxena A, et al. Bayesian model selection and parameter estimation for fatigue damage progression models in composites. *International Journal of Fatigue* 2015; 70: 361-373, <http://dx.doi.org/10.1016/j.ijfatigue.2014.08.003>.
- 4 Huang Z Y, Xu Z G, Wang W H, et al. Remaining useful life prediction for a nonlinear heterogeneous Wiener process model with an adaptive drift. *IEEE Transactions on Reliability* 2015; 64(2): 687-700, <http://dx.doi.org/10.1109/TR.2015.2403433>.
- 5 Gebraeel N, Elwany A Pan J. Residual life predictions in the absence of prior degradation knowledge. *IEEE Transactions on Reliability* 2009; 58(1): 106-117, <http://dx.doi.org/10.1109/TR.2008.2011659>.
- 6 Gebraeel N, Lawley M A, Li R, et al. Residual-life distributions from component degradation signals: a Bayesian approach. *IIE Transactions* 200; 37(6): 543-557.
- 7 Guida M, Penta F. A Bayesian analysis of fatigue data. *Structural Safety* 2010; 32:64-76, <http://dx.doi.org/10.1016/j.strusafe.2009.08.001>.
- 8 Jiang X M, Yuan Y, Liu X. Bayesian inference method for stochastic damage accumulation modeling. *Reliability Engineering & System Safety* 2013; 111:126-38, <http://dx.doi.org/10.1016/j.res.2012.11.006>.
- 9 Jin G, Matthews D E, Zhou Z. A Bayesian framework for on-line degradation assessment and residual life prediction of secondary batteries in spacecraft. *Reliability Engineering & System Safety* 2013;113:7-20, <http://dx.doi.org/10.1016/j.res.2012.12.011>.
- 10 Karandikar J M, Kim N H, Schmitz T L. Prediction of remaining useful life for fatigue-damaged structures using Bayesian inference. *Engineering Fracture Mechanics* 2012; 96:588-605, <http://dx.doi.org/10.1016/j.engfracmech.2012.09.013>.
- 11 Liao C M, Tseng S T. Optimal design for step-stress accelerated degradation tests. *IEEE Transactions on Reliability* 2006; 55: 59-66, <http://dx.doi.org/10.1109/TR.2005.863811>.
- 12 Liao H, Elsayed E A. Reliability inference for field conditions from accelerated degradation testing. *Naval Research Logistics* 2006; 53(6): 576-587, <http://dx.doi.org/10.1002/nav.20163>.
- 13 Ling M H, Tsui K L, Balakrishnan N. Accelerated degradation analysis for the quality of a system based on the Gamma process. *IEEE Transactions on Reliability* 2015; 64(1): 463-472, <http://dx.doi.org/10.1109/TR.2014.2337071>.
- 14 Lim H, Yum B J. Optimal design of accelerated degradation tests based on wiener process model. *Journal of Applied Statistics* 2011; 38:309-325, <http://dx.doi.org/10.1080/02664760903406488>.
- 15 Meeker W Q, Escobar L A. Accelerated degradation tests: modeling and analysis. *Technometrics* 1998; 40(2): 89-99, <http://dx.doi.org/10.1080/00401706.1998.10485191>.
- 16 Ntzoufras I. *Bayesian Modeling Using WinBUGS*: John Wiley & Sons; 2009, <http://dx.doi.org/10.1002/9780470434567>.
- 17 Padgett W J, Tomlinson M A. Inference from accelerated degradation and failure data based on Gaussian process models. *Lifetime Data Analysis* 2004; 10:191-206, <http://dx.doi.org/10.1023/B:LIDA.0000030203.49001.b6>.
- 18 Park C, Padgett W J. Stochastic Degradation Models With Several Accelerating Variables. *IEEE Transactions on Reliability* 2006; 55: 379-390, <http://dx.doi.org/10.1109/TR.2006.874937>.
- 19 Peng C Y, Tseng S T. Statistical lifetime inference with Skew-Wiener linear degradation models. *IEEE Transactions on Reliability*. 2013; 62(2); 338-350, <http://dx.doi.org/10.1109/TR.2013.2257055>.
- 20 Rigat F, Mira A. Parallel hierarchical sampling: A general-purpose interacting Markov chains Monte Carlo algorithm. *Computational Statistics & Data Analysis* 2012; 56:1450-67, <http://dx.doi.org/10.1016/j.csda.2011.11.020>.
- 21 Santini T, Morand S, Fouladirad M, et al. Accelerated degradation data of SiC MOSFETs for lifetime and remaining useful life assessment. *Microelectronics Reliability* 2014; 54: 1718-1723, <http://dx.doi.org/10.1016/j.microrel.2014.07.082>.
- 22 Si X S, Wang W B, Hu C H, et al. Remaining useful life estimation - a review on the statistical data driven approaches. *European Journal of Operational Research* 2011; 213:1-14, <http://dx.doi.org/10.1016/j.ejor.2010.11.018>.
- 23 Si, X S, Wang W B, Hu C H, et al. Estimating remaining useful life with three-source variability in degradation modeling. *IEEE Transactions on Reliability* 2014; 63(1): 167-190, <http://dx.doi.org/10.1109/TR.2014.2299151>.
- 24 Thas O, Ottoy J P. Some generalizations of the Anderson-Darling statistic. *Statistics & Probability Letters* 2003; 64:255-61, [http://dx.doi.org/10.1016/S0167-7152\(03\)00169-X](http://dx.doi.org/10.1016/S0167-7152(03)00169-X).
- 25 Wang L, Pan R, Li X, Jiang T. A Bayesian reliability evaluation method with integrated accelerated degradation testing and field information. *Reliability Engineering & System Safety* 2013; 112:38-47, <http://dx.doi.org/10.1016/j.res.2012.09.015>.
- 26 Wang H W, Xu T X, Mi Q L. Lifetime prediction based on Gamma processes from accelerated degradation data. *Chinese Journal of Aeronautics* 2015; 28(1): 172-179, <http://dx.doi.org/10.1016/j.cja.2014.12.015>.
- 27 Wang H W, Xu T X, Wang W Y. Remaining life prediction based on Wiener processes with ADT prior information. *Quality and Reliability Engineering*, <http://dx.doi.org/10.1002/qre.1788>.
- 28 Wang H W, Xu T X, Zhao J Z. Residual Life prediction method of fusing accelerated degradation and field degradation data. *Acta Aeronautica et Astronautica Sinica* 2014; 35(12):3350-3357.
- 29 Wang X. Wiener processes with random effects for degradation data. *Journal of Multivariate Analysis* 2010; 101:340-51, <http://dx.doi.org/10.1016/j.jmva.2008.12.007>.
- 30 Wang X L, Balakrishnan N, Guo B. Residual life estimation based on a generalized Wiener degradation process. *Reliability Engineering and System Safety* 2014; 124: 13-23, <http://dx.doi.org/10.1016/j.res.2013.11.011>.
- 31 Whitmore G A, Schenkelberg F. *Modelling Accelerated Degradation Data Using Wiener Diffusion With A Time Scale Transformation*. *Lifetime Data Anal* 1997; 3:27-45, <http://dx.doi.org/10.1023/A:1009664101413>.
- 32 Yang Z, Chen Y X, Li Y F, et al. Smart electricity meter reliability prediction based on accelerated degradation testing and modeling. *Electrical Power and Energy Systems* 2014; 56: 209-219, <http://dx.doi.org/10.1016/j.ijepes.2013.11.023>.

33. Ye Z S, Chen L P, Tang L C, et al. Accelerated degradation test planning using inverse Gaussian process. IEEE Transactions on Reliability 2014; 63(3): 750-763, <http://dx.doi.org/10.1109/TR.2014.2315773>.
34. Zaidan M A, Harrison R F, Mills A R, et al. Bayesian hierarchical models for aerospace gas turbine engine prognostics. Expert Systems with Applications 2015; 42:539-553, <http://dx.doi.org/10.1016/j.eswa.2014.08.007>.
35. Zhou Y Q, Weng C X, Ye X T. Study on Accelerated factor and condition for constant failure mechanism. Systems Engineering and Electronics 996; 18: 55-67.

Hao-Wei WANG**Ke-Nan TENG**

Naval Aeronautical and Astronautical University

The second road, 188 Yantai, China

E-mail: 13705355730@139.com, wyg2010123@126.com

Andrzej KOSUCKI
Piotr MALENTA

THE POSSIBILITIES OF REDUCING THE OPERATIONAL LOAD OF HOISTING MECHANISMS IN CASE OF DYNAMIC HOISTING

MOŻLIWOŚCI ZMNIEJSZENIA OBCIĄŻEŃ EKSPLOATACYJNYCH MECHANIZMÓW DŹWIGNIC DLA PRZYPADKU DYNAMICZNEGO PODNOSZENIA ŁADUNKU*

The simulation and experimental tests of hoisting mechanism in case of dynamic lifting the payload with clearance of ropes are presented in this paper. The minimization methods of the overloading of hoisting mechanisms were described. Basing on simulation tests the method that assured minimization of dynamics overloading with a few dozen to a few percent was introduced. It was determined the impact of the level of sensitivity of forces in ropes measurement on minimization of the overloading. The examples of the method implementation used for the real hoisting mechanism were shown.

Keywords: hoisting winch, overloads, control.

W artykule przedstawiono badania symulacyjne i eksperymentalne mechanizmu podnoszenia dla przypadku podrywania ładunku. Opisane zostały metody zmniejszania przeciążeń układu napędowego mechanizmów podnoszenia. Wskazano w oparciu o badania symulacyjne metodę zapewniającą minimalizację przeciążeń dynamicznych w czasie podrywania ładunku z kilkudziesięciu do kilku procent. Określony został wpływ poziomu czułości pomiaru sił w linach na minimalizację przeciążeń. Zaprezentowano przykłady zastosowań metody na rzeczywistej wciągarkie bębnowej.

Słowa kluczowe: wciągarka, przeciążenia, sterowanie.

1. Introduction

Besides the reliability, main requirements for vertical transport are positioning, use of power and reducing of the dynamic loads. For the hoisting mechanism the worst case in terms of appearing overloads is when the lifting operation starts when ropes have clearance. This case is called a jerk of a payload. The case when the ropes clearance is so big that when the ropes tensing began, the angular speed of the drum is near the reference speed. The research of overloads in drive systems usually comes up in the context of their impact on the steel structures of devices. For example in papers [1], [7] and [11] the tests of load dynamics of steel structures of the overhead cranes during payloads lifting were described. In [14], authors presented the model of the hoisting mechanism, where the stiffness of the girder has been taken into account. In these articles there were presented the studies of the behavior of the cranes structures under dynamic loads using FEM method. In [15] the influence of the hoisting mechanism operation on the crane structure was presented. There were presented waveforms of forces in ropes for different methods of increasing the drum speed from linear to inertial with various time constants. The problem of the crane structures load by vertical dynamic forces appeared also in [4] and [16], where the systems with moving mass were described. Reduction of dynamic overloads made by hoisting mechanisms operation provides measurable exploitation benefits, such as: minimization of the structure overload or reducing the power consumption. There were presented also methods of reduction of the steel structure loads by using dampers, eg. in [9]. Research of overloads of hoisting winches for various cases of lifting were described in [12]. The authors of [10] worked on modeling of hoisting mechanisms equipped with different drive systems.

The authors of [3] paid attention to necessity of consideration the various types of the loads of mechanisms caused eg. by the control methods and the limited scope of application of the cranes automa-

tion. The conclusion is that the control systems which reduce a temporary load should be used both for automatic and manual control of hoisting winches.

In [5] authors pointed the specificity of drives of hoisting winches, which: “are distinguished with respect of their requirements, regarding the control of speed and position and the acceleration phase carried with an active load”. The usage of modern drive systems based on frequency inverters, allows meet these requirements.

As can be seen the problem of overloads of hoisting mechanisms appears mainly in context of dynamic loads of supporting structures or research of dynamics of hoisting mechanisms. In our opinion, which is based on reading the available literature, the issues of reduce dynamic loads is presented only in context described above.

In the paper there is presented a drive system, which allows reduce dynamic overloads during lifting of a payload. Especially when a payload is jerk, the overloads are high. It was assumed that the proper control of a duty cycle allows reduce appearing overloads. Developed by authors, the method of minimization of dynamic overloads during lifting of the payload using continuous measure of the payload mass and constant power controller for hoisting mechanism are presented as well. Basing on developed models and both simulation and experimental tests, the results of minimization methods operation are shown.

2. The model of the hoisting winch

To examine the possibilities of minimization of the overload of the hoisting winch drive system, two experimentally verified models were used. The model, which inter alia was described in [2], of mechanical system of the hoisting winch and the model of the system: inverter - motor stator which was presented in [8].

(*) Tekst artykułu w polskiej wersji językowej dostępny w elektronicznym wydaniu kwartalnika na stronie www.ein.org.pl

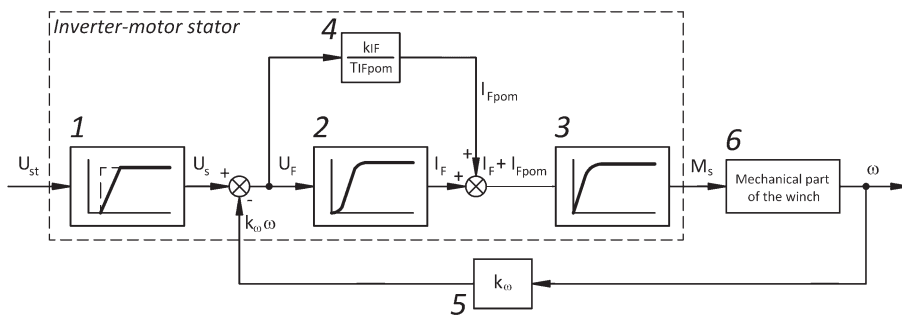


Fig. 1. The model of system: inverter - motor stator

The model of system: inverter - motor stator, which is presented on figure 1, was described using typical equations of dynamic elements. Elements 2, 3 and 4 are described respectively as inertial element second-order or first-order and as integral element. The integrating adjuster 1 was modeled as well. The task of this element is to limit the speed of increasing of dynamic values of the signal U_s as response on rapid change of the input signal U_{st} . The element 5 which converts motor speed to a voltage signal presents the existence of inner feedback of the speed ω_s inside the inverter.

Description in the space of state variables of the system presented on figure 1 is as follows:

$$\frac{dU_s}{dt} = \frac{1}{T_C} \times U_{SZ} \quad \text{— element 1}$$

$$\frac{dI_F'}{dt} = \frac{k_{IF} \times k_{wzm}}{T_{F1}^2} \times (U_s - k_E \times \omega) - \frac{T_{F2}^F}{T_{F1}^2} \times I_F' - \frac{1}{T_{F1}^2} \times I_F \quad \text{— element 2}$$

$$\frac{dI_F}{dt} = I_F'$$

$$\frac{dM_s}{dt} = \frac{k_{Ms}}{T_{Ms}} \times (I_F + I_{Fpom}) - \frac{1}{T_{Ms}} \times M_s \quad \text{— element 3}$$

$$\frac{dI_{Fpom}}{dt} = \frac{k_{IF}}{T_{IFpom}} \times (U_s - k_\omega \times \omega) \quad \text{— element 4}$$

The following markings were assumed in equations:

- U_s - control voltage
- I_F - stator current,
- I_{Fpom} - auxiliary stator current,
- M_s - torque on the motor stator,
- ω - angular speed of the motor,
- T_{F1}, T_{F2} - time constants of element 2,
- k_{IF} - conversion factor of elements 2 and 3,
- k_{wzm} - gain factor,
- T_{IFpom} - time constant of element 3,
- k_ω - conversion factor of angular speed
- k_{Ms} - gain factor of element 4,
- T_{Ms} - time constant of element 4.

The following state variables were specified:

- I_F - stator current,
- I_F' - auxiliary variable - current
- I_{Fpom} - auxiliary stator current,
- M_s - torque on the motor stator,
- U_s - control voltage

For the system described above, the control signal U_{st} proportional to the reference speed of the motor was the input signal. As the output signals an angular speed of the motor ω and a torque M_s were assumed. To determine a speed ω , the mechanical part of the hoisting winch should be modeled. Figure 2 presents the model of mechanical part of the hoisting winch and schema of the drive system.

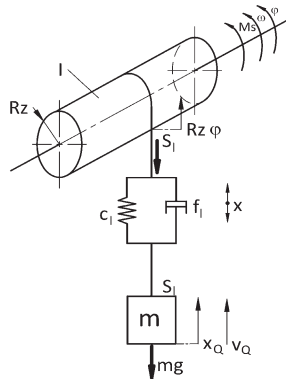


Fig. 2. The model of mechanical part of the hoisting winch and schema of the drive system.

The model is described in the space of state variables using between others rules presented in [13]. The mathematical model of the mechanical part of the hoisting winch in space of state variables is as follows:

$$\frac{d\omega}{dt} = \frac{1}{I_z} \times M_s - \frac{c_l \times x}{I_z} - \frac{R_z \times f_l}{I_z} \times \omega + \frac{f_l}{I_z} \times v_Q$$

$$\frac{dx}{dt} = R_z \times \omega + v_Q$$

$$\frac{dv_Q}{dt} = \frac{c_l}{m} \times x - \frac{R_z \times f_l}{m} \times \omega + \frac{f_l}{m} \times v_Q - g$$

where:

- x - elongation of a rope system
- I_z - effective moment of inertia of rotational parts of the hoisting winch
- m - mass of the payload
- R_z - effective radius
- c_l - effective stiffness of a rope system
- f_l - damping ratio
- v_Q - speed of the payload

The following state variables were established:

- x - elongation of a rope system
- v_Q - speed of the payload
- ω - angular speed of the motor,

Finally the description of the mechanical part of the hoisting winch, which includes drive system fed by the inverter was obtained. The following output variables were established:

- ω - angular speed of the motor
- v_Q - speed of the payload
- x - elongation of a rope system
- M_s - torque on the motor stator
- S_1 - force in ropes

The input for the system was voltage signal U which is inverter control signal and it is proportional to reference angular speed of the motor.

The solving of the model allowed to carry some simulation tests to determine dynamic behavior for the different cases of hoisting winch operation and varies control systems.

3. The methods of overload reduction during lifting

In case of the jerk of a payload – which gives the biggest overloads in drive system, a few methods and control systems allowing minimize overloads were checked.

Mostly used method of hoisting mechanism control consist in linear acceleration and deceleration (linear change of the speed during acceleration and deceleration phases), independently on initial state of the mechanism. In figure 3 are shown exemplary wavecharts of speed v_b , force in ropes S_1 and input signal U during the jerk of a payload with linear changes of input signal. The jerk of a payload occurs when after connection ropes with the payload, the clearance of the ropes remains. So, the start-up of the motor is practically without load. The steady speed of the motor (and drum) is reached when ropes still are with clearance. After deleting the clearance, the rope began to be tension, as it is shown in figure 3, seen as the rapid growth of the force in ropes. Lifting of the payload starts when force S_1 exceed the value of border force equal to the payload weight. The overload in presented

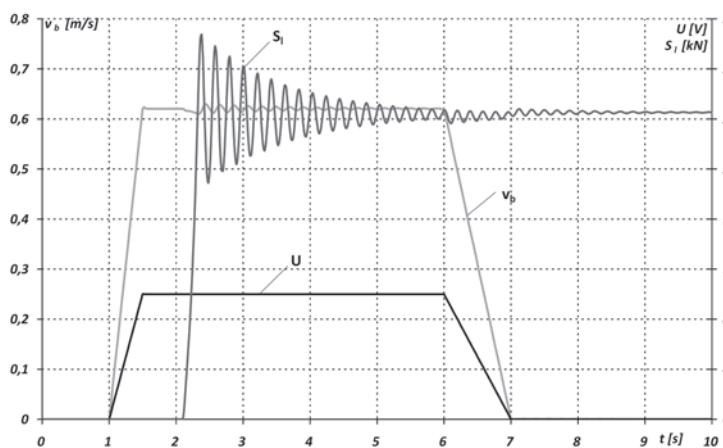


Fig. 3. Jerk of the payload with trapezoidal input

case reached 25% above the steady value.

This case concerned the payload with mass 2,5 tons, which was lifting with speed about 0.63 m/s.

The reduction this kind of overloads could be done eg. by increasing the acceleration time, but it is not always possible and desirable because of the longer time of the duty cycle.

One of the methods that allows reduce dynamics overloads is the start-up with preliminary speed, what was presented inter alia in [6]. An exemplary algorithm cover the following phases:

- preliminary movement with low speed (eg. 10 % of steady speed) during defined time

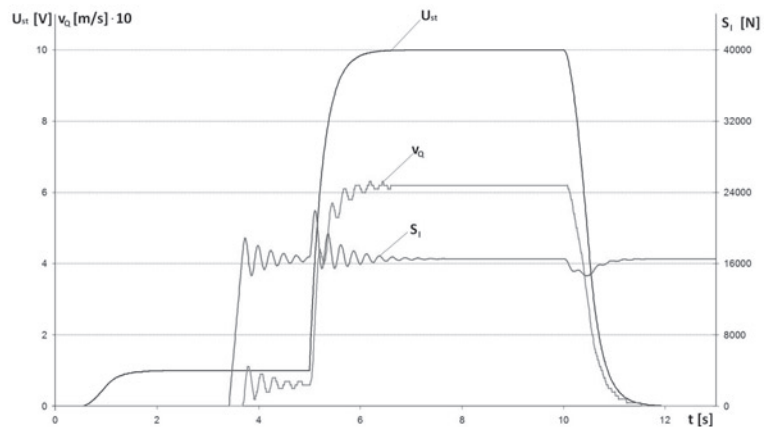


Fig. 4. Lifting the payload with preliminary speed

- measurement of the force in ropes
- movement with maximum allowed speed using constant power regulator

Figure 4 illustrates the operation of this system. The advantage of this method is the possibility of using constant power regulator, which increases efficiency of the machine and enables full power usage. The disadvantage is the necessity of deleting the clearance during preliminary movement. If not, the payload is still jerk. In addition, the constant power regulator will not operate properly because of wrong data about load. In cases of small payloads, the preliminary movement is redundant, because the times of the duty cycles are getting longer.

Disadvantages mentioned above could be removed by using the other algorithm of control, which is basing on following assumptions:

1. Lifting a payload with maximum allowed speed with continuous measurement of a force in ropes,
2. At the moment of the detection of the load follows:
 - a) stopping the lifting,
 - b) after establishing the conditions, the measurement of forces in ropes,
 - c) next, starting the lifting with maximum allowed speed.

It was important to define the proper level of force measurement sensitivity which is important because of reduction of overloads. The comparison of various settings of the force sensor are presented in figure 5, where the wavecharts of forces in ropes for different sensitivity thresholds, the levels of maximum forces and also the input functions are shown.

Application of a lower threshold of force sensor allows to reduce the dynamic overloads in ropes system. The comparison of the maximum overloads for cases presented on figure 5, which are calculated as quotient of a maximum and steady force, were as follows:

Sensor threshold	Without sensor	10 000 N	5 000 N	500 N
Overloads	1,252	1,217	1,161	1,097

The reduction of overload can reach over a dozen percent of steady value.

The implementation of this algorithm could be difficult. Figure 6 shows case when the second phase of the cycle starts with ropes clearance. This gives the effect of next payload jerk and consequently the absence of the overload reduction. It is important to assure the tensioning of the ropes before second phase starts.

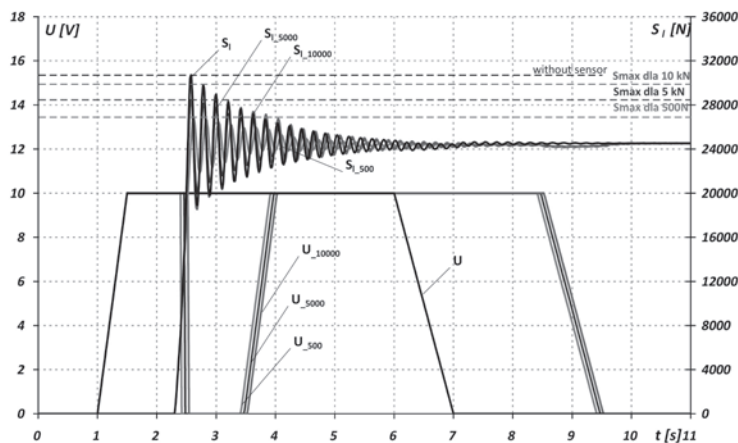


Fig. 5. The comparison of forces in ropes for different sensor thresholds

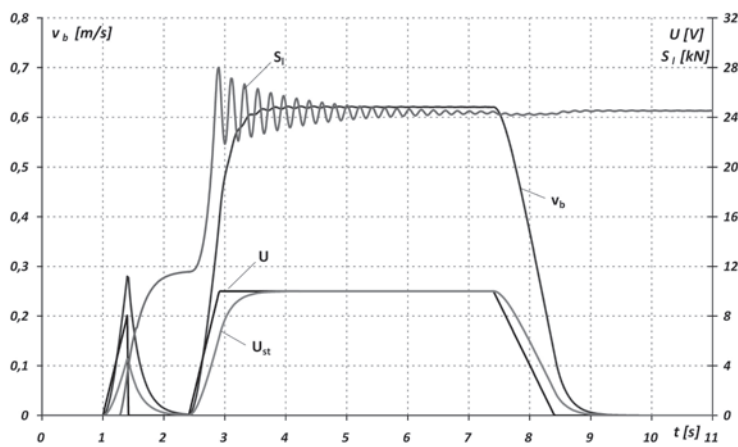


Fig. 6. Wavechart of force in ropes in case of low clearance

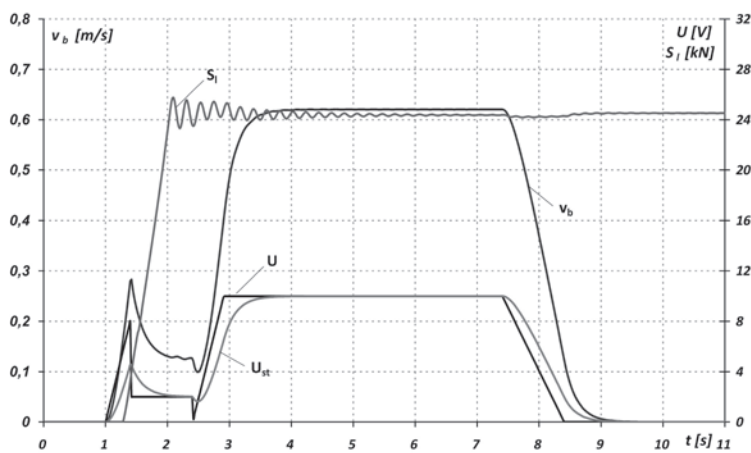


Fig. 7. Wavechart of force in ropes in case of reduced intermediate speed

One of solutions is replacing the stop of a movement by reduction of a speed. The speed should be at the low level which assures the tensioning of the ropes. A time of the movement depends on characteristic of the operation of the hoisting winch – speed and methods of payload fixing. This case is presented in figure 7. The overload is reduced to about 5% in contrary to 14% in case shown in figure 6.

The results of simulation tests carried on the model of hoisting winch, allowed to check the effectiveness of described method on real device.

4. The test stand

Good results of simulation tests of the system reducing overloads, allowed the experimental tests which should confirm good operation of the system installed on real winch. The assumptions were made that the ropes were cleared, the mass was defined and was standing on the ground. The trapezoidal input signal using varies times of acceleration (including step function) were also assumed. The tests were carried both with operating and switched off system of overload reduction.



Fig. 8. The laboratory overhead crane

The test stand consisted of hoisting winch installed on real overhead crane equipped with necessary control and measurement systems. Overhead crane was installed in Laboratory of Division of Working Machined, Drives and Control in Lodz University of Technology. The main parameters of the crane were as follows: capacity 50kN, span 10m and lifting height 6m. Described overhead crane is presented in figure 8.

All the mechanisms were equipped with the system: frequency inverter – asynchronous motor. Each inverter was managed by microprocessor controller which performed all the required functions of the control of the mechanism. In addition, the logic functions of the mechanisms such as control of mechanical brakes or limit switches were also managed by the controllers. The master controller managed operations of all controllers and the manipulator of manual control using BITBUS. It allowed both manual and automatic operation of the system.

The operating of hosting mechanism began with the information of the set position of the drum given by master computer. The whole duty cycle including acceleration, steady motion and deceleration is realized by the controller. For the experimental purposes the master controller was replaced by the outer computer.

The schema of the hoisting winch including control and measurement elements is presented in figure 9.

To assure correct operations of the system and acquisition of interested physical parameters, the following measurement systems were installed:

- measurement system of a force in ropes S_1 – using strain gauge below the compensatory pulley (used also to measure a payload mass)
- measurement system of an angular speed ω_s – using encoder mounted on the rotor of the electric motor
- measurement system of an angle position of the drum ϕ_b – using absolute encoder of angular position of the shaft

Working station AWS-842TP equipped with set of measuring and control cards was used to acquisition the measured physical values and the control

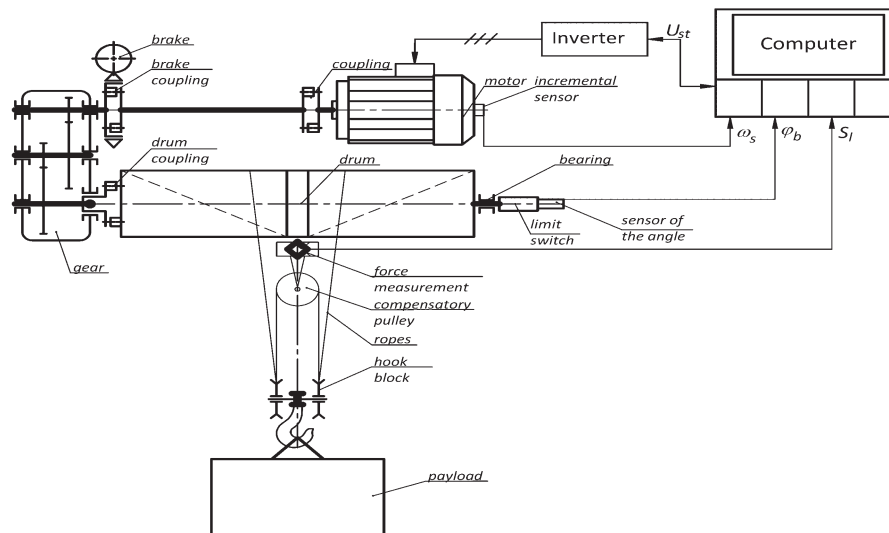


Fig. 9. The schema of the winch

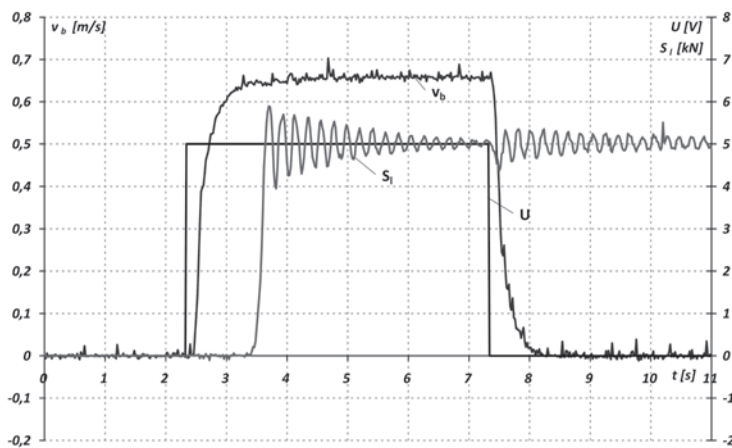


Fig. 10. The jerk of the payload without system of overloads reduction. Experimental tests

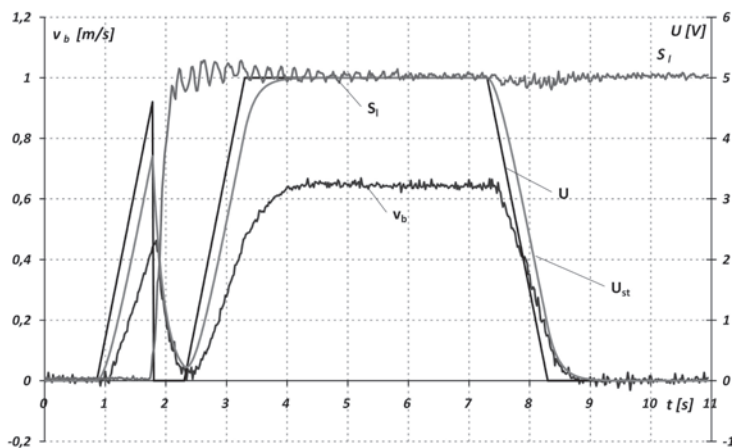


Fig. 11. The jerk of the payload with system of overloads reduction. Experimental tests

References

1. Bogdevičius M, Vika A. Investigation of The Dynamics of an Overhead Crane Lifting Process in a Vertical Plane. TRANSPORT 2005; XX (5): 176-180.
2. Bednarski S, Cink J, Malenta P. Pozycjonowanie ładunku w ruchu roboczym wciągarki bębnowej z napędem falownikowym. Materiały IV Konferencji Okrętownictwo i Oceanotechnika. Szczecin 1998: 15-24.

5. The experimental tests

The exemplary wavecharts taken from the experiment are presented in figures 10 and 11. The input signal U , voltage signal U_{st} controlling inverter, force in ropes S_l and real speed of rope on drum v_b taken from changes of the angle position of the drum φ_b are presented. The case of jerk of the payload without system of overloads reduction is shown in figure 10. The input signal is step signal. The payload weighed 500 kg.

The ropes tensing began more than 2 s after motor start-up, when motor rotates with speed close to synchronous. It results with the overload on the level more than 26% above the steady values.

Figure 11 shows wavecharts when system of overload reduction was operated in the mode of maximum speed start-up with constant power regulator. It shows that during start-up there appeared the small oscillation of the force in ropes, which slightly exceeding the steady values. Registered overloads were under 5%.

6. Summary

The tests of hoisting mechanism fed by inverter confirmed the correctness of operation of the control system, which was operated in the mode of maximum speed start-up with constant power regulator. Both simulation and experimental tests showed reduction of the overload from more than 25% to about 5%. It gives 80% reduction of the overload above the steady values. Operation of the reduction system did not influenced on steady values of speed of the ropes. The system can be used both in automatic and manual mode of control. The parameters which are responsible for proper drive operation eg. level of force measurement sensitivity were defined.

3. Eihab M, Abdel-Rahman, Ali H. Nayfeh, Ziyad N. Masoud. Dynamics and Control of Cranes: A Review. *Journal of Vibration and Control* 2003; 9: 863-908, <http://dx.doi.org/10.1177/1077546303009007007>.
4. Gašić V, Nenad Zrnić N, Obradović A, Bošnjak S. Consideration of Moving Oscillator Problem in Dynamic Responses of Bridge Cranes. *FME Transactions* 2011; 39: 17-24.
5. Grabowski E, Morawski A. Nowoczesne napędy falownikowe dźwignic. *Transport Przemysłowy* 2001; 1 (11): 33-37.
6. Grudziecki J, Malenta P, Uciński J. Zmniejszanie obciążeń dynamicznych w elementach mechanizmu podnoszenia. *Problemy Maszyn Roboczych* 2001; 18: 33-40.
7. Haniszewski T. Hybrid analysis of vibration of the overhead travelling crane. *Transport Problems* 2014; 9 (2): 89-100.
8. Kosucki A. Badanie transportu ładunków przy wykorzystaniu skojarzonych ruchów mechanizmów suwnic pomostowych. Łódź: z. 474 (1175), 2013.
9. Krukowski J, Maczyński A, Szczotka M. The Influence of a Shock Absorber on Dynamics of an Offshore Pedestal Crane. *Journal Of Theoretical And Applied Mechanics* 2012; 50, 4 (2012): 953-966.
10. Margielewicz J, Haniszewski T, Gąska D, Pypno C. Badania modelowe mechanizmów podnoszenia suwnic. *Polska Akademia Nauk*. Katowice: 2013.
11. Matyja T, Ślaskowski A. Modelling of the lift crane vibration caused by the lifting loads. *International Conference Zdvihací Zařízení v Teorii a Praxi*. Brno 2007: 98-105.
12. Michałowski S, Cichocki W. The Peak Dynamic Loading of a Winch in Term of the Rope Flexibility. *Key Engineering Materials* 2013; 542: 105-117, <http://dx.doi.org/10.4028/www.scientific.net/KEM.542.105>.
13. Newton I. *Mathematical Principles of Natural Philosophy*. NY: 1846.
14. Solazzi L, Incerti G, Petrogalli C. Estimation of the dynamic effect in the lifting operations of a boom crane. *Proceedings 28th European Conference on Modelling and Simulation*, 2014, <http://dx.doi.org/10.7148/2014-0309>.
15. Sun G., Kleeberger M, Liu J. Complete dynamic calculation of lattice mobile crane during hoisting motion. *Mechanism and Machine Theory* 2005; 40: 447-466, <http://dx.doi.org/10.1016/j.mechmachtheory.2004.07.014>.
16. Zrnić N, Gašić V, Bošnjak S, Dordević M. Moving Loads in Structural Dynamics of Cranes: Bridging the Gap Between Theoretical and Practical Researches. *FME Transactions* 2013; 41: 291-297.

Andrzej KOSUCKI

Piotr MALENTA

Lodz University of Technology

Department of Vehicles and Fundamentals of Machine Design

ul. Żeromskiego 116, 90-924 Łódź, Poland

E-mails: andrzej.kosucki@p.lodz.pl, piotr.malenta@p.lodz.pl

Zihua WANG
Junxing LI
Yongbo ZHANG
Huimin FU
Chengrui LIU
Sridhar KRISHNASWAMY

A NOVEL WIENER PROCESS MODEL WITH MEASUREMENT ERRORS FOR DEGRADATION ANALYSIS

ANALIZA DEGRADACJI Z ZASTOSOWANIEM NOWEGO MODELU PROCESU WIENERA UWZGLĘDNIAJĄCEGO BŁĘDY POMIAROWE

Degradation analysis can be used to assess reliability for complex systems and highly reliable products, because few or even no failures are expected in a reasonable life test span. In order to further our study on degradation analysis, an independent increment random process method with linear mean and standard deviation functions is presented to model practical degradation procedures. It is essentially a Wiener process method. Since measurement errors are often created by imperfect instruments, procedures and environments during degradation investigation, the measurement error is incorporated into the independent increment random process. Furthermore, statistical inferences of this model are discussed, and close forms of a product's median life and percentile of the failure time distribution (FTD) are also derived. The proposed method is illustrated and verified in a comprehensive simulation study and two practice applications for storage disks and Infrared light-emitting diodes. Meanwhile, the time-transformed Wiener process model with measurement error is considered as a reference method. Comparisons show that the proposed model can provide reasonable results, even in considerably small sample size circumstance.

Keywords: performance degradation, independent increment process, Wiener process model, linear mean function, linear standard deviation function, measurement error.

Analizę degradacji można stosować do oceny niezawodności wysoce niezawodnych złożonych systemów i produktów, ponieważ w ich przypadku istnieje bardzo niskie lub zerowe prawdopodobieństwo wystąpienia uszkodzenia w trakcie badania trwałości w przyjętym okresie eksploatacji. W artykule przedstawiono nowo opracowane podejście do modelowania procesu degradacji wykorzystujące metodę procesu o przyrostach niezależnych oraz pojęcia funkcji średniej liniowej i funkcji liniowego odchylenia standardowego. Zasadniczo jest to metoda oparta na procesie Wienera. Ponieważ badania degradacji często wiążą się z błędami pomiarowymi wynikającymi z niedoskonałości stosowanych narzędzi, procedur i warunków badawczych, opisywany proces o przyrostach niezależnych uwzględnia błędy pomiaru. Ponadto, w pracy omówiono wnioski statystyczne, jakie można wyciągnąć na podstawie przedstawionego modelu oraz wyprowadzono wzory ogólne na średnią długość życia produktu oraz na percentyl rozkładu czasu do uszkodzenia. Proponowaną metodę zilustrowano i zweryfikowano na podstawie kompleksowego badania symulacyjnego oraz przykładów praktycznego zastosowania modelu w odniesieniu do dysków pamięci masowej oraz diod podczerwieni. W artykule przedstawiono także model procesu Wienera z transformowanym czasem uwzględniający błąd pomiaru, który posłużył za model referencyjny. Porównania pokazują, że proponowany model może dawać poprawne wyniki, nawet przy bardzo małej liczbie próby.

Słowa kluczowe: obniżenie charakterystyk, proces o przyrostach niezależnych, model procesu Wienera, funkcja średniej liniowej, funkcja liniowego odchylenia standardowego, błąd pomiaru.

1. Introduction

High reliable components and systems have been becoming more and more common in engineering as well as in our everyday life. Conventional failure data based methods encounter serious challenges because one cannot get enough failure data through general or accelerated life tests. Since most components and systems degrade over time, and can be considered to be failed when the deterioration accumulates beyond a predefined level (also called threshold level), degradation data can be taken as rich source life information in reliability assessment [9]. Once the failure has been detected, it is possible to access the FTD, infer reliability and accordingly predict the remaining useful

life to take timely maintenance actions to avoid the catastrophic failures [12]. There has been a growing literature that is concerned with drawing reliability inferences from degradation data [8].

Lu and Meeker [6] concluded in their study that observed degradation on a specimen over time is a time series that can exhibit autocorrelation. Although they ignored the autocorrelation in their study, more and more deterioration models have taken this issue into consideration in the model construction procedure. Among these models, the Wiener process with positive drift is a favourable candidate due to its mathematical properties and physical interpretations [20]. The

regular Wiener process $\{\eta(t), t \geq 0\}$ with drift β and diffusion σ can be expressed as the well-adopted form [16, 18]:

$$\eta(t) = \beta\Lambda(t) + \sigma\mathbf{B}(\Lambda(t)) \quad (1)$$

where $\mathbf{B}(\cdot)$ denotes a standard Wiener process, and $\Lambda(t)$ is defined as a transformed time scale. From the basic definition of Wiener process, we know that $\{\eta(t), t \geq 0\}$ has s -independent and normally distributed increments; viz. $\Delta\eta(t) = \eta(t + \Delta t) - \eta(t)$ is s -independent of $\eta(t)$, and $\eta(t) \sim N(\beta\Lambda(t), \sigma^2\Lambda(t))$.

There has been considerable interest on the part of the scientists and engineers in applying this process in degradation reliability analysis. Whitmore and Schenkelberg [18] presented a Wiener diffusion process with power-law time scale transformation to model self-regulating heating cables. Tseng and Peng [14] adopted an exponential transformed time scale to describe the deterioration path of a specific light emitting diode (LED) product. Park and Padgett [10] developed a generalized cumulative damage approach by describing initial damage with this process.

In practical engineering, it is inevitable that possible heterogeneities within a product population may exist due to geometry, material and other variations throughout the population. Specimens from the same population may share some commonalities and exhibit certain unit-specific properties as well. Therefore, Wiener process model with mixed effects is developed, where fixed effects capture the common characteristics while random effects describe the unit-to-unit differences. In real applications, drift β for individual unit is usually assumed to be fixed but unknown, and follows a normal distribution $\beta \sim N(\mu, \kappa^2)$. This model was utilized by Crowder and Lawless [3] to analyze a wear procedure.

It should be noted from the Wiener process definition that the deterioration processes depicted by regular Wiener process and mixed effects models exhibit specific statistical properties. Certain relationship, also can be called limitation, exists between mean and variance because of the transformed time scale $\Lambda(t)$. Taking the linear transformed time scale situation (i.e., $\Lambda(t)$ is a linear function of test time) as an example, we should note that the regular Wiener process will illustrate both linear trend $\beta\Lambda(t)$ and variance $\sigma^2\Lambda(t)$. Although for the commonly used mixed effects model situation $\beta \sim N(\mu, \kappa^2)$, the Wiener process will exhibit a linear mean $\mu\Lambda(t)$ and a quadratic variance $\kappa^2\Lambda^2(t) + \sigma^2\Lambda(t)$, one should note that this quadratic variance is not a generalized one because of the only one transformed time scale $\Lambda(t)$.

To settle this problem, Tseng et al. [13] proposed a generalized Wiener process model for degradation analysis with two transformed time scales $\Lambda^{(1)}(t)$ and $\Lambda^{(2)}(t)$.

$$\eta(t) = \beta\Lambda^{(1)}(t) + \sigma\mathbf{B}(\Lambda^{(2)}(t)) \quad (2)$$

It can be concluded that Equation (2) is an improved degradation model comparing with Equation (1), because the previously mentioned correlation limitation between mean and variance of the regular Wiener process and mixed effects model can be broken through. It is worth noticing, however, that Tseng et al. [13] restricted their attention

to the case $\Lambda^{(1)}(t) = \Lambda^{(2)}(t)$ in their study, because they concluded that it was rather difficult to obtain an explicit form of the lifetime

distribution when $\Lambda^{(1)}(t) \neq \Lambda^{(2)}(t)$. Therefore, they only proposed a general Wiener process model form with two transformed time scales without any essential studies or applications. From this viewpoint, the first objective of this paper is to study a commonly encountered case of the generalized Wiener process model expressed by Equation (2) via theoretical, simulation and empirical means.

In our previous work [17], we constructed a Wiener process model:

$$\eta(t) = a + bt + \mathbf{B}(dt^2) \quad (3)$$

It can be concluded as a special case of the generalized two-transformed time scale Wiener model expressed by Equation (2), where drift β and diffusion σ are both constants, $\Lambda^{(1)}(t) = a + bt$ and $\Lambda^{(2)}(t) = dt^2$. Measurement errors were not considered in the modeling procedure, i.e., deterioration observations were supposed to only reflect the inherent randomness of degradation itself.

To further depict the commonly encountered degradation situation of linear trend and generalized quadratic variance, we propose an improved model:

$$\eta(t) = a + bt + \mathbf{B}((d_1 + d_2t)^2) \quad (4)$$

where a , b , d_1 and d_2 are model parameters relating to linear mean and quadratic variance features, common for all units. Therefore, increment $\Delta\eta(t) = \eta(t + \Delta t) - \eta(t)$ is also s -independent of $\eta(t)$.

Comparing with the previously discussed regular Wiener process and mixed effects models, Equation (4) can be considered as a more generalized Wiener process model for the commonly encountered linear degradation path situation, because it can break through the correlation limit due to the only one transformed time scale $\Lambda(t)$. More important, degradation model of Equation (4) also can give a closed-form of FTD, and standard errors and confidence intervals for the parameter estimators can be directly understood and derived. Meanwhile, comparing with the generalized Wiener model form of Equation (2), Equation (4) is a special case by letting the two trans-

formed time scales $\Lambda^{(1)}(t) = a + bt$ and $\Lambda^{(2)}(t) = (d_1 + d_2t)^2$, and the constant drift rate β and diffusion coefficient σ are incorporate into the transformed time scales.

On the other hand, it is inevitable that measurement errors may be introduced during the observation process in practical engineering. Therefore, Whitmore [18] described a Wiener diffusion model for measured degradation data that took both the inherent randomness of degradation itself and the measurement errors into account. He derived the sample log-likelihood function with the first differences of the inspections, the correlation among the observations on an item over time is consequently considered in his modeling procedure. Motivated by laser data [7], Peng and Tseng [11] proposed a generalized formulation of the linear degradation path in which the unit-to-unit variation, the time-dependent error structure and the measurement error were considered simultaneously. To utilize the first inspection of each unit, Ye et al. [20] improved the model in [18] and developed a time-transformed Wiener process model with measurement errors to analyze degradation of magnetic heads of hard disk drives. This

improvement makes efficient remedy in real application, especially when the number of observations associated with each unit is small.

Thus, motivated by the practical need of including measurement errors in degradation analysis, the second objective of this study is to develop a generalized Wiener process model subject to measurement errors. Throughout this paper, the deterioration measurement at time t is denoted by $Y(t)$, and the corresponding true level of degradation at this time is denoted by $\eta(t)$. Then the statistical model relating degradation measurement $Y(t)$ to the true deterioration level $\eta(t)$ is assumed to be the following:

$$Y(t) = \eta(t) + e(t) \quad (5)$$

where $e(t)$ denotes the measurement errors that are assumed to be i.i.d. realization of $e(t) \sim N(0, \sigma_e^2)$.

We call this proposed Wiener process model with measurement errors expressed by Equation (4) the simple model. And we will illustrate it in Section 2. In this study, consequently, we improve the Wiener process model of Equation (4) via taking measurement errors into consideration, and further investigate a more generalized model.

The remainder of the paper is organized as follows. Section 2 introduces the simple Wiener process degradation model with linear trend and quadratic variance. Section 3 takes measurement errors into the simple model and gives the model description, MLE for unknown parameter and initial guesses for optimization algorithm. In Section 4, the efficiency and reasonability of our methodology is validated comparing with the Wiener processes with measurement errors in [20] via a Monte Carlo simulation study. In Section 5, the proposed approach is illustrated by two applications including storage disks degradation analysis and Infrared light-emitting diodes (IRLEDs) degradation analysis, and comparative results are given. A summary and conclusion is given in Section 6.

2. The simple Wiener processes degradation model

Experimental results provide an observed sequence of degradation readings z over test time t for each sample unit. The observed degradation z is a unit's actual degradation. "Time" t could be real test time or some other measure like cycles in fatigue tests. We make the following general assumptions about the manner in which the test is conducted.

- 1) Sample units are randomly selected from a population or production process. We use this assumption for ensuring the independence of measurements for individual item, and ensuring the population reliability inference reasonability based on the tested sample.
- 2) The degradation is a non-return process (eg, when in discussion with unmaintainable systems with stable intensity of use); viz. a unit can be declared as having failed when its degradation reaches a critical threshold [4].
- 3) The first test time is prespecified, the same across all the test units, but not necessarily to be zero. This can be realized via proper transforming when the first test times are not all the same in practical degradation test. Then test times can be different for individual item, and may or may not be equally spaced in time.

Based on our previous study and analysis, the mean and standard deviation of some degradation process can both be considered as linear function of test time, or transformed test time when this relationship cannot be found directly. Consequently, in order to construct a generalized method, we define the following two transformation functions. One is an appropriate monotone increasing time transfor-

mation $x = f_1(t)$, where t denotes the test time, and x corresponds to the transformed test time. The other one is performance parameter transformation $y = f_2(z)$, where z denotes the measurement in the degradation test, and y is the transformed degradation value. These two transformation functions can be obtained by engineering experience, mechanistic knowledge (see the wearing theory in [15]) or data plotting (see the complex logarithmic transformation in [21]). Particularly, let $x = t$ and $y = z$ when linear mean relationship between degradation measurement z and test time t can be established directly.

Then the Wiener process proposed in this paper with linear mean $\mu(x) = a + bx$ and linear standard deviation $\sigma(x) = d_1 + d_2x$ can be defined through the following assumptions.

- 1) Suppose m items are put into test. The performance of unit i is measured (or inspected) at n_i prespecified times $t_1 < t_{i2} < \dots < t_{in_i}$ with corresponding measurements $z_{i1}, z_{i2}, \dots, z_{in_i}$, $i = 1, 2, \dots, m$.
- 2) If necessary, construct the time transformation $x = f_1(t)$ and/or performance parameter transformation $y = f_2(z)$. Then the transformed performance increments $y_{i2} - y_{i1}, y_{i3} - y_{i2}, \dots, y_{in} - y_{i(n-1)}$ are inter-independent for all items $i = 1, 2, \dots, m$.
- 3) The increment $y_{ij} - y_{i(j-1)}$ follows a normal distribution:

$$y_{ij} - y_{i(j-1)} \sim N\left(b(x_{ij} - x_{i(j-1)}), 2d_1d_2(x_{ij} - x_{i(j-1)}) + d_2^2(x_{ij}^2 - x_{i(j-1)}^2)\right) \quad (6)$$

$$i = 1, 2, \dots, m \quad j = 2, 3, \dots, n$$

where $b = \partial\mu(x)/\partial x$ is the constant mean degradation rate; and $d_2 = \partial\sigma(x)/\partial x$ depicts the increasing rate of standard deviation, also a constant.

- 4) The first transformed measurement y_{i1} is independent of the increments $y_{i2} - y_{i1}, y_{i3} - y_{i2}, \dots, y_{in} - y_{i(n-1)}$ and follows a normal distribution:

$$y_{i1} \sim N(\mu_1, \sigma_1^2) \quad i = 1, 2, \dots, m \quad (7)$$

where μ_1 and σ_1^2 are the mean and variance of the transformed degradation measurements at the first transformed test time x_1 .

Based on the properties of Wiener processes and the model assumptions mentioned above, y_{ij} also follows a normal distribution:

$$y_{ij} = a + bx_{ij} + \varepsilon(x_{ij})$$

$$\varepsilon(x_{ij}) \sim N\left(0, (d_1 + d_2x_{ij})^2\right) \quad (8)$$

$$\text{Cov}(\varepsilon(x_{ij}), \varepsilon(x_{ik})) = (d_1 + d_2x_{ij})^2 \quad x_{ij} \leq x_{ik}$$

where a , b , d_1 and d_2 are unknown parameters, common for all items. We can further concluded that variance of y_{ij} can be depicted by $\text{Var}(y_{ij}) = \sigma^2(x_{ij}) = (d_1 + d_2x_{ij})^2$.

From the Wiener process definition, its standard deviation can be concluded to be an increasing function of time, which yields that

$d_1 \geq 0$ and $d_2 > 0$. Particularly, when $d_1 = 0$, standard deviation will be $\sigma(x) = d_2 x$, then the degradation model will become the one we have established in [17]. Based on the statistical models expressed by Equation (2) and Equation (8), our proposed methodology is essentially the Wiener process model $y_t = a + bx + B((d_1 + d_2 x)^2)$ from a different viewpoint, where the statistical properties can be intuitively drawn.

3. The improved model with measurement errors

3.1. Model Assumption

Let $x = t$, $y = z$, and suppose $\eta(t)$ is a unit's actual degradation. Then, based on the statistical models expressed by Equation (4) and Equation (5), the statistical model relating degradation measurement $Y(t)$ to the true deterioration level $\eta(t)$ is assumed to be the following:

$$Y(t) = a + bt + B((d_1 + d_2 t)^2) + e(t) \quad (9)$$

where $e(t)$ denotes the measurement errors that are assumed to be i.i.d. realization of $e(t) \sim N(0, \sigma_e^2)$. The $e(t)$ is assumed to be mutually independent of each other and of the $\eta(t)$.

Suppose the deterioration is inspected at ordered times $t = \{t_1, t_2, \dots, t_n\}$, with observed degradations $\{Y_1 = y_1, Y_2 = y_2, \dots, Y_n = y_n\}$, where $Y_i = \eta_i + e_i$. Define the increment $\Delta Y_1 = Y_1$, $\Delta y_1 = y_1$, $\lambda_1 = a + bt_1$ and $\Delta Y_i = Y_i - Y_{i-1}$, $\Delta y_i = y_i - y_{i-1}$, $\lambda_i = b(t_i - t_{i-1})$ for $i = 2, 3, \dots, n$. Then $\Delta Y = \{\Delta Y_1, \dots, \Delta Y_n\}$ follows a multivariate normal distribution $N(b\lambda, \Sigma)$ with a joint probability density function (PDF):

$$f_{\Delta Y}(\Delta y) = (2\pi)^{-\frac{n}{2}} |\Sigma|^{-\frac{1}{2}} \exp\left[-\frac{1}{2}(\Delta y - \lambda)' \Sigma^{-1}(\Delta y - \lambda)\right] \quad (10)$$

where $\Delta y = (\Delta y_1, \Delta y_2, \dots, \Delta y_n)'$ is a realization of ΔY , $\lambda = (\lambda_1, \lambda_2, \dots, \lambda_n)'$, and the variance matrix Σ is a positive definite matrix with the (i, j) th element given by:

$$\Sigma_{i,j} = \text{cov}(\Delta Y_i, \Delta Y_j | b) = \begin{cases} (d_1 + d_2 t_i)^2 + \sigma_e^2 & i = j = 1 \\ 2d_2 \Delta t_i (d_1 + d_2 \bar{t}_i)^2 + 2\sigma_e^2 & i = j > 1 \\ -\sigma_e^2 & i = j+1 \text{ or } i = j-1 \\ 0 & \text{otherwise} \end{cases} \quad (11)$$

where $\Delta t_i = t_i - t_{i-1}$ and $\bar{t}_i = (t_i + t_{i-1})/2$, $i = 2, 3, \dots, n$.

3.2. Failure Time Distribution

The distribution function of the degradation characteristic y at time t can be given by:

$$F_Y(y|t) = \Phi\left(\frac{y - a - bt}{\sigma_0(t)}\right) \quad (12)$$

where $\sigma_0(t) = \sqrt{(d_1 + d_2 t)^2 + \sigma_e^2}$, and $\Phi(\cdot)$ is the distribution function of the standard normal distribution.

The failure state of the product can be defined by the event $y > D_f$ or $y < D_f$, where D_f is a particular "critical" level for product performance. According to this definition, product reliability is the probability of the product being in normal state in the time interval $[0, t]$. Consequently, FDT can be defined as:

$$F_T(t | D_f) = P\{T \leq t | D_f\} = 1 - \Phi\left(\frac{D_f - \mu(t)}{\sigma_0(t)}\right) \quad (13)$$

if $b > 0$, or as:

$$F_T(t | D_f) = P\{T \leq t | D_f\} = \Phi\left(\frac{D_f - \mu(t)}{\sigma_0(t)}\right) \quad (14)$$

when $b < 0$.

As important characteristics, the FTD percentiles are elemental in reliability and safety analysis. Let t_p be the 100 p th percentile of the FTD, i.e. an average of 100(1 - p)% of the population of the product will not fail before t_p . Then solving:

$$F_T(t | D_f) = p \quad (15)$$

with respect to t yields the percentile t_p . Taking $p = 0.50$ for example, the median life associated with the FTD in practical applications, can be derived.

3.3. Parameter Estimation

Let Θ be the vector of all unknown parameters; viz. $\Theta = (a, b, d_1, d_2, \sigma_e^2)$. Suppose that the degradation processes of m units have common inspection times given by t . The degradation measurements for unit k are given by $y_k = \{y_{k1}, y_{k2}, \dots, y_{kn}\}$. Again, we work on the increments Δy_k . Based on Equation (10) and Equation (11), the log likelihood function can be written as:

$$l(Y | \Theta) = C - \frac{m}{2} \ln |\Sigma| - \frac{1}{2} \sum_{k=1}^m (\Delta y_k - \lambda)' \Sigma^{-1} (\Delta y_k - \lambda) \quad (16)$$

where C denotes a generic constant that may change from line to line throughout this paper.

Subsequently, the maximum likelihood estimation (MLE) of $\Theta = (a, b, d_1, d_2, \sigma_e^2)$ can be obtained by maximizing the log likelihood function. However, it is very tough for direct constrained optimization of the log-likelihood function Equation (16). The genetic algorithm (GA) provides a possible way for resolving this problem. GA can be understood as an "intelligent" probabilistic search algorithm which can be applied to a variety of combinatorial optimization problems. GA is composed of evaluation-step, selection-step and reproduction-step. This evaluation-selection-reproduction cycle is repeated until a satisfactory solution is found. GA is considerably simple and converges reliably. A more comprehensive overview of GAs can be found in [1, 5].

3.4. Initial Guesses

When GA is applied to numerically maximize the log likelihood function, we start with an initial guess that is reasonably close to the MLE of the unknown parameters $\Theta = (a, b, d_1, d_2, \sigma_e^2)$. This start is especially important if the data size is large (i.e., a large prespecified inspection times n for each unit), because under this scenario the likelihood function becomes much more complex with possibly many local optima, and each step takes a long time to evaluate. A bad starting point would result in a very slow convergence, as well as a local optimum far away from the true MLE. This subsection develops a two-step procedure to make an educated guess for the initial intervals of the unknown parameters. The basic idea is as follows. For m degradation units, the rough estimates for a and b can be obtained by fitting the degradation data based on the standard least squares approach. Then, by treating the rough estimators as the true values, the problem reduces to the estimation of the unknown parameters d_1, d_2 and σ_e^2 . The detailed procedure is as follows:

Step 1. Get rough estimates of a and b by minimizing the mean

$$\text{squared error (MSE)} \quad \text{MSE} = \sum_{i=1}^n (\bar{y}_i - a - bt_i)^2, \text{ where}$$

$$\bar{y}_i = \frac{1}{m} \sum_{j=1}^m y_{ij}.$$

Step 2. By fixing a and b at the rough estimates obtained from

step 1, get rough estimates of d_1, d_2 and σ_e^2 by maximizing the log likelihood function $l(d_1, d_2, \sigma_e^2)$.

After obtaining the rough estimates from the above two-step procedure, legitimate initial guesses of d_1, d_2 and σ_e^2 are obtained. In conjunction with the initial guesses of a and b from Step 1, the starting intervals of the unknown parameters for maximizing the log likelihood function Equation (16) based on GA are determined.

4. Simulation Experiments

To demonstrate the reasonability of the proposed independent increment process degradation approach, a comprehensive Monte Carlo simulation study is conducted. For clear, let M_0 denote the proposed model. The Wiener process with measurement errors in [20] is considered as a reference method M_1 for comparison. To settle the linear degradation path problem, we assume the transformed time scale to be $\Lambda(t) = a + bt$, and let $\beta \sim N(\mu, \kappa^2)$ be a normally distributed random effect. As discussed in Section 1, the degradation process then follows a normal distribution with a linear mean and quadratic variance $Y(t) \sim N(\mu\Lambda(t), \kappa^2\Lambda^2(t) + \sigma_e^2\Lambda(t) + \sigma_e^2)$. Without loss of generality in simulation, degradation data are first simulated based on the proposed model, and then the model presented in [20] and our model are adopted to fit the simulated degradation. Based on simulation studies, we found that if the degradation model of Equation (10) is utilized to generate the deg-

radation data, not all simulated deterioration processes can be properly depicted by [20] because the limitation between mean and variance functions. To illustrate this important issue, we give two examples here.

4.1. Example 1

Without loss of generality, we simulate the degradation data of m products with parameters $a=3.5$, $b=1.8$, $d_1=0.5$, $d_2=0.18$ and $\sigma_e^2=1$. Each product is measured n times with the measured frequency of $\Delta t=1$. Given that the degradation threshold is $D_f=24$. The value of (n, m) is chosen to be (10, 5), (10, 10), (10, 20) and (15, 5) sequentially. For each combination of (n, m) , MSE and the mean relative error (MRE) for model parameters $(a, b, d_1, d_2, \sigma_e^2)$ of the proposed model are estimated based on 5000 Monte Carlo replications. Furthermore, the MSEs and the MREs of the median life $t_{0.5}$ and the 5th percentile of FTD $t_{0.05}$ are obtained to compare the estimated accuracy of the proposed model with the reference model. The results obtained are listed in Table 1 and Table 2 respectively.

Table 1 shows that the MSE and MRE of parameters based on the proposed model are considerably small, and when the number of test unit m increases, the MSE and MRE of parameters become smaller. When the number of measured time points n increases, the MSE and MRE of parameters also become smaller but not significantly. One should further note that the MRE of d_1 , d_2 and σ_e^2 are relatively big, this is because their true values are considerably small, then any small estimation bias will lead to a rather large relative error.

From Table 1 and Table 2, it can be observed that the MSE and MRE of the median life and the 5th percentile of FTD based on our model are significantly smaller than the estimated results obtained by the reference model. In addition, the MRE of the median life are less than 0.05 when the sample size is greater than 10 for both methods. However, for the proposed model, MRE is less than 0.05 even for a sample size of 5. For all situations, MRE of the 5th percentile of FTD based on our model are only nearly half of that based on the reference model. Therefore, for the purpose of obtaining more accurate results, proper degradation models should be considered. In other words, if the degradation model is mis-specified, it may lead to unreliable results.

Table 1. MSE and MRE of the estimates from M_0

(n, m)	(10,5)		(10,10)		(10,20)		(15,5)	
	MSE	MRE	MSE	MRE	MSE	MRE	MSE	MRE
a	0.26380	0.11849	0.12397	0.08077	0.06180	0.05696	0.23061	0.10861
b	0.01487	0.05400	0.00726	0.03827	0.00375	0.02691	0.01058	0.04576
d_1	0.11069	0.58424	0.06927	0.43850	0.04552	0.34930	0.10608	0.56923
d_2	0.00694	0.37162	0.00318	0.24760	0.00166	0.17936	0.00309	0.24288
σ_e^2	0.11534	0.27040	0.05950	0.19331	0.02812	0.13462	0.08533	0.23154
$t_{0.5}$	0.45964	0.04661	0.21803	0.03254	0.11324	0.02354	0.33809	0.04058
$t_{0.05}$	0.49521	0.05963	0.20037	0.03826	0.10238	0.02765	0.29164	0.04591

Table 2. MSE and MRE of the median life and the 5th percentile of FTD from M_1

(n, m)	(10,5)		(10,10)		(10,20)		(15,5)	
	MSE	MRE	MSE	MRE	MSE	MRE	MSE	MRE
$t_{0.5}$	1.28479	0.07428	0.55868	0.04963	0.29128	0.03565	1.23724	0.07304
$t_{0.05}$	1.35546	0.09738	0.65970	0.06972	0.38257	0.05354	1.01684	0.08234

To further compare the difference, we calculate the log-likelihood function (Log-LF) for each simulated data set. Then the average Log-LF and the corresponding Akaike information criterion (AIC) value are obtained, and the results are displayed in Table 3.

Table 3. Comparison between M_0 and M_1

(n, m)	M_0		M_1	
	Log-LF	AIC	Log-LF	AIC
(10,5)	-84.74	179.49	-87.37	186.74
(15,5)	-131.85	273.70	-136.49	284.98
(10,10)	-172.31	354.61	-176.53	365.06
(10,20)	-346.60	703.20	-355.40	722.80

Table 4. MSE and MRE of the estimates from M_0 with $\sigma_e^2=2$

(n, m)	(10,5)		(10,10)		(10,20)		(15,5)	
	MSE	MRE	MSE	MRE	MSE	MRE	MSE	MRE
a	0.35732	0.13585	0.18803	0.09929	0.09070	0.06848	0.30942	0.12606
b	0.01693	0.05755	0.00896	0.04196	0.00445	0.02960	0.01112	0.04683
d_1	0.11282	0.60780	0.08987	0.52449	0.05958	0.40829	0.12081	0.61106
d_2	0.00887	0.43454	0.00492	0.31110	0.00232	0.21554	0.00442	0.29287
σ_e^2	0.28193	0.22025	0.16406	0.16294	0.08109	0.11429	0.22876	0.19370
$t_{0.5}$	0.46760	0.04703	0.24449	0.03450	0.12272	0.02463	0.34283	0.04061
$t_{0.05}$	0.49531	0.06087	0.23498	0.04215	0.11174	0.02923	0.32773	0.04890

Table 5. MSE and MRE of the median life and the 5th percentile of FTD from M_1 with $\sigma_e^2=2$

(n, m)	(10,5)		(10,10)		(10,20)		(15,5)	
	MSE	MRE	MSE	MRE	MSE	MRE	MSE	MRE
$t_{0.5}$	1.03008	0.06834	0.56829	0.04996	0.30952	0.03654	1.46605	0.07764
$t_{0.05}$	1.09847	0.09086	0.66783	0.07094	0.39708	0.05587	1.13559	0.08756

For each combination of (n, m) shown in Table 3, it is clear that the proposed model always outperforms the reference model both in terms of the Log-LF and AIC. Therefore, in some cases, it is necessary to use the proposed model to capture the degradation over time for obtaining more accurate results.

4.2. Example 2

To test the effect of measurement error, let $\sigma_e^2=2$ and keep other parameters unchanged, we simulate the degradation data.

For each combination of (n, m) , the MSE and the MRE for parameters $(a, b, d_1, d_2, \sigma_e^2)$

of the proposed model are again estimated based on 5000 Monte Carlo replications. Furthermore, the MSE and the MRE of the median life $t_{0.5}$ and the 5th percentile of FTD $t_{0.05}$ are obtained to compare the estimated accuracy of the two models. The results are displayed in Table 4 and Table 5.

From Table 4 and Table 5, it can be concluded that MSE and MRE of parameters are small. MSE and MRE of median life and the 5th percentile of FTD based on our model are smaller than the reference model. Moreover, the MSE and MRE is a little larger than that in Section 4.1 because the measurement error increases, but this change is not very significant. It shows that our model and the reference model still can provide precise estimates even when the measurement error becomes larger. However, the estimated results are more accuracy based on our model.

5. Illustrative Example

5.1. Storage disks degradation modeling

The block error rates of magneto-optic data storage disks increases over time, and this increase leads to a soft failure when the block error rate reaches a critical value. Many tests have been carried out to collect degradation data to investigate the degradation behavior of magneto-optic data storage disks. A dataset was presented in [7], where 16 units were tested for 2000 hours at 80 °C and 85% relative humidity. The failure threshold level of block error rate is $D_f=5$. The degradation paths are depicted in Fig. 1.

We firstly begin with a preliminary statistical analysis by calculating the mean $\mu(t)$ and standard deviation $\sigma(t)$ at each measured time point, and the results are shown in Fig. 2. From Fig. 2, we can observe that the mean degradation path and the standard deviation are

Table 6. Comparisons of two fitted degradation models

Model	Parameters							
	a	b	μ	κ^2	σ^2	σ_e^2	Log-LF	AIC
M_1	0.3187	0.1320	1.9340	0.0060	0.2092	0.0054	30.30	-48.60
M_0	a	b	d_1	d_2	–	σ_e^2	Log-LF	AIC
	0.5573	0.2187	0.2322	0.0604	–	0.0025	32.29	-54.57
M_2	0.5647	0.2135	0.2334	0.0708	–	–	30.23	-52.46

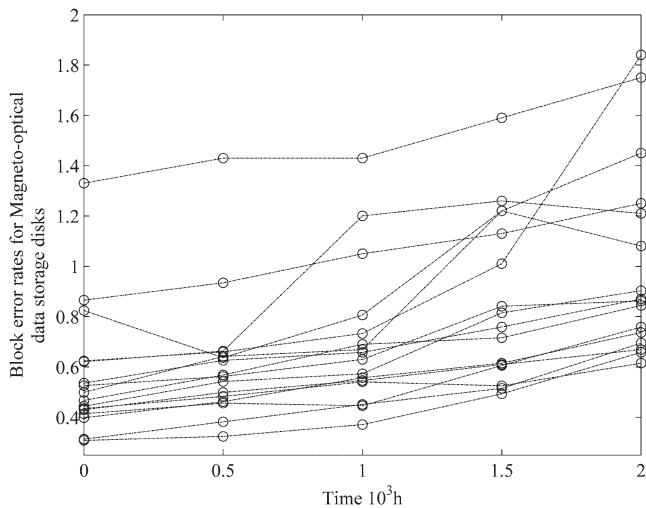


Fig. 1. Degradation paths of 16 magneto-optical data storage disks

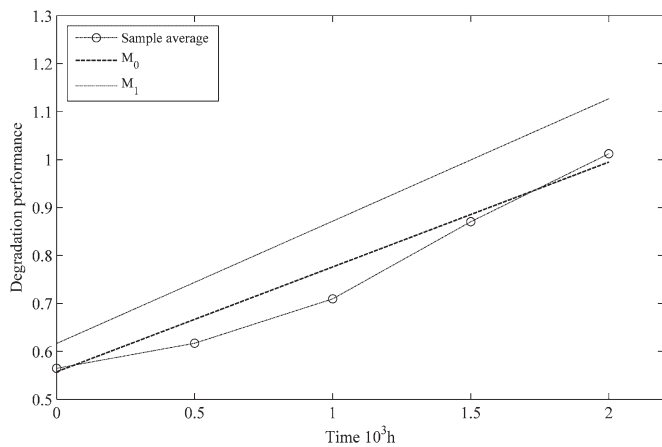
Fig. 3. Estimated mean paths based on M_0 and M_1

Table 7. The estimated median life and 10th percentile of FTD

Failure time/ 10^3 h	Model	
	M_0	M_1
$\hat{t}_{0.50}$	20.31	17.17
$\hat{t}_{0.10}$	14.00	13.70

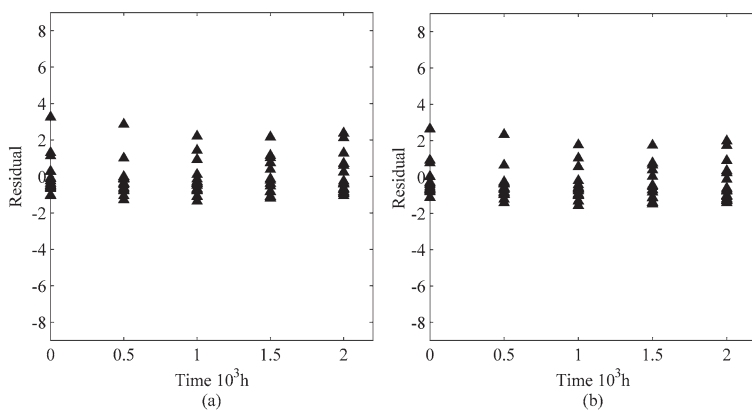
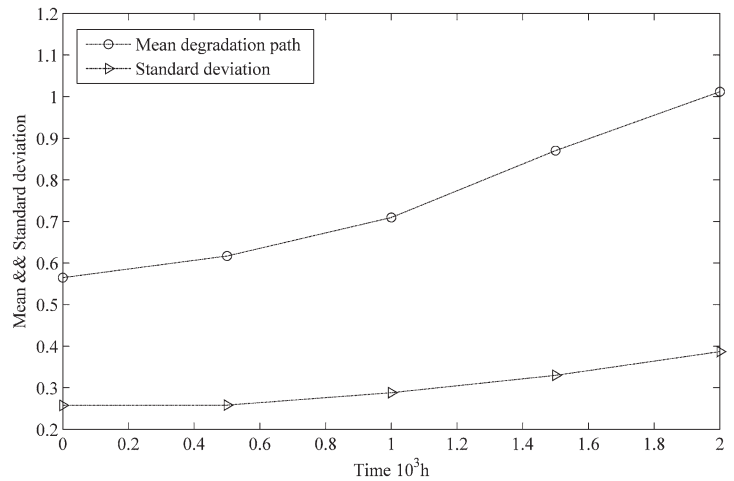
Fig. 5. Residual plot for degradation data: (a) the proposed model M_0 ; (b) the reference model M_1 

Fig. 2. Mean and standard deviation path

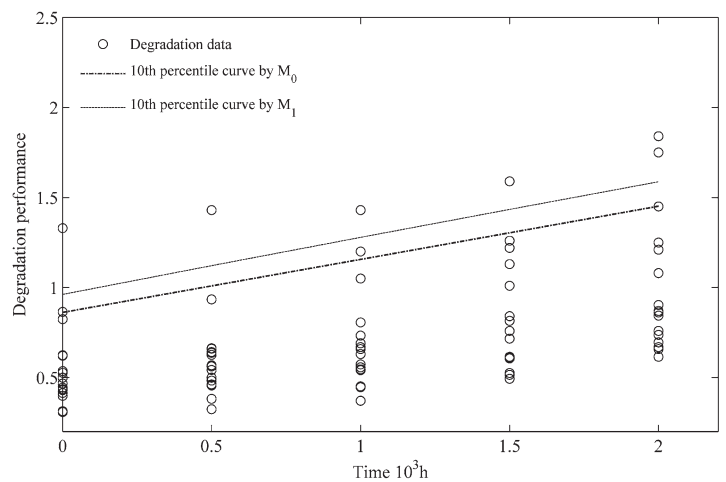


Fig. 4. Estimated 10th percentile curve of the two approaches

approximately linear over time. In such a case, the proposed model can effectively capture the degradation of storage disks without any transformation of test time and performance; viz. $x = t$ and $y = z$.

For comparison, let the time-transformed be $\Lambda(t) = a + bt$ in the reference model M_1 . We firstly apply M_0 and M_1 to fit the degradation data shown in Fig.1 to study the efficiency of the proposed model M_0 . Moreover, to show the necessity of incorporating measurement errors into the degradation model, the proposed model that removed the measurement error term is considered as model M_2 and used to fit the degradation data. The Log-LF values and the AIC values are calculated to test the fit of each model. The obtained results are summarized in Table 6. From Table 6, it is clear that the proposed model gives a better fitting both in terms of the Log-LF and AIC.

To demonstrate the goodness of fit, the mean degradation paths estimated from the two approaches are compared with the sample average. Based on the estimates in Table 6, the estimated mean degradation paths are shown in Fig. 3, which shows that the estimated mean degradation path based on the proposed model is in conjunction with the sample average, and the two curves tally quite well. However, the estimated mean degradation path from the reference model M_1 does not match the sample average well.

For further illustration, we calculate the 10th percentile of the block error rates of magneto-optical data storage disks. The estimated results are shown in Fig. 4. The 10th percentile of the block error rates $\hat{y}_{0.1}(t)$ means that 90% of the population of the disks performance degradation $y(t)$ should be below

$\hat{y}_{0.1}(t)$. In the test span, 80 performance degradation data are measured. From Fig. 4, we observe that there are 8 above the 10th percentile of the block error rates $\hat{y}_{0.1}(t)$ estimated from the proposed model M_0 , while 6 performance degradation data above that from the reference model M_1 . Therefore, the proposed model gives more accurate results.

The median life and the 10th percentile of FTD, which play an important role in making maintenance plan, are estimated through the two approaches, as given in Table 7. As we know that, the estimated variance determines the interval between the median life $\hat{t}_{0.50}$ and the 10th percentile of FTD $\hat{t}_{0.10}$, and a larger variance estimation leads to a larger interval. From Table 7, we can observe that the interval between the median life $\hat{t}_{0.50}$ and the 10th percentile of FTD $\hat{t}_{0.10}$ obtained from the reference model is smaller than that from the proposed method. This means a smaller variance estimation is obtained by the reference approach. As previously discussed, the mean degradation path of the proposed model better fits the sample average, and the 10th percentile of the block error rates of the proposed model is more reasonable. Consequently, if the results listed in Table 7 are used for maintenance schedule, the reference model will lead to premature maintenance which can reduce the product's utilization.

In addition, the residual plots are given based on the proposed model over time, the results are shown as Fig. 5. Fig. 5 indicates that the two models both perform well.

5.2. Infrared light-emitting diodes degradation modeling

Infrared light-emitting diodes (IRLEDs) are high-reliability optoelectronic devices widely used in communication systems. The performance of the devices is measured mainly by the variation ratio of

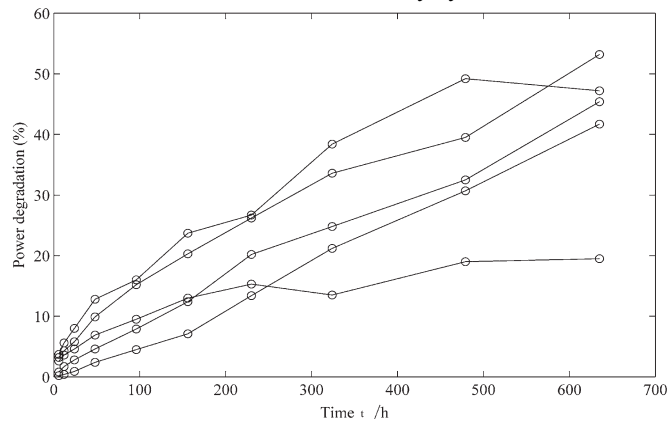


Fig. 6. The ratio of luminous power

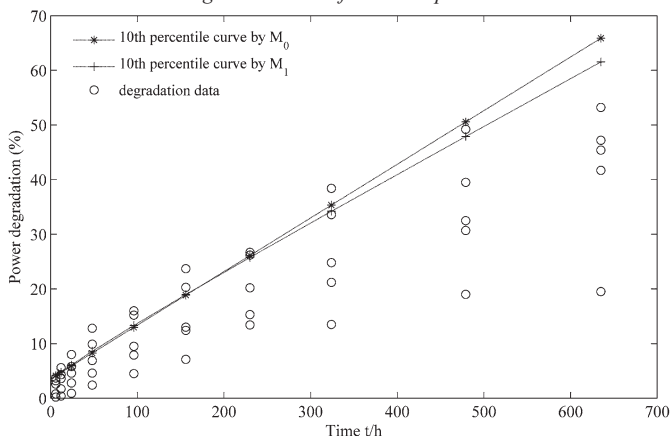


Fig. 7. Estimated 10th percentile performance curve of M_0 and M_1

Table 8. Comparisons of two fitted degradation models

Model	Parameters							
M_1	a	b	μ	κ^2	σ^2	σ_e^2	Log-LF	AIC
	1.7886	0.0909	0.8176	0.0082	1.1997	0.0078	-110.69	233.38
M_0	a	b	d_1	d_2	--	σ_e^2	Log-LF	AIC
	1.6572	0.0760	1.4662	0.0173	--	0.0075	-110.69	231.38
M_2	1.6169	0.0805	1.3107	0.0180	--	--	-112.49	232.97

Table 9. Comparisons of median life and 10th percentile of FTD

Failure time/h	Model	
	M_0	M_1
$\hat{t}_{0.50}$	228.05	235.86
$\hat{t}_{0.10}$	157.50	156.31

luminous power. To estimate the reliability, 5 units were tested at the operating current of 320 mA. A failure is said to have occurred if the ratio is greater than 19%. The original data are presented in [19], as shown in Fig. 6.

According to a preliminary statistical analysis, we observe that it is not necessary to transform the time and performance. Again, M_0 , M_1 and M_2 are used to fit the data respectively. The ML estimates of the parameters and the maximum log-likelihood values are summarized in Table 8. From Table 8, it can be observed that although the maximum log-likelihood values are equal, the number of the unknown parameters of M_0 is less than the other two models.

To test the goodness-of-fit, we calculate the median life $\hat{t}_{0.50}$ and the 10th percentile of the FTD $\hat{t}_{0.10}$ based on M_0 and M_1 respectively, and the results are given in Table 9. From the definition viewpoint, the 10th percentile of the FTD $\hat{t}_{0.10}$ means that an average of 90% of the population of products will not fail before $\hat{t}_{0.10}$. On the other hand, we know that the distance between $\hat{t}_{0.50}$ and $\hat{t}_{0.10}$ corresponds to the estimated dispersion. From Table 9, it is clear that the variance inferred from the proposed method M_0 evolves slower than that from the reference method M_1 .

Furthermore, the 10th percentiles of the ratio of luminous power of 5 IRLEDs are given by the proposed model and the reference model respectively. The results are depicted in Fig. 7. As can be seen from this figure, the ratio of the number of test data above the 10th percentile and the total number of test data obtained by the proposed model is more close to 10%. Meanwhile, the residual plots shown in Fig. 8 also demonstrate that the proposed model can perform well.

The reliability is estimated based on the proposed model. Meanwhile, we extrapolate the degradation paths to the failure threshold to obtain the pseudo failure time for each unit and calculate the empirical reliability by Kaplan-Meier method. The results are displayed in Fig. 9. Fig. 9 shows that the estimated reliability curve performs well with the empirical reliability.

Moreover, from the viewpoint of sample size, there are 5 units in IRLEDs degradation test. And 5 can be considered as a small sample. So it can be concluded that the proposed approach can ensure a good performance no matter the sample size is large enough or considerably small.

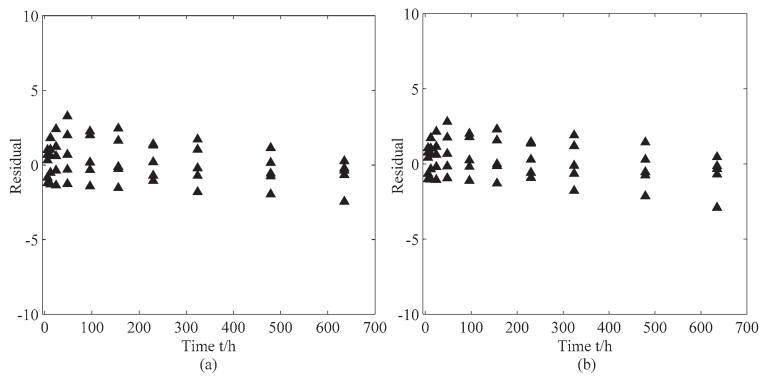


Fig. 8. Residual plot for degradation data: (a) the proposed model M_0 ; (b) the reference model M_1

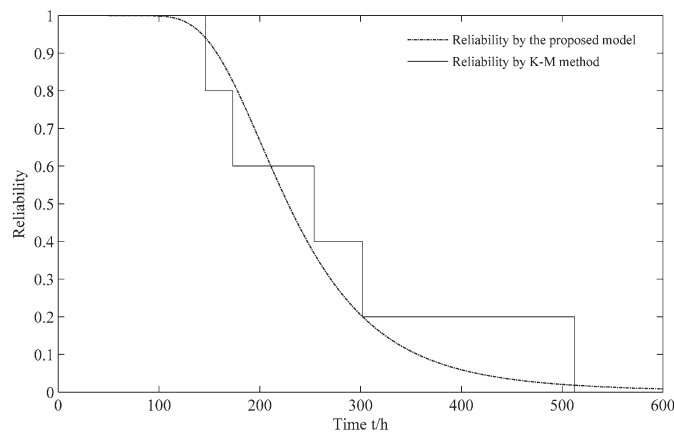


Fig. 9. Reliability function

6. Conclusion

In this paper, we propose a Wiener process model with linear mean function and standard deviation function, which allows us to take measurement error into considerations simultaneously. Comparing with the traditional time-transformed Wiener process, the proposed model can be considered as a more generalized Wiener process model with two different transformed time scales. Statistical inferences of this model are discussed, and a close form of product's median life and percentile of the FTD are also derived.

Simulation studies show that analysis precision can be enhanced while involving more items or setting more inspection times, and reasonable median life and FTD percentiles can still be derived with a considerably small sample size of $m = 5$ via the proposed method. Empirical studies with storage disks and IRLDs degradation illustrate the reasonability and effectiveness of the proposed approach.

Acknowledgement

The authors are grateful to the anonymous reviewers, and the editor, for their critical and constructive review of the manuscript. This study was co-supported by the National Natural Science Foundation of China (Grant No. 11202011 and 61203093), National Basic Research Program of China (973 Program) (Grant No. 2012CB720000), and Fundamental Research Funds for the Central Universities (Grant No. YWK13HK11).

References

1. Beasley J E, Chu P C. A genetic algorithm for the set covering problem. *European Journal of Operational Research* 1996; 94: 392-404, [http://dx.doi.org/10.1016/0377-2217\(95\)00159-X](http://dx.doi.org/10.1016/0377-2217(95)00159-X).
2. Chaluvadi V N H. Accelerated life testing of electronic revenue meters. In: Clemson University, 2008.
3. Crowder M, Lawless J. On a scheme for predictive maintenance. *European Journal of Operational Research* 2007; 176: 1713-1722, <http://dx.doi.org/10.1016/j.ejor.2005.10.051>.
4. Hamada M S, Wilson A, Reese C S, Martz H. Bayesian reliability: Springer Science & Business Media: 2008, <http://dx.doi.org/10.1007/978-0-387-77950-8>.
5. Lawrence D. Handbook of genetic algorithms. Van No strand Reinhold, New York 1991.
6. Lu C J, Meeker W Q. Using Degradation Measures to Estimate a Time-to-Failure Distribution. *Technometrics* 1993; 161-174, <http://dx.doi.org/10.1080/00401706.1993.10485038>.
7. Meeker W Q, Escobar L A. Statistical methods for reliability data: John Wiley & Sons: 2014.
8. Meeker W Q, Hamada M. Statistical tools for the rapid development and evaluation of high-reliability products. *Reliability, IEEE Transactions on* 1995; 44: 187-198, <http://dx.doi.org/10.1109/24.387370>.
9. Nair V N. [Estimation of Reliability in Field-Performance Studies]: Discussion. *Technometrics* 1988; 379-383.
10. Park C, Padgett W J. New cumulative damage models for failure using stochastic processes as initial damage. *Reliability, IEEE Transactions on* 2005; 54: 530-540.
11. Peng C, Tseng S. Mis-specification analysis of linear degradation models. *Reliability, IEEE Transactions on* 2009; 58: 444-455.
12. Pham H T, Yang B, Nguyen T T. Machine performance degradation assessment and remaining useful life prediction using proportional hazard model and support vector machine. *Mechanical Systems and Signal Processing* 2012; 32: 320-330, <http://dx.doi.org/10.1016/j.ymssp.2012.02.015>.
13. Tseng S T, Tang J, Ku I H. Determination of burn-in parameters and residual life for highly reliable products. *Naval Research Logistics (NRL)* 2003; 50: 1-14, <http://dx.doi.org/10.1002/nav.10042>.
14. Tseng S, Peng C. Stochastic diffusion modeling of degradation data. *Journal of Data Science* 2007; 5: 315-333.
15. Wang W, Dragomir-Daescu D. Reliability quantification of induction motors-accelerated degradation testing approach. In: *Reliability and Maintainability Symposium, 2002. Proceedings. Annual: IEEE* 2002: 325-331.
16. Wang X. Wiener processes with random effects for degradation data. *Journal of Multivariate Analysis* 2010; 101: 340-351, <http://dx.doi.org/10.1016/j.jmva.2008.12.007>.
17. Wang Z, Fu H, Zhang Y. Analyzing Degradation by an Independent Increment Process. *Quality and Reliability Engineering International* 2014; 30: 1275-1283, <http://dx.doi.org/10.1002/qre.1547>.

18. Whitmore G A, Schenkelberg F. Modelling accelerated degradation data using Wiener diffusion with a time scale transformation. *Lifetime Data Analysis* 1997; 3: 27-45, <http://dx.doi.org/10.1023/A:1009664101413>.
19. Yang G. *Life cycle reliability engineering*: John Wiley & Sons 2007, <http://dx.doi.org/10.1002/9780470117880>.
20. Ye Z, Wang Y, Tsui K, Pecht M. Degradation data analysis using Wiener processes with measurement errors. *Reliability, IEEE Transactions on* 2013; 62: 772-780.
21. Zuo M J, Jiang R, Yam R. Approaches for reliability modeling of continuous-state devices. *Reliability, IEEE Transactions on* 1999; 48: 9-18, <http://dx.doi.org/10.1109/24.765922>.

Zhijia WANG**Junxing LI****Yongbo ZHANG****Huimin FU**

School of Aeronautic Science and Engineering

Beihang University

XueYuan Road No.37

HaiDian District

Beijing 100083, China

Chengrui LIU

Science and Technology on Space Intelligent Control

Laboratory

Beijing Institute of Control Engineering

No.16 3th South Zhongguancun Street

Haidian District

Beijing 100191, China

Sridhar KRISHNASWAMY

Department of Mechanical Engineering

Northwestern University

633 Clark Street, Evanston

IL 60208

Evanston, USA

E-mail: wangzhijia@buaa.edu.cn, lijun-xing2008@163.com,
zhangyongbo@buaa.edu.cn, fuhuimin@263.net,
liuchengrui@buaa.edu.cn, s-krishnaswamy@northwestern.edu

Łukasz Stawiński

EXPERIMENTAL AND MODELING STUDIES OF HYDROSTATIC SYSTEMS WITH THE COUNTERBALANCE VALVES WHICH ARE USED IN HYDRAULIC LIFTING SYSTEMS WITH PASSIVE AND ACTIVE LOAD

EKSPERYMENTALNE I MODELOWE BADANIA UKŁADU HYDRAULICZNEGO Z ZAWORAMI HAMUJĄCYMI TYPU COUNTERBALANCE STOSOWANYMI W UKŁADACH DŹWIGOWYCH Z OBCIĄŻENIEM BIERNYM I CZYNNYM*

The article describes the structure and principle of the brake valve type counterbalance and the impact of its setup on the operating safety of hydrostatic systems with variable load, and in particular the problem of vibration and instability of operation of such systems after stop and restart with the active load. Mathematical and physical models of the valve and hydrostatic system with variable load have been developed. The models have been verified on the test bench, on which it is possible to the formation of arbitrary diagrams and extortion. The static and dynamic characteristics of the valve and the key operating parameters of the hydrostatic system that affect its useful properties have been shown. The simulation studies, which identify critical design parameters of the valve, that are crucial to the behaviour of the valve, and thus, hydrostatic system, has been carried out.

Keywords: operating safety of machines, hydrostatic systems, braking valves, counterbalance valve, platforms, cranes.

Artykuł opisuje budowę oraz zasadę działania zaworu hamującego typu counterbalance oraz wpływ jego nastaw na bezpieczeństwo pracy układów hydrostatycznych przy zmieniającym się obciążeniu, a w szczególności problem drgań i niestabilności pracy takiego układu hydrostatycznego po zatrzymaniu i ponownym uruchomieniu po przejściu z obciążenia biernego na czynne. Opracowane zostały modele matematyczne i fizyczne zaworu oraz układu hydrostatycznego ze zmiennym obciążeniem, które zweryfikowano na stanowisku badawczym, na którym możliwe jest kształtowanie dowolnych przebiegów i wymuszeń. Zamieszczone zostały charakterystyki statyczne i dynamiczne zaworu oraz przebiegi kluczowych parametrów pracy układu hydrostatycznego, które mają wpływ na jego właściwości użytkowe. Przeprowadzone badania symulacyjne identyfikują krytyczne parametry konstrukcyjne zaworu, które mają kluczowe znaczenie na zachowanie się zaworu, a co za tym idzie, układu hydrostatycznego. Słowa kluczowe: bezpieczeństwo obsługi maszyn, układy hydrostatyczne, zawór hamujący, counterbalance, dźwigi kosztowe, żurawie.

Słowa kluczowe: bezpieczeństwo obsługi maszyn, układy hydrostatyczne, zawór hamujący, counterbalance, dźwigi kosztowe, żurawie.

1. Introduction

The hydrostatic systems with variable load, as well as the value and the nature of action, are used in many industries. There may be different hydraulic solutions using the appropriate braking valves (Fig. 1.1), whose tasks include brake piston rod loaded with cargo, where it is necessary to receive power during lowering, including excavators, wheel loaders or cranes. With the correct setting, the valve also controls the movement of the piston rod with the variable load through the work cycle (for example – eject and/or return movement of the piston rod). Thus it provides a stable work with active force (the force vector and velocity vector are in the same sense) and passive force (the force vector and velocity vector have opposite sense). Examples of applications with braking valves are: scissor lifts, hydraulic cranes or containers lifting systems in garbage trucks. Importantly, all of the hydraulic machines operating in the EU, working as cranes or lift loads above 1 tonne, must be secured before breaking wires. This protection is achieved thanks to braking valves. The main European document that describes the essential safety requirements for currently marketed or put into using of machinery in the European Union is di-

rective 2006/42/EC. In the field of hydraulic systems and components of machines, the norm harmonized with the Directive 2006/42/EC is accordingly BS EN ISO 4413 (Drives and hydraulic control – General rules and safety requirements for systems and their components). One of the most important feature of the norm is to realize manufacturers and service staff of machines, etc., what are the dangers of using a hydraulic system. To the most notable include, among others, these about the typically mechanical origin, for example, associated with moving actuators, inadequate material strength of the components or accumulation of energy. Another important group are those resulting from the failure of the machine control system, for example, manifesting unusual reactions machines and systems as a result of loss of power supply or unexpected extrudes of machine parts or substances. It should be noted that the safety of these installations often depends on the reliability of the control circuit. For this purpose, in their construction it is necessary to take into account the requirements of the PN-EN ISO 13849-1 – Parts of control systems security. Research on this valve have been undertaken before those provisions came into effect and according to the data sheet of one of manufacturer [8] which gave only a small, incomplete and general information – the flow

(*) Tekst artykułu w polskiej wersji językowej dostępny w elektronicznym wydaniu kwartalnika na stronie www.ein.org.pl

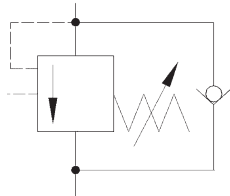


Fig. 1.1. Braking valve type counterbalance – graphic symbol

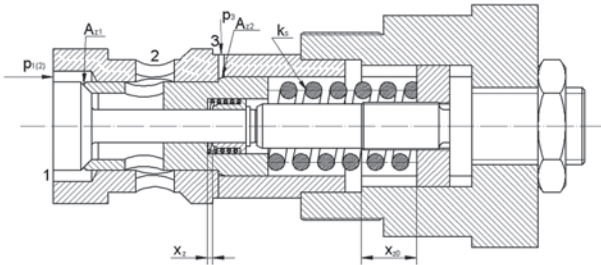


Fig. 1.2. Braking valve type UZPHD10 (Ponar Wadowice) – constructional scheme

Table 1. Braking valve type UZPHD10 (Ponar Wadowice) – work parameters

Working fluid	Mineral oil
Nominal viscosity liquids	37 mm ² /s in temp. 328 K (55°C)
Liquid viscosity range	2,8 to 328 mm ² /s
The optimum working temperature (fluid in a tank)	313 to 328 (40 to 55°C)
Temperature range	243 to 343 (-30 to 70°C)
Required fluid filtration	16 µm
Recommended fluid filtration	10 µm
Max. pressure of work	30 MPa
Max. flow	120 dm ³ /min
Checkvalve opening pressure	0.2 MPa
Ratio of the opening valve	4.5
Mass	0.45 kg

characteristics and the flow resistance characteristics through check-valve (flow through the valve in the opposite direction without the need to throttle). Table 1 presents work parameters for this specific braking valve from Ponar Wadowice. Therefore it seems appropriate to conduct a more thorough analysis of the brake valve's behavior at its various settings and the possibilities of control, which is included in this article.

During operation of these systems there may appear vibrations, uncontrolled movements of the piston rod, as well as the power losses during the lowering of loads (active load) – the issues discussed subsequently various examples of machines in the literature [1, 2, 3, 4, 6, 7, 9, 10, 14, 17]. In the papers [1, 3, 11], there are also negative energetic aspects, which are inherent to the inappropriate use of valves, for example, very high pressure in hydraulic systems and heating of the oil, which means there is the outflow of energy as heat. However, specialist literature does not discuss the problem that may arise in such systems, namely a negative pressure in one of the chambers of the actuator and the cavitation phenomenon which are dangerous and may lead to the destruction of the system. The worst situation is when machine works with an active force, for example, lowering the load. Insufficient pump capacity and excessive speed of the piston rod can reduce the pressure in the supply line actuator, which can be a cause of pressure below atmospheric. The adverse situation may also occur in case of a power failure, in the moment when the system is loaded actively. During the restart difficulties with smooth and controlled start-up and operation of the actuator are observed, and thus the entire mechanism, especially at large masses of cargo and supporting structures. It is important, therefore, that the system ensured the safety work of the entire device, including safe control and operation.

Because of the need for accuracy of hydraulic actuators, the research on the control systems of movement of the piston rod, the braking and start-up, in varying operating conditions is needed. The interest in these issues on the part of the engineering industry and the transport was a direct reason to work on the construction of position to study the behavior of systems with variable load for different hydraulic solutions. The involved system is designed for solutions with a pump fixed or variable capacity unit with double-acting actuator, as part of an executive with the ability to change its load, as well as the value and the nature of action. In the Division of Working Machines, Drives and Control at the Technical University of Lodz laboratory stand was built (Fig. 2) for testing hydraulic systems with variable load cylinder, equipped with two identical counterbalance valves.

The entire system is described in the literature [13], simulation test system were included in the article [12], and model verification position was included in the author PhD thesis. The counterbalance valve model was verified by experimental investigations of the system and thus helped further simulation of the valve itself. The graphs below show the diagrams of variables, during the piston rod extends (Fig. 3.1 - Fig. 3.3) and during its return to the cylinder of the hydraulic actuator (Fig. 3.4 - Fig. 3.6) at variable load, constant capacity hydraulic pump and fixed valve settings. Spring pre-tension in the valves is different for the different directions, due to the different surfaces (side of the piston or the piston rod cross-sectional area). Therefore, remember to set the valves for the various directions of the actuator, so as not to expose themselves for dangerous situations. The results confirm the good quality of the model. Average deviations are as follows:

- ejection of the piston rod:
 $\delta p_2 = 4.95\%$, $\delta p_3 = 11.29\%$ – deviations of the control pressure p_2 i p_3 ,
 $\delta L_{sil} = 2.45\%$ – deviations of the whole length of the actuator L_{sil} ,
 $\delta v = 2.62\%$ – deviations of the piston rod velocity v_T

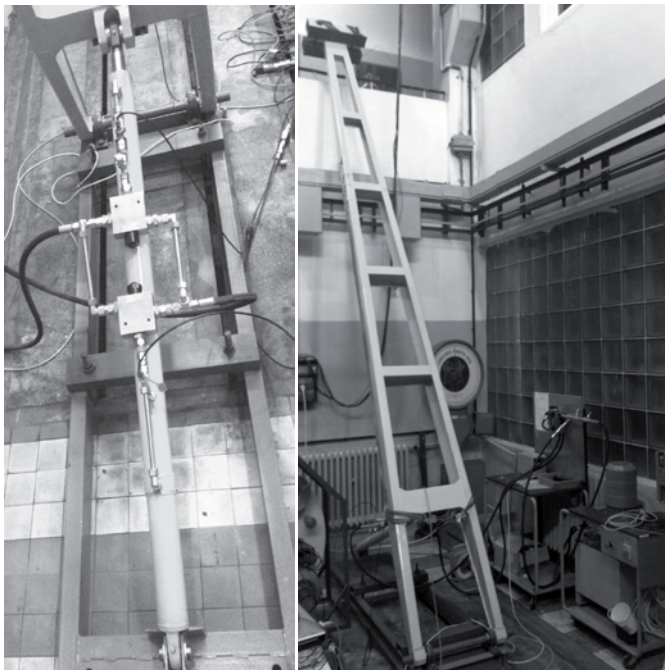


Fig. 2. The test stand for hydrostatic systems with variable load

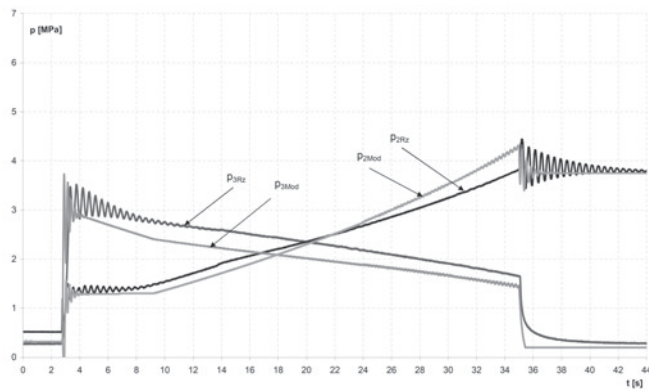


Fig. 3.1. Experimental and model waveforms of control pressures p_2 and p_3 of the braking valves during the eject of piston rod

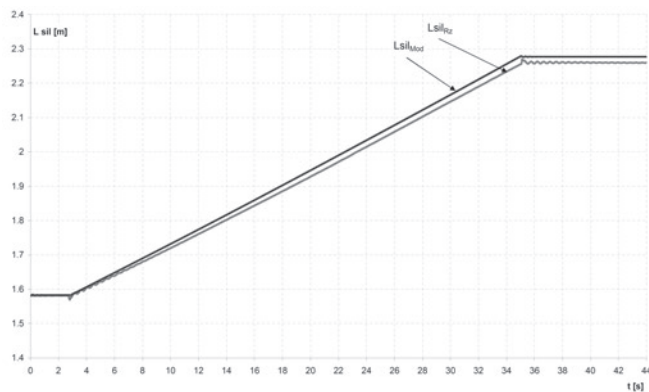


Fig. 3.2. Experimental and model waveforms of whole length of actuator L_{sil} during the eject of piston rod.

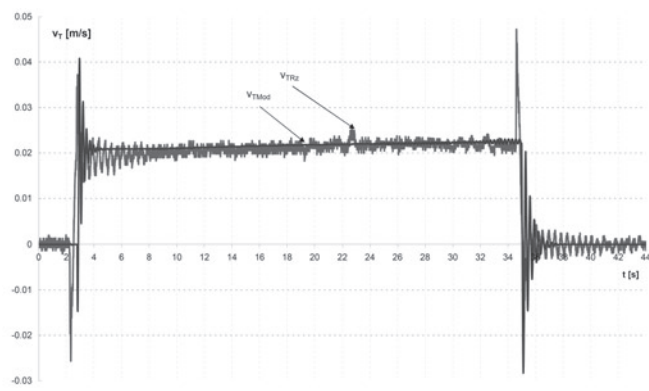


Fig. 3.3. Experimental and model waveforms of speed of actuator v_T during the eject of piston rod

- return movement of the piston rod:
 $\delta p_1 = 5.98\%$, $\delta p_3 = 13.40\%$ – deviations of the control pressure p_2 i p_3 ,
 $\delta L_{sil} = 2.45\%$ – deviations of the whole length of the actuator L_{sil} ,
 $\delta v = 1.12\%$ – deviations of the piston rod velocity v_T .

2. Analysis of the braking valve type counterbalance

The counterbalance valve is controlled by two independent pressures. Their weighted sum gives a signal to open the valve. Due to the construction of the valve (Fig. 1.2) pressure p_3 gives much larger amplification than pressure p_1 . The valve can be operated in both directions of flow movement, as the braking valve (1→2) or check valve (2→1).

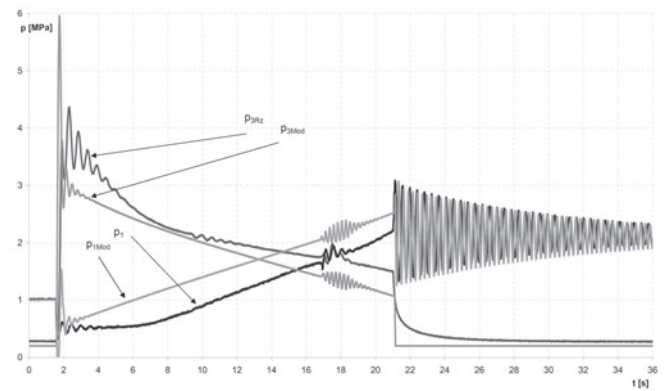


Fig. 3.4. Experimental and model diagrams of control pressures p_1 and p_3 of the braking valves during the return movement of piston rod

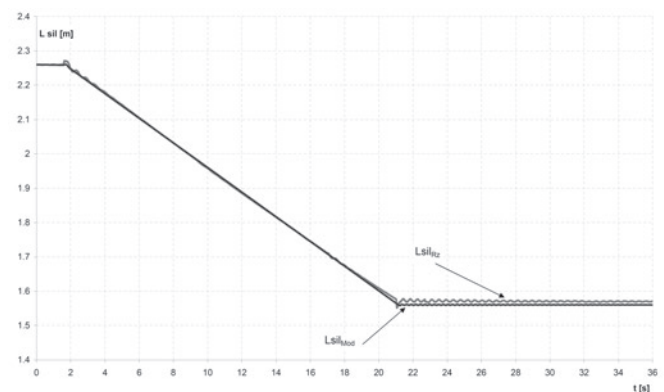


Fig. 3.5. Experimental and model diagrams of whole length of actuator L_{sil} during the return movement of piston rod

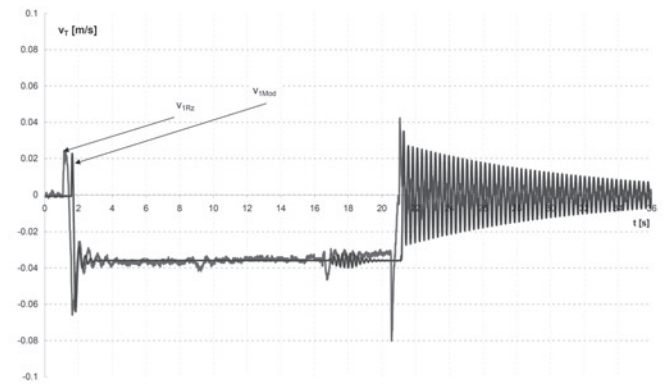


Fig. 3.6. Experimental and model diagrams of speed of actuator v_T during the return movement of piston rod

Flow from channel 1 to channel 2 is structurally restricted by the plunger which is based on the spring. As long as the pressure p_1 and p_3 , acting on two sections A_{z1} and A_{z2} , not overcome the force of the spring, the piston does not move and fluid cannot flow. In addition, the design of the valve allows to adjust initial deflection of spring x_{z0} , which gives the possibility to force the corresponding value of total pressures required to open the valve. This parameter determines a hydrostatic system response to the input value, and its choice is crucial for the proper operation of the system. The mathematical description of the valve was analyzed based on the literature [5, 15, 16], in which the physical and mathematical models of pressure valves with indirect and direct action with one and/or two control pressures was described.

The condition of the valve opening and start-up flow is to fulfilled the dependence (1):

$$p_1 \cdot A_{z1} + p_3 \cdot A_{z2} > k_s \cdot x_{z0} \quad (1)$$

where:

- A_{z1} – cross-sectional area of the brake valve plunger,
- A_{z2} – cross-sectional area of an additional element brake valve plunger,
- k_s – stiffness of the spring,
- x_{z0} – initial deflection of the spring.

The flow through the resulting orifice defines the equation (2). The displacement of the plunger within the valve is limited by the construction of the valve (3).

$$Q_{sz} = A_{sz} \cdot c_{sz} \cdot \sqrt{\frac{2 \cdot p_1}{\rho}}, \quad (2)$$

$$Q_{sz} = f(x_z), \quad (3)$$

where:

- Q_{sz} – volume of the fluid flows through the valve,
- A_{sz} – cross-sectional area of the valve orifice,
- c_{sz} – discharge coefficient of the flow rate
- ρ – fluid density
- x_z – deflection range of the spring during the movement of the plunger

The equation of motion of the plunger within the valve (4):

$$m_{zt} \frac{dv_z}{dt} = p_{1(2)} \cdot A_{z1} + p_3 \cdot A_{z2} - k_{1s} \cdot (x_{z0} + x_z) - f_{vz} \cdot v_z, \quad (4)$$

where:

- m_{zt} – mass of the plunger,
- v_z – velocity of the plunger within the valve,
- f_z – hyper viscous drag coefficient within the valve,

Based on measurements of the actual geometry of the valve and an analysis of its assembly drawing, which has been given by the manufacturer the company „Ponar Wadowice” a physical and mathematical model of such a valve has been created. Its description has been brought to the state variables and solved by numerical methods using computer software Lazarus. Block model used in the description was presented below (Fig. 4).

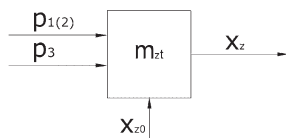


Fig. 4. The block model of the counterbalance valve

The simulation program with a simple interface which allows to observe the response of the valve to change of operating conditions and settings has been developed.

3. The simulation tests valve

The scope of research includes:

- changing the counterbalance valve setting with a constant flow,

- changing the counterbalance valve setting with a variable flow,
- control of opening the valve with a single pressure p_1 ,
- control opening the valve with two pressure p_1 and p_3

Oil is directed onto the surface of A_{z1} (Fig. 1.2), which, in the absence of flow through the valve, increases the pressure p_1 to a value required to overcome the force of spring initial deflection. With the increase of the control pressure p_3 the gap expands in the valve and the pressure p_1 decreases to a point in which the valve is fully open. Further increase of pressure p_3 does not affect the movement of the valve piston, which abuts the stopper ring. Characteristics of pressure valve (Fig. 5) correspond to the theoretical assumptions, which appear in the literature [2]. Displacement of the piston x_z , at a given adjustment and a constant input function by the flow, presented in Fig. 6.

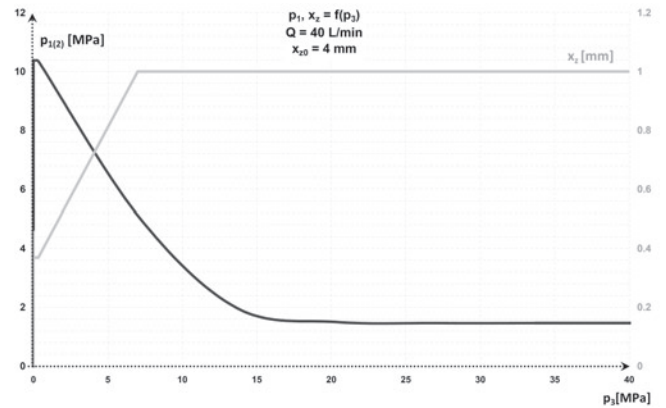


Fig. 5. Static characteristic and displacement of plunger inside the valve x_z with constant deflection of the spring x_{z0}

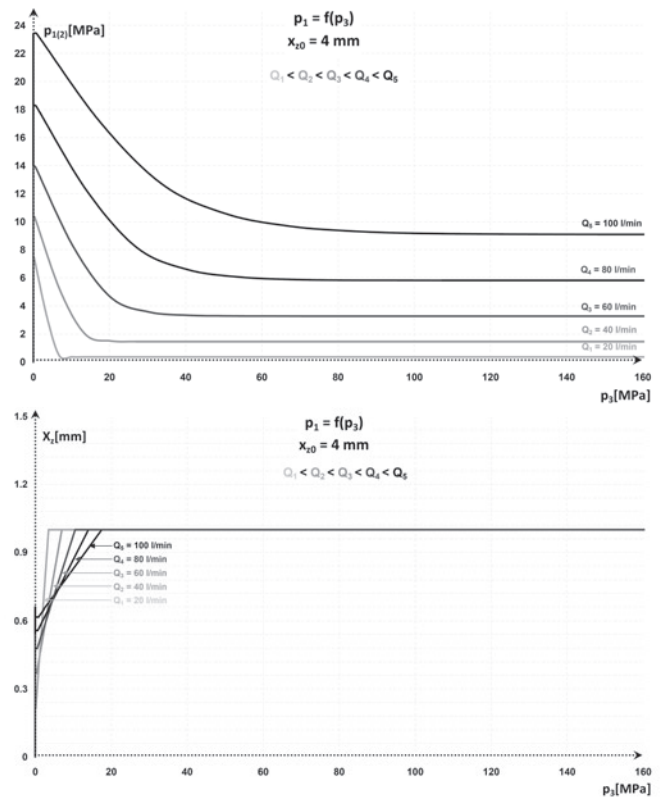


Fig. 6. Braking valve static characteristics and displacement plunger inside the valve x_z for different values of flow with constant deflection of the spring x_{z0}

To investigate the behavior of the valve at its various settings simulation tests at a constant flow rate have been carried out. The

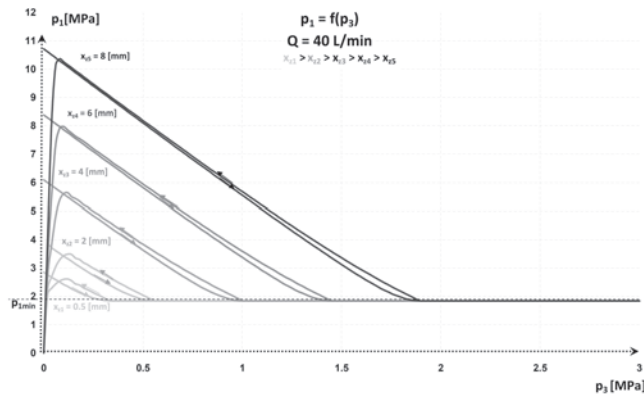


Fig. 7. The static characteristics of the braking valve for the specified flow at different deflection of the springs x_{z0}

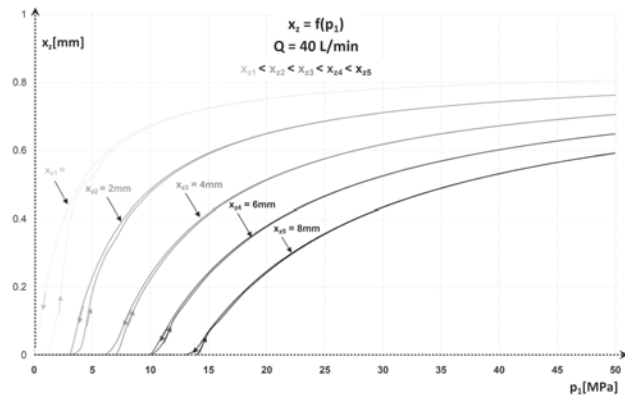


Fig. 8. Characteristics of displacement plunger inside the valve at different deflection of the spring x_{z0} . Initial phase of opening the valve

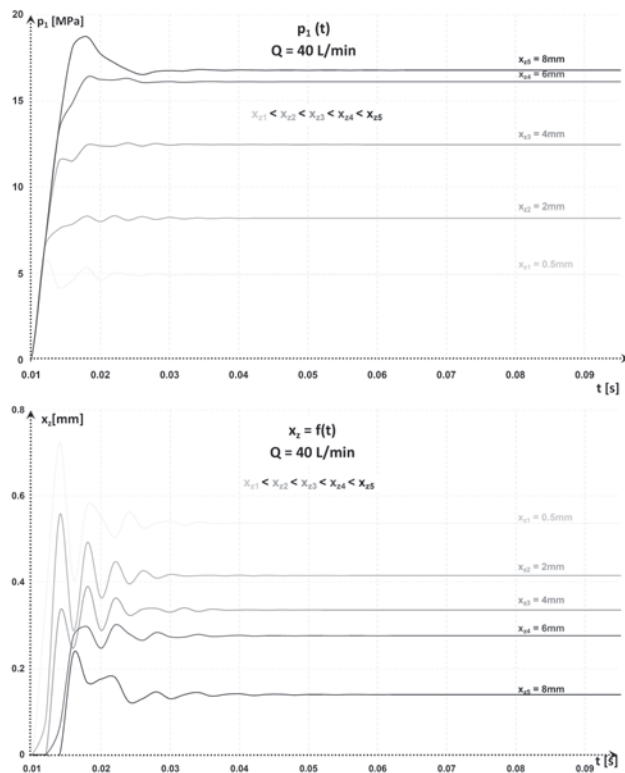


Fig. 9. Control pressures p_1 and displacements of the plunger inside the valve x_z characteristics at different deflection of the spring x_{z0}

counterbalance valve characteristics shown in Fig. 7. Through increase or decrease the pressure p_3 has been checked hysteresis effect, that is dependence of the current state of the system to the state in the preceding moments.

The sum of control pressures p_1 and p_3 , needed to open the valve, varies with the change in the valve setting x_{z0} . The flow through the valve at a smaller initial deflection of the spring occurs at low pressure p_3 and low increasing of its is needed to fully open the valve. The valve is then very sensitive and works well at low loads, where precision counts. The opposite situation occurs when the valve setting is large and need a greater control signal. We achieve then high pressure p_1 and it is needed in addition sufficiently large p_3 . Hysteresis occurs in the test valve, but it decreases with the increase in the spring stiffness and initial deflection of spring.

To accurately trace the plunger displacement inside the valve, simulation tests of the valve, forced only by pressure p_1 with absence of p_3 , has been done. Accordingly, by slowly increasing and decreasing the input signal p_1 , the appearance of hysteresis verified that occurs in the initial phase of opening of the valve, as shown in the enlarged view in Fig. 8. A further increase of pressure p_1 results an increase in movement of the plunger inside the valve, to the fully opened position, that is, the back of the plunger of the thrust ring.

To pay more attention to the dynamics of the valve and to show its reaction to the linear forcing the simulation tests have been done. The input signal flow was directed to a circuit coupled to the channel 1. Sample diagrams of pressure and plunger movement inside the valve for different initial settings of the spring show in Fig. 9. The higher initial setting of the valve, the bigger pressure p_1 and the noticeable jump of this pressure appear after the valve is opened and the displacement of the plunger is smoother, without any vibrations. A lower setting results a higher susceptibility of the piston to vibrations during the opening. However, the pressure required to open the valve is reduced, without pressure peaks. The time of the valve opens is changing and it occurs more rapidly at low settings of the valve, when the valve is forced by the same input signal.

The control of the valve opening by means of one pressure p_1 is encountered in practice very often. In this case, the valve acts as a pressure valve. Its operation will be similar to the braking valve with an internal control (Fig. 10), which is used to stop or hold a load back when the actuator does not need full power at the end of stroke. In the literature, it is sometimes called a over-centre (over-center) valve [3, 6] or internally piloted counterbalance valve [7], as opposed to dual-pressure valve (internally/externally piloted counterbalance valve), which was the subject of this paper. This type of counterbalance valve retards continuously, so it resists flow even after work contact stops the actuator. Power supply can be reduced and it allows to reduce pressure in the system and, in case of emergency, its stop and re-start occurs smoothly without shock and overload. However, the disadvantage of this valve is necessity to adjust the valve at each change of load.

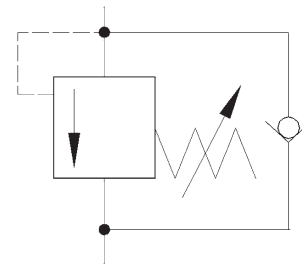


Fig. 10. The braking valve type counterbalance with internal pilot control - a graphic symbol

4. Evaluation of the impact of setting the braking valve on the behavior of the hydraulic system

Based on experimental studies of the valve on the test stand the behavior of a system with counterbalance valves in various operating conditions of hydrostatic system was examined. Below there are examples of diagrams at the wrong settings of valves in the least favorable cycle, the so-called emergency. It means that, when the passage is in an active load it is switched off (approximately 12th second of movement) and then re-powered (approximately 18th second of movement) (Fig. 11 and Fig. 12). Unfortunately, in the case of mismatched settings of the valve, system vibrates, and the pressure reaches large and useless value.

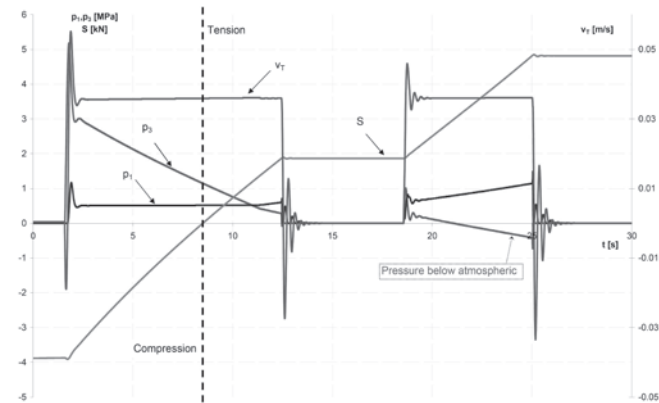


Fig. 11. The piston speed v_T , control pressures of the valve p_1 and p_3 , force acting on the piston rod S during the emergency cycle with too low stiffness of the spring in the counterbalance valve

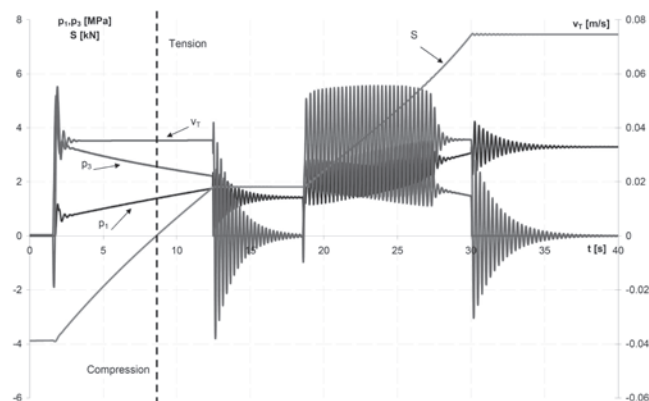


Fig. 12. The piston speed v_T , control pressures of the valve p_1 and p_3 , force acting on the piston rod S during the emergency cycle with too high stiffness of the spring in the counterbalance valve

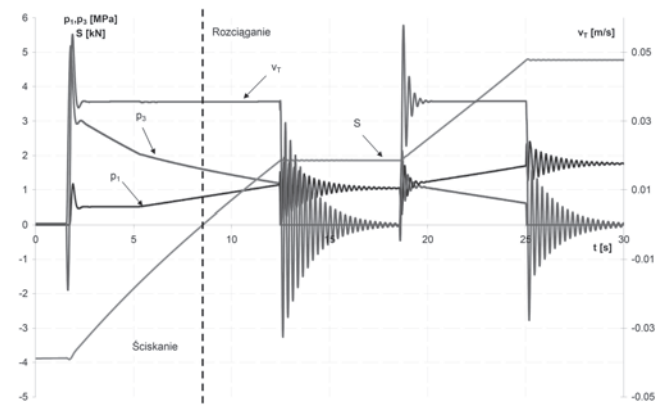


Fig. 13. The piston speed v_T , control pressures of the valve p_1 and p_3 , force acting on the piston rod S during the emergency cycle with correct stiffness of the spring in the counterbalance valve

While well-chosen setting valves (Fig. 13), the system moves smoothly both with a passive and active load, which gives a stable machine behavior and safety of its work. Thanks to the correct settings also provide low operating pressure, which has a positive effect on energy balance, that is a key element of today's research.

5. Conclusions

Choosing the setting of braking valves, all the conditions in which it will be working in the hydraulic system must be considered. Any change in the conditions requires different settings of the counterbalance valve. The above developed results show that the correct settings of the counterbalance valve provide smooth and stable behavior of the hydraulic system even in the case of lack of power supply. The paper discusses the simulation programs, both for the valve and for the hydrostatic system, so it is possible to analyze various parameters of any system. In addition, we have the ability to choose the right setting of the counterbalance valve, which will provide a fully controlled movement of the piston rod under all load conditions in any hydrostatic system with actuator.

References

- Andersen Bo, R. Energy efficient load holding valve. The 11th Scandinavian International Conference on Fluid Power. Linköping, 2009.
- Bednarski S., Kontrolowany ruch siłownika z obciążeniem czynnym. *Hydraulika i Pneumatyka* 2012; 2: 10-14.
- Cochran K. Cartridge valve and manifold technologies - a components approach to improved energy efficiency. Energy efficient hydraulics and pneumatics conference. Rosemont, 2012.
- Dabholkar R., Indulkar S., Overcenter valves are key to hydraulic control. Design World. www.designworldonline.com, 2012.
- Dasgupta K., Watton J. Modeling and dynamics of a two-stage pressure rate controllable relief valve: A bondgraph approach. *International Journal of Modelling and Simulation* 2008; 28: 11-19, <http://dx.doi.org/10.2316/Journal.205.2008.1.205-4336>.
- Hitchcox, A. The truth about problem valves. *Hydraulics & Pneumatics*. The Penton Media Buildings. Cleveland, 2009.
- Johnson J. L., Counterbalance Valve Circuits, *Hydraulics & Pneumatics*, The Penton Media Building. Cleveland, 2009.
- Karta katalogowa nr WK 498 500 firmy Ponar-Wadowice.
- Nordhammer P. A., Bak M. K., Hansen M. R. A method for reliable motion control of pressure compensated hydraulic actuation with counterbalance valve, 12th International Conference on Control. Automation and Systems 2012; 1: 759-763.
- Nordhammer P. A., Bak M. K., Hansen M. R. Controlling the slewing motion of hydraulically actuated crane using sequential activation of counterbalance valve, 12th International Conference on Control. Automation and Systems 2012; 1: 773-778.

11. Ritelli G. F. Energetic and dynamic impact of counterbalance valve in fluid power machines. *Energy Conversion and Management* 2013; 76: 701-711, <http://dx.doi.org/10.1016/j.enconman.2013.08.021>.
12. Stawiński, Ł. Badania symulacyjne układu hydrostatycznego z zaworem counterbalance. Międzynarodowa konferencja naukowo-techniczna: Napędy i Sterowanie Hydrauliczne i Pneumatyczne 2012; 1: 246-254.
13. Stawiński, Ł. Stanowisko laboratoryjne do badań układów hydrostatycznych ze zmiennym obciążeniem. *Hydraulika i Pneumatyka* 2014; 1: 9-12.
14. Stawiński, Ł. Układy hydrostatyczne do napędu siłowników przy zmiennym kierunku obciążania tłoczyska. *Hydraulika i Pneumatyka* 2011; 1: 17-20.
15. Stryczek S. Napęd hydrostatyczny - elementy. WNT, Warszawa 1998.
16. Tomczyk J. Modele dynamiczne elementów i układów napędów hydrostatycznych WNT, Warszawa 1999.
17. Zhao L., Xinhui L., Tongjian W., Influence of counterbalance valve parameters on stability of the crane lifting system, *International Conference on Mechatronics and Automation*. Xi'an, 2010; 1: 1010-1014.

Łukasz STAWIŃSKI

Faculty of Mechanical Engineering

Lodz University of Technology

Department of Vehicles and Fundamentals of Machine Design

ul. Żeromskiego 116, 90-924 Łódź, Poland

E-mail: lukasz.stawinski@p.lodz.pl

Grzegorz DOMBEK
Zbigniew NADOLNY

LIQUID KIND, TEMPERATURE, MOISTURE, AND AGEING AS AN OPERATING PARAMETERS CONDITIONING RELIABILITY OF TRANSFORMER COOLING SYSTEM

RODZAJ CIECZY, TEMPERATURA, ZAWILGOCENIE ORAZ ZESTARZENIE JAKO PARAMETRY EKSPLOATACYJNE WARUNKUJĄCE NIEZAWODNOŚĆ UKŁADU CHŁODZENIA TRANSFORMATORA*

The article presents research results of thermal properties of insulating liquids used in power transformer cooling system. The authors analyzed the influence of such factors, as the kind of the liquid, temperature, moisture and ageing rate of the liquid on thermal properties of the liquids. The analyzed properties of the liquids were thermal conductivity coefficient λ , kinematic viscosity ν , density ρ , specific heat c_p , and thermal expansion factor β . These properties determine the ability of the liquid to heat transport – heat transfer factor α – what means the properties describe reliability of power transformer cooling system. The authors calculated the factor of heat transfer by the investigated insulating liquids on the basis of measured values of thermal properties.

Keywords: power transformers, insulating liquids, heat transfer factor, moisture, ageing.

W artykule przedstawiono wyniki badań właściwości cieplnych cieczy elektroizolacyjnych, wykorzystywanych w układzie chłodzenia transformatora wysokiego napięcia. Dokonano analizy wpływu takich czynników jak rodzaj cieczy, temperatura, stopień jej zawilgocenia oraz zestarzenia na właściwości cieplne cieczy. Analizowanymi właściwościami cieczy były przewodność cieplna właściwa λ , lepkość kinematyczna ν , gęstość ρ , ciepło właściwe c_p oraz rozszerzalność cieplna β . Właściwości te określają zdolność cieczy do transportu ciepła – współczynnik przejmowania ciepła α , a tym samym warunkują niezawodność układu chłodzenia transformatora. Na podstawie zmierzonych przez autorów wartości właściwości cieplnych określony został współczynnik przejmowania ciepła badanych cieczy elektroizolacyjnych.

Słowa kluczowe: transformatory energetyczne, ciecze elektroizolacyjne, współczynnik przejmowania ciepła, zawilgocenie, zestarzenie

1. Introduction

Temperature distribution in power transformer plays a crucial role in providing proper work of the transformer [8, 15-17]. Too high temperature results in many negative effects, which can cause threats for the device itself, the maintenance personnel, and the natural environment [4, 5]. Raised temperature in the transformer affects acceleration of insulating system ageing. The ageing may result in deterioration of many properties of the insulating system, such as resistance drop, increase of dielectric losses $\tan(\delta)$, moisture increase [6, 13, 14, 22, 26]. The mentioned above results were often a reason of transformer breakdown or destruction in the past [9].

Heat transport in the transformer goes along the following way: heat source \rightarrow paper impregnated with insulating liquid \rightarrow insulating liquid \rightarrow tank \rightarrow air [18]. Thus, the insulating liquid plays an important role in heat transport. This process is connected with the effect of heat transfer by the liquid and it depends on a number of liquid thermal properties, such as thermal conductivity, viscosity, specific heat, density, and thermal expansion.

The insulating liquid changes its ageing and moisture rate and works in wide range of temperature during operation. Investigations of aged and moisture liquid and in various temperature are made mainly for dielectric properties (not for thermal properties). In [3] there are information about the influence of ageing rate of liquid on dielectric

properties, such as electric permittivity, dielectric losses $\tan(\delta)$ and dielectric strength. The influence of liquid moisture on its dielectric losses and electric permittivity is described in [25]. However, the influence of temperature on dielectric properties, such as dielectric strength and dielectric losses $\tan(\delta)$, is presented in [23].

There is no information about detailed thermal properties of insulating liquid in literature. There is information regarding to just new liquid (not aged and not moisture) and for chosen value of temperature. Manufacturers of insulating liquid give information concerning to thermal properties for temperature usually not higher than 40°C [1, 7, 19]. It is possible to find not complete information regarding to thermal properties of new insulating liquid [6, 21, 24]. However, the influence of temperature only on one from many thermal properties (kinematic viscosity) and only for new insulating liquid is described in [20]. Summarizing, it is possible to say that there is not so many investigations regarding to the influence of ageing and moisture on thermal properties of insulating liquid.

It can be a reason of mistakes during transformer design. Temperature distribution, as a result of computer simulation, which was obtained on the basis of thermal properties just for one value of temperature, can be a sample of the mistakes.

Complete knowledge about thermal properties of liquid for various rates of ageing and moisture, and for various values of tempera-

(*) Tekst artykułu w polskiej wersji językowej dostępny w elektronicznym wydaniu kwartalnika na stronie www.ein.org.pl

ture, is necessary and will bridge a gap in literature, what is a genesis of the paper.

2. Aim and range of the investigations

The influence of kind of liquid, temperature, moisture and ageing on thermal properties of the insulating liquid (thermal conductivity coefficient λ , kinematic viscosity ν , density ρ , specific heat c_p , thermal expansion factor β) was the aim of the investigations. These properties describe the ability of the liquid to heat transfer – heat transfer factor α . On the basis of thermal properties, measured by authors, the factor α was determined using the following formula:

$$\alpha = n+1 \sqrt{c \cdot \lambda^{1-n} \cdot g^n \cdot \delta^{3n-1} \cdot \beta^n \cdot \rho^n \cdot c_p^n \cdot \nu^{-n} \cdot q^n} \quad (1)$$

where: α – heat transfer factor of the liquid [$\text{W} \cdot \text{m}^{-2} \cdot \text{K}^{-1}$], n , c – constants dependent on the flow character, temperature and geometry, λ – thermal conductivity coefficient [$\text{W} \cdot \text{m}^{-1} \cdot \text{K}^{-1}$], g – acceleration of gravity [$\text{m} \cdot \text{s}^{-2}$], δ – characteristic dimension dependent on the flow character [m], β – thermal expansion [K^{-1}], ρ – density [$\text{g} \cdot \text{l}^{-1}$], c_p – specific heat [$\text{J} \cdot \text{kg}^{-1} \cdot \text{K}^{-1}$], ν – kinematic viscosity [$\text{mm}^2 \cdot \text{s}^{-1}$], q – surface thermal load [$\text{W} \cdot \text{m}^{-2}$].

Measurements of the mentioned above thermal properties were taken according to appropriate standards [2, 10-12]. The measurements were done on measurement systems, which in most cases had been designed, built, and tested by the authors.

3. Measurement results

3.1. Influence of a liquid kind on thermal properties of insulating liquids

Table 1 presents measurement results of five thermal properties and calculation results of the heat transfer factor α depending on a kind of insulating liquid. A comparative analysis was added with the assumption that the reference liquid will be mineral oil. This choice was supported by the fact that at present it is the most frequently used insulating liquid in transformers.

Thermal conductivity λ of both the esters was much higher than thermal conductivity of mineral oil. Conductivity of synthetic ester was higher than mineral oil conductivity by 18.8%. Conductivity of natural ester was higher than mineral oil conductivity by 36.8%.

Kinematic viscosity ν of the esters was much higher than viscosity of the mineral oil. Viscosity of synthetic ester was higher than mineral oil viscosity by 223%. Viscosity of natural ester was higher than mineral oil viscosity by 230%.

Specific heat c_p of the esters was higher than specific heat of mineral oil. Specific heat of synthetic ester was higher than specific heat

of mineral oil by 0.2%. Specific heat of natural ester was higher than specific heat of mineral oil by 6.6%.

Density ρ of the esters was higher than mineral oil density. Density of synthetic ester was higher than mineral oil density by 11.2%. Natural ester density was higher than mineral oil density by 5.8%.

Thermal expansion β of the esters was comparable to mineral oil expansion. Thermal expansion of synthetic ester was higher than mineral oil expansion by 1.1%. Thermal expansion of natural ester was less than mineral oil expansion by 1.1%.

The heat transfer factor α of both esters, calculated on the basis of the mentioned above measurement results, was less than the mineral oil factor. The heat transfer factor of synthetic ester was less than the heat transfer factor of mineral oil by 16.2%. The heat transfer factor of natural ester was less than the heat transfer factor of mineral oil by 10.1%. This means that mineral oil has the best properties of carrying away heat outside of all the studied liquids.

A lower heat transfer factor of synthetic and natural esters, in comparison to mineral oil, was caused by much higher viscosity (by over 200%) of the esters. Higher ester viscosity, in comparison to mineral oil viscosity, results from their chemical composition and is connected with substantially larger internal friction forces of the esters. When a liquid is in motion, the neighbouring liquid layers move with different velocities, and acting mutually with internal friction forces. The effect of liquid viscosity can be explained by momentum exchange between the adjacent layers of flowing liquid. This exchange takes place as a result of migrating liquid particles from one layer to the other. The particles that migrate from the layer moving more slowly to the layer moving faster cause a momentum decrease of the faster layer.

3.2. Influence of temperature on thermal properties of insulating liquids

Table 2 presents measurement results of five thermal properties and calculation results of the heat transfer factor α as a function of insulating liquid temperature. A comparative analysis was done assuming that the reference temperature will be 25°C.

With temperature increase from 25°C to 80°C, thermal conductivity λ of all the kinds of liquids slightly decreased. For mineral oil, thermal conductivity decreased by 5.3%, for synthetic ester by 4.4%, and for natural ester by 3.9%.

Temperature increase also resulted in a considerable drop of kinematic viscosity ν independently of a liquid kind. For mineral oil, viscosity decreased by 80%, for synthetic ester by 85%, and for natural ester by 80%.

The temperature increase from 25°C to 80°C caused an increase of specific heat c_p of all the analyzed liquids. For mineral oil, specific heat increased by 15%, for synthetic ester by 13%, and for natural ester by 11%.

With temperature increase, density ρ of all the liquids decreased a little. For mineral oil it was 4.0%, for synthetic ester 3.9%, and for natural ester 4.0%.

The temperature increase from 25°C to 80°C also caused a slight increase of thermal expansion β . For mineral oil this increase was 6.7%, for synthetic ester 4.0%, and for natural ester 8.1%.

Temperature increase caused an increase of the heat transfer factor α , independently of the liquid kind. This increase was 51% for mineral oil, 63% for synthetic ester, and 51% for natural ester. This means the higher the temperature the better the liquid carries away heat outside.

The heat transfer factor of a liquid was most heavily affected by viscosity, which was caused by a higher temperature. A drop of liquid viscosity, caused by a higher temperature, should be associated with a decrease of attraction forces acting among liquid particles resulting from their kinetic energy. This results in a drop of internal friction forces and viscosity decrease.

Table 1. Measurement results of five thermal properties of the liquids and calculation results of the heat transfer factor α depending on a kind of insulating liquid; temperature $T=25^\circ\text{C}$, new and dry liquid

Property	Mineral oil	Synthetic ester	Natural ester
Thermal conductivity λ [$\text{W} \cdot \text{m}^{-1} \cdot \text{K}^{-1}$]	0.133	0.158	0.182
Kinematic viscosity ν [$\text{mm}^2 \cdot \text{s}^{-1}$]	17.08	55.14	56.29
Specific heat c_p [$\text{J} \cdot \text{kg}^{-1} \cdot \text{K}^{-1}$]	1902	1905	2028
Density ρ [$\text{kg} \cdot \text{m}^{-3}$]	867	964	917
Thermal expansion β [K^{-1}]	0.00075	0.00076	0.00074
Heat transfer factor α [$\text{W} \cdot \text{m}^{-2} \cdot \text{K}^{-1}$]	82.35	69.04	73.46

Table 2. Measurement results of five thermal properties and calculation results of the heat transfer factor α as a function of insulating liquid temperature; new and dry liquid

Property	Mineral oil	
	25°C	80°C
Thermal conductivity λ [W·m ⁻¹ ·K ⁻¹]	0.133	0.126
Kinematic viscosity ν [mm ² ·s ⁻¹]	17.08	3.43
Specific heat c_p [J·kg ⁻¹ ·K ⁻¹]	1902	2187
Density ρ [kg·m ⁻³]	867	832
Thermal expansion β [K ⁻¹]	0.00075	0.00080
Heat transfer factor α [W·m ⁻² ·K ⁻¹]	82.35	124.67
Property	Synthetic ester	
	25°C	80°C
Thermal conductivity λ [W·m ⁻¹ ·K ⁻¹]	0.158	0.151
Kinematic viscosity ν [mm ² ·s ⁻¹]	55.14	8.11
Specific heat c_p [J·kg ⁻¹ ·K ⁻¹]	1905	2149
Density ρ [kg·m ⁻³]	964	926
Thermal expansion β [K ⁻¹]	0.00076	0.00079
Heat transfer factor α [W·m ⁻² ·K ⁻¹]	69.04	112.24
Property	Natural ester	
	25°C	80°C
Thermal conductivity λ [W·m ⁻¹ ·K ⁻¹]	0.182	0.175
Kinematic viscosity ν [mm ² ·s ⁻¹]	56.29	11.50
Specific heat c_p [J·kg ⁻¹ ·K ⁻¹]	2028	2259
Density ρ [kg·m ⁻³]	917	880
Thermal expansion β [K ⁻¹]	0.00074	0.00080
Heat transfer factor α [W·m ⁻² ·K ⁻¹]	73.46	111.06

3.3. Moisture influence on thermal properties of insulating liquids

Table 3 presents measurement results of five thermal properties and calculation results of the heat transfer factor α as a function of insulating liquid moisture. A comparative analysis was done by comparing thermal properties of a moistened and dry liquid.

Preparation of the liquids (both dried and moistened) consisted in drying and moistening samples of mineral oil, synthetic ester, and natural ester in the same conditions. As a result of different water solubility, dry and moistened samples of the particular liquids had different water contents. For dry samples, moisture was 2 ppm for mineral oil, 45 ppm for synthetic ester, and 34 ppm for natural ester. In turn, for moistened samples, moisture was equal to 46 ppm for mineral oil, 1875 ppm for synthetic ester, and 822 ppm for natural ester.

With moisture increase, thermal conductivity λ of all the insulating liquids practically remained the same. For mineral oil, conductivity increased slightly by 0.8% and for the esters it remained at the same level.

Moisture increase resulted in a tenuous drop of liquid kinematic viscosity ν . Mineral oil viscosity remained at the same level. Synthetic ester viscosity decreased by 3.7%, whereas of natural ester by 2.4%.

Liquid moisture increase brought a certain increase of their specific heat c_p . Specific heat of mineral oil increased by 6.0%, synthetic ester by 3.7%, and natural ester by 0.8%.

Insulating liquid moisture had no effect on their density ρ , which was independent of the liquid kind.

Liquid moisture did not cause any larger changes of thermal expansion β . The expansion of mineral oil and synthetic ester remained at the same level, whereas for natural ester it decreased by 1.4%.

Moisture increase caused a slight increase of the heat transfer factor α , independently of the liquid kind. This increase was 1.1% for mineral oil, 1.9% for synthetic ester, and 0.4% for natural ester. It means the higher moisture the better ability of liquid to heat transfer.

A slight increase of the heat transfer factor of the liquid, caused by its moisture should be linked with specific heat increase. Specific heat of dry insulating liquid is equal to about 2000 J·kg⁻¹·K⁻¹, whereas of pure water it is 4190 J·kg⁻¹·K⁻¹. This means that insulating liquid moisture resulted in its increase of specific heat c_p , and its effect was an increase of the heat transfer factor α .

3.4. Influence of ageing on thermal properties of insulating liquids

Table 4 presents measurement results of five thermal properties and calculation results of the heat transfer factor α as a function of ageing rate of an insulating liquid. A comparative analysis was done by comparing thermal properties of a new and aged liquid.

A new liquid meant that the authors used for the research liquid samples supplied directly from the manufacturer. The acid number was less than 0.010 mg_{KOH}·g⁻¹_{oil} for mineral oil, less than 0.030 mg_{KOH}·g⁻¹_{oil} for synthetic ester, and equal to 0.020 mg_{KOH}·g⁻¹_{oil} for natural ester.

An aged liquid of all the three kinds meant that the ageing process was progressing in the same conditions. This resulted in a little different values of the acid number for the particular kinds of the liquids. The acid number was equal to 0.135 mg_{KOH}·g⁻¹_{oil} for mineral oil, 0.175 mg_{KOH}·g⁻¹_{oil} for synthetic ester, and 0.173 mg_{KOH}·g⁻¹_{oil} for natural ester.

With an increase of the liquid ageing rate, thermal conductivity λ of all the insulating liquids practically remained unchanged. For

Table 3. Measurement results of five thermal properties and calculation results of the heat transfer factor α as a function of insulating liquid moisture; temperature $T=25^\circ\text{C}$, new liquid

Property	Mineral oil	
	dry	moistened
Thermal conductivity λ [W·m ⁻¹ ·K ⁻¹]	0.133	0.132
Kinematic viscosity ν [mm ² ·s ⁻¹]	17.08	17.08
Specific heat c_p [J·kg ⁻¹ ·K ⁻¹]	1902	2017
Density ρ [kg·m ⁻³]	867	867
Thermal expansion β [K ⁻¹]	0.00075	0.00075
Heat transfer factor α [W·m ⁻² ·K ⁻¹]	82.35	83.26
Property	Synthetic ester	
	dry	moistened
Thermal conductivity λ [W·m ⁻¹ ·K ⁻¹]	0.158	0.158
Kinematic viscosity ν [mm ² ·s ⁻¹]	55.14	53.09
Specific heat c_p [J·kg ⁻¹ ·K ⁻¹]	1905	1975
Density ρ [kg·m ⁻³]	964	964
Thermal expansion β [K ⁻¹]	0.00076	0.00076
Heat transfer factor α [W·m ⁻² ·K ⁻¹]	69.04	70.32
Property	Natural ester	
	dry	moistened
Thermal conductivity λ [W·m ⁻¹ ·K ⁻¹]	0.182	0.182
Kinematic viscosity ν [mm ² ·s ⁻¹]	56.29	54.96
Specific heat c_p [J·kg ⁻¹ ·K ⁻¹]	2028	2044
Density ρ [kg·m ⁻³]	917	916
Thermal expansion β [K ⁻¹]	0.00074	0.00073
Heat transfer factor α [W·m ⁻² ·K ⁻¹]	73.46	73.77

Table 4. Measurement results of five thermal properties of the liquids and calculation results of the heat transfer factor α as a function of ageing rate of an insulating liquid; temperature $T=25^{\circ}\text{C}$

Property	Mineral oil	
	new	aged
Thermal conductivity λ [$\text{W}\cdot\text{m}^{-1}\cdot\text{K}^{-1}$]	0.133	0.133
Kinematic viscosity ν [$\text{mm}^2\cdot\text{s}^{-1}$]	17.08	19.09
Specific heat c_p [$\text{J}\cdot\text{kg}^{-1}\cdot\text{K}^{-1}$]	1902	1972
Density ρ [$\text{kg}\cdot\text{m}^{-3}$]	867	866
Thermal expansion β [K^{-1}]	0.00075	0.00075
Heat transfer factor α [$\text{W}\cdot\text{m}^{-2}\cdot\text{K}^{-1}$]	82.35	80.79
Property	Synthetic ester	
	new	aged
Thermal conductivity λ [$\text{W}\cdot\text{m}^{-1}\cdot\text{K}^{-1}$]	0.158	0.157
Kinematic viscosity ν [$\text{mm}^2\cdot\text{s}^{-1}$]	55.14	54.43
Specific heat c_p [$\text{J}\cdot\text{kg}^{-1}\cdot\text{K}^{-1}$]	1905	2046
Density ρ [$\text{kg}\cdot\text{m}^{-3}$]	964	964
Thermal expansion β [K^{-1}]	0.00076	0.00076
Heat transfer factor α [$\text{W}\cdot\text{m}^{-2}\cdot\text{K}^{-1}$]	69.04	70.28
Property	Natural ester	
	new	aged
Thermal conductivity λ [$\text{W}\cdot\text{m}^{-1}\cdot\text{K}^{-1}$]	0.182	0.182
Kinematic viscosity ν [$\text{mm}^2\cdot\text{s}^{-1}$]	56.29	60.36
Specific heat c_p [$\text{J}\cdot\text{kg}^{-1}\cdot\text{K}^{-1}$]	2028	2012
Density ρ [$\text{kg}\cdot\text{m}^{-3}$]	917	917
Thermal expansion β [K^{-1}]	0.00074	0.00075
Heat transfer factor α [$\text{W}\cdot\text{m}^{-2}\cdot\text{K}^{-1}$]	73.46	72.29

synthetic ester, conductivity decreased slightly by 0.6%, whereas for mineral oil and natural ester, it remained at the same level.

Increase of the liquid ageing rate in most cases caused increase of its kinematic viscosity ν . Mineral oil viscosity increased by 11.8%, natural ester viscosity by 7.3%. By contrast, synthetic ester viscosity decreased slightly by 1.3%.

With an increase of the liquid ageing rate, specific heat c_p increased in most of the insulating liquids. Specific heat of mineral oil increased by 3.7% and of the synthetic ester by 7.4%. By contrast, specific heat of natural ester decreased by 0.8%.

The liquid ageing rate practically had no effect on its density ρ . Independently of the liquid kind, density remained at an unchanged level.

The ageing rate did not cause any substantial changes of thermal expansion β . Expansion of mineral oil and synthetic ester remained at the same level, whereas for natural ester it increased by 1.3%.

The ageing rate of insulating liquid did not affect significantly and explicitly the heat transfer factor α . Ageing caused a slight decrease of factor α by 1.9% for mineral oil and by 1.6% for natural ester. By contrast, for synthetic ester, ageing caused a slight increase of factor α by 1.8%.

The lack of clear changes of factor α was caused by the fact that with an increase of the liquid ageing rate its kinematic viscosity ν (causing a drop of factor α) was increasing and simultaneously, its specific heat c_p (causing a rise of factor α) was increasing. This means that liquid ageing practically has no influence on its ability to carry heat away to the surrounding. Viscosity increase was probably caused by the fact that with an increase of the ageing rate, solid products of this process are created. By contrast, increase of specific heat, accompanying liquid ageing resulted from the fact that solid products of this process have higher specific heat than pure insulating liquid.

4. Conclusions

The kind of insulating liquid has a considerable influence on its heat transfer factor α . It was found on the basis of the research that mineral oil has the highest factor α of the investigated liquids. The esters had factor α lower by over ten percent. It is viscosity of the analyzed liquids, which plays a crucial role. Viscosity of mineral oil was three times lower than viscosity of both kinds of the esters. From the viewpoint of transformer cooling, this means that mineral oil is a more effective liquid in comparison to synthetic or natural ester.

Temperature has significant influence on the heat transfer factor α of the analyzed liquids. A temperature increase from 25°C to 80°C resulted in an increase of factor α by over 50% regardless of the liquid kind. It was affected by viscosity, which decreased 5÷6 times with temperature rise, regardless of the liquid kind. This means that the higher the temperature in the transformer the more effectively heat will be carried away to the surrounding by insulating liquid.

Moisture does not have essential significance for the heat transfer factor α in the investigated insulating liquids. Moisture caused an increase of factor α by hardly 2%, regardless of the liquid kind. This rise should be linked with an increase of liquid specific heat by a few percent. That means moisture does not affect transformer cooling conditions.

Liquid ageing does not have explicit influence on the heat transfer factor α of the analyzed liquids. Changes of factor α were hardly 2%. It was on one hand viscosity increase and on the other hand specific heat increase, which were involved. This means that liquid ageing does not have substantial influence on transformer cooling conditions.

References

1. ABB Inc. Biotemp. Biodegradable dielectric insulating fluid. Product brochure 2009.
2. ASTM D 1903-96. Standard test method for coefficient of thermal expansion of electrical insulating liquids of petroleum origin, and askarels.
3. Borsi H, Gockenbach E. Performance and new application of ester liquids. IEEE 14th International Conference on Dielectric Liquids 2002; 203-206.
4. Borsi H, Gockenbach E, Wasserberg V, Werle P. New devices for a dry type transformer protection and monitoring system. 6th International Conference on the Properties and Applications of Dielectric Materials 2000: 567-570.
5. Borucki S, Boczar T, Cichoń A. Investigation of the acoustic pressure distribution occurring around an aerial substation adjacent to apartment buildings. Archives of Acoustics 2007; 32: 291-297.
6. CIGRE Brochure 436. Experiences in service with new insulating liquids. 2010.
7. Cooper Power Industries. Envirottemp FR3 Bulletin 2001; 00092.
8. Feser K, Radakovic Z. A new method for the calculation of the hot-spot temperature in power transformers with ONAN cooling. IEEE Transaction on Power Delivery 2003; 18: 1284-1292, <http://dx.doi.org/10.1109/TPWRD.2003.817740>.

9. Gielniak J, Graczkowski A, Morańda H, Przybyłek P, Walczak K, Nadolny Z, Mościcka-Grzesiak H, Feser K, Gubański S M. Moisture in cellulose insulation of power transformers - statistics. IEEE Transactions on Dielectrics and Electrical Insulation 2013; 20: 982-987, <http://dx.doi.org/10.1109/TDEI.2013.6518968>.
10. ISO 3104:1994. Petroleum products - Transparent and opaque liquids - Determination of kinematic viscosity and calculation of dynamic viscosity.
11. ISO 3675. Crude petroleum and liquid petroleum products -Laboratory determination of density - Hydrometer method.
12. ISO 649-1:1981. Laboratory glassware - Density hydrometers for general purposes - Part 1: Specification.
13. Koch M, Krueger M, Tenbohlen S. On-site methods for reliable moisture determination in power transformers. IEEE/PES Transmission and Distribution Conference and Exposition 2010: 1-6.
14. Koch M, Tenbohlen S, Rosner M. Moisture ingress in free breathing transformers. International Conference on Condition Monitoring and Diagnosis 2008: 646-650.
15. Łopatkiewicz R, Nadolny Z. Temperature field on high voltage power transformer. Przegląd Elektrotechniczny 2008; 84: 50-52.
16. Łopatkiewicz R, Nadolny Z, Przybyłek P. Influence of water content in paper on its thermal conductivity. Przegląd Elektrotechniczny 2010; 86: 55-58.
17. Łopatkiewicz R, Nadolny Z, Przybyłek P. The influence of water content on thermal conductivity of paper used as transformer windings insulation. IEEE International Conference on the Properties and Applications of Dielectric Materials 2012: 1-4, <http://dx.doi.org/10.1109/icpadm.2012.6318991>.
18. Łopatkiewicz R, Nadolny Z, Przybyłek P, Sikorski W. The influence of chosen parameters on thermal conductivity of windings insulation describing temperature in transformer. Przegląd Elektrotechniczny 2012; 88: 126-129.
19. M&I Materials Ltd. Midel 7131 Synthetic ester transformer fluid. Product guide 2014.
20. Perrier C, Beroual A, Bessede J L. Improvement of power transformers by using mixtures of mineral oil with synthetic esters. IEEE Transactions on Dielectrics and Electrical Insulation 2006; 13: 556-564, <http://dx.doi.org/10.1109/TDEI.2006.1657968>.
21. Perrier C, Ryadi M, Bertrand Y, Tran Duy C. Comparison between mineral and ester oil. Cigre Session 2010; D1-102: 1-10.
22. Przybyłek P, Nadolny Z, Mościcka-Grzesiak H. Bubble effect as a consequence of dielectric losses in cellulose insulation. IEEE Dielectric and Electrical Insulation 2010; 13: 919-925, <http://dx.doi.org/10.1109/tdei.2010.5492266>.
23. Suwarno, Darma I S. Dielectric properties of mixtures between mineral oil and natural ester. International Symposium on Electrical Insulating Materials 2008; 514-517.
24. Tenbohlen S, Koch M, Vukovic D, Weinlader A, Baum J, Harthun J, Schafer M, Barker S, Frotscher R, Dohnal D, Dyer P. Application of vegetable oil-based insulating fluids to hermetically sealed power transformers. Cigre Session 2008; A2-102: 1-8.
25. Trnka P, Mentlik V, Svoboda M. The effect of moisture content on electrical insulating liquids. IEEE 18th International Conference on Dielectric Liquids 2014; 1-4, <http://dx.doi.org/10.1109/icdl.2014.6893120>.
26. Wolny S, Adamowicz A, Lepich M. Influence of temperature and moisture level in paper-oil insulation on the parameters of the Cole-Cole model. IEEE Transaction on Power Delivery 2014; 29: 246-250, <http://dx.doi.org/10.1109/TPWRD.2013.2270917>.

Grzegorz DOMBEK

Zbigniew NADOLNY

Institute of Electrical Power Engineering

Poznan University of Technology

ul. Piotrowo 3a, 60-965 Poznań, Poland

E-mail: grzegorz.dombek@put.poznan.pl, zbigniew.nadolny@put.poznan.pl

Ji-Min LU
Fares INNAL
Xiao-Yue WU
Yiliu LIU
Mary Ann LUNDTEIGEN

TWO-TERMINAL RELIABILITY ANALYSIS FOR MULTI-PHASE COMMUNICATION NETWORKS

ANALIZA NIEZAWODNOŚCI PAR TERMINALI W WIELOFAZOWYCH SIECIACH KOMUNIKACYJNYCH

Most researches of network reliability generally assume that the system structures do not change with time. This paper presents the concept of multi-phase network systems (MPNS) to consider dynamic characteristics of networks, and analyze the reliability of MPNS. MPNS reliability is evaluated through a cross-phase binary decision diagram (BDD). The BDD-based algorithm can act as a platform to consider various components behaviors such as repair and growing pressure. Case study shows that the proposed MPNS concept is an effective description of some practical communication networks, and the cross-phase BDD model is efficient in analyzing MPNS reliability.

Keywords: Binary decision diagram, component-behavior model, multi-phase network systems, system reliability.

Większość badań niezawodności sieci ogólnie przyjąć, że struktury systemu nie zmieniają się w czasie. W artykule przedstawiono koncepcję systemów sieciowych wielofazowych (MPNS) rozpatrywanie dynamicznych właściwości sieci i analizy niezawodności MPNS. MPNS niezawodność jest oceniany przez cross-fazowego schematu decyzyjnego binarny (BDD). Algorytm z siedzibą w BDD może działać jako platforma do rozważenia różnych komponentów zachowań, takich jak naprawy i rosnącej presji. Studium przypadku pokazuje, że proponowana koncepcja MPNS jest skutecznym opis niektórych praktycznych sieci komunikacyjnych, a cross-fazowego modelu BDD jest skuteczny w analizie MPNS niezawodność.

Słowa kluczowe: Binarny schemat decyzji, model zachowania komponentów, systemów sieciowych wielofazowe, niezawodność systemu.

1. Introduction

Network has become a common and effective description for many engineering systems such as transportation, communications, and gas-pipeline systems. In graph theory, the network is usually denoted as $G=(V,E)$, where V is the vertex set representing terminals (bus stop, switchboard, etc.), and E is the edge set representing links (road, cable, etc.). Graph theory further classifies edges into directed and undirected edges. Communication networks, as well as transportation systems, are typical examples of undirected networks. In literature, networks structures normally remain unchanged during the entire mission. However, changing network structures and varying stress on components have become increasingly common in many engineering applications. This kind of systems can be termed as the multi-phase network systems (MPNS) in comparison to traditional single-phase network systems (SPNS). A typical example of MPNS is the satellite telemetry, tracking and control (TT&C) system which is responsible for the data transmission between satellites and ground facilities. In satellite TT&C systems, communications between a certain ground station and a target satellite usually rely on many relay satellites. As different relay satellites fly over the ground station, the communication networks changes its link structures and constitutes a MPNS.

Two-terminal reliability (or terminal-pair reliability) is one of key concern in the design and maintenance of network systems. Take communication systems for instance. The two-terminal reliability can be considered as the probability of successfully transmitting data from

one source to one receiver. Researches on two-terminal reliability of single-phase networks have been extensively conducted since 1970s. Early methods are mainly based on the enumeration of minimal paths/cuts, or based on the factoring theory. In minimal paths/cuts methods [2, 9, 16, 23, 25, 28], the reliability is evaluated by enumerating all minimal paths/cuts and summing the probabilities of their disjoint forms. A *path* is a set of network components (edges/vertices) such that if these components are operational, the system is up. A *path* is minimal if it has no proper subpaths. Conversely a *cut* can be considered as a set of network components such that if these components fail, the system is down. Some research [1, 22] shows that the number of cuts is usually much smaller than the number of paths for many practical systems, meaning that cut-based methods (i.e. to calculate the unreliability) have better performance. However, both paths and cuts based method have difficulties in applying to large networks since the number of paths/cuts may grow exponentially with the network size.

In contrast to paths/cuts based approaches, factoring methods (or decomposition/ topology methods) may exhibit better performance, especially combined with some reduction techniques [27, 30, 31, 38]. In factoring methods, a certain component of the network is chosen and then the network is decomposed into two subnetworks. One sub-network assumes the component is up and the other subnetwork assumes the component is down. Another version of this method does not choose a single component, but replaces some special substructures by smaller ones [8, 12]. Some experiments [32, 43] show that

factoring methods (with reduction) are more effective than classical minimal paths/cuts methods.

Methods for network reliability analysis are normally based on Boolean algebra [36], fault tree [40], digraph [4, 5, 18, 19], and BDD [37, 45, 49]. Kelly and Bartlett [4, 5, 18, 19] compare the digraph methods with the fault-tree methods in system fault diagnostics. In the 1990s, binary decision diagrams (BDD) based approaches [11, 14, 15, 19, 22, 33, 47] became increasingly popular for network analysis. A strength of BDD-based methods is that the BDD provides a succinct and disjoint description of system success/failure. Another strength is that BDD can act as a platform to consider various engineering problems such as common cause failure (CCF) [47], imperfect vertices [22], k -terminal network reliability [15], etc. The efficiency of BDD methods are measured by the BDD size which depends heavily on the chosen orderings of BDD variables. Hence, a big challenge facing BDD-based methods is the determination of the optimal orderings strategy and the automatic generation of BDD for large systems. Although literature [6] shows that improving the variable ordering of BDD is NP -complete, Friedman [11] proposes an algorithm (of time

complexity $O(n^2 3^n)$) to find the optimal variable ordering. For small networks, existing ordering algorithms (such as breadth-first searching [19, 44]) can usually generate a BDD which is succinct enough for reliability computation.

From literature it can be seen that extensive efforts have been expended to evaluate the reliability of single-phase network. Nevertheless, we can hardly find the solution to analyze MPNS reliability. Some approaches [10] may consider changes in network connectivity, but they seldom make allowance for multi-phase characteristics such as the varying system configuration, changing failure rates, and repair activities of network components, etc. Based on the BDD merging technique, this paper proposes a non-simulation approach to analyze the MPNS reliability. Additionally, the proposed method uses “o analyze the ration, changing component-behavior model” to consider phenomena such as the components repair, changes in failure rates, and multi-state components. Our method can be extended to consider unreliable vertices by minor modification to the algorithm.

The remainder of the paper is organized as follows. In Section 2, readers are briefed on the basics of phased-mission systems and BDD. In Section 3, the proposed BDD-based algorithm is presented as the mean to evaluate MPNS reliability. In Section 4, we insert the component-behavior model into the BDD-based method to analyze MPNS with repairable edges/vertices. Section 5 depicts two cases to show that MPNS is effective in analyzing the reliability of communication systems. Finally, we draw the conclusions in Section 6.

2. Preliminary knowledge

2.1. Brief of phased-mission-system reliability

The phased-mission systems (PMS), or multi-phase mission systems, describe the systems in which the components stress and system structure may change from phase to phase. An example of PMS is the rocket launching mission where the boosters, engines, and solar panels are used at different time, resulting in different system structures in different phases. A challenge facing the reliability evaluation of PMS is the dependency problem which means a single component may appear repeatedly across phases. As consequence, the reliability of PMS is not the simple multiplication of the reliability of each phase. Such challenge does not appear in single-phase systems.

Researches in the field of PMS reliability are prevalent. Existing non-simulation approaches are normally based on Boolean algebra [36], fault tree (FT) [40], BDD [37, 45, 49] and Markov chains [3, 18, 34, 35, 50], etc. Markov-chains based approaches are mainly used to analyze PMS with repairable components. In contrast, the BDD, FT,

and Boolean-algebra based algorithms are relatively more efficient in analyzing non-repairable components. A significant challenge facing most existing PMS researches is that they cannot be applied to large PMS (contain up to 100 components & phases). For large systems, most PMS approaches will encounter various explosion problems, such as the state-space explosion for Markov-chain models and the BDD-size explosion for BDD models.

Fortunately, methods analyzing small-scale PMS reliability are relatively mature (especially the BDD and Markov-chain based methods). These methods have been expanded to consider various engineering problems, such as the imperfect coverage [46], combinatorial phase requirements [24], and CCF [45, 46] etc. For PMS reliability, a remarkable algorithm is the BDD-Markov combined method [41] which builds a separate Markov chain for each component. The separate Markov chain and associated matrices manipulation can be termed as the “component behavior model” [24] which is able to depict various components’ failure and repair activities in a given phase. One strength of the component-behavior model lies in its efficiency in analyzing PMS with many repairable components, while traditional Markov-chain models are difficult to deal with such PMS. This paper uses the component-behavior model to allow for various component activities (such as repair and idle) and their effects on network reliability.

A noticeable difference between PMS and MPNS is that some PMS approaches cannot be applied to MPNS. For instance, the reliability block diagram (RBD) based methods and the FT methods are inapplicable to MPNS. This paper uses the BDD-based method to analysis MPNS reliability.

2.2. BDD method for reliability evaluation

BDD or ordered BDD (OBDD) based methods [14, 15, 19, 22, 33, 47] have been widely used in analyzing network reliability since 1990s. BDD is a directed graph based on Shannon decomposition. The Shannon decomposition for a Boolean function f is defined as:

$$f = x \cdot f_{x=1} + \bar{x} \cdot f_{x=0} \quad (1)$$

where x is one of the decision variables, and $f_{x=1}$ is the expression of f at $x=1$ (i.e. x is true). By choosing an ordering over all variables, a given Boolean expression (such as Eq.) can be expressed as a binary tree by recursively applying the Shannon decomposition. Such decomposition may result in a space-consuming BDD if no proper variable ordering is chosen. Basically, reliability evaluation based on BDD contains the following two steps.

Step (1) – Choose an ordering strategy for network components, and generate BDD according to the chosen ordering. The chosen ordering strategy should ensure the resulting BDD as succinct as possible as the size of BDD depends heavily on the ordering. Readers may refer to [7, 17, 29] for an overview about the existing ordering methods.

Step (2) – Calculate the network reliability based on the BDD.

In general, reliability evaluation based on BDD can be categorized into two types: one is the bottom-up algorithm which traverses all BDD nodes; the other one is the top-down algorithm which enumerates all BDD paths. In the bottom-up algorithm, we calculate the probability associated with each node, from the bottom node to the top node using a recursive method based on the Shannon Decomposition of Eq. . The probability of the top node equals to the system reliability. For instance, assume the reliability of each edge (a, b, j) is 0.9 (independent of time). The bottom-up evaluation of BDD is illustrated in Fig. 1.

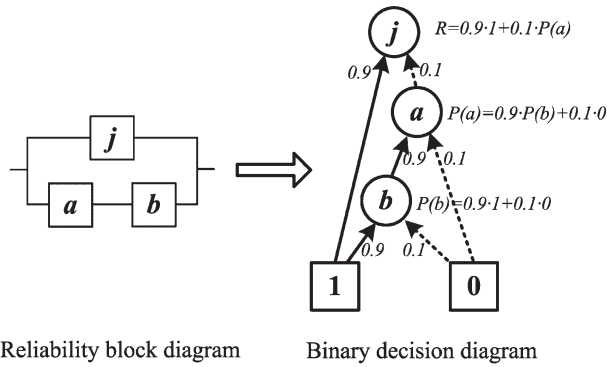


Fig. 1. Bottom-up reliability evaluation based on BDD nodes

On the other hand, the top-down algorithm calculates the probability of each BDD path which connects the top node with the bottom node $\bar{1}$. And then it sums up the probabilities of these paths to obtain the system reliability. For the system in Fig. 2, there are two paths from j to $\bar{1}$ (see Fig. 2), therefore the system reliability is $R = \Pr\{j\} + \Pr\{\bar{j} a b\}$ where \bar{j} represents that j fails during the mission.

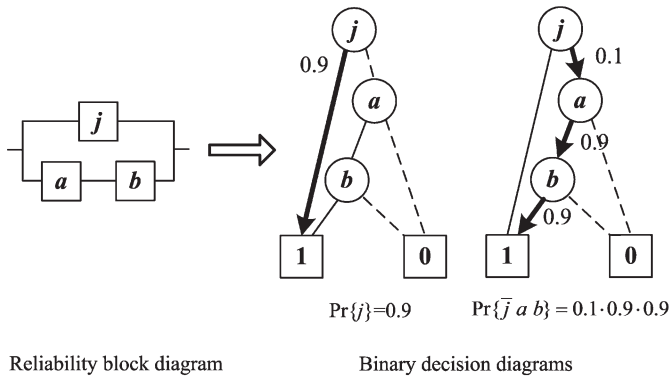


Fig. 2. Top-down reliability evaluation based on BDD paths

Compared with the top-down algorithm, the bottom-up algorithm may be more efficient to traditional (single-phase) systems as the number of BDD nodes is normally smaller than the number of BDD paths. However, for PMS, just the opposite is true. That is because the bottom-up algorithm is applicable only to BDD where nodes of the latter phase are placed higher than (or in front of) nodes of the former phase. For PMS, such BDD are almost too complex to generate. Hence the algorithm in the next section uses the top-down algorithm which is applicable to a variety of BDD.

3. BDD analysis for MPNS

In this section, a BDD-based method is proposed to analyze MPNS reliability. Generally it contains two steps: the first step is to produce the cross-phase BDD of MPNS; the second step is to calculate MPNS reliability based on the cross-phase BDD.

Step 1: BDD generation for the entire MPNS

The algorithm begins with the separate generation of BDD for every phase with classical methodologies [44]. And then these BDD are integrated together to form the final BDD of the entire MPNS. To illustrate the algorithm, consider a 3-phase MPNS which is illustrated in Fig. 3.

There are plentiful methods of generating BDD for networks in Fig. 3. Here we use the generation algorithm in [44]. Take the bridge

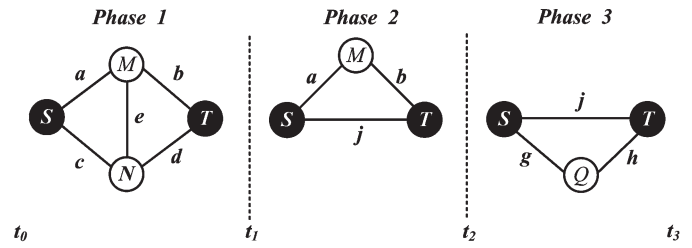


Fig. 3. MPNS example with 3 phases and duplicating components

network in Fig. 3 (first phase) for example, minimal paths are ab , aed , cd , and ceb ; hence the Boolean function of the phase-1 network is:

$$F_{\text{phase1}} = ab + aed + cd + ceb \quad (2)$$

In Eq. (2), let $L(x)$ be the length of Boolean variable x . $L(x)$ is defined as the length of the shortest minimal path containing x . For instance, the length of Boolean variable a is $L(a)=2$ because the shortest minimal path containing a is ab (aed is not shortest); similarly $L(b)=L(c)=L(d)=2$, and $L(e)=3$. And then F_{phase1} is decomposed by the Boolean variable whose length is shortest, meaning that a is chosen (b , c , and d are also appropriate here), i.e.:

$$\begin{aligned} F_{a=1} &= b + ed + cd + ceb \\ F_{a=0} &= cd + ceb \end{aligned} \quad (3)$$

When there are more than one Boolean variables whose lengths are shortest, we choose the variable which appears most frequently in Eq. (2). Above decomposition process (Eq. (3)) will repeat to form the BDD of each phase, as shown in Fig. 4. In Fig. 4, BDD node x_i represents the behavior of edge x during phase i . For instance, j_2 represents the behavior of edge j during phase 2. In this section, the assumption that all network vertices are perfectly reliable excludes network vertices from BDD.

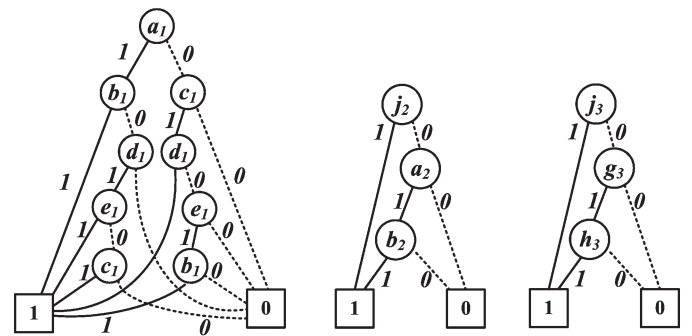
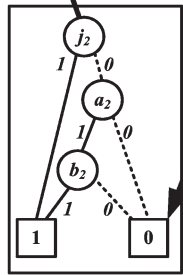
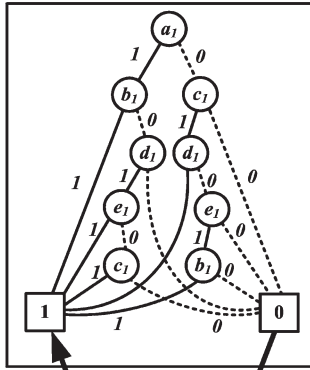


Fig. 4. BDD of phase 1, 2, and 3

Next, we integrate above BDD one-by-one to form a large BDD of the entire MPNS. To do this, we combine the top node in the next-phase BDD with the bottom node $\bar{1}$ in the former-phase BDD (see Fig. 5), based on the assumption of AND logic between phases (i.e., the system can progress into the task of the next phase only when it successfully finishes the previous-phase task.). In case studies readers will find this assumption common in practical MPNS. The new cross-phase BDD represents the system behavior (success/failure) from phase 1 to phase 2. Although the BDD combining solution can

be found in [41], it is applied to network systems for the first time. After the last-phase BDD is merged, we obtain the final BDD of the entire MPNS, which is shown in Fig. 6.

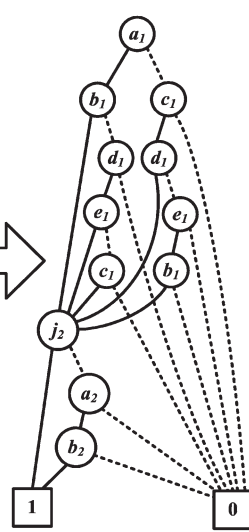
BDD of phase 1



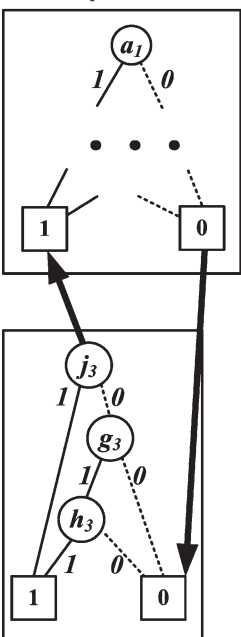
BDD of phase 2

Fig. 5. Generation of BDD for phase 1-2

BDD of phase 1-2



BDD of phase 1-2



BDD of phase 3

BDD of the entire MPNS

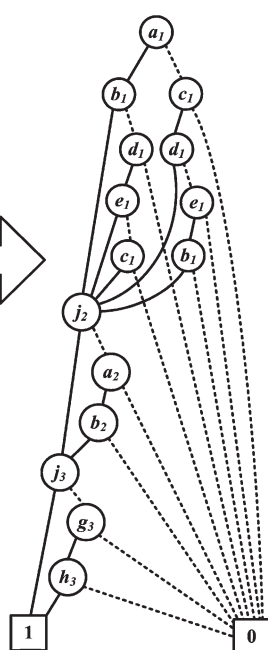


Fig. 6. Generation of the final BDD for the entire MPNS

Step 2: Reliability evaluation after the cross-phase BDD is generated

As mentioned in section 2, there are two algorithms available to the BDD-based evaluation. One is the bottom-up algorithm which traverses all BDD nodes, while the other one is the top-down algorithm which enumerates all BDD paths. Here, we use the top-down algorithm because it is applicable to a wide range of BDD (i.e., it does

not require that latter-phase nodes are placed higher than former-phase nodes.).

In order to evaluate MPNS reliability, we first find 20 paths from node a_1 to $\bar{1}$ ($20 = 5 \times 2 \times 2$; 5 paths for phase 1; and 2 paths for phase 2-3). And then the system reliability is the sum of probabilities of these 20 paths, i.e.:

$$R_{MPNS} = \sum_{m=1}^{20} \Pr\{path_m\} \quad (4)$$

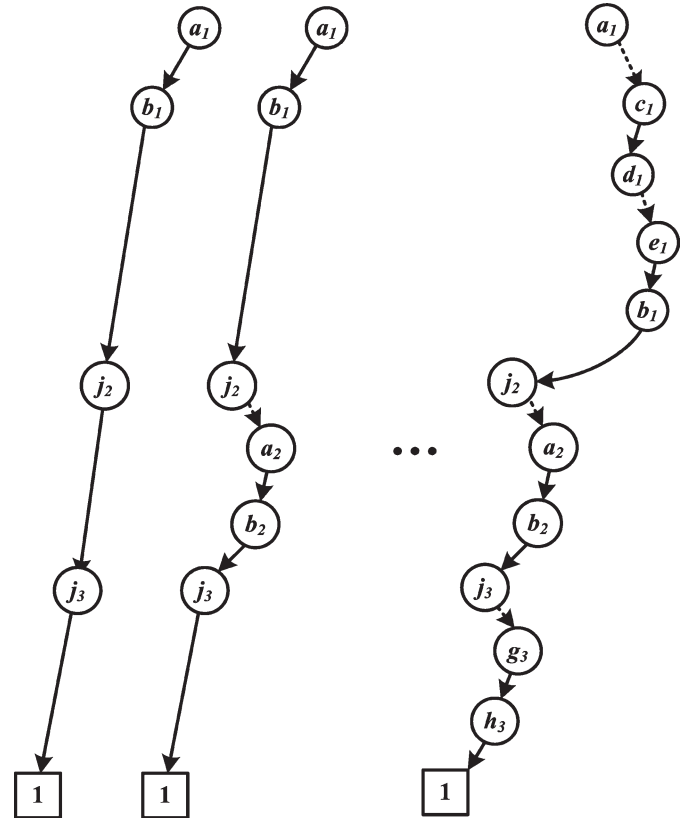


Fig. 7. Twenty paths connecting the top node with the bottom node

In Eq. (4), $\Pr\{path_m\}$ is the probability of the m^{th} BDD path. For instance, the $path_2$ ($a_1 \xrightarrow{1} b_1 \xrightarrow{1} j_2 \xrightarrow{0} a_2 \xrightarrow{1} b_2 \xrightarrow{1} j_3 \xrightarrow{1} \bar{1}$) indicates that edges a and b should keep operational during phase 1 and phase 2; meanwhile j fails and is repaired during phase 2, and then functions successfully during phase 3. By assuming edges are independent we have:

$$\Pr\{path_2\} = \Pr\{a_1 a_2\} \cdot \Pr\{b_1 b_2\} \cdot \Pr\{\bar{j}_2 j_3\} \quad (5)$$

Eq. (5) is easy to calculate when specific probability distribution functions of edges are provided. However, calculation based on Eq. will be complex when the number of phases increases and edges become repairable. In the next section we present the component-behavior model to solve this problem.

4. Method Expansion

In this section, we show that some new techniques can be inserted into the proposed method to consider various engineering problems. The first challenge presented in this section is the multi-phase repair

of network components. The second challenge is the failure occurred in network vertices. Both problems are common in engineering applications.

4.1. Challenge 1: repair in MPNS components

Here, we present a component-behavior model [24] to allow for the complex multi-phase repair/failure activities of components, based on the following assumptions.

(1) Repaired components are reused only in the next phase. (i.e., repaired components cannot be reused immediately until the next phase begins.)

(2) Components' life and repair time are independent variables of exponential distributions.

The component-behavior model is valuable because the traditional approach is too complicated to analyze multi-phase repair. For instance, consider the BDD path $\bar{j}_1\bar{j}_2\bar{j}_3j_4$ which indicates that the state of j is down sometime during phase 1 (the same happens in phase 2 and 3), but the state of j is always up during phase 4. Traditional methods usually need to discuss $\Pr\{\bar{j}_1\bar{j}_2\bar{j}_3j_4\}$ in a way like Eq. (6).

$$\begin{aligned} \Pr\{\bar{j}_1\bar{j}_2\bar{j}_3j_4\} &= \Pr\{X\}\Pr\{Y\}\Pr\{Z\} \cdot \Pr\{\bar{j}_1\bar{j}_2\bar{j}_3j_4|XYZ\} + \Pr\{\bar{X}\}\Pr\{\bar{Y}\}\Pr\{Z\} \cdot \Pr\{\bar{j}_1\bar{j}_2\bar{j}_3j_4|\bar{X}YZ\} + \\ &\Pr\{X\}\Pr\{\bar{Y}\}\Pr\{Z\} \cdot \Pr\{\bar{j}_1\bar{j}_2\bar{j}_3j_4|X\bar{Y}Z\} + \Pr\{\bar{X}\}\Pr\{Y\}\Pr\{Z\} \cdot \Pr\{\bar{j}_1\bar{j}_2\bar{j}_3j_4|\bar{X}YZ\} \end{aligned} \quad (6)$$

where events X, Y, Z represent that j is repaired during phase 1, 2, 3, respectively. Events $\bar{X}, \bar{Y}, \bar{Z}$ represent that j is not repaired (after failure) during phase 1, 2, 3, respectively. The event $\bar{j}_1\bar{j}_2\bar{j}_3j_4|\bar{X}\bar{Y}Z$ represents that the state of j is never repaired during phase 1 and 2; in phase 3 j is repaired sometime but fails again; finally j stays operational in phase 4. Apparently such decomposition is too cumbersome to implement.

In order to provide a concise approach, we propose the "component-behavior model" [24] which is effective in analyzing various behavior of components. Take the system in Fig. 2 for

instance, matrices $\mathbf{U}_i^{(k)}$ and $\mathbf{D}_i^{(k)}$ (represent k is up and down in phase i , respectively) replace the constant edge reliability (0.9), as shown in Fig. 8.

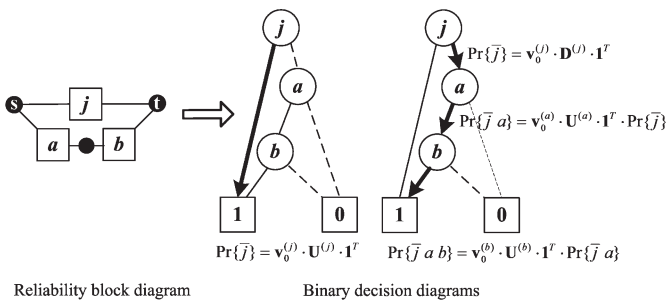


Fig. 8. Component-behavior model integrated with BDD

In Fig. 8, the initial state vector $\mathbf{v}_0^{(k)} = (1, 0)$ for initially operational binary-state edge k . The column vector $\mathbf{1}^T = (1, 1)^T$. In Fig. 8 we use a matrix $(\mathbf{C}_i^{(k)})$ to represent the behavior of certain network edge k during phase i . i.e.:

$$\mathbf{C}_i^{(k)} = \begin{cases} \mathbf{E}_i^{(k)}, & \text{if the state of } k \text{ is either operational or down in phase } i \\ \mathbf{U}_i^{(k)}, & \text{if component } k \text{ stays operational during phase } i \\ \mathbf{D}_i^{(k)}, & \text{if component } k \text{ is down sometime in phase } i \\ \mathbf{R}_i^{(k)}, & \text{if component } k \text{ continues repairs in phase } i \\ \mathbf{I}, & \text{if the state of } k \text{ remains unchanged in phase } i \end{cases} \quad (7)$$

In Eq., the expression of $\mathbf{E}_i^{(k)}, \dots, \mathbf{R}_i^{(k)}$ can be found in [24]. For instance, $\mathbf{U}_i^{(k)}, \mathbf{E}_i^{(k)}$, and $\mathbf{D}_i^{(k)}$ are of the form:

$$\mathbf{U}_1^{(k)} = \exp\left(\begin{bmatrix} -\lambda_i^k & \lambda_i^k \\ 0 & 0 \end{bmatrix} \cdot T_i\right) \cdot \begin{bmatrix} 1 & 0 \\ 0 & 0 \end{bmatrix}, \mathbf{E}_1^{(k)} = \exp\left(\begin{bmatrix} -\lambda_i^k & \lambda_i^k \\ \mu_i^k & -\mu_i^k \end{bmatrix} \cdot T_i\right), \mathbf{D}_1^{(k)} = \mathbf{E}_1^{(k)} - \mathbf{U}_1^{(k)} \quad (8)$$

where λ_i^k is the failure rate of k during phase i (μ_i^k is the repair rate); T_i is the duration of phase i . By applying the evaluation algorithm (Fig. 8) to the cross-phase BDD of MPNS, we can evaluate the reliability of MPNS with repairable edges easily. It should be noted that the method in this section is effective even when components becomes non-repairable (At this case let $\mu_i^k = 0$).

For instance, reconsider the BDD path $a_1b_1\bar{j}_2a_2b_2j_3$ which is mention in Eq. (see Section 3). We have:

$$\begin{aligned} \Pr\{a_1a_2\} &= \mathbf{v}_0^{(a)} \cdot \mathbf{U}_1^{(a)} \cdot \mathbf{U}_2^{(a)} \cdot \mathbf{E}_3^{(a)} \cdot \mathbf{1}^T \\ \Pr\{b_1b_2\} &= \mathbf{v}_0^{(b)} \cdot \mathbf{U}_1^{(b)} \cdot \mathbf{U}_2^{(b)} \cdot \mathbf{E}_3^{(b)} \cdot \mathbf{1}^T \\ \Pr\{\bar{j}_2j_3\} &= \mathbf{v}_0^{(j)} \cdot \mathbf{E}_1^{(j)} \cdot \mathbf{D}_2^{(j)} \cdot \mathbf{U}_3^{(j)} \cdot \mathbf{1}^T \end{aligned} \quad (9)$$

The probability of $a_1b_1\bar{j}_2a_2b_2j_3$ can be expressed as:

$$\Pr\{a_1b_1\bar{j}_2a_2b_2j_3\} = (\mathbf{v}_0^{(a)}\mathbf{U}_1^{(a)}\mathbf{U}_2^{(a)}\mathbf{E}_3^{(a)}\mathbf{1}^T) \cdot (\mathbf{v}_0^{(b)}\mathbf{U}_1^{(b)}\mathbf{U}_2^{(b)}\mathbf{E}_3^{(b)}\mathbf{1}^T) \cdot (\mathbf{v}_0^{(j)}\mathbf{E}_1^{(j)}\mathbf{D}_2^{(j)}\mathbf{U}_3^{(j)}\mathbf{1}^T) \quad (10)$$

$$\begin{aligned} a_1 &\xrightarrow{\text{up}} \mathbf{U}_1^{(a)}; a_2 \xrightarrow{\text{up}} \mathbf{U}_2^{(a)}; a_3 \xrightarrow{\text{not specified}} \mathbf{E}_3^{(a)}; \\ b_1 &\xrightarrow{\text{up}} \mathbf{U}_1^{(b)}; b_2 \xrightarrow{\text{up}} \mathbf{U}_2^{(b)}; b_3 \xrightarrow{\text{not specified}} \mathbf{E}_3^{(b)}; \\ j_1 &\xrightarrow{\text{Not specified}} \mathbf{E}_1^{(j)}; j_2 \xrightarrow{\text{down}} \mathbf{D}_2^{(j)}; j_3 \xrightarrow{\text{up}} \mathbf{U}_3^{(j)}; \end{aligned}$$

Fig. 9. BDD path interpretation according to the component-behavior model

In fact, $a_1b_1\bar{j}_2a_2b_2j_3$ does not clarify the behavior of the edge j during the first phase. Hence in Eq. the matrix $\mathbf{E}_1^{(j)}$ is used to represent that j may fail even if it is not used during phase 1. Conversely we can replace $\mathbf{E}_1^{(j)}$ with the identity matrix \mathbf{I} based on the assumption that j will maintain its initial state (operational) during phase 1. In this case Eq. (11) becomes:

$$\Pr\{a_1b_1\bar{j}_2a_2b_2j_3\} = (\mathbf{v}_0^{(a)}\mathbf{U}_1^{(a)}\mathbf{U}_2^{(a)}\mathbf{E}_3^{(a)}\mathbf{1}^T) \cdot (\mathbf{v}_0^{(b)}\mathbf{U}_1^{(b)}\mathbf{U}_2^{(b)}\mathbf{E}_3^{(b)}\mathbf{1}^T) \cdot (\mathbf{v}_0^{(j)} \cdot \mathbf{I} \cdot \mathbf{D}_2^{(j)}\mathbf{U}_3^{(j)}\mathbf{1}^T) \quad (11)$$

From Fig. 9 we can see it is easy to interpret BDD paths into corresponding matrices, making it practical to implement in computer

languages. By summing the probabilities of all BDD paths we can obtain the reliability of MPNS, i.e.:

$$R_{MPNS} = \sum_{m=1}^s \Pr\{path_m\} \quad (12)$$

where s is the number of paths linking the top node with the bottom node $\bar{1}$ in the cross-phase BDD. In summary, the algorithm proposed in this section can be illustrated by Fig. 10.

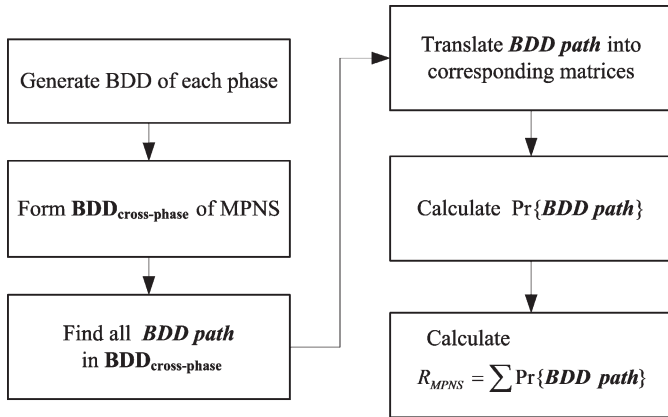


Fig. 10. BDD and component-behavior combined method for MPNS reliability analysis

4.2. Challenge 2: unreliable vertices

In many realistic engineering applications, network vertices may fail as well as edges. These vertices are termed as unreliable vertices (or imperfect vertices). In literature we can find some researches [22, 26, 40, 39] allowing for unreliable vertices. Kuo et. al. [22] replace edges with the entities which combines both edges and vertices, and use the entities to build BDD. This approach is called "Incident edge substitution". In factoring-theorem algorithms, unreliable vertices are taken into consideration by factoring on vertices as well as on edges. In our approach, both vertices and edges are considered as BDD variables, and meanwhile the BDD generation algorithm [44] is applied to both of them.

Consider the MPNS in Fig. 3, the BDD generation technique [22] is applied to both networks edges and vertices, resulting in BDD of Fig. 11. Next, three BDD are combined one-by-one as we did in Section 3.1 to generate a final cross-phase BDD of MPNS. Based on the cross-phase BDD we can evaluate the reliability of MPNS. In the

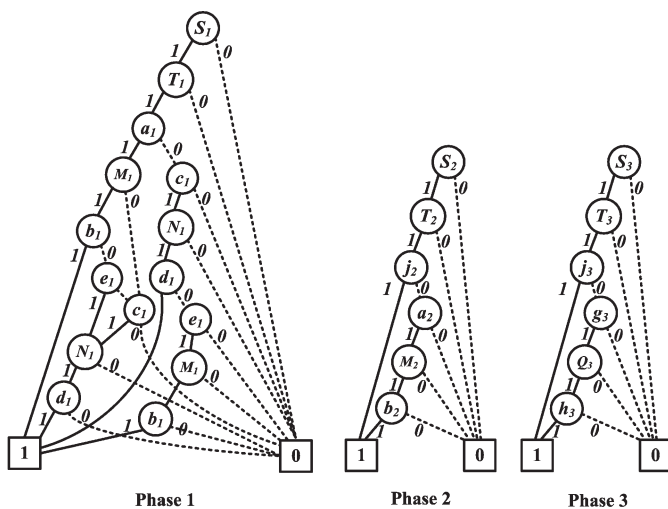


Fig. 11. Network BDD considering vertices & links failure

next section we propose two practical cases which consider repairable components and unreliable vertices, respectively.

5. Case study

5.1. Satellite telemetry, tracking & control (TT&C) mission

In the satellite telemetry, tracking & control (TT&C) mission, high reliability is one of the top concern for communication-system designers. To ensure reliable communications, some on-orbit satellites usually act as the repeater between the source ground station and the target satellite. For instance in Fig. 12, a relay satellite Sat_1 may retransmit signals when the target Sat_2 is not directly visible to the ground-station facility Fac_1 .

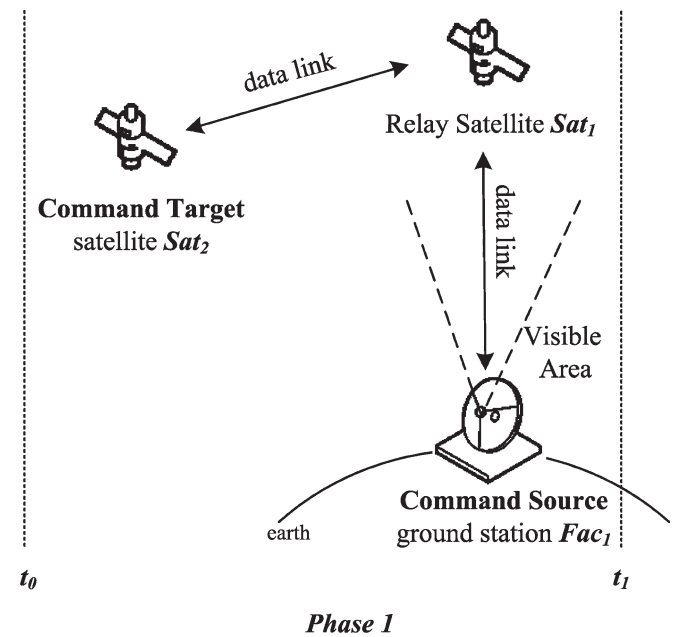


Fig. 12. Relay satellite between the source ground facility and the target satellite

For practical satellite navigation systems, there exist several data-relay alternatives. By considering relay satellites as vertices, the communication scheme can be interpreted as a network which is shown in Fig. 13.

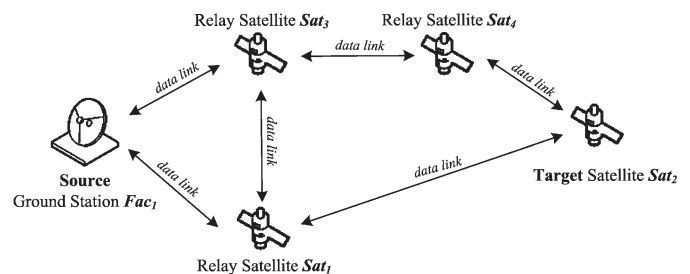


Fig. 13. Relay satellites and combination links in a certain phase

As different non-geostationary satellites fly over the source ground station. Data links in the previous phase may become invalid as the original relay satellites are no longer invisible to the ground facility. Hence it leads to the changing communication structures in different phases, as shown in Fig. 14. This changing system structure can be extracted as a MPNS model (see Fig. 15).

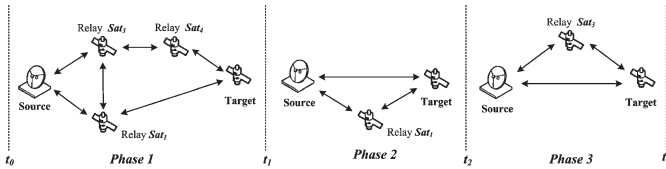


Fig. 14. Changing communication links in the spacecraft TT&C mission

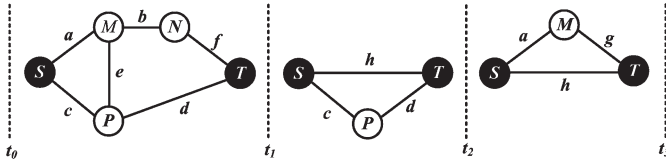


Fig. 15. MPNS of the spacecraft TT&C mission

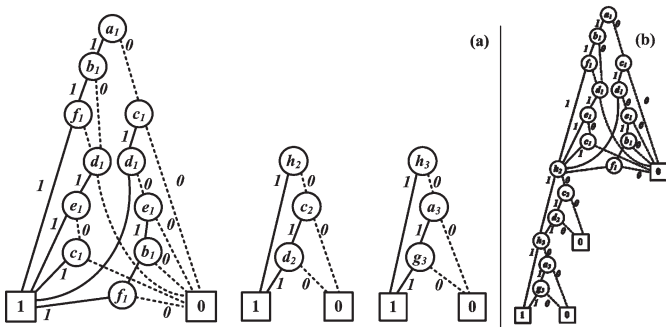


Fig. 16. BDD for the satellite TT&C systems

In order to evaluate the reliability of MPNS, we generate BDD (Fig. 16(a)) for different phases according to the algorithm in Section 3 [44]. These BDD are combined together to form a cross-phase BDD of MPNS (Fig. 16(b)). The reliability of MPNS is evaluated by the top-down algorithm. For the cross-phase BDD, there are 28 vectors which correspond to 28 paths from a_1 to $\bar{1}$. (7 paths for phase 1; 2 paths for phase 2, and 2 paths for phase 3; we have $28 = 7 \times 2 \times 2$ paths for the cross-phase BDD.)

For instance, the probability of $path_1 (a_1 \xrightarrow{1} b_1 \xrightarrow{1} f_1 \xrightarrow{1} h_2 \xrightarrow{1} h_3 \xrightarrow{1} \bar{1})$ is:

$$\Pr\{path_1\} = (v_0^{(a)} \cdot U_1^{(a)} \cdot [1,1]) \cdot (v_0^{(b)} \cdot U_1^{(b)} \cdot [1,1]) \cdot (v_0^{(c)} \cdot E_1^{(c)} \cdot [1,1]) \cdot (v_0^{(d)} \cdot E_1^{(d)} \cdot [1,1]) \cdot (v_0^{(e)} \cdot E_1^{(e)} \cdot [1,1]) \cdot (v_0^{(f)} \cdot U_1^{(f)} \cdot [1,1]) \cdot (v_0^{(g)} \cdot E_1^{(g)} \cdot [1,1]) \cdot (v_0^{(h)} \cdot I_1^{(h)} \cdot U_2^{(h)} \cdot U_3^{(h)} \cdot [1,1]) \quad (13)$$

where $U_1^{(a)}$ indicates that edge a keeps operational during phase 1.

$E_1^{(c)}$ indicates that the behavior of c in phase 1 is either up or down.

$I_1^{(h)} U_2^{(h)} U_3^{(h)}$ indicates that the state of h remains unchanged during phase 1, and keeps operational during phase 2 and phase 3. The MPNS reliability is the sum of all $\Pr\{path_i\}$, i.e.:

$$R_{MPNS} = \sum_i \Pr\{path_i\} \quad (14)$$

In order to verify the above algorithm, we compare results of our method and that of the simulation method under two scenarios. The first scenario considers all communication links as nonrepairable and their life are independent variables of exponential distributions, failure rates $[\lambda_a, \lambda_b, \dots, \lambda_h] = [0.2, 0.22, 0.24, \dots, 0.34]$ (unit: probability per hour), and failure rates do not change across phases. Let

$[T_1, T_2, T_3] = [1, 1, 1]$ (hour) be the duration of phase 1-3. System reliability calculated by our approach and the simulation approach are shown in Table. 1.

Figures in Table. 1 show that our result is very close to the simulation result. The Monte Carlo simulation is carried out with the software of Windchill Quality Solutions (formerly Relx) [42]. The number of simulation iteration is 10^6 . Additionally, results of Monte Carlo simulation is very close to the Petri-net simulation results of the GRIF software [13]. From the 5th row data of Table. 1 we can see that the proposed method is able to detect the sudden reliability drop at the phase-transition moment.

Table 1. Reliability of MPNS with nonrepairable links

Time	System Reliability	
	Proposed method	Monte Carlo simulation
0 (Start of phase 1)	1	1
1 (End of phase 1)	0.85400	0.85394
1.001 (Start of phase 2)	0.85399	0.85390
2 (End of phase 2)	0.71389	0.71386
2.001 (Start of phase 3)	0.69466	0.69458
3 (End of phase 3)	0.57323	0.57334

In the second scenario, we suppose all communication links are repairable (exponential distributed repair time) and their repair rates are $[\mu_a, \mu_b, \dots, \mu_h] = [0.4, 0.42, 0.44, \dots, 0.54]$ (μ_i do not change across phases, and other parameters equals to that in the scenario 1.). Figures in Table. 2 show that results of our method (1st column data) are slightly different from that of the simulation method (3rd column data).

Table 2. Reliability of MPNS with repairable links

Time	System Reliability		
	Proposed method (Original system)	Proposed method (more accurate) (Divide 1 phase into 4 phases)	Monte Carlo simulation
0 (Start of phase 1)	1	1	1
1 (End of phase 1)	0.8540	0.8656	0.8715
2 (End of phase 2)	0.7213	0.7415	0.7510
3 (End of phase 3)	0.5905	0.6164	0.6231

When the system contains repairable components, the proposed method generates accurate results only on the assumption that repaired units can be reused only in the next phase (cannot be reused immediately until next phase). Without this assumption our method only provides an approximate result (i.e., data differences between 1st column and 3rd column in Table 2). In Monte Carlo simulation, no such assumption exists and thus simulation approach generates a more accurate (higher) result than our method. Fortunately the impact of our assumption can be diminished by dividing one mission phase into multiple ones. We divide one phase into four phases and obtain more accurate results which is shown in the 2nd column of Table. 2. Figures in the 2nd column are close to the simulation results, partly demonstrating the effectiveness of the proposed method in analyzing repairable components.

5.2. Speed-monitoring mission

In railway systems, speed detection has become an indispensable security measure to avoid clashes and delay. A common speed-monitoring equipment is the radar speedometer which uses the Doppler effect to analyze the speed of trains. In addition, laser speedometers are normally installed near railway stations as an alternative to supervise the incoming train. Consider a train P scheduled to move across Station α , β , and γ , as shown in Fig. 17. Radar speedometers M and N measure the speed of the train and directly transmit data to the control center Q . In addition, laser sensors $A \sim F$ measure the speed when P approaches railway stations. Data from $A \sim F$ can be directly transmitted to Q , or gathered at specific sensors to be transmitted together.

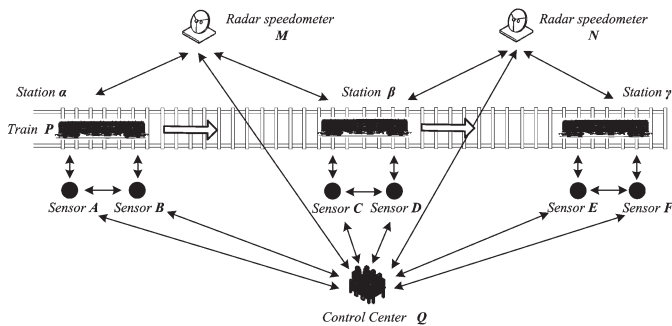


Fig. 17. Train-speed monitoring mission.

Our aim is to analyze the reliability of the speed-monitoring system when the train approaches stations. Apparently MPNS is an effective description for the system. We decompose the mission into three phases to obtain a MPNS which is shown in Fig. 18. Suppose both edges and vertices are prone to failure (except P and Q), the proposed algorithm generates the BDD for each phase (Fig. 19 considers uMv or sNt as an entity) and combines them together to form a cross-phase BDD. The system reliability is the sum of probabilities of all BDD paths. (There are $392 = 7 \times 8 \times 7$ paths in the cross-phase BDD; 7 paths for phase 1; 8 path for phase 2; and 7 paths for phase 3)

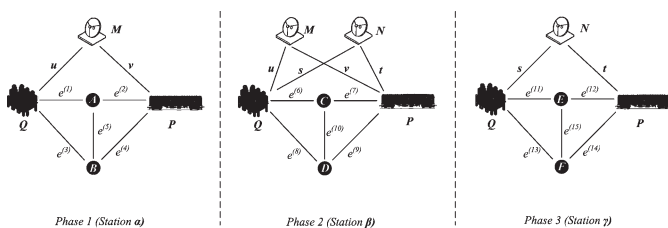


Fig. 18. MPNS model for the train-speed monitoring system.

By setting the following parameters we can compare our results with simulation results (generated by Windchill [42] and GRIF software [13]), as shown in Table. 3.

- (1) Failure rates of all components $\lambda = 0.1$ (failure rates remain unchanged across phases; life of components are exponentially distributed independent variables.);
- (2) All components are non-repairable;
- (3) Phase duration $[T_1, T_2, T_3] = [1, 1, 1]$ hour.

From cases in this section it can be seen that MPNS is a useful tool to model some communication projects. Figures in Table. 3 show that the proposed evaluation method can calculate an accurate reliability of multi-phase networks.

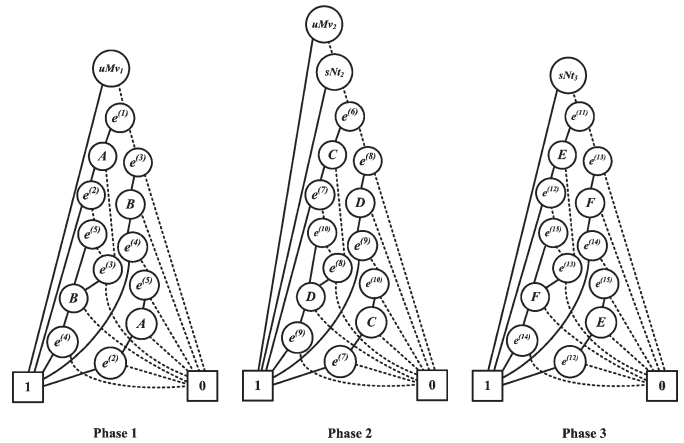


Fig. 19. BDD of each phase in MPNS

Table 3. Reliability of the speed-monitoring system

Time	System Reliability	
	Proposed method	Monte Carlo simulation
0 (Start of phase 1)	1	1
1 (End of phase 1)	0.98543	0.98544
2 (End of phase 2)	0.97908	0.97909
3 (End of phase 3)	0.95445	0.95449

6. Conclusion

The paper proposes an BDD-based algorithm to evaluate the reliability of MPNS. From literatures we find existing methods do not take dynamic characteristics of networks into consideration. Hence this paper introduces the concept of MPNS to consider some dynamic characteristics which include the varying system configuration, changing components' failure rates, and repair activities during the mission. From case study it can be seen that MPNS is the effective description of many communication systems.

The reliability of MPNS is evaluated with the cross-phase BDD which is generated by merging BDD of different phases. When the number of phase in MPNS increases, the merging step is easier to implement in computers compared to the backward ordering in [49]. Another strength of the BDD-based approach is that it can be further expanded to consider repairable edges and failure in vertices.

Future efforts will focus on the k-terminal reliability analysis of MPNS, and the reliability analysis of directed MPNS with CCF. Additionally, truncation of the cross-phase BDD can also be taken into consideration to make our approach applicable to large MPNS.

Acknowledgement

Authors express their gratitude to the reviewer's comment about the digraph (and Signed Directed Graphs) based methods. This research is partly carried out with the Reliability, Availability, Maintainability and Safety (RAMS) group at the Norwegian University of Science and Technology (NTNU), and it is funded by the National Natural Science Foundation of China with the grant no. 71071159.

References

1. Aggarwal KK, Chopra YC, Bajwa JS. Modification of cutsets for reliability evaluation of communication systems. *Microelectronics Reliability* 1982; 22(3): 337-340, [http://dx.doi.org/10.1016/0026-2714\(82\)90005-1](http://dx.doi.org/10.1016/0026-2714(82)90005-1).
2. Ahmad SH. Simple enumeration of minimal cutsets of acyclic directed graph. *IEEE Transactions on Reliability* 1988; 37(5): 484-487, <http://dx.doi.org/10.1109/24.9868>.
3. Alam M, Alsaggaf UM. Quantitative reliability evaluation of repairable phased-mission systems using Markov approach. *IEEE Transactions on Reliability* 1986; 35(5): 498-503, <http://dx.doi.org/10.1109/TR.1986.4335529>.
4. Bartlett LM, Hurdle EE, Kelly EM. Integrated system fault diagnostics utilising digraph and fault tree-based approaches. *Reliability Engineering and System Safety* 2009; 94(6): 1107-1115, <http://dx.doi.org/10.1016/j.res.2008.12.005>.
5. Bartlett LM, Hurdle EE, Kelly EM. Comparison of digraph and fault tree based approaches for system fault diagnostics. *Proceedings of the European Safety and Reliability Conference (ESREL)* 2006; 1: 191-198.
6. Bollig B, Wegener I. Improving the variable ordering of OBDDs is NP-complete. *IEEE Transactions on Computers* 1996; 45(9): 993-1002, <http://dx.doi.org/10.1109/12.537122>.
7. Bouissou M, Bruyere F, Rauzy A. BDD based fault-tree processing: a comparison of variable ordering heuristics. *Proceedings of European Safety and Reliability Association Conference (ESREL)* 1997, <http://dx.doi.org/10.1016/b978-008042835-2/50231-9>.
8. Choi MS, Jun CH. Some variants of polygon-to-chain reductions in evaluating reliability of undirected network. *Microelectronics Reliability* 1995; 35(1): 1-11, [http://dx.doi.org/10.1016/0026-2714\(94\)P1833-X](http://dx.doi.org/10.1016/0026-2714(94)P1833-X).
9. Colbourn CJ, *The combinatorics of network reliability*, Oxford University Press: London, 1987.
10. Cook JL, Ramirez-Marquez JE. Two-terminal reliability analyses for a mobile ad hoc wireless network. *Reliability Engineering and System Safety* 2007; 92(6): 821-829, <http://dx.doi.org/10.1016/j.res.2006.04.021>.
11. Friedman SJ, Supowit KJ. Finding the optimal variable ordering for binary decision diagrams. *Proceedings of the 24th ACM/IEEE Design Automation Conference* 1987: 348-356, <http://dx.doi.org/10.1145/37888.37941>.
12. Gadani J. System effectiveness evaluation using star and delta transformations. *IEEE Transactions on Reliability* 1981; 30(1): 43-47, <http://dx.doi.org/10.1109/TR.1981.5220959>.
13. GRIF-Workshop Software, SATODEV LLC 2014; <http://grif-workshop.com/>.
14. Hardy G, Lucet C, Limnios N. Computing all-terminal reliability of stochastic networks with binary decision diagrams. *11th International Symposium on Applied Stochastic Models and Data Analysis* 2005: 17-20.
15. Hardy G, Lucet C, Limnios N. K-terminal network reliability measures with binary decision diagrams. *IEEE Transactions on Reliability* 2007; 56(3): 506-515, <http://dx.doi.org/10.1109/TR.2007.898572>.
16. Hariri S, Raghavendra CS. SYREL: A symbolic reliability algorithm based on path and cutset methods. *IEEE Transactions on Computers* 1987; 100(10): 1224-1232, <http://dx.doi.org/10.1109/TC.1987.1676862>.
17. Huang HZ, Zhang H, Li Y. A new ordering method of basic events in fault tree analysis. *Quality and Reliability Engineering International* 2012; 28(3): 297-305, <http://dx.doi.org/10.1002/qre.1245>.
18. Kelly EM, Bartlett LM. Enhanced diagnosis of faults using the digraph approach applied to a dynamic aircraft fuel system. *Proceedings of the first international conference on availability, reliability and security (ARES)* 2006.
19. Kelly EM, Bartlett LM. Application of the digraph method in system fault diagnostics. *Proceedings of the first international conference on availability, reliability and security (ARES)* 2006, <http://dx.doi.org/10.1109/ARES.2006.31>.
20. Kim K, Park KS. Phased-mission system reliability under Markov environment. *IEEE Transactions on Reliability* 1994; 43(2): 301-309, <http://dx.doi.org/10.1109/24.295013>.
21. Kuo SY, Lu SK, Yeh FM. Determining terminal-pair reliability based on edge expansion diagrams using OBDD. *IEEE Transactions on Reliability* 1999; 48(3): 234-246, <http://dx.doi.org/10.1109/24.799845>.
22. Kuo SY, Yeh FM, Lin HY. Efficient and exact reliability evaluation for networks with imperfect vertices. *IEEE Transactions on Reliability* 2007; 56(2): 288-300, <http://dx.doi.org/10.1109/TR.2007.896770>.
23. Locks MO. A minimizing algorithm for sum of disjoint products. *IEEE Transactions on Reliability* 1987; 36(4): 445-453, <http://dx.doi.org/10.1109/TR.1987.5222436>.
24. Lu JM, Wu XY. Reliability evaluation of generalized phased-mission systems with repairable components. *Reliability Engineering and System Safety* 2014; 121: 136-145, <http://dx.doi.org/10.1016/j.res.2013.08.005>.
25. Lu JM, Wu XY, Liu Y, Mary Ann Lundteigen. Reliability analysis of large phased-mission systems with repairable components based on success-state sampling. *Reliability Engineering and System Safety* 2015; 142: 123-133, <http://dx.doi.org/10.1016/j.res.2015.05.010>.
26. Netes VA, Filin BP. Consideration of node failures in network-reliability calculation. *IEEE Transactions on Reliability* 1996; 45(1): 127-128, <http://dx.doi.org/10.1109/24.488928>.
27. Page LB, Perry JE. Reliability of directed networks using the factoring theorem. *IEEE Transactions on Reliability* 1989; 38(5): 556-562, <http://dx.doi.org/10.1109/24.46479>.
28. Rai S, Kumar A, Prasad EV. Computing terminal reliability of computer network. *Reliability Engineering* 1986; 16(2): 109-119, [http://dx.doi.org/10.1016/0143-8174\(86\)90079-X](http://dx.doi.org/10.1016/0143-8174(86)90079-X).
29. Rauzy A. Binary decision diagrams for reliability studies. *Handbook of Performability Engineering*. Springer: London, 2008: 381-396.
30. Resende LI. Implementation of a factoring algorithm for reliability evaluation of undirected networks. *IEEE Transactions on Reliability* 1988; 37(5): 462-468, <http://dx.doi.org/10.1109/24.9862>.
31. Resende MG. A program for reliability evaluation of undirected networks via polygon-to-chain reductions. *IEEE Transactions on Reliability* 1986; 35(1): 24-29, <http://dx.doi.org/10.1109/TR.1986.4335334>.
32. Satyanarayana A, Chang MK. Network reliability and the factoring theorem. *Networks* 1983; 13(1): 107-120, <http://dx.doi.org/10.1002/net.3230130107>.
33. Singh H, Vaithilingam S, Anne RK. Terminal reliability using binary decision diagrams. *Microelectronics Reliability* 1996; 36(3): 363-365, [http://dx.doi.org/10.1016/0026-2714\(95\)00087-9](http://dx.doi.org/10.1016/0026-2714(95)00087-9).

34. Smotherman MK, Geist RM. Phased mission effectiveness using a nonhomogeneous Markov reward model. *Reliability Engineering and System Safety* 1990; 27(2): 241-255, [http://dx.doi.org/10.1016/0951-8320\(90\)90057-T](http://dx.doi.org/10.1016/0951-8320(90)90057-T).
35. Smotherman MK, Zemoudeh K. A non-homogeneous Markov model for phased-mission reliability analysis. *IEEE Transactions on Reliability* 1989; 38(5): 585-590, <http://dx.doi.org/10.1109/24.46486>.
36. Somani AK, Trivedi KS. Phased-mission system analysis using Boolean algebraic methods. *Proceedings of ACM/SIGMETRICS conference on Measurement and modeling of computer systems* 1994: 98-107, <http://dx.doi.org/10.1145/183019.183029>.
37. Tang ZH, Dugan JB. BDD-based reliability analysis of phased-mission systems with multimode failures. *IEEE Transactions on Reliability* 2006; 55(2): 350-360, <http://dx.doi.org/10.1109/TR.2006.874941>.
38. Theologou OR, Carlier JG. Factoring and reductions for networks with imperfect vertices. *IEEE Transactions on Reliability* 1991; 40(2): 210-217, <http://dx.doi.org/10.1109/24.87131>.
39. Torrieri D. Calculation of node-pair reliability in large networks with unreliable nodes. *IEEE Transactions on Reliability* 1994; 43(3): 375-377, <http://dx.doi.org/10.1109/24.326428>.
40. Vaurio JK. Fault tree analysis of phased mission systems with repairable and non-repairable components. *Reliability Engineering and System Safety* 2001; 74(2): 169-180, [http://dx.doi.org/10.1016/S0951-8320\(01\)00075-8](http://dx.doi.org/10.1016/S0951-8320(01)00075-8).
41. Wang D, Trivedi KS. Reliability analysis of phased-mission system with independent component repairs. *IEEE Transactions on Reliability* 2007; 56(3): 540-551, <http://dx.doi.org/10.1109/TR.2007.903268>.
42. Windchill Quality Solutions (formerly Relex) Version 10 Software, PTC Product & Service Advantage LLC 2014; <http://www.ptc.com/product/windchill>.
43. Wood RK. A factoring algorithm using polygon-to-chain reductions for computing K-terminal network reliability. *Networks* 1985; 15(2): 173-190, <http://dx.doi.org/10.1002/net.3230150204>.
44. Wu XY. Reliability modeling and reliability analysis of complex correlative systems. PhD degree thesis of National University of Defense Technology China, 2000.
45. Xing L, Levitin G. BDD-based reliability evaluation of phased-mission systems with internal/ external common-cause failures. *Reliability Engineering and System Safety* 2013; 112: 145-153, <http://dx.doi.org/10.1016/j.res.2012.12.003>.
46. Xing L. Reliability evaluation of phased-mission systems with imperfect fault coverage and common-cause failures. *IEEE Transactions on Reliability* 2007; 56(1): 58-68, <http://dx.doi.org/10.1109/TR.2006.890900>.
47. Xing L. An efficient binary-decision-diagram-based approach for network reliability and sensitivity analysis. *IEEE Transactions on Systems, Man and Cybernetics, Part A: Systems and Humans* 2008; 38(1): 105-115, <http://dx.doi.org/10.1109/TSMCA.2007.909493>.
48. Xing L, Dugan JB, Morissette BA. Efficient reliability analysis of systems with functional dependence loops. *Eksplotacja i Niezawodność – Maintenance and Reliability* 2009; 43(3): 65-69.
49. Zang X, Sun H, Trivedi KS. A BDD-based algorithm for reliability analysis of phased-mission systems. *IEEE Transactions on Reliability* 1999; 48(1): 50-60, <http://dx.doi.org/10.1109/24.765927>.
50. Zhang T, Bai GH, Guo B. Success probability model of phased mission systems with limited spares. *Eksplotacja i Niezawodność – Maintenance and Reliability* 2012; 14(1): 24-32.

Ji-Min LU

College of Information System and Management
National University of Defense Technology
De Ya Road 109, Changsha, Hunan 410073, China

Fares INNAL**Yiliu LIU****Mary Ann LUNDTEIGEN**

Department of Production and Quality Engineering
Norwegian University of Science and Technology, Valgrinda, N-7491
Trondheim, Norway

Xiao-Yue WU

College of Information System and Management
National University of Defense Technology
De Ya Road 109, Changsha, Hunan 410073, China

E-mails: jeemanlv@gmail.com, innal.fares@hotmail.fr, yiliu.liu@ntnu.no,
mary.a.lundteigen@ntnu.no, xiaoyuewucn@gmail.com

Witold PAWLOWSKI
Lukasz KACZMAREK
Petr LOUDA

THEORETICAL AND EXPERIMENTAL MODAL ANALYSIS OF THE CYLINDER UNIT FILLED WITH PUR FOAM

TEORETYCZNA I EKSPERYMENTALNA ANALIZA MODALNA ZESPOŁU BĘBNA WCIĄGARKI WYPEŁNIONEGO PIANKĄ POLIURETANOWĄ

In the paper the dynamic properties of the cylinder unit as a part of the theatre scenography lifting mechanism have been investigated. The noise and vibration problem of the cylinder unit when lifting loads turned out to be the crucial limit in application of the whole mechanism for lifting scenography elements on a theatre stage. The construction of the mechanism was examined and the main source of noise was identified as the cylinder unit. Theoretical modal analysis confirmed that thesis. Experimental modal analyses of the hollow cylinder unit as well as the cylinder with the PUR foam filling were performed. The results showed significant improvement of the dynamic properties due to the vibration amplitude decrease for the first three vibration modes of the filled cylinder. The research method of modal analysis turned out to be highly efficient in dynamic properties determination in the industrial practice. The method of improving the dynamic properties of the mechanical construction by filling closed regions with PUR foam is of a great importance for industrial application and seems to be economically effective.

Keywords: *dynamic properties, noise and vibration, theoretical and experimental modal analysis, PUR foam.*

W artykule przedstawiono badania dynamicznych właściwości zespołu bębna wciągarki służącej do podnoszenia scenografii teatralnej. Problem nadmiernego hałasu i drgań wciągarki podczas podnoszenia elementów scenografii okazał się istotnym problemem użytkowym ograniczającym możliwości zastosowania urządzenia w teatrze. Przeprowadzono analizę konstrukcji mechanizmu wciągarki i wskazano zespół bębna jako źródło nadmiernego hałasu. Tę tezę potwierdzono przeprowadzając teoretyczną analizę modalną zespołu bębna. W części doświadczalnej badań przeprowadzono analizę modalną oryginalnego, pustego zespołu bębna a następnie zespołu wypełnionego pianką poliuretanową. Otrzymano wyniki badań doświadczalnych, na podstawie których dokonano obserwacji, że amplituda pierwszych trzech postaci drgań swobodnych analizowanego zespołu została znacznie obniżona, co skutkuje znaczną redukcją hałasu generowanego przez bęben wypełniony pianką poliuretanową. Analiza modalna okazała się wysoce przydatna w praktyce przemysłowej w celu określania dynamicznych właściwości urządzenia mechanicznego. Na podstawie wyników przeprowadzonych badań modalnych sformułowano wniosek, że metoda wypełniania zamkniętych obszarów konstrukcji mechanicznych pianką poliuretanową w celu poprawienia właściwości dynamicznych urządzenia może być szeroko wykorzystana w praktyce przemysłowej ze względu na wysoką skuteczność oraz ważny aspekt ekonomiczny w postaci niskiej ceny takiego rozwiązania.

Słowa kluczowe: *właściwości dynamiczne, hałas i drgania, teoretyczna i eksperymentalna analiza modalna, pianka poliuretanowa.*

1. Introduction

Vibration can be considered as an undesired phenomenon in mechanical mechanisms as far as it decreases lifetime of the machine, limits its performance, influences other machines in the neighborhood or induces high level of noise. There are some application areas where the latter reason is referred to as the crucial one. All the measures which must be undertaken in those circumstances focus on either identifying and removing the excitation sources or minimizing harmful results of vibration. When it is not possible to change construction of vibrating mechanism and sources of vibration are beyond control the efficient way to improve machine dynamic behavior parameters is to enhance damping properties of the mechanical system. This approach can be realized as active or passive damping. Active damping methods include application of specially designed and adaptively controlled actuators which counteract the vibration motion and use springs of variable rigidity coefficient, viscous dampers with actively controlled internal flow, dampers with non-newton fluids etc. Those solutions are very efficient when well-tuned but expensive and dif-

ficult to be inserted into the existing design. That is why passive ways of vibration damping are the most often applied applications.

To solve the noise and vibration problems and identify the dynamic properties of the mechanical systems new research methods both theoretical and experimental must be applied. In the past three decades, modal analysis has become a major technology in the quest for determining, improving and optimizing dynamic characteristics of engineering structures [6, 8, 12]. It has been successfully applied to solve structural dynamic problems in mechanical [5, 7, 9, 15, 16] and aeronautical [14] engineering. Recently modal analysis has also found its broad applications for civil and building [11] structures, biomechanical and harvest [3] problems, space structures, electrics and electronics [2] acoustical instruments [1], transportation [10] and nuclear plants.

The origin of presented research is the technical problem of the curtain lifting mechanism making too much noise to be applied in a theatre. The mechanisms of scenography changing must work smoothly and quietly during a play otherwise they attract the spectators' attention spoiling the art effect.

2. The object of research

The whole mechanism of a scenography lift consists of an electrical motor combined with a reducing gear box, the cylinder unit with bearings supported in the frame of the machine. The cylinder unit is a welded construction of the shaft, two flanges and the cylinder. The cylinder of 1000 mm long is supported on two flanges which connect it to the main shaft of ca. 1400 mm long. The elements are mutually located by means of the shapes tolerated as normal running fit. The parts of the unit are connected with standard filled welds. The original construction of the cylinder unit is presented in Fig.1.

On the external surface of the cylinder there is an u-groove distributed helicoidally which is designed to guide a rope winding on the cylinder. The whole construction is made of structural steel. The cylindrical surfaces for bearings are ground to obtain required tolerances. The whole unit mass is ca. 160 kg.

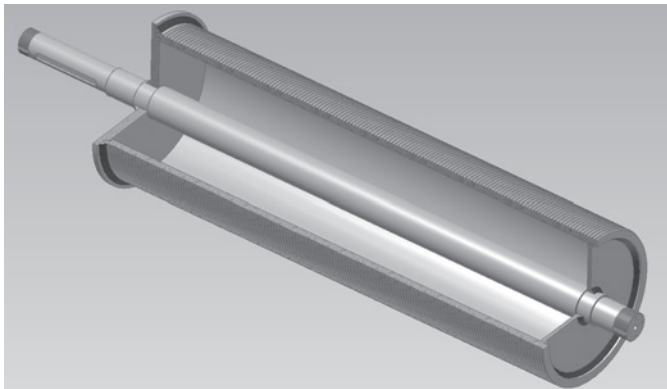


Fig. 1. The original construction of the cylinder unit

The construction presented in Fig.1 is optimal from the strength point of view. However, the hollow region inside the cylinder makes the unit susceptible to dynamic excitation because the cylinder is supported only on both sides without any support along its generating line. That is the reason why the cylinder is prone to vibrating with high amplitude rates which makes loud noise.

3. Problem definition and proposed solution

The analysis of the lifting mechanism and the preliminary experimental noise tests showed the source of the highest sound intensity not around the motor and gear but in the middle of the winding cylinder. It proved that the reason of the noise and vibration is an instability of the mechanical system of the cylinder unit of the machine. That fact had to be verified by thorough theoretical and experimental investigation.

The solution of the vibration minimizing problem had to be easy-applicable and inexpensive because the production of the lifting mechanisms should remain competitive. The solution which was chosen was a passive way of vibration damping by inserting additional material of high damping properties into the existing structure. The large region inside the cylinder seemed to be the best space to insert vibration damping material. It needed creating some inlet hole through which the material should be inserted. The other limitation was the density of the material. The overall mass of the lifting mechanism should not be increased too much because all the construction assumptions and solutions could not be altered. Additionally, the applied material should be incombustible. Considering all those limitations and assumptions the PUR foam of low-expansibility was chosen for further research. That material is of low density (ca. 20kg/m³ after curing) and very good adhesion properties. Its low-expansibility makes that material structure very advantageous for vibration damping because it has small void spaces after curing.

The proposed solution needs to be investigated numerically and experimentally in order to evaluate the influence of the additional material of PUR foam on the dynamic properties of the whole cylinder unit.

4. Theoretical and experimental modal analysis

Modal analysis is the process of determining the inherent dynamic characteristics of a system in forms of natural frequencies, damping factors and mode shapes, and using them to formulate a mathematical model for its dynamic behavior. The formulated mathematical model is referred to as the modal model of the system and the information for the characteristics are known as its modal data [6]. The system must meet several requirements in order to apply the modal analysis method for its examination i.e. it has to be linear, time-invariant and observable and it must obey the Maxwell's reciprocity theorem. These basic prerequisites must be checked and fulfilled prior performing modal analysis test of the system. The modal analysis (MA) can be performed as theoretical, experimental or operational modal analysis. Theoretical MA usually applies Finite Element Method (FEM) to solve dynamic problems of the analyzed structure. The procedures of solving the MA problem are usually implemented in the 3D CAD software systems, which is very convenient because the analyses are performed in the same graphic environment as the design process.

The experimental modal analysis comprises deriving the dynamic properties of analyzed structure by means of experimentally obtained characteristics of input signal - excitation force and corresponding characteristics of vibration response signal of the system (acceleration, velocity or position). The modal identification test is subjected to the prerequisites of the modal analysis method. It returns information in the form which can be applied for further evaluation process in order to achieve the required information on the dynamic properties of the analyzed system. The information can be also applied in the model of the machine when the mathematical form of the obtained characteristics is properly defined. Additionally, the mathematical form of that definition must comply with the actual form of the whole model of analyzed system.

Modal analysis can be considered as transformation of a complex dynamic system into a set of single-degree-of-freedom systems [4, 6]. If the aim of research is to determine frequency of free vibrations of the system, modal analysis can be limited to simple identification modal test for deriving frequency response function (FRF) of the system. FRF is a transfer function and is expressed in frequency domain.

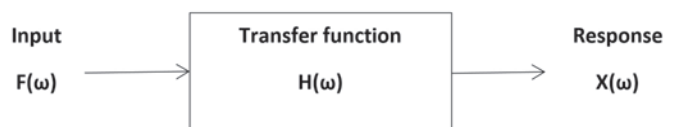


Fig. 2. The linear mechanical system

For the linear system (Fig. 2) the following formula can be expressed – Eq. (1):

$$X(\omega) = H(\omega) \cdot F(\omega) \quad (1)$$

The transfer function $H(\omega)$ is the complex function which is formulated as follows – Eq. (2):

$$H(\omega) = \frac{X(\omega)}{F(\omega)} \quad (2)$$

The FRF reflects dynamic properties of the investigated system. It represents relation between the response of the system (e.g. position, velocity, acceleration) and input force for the certain pair of measurement points of response and excitation. The important feature of the frequency response function is the fact, that it describes dynamic properties of the investigated system regardless the type of excitation signal (harmonic, impulse or random) during measurements. The FRF provides qualitative and quantitative evaluation of the dynamic system resonance of the machine tool [13].

The experimental modal analysis procedure can be performed by single input-single output (SISO) method, single input – multiple outputs (SIMO) or multiple inputs – multiple outputs (MIMO). These methods differ not only in the measurement equipment requirements but also in the required aim of the research and the accuracy of the analysis results.

SISO method is used mainly when only two-channel data acquisition measurement system is available and the resultant FRF can be limited to several point of measurement. It is usually applied when impact hammer test is performed (force input signal and acceleration output signal). The method can be applied as roving hammer (fixed accelerometer) or fixed hammer (roving accelerometer) procedure. In practice the roving hammer procedure is much more convenient because it does not require reinstalling the accelerometer from one point of measurement to another as it is in the fixed hammer procedure. The problems arise with normalizing input signal for every measurement point. Therefore averaging procedure must be introduced.

SIMO method enables application of the harmonic exciter as in input signal generator for simultaneous exciting many points of response measurement. It requires multi-channel data acquisition system and gives more accurate results than SISO method, because the same excitation signal is used for all analyzed response points while performing modal analysis.

MIMO is more hardware-requiring method but it returns much thorough information of the analyzed system than SISO or SIMO method. It is usually applied when the multi-channel data acquisition system is available. The selected input points can be excited with different force characteristics in order to enhance accuracy and efficiency of the modal analysis.

In the further analysis the SISO method was applied because of the limitations of the measurement system which was used.

5. Research method

The theoretical modal analysis was performed in order to obtain modal shapes and their frequencies of the cylinder unit. The 3D CAD software applied in that study is Autodesk Inventor 2015 Professional. In that system the 3D model of all the parts and welded assembly were created. In order to perform the analysis efficiently some simplifications of the analyzed model were applied. They comprised excluding small holes on the surface of the cylinder and the helicoidal groove. The simplifications were applied in order to speed-up the analysis. In the case of small elements modelling the finite elements dimension must be lower and it increases the number of elements, knots and equations to be solved. The simplifications introduced in the model change the dynamic properties of the whole system slightly but not significantly. The elements materials properties were assigned from the Inventor library according to the construction documentation. Subsequently, the boundary conditions of the analysis were defined.

The theoretical modal analysis requires indicating the support of analyzed construction. For the numerical analysis the cylindrical surfaces of bearing contact were defined as fixed support. The assembly analysis requires definition of contacts among the elements of construction. The default contact type is bonded contact of the surfaces which are closer to each other than tolerance of 0.01mm. Considering the real way of connecting elements within the construction the bonded contacts were only applied between every weld and welded element. The other automatically created contacts were discarded in analysis. That method of contact definition reflected the real way of elements connection. The finite elements net was created with default settings (tetrahedrons) of the analytical program.

The experimental modal analysis was performed in order to obtain modal shapes, their frequencies and evaluate magnitude rates of the frequency response functions in the resonances of the cylinder unit structure. The impulse excitation was exerted by means of a modal hammer. The response was measured with an accelerometer. The signals both from the hammer and the accelerometer were acquired and analyzed in the PULSE system. The PULSE LITE system [17] by Brüel&Kjær consists of the measurement module 3560L, the FFT analysis software, the accelerometer 4514 [18] and the modal hammer 8206-003 [19].

The points of input (excitation) and response (acceleration) measurement were chosen on the cylinder and the shaft in one plane because the whole construction is axially symmetrical. The accelerometer was placed in the middle of the cylinder length for in that point one can expect the highest rates of vibration amplitude. The sensor was mounted on the cylinder with the bee wax, which is reported to as one of the best way of connecting the accelerometer to the measured surface [13].

In the case of noise in the output signal the H1 estimator of FRF [13] is applied the value of which approaches the real FRF with the growing number of measurement repetitions. The H1 estimator is equal to the cross spectrum, between the response and force, divided by the autospectrum of the force. The H1 estimator minimizes the output noise effect. That is why 3 repetitions of every measurement were applied in the experimental test procedure.

6. Results of research

Numerical simulations were performed in the Simulation module of Autodesk Inventor 2015 Professional system. Firstly, the original welded construction of the cylinder unit was examined (Fig.1). The first 20 modes of the hollow unit were investigated. The results obtained in simulation are presented in Table 1.

The modes obtained in numerical simulation are multiplied because analytical software recognizes modes of the same shape distributed in different planes of symmetry. Therefore modes No 3 and 4 are the same modes in two perpendicular planes respectively. The same situation is in the case of the following pairs: 5 and 6, 7 and 8, 9 and 10 etc. From the noise point of view the modes presented in the figures 3, 4 and 5 are of particular interest. These mode shapes can be strong sources of noise. The other shapes refer to the shaft modes which vibrates inside the cylinder.

The legend on the side of graph shows the displacements of the analyzed elements deformed during vibration of certain mode and frequency but it should be noted that these values are introduced into simulation only for comparing purposes. They do not represent real

Table 1. Frequencies of the first 20 modes of the hollow cylinder unit

Mode N°	1	2	3	4	5	6	7	8	9	10
Frequency [Hz]	191,58	243,31	247,01	247,08	520,23	520,31	649,62	649,82	667,17	667,48
Mode N°	11	12	13	14	15	16	17	18	19	20
Frequency [Hz]	772,38	785,29	1079,32	1083,96	1102,46	1103,95	1277,07	1278,87	1450,98	1508,05

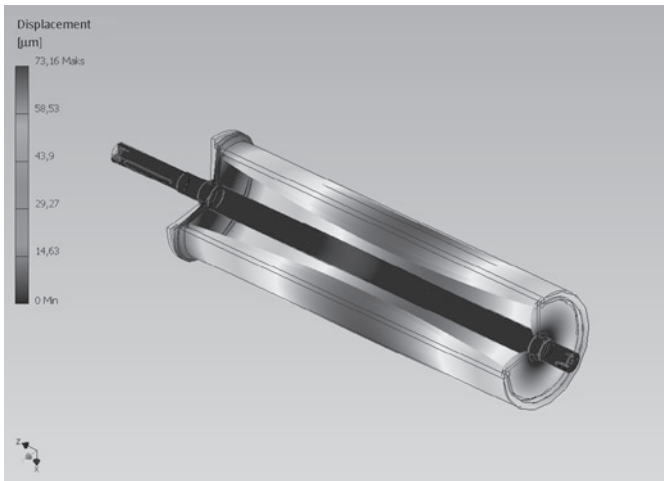


Fig. 3. The 6th mode of the cylinder unit (520 Hz)

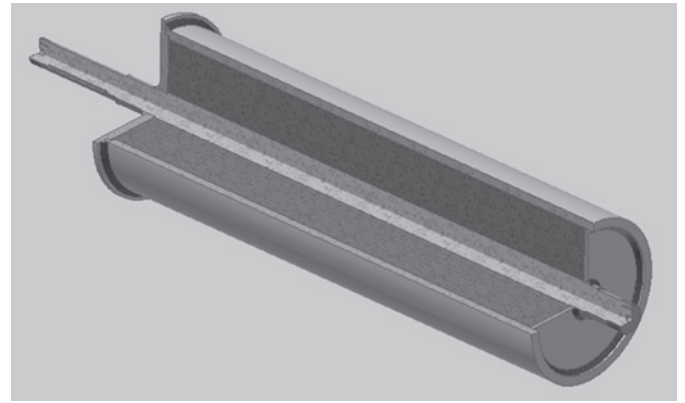


Fig. 6. The modified construction of the cylinder unit

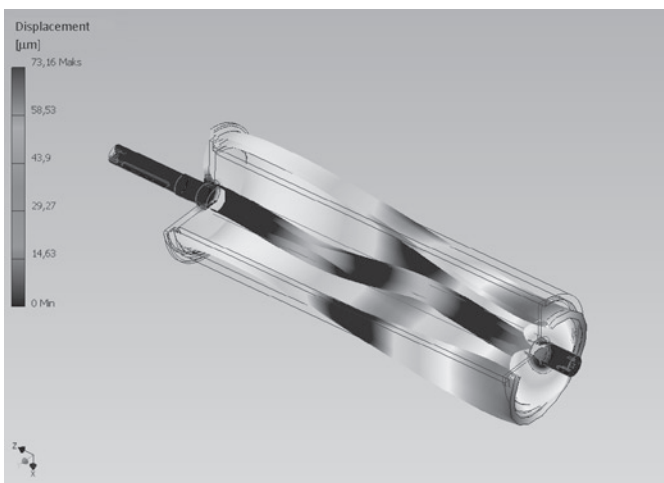


Fig. 4. The 15th mode of the cylinder unit (1102 Hz)

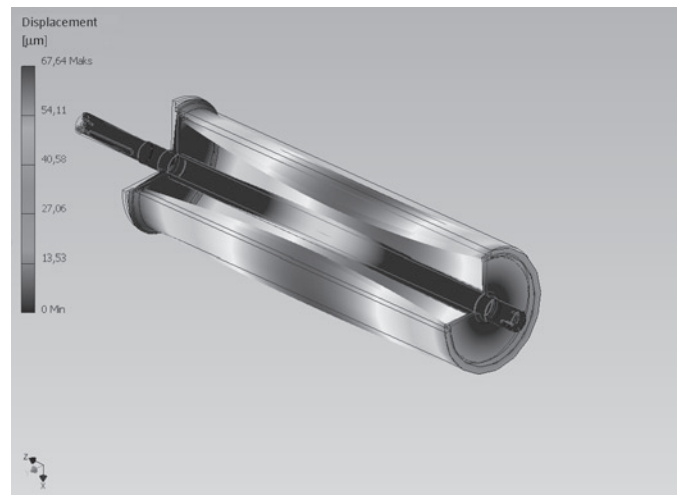


Fig. 7. The 6th mode of the cylinder unit (560 Hz)

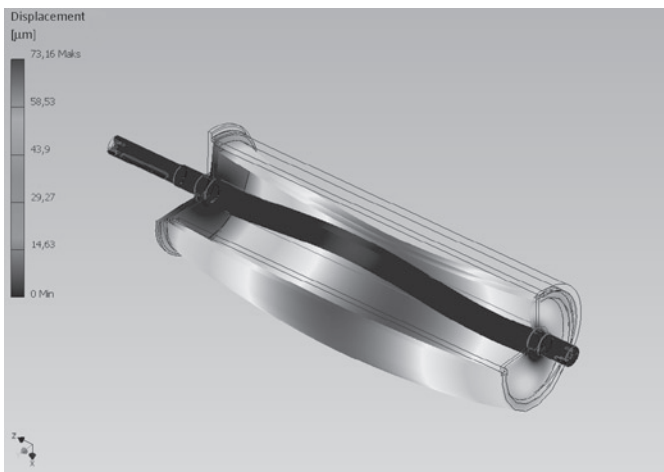


Fig. 5. The 19th mode of the cylinder unit (1451 Hz)

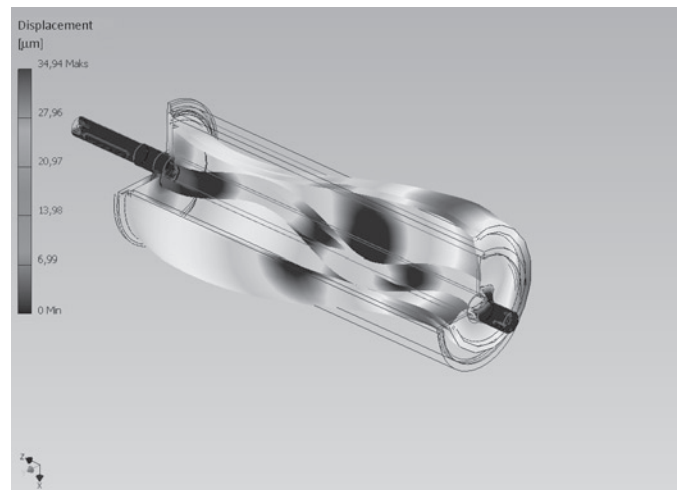


Fig. 8. The 15th mode of the cylinder unit (1230 Hz)

Table 2. Frequencies of the first 20 modes of the modified cylinder unit

Mode N°	1	2	3	4	5	6	7	8	9	10
Frequency [Hz]	294,43	294,51	300,90	358,31	557,62	560,00	695,12	704,57	705,36	735,48
Mode N°	11	12	13	14	15	16	17	18	19	20
Frequency [Hz]	773,27	783,97	1155,58	1226,01	1230,00	1309,49	1309,61	1420,84	1480,59	1500,36

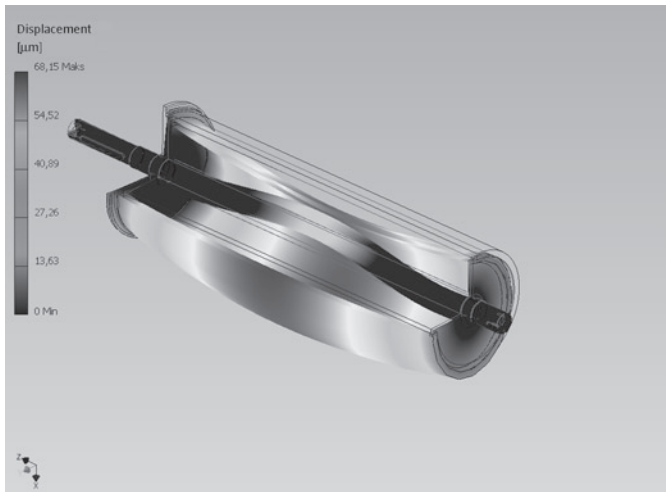


Fig. 9. The 19th mode of the cylinder unit (1481 Hz)

deflections of the elements but reflect damping capabilities of the mechanical system when comparing one boundary situation or construction to another.

Having performed simulations of the original cylinder unit the modification of its constructions was created. The inside of the cylinder element was filled with material of PUR foam (Fig. 6). The material was supposed to be inserted by a hole of about 20mm diameter in one flange of the unit. The hole was not modelled in analytical software because it is insignificant for simulation results.

To perform simulation the model of the PUR foam material had to be introduced into Autodesk Inventor Material Library. The parameters of the PUR foam material were obtained from the producer sources and implemented into the Library. Due to the fact that the PUR foam sticks to the metal surfaces strongly the contacts of the material with the steel elements of the unit were taken into consideration and modelled as bonded contacts.

The results obtained with the same boundary conditions are presented in Table 2.

The frequencies for the corresponding modes of the filled cylinder unit are slightly higher than those of the hollow unit. It is a result of adding lightweight material of considerable stiffness. The modes presented in Fig. 7, 8 and 9 are similar to the corresponding modes of the hollow unit shown in Fig. 3, 4 and 5.

Analyzing the maximum deflection values (the legend in Fig. 3, 4, 5, 7, 8 and 9) it can be noted that for the presented modes the rate of deflection for modified construction of the cylinder unit is lower than for hollow cylinder unit.

The numerical modal analysis gave promising results which indicate that it is possible to obtain good results in reality. It is experimental modal analysis which can fully justify the modification of the construction and support the thesis of achieving significantly higher

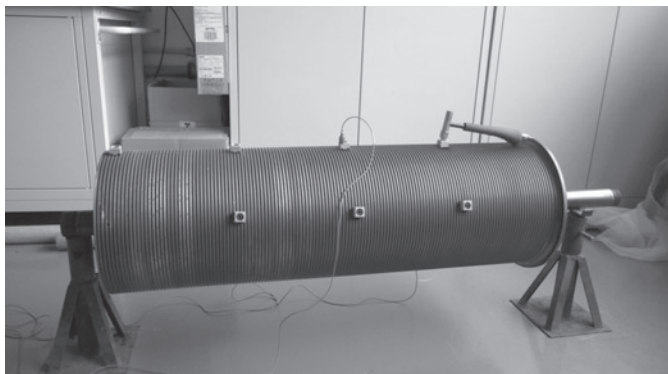


Fig. 10. The modal test rig of the cylinder unit

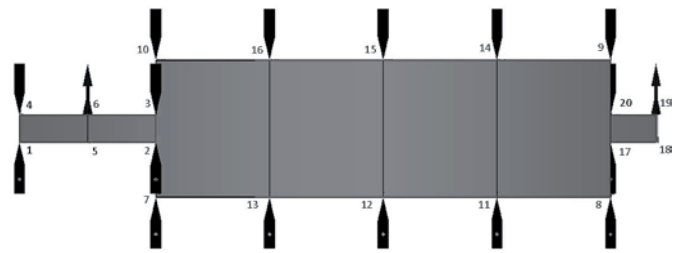


Fig. 11. The measurement points distribution

rates of structural damping by applying PUR foam filling of the hollow regions of the construction which will solve the problem of too much noise of the cylinder unit.

Experimental modal analysis was performed on the test rig presented in Fig. 10. The cylinder unit was supported in two holders in the places where the unit is normally supported in the whole construction of the lift. The way of supporting was not the same as in target construction because not the whole cylindrical surfaces are fixed. Nevertheless the mass of the whole unit is so high that it should influence obtained results insignificantly.

The response accelerometer was placed in the middle of the cylinder generating line. The hammer impact points were distributed evenly along the generating line symmetrically on both sides of the cylinder in one plane. The measurement points distribution is presented in Fig. 11. The impact points are indicated with black hammer symbols, the supporting points are indicated with arrows and the response accelerometer is placed in point number 15.

The hollow cylinder unit was analyzed modally three times. All the attempts gave similar results of the structural vibration properties of the cylinder unit system. The analysis showed that there are three main modes which are dominant for the whole unit construction. The magnitude of FRF H1 estimate for the point situated opposite the response accelerometer for the hollow cylinder unit is presented in Fig. 12.

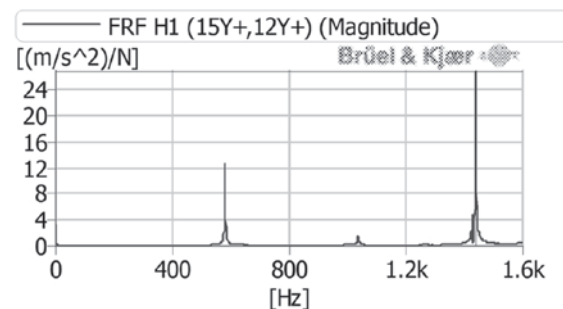


Fig. 12. The magnitude of FRF H1 spectrum of the hollow cylinder unit

The resultant frequencies and H1 magnitudes of three main modes are as follows:

- The first mode $f=580$ [Hz] $|H1|=12.61$ [$m/s^2/N$],
- The second mode $f=1035$ [Hz] $|H1|=1.49$ [$m/s^2/N$],
- The third mode $f=1439$ [Hz] $|H1|=26.83$ [$m/s^2/N$].

The graphical form of the modes are presented in Fig. 13, 14 and 15.

After filling the cylinder with PUR foam and curing time of one day the analysis was performed again in the same arrangements of impact and response points.

The magnitude of FRF H1 estimate for the point situated opposite the response accelerometer is presented in Fig. 16.

The results obtained after modal analysis are as follows:

- The first mode $f=577$ [Hz] $|H1|=3.51$ [$m/s^2/N$],
- The second mode $f=1038$ [Hz] $|H1|=0.70$ [$m/s^2/N$],
- The third mode $f=1436$ [Hz] $|H1|=2.35$ [$m/s^2/N$].

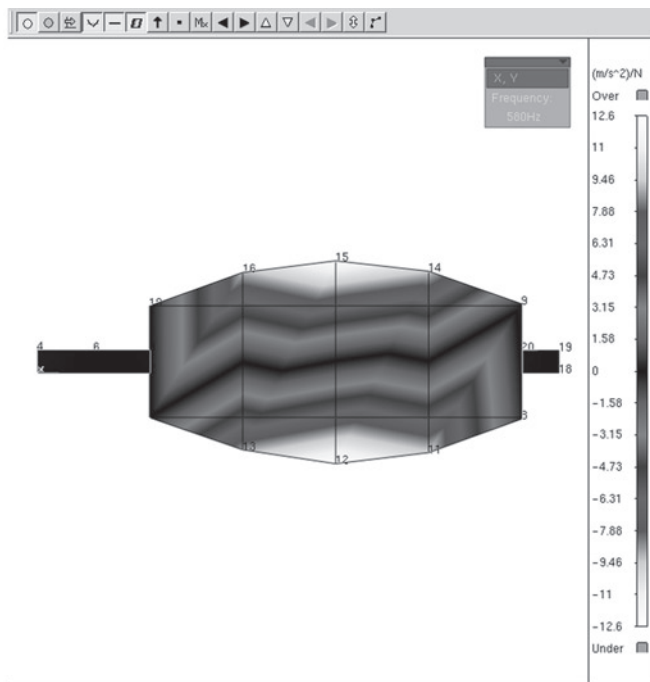


Fig. 13. The first mode of the hollow cylinder unit

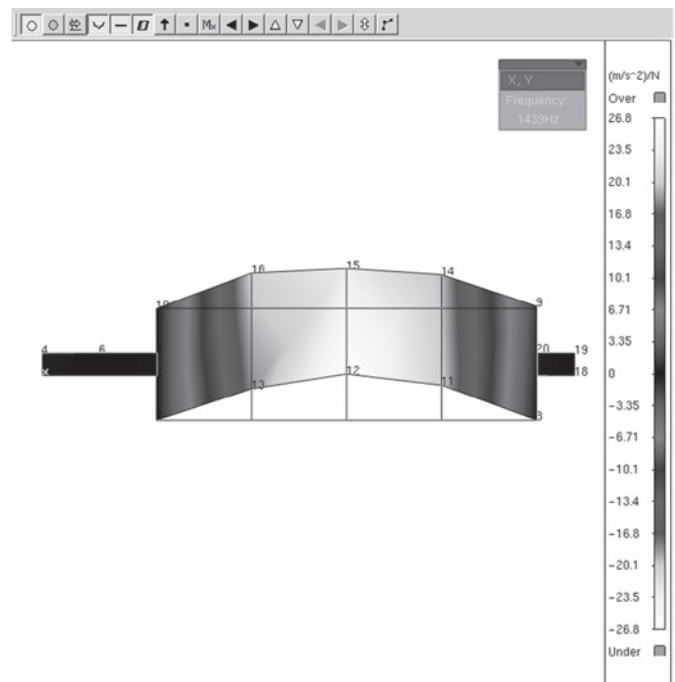


Fig. 15. The third mode of the hollow cylinder unit

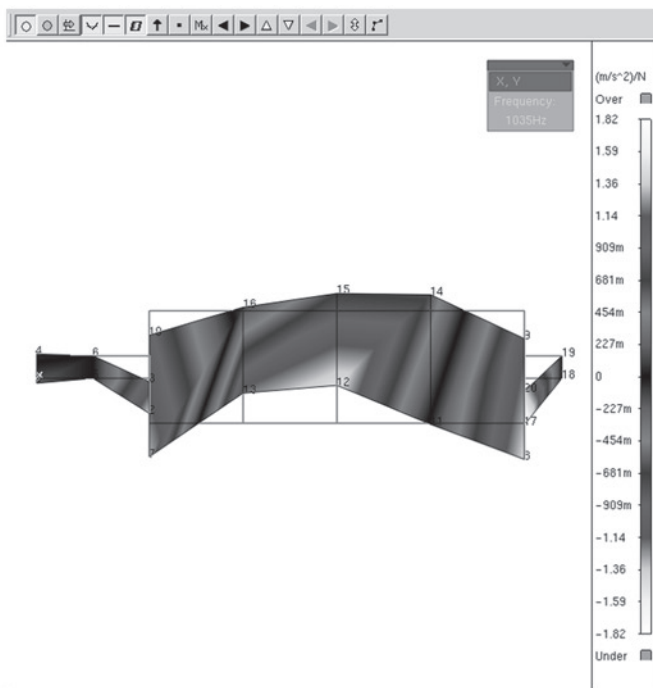


Fig. 14. The second mode of the hollow cylinder unit

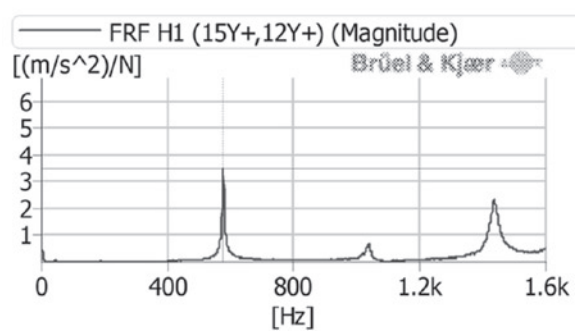


Fig. 16. The magnitude of FRF H1 spectrum of the PUR foam filled cylinder unit

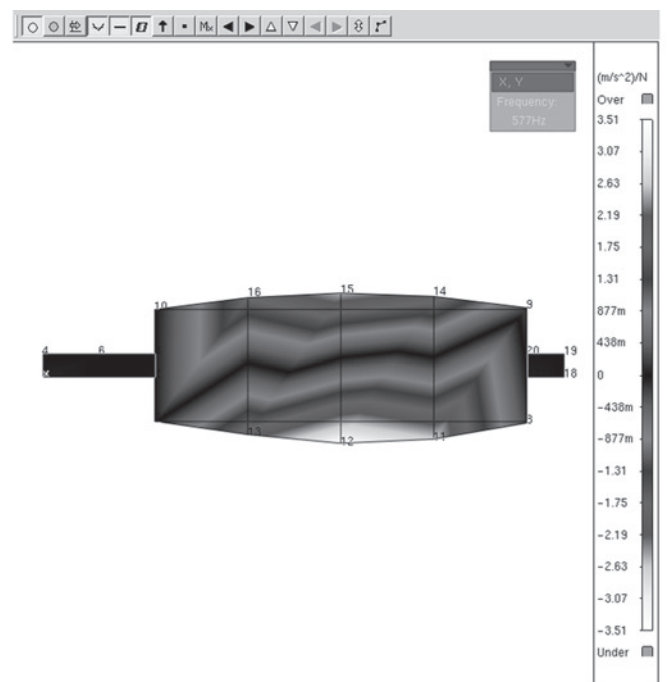


Fig. 17. The first mode of the filled cylinder unit

The graphical form of the modes are presented in Fig. 17, 18 and 19.

The results of magnitude of FRF H1 of the hollow and filled cylinder unit are presented in Fig. 20.

The procedure of experimental modal analysis was repeated on the next day, after two days of foam curing. The results which were obtained after two days of curing fully correspond to those after one day, which proved that curing time of one day is sufficient to obtain result of structural damping properties enhancement.

The results (Fig. 20) show that the filled cylinder unit vibrates less intensively than it can be noted in the case of the hollow cylinder unit. During experimental part of the research it could be heard by ear that

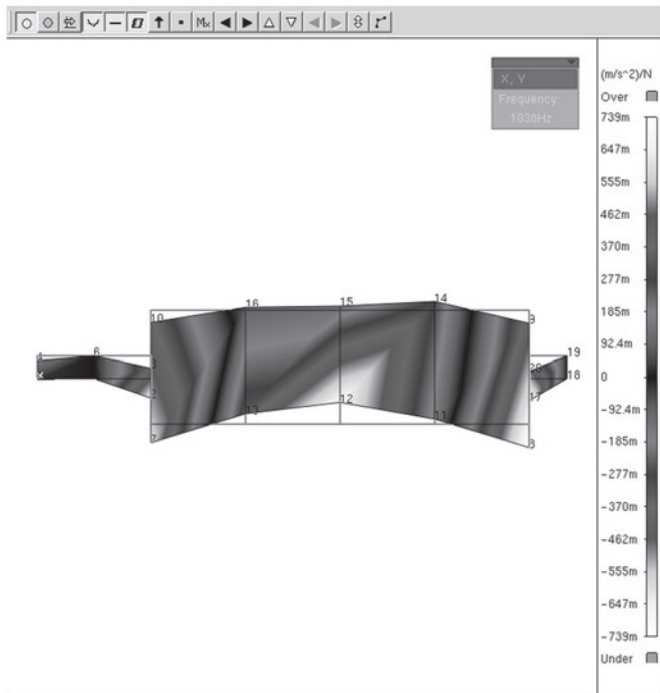


Fig. 18. The second mode of the filled cylinder unit

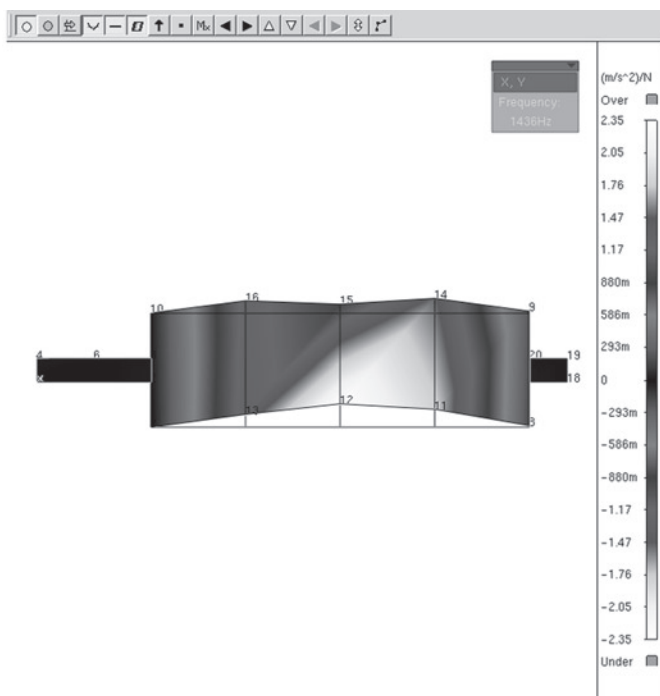


Fig. 19. The third mode of the filled cylinder unit

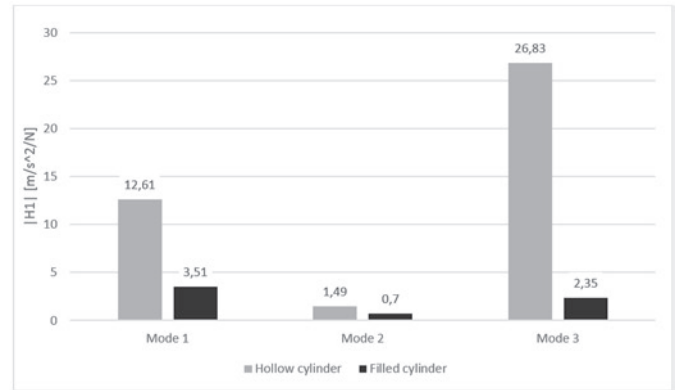


Fig. 20. The magnitude of FRF H1 of the hollow and filled cylinder unit

the impacts sounded muffled after filling the cylinder with PUR foam. The experimental modal results fully supported the sensual effects.

7. Conclusions

The results obtained in numerical and experimental modal analysis showed that filling the cylinder with PUR foam of low-expansibility appeared to be very efficient solution for noise and vibration problem of the cylinder unit of lift mechanism. The method of PUR foam application seems to be very easy to perform and low-cost soundproofing method.

Both numerical and experimental modal analysis procedures applied in that case fully supported the thesis of the enhancing the construction damping capabilities by inserting the material of PUR foam of low-expansibility into the hollow regions of resonant structure. The results of the research are of great value for the cylinder manufacturer making his product competitive and high-quality with only a slight additional workload and cost.

Acknowledgement:

The paper was supported in part by the project MŠMT EUREKA CZ LF13009, E!6727 and by the project LO1201 obtained through the financial support of the Ministry of Education, Youth and Sports of Czech Republic in the framework of the targeted support of the "National Programme for Sustainability I" and the OPR&DI project Centre for Nanomaterials, Advanced Technologies and Innovation CZ.1.05/2.1.00/01.0005.

References

1. Chomette, B., and Carrou, J-L., Operational Modal Analysis Applied to the Concert Harp. Mechanical Systems and Signal Processing 2015: 81-91, <http://dx.doi.org/10.1016/j.ymssp.2014.10.011>.
2. Brecher, Ch., Baumler, S., and Guralnik, A. Experimental Modal Analysis Using a Tracking Interferometer. CIRP Annals – Manufacturing Technology 2014: 345-348.
3. Ebrahimi, R., Esfahanian, M., and Ziaei-Rad, S. Vibration Modeling and Modification of Cutting Platform in a Harvest Combine by Means of Operational Modal Analysis (OMA). Measurement 2013: 3959-3967, <http://dx.doi.org/10.1016/j.measurement.2013.07.037>.
4. Ewins, D.J. Modal Testing: Theory and Practice. Research Studies Press, 2nd edition, UK, 2000.
5. Gagnol, V., Le, T.P., and Ray, P. Modal Identification of Spindle-tool Unit in High-speed Machining. Mechanical Systems and Signal Processing 2011: 238-239, <http://dx.doi.org/10.1016/j.ymssp.2011.02.019>.

6. He, J., and Fu, Z., Modal Analysis. Butterworth-Heinemann, 2001.
7. Li, B., Cai, H., Mao, X., Huang, J., and Luo, B., Estimation of CNC Machine Tool Dynamic Parameters Based on Random Cutting Excitation Through Operational Modal Analysis. *International Journal of Machine Tools & Manufacture* 2013: 26-40, <http://dx.doi.org/10.1016/j.ijmachtools.2013.04.001>.
8. Kęcik K., Rusinek R., and Warminski J., Modelling of high-speed milling process with frictional effect. *Journal of Multi-body Dynamics, Proceedings of the Institution of Mechanical Engineers Part K*, 2013; 1(1): 3-11, doi:10.1177/1464419312458636.
9. Matsuo, M., Yasui, T., Inamura, T., and Matsumura, M. High-speed Test of Thermal Effects for a Machine Tool Structure Based on Modal Analysis. *Precision Engineering* 1986: 72-78, [http://dx.doi.org/10.1016/0141-6359\(86\)90089-9](http://dx.doi.org/10.1016/0141-6359(86)90089-9).
10. Nangolo, N.F., Soukup, J., Rychlikova, L., and Skocilas, J. A Combined Numerical and Modal Analysis on Vertical Vibration Response of Railway Vehicle. *Procedia Engineering* 2014: 310-319, <http://dx.doi.org/10.1016/j.proeng.2014.12.136>.
11. Rahmatalla, S., Hudson, K., Liu, Y., and Eun, H.Ch. Finite Element Modal Analysis and Vibration-waveforms in Health Inspection of Old Bridges. *Finite Elements in Analysis and Design*, 2014: 40-46, <http://dx.doi.org/10.1016/j.finel.2013.09.006>.
12. Rusinek R., Stability criterion for aluminium alloy milling expressed by recurrence plot measures. *Proceedings of the Institution of Mechanical Engineers, Part B, Journal of Engineering Manufacture* 2012; 226 (12): 1976-1985, <http://dx.doi.org/10.1177/0954405412462779>.
13. Uhl T. Komputerowo wspomagana identyfikacja modeli konstrukcji mechanicznych. Warszawa: WNT, 1997.
14. Vivo, A., Brutti, C., and Leofanti, J. Modal Shape Identification of Large Structure Exposed to Wind Excitation by Operational Modal Analysis Technique. *Mechanical Systems and Signal Processing* 2013: 195-206, <http://dx.doi.org/10.1016/j.ymssp.2013.03.025>.
15. Zaghbani, I., and Songmene, V. Estimation of Machine Tool Dynamic Parameters During Machining Operation Through Operational Modal Analysis. *International Journal of Machine Tools & Manufacture* 2009: 947-957, <http://dx.doi.org/10.1016/j.ijmachtools.2009.06.010>.
16. Zhang, G.P., Huang, Y.M., Shi, W.H., and Fu, W.P. Predicting Dynamic Behaviours of a Whole Machine Tool Structure Based on Computer-aided Engineering. *International Journal of Machine Tools & Manufacture* 2003: 699-706, [http://dx.doi.org/10.1016/S0890-6955\(03\)00026-9](http://dx.doi.org/10.1016/S0890-6955(03)00026-9).
17. Product Data. Pocket Front-end, Type 3560 L, PULSE Lite Software, Types 7781, 7782, 7783. Brüel&Kjær, 2005.
18. Product Data. DeltaTron® Accelerometers, Types 4514, 4514-001, 4514-002, 4514-004, 4514-B, 4514-B-001, 4514-B-002 and 4514-B-004. Brüel&Kjær, 2006.
19. Product Data. Impact Hammers - Types 8206, 8206-001, 8206-002 and 8206-003. Brüel&Kjær, 2006.

Witold PAWLOWSKI

Institute of Machine Tools and Production Engineering
Lodz University of Technology
ul. Stefanowskiego 1/15, 90-924 Lodz, Poland

Lukasz KACZMAREK

Institute of Material Science and Engineering
Lodz University of Technology
ul. Stefanowskiego 1/15, 90-924 Lodz, Poland

Petr LOUDA

Institute for Nanomaterials, Advanced Technologies and Innovation
Technical University of Liberec
Bendlova 1407/7, 461-17 Liberec 1, Czech Republic

E-mails: witold.pawlowski@p.lodz.pl, lukasz.kaczmarek@p.lodz.pl,
petr.louda@tul.cz

Andrzej ŻUCHOWSKI

ANALYSIS OF THE INFLUENCE OF THE IMPACT SPEED ON THE RISK OF INJURY OF THE DRIVER AND FRONT PASSENGER OF A PASSENGER CAR

OCENA WPŁYWU PRĘDKOŚCI ZDERZENIA NA RYZYKO OBRAŻEŃ KIEROWCY I PASAŻERA SAMOCHODU OSOBOWEGO*

The subject of the analysis was the influence of the speed, at which a personal car hit an obstacle, on the risk of injury of the driver and the passenger sitting in the front seat. With this goal in mind, several hundred of crash tests were analysed, published on the Internet by National Highway Traffic Safety Administration (USA). The analysis focuses on the cases involving a frontal impact of the car on a rigid barrier. For the purpose of assessing the forces acting on a dummy, Head Injury Criterion (HIC_{36}) and Chest Acceleration (C_{Acc}), were applied, calculated on the basis of the resulting acceleration of head and chest of the dummy. Separate analyses were performed for the forces acting on the dummy representing 50-centile man (M50) and 5-centile woman (F5). A statistical analysis of the results of the crash tests was performed in order to determine the typical values of HIC_{36} and C_{Acc} factors, as well as the risk of severe injury of the driver and the passenger at a given collision speed. The risk of injury was calculated on the basis of provided in the research literature so-called injury risk curves. It was determined that increasing the speed at which a car hits an obstacle from 25 km/h up to 56 km/h results in the increase in the risk of severe injury (AIS4) of the driver and the passenger from 2 to 10%. Some functions were proposed, describing the relation between the risk of injury and the velocity of collision.

Keywords: road accidents, crash tests, impact speed, risk of injury.

Rozważono wpływ prędkości uderzenia samochodu osobowego w przeszkodę na ryzyko obrażeń kierowcy oraz pasażera na przednim fotelu. W tym celu wykorzystano wyniki kilkuset testów zderzeniowych, udostępnionych w Internecie przez National Highway Traffic Safety Administration (USA). Uwagę skupiono na czołowe uderzenie samochodu w sztywną barierę. Podczas oceny obciążeń manekinów wykorzystano wskaźniki obrażeń głowy HIC_{36} oraz torsu C_{Acc} , które oblicza się na podstawie wypadkowego przyspieszenia działającego na głowę i tors manekina. Oddzielnie rozważono obciążenia manekina reprezentującego 50-centylowego mężczyznę (M50) oraz 5-centylową kobietę (F5). Przeprowadzono statystyczną ocenę wyników testów zderzeniowych, której celem było określenie dominujących wartości wskaźników HIC_{36} i C_{Acc} oraz ryzyka ciężkich obrażeń kierowcy i pasażera przy danej prędkości zderzenia. Ryzyko obrażeń obliczono na podstawie dostępnych w literaturze tzw. funkcji ryzyka obrażeń. Ustalono, że zwiększenie prędkości uderzenia samochodu w przeszkodę z 25 km/h do 56 km/h zwiększa ryzyko ciężkich obrażeń (AIS4) kierowcy i pasażera z 2 do 10%. Zaproponowano funkcje wiążące ryzyko obrażeń i prędkość zderzenia.

Słowa kluczowe: wypadki drogowe, testy zderzeniowe, prędkość zderzenia, ryzyko obrażeń.

1. Introduction

Speed is a basic operating parameter of a car, taken into account while designing roads and streets, determining the total time of the journey but also the risk of a traffic accident and the severity of its possible results. Legal provisions setting limits to the speed are a common solution to the problem of the abovementioned danger. However, this solution is often inefficient because many drivers violate the limits. In the European Union, 40-50% of the drivers exceed the speed limit on a given stretch of the road, with 10-20% of drivers driving at 10 km/h or more above the limit [22]. As the research conducted in Poland in 2013-2014 indicate, about 30% of the drivers drive at more than 10 km/h above the speed limit [2]. Improving the measures of supervision results in the decreasing share of the accidents caused by the excessive speed is in the last couple of years, from 31% in 2007 to 26% in 2014. With regard to the number of fatalities it is a change from 47% to 39%.

When setting the speed limit and deciding on the measures of supervision to be applied, many factors are taken into account, connected with the road geometry and its visibility, the condition of the surface, intensity and structure of the traffic among others. Another important issue is the influence of the speed on the results of the acci-

dents [5, 21]. Event data recorders (EDR), which are gaining popularity among car users, make it easier to examine the relations between the velocity of the collision and the injury to the occupants of the vehicle [3, 4, 8, 9]. However, determining the possible injuries on the basis of the measured forces acting on a dummy during a crash test is still a difficult task.

Normative requirements regarding crash tests of the cars usually specify one value of test speed (e.g. ECE UN Regulations No 44, 80, 94 and 95). The results of laboratory tests, assessing the influence of the collision speed on the forces acting on the occupants of the vehicle are rarely published, the apparent reason being the costs of this kind of research. On order to limit the costs, the tests are sometimes conducted with one and the same car hitting the obstacle at several different values of speed. For example, paper [14] presents the results of the research on the forces acting on the driver of a SUV car at the velocity 4, 10 and 43 km/h, and in paper [20] the results are described of a bus at 4, 7 and 30 km/h. The results of model tests are published more often. Papers [10, 12] describe analyses of the forces acting on the model dummies at 70-90 km/h, which is much more than in the case of typical crash tests (30-64 km/h). The results of the research on the influence of the car collision speed on the other variables are used

(*) Tekst artykułu w polskiej wersji językowej dostępny w elektronicznym wydaniu kwartalnika na stronie www.ein.org.pl

to assess to test the effectiveness of passive safety devices, but also to model the injuries of the driver for the purpose of activating eCall system (automatic notification of the accident) [12] or to assess the costs of traffic accidents [10].

The purpose of the paper is to discuss the assessment of the influence of the car collision speed on the dynamic load on the driver and the passenger sitting in the front seat, in the case of a car hitting a rigid barrier. This kind of tests is used to assess the risk of injury of the occupants of the vehicle. The risk was calculated on the basis of so-called *injury risk curves* presented in the research literature, functions which take into account the forces acting on the head and the chest of the dummies. The analysis involves the results of the crash tests published on the Internet by *National Highway Traffic Safety Administration* [24]. The results of the assessment of the risk of injury, performed on the basis of the laboratory tests, are applied to the data on the car accidents. The work was aimed at identifying the vehicle design and operation factors that are decisive for the loads on vehicle passengers during a road accident and for the necessity of reducing the loads to a minimum.

2. Collision speed and the results of the car accident

The results of a traffic accident depend on a variety of factors connected with the variables of movement and the kind of the vehicle, properties of the road and its surroundings (type of the obstacle) and the human factors (anthropometric features, age, health). The main parameters taken into account are the speed at which the vehicle hits the obstacle (or another car), the direction of impact (frontal, side) or the type of the protective devices used in the car. Another important features include the weight and height of the occupant of the car, his or her place in the car, and position on the seat [15, 25, 28]. A number of tests indicate that the effectiveness of the protective devices depends on the manner of use (e.g. proper positioning and tension of the seat belt, proper infant restraint) [29]. This is why the assessment of the influence of the impact speed (which is one of the many operating factors) on the results of the collision requires that the other factors are constant throughout the tests.

In the assessment of the injuries during the traffic accidents, a six-degree scale called AIS (*Abbreviated Injury Scale*) is often used, where specific kinds of injuries were assigned a certain level, expressed as a number. The higher the number, the greater the threat to life. For example, AIS3+ denotes injuries of AIS3 degree or higher. *Maximum AIS Scale* (MAIS) is used to describe the condition of the injured with multiple injuries [17].

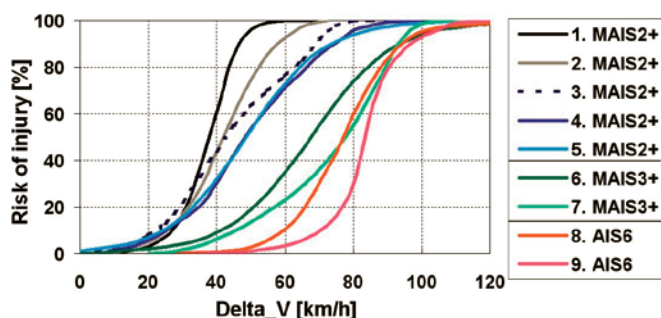


Fig. 1. Risk of injury of the driver and the passenger on the front seat during a frontal impact (the lines are described in Table 1)

Table 1. Data on the accidents involved in the assessment of injury risk presented in Figure 1

Number of line on Fig. 1	Degree of injury	Number of the injured	Impact type	Country	Source
1	MAIS2+	11 (D+FP)*	C-T	Sweden	[18]
2		55 (D+FP)		Sweden	
3		30 men and 12 women (D)	C-C	Australia	[9]
4		64 (D+FP)		Sweden	[8]
5	MAIS3+	145 (D+FP)	C-C (88%), C-O (12%)	USA	[4]
6		15 (D+FP)		Sweden	[8]
7	AIS6	64 (D)	C-C	Great Britain	[16]
8		no data		Sweden	[23]
9					

*) D – driver, FP – passenger on the front seat

On the basis of the analysis of the data on the traffic accidents, statistical models are developed, making it possible to assess the influence of the impact speed on the risk of injury of the occupants of the vehicle. On the basis of several research papers from 2003-2012 [4, 8, 9, 16, 18, 23], injury risk curves were calculated for the occupants of the vehicle (logistic regression), presented in Figure 1, regarding the cases of frontal impact (overlap above 25%, impact angle within $\pm 30^\circ$). The lines on the chart denote the risk of MAIS2+, MAIS3+ and AIS6 injury, the last one being a fatal injury. The injuries are classified as MAIS2 in case of e.g. concussion with a loss of consciousness, jaw or basal skull fracture, lung or heart contusion, fracture of 4 and more ribs at one side [12, 17, 21]. Some data on the accidents involved in the analysis presented in Figure 1 are presented in Table 1. The data consider the driver and the passenger on the front seat (men and women in various age), with their seatbelts fastened, during a frontal impact of a passenger car, respectively: with another personal car (C-C) with a truck (C-T), or with an obstacle (C-O).

The change in vehicle velocity over the duration of the crash event ΔV was determined on the basis of the data from the devices recording the variables of the movement of the cars (CPR – *Crash Pulse Recorder*, EDR – *Event Data Recorder*), mounted in some cars even since 1992 [9]. During a frontal crash impact involving two cars, A and B, moving at V_A and V_B speed, respectively, the change in vehicle velocity depends on their mass, m_A and m_B , respectively, according to the principle of the conservation of linear momentum [21].

$$\begin{aligned}\Delta V_A &= (V_A + V_B) \cdot m_B / (m_A + m_B) \\ \Delta V_B &= (V_A + V_B) \cdot m_A / (m_A + m_B)\end{aligned}\quad (1)$$

Assuming that the duration of the impact phase is the same for both of the vehicles (about 0.1–0.2 s), ΔV determines the deceleration of a car, which in turn determines the value of inertial forces acting on the car and its occupants, therefore determining the severity of the crash. As we can infer from (1), the deceleration is higher in the case of lighter cars. If the weight of the cars is equal, $\Delta V_A = \Delta V_B = 0.5 \cdot (V_A + V_B)$. If a car hits a stationary, non-deformable obstacle, at speed V , $\Delta V \approx V$.

The results presented in Figure 1 confirm that there is a strong dependency between the risk of injuries and ΔV . As for MAIS2+ injuries, it was proved that a frontal impact involving a passenger car and a lorry is more dangerous, than in case of the same type of impact involving two passenger cars (lines no 1 and 2). Important observations include:

- quite a high difference between the shape of the lines referring to a given degree of injuries (with the exception of lines 4 and 5, where the functions of MAIS2+ risk, determined on the basis of research on the accidents in Sweden and USA, are similar);
- risk lines 6 and 7 (MAIS3+) are quite close to lines 8 and 9 (AIS6), that is in the place where the lines are expected regarding AIS4 and AIS5 injuries;
- similarities between lines 7 and 8 when $\Delta t_{V>70}$ km/h, despite the fact that the lines refer to different degrees of injury (MAIS3+ and AIS6).

These results show that it is difficult to develop a function (model) that would describe the dependence of the risk of injuries on the speed of collision, and the small number of accidents (Table 1) results in a low statistical representativeness of those functions. The confidence intervals for some of the abovementioned risk functions are presented in [4, 16].

The differences in the risk lines presented in Figure 1, referring to the same degree of injury, may result from the factors other than the abovementioned criteria of similarity of accidents. For example, the accidents analysed include cars manufactured in different years, and therefore with different passive safety systems. We know that all the people injured had their seatbelts fastened but there is no information on the construction of those belts (lock tensioners, force limiters), which has a very significant effect on the forces acting on the person protected and therefore on the injuries [27]. The age and the anthropometric features of the driver and of the passenger are also important [3, 13].

3. Indicators of the risk of injury

The injuries of the driver and the passengers during a traffic accident are caused by dynamic loads, resulting by stopping the car suddenly. The loads are measured in the crash tests usually as accelerations and forces acting on the various parts of the dummy. Further analysis focuses on the acceleration of the head and the chest (torso) of the dummies, representing a 50-centile man (M50) and a 5-centile woman (F5). Two indicators are applied:

- HIC_{36} , Head Injury Criterion, calculated for a time interval of up to 15 ms;
- C_{Acc} , maximum resultant torso acceleration [g], acting for a period of at least 3 ms.

HIC_{36} indicator is calculated on the basis of the acceleration of the head and time of the acceleration [1, 21]:

$$HIC_{36} = \max \left[\frac{1}{(t_2 - t_1)} \int_{t_1}^{t_2} a_H(t) dt \right]^{2,5} \cdot (t_2 - t_1) \quad (2)$$

where:

$a_H(t)$ – resultant acceleration of the centre of the head [g] (CFC100 filtration), calculated on the basis of the component accelerations, measured in three mutually perpendicular directions;
 $\Delta t = t_2 - t_1 \leq 0.036$ s – length of time [s] with the highest values of $a_H(t)$.

C_{Acc} indicator is calculated from the resultant chest acceleration $a_C(t)$, while its components, measured in three mutually perpendicular directions, were filtered with CFC180 [1]. Figure 2 presents an exemplary resultant acceleration of head and chest. The blue lines denote

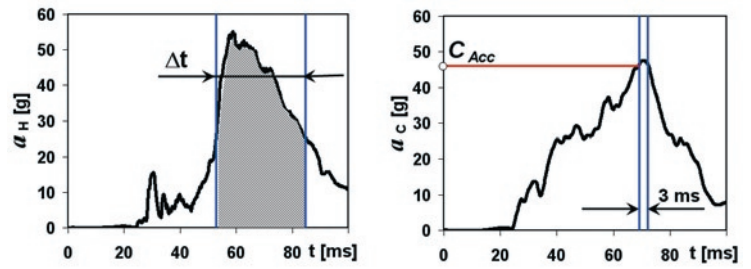


Fig. 2. Resultant acceleration of the head and chest of the dummy (example)

the time span where the indicators are calculated. The hatched area under $a_H(t)$ line denotes the integral of the expression (2).

The values of HIC_{36} and C_{Acc} indicators are used to calculate the risk (probability) of injuries of the head and chest. Injury risk curves for severe injuries (AIS4+) of the head and chest [1, 11, 25] were applied:

$$P_{head}(AIS4+) = \{1 + \exp[5,02 - 0,00351 \cdot HIC_{36}]\}^{-1} \quad (3)$$

$$P_{chest}(AIS4+) = \{1 + \exp[5,55 - 0,0693 \cdot C_{Acc}]\}^{-1} \quad (4)$$

Risk curves are presented in Figure 3, denoting the risk in percentage. The limit values for M50 and F5 dummies are, respectively, $HIC_{36} = 1000$ i $C_{Acc} = 60$ g [1, 21]. The risk of severe injury AIS4+

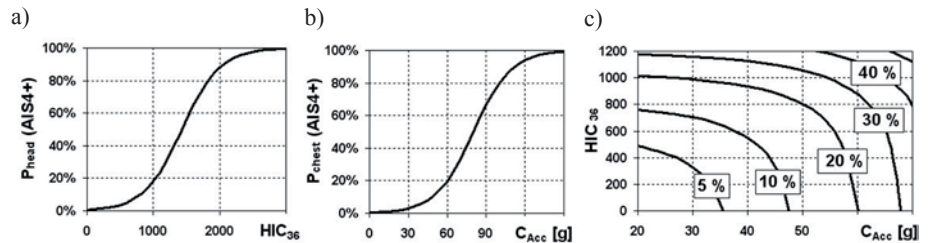


Fig. 3. Risk of severe injury (AIS4+) of head and chest of M50 and F5 dummies (a and b) and the risk curves P_{comb} (c)

of head and chest does not exceed 20% in this case, but it increases rapidly when the limit values are exceeded (Figure 3 a, b). The same functions hold for M50 and F5 dummies.

The loads at head and chest usually do not change to such a degree when the conditions of the crash test are changed, e.g. when the speed of the collision is changed. This is why combined injury probability criterion P_{comb} was used to assess the loads on the dummies [1, 11]:

$$P_{comb} = 1 - (1 - P_{head}) \cdot (1 - P_{chest}) = P_{head} + P_{chest} - P_{head} \cdot P_{chest} \quad (5)$$

In the further part of the analysis, $HIC_{36} = f(C_{Acc})$ chart was applied, presented in Figure 3c, where the lines indicate the values of HIC_{36} and C_{Acc} , at which the values of $P_{comb}(AIS4+)$ indicator (risk of severe injury) are 5, 10, 20, 30 and 40%, respectively.

4. Selection of the crash tests for the analysis

For the purpose of the analysis of the influence of the impact speed on the dynamic load on the driver and on the passenger, the results of crash tests published in the Internet by *National Highway Traffic Safety Administration* were applied [24]. NHTSA database includes the results of over 7000 crash tests of the cars from 1965-2016, conducted under various conditions (different types of impact, barrier



Fig. 4. Frontal impact of a car with a rigid barrier [24]



types, velocity of collision etc.), with the special focus on the frontal impact of a car on a rigid, plain barrier, placed perpendicularly to the direction of the drive (Figure 4).

Crash tests of the cars produced in 1990-2010 were chosen for the analysis, where the dummies placed on the front seats had their seatbelts fastened, and were protected with a front airbag (Figure 4). The cars manufactured more recently were omitted because, for the records from 2011 on, NHTSA database includes the values HIC_{15} ($\Delta t \leq 15$ ms), which replaced HIC_{36} ($\Delta t \leq 36$ ms).

The speed with which the car hits the barrier is only one of many factors influencing the load on the dummies. This is why for the purpose of further analysis the results of the crash tests were divided into several groups in such a manner as to limit the influence of the other factors on the result of the assessment performed for the purpose of the analysis described in the paper. The first two groups of results (data) were obtained with grouping the crash tests according to the car's manufacturing year (standard of the used passive safety systems):

- the models manufactured in 1990-1999;
- the models manufactured in 2000-2010.

The indicators connected with the driver and the passenger were analysed separately due to the fact that the loads on the same dummies may differ significantly if placed on different seats in the car [25, 28]. For example, the values of HIC_{36} and C_{Acc} indicators in Figure 5, regarding M50 dummy placed on the driver and passenger seat were compared (422 tests, cars from 2000-2010, speed 56 km/h). The differences in HIC_{36} for the driver and the passenger were as following:

- not more than $\pm 10\%$ in 111 tests (26% of the results are between the red lines);
- more than 20% in 211 tests (50% of the tests).

The differences in C_{Acc} for the driver and the passenger were as following:

- not more than $\pm 10\%$ in 274 tests (65% of the results are between the red lines);
- more than 20% in 31 tests (7% of the tests).

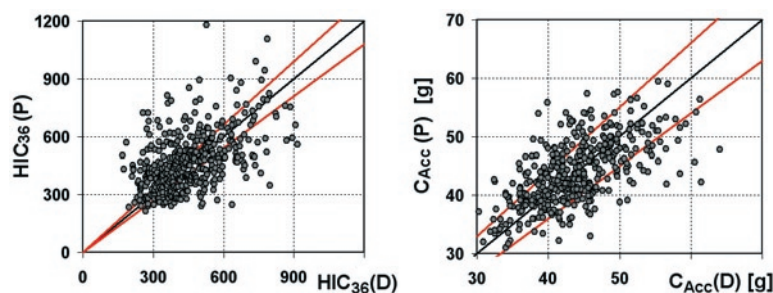


Fig. 5. Comparison of HIC_{36} and C_{Acc} indicators, calculated for M50 dummy placed on the driver's seat (D) and on the passenger's seat (P); cars from 2000-2010 (56 km/h)

The passenger cars have different construction of the frontal crumple zone, which significantly influences the process of deformation of the zone upon hitting the obstacle, and therefore also the deceleration of the car [26]. This is why the further division of the crash tests into the categories was based on the type of the car. The greatest number was that of „classic“ cars (61% of the tests, weight of the car during the crash test: 932-2562 kg)

– a category including hatchback, sedan, coupe, kombi and convertible cars. Vehicles of that category have similar construction of the integral body. Moreover, the following types of cars are included:

- utility vehicles, with a reinforced chassis, drive usually 4x4 (20% of the tests, weight 1298-2917 kg);
- pickups, with a frame chassis (11% of the tests, weight 1447-3054 kg);
- vans (8% of the tests, weight 1661-2721 kg, including mini-vans).

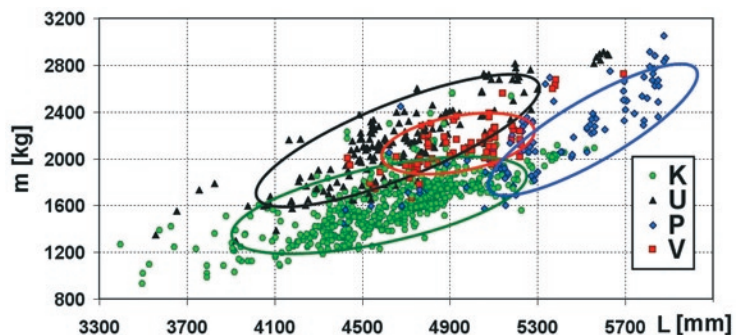


Fig. 6. Comparison of mass (m) and length (L) of the passenger cars (according to [24]): K – classic; U – utility vehicles; P – pickups; V – vans

In order to present the differences between the four types of cars, their weights and length were compared in Figure 6.

Further analysis includes:

- 788 tests with Hybrid III M50 dummies on the front seats (in 55 tests from 1990-1995, there were Hybrid II dummies on the passenger seat);
- 125 tests with Hybrid III F5 dummies on the front seats.

Table 2 provides information on the number of tests at a given collision speed, with regard to the manufacturing year and type of the car (acc. to NHTSA classification), as well as the kind of a dummy. The greatest number of tests were performed at nominal speed with which the car hit the obstacle: 40, 48 and 56 km/h (25, 30 and 35 miles per hour, respectively), where the usual speed in the case of M50 dummy was usually 56 km/h, whereas in the case of F5 it was usually 48 km/h. The real value of the speed at which the car hit the obstacle was usually within the range of ± 1 km/h from the nominal value.

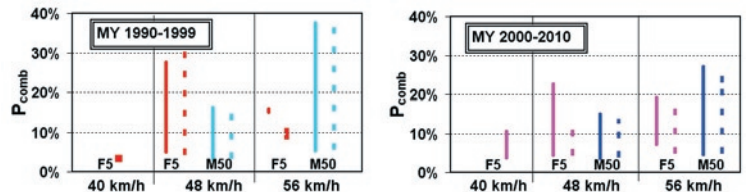
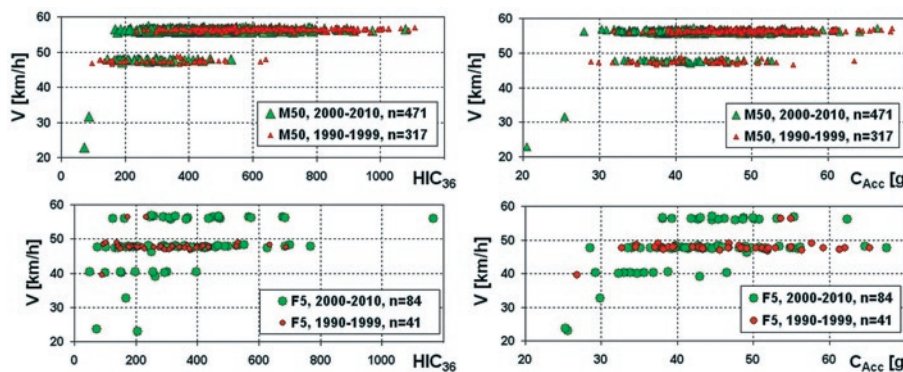
5. Preliminary assessment of the influence of the impact speed on the loads of a dummies

At this stage of the analysis, all types of cars were taken into account (Figure 6). In Figure 7, the values of HIC_{36} and C_{Acc} were presented with regard to the speed at which the car hit the barrier. The values refer to M50 and F5 dummies placed

Table 2. Number of the crash tests included in the analysis (K – classic, U – utility vehicles, P – pickups, V – vans and minivans)

Impact speed	Manufacturing year of a car	K		U		P		V		Total	
		M50	F5	M50	F5	M50	F5	M50	F5	M50	F5
<40 km/h	2000-2010	2	3			0				2	3
40 km/h	1990-1999	0	1			0				0	1
	2000-2010	0	7	0	0	0	1	0	2	0	10
48 km/h	1990-1999	28	30	9	1	3	4	6	3	46	38
	2000-2010	40	37	2	3	3	5	2	4	47	49
56 km/h	1990-1999	171	2	41	0	29	0	30	0	271	2
	2000-2010	218	16	127	0	50	2	27	4	422	22
Total		459	96	179	4	85	12	65	13	788	125

on the driver's seat. What is interesting, there was a huge dispersion of the values of the indicators at a given speed, irrespectively of the cars' year of production and the type of the dummy. For example, the values of HIC_{36} when the car hit the barrier 56 km/h speed for M50 dummy were within the range of 176-1079 (cars from 2000-2010). This result shows that the effectiveness of protective devices used in cars varies greatly. The effect of the speed at which the car hits the barrier is more visible in case of

Fig. 8. Influence of the impact speed on the value of risk P_{comb} (AIS4+); (solid lines – driver; dashed lines – passenger)Fig. 7. Influence of the impact speed on the values of HIC_{36} and C_{Acc} for M50 and F5 dummies placed on the driver's seatTable 3. Ranges of HIC_{36} and C_{Acc} as well as P_{head} , P_{chest} , P_{comb} risk factors

Dummy	M50				F5					
	1990-1999		2000-2010		1990-1999			2000-2010		
MY										
V [km/h]	48	56	48	56	40	48	56	40	48	56
n	44	265	48	417	1	36	2	10	46	20
Ranges of the indicators calculated for the dummy on the driver seat										
HIC_{36}	90-518	238-1088	144-532	169-894	90	96-636	174-234	51-396	75-628	126-686
C_{Acc} [g]	27-55	32-71	32-53	28-61	27	33-65	54-55	29-47	28-56	38-55
P_{head} [%]	1-4	1-23	1-4	1-13	1	1-6	1	1-3	1-6	1-7
P_{chest} [%]	2-15	3-35	3-13	3-21	2	4-26	14-15	3-9	3-16	5-15
P_{comb} [%]	3-16	5-38	5-15	5-27	3	5-28	15-16	4-11	5-23	7-19
Ranges of the indicators calculated for the dummy on the passenger seat (next to the driver)										
n^*	38	192	43	417	0	34	2	10	45	18
HIC_{36}	80-573	181-1163	101-536	214-902	-	69-723	174-261	93-298	91-678	196-712
C_{Acc} [g]	26-53	35-64	28-50	29-59	-	32-67	43-47	31-44	30-49	30-52
P_{head} [%]	1-5	1-28	1-4	1-14	-	1-8	1-2	1-2	1-7	1-7
P_{chest} [%]	2-13	4-24	3-11	3-19	-	3-29	7-9	3-7	3-11	3-13
P_{comb} [%]	4-15	6-37	4-14	5-25	-	5-31	9-10	5-9	5-13	5-18

M50 dummy load that in the case of F5. The values of HIC_{36} and C_{Acc} for F5 dummy are within a similar range at 48 and 56 km/h (cars from 2000-2010). As for M50 dummy, the maximum values of HIC_{36} at 56 km/h are about two times higher than at 48 km/h. The maximum values of C_{Acc} for M50 dummy at 56 km/h are about 30% higher than at 48 km/h.

In further analysis of the influence of the impact speed on the injuries of the occupants of the vehicle, the results of 24 tests were omitted where the values of HIC_{36} and C_{Acc} indicators at a given collision speed were significantly higher than in the other cases (cf. Fig. 7). Table 3 presents the ranges of HIC_{36} and C_{Acc} indicators and the risk

of severe injury (AIS4+) P_{head} , P_{chest} , P_{comb} of the driver and the passenger calculated on the basis of (3)-(5).

The number of the tests with a passenger (n^*) is smaller than the number of the tests with the driver (n) because the results were omitted that do not meet the abovementioned similarity criteria of the conditions of tests, e.g. there was no air cushion for the passenger in some of the older car models, or there was a different dummy on the passenger seat.

There was a significant range, that is the difference between the minimum and maximum value, for HIC_{36} and C_{Acc} , at a given collision speed, which makes it more difficult to analyse the impact of the speed on head and chest in-

ries. Minimum values of head injury indicator are usually $HIC_{36} < 900$ and $C_{Acc} < 60$ g for the chest. The risk of severe injury (AIS4+) in these cases is not higher than 14% (head) and 20% (chest). The load on the chest determines the total risk of injury P_{comb} , irrespective of the speed of the car.

In Figure 8, collision speed and the risk of severe injury P_{comb} are juxtaposed. Taking into account the results for the two dummies (M50 and F5) placed on the driver's seat and on the passenger's seat, the following ranges of the risk of injury were determined:

– cars manufactured in 1990-1999	– cars manufactured in 2000-2010
$P_{comb} = 4 \div 31\%$ at 48 km/h;	$P_{comb} = 4 \div 11\%$ at 40 km/h (F5 only);
$P_{comb} = 5 \div 38\%$ at 56 km/h;	$P_{comb} = 4 \div 23\%$ at 48 km/h;
	$P_{comb} = 5 \div 27\%$ at 56 km/h.

6. Statistical analysis of the influence of the impact speed on the loads on the dummies

6.1. The scope of the analysis

A more detailed analysis of the influence of the speed at which the car hit the obstacle on the loads and injury risk of the occupants of the car was performed on the basis of the statistical analysis of the values of HIC_{36} and C_{Acc} indicators and values of risk factors P_{head} , P_{chest} , P_{comb} , applied as random variables. In order to analyse the properties of the probability distribution, histograms were prepared. On the basis of the number of crash tests n and the range R of a given indicator, the values x_1, x_2, \dots, x_n were grouped into k intervals (bins) with the length of h (bin interval), taking into account [6, 7]:

$$k \approx \sqrt{n}; k \leq 5 \log(n); h \approx \frac{R}{k} \quad (6)$$

In this manner, every i^{th} bin was assigned n_i number of indicators (number of the elements in a given bin) and the relative number of elements p_i (frequency), cumulated number of elements c_i , and the distribution function F in the upper limits of x_i^+ bins:

$$p_i = \frac{n_i}{n}; c_i = \sum_{j=1}^i n_j, i = 1, 2, \dots, k; F(x_i^+) = \frac{c_i}{n} \quad (7)$$

On the basis of the histograms, mode was calculated [6]:

$$Mo = x_m^- + h \cdot \frac{n_m - n_{m-1}}{2n_m - n_{m-1} - n_{m+1}} \quad (8)$$

where: m – number of the bin with the greatest number of elements; x_i^- , n_m – lower limit and number of elements of the bin where the mode is located.

The coefficient of skewness As and kurtosis Ku was used to assess asymmetry and flattening (concentration) of the analysed patterns of distribution [6]:

$$As = \frac{\bar{x} - Me}{s}; Ku = \frac{\mu_4}{s^4} \quad (9)$$

where: \bar{x} – arithmetic mean, Me – median, s – standard deviation, μ_4 – fourth moment about the mean.

The asymmetry coefficient $As=0$ for symmetric distribution ($\bar{x} = Me = Mo$), $As < 0$ for left-skewed distribution ($Mo > Me > \bar{x}$) and $As > 0$ for right-skewed distribution ($Mo < Me < \bar{x}$). The higher the absolute value of the asymmetry coefficient, the stronger the asymmetry of distribution. Kurtosis $Ku > 3$ and $Ku < 3$ characterises distribution patterns with more, or less concentration than in the case of normal distribution, for which $Ku=3$ [6].

6.2. Effect of the year of production, type and weight of the car on the HIC_{36} and C_{Acc}

In point 5, the influence of the impact speed on the values of HIC_{36} and C_{Acc} indicators was analysed, separately for the cars from 1990-1999 and from 2000-2010. At this stage, it was analysed whether there may be a relation between the type and the weight of the car and the high dispersion of the values of HIC_{36} and C_{Acc} indicators at a given speed of collision.

Figure 9a presents the values of HIC_{36} and C_{Acc} indicators for M50 dummy (a driver) in classic cars. The values of HIC_{36} and C_{Acc} indicators were juxtaposed with the injury risk curves (cf. Fig. 3c). A clear difference between the loads on the dummies in case of older and newer cars is confirmed by the distribution functions of the risk of injury P_{comb} .

In Figure 9b, the values of HIC_{36} and C_{Acc} are presented for M50 dummy (the driver) in the following types of cars: classic (K), utility vehicle (U), pick-ups (P) and vans (V) from 2000-2010. Classic cars, which are the most numerous, are additionally divided into four groups, each of different weight (Fig. 9c). Risk distribution P_{comb} , expressed as a distribution function $F(P_{comb})$, are similar both for differ-

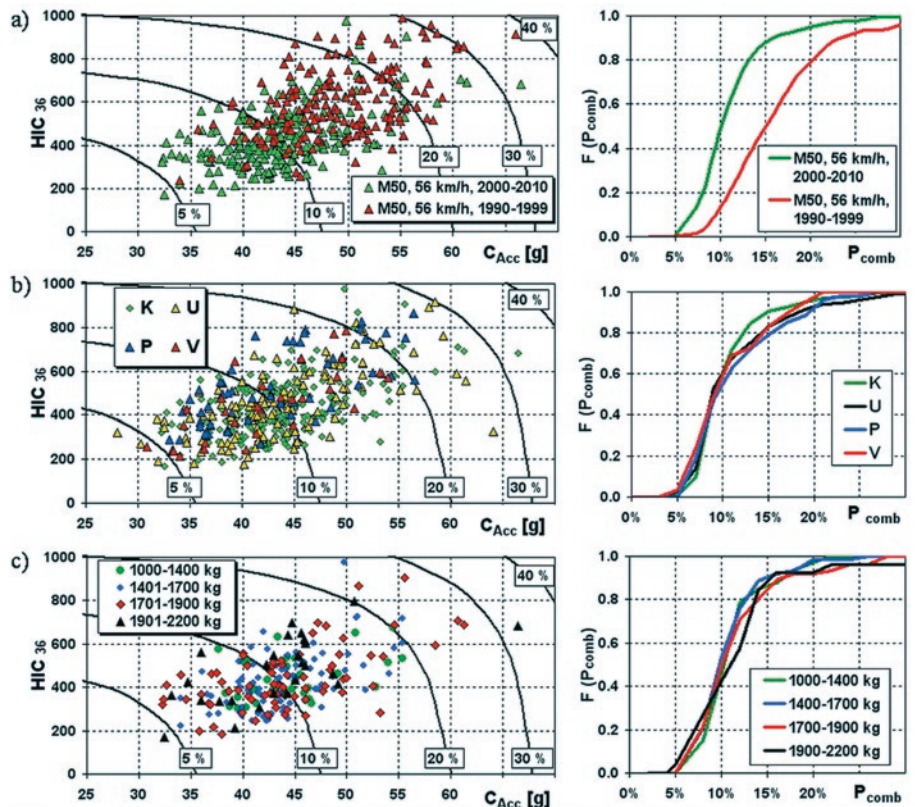


Fig. 9. HIC_{36} and C_{Acc} indicators and the distribution functions of the injury risk P_{comb} (AIS4+) (M50, 56 km/h); a) cars from 1990-1999 and 2000-2010; b) various types of cars from 2002-2010; c) different values of weight of classic cars (C) from 2000-2010.

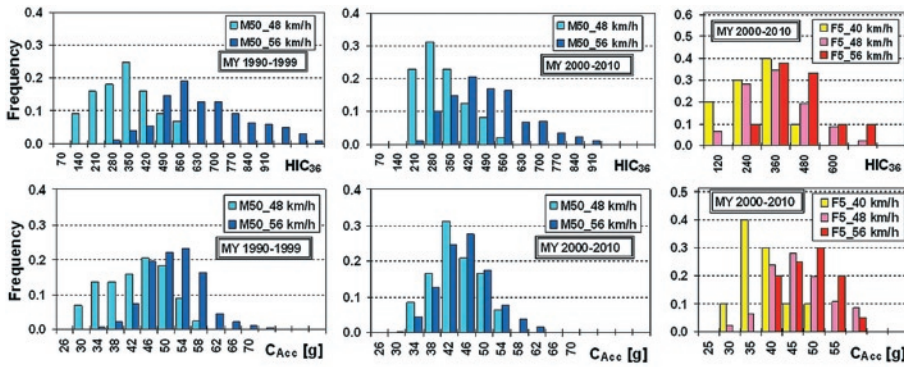


Fig. 10. Histograms of the frequency of HIC_{36} and C_{Acc} indicators for the dummies on the driver's seat; M50 (48 and 56 km/h) and F5 (40, 48 and 56 km/h)

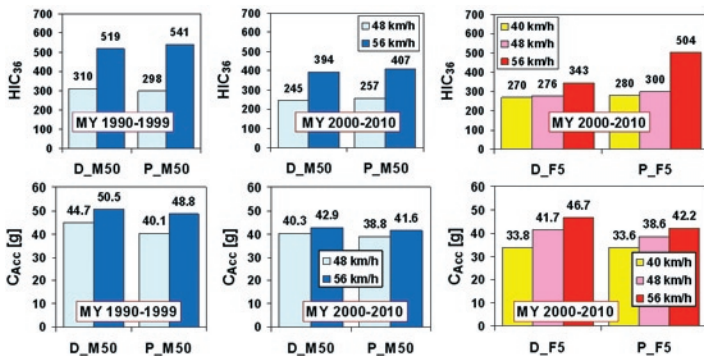


Fig. 11. Mode values of HIC_{36} and C_{Acc} indicators (M50 and F5) for the driver (D) and for the passenger (P) in case of a car hitting the obstacle at 40, 48 and 56 km/h

ent types of cars and for different weight of classic cars. Therefore, no significant relation was discovered between the type or weight of the car and the distribution of HIC_{36} and C_{Acc} indicators.

On the basis of the above findings, the crash tests were divided into 14 groups (7 with the driver and 7 with the passenger), listed above in Table 3 (8 groups of the tests with M50 dummy and 6 groups of the tests with F5 dummy). Due to a small number of tests involving

Table 4. Values of the parameters describing the properties of risk P_{comb} distribution

Dummy	M50								F5					
Place	Driver				Passenger				Driver			Passenger		
MY	1990-1999		2000-2010		1990-1999		2000-2010		2000-2010					
V [km/h]	48	56	48	56	48	56	48	56	40	48	56	40	48	56
Group	I	II	III	IV	V	VI	VII	VIII	IX	X	XI	XII	XIII	XIV
<i>n</i>	44	265	48	417	38	192	43	417	10	46	20	10	45	18
<i>R</i> [%]	12.9	32.2	10.3	22.5	11.5	31.3	9.4	19.4	6.8	18.2	11.8	4.3	7.9	12.5
<i>h</i> [%]	1.8	2.5	1.8	1.5	1.8	2.5	1.8	1.5	3.0	3.0	3.0	3.0	3.0	3.0
\bar{x} [%]	9.3	17.2	8.6	11.2	7.9	16.9	7.8	11.2	6.3	10.4	11.4	6.3	7.9	11.1
<i>Me</i> [%]	9.3	15.8	8.1	10.0	7.4	15.8	7.3	10.3	5.2	9.1	10.9	5.9	7.6	11.0
<i>Mo</i> * [%]	8.6	13.8	7.7	8.7	7.6	14.0	6.6	8.6	5.0	7.8	9.8	5.5	7.3	10.7
<i>s</i> [%]	3.1	6.8	2.6	4.4	3.0	6.5	2.4	3.9	2.1	4.6	3.4	1.5	2.3	3.3
<i>q</i> _{0.25} [%]	7.2	12.2	6.7	8.2	5.4	11.9	6.0	8.3	4.5	7.0	8.5	5.1	5.9	8.8
<i>q</i> _{0.75} [%]	11.6	20.7	10.4	13.1	9.1	20.4	9.2	13.4	7.5	12.2	12.9	6.9	9.9	12.9
<i>As</i>	0.01	0.20	0.18	0.26	0.15	0.17	0.22	0.25	0.49	0.28	0.17	0.26	0.14	0.03
<i>Ku</i>	2.36	3.23	2.61	4.64	2.84	3.36	2.82	3.71	2.21	3.11	2.65	1.97	1.90	2.21

* Mode values of P_{comb} indicator calculated in accordance with (8). The differences between mode values of P_{comb} indicator calculated on the basis of mode HIC_{36} and C_{Acc} indicators (from Fig. 11) and acc. to (8) for 9 groups are not higher than 5% for the rest of the groups (I, II, IV, IX and XI), the differences remaining at the level of 8-12%.

the cars from 1990-1999 and F5 dummy, at 40 and 56 km/h, they were omitted in the further analysis.

6.3. Effect of the impact speed on the modes of HIC_{36} and C_{Acc} indicators

The histograms of HIC_{36} and C_{Acc} indicators regarding the loads on the dummies on the driver's seat are presented in Figure 10 (similar distributions were prepared for the passenger). On the abscissa axis, there are values of the upper limits of x_i^+ bins. The frequency p_i is lo-

cated on the axis of ordinates (7). The number of elements in the tests was presented above in Table 3. On the basis of (6), bin intervals were applied $h_{HIC}=70$ and $h_{CAcc}=4$ g for the indicators regarding M50 dummy, as well as $h_{HIC}=120$ and $h_{CAcc}=5$ g for the indicators regarding F5 dummy.

On the basis of the analysis of the measures of location, shape and dispersion of the distribution patterns analysed, described in point 6.1, it was determined that the distribution of HIC_{36} and C_{Acc} indicators has a very weak ($|As|<0.2$) right-side skewness ($As>0$, that is $\bar{x} > Mo$), and concentration lower than in the case of normal distribution (usually $Ku \in (1.7; 2.9)$, and only for 2 groups $Ku>3$). Due to the asymmetry of the distribution of the HIC_{36} and C_{Acc} indicators, mode values Mo were applied to describe the maximum of their density functions (Fig. 11).

Increase in the impact speed of the car from 48 to 56 km/h has a greater influence on the increase in the mode value of HIC_{36} than C_{Acc} . On the basis of dependencies (3) and (4), it was determined that such an increase in speed results in the increase in mode value of the risk of severe injury of head (from 2 to 4%) and chest (from 5-6% to 7-11%).

It was proved that the increase in the impact speed has a greater influence on the loads on M50 dummy in case of older cars (cf. 9a and 11). Moreover, the mode values of HIC_{36} and C_{Acc} indicators for M50 dummies on the driver's and passenger's seat are similar at a given speed. However, at 56 km/h, the mode values of HIC_{36} indicator are

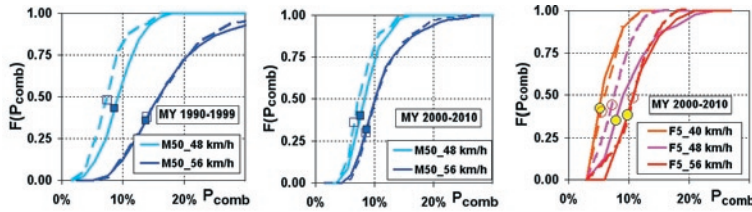


Fig. 12. Distribution functions of the injury risk P_{comb} (AIS4+) of the dummies on the driver's seat (continuous lines) and on the passenger's seat (dashed lines) at the speed with which the car hits the obstacle 40, 48 and 56 km/h

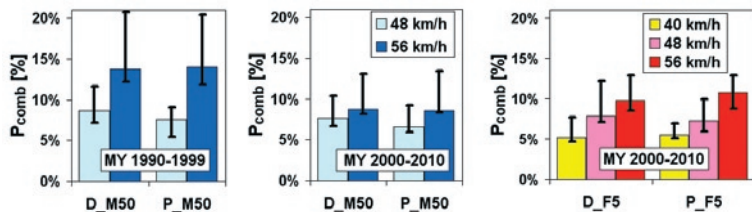


Fig. 13. Mode values of the injury risk P_{comb} (AIS4+) for the driver (D) and for the passenger (P) in the case of a car hitting the obstacle at 40, 48 and 56 km/h (M50 and F5 dummies)

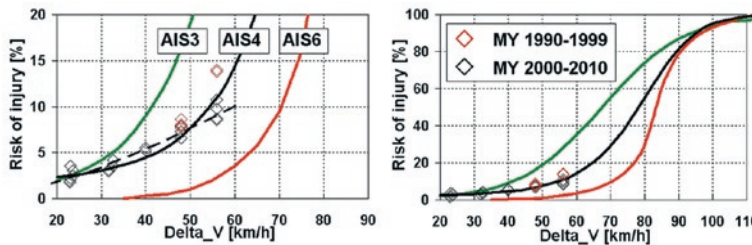


Fig. 14. Risk of injury of the driver and of the passenger on the front seat during a frontal impact as a function of ΔV (on the left, there is a fragment of the chart from the right); "AIS3" line acc. to [4], "AIS6" line acc. to [23]

significantly higher for F5 dummies on the place of the passengers than on the place of the driver.

6.4. Effect of the impact speed on the modes of injury risk P_{comb}

Distribution of the risk of injury P_{comb} was assessed also on the basis of histograms. In Table 4, values are presented of the parameters describing the properties of risk P_{comb} distribution in 14 data groups (I-XIV). On the basis of (6), bin intervals h were applied of 1.5, 1.8 and 2.5% for M50 dummy, and $h=3\%$ for F5 dummy.

Distribution in every group is characterised by right-side asymmetry ($As>0$), with very weak ($|As|<0.2$) or low intensity of the asymmetry ($|As|<0.4$). The arithmetical mean is 8-33% higher than Mo , and standard deviation $s \in (1.5\%; 6.8\%)$. In case of 5 groups (II, IV, VI, VIII, X) the concentration is higher than in the case of normal distribution ($Ku>3$), and in the rest of the groups $Ku \in (1.97; 2.84)$.

In Figure 12, distribution functions of risk P_{comb} are presented, regarding dummies on the seat of the driver and the passenger. The points indicate mode values of injury risk P_{comb} . The modes are located between the quartile $q_{0.25}$ and the median Me . What is important is that there are differences of the distribution regarding the driver and the passenger at 48 km/h speed.

The mode values of injury risk P_{comb} (AIS4+) of the driver and the passenger from Table 4 are presented in Figure 13, where the ranges of the variable are marked ($Mo-q_{0.25}$; $q_{0.75}-Mo$), with 50% of the results in every 14 groups.

On the basis of the mode values of injury risk P_{comb} , it was discovered that the increase in the speed at which the car hits the obstacle:

- from 48 to 56 km/h increases the risk of injury (AIS4+) in the case of a 50-centile man from 8 to 14% in the cars from 1990-1999 and from 7 to 9% in the cars from 2000-2010;
- from 40 to 56 km/h increases the risk of injury (AIS4+) in the case of a 5-centile woman from 5 to 10% in the cars from 2000-2010.

Generalized results of the analysis of the influence of the speed in case of a frontal impact on the risk of injury for the driver and for the passengers on the front seat are presented in Figure 14. The points on the charts at the speed of 40, 48 and 56 km/h denote mode values from Figure 13, while points at $\Delta V < 40$ km/h represent the values of the risk of injury P_{comb} for the driver and for the passenger, calculated on the basis of the results of two tests with M50 dummy and three tests with F5 dummy (cf. Fig. 7 and tab. 2).

The points on the charts and the behaviour of AIS3 and AIS6 risk functions (lines 6 and 9 in Fig. 1) were used to approximate the results with the following function ("AIS4" line in Fig. 14):

$$P_{comb}(AIS4+) = \{1 + \exp[3,9 - 4,1 \cdot (\Delta V / 80)^{2,3}]\}^{-1} \quad (10)$$

where ΔV [km/h] is the change in vehicle velocity over the duration of the crash.

The injury risk of the occupants on the front seats of the cars from 2000-2010 during a frontal impact at $\Delta V < 60$ km/h can be described with the following approximating function (dashed line in Fig. 14):

$$P_{comb}(AIS4+) = 0,017 \cdot \Delta V^{1,56} \quad (11)$$

with a high value of the coefficient of determination $R^2=0,920$.

7. Summary

The analysis of the results of several hundred of crash tests made it possible to assess the influence of the impact speed on the injury risk for the driver and for the passenger on the front seat, with their seatbelts fastened and protected with an airbag. The speed of collision is but one of many factors with an influence on the risk of injuries for the occupants of the car. Due to the above, the analysis was conducted in older and newer cars, separately for F5 and M50 dummies and for two different places in the car (on the driver's seat and on the passenger's seat).

The analysis of the injury risk includes the loads on head and chest (HIC_{36} i C_{Acc} indicators). Significant dispersion of these indicators made the analysis harder (pt. 5). This is why the values of HIC_{36} and C_{Acc} were determined statistically, by specifying their parameters of distribution. On the basis of the mode values of the risk of injury P_{comb} , it was determined that the increase in the speed at which the car hits the obstacle from 40 to 56 km/h increases the risk of severe injury (AIS4+) in the case of a 5-centile woman from 5 to 10%. The risk of injury in the case of a 50-centile man was assessed at the collision speed of 48 and 56 km/h. The increase in speed in such a case increases the risk of severe injury from 8 to 14% in the cars from 1990-1999 and from 7 to 9% in the cars from 2000-2010.

To sum up the results – it was determined that the increase in the speed at which the car hits the obstacle from 25 to 56 km/h increases the risk of severe injury (AIS4+) for the driver and for the passenger from 2 to 10%. The value of the risk of injury P_{comb} is determined by the loads on the chest, irrespective of the speed at which the car

hits the obstacle. The results of the analysis were used to describe the

dependency of the risk of severe injury (AIS4+) for the driver and for the passenger from ΔV parameters with functions (10) and (11).

References

1. Cichos D, Otto M, Zölsch S, Clausnitzer S, Vetter D, Pfeiffer G, de Vogel D, Schaar O. Crash analysis criteria description. Arbeitskreis Messdatenverarbeitung Fahrzeugsicherheit. Germany 2011.
2. Dąbrowska-Loranc M, Wojsz T. Prędkość pojazdów w Polsce w 2014 r. Krajowa Rada Bezpieczeństwa Ruchu Drogowego. Warszawa 2014.
3. Funk J R, Cormier J M, Gabler H C. Effect of Delta-V errors in NASS on frontal crash risk calculations. 52nd AAAM Annual Conference Annals of Advances in Automotive Medicine 2008.
4. Gabauer D J, Gabler H C. Comparison of roadside crash injury metrics using event data recorders. Accident Analysis and Prevention 2008; 40: 548-558, <http://dx.doi.org/10.1016/j.aap.2007.08.011>.
5. Gaca S, Suchorzewski W, Tracz M. Inżynieria ruchu drogowego. WKŁ, Warszawa 2008.
6. Kot S M, Jakubowski J, Sokołowski A. Statystyka. Wydawnictwo Difin SA, Warszawa 2011.
7. Kukula K. Elementy statystyki w zadaniach. Wydawnictwo Naukowe PWN, Warszawa 1998.
8. Kullgren A. Dose-response models and EDR data for assessment of injury risk and effectiveness of safety systems. IRCOBI Conference, Bern, Switzerland 2008: 3-14.
9. Kullgren A, Krafft M, Tingvall C, Lie A. Combining crash recorder and paired comparison technique: Injury risk functions in frontal and rear impacts with special reference to neck injuries. The 18th International Technical Conference on the Enhanced Safety of Vehicles, Paper Number 404, Nagoya, Japan 2003.
10. Liu W C, Doong J L, Tsai S L, Lai C H, Jeng M C. Integrated model of simulated occupant injury risk and real medical costs. Journal of Safety Research 2009; 40: 461-468, <http://dx.doi.org/10.1016/j.jsr.2009.09.006>.
11. Opportunities exist to enhance NHTSA's New Car Assessment Program. United States Government Accountability Office, GAO-05-370. USA 2005.
12. Pijanowski B, Żardecki D. Selected vehicle monitoring problems with the e-Call system taken as an example. The Archives of Automotive Engineering 2013; 3: 25-41.
13. Prochowski L, Kochanek H. Analiza wieku i obrażeń ofiar wypadków drogowych w aspekcie programowania ratownictwa drogowego. Logistyka 2015; 4: 1082-1090.
14. Prochowski L, Żuchowski A, Zielonka K. Analysis of the influence of the speed of impact against an obstacle on the dynamic loads acting on occupants of an automotive vehicle with body-on-frame design of the load bearing structure. The Archives of Automotive Engineering 2011; 4: 53-73.
15. Prochowski L, Żuchowski A. Analysis of the influence of passenger position in a car on a risk of injuries during a car accident. Eksploatacja i Niezawodność-Maintenance and Reliability 2014; 16(3): 360-366.
16. Richards D, Cuerden R. The relationship between speed and car driver injury severity. Road Safety Web Publication No.9, Transport Research Laboratory, Department for Transport, London 2009.
17. Schmitt K U, Niederer P F, Muser M H, Walz F. Trauma biomechanics. Accidental injury in traffic and sports. Springer-Verlag Berlin Heidelberg 2010.
18. Strandroth J, Rizzi M, Kullgren A, Tingvall C. Head-on collisions between passenger cars and heavy goods vehicles: Injury risk functions and benefits of Autonomous Emergency Braking. IRCOBI Conference 2012: 342-351.
19. Symon E. Wypadki drogowe w Polsce (lata 2001-2014), <http://statystyka.policja.pl>.
20. Vincze-Pap S, Csiszár A. Real and simulated crashworthiness tests on buses. The 19th International Technical Conference on the Enhanced Safety of Vehicles, Washington, 2005.
21. Wicher J. Bezpieczeństwo samochodów i ruchu drogowego. WKŁ, Warszawa 2012.
22. Wicher J. Is it worth limiting the travel speed? The Archives of Automotive Engineering 2015; 69(4): 105-114.
23. Wramborg P. A new approach to a safe and sustainable road structure and street design for urban areas. Proceedings of the Road Safety on Four Continents Conference, Warsaw 2005.
24. www.nhtsa.gov.
25. Żuchowski A. Risk of injury for the front and rear seat passengers of the passenger cars in frontal impact. Journal of KONES Powertrain and Transport 2012; 19(3): 507-518, <http://dx.doi.org/10.5604/12314005.1138166>.
26. Żuchowski A. The use of energy methods at the calculation of vehicle impact velocity. The Archives of Automotive Engineering 2015; 68(2): 85-111.
27. Żuchowski A, Jackowski J. Analysis of properties of operation of the supporting equipment for the seat belts. Journal of KONES Powertrain and Transport 2011; 18(1): 697-704.
28. Żuchowski A, Prochowski L. The analysis of safety of rear seat occupants of a passenger car during the road accident. The Archives of Automotive Engineering 2011; 53(3): 83-98.
29. Żuchowski A, Wicher J. Influence of the pre-tightening of seat belts on the loads acting on rear seat occupants during a frontal collision. The Archives of Automotive Engineering 2013; 2: 93-110, <http://dx.doi.org/10.5604/1234754X.1066779>.

Andrzej ŻUCHOWSKI

Institute of Motor Vehicles and Transportation
Faculty of Mechanical Engineering
Military University of Technology
ul. Gen. S. Kaliskiego 2, 00-908 Warsaw, Poland
E-mail: andrzej.zuchowski@wat.edu.pl

Yi-Chao YIN
Hong-Zhong HUANG
Weiwen PENG
Yan-Feng LI
Jinhua MI

AN E-BAYESIAN METHOD FOR RELIABILITY ANALYSIS OF EXPONENTIALLY DISTRIBUTED PRODUCTS WITH ZERO-FAILURE DATA

METODA BAYESOWSKIEJ ESTYMACJI WARTOŚCI OCZEKIWANEJ DLA PRODUKTÓW O ROZKŁADZIE WYKŁADNICZYM WYKORZYSTUJĄCA DANE O NIEZAISTNIAŁYCH USZKODZENIACH

This paper investigate an E-Bayesian estimation as a reliability analysis method for the seekers to deal with the zero-failure life testing data. Firstly, we introduce an E-Bayesian estimation for the exponential distribution, and then propose a zero-failure model with assumptions. Using the proposed model, we set up a series of life tests for the seekers, and apply the E-Bayesian estimation on the observed zero-failure data to calculate the failure rate and reliability of the seekers. Finally, the reliability estimation results of the seekers demonstrate the performance of the proposed method.

Keywords: E-Bayesian estimation, exponential distribution, zero-failure data, failure rate, hierarchical Bayesian estimation.

W pracy analizowano estymację bayesowską wartości oczekiwanej jako metodę analizy niezawodności urządzeń naprowadzających w przypadkach, gdy dane z badań trwałości są danymi o uszkodzeniach niezaistniałych (zerowych). W pierwszej części pracy opisano E-estymację bayesowską dla rozkładu wykładniczego, a następnie zaproponowano model uszkodzeń niezaistniałych oraz opisano jego założenia. Wykorzystując zaproponowany model, zaprojektowano i zrealizowano serię badań trwałości urządzeń naprowadzających jak również zastosowano E-estymację bayesowską w celu obliczenia intensywności uszkodzeń oraz niezawodności badanych urządzeń. Wyniki oceny niezawodności urządzeń naprowadzających potwierdzają przydatność proponowanej metody.

Słowa kluczowe: estymacja bayesowska wartości oczekiwanej, rozkład wykładniczy, dane o niezaistniałych uszkodzeniach, intensywność uszkodzeń, hierarchiczna estymacja bayesowska.

1. Introduction

Reliability is the probability of a component or system working regularly. Reliability technology was firstly applied in the fields of nuclear industry, aviation and aerospace, and then was spread to the industries of electronic, metallurgy, mechanical and so on. The researches and analyses on the reliability theories and applications have lasted for decades. Now reliability has become one of the most important areas in the industry. With the improvement of reliability applications, products with high reliability require a long time to obtain the failure data in normal life tests. Actually, zero-failure data is often detected in Type I Censoring life tests.

The early research about zero-failure data started by Bartholomew [1], who firstly used the test time as the estimate of the average life, which was obviously too small. Martz and Waller [12] developed a method for an exponential failure-time model and a gamma prior distribution on the failure rate. Chow and Shao [2, 3] used a regression model and the weighted least squares method for accessing the shelf-lives of drug products. Miller, Morell and Noonan [13] provided the formulae for the probability of failure with zero-failure data based on some assumptions of Bayesian prior distribution, and gave an example of failure rate estimation with zero-failure data. Han [4, 5] developed an E-Bayesian estimate method based on hierarchi-

cal Bayesian estimation, which was proved to be feasible for zero-failure data. Liu [9] investigated the applications of E-Bayesian estimation for exponential life distribution. Based on the researches of E-Bayesian estimation, we introduce a reliability analysis method for the seekers, which is more convenient and effective for zero-failure data of exponential distribution.

The remainder of the paper is organized as follows. Section 2 presents a brief description of E-Bayesian method for the failure rate estimation of exponential distribution. In Section 3 we introduce the assumptions for reliability testing with zero-failure data. In Section 4 we provide an E-Bayesian method for exponential distribution with zero-failure data. In Section 5 we illustrate how the proposed E-Bayesian method can deal with zero-failure data in life testing, and compare it with different zero-failure analysis methods. In Section 6 We give some comments and conclusions.

2. E-Bayesian estimation for the failure rate of exponential distribution

Exponential life distribution is suitable for the electronic products, so it is widely applied in the field of electronic reliability. For example, it is used as the life distribution of semiconductor devices

both in Japanese industry standards and American military standards. The density function of exponential distribution is:

$$f(t) = \lambda \exp(-\lambda t) \quad (1)$$

where $t > 0$, $\lambda > 0$, and λ is the failure rate of the exponential distribution.

Han introduced the definition of E-Bayesian estimation in [8]. Assume that $\hat{\lambda}(t)$ is a continuous function defined on the interval R ,

and $t \in R$. If $\int_{\Omega} |\hat{\lambda}(t)| \pi(t) dt < \infty$, the definition of expected Bayesian (E-Bayesian) estimation is:

$$\hat{\lambda}_{EB} = \int_{\Omega} \hat{\lambda}(t) \pi(t) dt \quad (2)$$

where Ω is the interval of the hyper parameter t , $\pi(t)$ is the density function in Ω , $\hat{\lambda}(t)$ is Bayesian estimation for λ . From the E-Bayesian definition of failure rate λ , we can obtain:

$$\hat{\lambda}_{EB} = \int_{\Omega} \hat{\lambda}(t) \pi(t) dt = E_t[\hat{\lambda}(t)] \quad (3)$$

We can see that $\hat{\lambda}_{EB}$ is the mathematical expectation of hyper parameter t in the Bayesian estimation $\hat{\lambda}(t)$.

It is noticeable that E-Bayesian estimation is different from hierarchical Bayesian estimation. However, there are some connections between the E-Bayesian estimation and hierarchical Bayesian estimation, see [5,8] for further details.

3. Assumptions for zero-failure data

Different kinds of censored data are often gathered in reliability and life tests. For Type I Censoring test, especially in the tests of high-reliability products with small samples, zero-failure data are frequently collected. With the development of technology, zero-failure data attracted wide attention, and the researches on zero-failure data needs intensive studies.

In reliability tests, we assume that the distribution function of product life T is $F(t)$, follow the two steps:

- Take n samples and divide them into m groups. The number of the sample in the i th group is n_i , $i = 1, 2, 3, \dots, m$, $\sum_{i=1}^m n_i = n$.
- Assume that each group starts testing at the same time 0, the i th group stops at time t_i , $0 < t_1 < t_2 < \dots < t_m$, and no product fails during the whole test. Then (t_i, n_i) is called zero-failure data.

The test starts at time 0 with m group, group 1 stops testing until time t_1 , group 2 stops testing until time t_2 . It goes on until time t_m , group m stops testing, when all tests come to the end. We can obtain:

$$S_j = \sum_{i=j}^m n_i, \quad j = 1, 2, 3, \dots, m \quad (4)$$

There is not any failure during the test, from time t_j onwards, S_j samples are still under test. So we can suggest that there are S_j samples of which life is more than t_j , $j = 1, 2, \dots, m$.

According to the above, we can make some assumptions as follows:

- When the time of the reliability test is $t_0 = 0$, the failure rate of the product is 0, which is $p_0 = P(T \leq 0) = F(0) = 0$.
- $S_j = \sum_{i=j}^m n_i$, $j = 1, 2, 3, \dots, m$, that means at time t_j , there are S_j samples whose life are longer than t_j , $j = 1, 2, \dots, m$.
- The failure rate at time t_j is $p_j = P(T \leq t_j)$, $0 < t_1 < t_2 < \dots < t_m$. Then the reliability of the product at time t_j is $R = 1 - p_j = P(T > t_j)$, $p_0 < p_1 < \dots < p_m$.

4. E-Bayesian model for exponential distribution with zero-failure data

If the life distribution of the product is exponential distribution, the density function is as follows:

$$f(t) = \lambda \exp(-\lambda t), t > 0 \quad (5)$$

where λ is the failure rate of the exponential distribution, and $\lambda > 0$.

Assume the prior distribution of λ is a Gamma distribution, the density function is:

$$\pi(\lambda | a, b) = \frac{b^a}{\Gamma(a)} \lambda^{a-1} \exp(-b\lambda) \quad (6)$$

where a and b are both hyper parameters with $a > 0$, $b > 0$, $\lambda > 0$, and $\Gamma(a) = \int_0^\infty t^{a-1} e^{-t} dt$ is a Gamma function.

Usually the failure rate of a high quality product is less than that of a low quality product with the failure data, which fits for the reliability theory. According to that model, Xu and Liu [15] proposed a decreasing function for prior distribution of failure rate λ . The derivative of the density function $\pi(\lambda | a, b)$ is:

$$\frac{d\pi(\lambda | a, b)}{d\lambda} = \frac{b^a \lambda^{a-2} \exp(-b\lambda) ((a-1) - b\lambda)}{\Gamma(a)} \quad (7)$$

It can be seen that when $0 < a < 1$ and $b > 0$, from Eq. (6) one can find that the prior distribution $\pi(\lambda | a, b)$ is a decreasing function for λ . For Bayesian estimation, when $0 < a < 1$, the increasing of parameter b makes the reliability robustness decreasing. Thus we set an upper bound c for parameter b , then the range of b is $0 < b < c$ (c is a constant). Assuming the prior distribution of a is $U(0, 1)$ and that of b is $U(0, c)$ [9]. So we can obtain the density functions of a and b as:

$$\pi(a) = 1(0 < a < 1), \pi(b) = \frac{1}{c}(0 < b < c)$$

In Type I Censoring tests of exponential distribution samples, if there are X_i samples failed in test $i (i = 1, 2, \dots, m)$, i is the number of Type I Censoring tests. Based on [10], the failure number X_i is subject to Poisson distribution with the parameters t_i, n_i and λ :

$$P\{X_i = r_i\} = \frac{(t_i n_i \lambda)^{r_i}}{(r_i)!} \exp(-t_i n_i \lambda) \quad (8)$$

where $r_i = 0, 1, \dots, n$, and $i = 1, 2, \dots, m$.

The likelihood function of λ is:

$$L(X_i | \lambda) = \prod_{i=1}^m P\{X_i = r_i\} = \left[\prod_{i=1}^m \frac{(t_i n_i \lambda)^{r_i}}{(r_i)!} \right] \exp(-N\lambda) \quad (9)$$

under zero-failure condition, which means $r_i = 0, i = 1, 2, \dots, m$, we can note that $L(0 | \lambda) = \exp(-N\lambda)$.

If the prior density function $\pi(\lambda | a, b)$ is exactly as Eq. (6), according to Bayes theory, the posterior density function of λ is:

$$\begin{aligned} h(\lambda | 0) &= \frac{\pi(\lambda | a, b) L(0 | \lambda)}{\int_0^\infty \pi(\lambda | a, b) L(0 | \lambda) d\lambda} = \frac{\frac{b^a}{\Gamma(a)} \lambda^{a-1} \exp(-b\lambda) \exp(-N\lambda)}{\int_0^\infty \frac{b^a}{\Gamma(a)} \lambda^{a-1} \exp(-b\lambda) \exp(-N\lambda) d\lambda} \\ &= \frac{\lambda^{a-1} \exp[-(N+b)\lambda]}{\int_0^\infty \lambda^{a-1} \exp[-(N+b)\lambda] d\lambda} = \frac{(N+b)^a}{\Gamma(a)} \lambda^{a-1} \exp[-(N+b)\lambda] \end{aligned} \quad (10)$$

The Bayesian estimation of λ under square loss is:

$$\hat{\lambda}_B = \int_0^\infty \lambda h(\lambda | 0) d\lambda = \frac{(N+b)^a}{\Gamma(a)} \int_0^\infty \lambda^a \exp[-(N+b)\lambda] d\lambda = \frac{a}{N+b} \quad (11)$$

We can obtain E-Bayesian estimation of the failure rate λ , which is:

$$\hat{\lambda}_{EB} = \frac{1}{c} \int_0^c \int_0^1 \frac{a}{N+b} da db = \frac{1}{2c} \int_0^c \frac{1}{N+b} db = \frac{1}{2c} \ln \frac{N+c}{N} \quad (12)$$

where $N = \sum_{i=1}^m t_i n_i$, (t_i, n_i) is the zero-failure data in the life tests,

$i = 1, 2, \dots, m$.

5. Experimental verification and model application

In order to verify the proposed E-Bayesian estimation model, we set up a reliability test by subjecting specimens to a series of life tests under different working circumstances. Then the life data are collected and analyzed to obtain the life time of the specimens. The purpose of this experiment is to estimate the reliability of the seekers with a simplified estimation model for engineering applications.

The samples were tested in different test environments. None of them failed during the test, and these observations are shown in Table 5.1. Assume that differences between the test environments have no effect on the life time. We can assume that all the seekers were tested at the same time, thus we can obtain the zero-failure working time data of the observations, which are shown in Table 5.2.

According to Eq. (12), we have $N = \sum_{i=1}^m t_i n_i = 2051$, and we can

obtain the E-Bayesian estimation of the failure rate $\hat{\lambda}_{EB}$.

There are two methods to take zero-failure information into consideration. Han M. [6] proposed a model for $m+1$ Type I Censoring test, which is:

$$t_{m+1} = t_m + \frac{1}{m-1} \sum_{i=2}^m (t_i - t_{i-1}), \quad n_{m+1} = \left[\frac{1}{m} \sum_{i=1}^m n_i \right] \quad (13)$$

where $\left[\frac{1}{m} \sum_{i=1}^m n_i \right]$ means rounding down for $\frac{1}{m} \sum_{i=1}^m n_i$. Then we can obtain

$$M = \sum_{i=1}^{m+1} t_i n_i, \quad \text{and} \quad \hat{\lambda}_{EB1} = \frac{1}{2c} \ln \frac{M+c}{M}.$$

According to the average remaining life method, Wu [14] developed another model for t_{m+1} with zero-failure data:

$$t'_{m+1} = t_m + \frac{1}{\lambda}, \quad n_{m+1} = \left[\frac{1}{m} \sum_{i=1}^m n_i \right] \quad (14)$$

Table 5.1 Working time of the seekers

Test Sample	Working Time (h)				
	Test Environment A	Test Environment B	Test Environment C	Test Environment D	Test Environment E
a	10	40	45	162	72
b	10	/	/	162	68
c	12	12	3	45	105
d	10	13	3	50	102

Table 5.2 Zero-failure data of the tested seekers

Test Sample	Failure Number	Total Working Time (Censoring Time t_i)	Cumulative Zero-failure Number (Test Sample n_i)
c	0	177h	4
d	0	178h	3
b	0	240h	2
a	0	329h	1

Table 5.3 The results of E-Bayesian estimation for failure rate

c	300	500	1000	2000	3000	4000	5000	6000
$\hat{\lambda}_{EB} \times 10^{-4}$	2.2752	2.1815	1.9857	1.7015	1.5020	1.3523	1.2348	1.1395
$\hat{\lambda}_{EB1} \times 10^{-4}$	1.5885	1.5415	1.4384	1.2771	1.1552	1.0591	0.9808	0.9155
$\hat{\lambda}_{EB2} \times 10^{-4}$	0.3568	0.3428	0.3133	0.2695	0.2383	0.2145	0.1957	0.1804
$\hat{\lambda}_H \times 10^{-4}$	4.4515	4.2156	3.7409	3.0948	2.6687	2.3629	2.1307	1.9472

Table 5.4 The results of E-Bayesian estimation for reliability

c	300	500	1000	2000	3000	4000	5000	6000
\hat{R}_{EB}	0.9555	0.9573	0.9610	0.9665	0.9704	0.9733	0.9756	0.9774
\hat{R}_{EB1}	0.9687	0.9696	0.9716	0.9748	0.9772	0.9790	0.9806	0.9819
\hat{R}_{EB2}	0.9929	0.9932	0.9938	0.9946	0.9952	0.9957	0.9961	0.9964
\hat{R}_H	0.9148	0.9191	0.9279	0.9400	0.9480	0.9538	0.9583	0.9618

where λ is a unknown parameter, we use E-Bayesian estimation $\hat{\lambda}_{EB}$ instead of λ . Then we can obtain $M' = \sum_{i=1}^m t_i n_i + t'_{m+1} n_{m+1}$, and

$$\hat{\lambda}_{EB2} = \frac{1}{2c} \ln \frac{M' + c}{M'}.$$

As reported in [11], the range of c is $300 \leq c \leq 6000$, which is reasonable in engineering practice. Based on Eq. (12), we calculate the values of λ with different c , and compare with the hierarchical Bayesian estimation [7]. The results are shown in Table 5.3.

According to [9], the reliability of exponential distribution with zero-failure data (t_i, n_i) is as follows:

$$\hat{R}(t) = \exp(-\hat{\lambda}t) \quad (15)$$

where t is the moment for estimating the product reliability under the exponential distribution. The results of E-Bayesian estimation for reliability ($t = 200h$) are shown in Table 5.4.

These estimation results accord with the practical situation of the seekers. Based on the results, it can be inferred that after taking zero-failure data into consideration, the reliability estimation method of the products is significantly improved. Compared with the average remaining life method for zero-failure data, Eq. (13) makes the results more conservative, which is more acceptable in engineering applications.

6. Concluding remarks

In this paper, a reliability analysis method based on the E-Bayesian estimation for zero-failure data is proposed to estimate the reliability of seekers. By integrating the zero-failure information, the precision of estimation results of reliability increases greatly based on the hierarchical Bayesian estimation. Furthermore, the experiment results demonstrate that E-Bayesian method makes the calculation process easier and more effective for exponential distribution products. In addition, smaller c makes the results more conservative in engineering practices.

However, there are still some problems with reliability analysis of zero-failure data. When using Bayesian model for analyzing zero-failure data, the influence of assumptions about the parameters on final results is obscure. In addition, appropriate parameters and models selections for engineering applications need a further investigation.

Acknowledgement

This research was supported by the National Natural Science Foundation of China under contract number 11272082.

References

- Bartholomew D J. A problem in life testing. Journal of the American Statistical Association 1957; 52(279): 350-355, <http://dx.doi.org/10.1080/01621459.1957.10501394>.
- Chow S C and Shao J. Test for batch-to-batch variation in stability analysis. Statistics in medicine 1989; 8(7): 883-890, <http://dx.doi.org/10.1002/sim.4780080712>.
- Chow S C and Shao J. Estimating drug shelf-life with random batches. Biometrics 1991; 1071-1079, <http://dx.doi.org/10.2307/2532659>.
- Han M and Ding Y. Synthesized expected Bayesian method of parametric estimate. Journal of Systems Science and Systems Engineering 2004; 13(1): 98-111, <http://dx.doi.org/10.1007/s11518-006-0156-0>.
- Han M. Expected Bayesian estimation of failure probability and its character. Acta Mathematica Scientia 2007; 3: 013.
- Han M. The synthesize hierarchical Bayesian estimation of failure rate of zero-failure data, Operations Research and Management Science 1999; 8(1): 1-5.
- Han M. The hierarchical Bayesian estimation of failure-rate of exponential distribution of zero-failure data. Journal of Engineering Mathematics 1998; 15(4): 135-138.
- Han M. E-Bayesian estimation and hierarchical Bayesian estimation of failure rate. Applied Mathematics A Journal of Chinese Universities 2008; 23(4): 399-407.
- Liu Y F. Some applications of Bayes method in the study for the reliability of zero-failure data. China: Wenzhou University 2011.
- Mao S, Tang Y and Wang L. Reliability Statistics. Beijing: Higher Education Press 2008.
- Mao S. Statistical analysis of zero failure data. Mathematical Statistics and Applied Probability 1989; 4: 489-506.

12. Martz Jr H F and Waller R A. Bayesian Zero-Failure (BAZE) reliability demonstration testing procedure. *J. Qual. Technol* 1979; 11(3).
13. Miller K W, Morell L J, Noonan R E, et al. Estimating the probability of failure when testing reveals no failures. *IEEE Transactions on Software Engineering* 1992; 18(1): 33-43, <http://dx.doi.org/10.1109/32.120314>.
14. Wu X. Inspection with errors. *Chinese Journal of Applied Probability and Statistics* 1993; 9(3): 310-318.
15. Xu T, Liu H and Chen Y. Synthetic expected Bayesian estimation of failure rate in the case of zero failure data. *Journal of Applied Statistics and Management* 2011; 30(4): 644-654.

Yi-Chao YIN
Hong-Zhong HUANG
Weiwen PENG
Yan-Feng LI
Jinhua MI

Institute of Reliability Engineering
University of Electronic Science and Technology of China
No. 2006, Xiyuan Avenue, West Hi-Tech Zone
Chengdu, Sichuan, 611731, P. R. China

E-mail: hzhuang@uestc.edu.cn

Michael MUTINGI
Charles MBOHWA
Venkata P. KOMMULA

MULTI-CRITERIA RELIABILITY OPTIMIZATION FOR A COMPLEX SYSTEM WITH A BRIDGE STRUCTURE IN A FUZZY ENVIRONMENT: A FUZZY MULTI-CRITERIA GENETIC ALGORITHM APPROACH

WIELOKRYTERIALNA OPTYMALIZACJA NIEZAWODNOŚCI ZŁOŻONEGO SYSTEMU O STRUKTURZE MOSTKOWEJ W ŚRODOWISKU ROZMYTYM. METODA ROZMYTEGO WIELOKRYTERIALNEGO ALGORYTMU GENETYCZNEGO

Optimizing system reliability in a fuzzy environment is complex due to the presence of imprecise multiple decision criteria such as maximizing system reliability and minimizing system cost. This calls for multi-criteria decision making approaches that incorporate fuzzy set theory concepts and heuristic methods. This paper presents a fuzzy multi-criteria nonlinear model, and proposes a fuzzy multi-criteria genetic algorithm (FMGA) for complex bridge system reliability design in a fuzzy environment. The algorithm uses fuzzy multi-criteria evaluation techniques to handle fuzzy goals, preferences, and constraints. The evaluation approach incorporates fuzzy preferences and expert choices of the decision maker in regards to cost and reliability goals. Fuzzy evaluation gives the algorithm flexibility and adaptability, yielding near-optimal solutions within short computation times. Results from computational experiments based on benchmark problems demonstrate that the FMGA approach is a more reliable and effective approach than best known algorithm, especially in a fuzzy multi-criteria environment.

Keywords: multi-criteria optimization, reliability optimization, complex bridge system, genetic algorithm.

Optymalizacja niezawodności systemu w środowisku rozmytym to problem złożony ze względu na konieczność wzięcia pod uwagę wielu niedokładnie określonych kryteriów decyzyjnych, takich jak maksymalizacja niezawodności systemu i minimalizacja kosztów. Wymaga ona zastosowania wielokryterialnych metod podejmowania decyzji, które łącząby pojęcia z zakresu teorii zbiorów rozmytych oraz metody heurystyczne. W niniejszej pracy przedstawiono rozmyty wielokryterialny model nieliniowy (FMGA) oraz zaproponowano rozmyty wielokryterialny algorytm genetyczny do projektowania niezawodności złożonych systemów mostkowych w środowisku rozmytym. Algorytm wykorzystuje techniki rozmytej oceny wielokryterialnej do określania rozmytych celów, preferencji oraz ograniczeń. Metoda oceny uwzględnia rozmyte preferencje i eksperckie wybory decydenta dotyczące kosztów oraz celów niezawodnościowych. Ocena rozmyta nadaje algorytmowi cechy elastyczności oraz adaptacyjności, pozwalając na otrzymanie niemal optymalnych rozwiązań w krótkim czasie obliczeniowym. Wyniki eksperymentów obliczeniowych opartych na problemach wzorcowych pokazują, że podejście z zastosowaniem FMGA jest bardziej niezawodne i wydajne niż najbardziej znany algorytm, zwłaszcza w rozmytym środowisku wielokryterialnym.

Słowa kluczowe: optymalizacja wielokryterialna, optymalizacja niezawodności, złożony system mostkowy, algorytm genetyczny.

1. Introduction

Reliability is central to productivity and effectiveness of real world industrial systems [22, 35]. To maximize productivity, the systems should always be available. However, it is difficult for an industrial system, comprising several complex components to survive over time since its reliability directly depends on the characteristics of its components. Failure is inevitable, such that system reliability optimization has become a key subject area in industry. Developing effective system reliability optimization is imperative. Two approaches for system reliability improvement are: (i) using redundant elements in subsystems, and (ii) increasing the reliability of system components.

Reliability-redundancy allocation maximizes system reliability via redundancy and component reliability choices [23], with restrictions on cost, weight, and volume of the resources. The aim is to find a trade-off between reliability and other resource constraints [22]. Thus, for a highly reliability system, the main problem is to balance reliabil-

ity enhancement and resource consumption. A number of approaches in the literature focus on the application of metaheuristic methods for solving system reliability optimization problems [9, 7, 27, 15, 33, 34, 10, 13]. However, real-life reliability optimization problems are complex:

- (i) management goals and the constraints are often imprecise;
- (ii) problem parameters as understood by the decision maker may be vague; and,
- (iii) historical data is often imprecise and vague.

Uncertainties in component reliability may arise due to variability and changes in the manufacturing processes that produce the system component. Such uncertainties in data cannot be addressed by probabilistic methods which deal with randomness. Therefore, the concept of fuzzy reliability is more promising [2, 4, 5, 6, 30, 31]. Contrary to

probabilistic models, fuzzy theoretic approaches address uncertainties that arise from vagueness of human judgment and imprecision [26, 3, 28, 1, 13, 14].

A number of methods and applications have been proposed to solve fuzzy optimization problems by treating parameters (coefficients) as fuzzy numerical data. [31, 11, 20, 21, 24]. In a fuzzy multi-criteria environment, simultaneous reliability maximization and cost minimization requires a trade-off approach. Metaheuristics are a potential application method for such complex problems [9]. Population based metaheuristics are appropriate for finding a set of solutions that satisfy the decision maker's expectations. This calls for interactive fuzzy multi-criteria optimization which incorporates preferences and expectations of the decision maker, allowing for expert judgment. Iteratively, it becomes possible to obtain the most satisfactory solution.

In light of the above issues, the aim of this research is to address the system reliability optimization problem for a complex bridge system in a fuzzy multi-criteria environment. Specific objectives of the research are (1) to develop a fuzzy multi-criteria decision model for the problem; (2) to use an aggregation method to transform the model to a single-criteria optimization problem; and, (3) to develop a multi-criteria optimization method for the problem.

The rest of the paper is organized as follows: The next section describes the problem formulation for the complex bridge system. Section 3 provides a general fuzzy multi-criteria optimization modelling approach. In Section 4, a fuzzy multi-criteria genetic algorithm approach is proposed. Computational experiments, results and discussions are presented in Section 5. Section 6 concludes the paper.

2. Problem formulation

This section presents the mathematical formulation for the reliability optimization for a complex bridge system. In the real world, a typical complex bridge system [23] comprises five components or subsystems. The general structure of the complex bridge system is illustrated in Fig. 1.

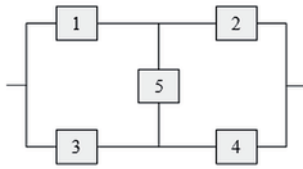


Fig. 1. The schematic diagram of the complex bridge system

The aim is to maximize system reliability, subject to multiple linear constraints. In this respect, we present the following notations and assumptions;

Notations:

m	the number of subsystems in the system
n_i	the number of components in subsystem i , $1 \leq i \leq m$
n	$\equiv (n_1, n_2, \dots, n_m)$, the vector of the redundancy allocation for the system
r_i	the reliability of each component in subsystem i , $1 \leq i \leq m$
r	$\equiv (r_1, r_2, \dots, r_m)$, the vector of the component reliabilities for the system
q_i	$= 1 - r_i$, the failure probability of each component in subsystem i , $1 \leq i \leq m$
$R_i(n_i)$	$= 1 - q_i^{n_i}$, the reliability of subsystem i , $1 \leq i \leq m$
R_s	the system reliability
g_i	the i^{th} constraint function

w_i	the weight of each component in subsystem i , $1 \leq i \leq m$
v_i	the volume of each component in subsystem i , $1 \leq i \leq m$
c_i	the cost of each component in subsystem i , $1 \leq i \leq m$
V	the upper limit on the sum of the subsystems' products of volume and weight
C	the upper limit on the cost of the system
W	the upper limit on the weight of the system
b	the upper limit on the resource
α_i, β_i	parameters in constraint functions of subsystem i

Assumptions

1. The availability of the components is unlimited;
2. The weight and product of weight and square of the volume of the components are deterministic;
3. The redundant components of individual subsystems are identical;
4. Failures of individual components are independent;
5. All failed components will not damage the system and are not repaired.

The problem can be formulated as a mixed integer nonlinear programming model as follows [8, 34, 35]:

$$\begin{aligned}
 \text{Max} \quad & \eta(r, n) = R_1 R_2 + R_3 R_4 + R_1 R_4 R_5 + R_2 R_3 R_5 + 2R_1 R_2 R_3 R_4 R_5 \\
 & - R_1 R_2 R_3 R_4 - R_1 R_2 R_3 R_5 - R_1 R_2 R_4 R_5 - R_1 R_3 R_4 R_5 - R_2 R_3 R_4 R_5 \\
 \text{Subject to:} \quad & g_1(r, n) = \sum_{i=1}^m w_i v_i^2 n_i^2 \leq V \\
 & g_2(r, n) = \sum_{i=1}^m \alpha_i (-1000/\ln r_i)^{\beta_i} (n_i + \exp(n_i/4)) \leq C \\
 & g_3(r, n) = \sum_{i=1}^m w_i n_i \exp(n_i/4) \leq W \\
 & 0 \leq r_i \leq 1, n_i \in \text{positive integer}, 1 \leq i \leq m
 \end{aligned} \quad (1)$$

where, $\eta(\cdot)$ denotes the system reliability, and expressions $g_1(\cdot)$, $g_2(\cdot)$, and $g_3(\cdot)$ represent the total volume, cost, and weight of the system, respectively.

In the next section, we propose a general approach to fuzzy multi-criteria optimization, in the context of system reliability optimization.

3. Fuzzy multi-criteria optimization modelling

In a fuzzy environment, the aim is to find a trade-off between reliability, cost, weight and volume. A common approach is to simultaneously maximize reliability and minimize cost. Constraints are transformed into objective functions, so that reliability and other cost functions can be optimized jointly. This is achieved through the use of membership functions, which are easily applicable and adaptable to the real life decision process.

In general, the fuzzy multi-criteria optimization problem can be represented by the following [13, 29];

$$\begin{aligned}
 \text{Min} \quad & \tilde{\eta}(x) \\
 \text{Subject to:} \quad & g_z(x) \leq \text{or } \equiv \text{ or } \geq 0 \quad z = 1, 2, \dots, p \\
 & v_q \leq x_q \leq \bar{v}_q \quad q = 1, 2, \dots, Q
 \end{aligned} \quad (2)$$

where, $x = (x_1, x_2, \dots, x_Q)^T$, is a vector of decision variables that optimize a vector of objective functions, $\tilde{\eta}(x) = \{\tilde{\eta}_1(x), \tilde{\eta}_2(x), \dots, \tilde{\eta}_h(x)\}$ are

h individual objective functions over the decision space X ; v_q and \bar{v}_q are lower and upper bounds on the decision variable x_q , respectively. Note that expressions $g_1(\cdot)$, $g_2(\cdot)$ and $g_3(\cdot)$ in (1) are converted into objective functions.

Fuzzy set theory permits gradual assessment of membership, in terms of a suitable function that maps to the unit interval $[0,1]$. Membership functions such as Generalized Bell, Gaussian, Triangular and Trapezoidal can represent the fuzzy membership [31]. Linear membership functions can provide good quality solutions with much ease, including the widely recommended triangular and trapezoidal membership functions [6, 8, 11, 30, 31]. Thus, we use linear functions to define fuzzy memberships of objective functions (or decision criteria).

Let a_t and b_t denote the minimum and maximum feasible values of each objective function $\tilde{\eta}_t(x)$, $t = 1, 2, \dots, h$, where h is the number of objective functions. Let μ_{η_t} denote the membership function corresponding to the objective function f_t . Then, the membership function corresponding to minimization and maximization is defined based on satisfaction degree. Fig. 2 illustrates the linear membership functions defined for minimization and maximization.

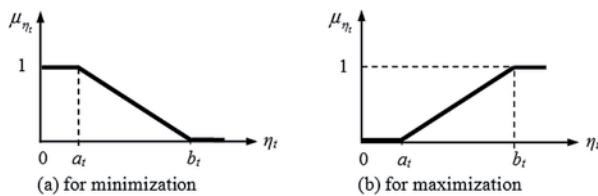


Fig. 2. Fuzzy membership functions for $\eta_t(x)$

As shown in Fig. 2(a), the linear membership function is suitable for representing cost functions that should be minimized. The membership function is represented as follows;

$$\mu_{\eta_t}(x) = \begin{cases} 1 & \eta_t(x) \leq a_t \\ \frac{b_t - \eta_t(x)}{b_t - a_t} & a_t \leq \eta_t(x) \leq b_t \\ 0 & \eta_t(x) \geq b_t \end{cases} \quad (3)$$

The linear membership function shown in Fig. 2(b) is suitable for representing profit functions that should be maximized. The membership function is represented as follows;

$$\mu_{\eta_t}(x) = \begin{cases} 0 & \eta_t(x) \leq a_t \\ \frac{\eta_t(x) - a_t}{b_t - a_t} & a_t \leq \eta_t(x) \leq b_t \\ 1 & \eta_t(x) \geq b_t \end{cases} \quad (4)$$

Having defined the fuzzy model using membership functions, the corresponding crisp model is formulated. Fuzzy evaluation enables FMGA to cope with infeasibilities which is otherwise impossible with crisp formulation. This gives the algorithm speed and flexibility, which ultimately improves the search power of the algorithm.

4. A fuzzy multi-criteria genetic algorithm approach

FMGA is an improvement from the classical genetic algorithm (GA). GA is a stochastic global optimization technique that evolves a population of candidate solutions by giving preference of survival

to quality solutions, while allowing some low quality solutions to survive, to maintain diversity in the population [18]. Each candidate solution is coded into a string of digits, called chromosomes. New offspring are obtained from probabilistic genetic operators, such as selection, crossover (at probability p^c), mutation (at a probability p^m), and inversion [16]. A comparison of new and old (parent) candidates is done based on a given fitness function, retaining the best performing candidates into the next population. Characteristics of candidate solutions are passed through generations using genetic operators. The overall flow of the FMGA is presented in Fig. 3.

Algorithm 1. The FMGA Pseudo-Code

```

1. Begin
2.   Input: FMGA parameters;  $p^c, p^m, popsize, maxgen, w_1, \dots, w_h$ ;
3.   Initialize pop:  $t = 0; P(0)$ ;
4.   Repeat
5.     Selection(){
6.       evaluation ( $P(t)$ );
7.       create temporal population,  $temp(t)$ 
8.     }
9.     Crossover(){
10.      select 2 chromosomes from  $temp(t)$ ;
11.      apply crossover operator, repair if necessary
12.    }
13.    Mutation(){
14.      mutate  $P(t)$ ;
15.      add offspring to  $newpop(t)$ 
16.    }
17.    Replacement(){
18.      compare successively,  $spool(t)$  and  $oldpop(t)$  strings;
19.      take the ones that fare better;
20.      select the rest of the strings with probability 0.52
21.    }
22.    Diversification(){
23.      calculate population diversity  $h$ ;
24.      While ( $h < h_c$ )
25.        diversify  $P(t)$ ;
26.        recalculate  $h$ ;
27.      End While
28.    }
29.    evaluation ( $P(t)$ );
30.    New population(){
31.       $oldpop(t) = newpop(t)$ ;
32.      advance population,  $t = t + 1$ 
33.    }
34.  Until (termination criteria satisfied)
35. End

```

Fig. 3. The overall pseudo-code of the FMGA

4.1. Chromosome coding

Traditionally, candidate solutions were encoded as binary strings. In the FMGA, each candidate solution is encoded into a chromosome using the variable vectors n and r . An integer variable n_i is coded as a real variable and transformed to the nearest integer value upon objective function evaluating.

4.2. Initialization and evaluation

An initial population of the desired size, pop , is randomly generated. FMGA then computes the objective function for each string (chromosome). The string is then evaluated according to the overall objective function in the model.

To improve flexibility and to incorporate the decision maker's preferences into the model, we introduce user-defined weightings, $w = \{w_1, w_2, \dots, w_h\}$. We use the max-min operator to aggregate the membership functions of the objective functions, incorporating expert opinion. Thus, from models (1) and (2), constraints $g_1(\cdot)$, $g_2(\cdot)$, and $g_3(\cdot)$ which represent volume, cost, and weight, respectively, are transformed into objective functions using the fuzzy membership functions. This leads to a multiple criteria system reliability optimization model, consisting of five criteria namely, reliability, volume, cost, and weight. In addition, the model is converted into a single objective optimization model as follows:

$$\left. \begin{aligned} & \text{Max} \left(1 \wedge \frac{\lambda_1(x)}{w_1} \right) \wedge \left(1 \wedge \frac{\lambda_2(x)}{w_2} \right) \wedge \dots \wedge \left(1 \wedge \frac{\lambda_h(x)}{w_h} \right) \\ & \text{Subject to :} \\ & \lambda_t(x) = \mu_{\eta_t}(x) \quad w_t \in [1,0] \quad t=1,\dots,h \\ & v_q \leq x_q \leq \bar{v}_q \quad q=1,2,\dots,Q \end{aligned} \right\} \quad (5)$$

Here, $\mu_{\eta_t}(x) = \{\mu_{\eta_1}(x), \mu_{\eta_2}(x), \dots, \mu_{\eta_h}(x)\}$ signifies a set of fuzzy regions that satisfy the objective functions λ_t which denote the degree of satisfaction of the t^{th} objective; x is a vector of decision variables; w_t is the weighting of the t^{th} objective function; and symbol " \wedge " is the aggregate min operator. Thus, expression $(1 \wedge \lambda_1(x)/w_1)$ gives the minimum between 1 and $\lambda_1(x)/w_1$. Though $\lambda_1(x)$ are in the range $[0,1]$, the value of $\lambda_1(x)/w_1$ may exceed 1, howbeit, the final value of $(1 \wedge \lambda_1(x)/w_1)$ will always lie in $[0,1]$. A FMGA approach is used to solve the model.

4.3. Selection and crossover

Several selection strategies have been suggested in [16]. The remainder stochastic sampling without replacement is preferred; each chromosome j is selected and stored in the mating pool according to the expected count e_j ;

$$e_j = \frac{f_j}{\sum_{j=1}^{pop} f_j / pop} \quad (6)$$

where, f_j is the objective function value of the j^{th} chromosome. Each chromosome receives copies equal to the integer part of e_j , while the fractional part is treated as success probability of obtaining additional copies of the same chromosome into the mating pool.

Genes of selected parent chromosomes are partially exchanged to produce new offspring. We use an arithmetic crossover operator which defines a linear combination of two chromosomes [25][29]. Assume a crossover probability of 0.41. Let p_1 and p_2 be two parents randomly selected for crossover. Then, the resulting offspring, q_1 and q_2 , are given by the following expression;

$$\begin{aligned} q_1 &= \varepsilon p_1 + (1 - \varepsilon) p_2 \\ q_2 &= (1 - \varepsilon) p_1 + \varepsilon p_2 \end{aligned} \quad (7)$$

where, ε represents a random number in the range $[0,1]$.

4.5. Mutation

Mutation is applied to every new chromosome so as to maintain diversity of the population, howbeit, at a very low probability. A uniform mutation probability rate of 0.032 is applied.

4.6. Replacement

At each generation or iteration, new offspring may be better or worse. As a result, nonperforming chromosomes should be replaced. A number of replacement strategies exist in the literature, e.g., probabilistic replacement, crowding strategy, and elitist strategy [26]. The proposed FMGA uses a hybrid of these strategies.

4.7. Termination

The FMGA algorithm uses two termination criteria to stop the iterations: when the number of generations exceeds the user-defined

maximum iterations, and when the average change in the fitness of the best solution over specific generations is less than a small number, which is 10^{-5} .

5. Computational illustrations

This section presents the computational experiments, results and discussions based on benchmark problems in [17, 19].

5.1. Computational experiments

We use the parameter values in [23] and define the specific instances of the problems as shown in Table 1.

Table 1. Basic data used for the bridge complex system

i	$10^5 a_i$	β_i	$w_i v_i^2$	w_i	V	C	W
1	2.330	1.5	1	7	110	175	200
2	1.450	1.5	2	8	110	175	200
3	0.541	1.5	3	8	110	175	200
4	8.050	1.5	4	6	110	175	200
5	1.950	1.5	2	9	110	175	200

The FMGA was implemented in JAVA on a 3.06 GHz speed processor with 4GB RAM. The FMGA crossover and mutation parameters were set at 0.45 and 0.035, respectively. A two-point crossover was used in this application. The population size was set to 20, and the maximum number of generations was set at 500. The termination criteria was controlled by either the maximum number of iterations, or the order of the relative error set at 10^{-5} , whichever is earlier. Whenever the best fitness f^* at iteration t is such that $|f_t - f^*| < \varepsilon$ is satisfied, then five best solutions are selected; where ε is a small number, which was set at value $\varepsilon = 10^{-5}$ for the computational experiments.

Expression (5) is used to solve benchmark problems. A fuzzy region of satisfaction is constructed for each criterion, that is, system reliability, cost, volume, and weight, denoted by λ_1 , λ_2 , λ_3 , and λ_4 , respectively. By using the constructed membership functions together with their corresponding weighting vectors, an equivalent crisp optimization formulation is obtained [29];

$$\left. \begin{aligned} & \text{Max} \left(1 \wedge \frac{\lambda_1(x)}{w_1} \right) \wedge \left(1 \wedge \frac{\lambda_2(x)}{w_2} \right) \wedge \left(1 \wedge \frac{\lambda_3(x)}{w_3} \right) \wedge \left(1 \wedge \frac{\lambda_4(x)}{w_4} \right) \\ & \text{Subject to :} \\ & \lambda_t(x) = \mu_{\eta_t}(x) \quad t=1,\dots,4 \\ & 0.5 \leq r_i \leq 1 - 10^{-6} \quad r_i \in [0,1] \\ & 1 \leq n_i \leq 10 \quad n_i \in \text{positive integers} \\ & 0.5 \leq R_s \leq 1 - 10^{-6} \quad R_s \in [0,1] \end{aligned} \right\} \quad (8)$$

The set $\omega = \{\omega_1, \omega_2, \omega_3, \omega_4\}$ are user-defined weightings in the range $[0.2,1]$ that indicate the bias towards specific decision criteria. To illustrate, given the weighting set $\omega = [1,1,1,1]$, the expert user expects no bias towards any criterion. On the contrary, set $\omega = [1,0.4,0.4,0.4]$, indicates preferential bias towards the region with higher reliability values as compared to the rest of the criteria equally weighted at 0.4. Consequently, the decision process considers the expert opinion and preferences of the decision maker.

Rather than prescribing a single solution to the user or decision maker, the FMGA interactively provides a population of near-optimal

solutions. The algorithm enables the decision maker to specify the minimum and maximum values of objective functions in terms of reliability η_1 , cost η_2 , volume η_3 , and weight η_4 . Table 2 provides a list of selected minimum and maximum values of the objective functions for the complex bridge system.

Table 2. Minimum and maximum values of objective functions

	η_1	η_2	η_3	η_4
b_t	1	180	190	110
a_t	0.6	60	70	20

Two experiments were conducted: Experiment 1 and Experiment 2.

5.1.1 Experiment 1

The aim of experiment 1 was to demonstrate the performance of the FMGA algorithm over time. As such, the algorithm was executed for 500 iterations, to show the results of intermediate solutions over time. A graphical analysis of the results was presented to show the performance behaviour of the algorithm.

5.1.2 Experiment 2

This purpose of experiment 2 was to make a comparative analysis of the performance of the FMGA algorithm against best known algorithms in the literature. Thus, the algorithm was executed 25 times, and the best five solutions were selected. The experimental results were compared with best known algorithms in [17] and [19], based on four performance criteria namely, reliability R_s , cost C_s , weight W_s , and volume V_s .

For further comparative analysis, an improvement measure is defined R_s , C_s , W_s and V_s values obtained. Thus, for each value, the percentage improvement I is defined according to the following expression:

$$I = ((v_s - v_{best}) / v_{best}) \times 100\% \quad (9)$$

where, v_s and v_{best} represent the FMGA solution value and the best known solution from literature. Computational results and the ensuing discussions are presented in the next section.

5.2 Computational results and discussions

This section presents the results of the computational experiments outlined in the previous section.

Table 3. FMGA performance against other algorithms

	Best 3 FMGA Solutions					Chen (2006) [8]	Wu et al. (2011) [35]
	$S_1 (r_i; n_i)$	$S_2 (r_i; n_i)$	$S_3 (r_i; n_i)$	$S_4 (r_i; n_i)$	$S_5 (r_i; n_i)$	$(r_i; n_i)$	$(r_i; n_i)$
1	0.790900512:4	0.828215087:2	0.825219610:3	0.817014473:3	0.820167554:3	0.81059326:3	0.82868361:3
2	0.867626123:3	0.819984805:3	0.853758959:3	0.845485199:3	0.851049098:3	0.85436730:3	0.85802567:3
3	0.902336897:3	0.894109978:4	0.894923994:3	0.913250236:3	0.905656019:3	0.88721528:3	0.91364616:2
4	0.803110963:1	0.833583709:1	0.757171007:2	0.812419422:1	0.750141630:2	0.72126594:3	0.64803407:4
5	0.625300922:1	0.763449829:1	0.677263922:1	0.682027145:1	0.640392747:2	0.71732358:1	0.70227595:1
R_s	0.9999928538	0.9999863254	0.9999758049	0.9999882710	0.9999731313	0.999958830	0.999889630
C_s	174.99949346	174.99999999	174.86624115805	174.99989705	174.81703492	175.00000000	174.9999960
W_s	196.988273245	180.13549794	177.41388514487	165.33338239	195.53463927	195.7352300	198.4395340
V_s	67.00	76.00	72.00	60.00	78.00	92.00000000	105.0000000

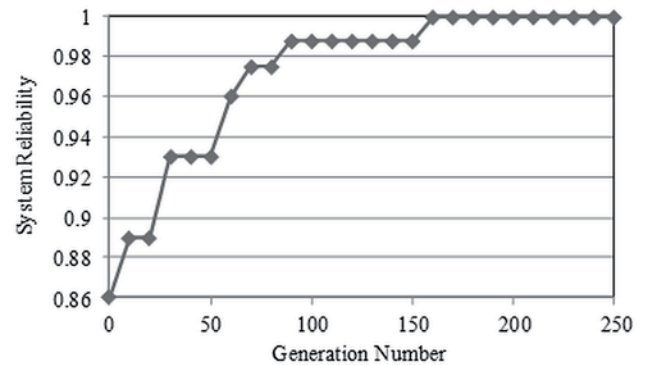


Fig. 4. Best system reliability value convergence over generations

5.2.1. Experiment 1 results

Figure shows a plot of the variation of the best fitness in each generation over a run time of 250 generations. After 250 generations, the following solution is obtained as the best solution: the maximum system reliability is $R_s = 0.999958830$. The reliability for the 5 constituent components are $r_1 = 0.81059326:3$, $r_2 = 0.85436730$, $r_3 = 0.88721528$, $r_4 = 0.72126594$ and $r_5 = 0.71732358$. The resulting system cost $C_s = 175.000$.

It can be seen that the algorithm converged to a desirable solution within about 200 iterations (generations). This indicates the potential of the algorithm in terms of computational efficiency.

5.2.2. Experiment 2 results

Computational results from experiment 2 showed the performance of FMGA as compared to other best known algorithms. The best five FMGA solutions were compared with the best results obtained from the literature [8][35].

Tables 3 presents the best five FMGA solutions, and the best known solutions obtained from [8] (with system reliability $R_s = 0.999958830$, cost $C_s = 175.00$, weight $W_s = 195.7352300$, and $V_s = 92.00$). It can be seen that, based on system reliability, cost, weight and volume, the five FMGA solutions are better than the best known results, except for a single weight value from solution S_1 (that is, 196.988273245) which is slightly higher than the best known (that is, 195.7352300). Further, all the five best FMGA solutions outperformed the solutions in [35], based on all performance criteria. This indicates that, overall, the FMGA performs better than the previous algorithms.

Table 4 presents the percentage improvement of the FMGA solutions, using the best known results as benchmarks. The improvements in reliability, cost, weight and volume are denoted by I_R , I_C , I_W and

Table 4. Percentage improvement of FMGA solutions over best known results

Improvement	S_1	S_2	S_3	S_4	S_5	Average
I_R	0.0034	0.0027	0.0017	0.0029	0.0014	0.0024
I_C	0.0003	0.0000	0.0764	0.0001	0.1046	0.0363
I_W	-0.6402	7.9698	9.3603	15.5321	0.1025	6.4649
I_V	27.1739	17.3913	21.7391	34.7826	15.2174	23.2609

I_R , respectively. The results show positive improvements of all the criteria. As indicated by the average values in the last column, there was remarkable improvement in volume, weight, cost and reliability, in that order of magnitude.

Overall, the proposed algorithm is more reliable and effective than existing algorithms in the literature. The algorithm offers a number of practical advantages to the decision maker, including the following:

- The FMGA method addresses the conflicting multiple objectives of the problem, giving a trade-off between the objectives;
- The approach accommodates the decision maker's fuzzy preferences;
- The method gives a population of alternative solutions, rather than prescribe a single solution;
- The method is practical, flexible and easily adaptable to problem situations.

In view of the above advantages, FMGA is a useful decision support tool for the practicing decision maker in system reliability optimization, especially in a fuzzy environment.

6. Conclusions

Decision makers in system reliability optimization seek to satisfy reliability enhancement and cost minimization. In a fuzzy environment, management goals and constraints are often imprecise and conflicting. One most viable and useful option is to use a fuzzy satisficing

approach that includes the preferences and expert judgments of the decision maker. This study provided a multi-criteria non-linear mixed integer program for reliability optimization of a complex bridge system. Using fuzzy multi-criteria evaluation, the model is converted into a single-objective model. Thus, FMGA uses fuzzy evaluation to find the fitness of candidates in each population. Illustrative computation experiments showed that the FMGA approach is highly capable of providing near optimal solutions.

Contrary to single-objective approaches which optimize system reliability only, FMGA provides satisficing solutions in the presence of fuzzy multiple criteria. Furthermore, the algorithm provides a population of good alternative solutions, which offers the decision maker a wide choice of practical solutions and an opportunity to consider other practical factors not included in the formulation. Therefore, the approach gives a robust method for system reliability optimization.

A fuzzy based approach is especially essential, given that, at design stage, the desired design information is not precisely known, which makes the problem rather ill-structured. As such, reliance on human experience and expert information is unavoidable. FMGA uses fuzzy theory concepts to effectively model the vagueness and imprecision of the expert knowledge, taking into account the conflicting multiple criteria. Computational results and comparative analysis showed that the proposed algorithm is more effective than best known algorithms in the literature.

Acknowledgement

This research work was financed by the University of Johannesburg, Johannesburg, South Africa, in the year 2015.

References

1. Bag S, Chakraborty D, Roy A. R. A production inventory model with fuzzy demand and with flexibility and reliability considerations. *Journal of Computers and Industrial Engineering* 2009; 56: 411–416, <http://dx.doi.org/10.1016/j.cie.2008.07.001>.
2. Bellman R, Zadeh L. Decision making in a fuzzy environment. *Management Science* 1970; 17: 141–164, <http://dx.doi.org/10.1287/mnsc.17.4.B141>.
3. Bing L, Meilin Z, Kai X. A practical engineering method for fuzzy reliability analysis of mechanical structures. *Reliability Engineering and System Safety* 2000; 67(3): 311–315, [http://dx.doi.org/10.1016/S0951-8320\(99\)00073-3](http://dx.doi.org/10.1016/S0951-8320(99)00073-3).
4. Cai K. Y, Wen C. Y, Zhang M. L. Fuzzy variables as a basis for a theory of fuzzy reliability in the possibility context. *Fuzzy Sets and Systems* 1991; 42: 145–172, [http://dx.doi.org/10.1016/0165-0114\(91\)90143-E](http://dx.doi.org/10.1016/0165-0114(91)90143-E).
5. Chen L. Multi-objective design optimization based on satisfaction metrics. *Engineering Optimization* 2001; 33: 601–617, <http://dx.doi.org/10.1080/03052150108940935>.
6. Chen S. M. Fuzzy system reliability analysis using fuzzy number arithmetic operations. *Fuzzy Sets and Systems* 1994; 64 (1): 31–38, [http://dx.doi.org/10.1016/0165-0114\(94\)90004-3](http://dx.doi.org/10.1016/0165-0114(94)90004-3).
7. Chen T. C, You P. S. Immune algorithm based approach for redundant reliability problems. *Computers in Industry* 2005; 56 (2): 195–205, <http://dx.doi.org/10.1016/j.compind.2004.06.002>.
8. Chen T-C. IAs based approach for reliability redundancy allocation problems. *Applied Mathematics and Computation* 2006; 182, 1556–1567, <http://dx.doi.org/10.1016/j.amc.2006.05.044>.
9. Coit D.W, Smith A.E. Reliability optimization of series-parallel systems using genetic algorithm. *IEEE Transactions on Reliability* 1996; R-45 (2), 254–260, <http://dx.doi.org/10.1109/24.510811>.
10. Deb K. An efficient constraint handling method for genetic algorithms. *Computer Methods in Applied Mechanics and Engineering* 2000; 186: 311–338, [http://dx.doi.org/10.1016/S0045-7825\(99\)00389-8](http://dx.doi.org/10.1016/S0045-7825(99)00389-8).
11. Delgado M, Herrera F, Verdegay J. L, Vila M. A. Post optimality analysis on the membership functions of a fuzzy linear problem. *Fuzzy Sets and Systems* 1993; 53 (1), 289–297, [http://dx.doi.org/10.1016/0165-0114\(93\)90400-C](http://dx.doi.org/10.1016/0165-0114(93)90400-C).
12. Duque O, Morifigo D. A fuzzy Markov model including optimization techniques to reduce uncertainty, *IEEE Melecon* 2004; 3 (1): 841–844, <http://dx.doi.org/10.1109/melcon.2004.1348077>.
13. Garg H, Sharma S. P, Multi-criteria reliability-redundancy allocation problem using particle swarm optimization. *Computers & Industrial*

- Engineering 2013; 64 (1): 247-255, <http://dx.doi.org/10.1016/j.cie.2012.09.015>.
14. Garg H. Sharma S. P. Stochastic behavior analysis of industrial systems utilizing uncertain data. ISA Transactions 2012; 51(6): 752–762, <http://dx.doi.org/10.1016/j.isatra.2012.06.012>.
 15. Giuggioli P., Marseguerra M., and Zio E. Multiobjective optimization by genetic algorithms: Application to safety systems. Reliability Engineering and System Safety, 2001; 72(1): 59–74, [http://dx.doi.org/10.1016/S0951-8320\(00\)00109-5](http://dx.doi.org/10.1016/S0951-8320(00)00109-5).
 16. Goldberg D. E. Genetic Algorithms: In Search, Optimization & Machine Learning. Addison-Wesley, Inc., MA, 1989.
 17. Hikita M, Nakagawa Y, Harihisa H. Reliability optimization of systems by a surrogate constraints algorithm. IEEE Transactions on Reliability 1992; R-41 (3): 473–480, <http://dx.doi.org/10.1109/24.159825>.
 18. Holland J. H. Adaptation in Natural and Artificial System. University of Michigan Press, Ann Arbor, MI, 1975.
 19. Hsieh Y.C, Chen T.C, Bricker D.L. Genetic algorithm for reliability design problems, Microelectronics and Reliability 1998; 38 (10): 1599-605, [http://dx.doi.org/10.1016/S0026-2714\(98\)00028-6](http://dx.doi.org/10.1016/S0026-2714(98)00028-6).
 20. Huang H. Z, Gu Y. K, Du X. An interactive fuzzy multi-criteria optimization method for engineering design. Engineering Applications of Artificial Intelligence 2006; 19(5): 451–460, <http://dx.doi.org/10.1016/j.engappai.2005.12.001>.
 21. Huang H. Z. Fuzzy multi-criteria optimization decision-making of reliability of series system. Microelectronics Reliability 1997; 37(3), 447–449, [http://dx.doi.org/10.1016/S0026-2714\(96\)00040-6](http://dx.doi.org/10.1016/S0026-2714(96)00040-6).
 22. Huang H. Z., Tian Z. G, Zuo M. J. Intelligent interactive multi-criteria optimization method and its application to reliability optimization. IIE Transactions 2005; 37 (11): 983–993, <http://dx.doi.org/10.1080/07408170500232040>.
 23. Kuo W, Prasad V. R. An annotated overview of system-reliability optimization. IEEE Transaction on Reliability 2000; 49 (2): 176–187, <http://dx.doi.org/10.1109/24.877336>.
 24. Mahapatra G. S, Roy T. K. Fuzzy multi-criteria mathematical programming on reliability optimization model. Applied Mathematics and Computation 2006; 174 (1): 643–659, <http://dx.doi.org/10.1016/j.amc.2005.04.105>.
 25. Mahapatra G. S, Roy P. A genetic algorithm approach for reliability of bridge network in fuzzy system. Journal of Information and Computing Science 2011; 6 (4): 243-254.
 26. Michalewicz Z. Genetic Algorithms + Data Structures = Evolutionary Programs. Springer, 1996, <http://dx.doi.org/10.1007/978-3-662-03315-9>.
 27. Moghaddam R. T., Safari J., and Sassani F. Reliability optimization of series–parallel systems with a choice of redundancy strategies using a genetic algorithm. Reliability Engineering and System Safety 2008; 93(4): 550–556, <http://dx.doi.org/10.1016/j.res.2007.02.009>.
 28. Mohanta D. K, Sadhu P.K, Chakrabarti R. Fuzzy reliability evaluation of captive power plant maintenance scheduling incorporating uncertain forced outage rate and load representation. Electric Power Systems Research 2004; 72(1), 73–84, <http://dx.doi.org/10.1016/j.epr.2004.04.001>.
 29. Mutingi M. System reliability optimization: A fuzzy multi-objective genetic algorithm approach. Eksploatacja i Niezawodność – Maintenance and Reliability 2014; 16 (3): 400–406.
 30. Onisawa T. An application of fuzzy concepts to modeling of reliability analysis. Fuzzy Sets and Systems 1990; 37 (3): 267–286, [http://dx.doi.org/10.1016/0165-0114\(90\)90026-3](http://dx.doi.org/10.1016/0165-0114(90)90026-3).
 31. Sakawa M. Fuzzy Sets and Interactive Multi-criteria Optimization. Plenum Press, New York, 1993, <http://dx.doi.org/10.1007/978-1-4899-1633-4>.
 32. Slowinski R. Fuzzy sets in decision analysis. Operations research and statistics. Boston: Kluwer Academic Publishers, 1998, <http://dx.doi.org/10.1007/978-1-4615-5645-9>.
 33. Wang Z, Chen T, Tang K, Yao X. A multi-objective approach to redundancy allocation problem in parallel-series systems. In Proceedings of IEEE Congress on Evolutionary Computation 2009: 582–589, <http://dx.doi.org/10.1109/cec.2009.4982998>.
 34. Wang Z., Tang K, Yao X. A memetic algorithm for multi-level redundancy allocation. IEEE Transactions on reliability 2010; 59(4): 754–765, <http://dx.doi.org/10.1109/TR.2010.2055927>.
 35. Wu P, Gao L, Zou D, Li S. An improved particle swarm optimization algorithm for reliability problems. ISA Transactions 2011; 50: 71-8, <http://dx.doi.org/10.1016/j.isatra.2010.08.005>.

Michael MUTINGI

Faculty of Engineering and the Built Environment
University of Johannesburg
P. O. Box 524, Auckland Park 2006, Johannesburg,
South Africa

Faculty of Engineering,
Namibia University of Science & Technology,
P Bag 13388 Windhoek
Namibia

E-mail: mmutingi@gmail.com

Charles MBOHWA

Faculty of Engineering and the Built Environment
University of Johannesburg
P. O. Box 524, Auckland Park 2006, Johannesburg, South
Africa

Venkata P. KOMMULA

Mechanical Engineering Department
University of Botswana
P Bag 0061, Gaborone, Botswana

E-mails: cmbowha@uj.ac.za, kommula@mopipi.ub.bw

Zhiao ZHAO
Jing QIU
Guanjun LIU
Yong ZHANG

RESEARCH ON TIME-VARYING CHARACTERISTICS OF TESTABILITY INDEX BASED ON RENEWAL PROCESS

BADANIE ZMIENNYCH W CZASIE WŁASNOŚCI WSKAŹNIKA TESTOWALNOŚCI NA PODSTAWIE PROCESU ODNOWY

Testability indices are used in the phases of testability design and testability demonstration. This paper focuses on fault detection rate (FDR), which is the most widely used testability index. Leading hypothesis suggests that the value of FDR of a system is usually a certain value. However, few attempts have been made to research the statistical characteristics of FDR. Considering the fault occurrence process and test uncertainty, FDR is time varying and a special statistical process. Under the assumption of perfect repairs, we build a fault occurrence model based on the renewal process theory. Supposing that test uncertainty is mainly induced by test fault, the renewal process is employed to depict the occurrence process of test faults. Simultaneously, we depict the process of test state change and then construct the fault detection logic based on the digraph model. Combining the fault occurrence model and the fault detection logic, we focus on the expectation of FDR, which is one of the key statistical characteristics. By comparison, we introduce the calculation method of expectation of FDR in two cases, including without considering test uncertainty and considering test uncertainty. To validate the conclusions presented in this paper, we carry on a simulation case using an integrated controller. Based on the theoretic and simulating methods, the expectation of FDR tends to be a constant with the increase of time under the assumptions made in this paper. The statistical characteristic of FDR presented in this paper would be the basic theoretical guide to testability engineering.

Keywords: testability index; fault detection rate; renewal process; test uncertainty; statistical characteristics.

Wskaźniki testowalności wykorzystuje się w fazach projektowania oraz potwierdzania testowalności. Przedstawiony artykuł poświęcony jest wskaźnikowi wykrywalności błędów (fault detection rate, FDR), który jest najczęściej stosowanym wskaźnikiem testowalności. Wiodąca hipoteza sugeruje, że wartość FDR dla danego systemu jest zwykle wartością pewną. Istnieje jednak niewiele badań na temat statystycznych własności FDR. Biorąc pod uwagę proces występowania błędów oraz niepewność pomiarów, współczynnik FDR można opisać jako zmienny w czasie specjalny proces statystyczny. Przy założeniu naprawy doskonałej, zbudowaliśmy model występowania błędów w oparciu o teorię procesu odnowy. Przyjmując, że niepewność testową wywołują głównie błędy testowe, wykorzystaliśmy proces odnowy do zobrazowania procesu występowania błędów testowych. Jednocześnie przedstawiliśmy proces zmiany stanu testu, a następnie zbudowaliśmy logikę wykrywania błędów w oparciu o model grafu skierowanego. Łącząc model występowania błędów z logiką wykrywania błędów, opracowaliśmy metodę obliczania wartości oczekiwanej FDR, która jest jedną z najważniejszych własności statystycznych tego wskaźnika. Dla porównania, metodę obliczania wartości oczekiwanej FDR zastosowaliśmy w dwóch przypadkach, z uwzględnieniem i bez uwzględnienia niepewności testowej. Aby zweryfikować wnioski przedstawione w niniejszej pracy, przeprowadziliśmy symulację z wykorzystaniem zintegrowanego kontrolera. Obliczenia teoretyczne i symulacja pokazują, że wartość oczekiwana FDR wraz z upływem czasu staje się wartością stałą w warunkach założonych w niniejszej pracy. Przedstawiona w artykule charakterystyka statystyczna FDR stanowi jedną z podstaw teoretycznych inżynierii testowej.

Słowa kluczowe: wskaźnik testowalności; wskaźnik wykrywalności błędów; proces odnowy; niepewność testu; własność statystyczna

1. Introduction

Reliability, maintainability and testability (RMT) have been integral parts of the equipment design. Equipment testability level has effects on operational reliability and maintainability [3], which improves the operational reliability and quick maintenance. For example, shortening mean time to repair (MTTR) needs high requirements of fault detection and isolation capability. After years of theoretical researches and engineering practices, testability index has formed a complete system. It is reported that the number of testability index is as many as dozens [13]. From the point view of clear definition and

easy demonstration, these testability indices, such as fault detection rate (FDR), fault isolation rate (FIR) and false alarm rate (FAR) etc., are widely used.

In particular, FDR is one of the most widely used testability index in many engineering practices. FDR is a measure of the capability that faults or failures occurring in the system can be detected by prescriptive test means. Briefly, FDR shows the system ability to indicate the occurred faults. FDR acts as the measure and constraint of the testability level in the design and demonstration phases. In the testability design stage, FDR is the constraint of the product testability level. During this stage, the product purchaser usually proposes a con-

tract value of FDR. In the testability demonstration stage, the contract value of FDR is the measure to validate product testability level. In this stage, the purchaser would decide whether to accept or reject the product using the statistical sampling method [7, 22, 23]. In order to validate the value of FDR of a series of products, it is assumed that the real value FDR of a test product is a certain number when we use the statistical sampling method [25]. The statistical sampling method is the core theory of the quality inspection. In a quality inspection procedure, the only source of the statistical error is due to random sampling. Currently, the demonstration test of FDR directly employs the theoretical assumptions adopted in the quality inspection. Therefore, if the FDR test based on the quality inspection theory can be used, it must accord to the assumption that the real value of FDR is an existing certain value and do not change. Moreover, the truth is that we pay little attention to the statistical characteristics of FDR. Accordingly, the research on statistical characteristics of FDR is crucial paramount.

FDR is a rate, which reflects the capability of automatic fault indication. Intuitively, the process of fault detection includes two steps. The first step is a fault occurs in a system. The second step, a test means, for example a Built-in Test (BIT), detects the occurred fault and give an indication to the operating or maintenance personnel. Therefore, to achieve the statistical characteristics of FDR, we must have more understandings of the laws of equipment fault occurrence and fault detection.

Modelling of fault occurrence is the key point of reliability and maintainability engineering [21]. The reliability level of a product is its inherent property, which decides the fault occurrence of a product. However, the fault occurrence process also depends on maintenance activities. For example, good maintenance activities can reduce the rate of occurrence of failure (ROCOF) [4]. On the contrary, poor maintenance actions would increase the ROCOF. From the point of view of existing testability engineering, the ROCOF of a product is considered to be constant and the fault interval obeys the exponential distribution [17]. Since the reliability tests carry out separately, testability staff only can obtain product fault information using reliability prediction method. The stochastic process model is related to models of repairable systems in the reliability and maintainability literature [1, 26, 28]. The widely used stochastic process models for repairable systems are the Poisson process, the renewal process (RP), the generalized renewal process (GRP) and the nonhomogeneous Poisson process (NHPP) [4, 11, 26]. The renewal process is commonly used if all the maintenance repairs are preventive maintenance, bringing the system to a "good-as-new" state each time (known as perfect repair). The renewal process (RP) is widely used to depict the fault occurrence process in systems with perfect repairs. The maintenance model was established based on the theory of renewal process and the periodic inspection interval is optimized [21]. Ji et al. [8] introduced to calculate time-varying failure probabilities based on a renewal-process-based model. Kim et al. simulated the failure and repair cycle of a component based on the alternating renewal process [10]. Reference [29] proposed a fault sample simulation approach for virtual testability demonstration test based on the renewal process theory.

The value of FDR is affected not only by the number of fault occurrence but also by the relationships of tests and faults. From a mathematical viewpoint, the dependency matrix (D matrix) can describe the certain relationship among faults and tests [5]. In a dependency matrix, the corresponding element in the D matrix is one when a test can detect a fault. On the contrary, the matrix element is zero when a fault is undetectable by a test. Considering the actual practice and theoretical study, the relation between a fault and a test is not purely zero or one. This relationship between fault and test is called as the uncertainty relation, also known as the test uncertainty. In this case, the relationship between a test and a fault can be depicted by a decimal between zero to one. Such D matrix is called the uncertainty dependency matrix. Reference [5] focuses on building the diagnostic strategy

based on the uncertainty correlation matrix. For the studies of sources of test uncertainty, reference [9] investigates that sensor faults are the main reasons causing the test uncertainty. References [18-20] focus on solving real-time multi-fault diagnosis problem using the theory of imperfect test. The definition of imperfect test is also a way to depict test uncertainty. They define the probability of detection and probability of false alarm to describe the test uncertainty. Accordingly, the relationship between a test and a fault is often uncertain. Generally, the test certainty is only the special case.

FDR is an important indicator of the testability level of a product. As a statistical and time varying parameter, its statistical characteristics are the main points of this paper. This paper proceeds as follow. Section 2 analyses the existing FDR test theory and describes the statistical property of FDR. Section 3 models the fault occurrence process using the renewal process theory. Test uncertainty based on the test fault model is described in Section 4. In Section 5, the expectation of FDR as the key stochastic characteristic is discussed. Section 6 gives a specific simulation example. Conclusions are given in Section 7.

2. Problem description

2.1. Existing test theory of FDR

The demonstration of FDR is carried out by artificially injecting faults into equipment. Then, the purchaser makes an acceptance/rejection decision according to the contractual requirement of FDR. The existing demonstration theory of FDR is mainly based on the sampling plan by attributes or sequential probability ratio test [15, 24]. The demonstration test of FDR is a Pass/Fail test. It means that each time of the test has two results, including successful detection or failed detection. The basic idea of the demonstration test of FDR is the receiver operating characteristic curve [6]. The characteristic curve $L(p)$ can be written as eq. (1). $L(p)$ is the probability $P\{f \leq c\}$ of an event $f \leq c$. Let f denote the number of failed tests of fault detection. The event $f \leq c$ denotes f is smaller or equal to a specified positive integer c :

$$L(p) = \sum_{i=0}^c C_n^i p^{n-i} (1-p)^i \quad (1)$$

where n is the number of test samples, c is the maximum number of allowable failed sample and p denotes the probability of success.

Using the sampling plan by attributes or sequential probability ratio test to carry on the FDR demonstration test, we must accept the implicit assumption that the FDR value of a system is a constant depicted as the parameter p in eq. (1). However, researchers have never proved this hypothesis theoretically or using FDR statistical data from the field. In order to validate the availability of this assumption, the statistical model of FDR would be built in next section.

2.2. Statistical model of FDR

FDR is defined as a rate, which the number of successfully detected faults is divided by the total number of occurred faults during the specified time interval. According to its definition, FDR is time varying. Here we use the notation $FDR(t)$ to represent fault detection rate at time t and $FDR(t)$ can be calculated as follows [30]:

$$FDR(t) = \frac{N^D(t)}{N(t)} \quad (2)$$

where $N(t)$ denotes the total occurred number of faults at time t and $N^D(t)$ denotes the total number of correctly detected faults at time t . Generally, the relationship of $N(t)$ and $N^D(t)$ must satisfy $N(t) \geq N^D(t)$.

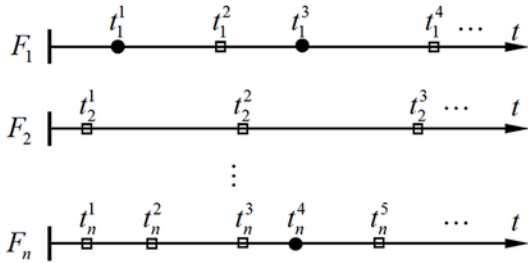


Fig. 1. Counting processes of fault detection in multiple faults system

Let $F = \{F_1, F_2, \dots, F_n\}$ denotes a fault set in a system. It means that faults occurred in this system are categorized as n groups. Generally, one of the groups is called a failure mode and we use the term fault to instead. As shown in Fig. 1, each fault F_i independently occurs at time $t_i^j (j=1, 2, \dots)$, where unfilled squares denote successfully detected faults and filled circles denote the undetected faults. Let $N_{F_i}(t)$ denote the total occurred number of the fault F_i at time interval $[0, t]$. Let $N_{F_i}^D(t)$ denotes the total number of correctly detected of the fault F_i at time interval $[0, t]$. Accordingly, the calculation of $FDR(t)$ can be further rewritten as follows:

$$\begin{aligned} FDR(t) &= \frac{\sum_{i=1}^n N_{F_i}^D(t)}{N(t)} \\ &= \frac{N_{F_1}^D(t)}{N(t)} + \frac{N_{F_2}^D(t)}{N(t)} + \dots + \frac{N_{F_n}^D(t)}{N(t)} \\ &= \frac{N_{F_1}^D(t)}{N_{F_1}(t)} \cdot \frac{N_{F_1}(t)}{N(t)} + \frac{N_{F_2}^D(t)}{N_{F_2}(t)} \cdot \frac{N_{F_2}(t)}{N(t)} + \dots + \frac{N_{F_n}^D(t)}{N_{F_n}(t)} \cdot \frac{N_{F_n}(t)}{N(t)} \\ &= \sum_{i=1}^n \lambda_{F_i}(t) \cdot r_{F_i}(t) \end{aligned} \quad (3)$$

where $\lambda_{F_i}(t) = N_{F_i}(t) / N(t)$ can be defined as an occurring weight, which denotes the proportion of occurred number $N_{F_i}(t)$ of the fault F_i to $N(t)$. The proportion $r_{F_i}(t) = N_{F_i}^D(t) / N_{F_i}(t)$ can be defined as the detection probability of the fault F_i . The values $\lambda_{F_i}(t)$ and $r_{F_i}(t)$ lie in an interval $[0, 1]$.

From eq. (3), we can clearly find that the value of $FDR(t)$ would be higher if occurring weights of the detectable faults increase. Here, the detectable faults mean that their detection probability $r_{F_i}(t)$ is not equal to zero. From the definition of eq. (2), $FDR(t)$ always lies in

the interval $[0, 1]$. As random variables $N(t)$ and $N^D(t)$ are time varying, $FDR(t)$ can be called a statistical process. As shown in Fig. 2, $FDR(t)$ fluctuates between zero to one. The dotted lines are the samples of $FDR(t)$. The heavy line is the expectation $E[FDR(t)]$ of the samples of $FDR(t)$. From the statistical views, we must pour much attention to the statistical characteristics of $FDR(t)$, such as the expectation $E[FDR(t)]$. Therefore, the trend and the statistical characteristics of $FDR(t)$ would be the key points in following sections.

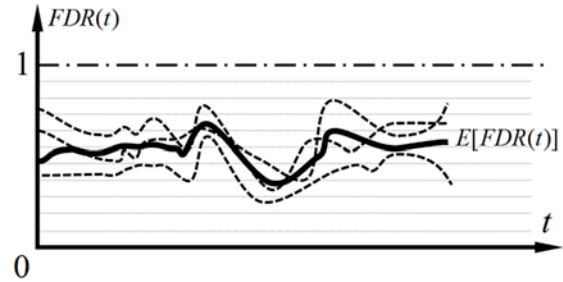


Fig. 2. Time varying characteristic of FDR

3. Fault occurrence model based on renewal process

The fault occurrence process is not only affected by its reliability level, but also affected by maintenance activities. Especially for repairable weapons and equipment, they have finite lifetimes that may require corrective maintenance during their lifetimes. During the whole life cycle, their fault occurrence situations should take the effects of maintenance activities into account. According to the effects on fault occurrence from the maintenance activity, maintenance activities can be divided into five categories [26]. Under the assumption of perfect repairs for repairable system, the system is assumed to restore to a 'good-as-new' state each time. Under this maintenance strategy, renewal process is widely used to depict the fault occurrence processes [27, 28].

In a renewal process, $N(t)$ denotes the number of faults occurred during time interval $[0, t]$. It is a counting process, which has the following properties.

- (1) $N(t) \geq 0$.
- (2) The value of $N(t)$ is an integer and increases monotonically.
- (3) At different times t and $s (s > t)$, the number of occurred fault is denoted as $N(s) - N(t)$ during the interval $[t, s]$. In a counting process, if the value of $N(s) - N(t)$ is only related to the length of the interval $[t, s]$ and has no relation with the starting count time t , this counting process is called an independent increment process.

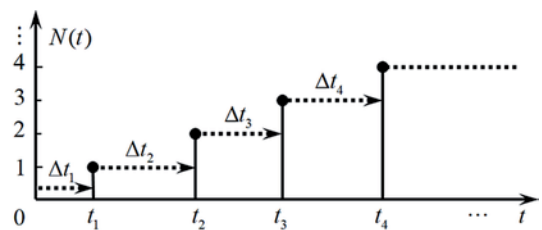


Fig. 3. Counting process of fault occurrence

A sample of counting process of fault occurrence is illustrated in Fig. 3. The fault occurrence times are (t_1, t_2, t_3, \dots) . We ignore the

repair time, i.e., the system is repaired and put into new operation immediately after a fault. Let t_i denote the occurring time of the i th fault. The interval $\Delta t_i = t_i - t_{i-1}$ ($i=1,2,\dots$) denotes the time interval length between the $(i-1)$ th fault and i th fault. Specially, $t_0 = 0$. We use the term interarrival time to depict the time interval between two successive faults. All of the interarrival times $\{\Delta t_i | i=1,2,\dots\}$ are considered independently and identically distributed. The n th fault occurrence time t_n can be written as:

$$t_n = \sum_{i=1}^n \Delta t_i \quad (4)$$

In the renewal process, the fault interval Δt_i obeys the same cumulative distribution function $F(t)$ of the interarrival time, namely $\Delta t_i \sim F(t)$ [10]. Shortly, we define the interarrival time function $F(t)$ to instead. And the probability density function is $f(t) = F'(t)$. The $F(t)$ may be the exponential distribution, Weibull distribution, log-normal distribution and Gamma distribution etc. Supposing that $F(t)$ obeys exponential distribution, the renewal process degenerates into a Poisson process. According to the current testability demonstration theory, the assumption that the interarrival time function is an exponential distribution represents that the fault occurrence process is a Poisson process. However, the Poisson process is just a special form of the renewal process [16]. Therefore, it is more universal using the renewal process to describe the process of fault occurrence.

From the mathematical description of the renewal process, it can be described by a function $M(t)$. $M(t)$ is called the renewal function, which is defined as the expectation of $N(t)$. It can be written as:

$$\begin{aligned} M(t) &= E[N(t)] \\ &= \sum_{n=1}^{\infty} nP\{N(t) = n\} \\ &= \sum_{n=1}^{\infty} n\{P\{N(t) \geq n\} - P\{N(t) \geq n+1\}\} \\ &= \sum_{n=1}^{\infty} n\{P\{t_n \leq t\} - P\{t_{n+1} \leq t\}\} \end{aligned} \quad (5)$$

where $P\{N(t) = n\}$ denotes the probability of n faults in $[0, t]$ and $n=0,1,2,\dots$.

The random variable t_n are the sum of n independent and identically random variables Δt_i , so we can rewrite $M(t)$ as:

$$\begin{aligned} M(t) &= \sum_{n=1}^{\infty} n\{F^n(t) - F^{n+1}(t)\} \\ &= \sum_{n=1}^{\infty} \{nF^n(t) - (n-1)F^n(t)\} \\ &= F^1(t) + \int_0^t M(t-x)dF(x) \end{aligned} \quad (6)$$

where $F^n(t)$ denotes the n -fold convolution of the time interval distribution function $F(t)$. $F^n(t)$ is the probability that the n th fault

occurs at time t . From the above analysis, $F(t)$, $F^n(t)$ and $M(t)$ can determine each other.

For the eq. (6), use the Laplace transform [16]:

$$M^*(s) = F^*(s) + M^*(s)F^*(s) \quad (7)$$

where $M^*(s)$ and $F^*(s)$ are the Laplace transform of $M(t)$ and $F(t)$ respectively.

Because $f(t) = F'(t)$, so $f(s) = sF(s)$. We can rewrite the eq. (7) as:

$$M^*(s) = \frac{F^*(s)}{1 - F^*(s)} \quad (8)$$

After obtaining the interarrival time function $F(t)$, the renewal function $M(t)$ can be calculated after the inverse Laplace transform of eq. (8).

4. Stochastic property modelling of fault detection

Realistically, the relationship between a fault and a test is uncertain in the actual operation of a system. This section focuses on modelling the test state change and describing fault detection logic.

The results of a test usually have three states, namely correct detection, missed detection and false alarm. The correct detection means that the test indication is consistent with the system occurred fault. The missed detection refers to when there exist a failure, but the test does not give the right fault indication or have no indication at all. A false alarm represents that the test indicates a fault but there is no fault really occurred in a system. References [19, 20] define the fault detection probability and the missed detection probability respectively to depict test uncertainty. Considering the definition of $FDR(t)$ according to eq. (2), it only relates to the existed faults whether they can be detected or not. Therefore, the false alarms would not be considered in this paper. So we define a test have two states, including normal state (give right fault indication) and error state (give wrong fault indication or no indication at all). For the sake of simplicity, test states are categorized as $\{0,1\}$, where 1 denotes the normal state and 0 represents the error state.

Reference [2] considered a test appears error state mainly because of sensor failures. Simple to understand, sensor failures mean that a sensor or test circuit itself is in fault. Generally, the reliability level and maintenance strategy of the tests are same as the product itself. Therefore, it is considered that fault occurrence rule of the test is consistent to product itself.

4.1. Digraph model of fault detection

In order to carry out the standardized description of fault detection in a system, $F = \{F_1, F_2, \dots, F_n\}$ denotes a fault set, which has n independent faults. The independence between faults refers to whether a fault occurs or not does not relate to any other faults in the fault set F . In addition, the system has m independent tests, which are grouped as a set $T = \{T_1, T_2, \dots, T_m\}$. The independence of a test has two meanings. Firstly, it means that whether the test is in error or normal state keeps independent to other tests. Secondly, a test whether can detect an existing fault is irrelevant to other tests. The relationships among faults and tests can be modelled by a digraph [20]. Fig.4 illustrates a schematic digraph depicting these relationships. In Fig.4, the upper layer nodes represent faults and the lower nodes refer to

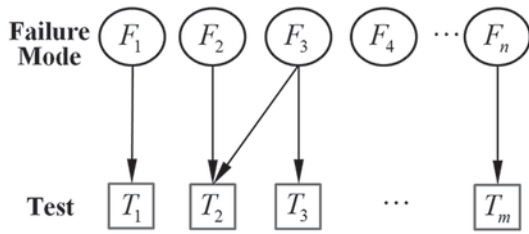


Fig. 4. Digraph of fault detection relationships

tests. In Fig. 4, if there exists the detection relationship between a fault and a test, there is a directed line connection between them.

For notation convenience, we defined the relevant fault set $RFS(T_j)$ of test T_j . The set $RFS(T_j)$ denotes a group of faults can be detected by test T_j . Mathematically, the set $RFS(T_j)$ must satisfy:

$$RFS(T_j) = \{F_i \mid F_i \in F \text{ and } r_{F_i}^{T_j} = 1\} \quad (9)$$

where $r_{F_i}^{T_j} = 1$ denotes that there exists the physical detection relationship between the test T_j and the fault F_i . On the contrary, we define $r_{F_i}^{T_j} = 0$ when the test T_j cannot detect the fault F_i . As shown in Fig. 4, taking the test T_2 as an example, the relevant fault set of T_2 is $RFS(T_2) = \{F_2, F_3\}$. Generally, $RFS(T_j) \neq \emptyset$, where \emptyset denotes an empty set.

Likewise, let $RTS(F_i)$ denote a relevant test set of the fault F_i . The $RTS(F_i)$ is a group of tests which can detect the fault F_i . The set $RTS(F_i)$ must satisfy the condition:

$$RTS(F_i) = \{T_j \mid T_j \in T \text{ and } r_{F_i}^{T_j} = 1\} \quad (10)$$

As shown in Fig. 4, the relevant test set of F_3 is $RTS(F_3) = \{T_2, T_3\}$. If a fault F_i cannot be detected by any test, it satisfies $RTS(F_i) = \emptyset$.

4.2. Modelling of test state change

The digraph model of between a test and a fault depict the static detection relationship. In this section, we model the test uncertainty based on the assumption of test state change. In reality, the state of a test could not be recognized automatically in the real situation. Generally, when a test does not give right indications to the occurred relevant faults, maintenance staff will affirm that the test is in error state. It means that the test T_i would be repaired and its state switches to be normal only the fault in the set $RFS(T_i)$ occurs. Otherwise, the test T_i will keep its error state. Accordingly, we define a test state change process to depict a test repeatedly change its state from normal to error state then from error to normal state.

To describe the test uncertainty, test fault can be described by the same way as the description of the system fault occurrence. We describe the test fault occurring model using the renewal process. Let

$t_{T_i}^j (j = 1, 2, \dots)$ denote the fault time sequence of the test T_i . It means

that the test state change from 1 to 0 at time $t_{T_i}^j (j = 1, 2, 3, \dots)$. The fault occurrence law of T_i can also be described by the renewal function $M_{T_i}(t)$. The meaning of $M_{T_i}(t)$ is consistent with the definition in Section 3. Simultaneously, let $\tilde{t}_{T_i}^j (j = 1, 2, 3, \dots)$ denote the repair time of T_i . It means that the test state change from 0 to 1 at time $\tilde{t}_{T_i}^j (j = 1, 2, 3, \dots)$.

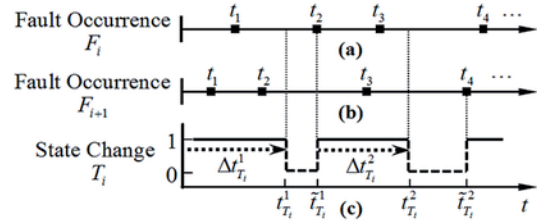


Fig. 5. Schematic diagram of test state change

Fig. 5 illustrates an example of state change process of a test T_i . The $RFS(T_i)$ of T_i is $\{F_i, F_{i+1}\}$. As shown in Fig. 5, the fault time $t_{T_i}^j (j = 1, 2, \dots)$ of T_i is decided by its interarrival time $\Delta t_{T_i}^j (j = 1, 2, \dots)$. The repair time $\tilde{t}_{T_i}^j (j = 1, 2, \dots)$ is related to the fault time of the faults in $RFS(T_i)$. Let $\min(t \mid t(RFS(T_i)) > t_{T_i}^j)$ denote the minimum time of occurring time of the faults in $RFS(T_i)$ after the j th fault $t_{T_i}^j$ of the test T_i . Consequently, the state change time of T_i can be depicted as follows:

$$\begin{cases} t_{T_i}^j = \tilde{t}_{T_i}^j + \Delta t_{T_i}^j, j = 1, 2, \dots \\ \tilde{t}_{T_i}^k = \min(t \mid t(RFS(T_i)) > t_{T_i}^j), k = j \end{cases} \quad (11)$$

Obviously, the fault time $t_{T_i}^j (j = 1, 2, \dots)$ of the test T_i would alternates with the repair time $\tilde{t}_{T_i}^j (j = 1, 2, \dots)$, which forms the state change process of T_i .

4.3. Description of fault detection logic

Because of the existence of state change process of a test, the detection probability of the fault F_i is less than 1. The event of fault detection can be modelled as follows.

For a fault F_i , if it is not detected by any tests, namely $RTS(F_i) = \emptyset$, F_i would not be detected in any case. For a detectable fault F_i , namely it satisfies $RTS(F_i) \neq \emptyset$. We define an event $A\{F_i(t)\}$ which represents the detection outcome of F_i at the fault occurring time t . The event $A\{F_i(t)\}$ has two states $\{s, f\}$. Let s denote that F_i is successfully detected and f represents the failed detection. Simultaneously, let $Normal[RTS(F_i(t))]$ denote the number

of normal tests in set $RTS[F_i(t)]$ at time t . Accordingly, we have the following relationship:

$$A\{F_i(t)\} = \{Normal[RTS(F_i(t))] \geq 1\} \quad (12)$$

where $\{Normal[RTS(F_i(t))] \geq 1\}$ denotes the value of $Normal[RTS(F_i(t))]$ must be more than or equal to 1.

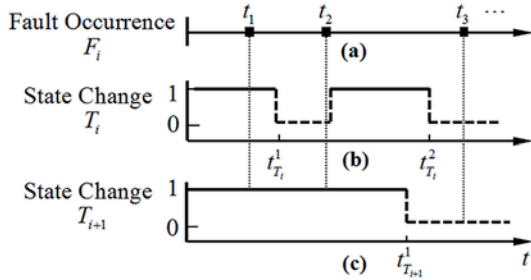


Fig. 6. Schematic diagram of fault detection process

Fig. 6 shows a fault detection process of fault F_i . Its $RTS(F_i)$ is the set $\{T_i, T_{i+1}\}$. The fault F_i occurs at $\{t_1, t_2, t_3\}$. According to the fault detection logic depicted in eq. (11), the values of $Normal[RTS[F_i(t)]]$ at (t_1, t_2, t_3) are 1, 2 and 0 respectively. So, results of the event $A\{F_i(t)\}$ at (t_1, t_2, t_3) are (s, s, f) .

5. Stochastic characteristics of FDR

In testability test engineering, we usually assume that tests have no uncertainty when the testability tests are carried out under laboratory conditions. It means that if the set $RTS(F_i)$ is nonempty, the fault F_i can be detected at every time when it occurs. For comparison, we divide in two cases to study the stochastic characteristic of $FDR(t)$. In Case 1, we assume that every test keeps normal state all the time. And in Case 2, both the fault occurrence randomness and test uncertainty are considered. In two cases, the final aim is the calculation of the statistical characteristics of $FDR(t)$. In this paper, we mainly focus on the expectation of $FDR(t)$, which is denoted as $E[FDR(t)]$.

5.1. Case 1

In this case, we make the following assumptions.

- (1) In the fault set $F = \{F_1, F_2, \dots, F_n\}$, each fault occurrence process obeys the renewal process;
- (2) The tests remain normal all the time. Namely, whether the failure mode F_i can be detected is determined. When a fault F_i is detectable, its detection probability r_{F_i} is equal to one and F_i can be detected at any time. Conversely, if a fault F_i is undetectable, its detection probability $r_{F_i}(t)$ is equal to zero and F_i is undetectable at any time.
- (3) Every fault F_i must obeys the same form of the interarrival time function $F(\Delta t; a_1, a_2, \dots)$. Only the distribution parameters a_1, a_2, \dots are different for different faults.

As the above assumptions, we define the detectable fault set F^D . The set F^D must satisfy

$$F^D = \{F_i \mid F_i \in F \text{ and } RTS(F_i) \neq \emptyset\} \quad (13)$$

Let $|F^D| = k$ represents the number of elements in the set F^D . According to the above assumption, $r_{F_i}(t)$ equals to one or zero. Accordingly, eq. (3) can be further described as:

$$\begin{aligned} FDR(t) &= \sum_{i=1}^n \lambda_{F_i}(t) \cdot r_{F_i}(t) \\ &= \sum_{i=1}^k \frac{N_{F_i}^D(t)}{N(t)} \end{aligned} \quad (14)$$

where $N_{F_i}^D(t)$ represents the occurred number of detectable fault F_i at time t and $F_i \in F^D$, $N(t)$ denotes the occurred number of all faults.

The expectation $E[FDR(t)]$ can be calculated as follows:

$$\begin{aligned} E[FDR(t)] &= E\left[\sum_{i=1}^k \frac{N_{F_i}^D(t)}{N(t)}\right] \\ &= \sum_{i=1}^k E\left[\frac{N_{F_i}^D(t)}{N(t)}\right] \end{aligned} \quad (15)$$

However, the comprehensive and accurate calculation of eq. (15) is a formidable work. We suppose that the elements in set $F = \{F_1, F_2, \dots, F_m\}$ keep independent. Combining eq. (5), the expectation $E[FDR(t)]$ can be approximately calculated as follows:

$$\begin{aligned} E[FDR(t)] &= \sum_{i=1}^k E\left[\frac{N_{F_i}^D(t)}{N(t)}\right] \\ &= \sum_{i=1}^k \frac{E[N_{F_i}^D(t)]}{E[N(t)]} \\ &= \sum_{i=1}^k \frac{M_{F_i}^D(t)}{\sum_{j=1}^n M_{F_j}(t)} \end{aligned} \quad (16)$$

where $M_{F_i}^D(t)$ refers to the renewal function of the detectable fault F_i^D . $M_{F_i}(t)$ denotes the renewal function of fault F_i .

From the above analysis, when the form of $F(t)$ changes, $M(t)$ and $E[FDR(t)]$ would have different forms. Based on the above description, the calculation of $M(t)$ is very complicated. Here, taking gamma distribution and exponential distribution for example, the calculation process of $E[FDR(t)]$ is presented.

- (1) $F(t)$ obeys gamma distribution

Suppose that the interarrival time function $F(t)$ is a gamma distribution, i.e.:

$$F(t) = 1 - e^{-\lambda t} \sum_{j=0}^{k-1} \frac{(\lambda t)^j}{j!} \quad (k=1, 2, 3, \dots) \quad (17)$$

The LS transform of $F(t)$ is as follows:

$$\begin{aligned} F^*(s) &= L[F(t)] \\ &= \frac{1}{s} - \frac{1}{s+\lambda} \sum_{j=1}^k \frac{\lambda^{j-1}}{s^j} \end{aligned} \quad (18)$$

Combine with eq. (8):

$$M^*(s) = \frac{\frac{1}{s} - \frac{1}{s+\lambda} \sum_{j=1}^k \frac{\lambda^{j-1}}{s^j}}{1 - \frac{1}{s} + \frac{1}{s+\lambda} \sum_{j=1}^k \frac{\lambda^{j-1}}{s^j}} = \frac{\lambda^k}{(s+\lambda)^k - \lambda^k} \quad (19)$$

The inverse LS transform of equation is as follows:

$$M(t) = \frac{\lambda t}{k} + \frac{1}{k} \sum_{j=1}^{k-1} \frac{\omega_j}{1 - \omega_j} [1 - e^{-\lambda t(1 - \omega_j)}] \quad (20)$$

where $\omega_j = e^{2\pi j i / k}$ ($j=1, 2, \dots, k-1$) is the distinct root of $s^k = 1$ and i is an imaginary order

From eq. (20), the limit of $M(t)$ is:

$$\lim_{t \rightarrow \infty} M(t) = \frac{\lambda t}{k} \quad (21)$$

According to eq. (21), $M(t)$ can be approximately calculated as:

$$M(t) \approx \frac{\lambda t}{k} = at \quad (22)$$

where $a = \lambda / k$. From eq. (22), $M(t)$ increases linearly with the prolonging of time.

Combine eq. (16) and (22), $E[FDR(t)]$ can be calculated as:

$$\begin{aligned} E[FDR(t)] &= \sum_{i=1}^k \frac{M_{F_i^D}(t)}{\sum_{j=1}^m M_{F_j}(t)} \\ &= \sum_{i=1}^k \frac{a_i t}{\sum_{j=1}^n a_j t} \\ &= const \end{aligned} \quad (23)$$

where $const$ refers to a constant.

(2) $F(t)$ obeys exponential distribution

When the interarrival time function $F(t)$ is exponentially distributed, namely $F(t) = 1 - e^{-\lambda t}$. It is a special situation of

when $F(t)$ obeys the gamma distribution and $k=1$. In this case, $E[N(t)] = \lambda t = M(t)$.

According to eq. (16), the value of $E[FDR(t)]$ can be calculated as:

$$\begin{aligned} E[FDR(t)] &= \sum_{i=1}^k \frac{\lambda_i t}{\sum_{j=1}^n \lambda_j t} \\ &= \frac{\sum_{i=1}^k \lambda_i t}{\sum_{j=1}^n \lambda_j t} \\ &= const \end{aligned} \quad (24)$$

For the other distribution forms, such as Weibull distribution, it is difficult to obtain the analytical expression of the renewal function $M(t)$. When the time interval Δt obeys the interarrival time function $F(t)$, the interarrival time Δt can be obtained using Monte Carlo simulation. Accordingly, we can use the Monte Carlo simulation to calculate $M(t)$ and $E[FDR(t)]$.

The core of Monte Carlo method is the process of generating random numbers. The method of generating random numbers includes the inverse distribution generation method and congruence method [12, 14]. Using in the computer simulation, the most widely used method is the inverse distribution method. The procedure is as follows:

- Step 1** Calculate the inverse distribution $\Delta t = F^{-1}(U)$ of the interarrival time function $F(\Delta t) = U$.
- Step 2** Generate random numbers u_1, u_2, \dots, u_k which obey a uniform distribution and the values of these numbers must lie between 0 to 1.
- Step 3** Calculating each $u_i \in u_1, u_2, \dots, u_k$ using $\Delta t_i = F^{-1}(u_i)$, we can get the interarrival time series $\Delta t_1, \Delta t_2, \dots, \Delta t_k$.

Under the assumption of certain test, the values of $M(t)$ and $E[FDR(t)]$ are only affected by the number of occurred faults. Fig. 7 illustrates the simulation procedure of a fault occurrence process.

The simulation can be concisely described as follows:

- Step 1** For the fault F_i and its interarrival time function is $F(t | F_i)$.
Generate the fault interval $\Delta t_{F_i}^j$ ($j=1, 2, 3, \dots$) using the random number generation method.
- Step 2** Calculate the fault time $t_{F_i}^j$ according to $t_{F_i}^j = t_{F_i}^{j-1} + \Delta t_{F_i}^j$, where $t_{F_i}^0 = 0$. When the $t_{F_i}^j$ reaches the t_{\max} , stop the simulation of F_i . Let t_{\max} denote the maximum time of fault occurrence.
- Step 3** Repeat the above two steps and obtain all the time sequences of fault in the set $F = \{F_1, F_2, \dots, F_n\}$.

After the above of three steps, we obtain one sample of fault occurrence process. In order to calculate $M(t)$ and $E[FDR(t)]$, we need repeat the simulation procedure. Here, we define the simulation time ST .

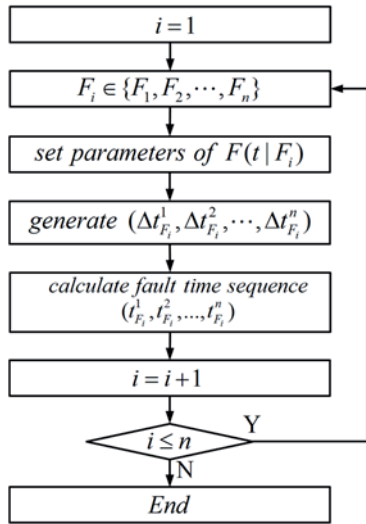
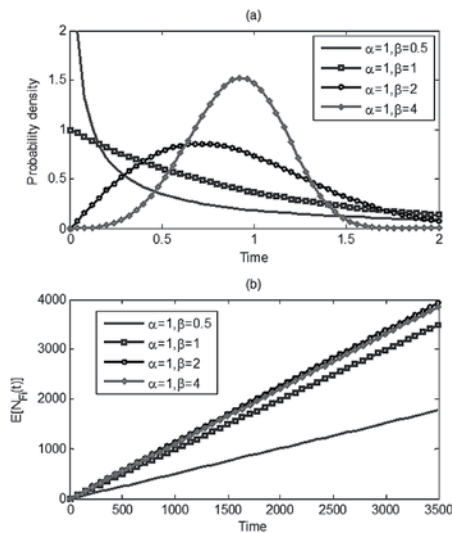


Fig. 7. Simulation flowchart of fault occurrence sequence

(3) $F(t)$ obeys Weibull distribution


 Fig. 8. $E[N_{F_i}(t)]$ under different parameters of Weibull distribution

When the interarrival time function is Weibull distribution, namely $F(t)=1-e^{-(\lambda t)^\alpha}$ and $t \geq 0$. Generally, the parameters λ and α denote shape parameter and scale parameter respectively. Let $E[N_{F_i}(t)]$ denote the expectation of cumulative number of a fault F_i at time t . According to the fault occurrence simulation procedure, we simulate the $E[N_{F_i}(t)]$ under four groups of representative distribution parameter as illustrated in Fig. 8. Fig. 8(a) depicts the probability density functions of four different distribution parameters. Fig. 8(b) illustrates four corresponding curves of $E[N_{F_i}(t)]$. We can clearly find that each $E[N_{F_i}(t)]$ increases linearly and can be approximately expressed as a function $E[N_{F_i}(t)] = at$, where a is a constant. Similar to the analysis of eq. (23), $E[FDR(t)]$ would tend to be a constant with the increase of time.

According to the theoretical and simulative method proposed in this section, when the fault occurrence process can be modelled by the

renewal process and without considering test uncertainty, the value of $E[FDR(t)]$ tends to be a constant.

5.2. Case 2

In Case 1, we neglect the test uncertainty. In this case, we would consider the test uncertainty as depicted in Section 4. All for the assumption made in Case 1 are applicable here. In addition, let $T = \{T_1, T_2, \dots, T_m\}$ the m independent tests in a system. Every T_i in the T will obeys the same interarrival time function $F(t; b_1, b_2, \dots, b_k)$, and only the distribution parameters b_1, b_2, \dots, b_k are different for different tests.

As shown in eq. (12), the detection condition of the fault F_i must satisfy $Normal[RTS(F_i(t))] \geq 1$. Generally, we define a characteristic function $FD(\cdot)$ which shows whether F_i can be detected. At time t , the detection state of the fault F_i can be written as:

$$FD(F_i(t)) = \begin{cases} 1, & Normal[RTS(F_i(t))] \geq 1 \\ 0, & \text{else} \end{cases} \quad (25)$$

Since we introduce the test uncertainty, the number of detected fault $N_{F_i}^D(t)$ cannot calculate according to the theory of the renewal process. Therefore, obtaining analytical expression of $E[FDR(t)]$ is a formidable work. So we propose the simulation method to calculate $E[FDR(t)]$.

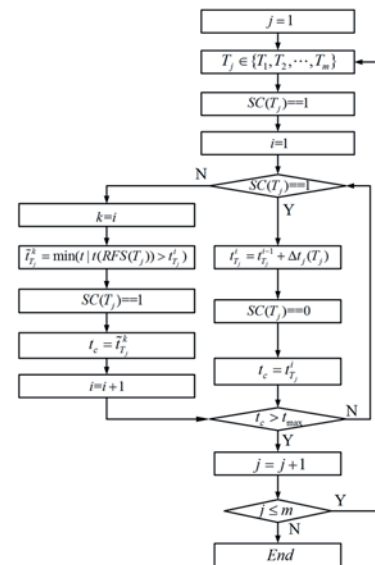


Fig. 9. Simulation flowchart of the process of test state change

To verify the expectation of $FDR(t)$, we must simulate the fault occurrence process and test state change process. In Case 1, we already introduce the simulation procedure of fault occurrence sequence. This section would give the simulation flowchart of test state change process.

First, let $SC(T_j)$ denote the state of test T_j . When the T_j is in normal state, $SC(T_j)=1$. On the contrary, $SC(T_j)=0$ represent T_j is in error state. As shown in Fig. 9, it depicts the simulation procedure of the test state change. It can be described as follows.

- Step 1** Set the state change time label $i = 1$. From the above description, the length of time $\Delta t_i(T_j)$ which a test T_j keep normal state is decided by its interarrival time function $F(\Delta t_i | T_j)$, namely $\Delta t_i(T_j) \sim F(\Delta t_i | T_j)$. When $SC(T_j) = 1$, the fault time $t_{T_j}^i$ of the test T_j can be calculated $t_{T_j}^i = t_{T_j}^{i-1} + \Delta t_j(T_j)$. Specially, $t_{T_j}^0 = 0$. At the time $t_{T_j}^i$, the T_j switches its state from normal to error.
- Step 2** When the state of test T_j is error, namely $SC(T_j) = 0$. As depicted in eq. (11), the repair time is $\tilde{t}_{T_j}^k = \min(t | t(RFS(T_j)) > t_{T_j}^i) \ (k = i)$. Then, $i = i + 1$.
- Step 3** Repeat the above two steps. When $t_{T_j}^i$ or $\tilde{t}_{T_j}^k$ reaches t_{\max} , stop the simulation of test T_j .
- Step 4** Repeat the above three steps, we would obtain a complete test state change sequence of T_j . Similarly, we can obtain the other tests' state change sequences.

After the simulation processes of fault occurrence and test state change, the vital step is the statistics the fault detection result. As described above, the fault F_i occurs at time t , its detection state (determine whether the fault can be detected or not) is decided by eq. (25). So

we can obtain the fault occurrences number $N_{F_i}(t)$ and successfully detected times $N_{F_i}^D(t)$ in the interval $[0, t]$. Likewise, complete the simulation processes of all of the faults in the set $F = \{F_1, F_2, \dots, F_n\}$. The total number occurred faults $N(t)$ and detected faults $N^D(t)$ can be calculated. Obtaining $N(t)$ and $N^D(t)$, we can calculate the $FDR(t)$ according to eq. (2) and obtain a sample curve of $FDR(t)$.

After the entire simulation, we obtain a sample curve of $FDR(t)$. Repeating the above process ST times, we would get ST simulation samples $\{FDR^1(t), FDR^2(t), \dots, FDR^{ST}(t)\}$. Employ the moment estimation method to calculate the expectation $E[FDR(t)]$ as follows:

$$E[FDR(t)] = \frac{\sum_{i=1}^{ST} FDR^i(t)}{ST} \quad (26)$$

After the whole simulation and calculation procedure, we obtain the $E[FDR(t)]$ and observe its change trend.

6. Simulation Case

To verify the theory and simulation method proposed in this paper, an integrated controller in the missile control system is taken as study case. It is used to simulating its fault detection process. Simultaneously, simulating calculation of $E[FDR(t)]$ is carried on.

The integrated controller is a LRU (Line Replaced Unit) level product. Its main functions are outputting the drive and control signals to the four rudders. The test relationship in the integrated controller is shown in Fig. 10.

As illustrated in Table 1, the integrated controller has 11 failure modes $\{F_1, F_2, \dots, F_{11}\}$. The detection method means the way to detect

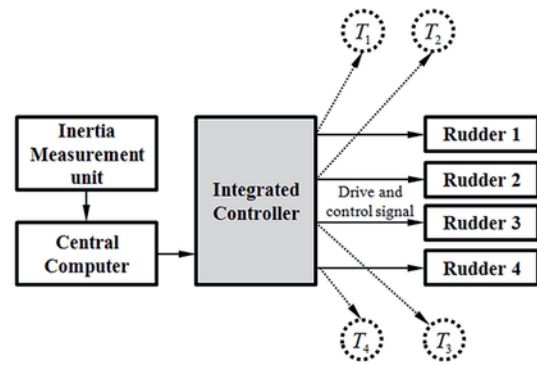


Fig. 10. Test relationship in the integrated controller

a fault, where ATE refers to the automatic test equipment. T_i refers to the Built-in Test. The manual test means refers to detect a fault manually. The distribution parameter denotes the parameter of the interarrival time function $F(\Delta t | F_i)$, where $F(\Delta t | F_i)$ obeys exponential distribution. During the simulation, we only count the fault which can be detected by BIT.

The interarrival time functions of tests T_1, T_2, T_3, T_4 are exponentially distributed and the parameter of each $F(\Delta t | T_i)$ is 1.408(year).

Table 1. Fault information of the integrated controller

Number	Failure Mode	Detection Method	Parameter of Interarrival Time Function (year)
F_1	1553B bus communication error	ATE	0.963
F_2	Self-test function failure	Manual test	0.079
F_3	All the rudder drive signals error	T_1, T_2, T_3, T_4	0.507
F_4	No Rudder 1 drive signal	T_1	0.710
F_5	No Rudder 2 drive signal	T_2	0.710
F_6	No Rudder 3 drive signal	T_3	0.710
F_7	No Rudder 4 drive signal	T_4	0.710
F_8	Error polarity signal to Rudder 1	T_1	0.152
F_9	Error polarity signal to Rudder 2	T_2	0.125
F_{10}	Error polarity signal to Rudder 3	T_3	0.125
F_{11}	Error polarity signal to Rudder 4	T_4	0.125

As shown in Fig. 10, the integrated controller has four independent outputs. In addition, each output is control and drive signal to a special rudder. In the integrated controller, there are four circuits (BIT) to monitor the 4-way signals. These four BITs denotes as $\{T_1, T_2, T_3, T_4\}$ respectively. The test digraph of the integrated controller is built as shown in Fig. 11. The upper nodes $\{F_1, F_2, \dots, F_{11}\}$ refer to faults. The lower nodes $\{T_1, T_2, T_3, T_4\}$ refer to tests. The faults F_1 and F_2 cannot be detected by any test in $\{T_1, T_2, T_3, T_4\}$. Specially, the fault F_3 can be detected by the tests $\{T_1, T_2, T_3, T_4\}$.

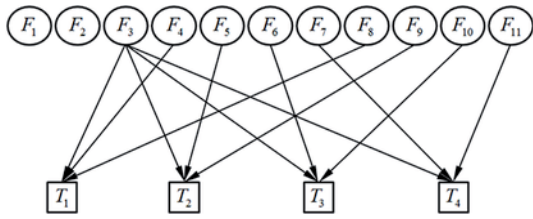


Fig. 11. Test digraph of the integrated controller

In the above discussion, it is divided into two cases to study the statistical characteristics of the $FDR(t)$. However, the simulation of two cases can be carried out together.

Set the simulation time $ST = 100$ and the maximum fault time to $t_{\max} = 20(\text{year})$.

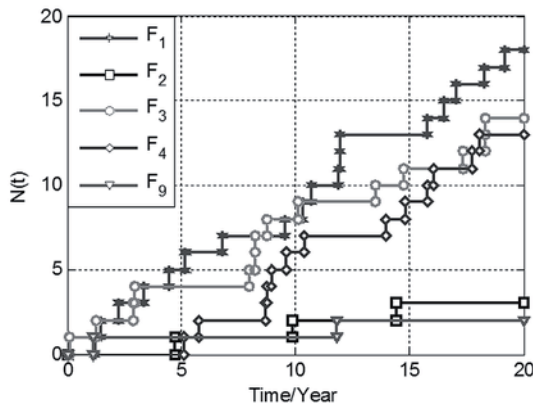


Fig. 12. Example of fault occurrence counting process

Firstly, generate the fault sequence sets of the 11 faults. Fig. 12 shows the fault occurrence counting processes of $\{F_1, F_2, F_3, F_4, F_9\}$. For the sake of clarity, it does not illustrate the fault occurrence counting processes of all the 11 faults. Each line in Fig. 11 represents a fault occurrence number $N_{F_i}(t)$ of fault F_i .

Secondly, repeat simulation of fault occurrence 100 times and obtain 100 samples of the fault occurrence processes.

Under the assumption certain test, the detected fault number $N^D(t)$ is the sum of the occurred number of faults which can be detected. Here, a fault F_i can be detected when it satisfies $RTS(F_i) \geq 1$. In the integrated controller, faults $F_3 \sim F_{11}$ are detectable and $\{F_1, F_2\}$ are undetectable.

Fig. 13 indicates the expectation of total number of occurred and detected faults, denoted as $E[N(t)]$ and $E[N^D(t)]$ respectively. Both $E[N(t)]$ and $E[N^D(t)]$ approximately linearly increase with the increase of time. $E[FDR(t)]$ can be approximately seemed as the

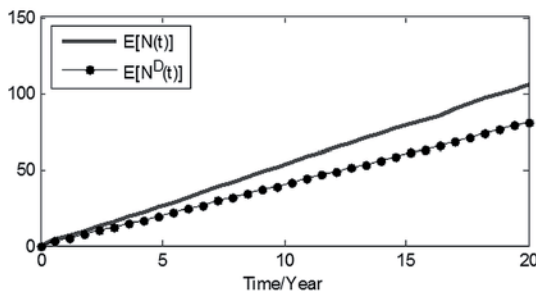
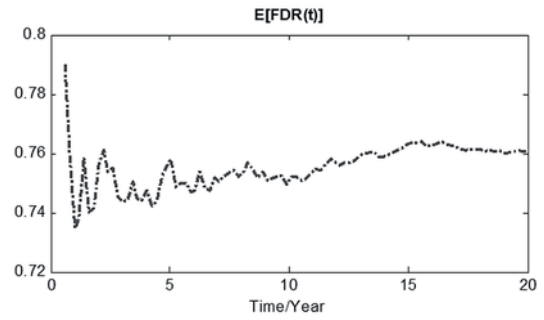
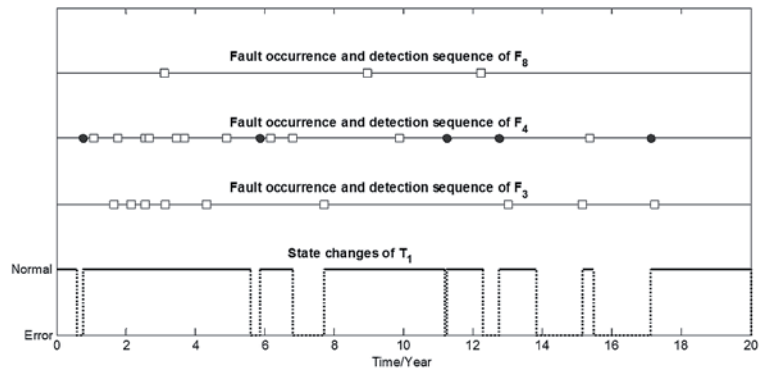


Fig. 13. Expectation of total number of occurred and detected faults


 Fig. 14. Time-varying process of $E[FDR(t)]$ under certain test assumption

division of $E[N^D(t)]$ and $E[N(t)]$. Accordingly, $E[FDR(t)]$ might gradually tend to a constant. According to the eq. (26), we can calculate the $E[FDR(t)]$ under the assumption of certain test.

Fig. 14 shows simulation result of $E[FDR(t)]$, where the expectation $E[FDR(t)]$ changes over time and fluctuates acutely at early period then gradually tend to be smoothed and stabilized. Then, we carry on the simulation process based on the assumption of test uncertainty. According to the test state change process and fault detection logic, we obtain four state change sequences of tests T_1, T_2, T_3, T_4 and fault detection outcomes. As shown in Fig. 15, the state change of test T_1 is displayed. Simultaneously, the fault occurrence and detection processes of $RFS(T_1) = \{F_3, F_5, F_8\}$ are shown. The fault is labelled as a square when it is detected at occurring time. On the other hand, it is labelled as a filled circle when it is not detected at occurring time.


 Fig. 15. State change of T_1 and fault occurrence processes of $RFS(T_1)$

Next, we count the detected number of faults according to the fault detection logic. By comparison, the expectation values of total number of occurred faults and detected faults in two cases are displayed in Fig. 16. All the three curves have linear increasing charac-

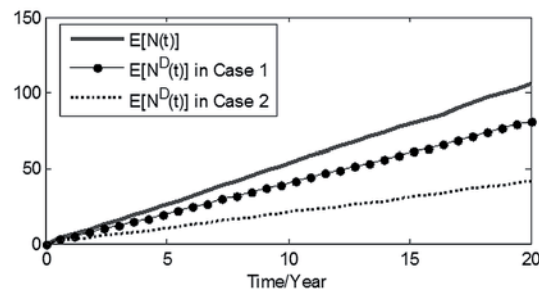


Fig. 16. Expectation of occurred and detected fault number in two cases

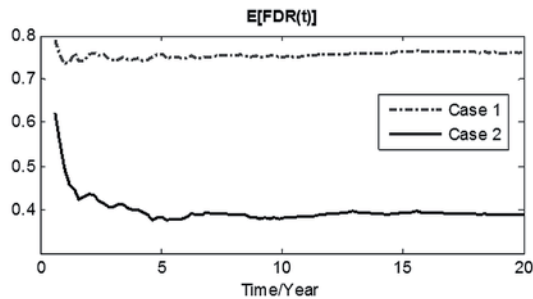


Fig. 17. Time-varying processes of the expectation of $FDR(t)$ in two cases

teristics. Considering test uncertainty in Case 2, the total number of detected faults is less than in Case 1.

In order to compare the $E[FDR(t)]$ in two cases, we display the $E[FDR(t)]$ curves in two cases in Fig. 17. As shown in Fig. 17, two $E[FDR(t)]$ curves have the same law. Both of them fluctuate acutely at the earlier period and gradually get to be stabilised with the increase of time. According to the simulation results in two cases, the FDR real value of the integrated controller could be assumed to be a certain value.

Acknowledgement

This research work is supported by National Natural Science Foundation of China (No. 61403408). We would like to thank the editor and the reviewers for their valuable suggestions and comments, which helped to improve our paper.

References

1. Attardi L, Pulcini G. A new model for repairable systems with bounded failure intensity. IEEE Transactions on Reliability 2005; 54(4): 572-574, <http://dx.doi.org/10.1109/TR.2005.858465>.
2. Banghart M, Fuller K. Utilizing confidence bounds in failure mode effects analysis (FMEA) hazard risk assessment. IEEE Aerospace Conference 2014: 1-6, <http://dx.doi.org/10.1109/AERO.2014.6836222>.
3. Barnett N, Bristol. In-service reliability, maintainability and testability demonstrations - 15 years of experience. Annual Reliability and Maintainability Symposium 2003: 587-592, <http://dx.doi.org/10.1109/RAMS.2003.118254>.
4. Coetzee J L. The role of NHPP models in the practical analysis of maintenance failure data. Reliability Engineering and System Safety 1997; 56(2): 161-168, [http://dx.doi.org/10.1016/S0951-8320\(97\)00010-0](http://dx.doi.org/10.1016/S0951-8320(97)00010-0).
5. Deng S, Jing B, et al. Yang Z. Test point selection strategy under unreliable test based on heuristic particle swarm optimization algorithm. IEEE Conference on Prognostics and System Health Management (PHM) 2012: 1 - 6, <http://dx.doi.org/10.1109/PHM.2012.6228884>.
6. Fan S, Pan M, et al. Catherine A. Intercept based performance evaluation of operation characteristic curve. International Conference on Computer Application and System Modeling 2010: V13-173-V13-175, <http://dx.doi.org/10.1109/ICCASM.2010.5622707>.
7. Feng K. Test-based study on verification model of detection rate in flight test phase. Flight Dynamics 2015; 33(4): 369-370, <http://dx.doi.org/10.13645/j.cnki.f.d.20150513.011>.
8. Ji G, Wu W, Zhang B, et al. A renewal-process-based component outage model considering the effects of aging and maintenance. International Journal of Electrical Power and Energy Systems 2013; 44(1): 52-59, <http://dx.doi.org/10.1016/j.ijepes.2012.07.035>.
9. Kacprzyński G J, Goebel K, et al. Vachtsevanos G. Methodologies for uncertainty management in prognostics. IEEE Aerospace Conference 2009: 7-8, <http://dx.doi.org/10.1109/AERO.2009.4839668>.
10. Kim H, Singh C. Reliability modeling and simulation in power systems with aging characteristics. IEEE Transactions on Power Systems 2010; 25(1): 21-27, <http://dx.doi.org/10.1109/TPWRS.2009.2030269>.
11. Li X, Jia Y, Wang P, et al. Renewable warranty policy for multiple-failure-mode product considering different maintenance options. Eksploatacja i Niezawodność - Maintenance and Reliability 2015; 17(4): 551-560, <http://dx.doi.org/10.17531/ein.2015.4.10>.
12. Liu Q, Zhao P. An analysis method of system mission reliability based on Monte Carlo method. Electronic Product Reliability and Environmental Testing 2013; 31(5): 17-20, <http://dx.doi.org/10.3969/j.issn.1672-5468.2013.05.005>.
13. Liu Y, Liu J, Jiang P, et al. Selection of equipment testability parameters based on improved AHP and fuzzy evaluation. China Measurement & Test 2015; 41(7): 23-24, <http://dx.doi.org/10.11857/j.issn.1674-5124.2015.07.006>.
14. Lu Z, Sun Y. Reliability calculating method of complex systems based on Monte Carlo method and genetic algorithm. Systems Engineering and Electronics 2008; 30(12): 2520-2521, <http://dx.doi.org/10.3969/j.issn.1672-5468.2013.05.005>.
15. Ma Y, Han J, et al. Li G. Testability demonstration method of electronic equipment based on hypergeometric distribution. IEEE International Conference on Industrial Engineering and Engineering Management 2008 <http://dx.doi.org/10.1109/IEEM.2008.4738256>.
16. Mitov K V, Omev E. Renewal processes. Springer, 2014, <http://dx.doi.org/10.1007/978-3-319-05855-9>.
17. Qiu J, Wang C, Liu G, et al. Testability demonstration for a flight control system based on sequential probability ratio test method. Proceedings of the Institution of Mechanical Engineers, Part G: Journal of Aerospace Engineering 2015; 229(3): 492-501, <http://dx.doi.org/10.1177/0954410014537239>.
18. Ruan S, Yu F, Meirina C, et al. Dynamic multiple fault diagnosis with imperfect tests. Proceedings of AUTOTESTCON 2004: 395 - 401, <http://dx.doi.org/10.1109/AUTEST.2004.1436895>.

7. Conclusions

This paper mainly focuses on the expectation of the statistical process $FDR(t)$, which is one of the most important statistical characteristics. The works of this paper can be concludes as follows.

- (1) This paper constructs the fault occurrence model based on renewal process.
- (2) This paper presents the test uncertainty model based the reality that test could be in fault and models the test state change process and fault detection logic.
- (3) We study the expectation of FDR in two cases, including considering test uncertainty and without considering test uncertainty. In these two cases, the expectations of $FDR(t)$ tend to be a constant along with the increase of time.
- (4) When a system obeys laws of fault occurrence and test uncertainty proposed in this paper, we prove the effectiveness of the assumption that the FDR value of a system exists a certain value. Accordingly, the FDR value of this kind of systems could be evaluated by the existing theory of testability demonstration. For systems with other fault occurrence laws, the effectiveness of the assumption needs further studies.

19. Ruan S, Zhou Y, Yu F, et al. Dynamic multiple-fault diagnosis with imperfect tests. *IEEE Transactions on Systems, Man, and Cybernetics—Part A: Systems and Humans* 2009; 39(6): 1225-1229, <http://dx.doi.org/10.1109/TSMCA.2009.2025572>.
20. Singh S, Kodali A, Choi K, et al. Dynamic multiple fault diagnosis: mathematical formulations and solution techniques. *IEEE Transactions on Systems, Man, and Cybernetics—Part A: Systems and Humans* 2009; 39(1): 160-163, <http://dx.doi.org/10.1109/TSMCA.2008.2007986>.
21. Su C, Zhou X. Maintenance optimization considering dependent competing failure based on renewal process. *International Conference on Quality, Reliability, Risk, Maintenance, and Safety Engineering* 2013: 620 - 625, <http://dx.doi.org/10.1109/QR2MSE.2013.6625657>.
22. Wang C, Qiu J, Liu G, et al. Testability demonstration test planning based on sequential posterior odds test method. *Proceedings of the Institution of Mechanical Engineers, Part O: Journal of Risk and Reliability* 2014; 228(2): 189-199, <http://dx.doi.org/10.1177/1748006X13508108>.
23. Wang C, Qiu J, Liu G, et al. Testability evaluation using prior information of multiple sources. *Chinese Journal of Aeronautics* 2014; 27(4): 867-874, <http://dx.doi.org/10.1016/j.cja.2014.03.029>.
24. Wang C, Qiu J, Liu G, et al. Testability verification based on sequential probability ratio test method. *IEEE AUTOTESTCON* 2013: 1-7, <http://dx.doi.org/10.1109/AUTEST.2013.6645066>.
25. Xu P, Liu S, et al. Li Y. Research on concept and model of testability test. *China Measurement & Test* 2006; 14(9): 1150-1151, <http://dx.doi.org/10.3321/j.issn:1671-4598.2006.09.010>.
26. Yanez M, Joglar F, et al. Modarres M. Generalized renewal process for analysis of repairable systems with limited failure experience. *Reliability Engineering and System Safety* 2002; 77(2): 167-180, [http://dx.doi.org/10.1016/S0951-8320\(02\)00044-3](http://dx.doi.org/10.1016/S0951-8320(02)00044-3).
27. Yang R, Zhao F, Kang J, et al. Inspection optimization model with Imperfect maintenance based on a three-stage failure process. *Eksplatacja i Niezawodnosc - Maintenance and Reliability* 2015; 17(2): 165-173, <http://dx.doi.org/10.17531/ein.2015.2.1>.
28. Zantek P F, Hanson T, Damien P, et al. A decision dependent stochastic process model for repairable systems with applications. *Operations Research Perspectives* 2015(2): 73-80, <http://dx.doi.org/10.1016/j.orp.2015.03.002>.
29. Zhang Y, Qiu J, Liu G, et al. A fault sample simulation approach for virtual testability demonstration test. *Chinese Journal of Aeronautics* 2012; 25(4): 598-604, [http://dx.doi.org/10.1016/S1000-9361\(11\)60424-X](http://dx.doi.org/10.1016/S1000-9361(11)60424-X).
30. Zhang Y, Qiu J, Liu G, et al. Fault sample generation for virtual testability demonstration test subject to minimal maintenance and scheduled replacement. *Mathematic Problems in Engineering* 2015, <http://dx.doi.org/10.1155/2015/645047>.

Zhiao ZHAO
Jing QIU
Guanjun LIU
Yong ZHANG

Science and Technology on Integrated Logistics Support
Laboratory, National University of Defense Technology
Changsha, Hunan 410073, China

College of Mechatronic Engineering and Automation, National
University of Defense Technology
Changsha, Hunan 410073, China

E-mails: zza19891013@126.com, qiuqing16@sina.com,
gjliu342@qq.com, zhangy21cn@126.com

Paweł OSTAPKOWICZ
Andrzej BRATEK

POSSIBLE LEAKAGE DETECTION LEVEL IN TRANSMISSION PIPELINES USING IMPROVED SIMPLIFIED METHODS

WERYFIKACJA MOŻLIWEGO POZIOMU WYKRYWALNOŚCI WYCIEKÓW W ZAKRESIE ZASTOSOWANIA ZMODYFIKOWANYCH UPROSZCZONYCH METOD DIAGNOSTYCZNYCH*

This paper deals with issues of detecting leaks in liquid transmission pipelines. It presents an overall comparison of three improved simplified methods, i.e. correlation analysis of pressure and flow rate, pressure monitoring and volume balance. Besides the well-known solutions, the authors also propose a detection algorithm with a new process variable structure and with two options of a resulting function. These methods do not require a complicated mathematical model and highly specialist measuring hardware. Their application and maintenance are easy and low cost. The interest of this paper is to determine the leakage detection level, when these methods are used for diagnosing single leakages under steady-state operating pipeline's conditions. The assessment, carried out on a laboratory water pipeline, was based on two performance indexes, i.e. a magnitude of a minimal leakage, which can be detected and the response time, i.e. time between the moment of beginning (occurrence) of leakage and the moment when it has been detected. The obtained results proved a high efficiency of proposed techniques in detection of leaks.

Keywords: fault detection, pipelines, leak detection methods, leakage detection level.

Artykuł dotyczy zagadnień diagnozowania wycieków z rurociągów przesyłowych cieczy z wykorzystaniem metod, które bazują na pomiarach wewnętrznych parametrów przepływu (zmiennych procesowych), tj.: strumienia i ciśnienia. Artykuł prezentuje porównanie trzech zmodyfikowanych uproszczonych technik, tj.: analizy korelacyjnej sygnałów ciśnienia i przepływu, monitorowania zmian ciśnienia i bilansu strumieni. Oprócz uprzednio znanych rozwiązań autorzy proponują również rozwiązanie algorytmu detekcyjnego o nowej strukturze zmiennych i o dwóch wariantach funkcji wynikowych. Metody nie wymagają zastosowania skomplikowanych modeli rurociągu, cechuje je niski koszt w sensie wymagań dotyczących urządzeń pomiarowych oraz łatwa realizacja i obsługa. Obszarem zainteresowania niniejszego artykułu jest określenie dla proponowanych metod wskaźników jakościowych, w przypadku diagnozowania pojedynczych wycieków w stanach ustalonych. Taka ocena dotyczy w szczególności ustalenia możliwego poziomu wykrywalności wycieku, tj. minimalnej wielkości wycieku, który może być wykryty. Innym określanym parametrem jest tzw. czas odpowiedzi, tj. czas od momentu wystąpienia wycieku do jego wykrycia. Podstawę weryfikacji stanowiły badania eksperymentalne przeprowadzone na stanowisku z modelem fizycznym rurociągu. Uzyskane wyniki potwierdziły wysoką skuteczność proponowanych technik wykrywania wycieków.

Słowa kluczowe: wykrywanie uszkodzeń, rurociągi, metody wykrywania wycieków, poziom wykrywalności wycieków.

1. Introduction

Liquid transmission pipelines may suffer from damages, which might result in leakages. Therefore, Leak Detection System (LDS) is an indispensable equipment of a pipeline installation. The main purpose of such system is to detect, locate, as well as determine the magnitude of occurred leak.

Most popular LDS are developed with the use of diagnostic methods, which are based on measurements of internal flow parameters, i.e. flow rate, pressure and fluid temperature. In the literature such methods are called *internal (analytical, indirect) methods* [2, 11, 17].

The implementation of leak diagnosis process is a rather complex issue. The existing internal methods, whose review might be found in the papers [4, 10, 11, 17, 19], on their own are not able to fulfill all mentioned above diagnostic tasks. Their utility is limited to certain, defined operational pipeline's states and leaks' characteristics. Thus,

elaboration of effective and reliable LDS requires applying of at least several internal methods working concurrently [17].

Taking into account that a LDS should first detect a leak, internal methods, which are responsible for this diagnostic task, acquire particular significance. In practice, one or several methods must be used to increase the reliability of LDS, which is defined as a degree of pipeline's operators confidence, i.e. absence of false alarms and also system's ability to detect any kind of occurred leak.

The most advanced solutions, aimed at leakage detection, are based on process dynamics models. An example of this method is the *inverse analysis method* [9, 19] and also so called methods with *automatic control approach* [1, 2, 10, 11, 16, 18]. Without doubt, the main advantage of both groups of methods is the ability to detect leaks in steady states as well as in transition states, resulting from a change in pipeline's operational conditions such as: an operating point change, valve's aperture and closure, pump's start-up or stoppage. However,

(*) Tekst artykułu w polskiej wersji językowej dostępny w elektronicznym wydaniu kwartalnika na stronie www.ein.org.pl

these methods are quite complex and their practical application involves solving many problems, which relate to constructing pipeline's mathematical model and developing its solutions, precise applying of diagnostic process methodology and appropriate diagnostic means.

In case of *inverse analysis methods*, their general idea consists in a comparison of model-generated data with measured data, i.e. minimizing the obtained deviations to enable leak detection and its localization, and depends on proper model fitting. Pipe's flow dynamic modelling mainly involves applying non-stationary equations of continuity and motion for fluids. In practice, it might be required to perform specific tests, which consist in enforcing transitional states in a shape of pressure impulses, generated by a valve's closure on the outer point of the pipeline [19]. Such tests significantly simplify pipeline's dynamics description, include leak's modelling and facilitate solving systems of equations due to better understanding of boundary conditions. However, in order to perform these tests correctly, it is necessary to control appropriately the valve's closure process, which is raised in [9]. Closing a valve on an operating pipeline always may be risky. Therefore, it might be required to introduce certain constraints to operating conditions in real-life i.e. decreasing the pressure values and volume of liquid.

In methods considered within context of *automatic control*, the mathematical model of liquid flow dynamics is mainly described in the state-space. A common solution is an implementation of state observers, which estimate process variables, for example, the flow rate at pipeline's inlet and outlet [1, 2, 10, 11] or other parameters to describe the flow e.g. the friction coefficient [2, 10, 11]. By applying a specific leak detection algorithm, it is possible to get the leak diagnosed and an alarm generated.

Considering a performance, in both mentioned above groups of methods, it creates strong requirements that measurement systems must meet. This results in high costs of LDS, related to the need of using the appropriate quantity of precise measurement instruments, well synchronized data transmission system and powerful computers. Such LDS should also be operated by high qualified staff.

Consequently, instead of these methods, simpler solutions are being used, including: mass balance, pressure/flow monitoring, pressure wave detection and correlation analysis of measured signals. In general, each method considers a single hydraulic phenomenon related to the leak occurrence which is the base to elaborate appropriate algorithms to detect leakages. Such simplified detection algorithms (SLDA), aimed at single leak detection in liquid transmission pipelines, consist the main area of focus of this paper.

The important advantages of SLDA are relatively low cost and ease of implementation. Taking into account other features, such as: duration of tests, disruption to normal system operation, complexity of the instrumentation, which according to [3] all together consist the comparison criteria for different leak diagnostic methods, in case of SLDA they also give satisfying results. From practical point of view, it is also worth seeing the SLDA implementation as an element of LDS. In a LDS even a single SLDA could be used, for example, on the basis of the mass or volume balance principle. However, more often a few SLDA are used, which, thanks to a proper synchronization, should verify each other and/or complement each other. This should result in being able to detect leaks not only in the state of steady flow, but also in other operational conditions during low operational transients. SLDA may be a part of more complex leak detection procedures, which use the mathematical models of liquid flow dynamics. The last solutions can be found in papers [1, 2, 10, 11]. In the paper [1] the comparison of the two advanced algorithms can be found. An algorithm configured on the above schema as a SLDA combination, "due to its good performance and good reliability is more appropriated to be implemented in industrial controllers", than the second one, which is far more computationally sophisticated.

Besides mentioned above characteristics, independently from using complex or simplified leak detection techniques, their practical usefulness is decided mainly on their efficiency. This is defined as the ability to detect a given volume of leakage in determined timeframe and with minimal number of false alarms. According to [18], pipeline's operators are interested in LDS solutions, which would enable leak detection of less than 1% nominal flow intensity. It would be better if such results were achieved both in steady state conditions and transient states. The operators are also interested in the evaluation of the smallest detectable leak, which might be achieved for a determined detection algorithm.

SDLA effectiveness depends on many factors, e.g. algorithm's structure. By the algorithm's structure we consider the overall elaborated solution of a given diagnostic method. This includes configuration of measurement devices (their number, location), their metrological characteristics (precision), signal sampling, measurement conditions (noise and distortion level) and techniques implemented for data processing and analysing, as well as the selection of the alarm thresholds. In relation to a pipeline, the following factors are significant: topography (e.g. diameter and length), a type of liquid (density, velocity of a pressure wave), flow conditions (flow and pressure rate). Moreover, essential also are the leak parameters, i.e.: its location, size (intensity), the nature of occurrence (rapid leaks or slowly increasing leakages), but also the size of a pipe damage and its development. The analysis of these issues might be found in papers [3, 7].

Unfortunately the effectiveness of commonly used nowadays SLDA is often below the expectations. In this paper we are interested in applying SLDA to diagnose singular liquid transmission pipeline leak in steady states. An example of such SLDA, which uses the negative pressure wave detection method, can be reviewed in [7]. The algorithm processes data obtained from two pressure sensors located at the inlet and outlet of a pipeline. Its performance assessment, which takes into account the smallest detectable leak, was based on carried out simulations, in which mathematical description for the amplitude change of negative pressure wave was used, being supplied by defined pipeline's parameters. The achieved smallest detectable leak, which amounted to about 1.4% of the nominal mass flow, overpasses however the reference value (i.e. 1%). Another SLDA system, which uses the mass-balanced leak detection method with correlation analysis, is presented in [10]. The algorithm runs on the basis of the mass flow rate measured only at the inlet and the outlet. It was experimentally verified on a gasoline pipeline. The presented results relate to only a single experiment, where the intensity of detected leak is 0.19% of the nominal mass flow rate.

It is worth highlighting that the SLDA are discussed or mentioned also in many other papers [5, 12]. Nevertheless, not always these papers encompass and present all information about their particular solutions and their effectiveness relating to the smallest detectable leak, which might considerably impede their potential analysis, modifications and implementation.

Considering the existent SLDA, we may notice that the effectiveness of similar solutions, in the sense of their overall methodology, might significantly vary. The authors consider applying an adequate solution structure of SLDA as a way to have SLDA effectiveness improved.

Therefore, the main goal of this paper is to present an overall comparison of a few modified SLDA solutions, taking also into account, the evaluation of their effectiveness. The presented set of detection algorithms is characterized by the fact that they combine different process variables i.e. flow and pressure signals, commonly measured at transmission pipelines. Besides the well-known solutions, the authors also propose a detection algorithm with a new variable structure and with two options of a resulting function. All presented SLDA solutions are focused on detection of a single leakage in a liquid transmission pipeline in steady state conditions.

It is worth mentioning that the authors focus especially on the leak detection issue. A great deal of attention is paid to the leak detection itself. This task is considered to be the most crucial activity from the LDS standpoint as it is the first, mandatory step to be completed in order to perform the leak position and flow estimation. Nevertheless, the leak localization was also considered in this paper, whereas estimation of a size of leakage was skipped in the presented results.

The proposed algorithms were tested in experiments carried out on a laboratory pipeline in a wide range of leak simulations. The basis of the evaluation was established by two primary performance indexes: the *smallest leakage detection level* and the *detection response time*. These parameters are directly related to the leak detection issue. While determining a leakage point, a location error was defined as a estimation's precision parameter.

The smallest detectable leak, which were achieved with elaborated algorithms, are lower than the defined reference value. According to the authors, solutions presented in this paper for modified SLDA - improved leakage detection techniques (algorithms) - and their results may provide valuable information for pipeline's operators.

This paper is organized as follows: the second chapter presents a description of typical measurement equipment of the transmission pipelines. The third chapter describes hydraulic phenomena related to leak occurrence. In the next section, the basic problems encountered during leak detection are discussed. The detailed description of the proposed algorithms might be found in the fifth chapter. The sixth section presents the laboratory pipeline and experiments' program overview. The next two chapters present the achieved results in diagnostic of simulated leaks and discuss the aspects of implementation of proposed algorithms in practice. Finally, overview of conclusions and some suggestions for future research are presented.

2. Pipeline measuring equipment

The liquid transmission pipelines are usually equipped with flowmeters and pressure transducers, installed at the inlet and outlet. Moreover, additional pressure sensors are often installed at regular intervals along the pipeline. The purpose of these sensors is to reduce the detection response time and improve the accuracy of the leak location.

Whereas measuring systems are the basis of SCADA (Supervisory Control and Data Acquisition) systems, which are used in pipelines to monitor and control pumping process, LDS system is usually their additional module.

The diagnostic data information, i.e. the measured pressure and flow rate signals, required by the leakage detection systems, should be continuously provided with defined sampling time T_p , without significant time delays. Moreover, the measurement systems should be error and noise resistant. However, the above mentioned disturbance issues might appear in case of long range transmission pipelines. According to [20], it is quite common, when only some useful measurement data is available.

3. Description of the leak phenomenon

Typical relationship between pressure (measured at the inlet and the outlet, and also at several points along the pipeline) and flow rate signals (measured at the inlet and the outlet) in the liquid transmission pipeline, before and after the occurrence of leak, is shown in Figure 1.

Assuming that a tight pipeline operates under stationary conditions, the pressure and flow rate along the pipe have stabilized values with low levels of fluctuations. Event of leak leads to changes of pressure and flow in the pipeline. At the beginning, a pressure drop takes place in the leak point. Afterwards, the pressure drop in the form of a negative wave propagates in both directions of the pipeline with the speed of sound. The profile of pressure wave propagation depends on the location of the leak, its size and the way it increases (which, in turn, depends on the development of damage to the pipeline). In case of sudden leaks (whose flow rate reaches the nominal value in short time after the moment of their occurrence), waves have clearly visible fronts (Fig. 1a). For slowly increasing leakages, where pressure changes have milder character, wave fronts have a smoother shape (Fig. 1c). Behind the wave front, the longer the distance is from the leak point, the smaller the pressure drop is in the pipeline. The observed pressure drops depend on the size of leakage, its position, and flow conditions.

Medium flow in the pipeline gets stabilized for a while after the occurrence of leakage with a new steady-state operating point. Comparing to the state before leakage, the flow rate in the section between the inlet and the leak point has increased, and the flow rate in the section from the leak point to the outlet has decreased (Fig. 1).

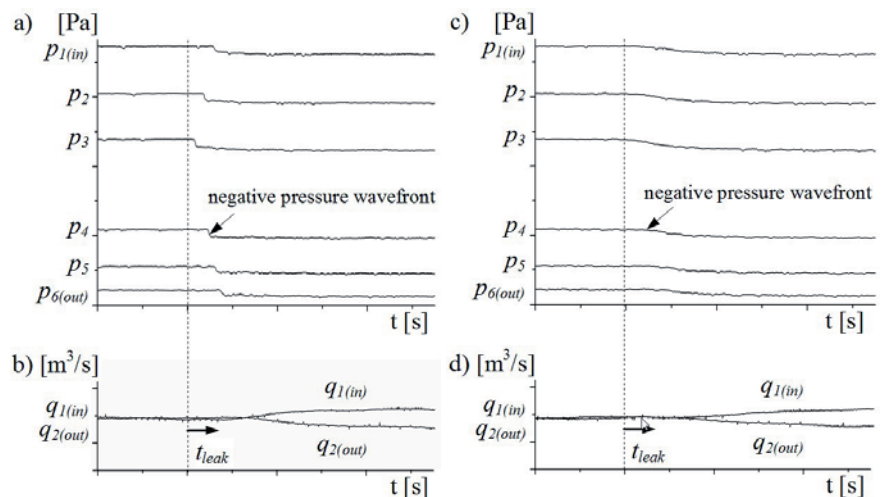


Fig. 1. Plots of sensor's signals at the laboratory pipeline with a single leak: p_1, \dots, p_6 - pressure along the pipeline, q_{in} , q_{out} - flow rate at the inlet and outlet; Clear changes in measurement signals' trends are caused by a large leak simulated at $t = t_{leak}$. These may be found in case of a sudden leakage: a) pressure, b) flow rate, and a slowly increasing one: c) pressure, d) flow rate.

4. Problems faced in leak detection

Profile and clarity of changes in measured pressure and flow rate signals (resulting from the course of leak phenomenon and metrological characteristics of measuring devices) essentially determine the leak detection level.

Such an exemplary situation is shown in Figure 2. The plots present the pressure and flow rate histograms in an experimental pipeline (which description can be found in section 6) initially operating in steady state conditions. Later the sudden leak of a 0.45% nominal flow rate was simulated at the point close to the middle of the pipe's length. We might observe that the pressure and flow rate variations are hardly noticeable, which is caused by a considerable level of noise in the signals.

We need to comment that pressure and flow rates in Figure 2 are not expressed in the SI units, but in the units that clearly represent flow's characteristics in the pipeline (pipeline's operators commonly

use the non SI units – e.g. m³/h as well). These units are also used through the next sections of this paper.

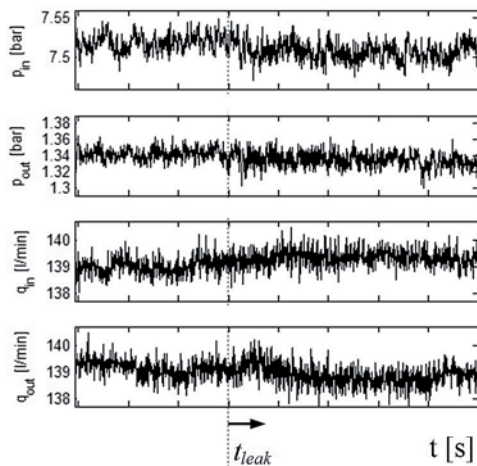


Fig. 2. Plots of measurement data collected on the laboratory pipeline for a small, sudden leakage: p_{in} , p_{out} – pressure at the inlet and outlet, and q_{in} , q_{out} – flow rate at the inlet and outlet respectively. Due to considerable level of noise in the data, it is difficult to notice small changes, provoked by the leakage, in the observed signal trends. The leakage of about 0.45% of the nominal flow rate was simulated close to the middle of the pipe's length at the time $t = t_{leak}$.

5. Theoretical characteristics of compared solutions

The proposed modified SLDA solutions are based on using measurement signals mentioned about in the chapter 2. They involve the following methods:

- correlation analysis (labeled “method I”),
- pressure monitoring (labeled “method II”),
- volume balance (labeled “method III”).

The presented descriptions of proposed solutions might be a basis of their practical application.

5.1. Method I

The proposed technique is based on correlation analysis. In contrast to similar solutions discussed in papers [1, 2, 10, 11], the authors propose to use the correlation analysis not only with regards to flow rate signals, but also to pressure signals [14, 15].

Using pressure signals is aimed at reducing the time required to detect a leak. Considering the pipeline's dynamics, pressure signals may sooner identify a leakage occurrence, than flow rate signals. This can be clearly noticed if we compare the signals measured at the pipe's inlet and outlet (see Fig. 1). Taking into account additional pressure sensors mounted along a pipeline, there is a possibility to detect a leak even quicker.

The algorithm based on the use of pressure signals may work independently. However, we need to remember that the pressure changes in a pipeline not always are a consequence of the leak occurrence. Similar symptoms of a leak, e.g. characteristic also for the wave propagation, might be observed for other flow conditions caused by valve regulation. It is difficult to differentiate them, what is mentioned by [12]. In order to avoid generating false alarms and increase credibility of a diagnosis, apart from using the algorithm, which is based on pressure signals, the second algorithm, based on flow rate signals, working concurrently may be applied.

Taking into account the above assumptions, a few SLDA were elaborated. All of them use the following different configurations of diagnostic signals:

- a) two flow rate signals measured at the inlet and outlet of the pipeline,

- b) two pressure signals measured at the inlet and outlet of the pipeline,
- c) two pressure signals measured at the inlet and outlet, and additionally at several points along the pipeline.

The structure of each algorithm, besides their general likeness, is characterized by the application of significant different elements. Their basis is the correlation analysis. Such analysis in consecutive steps of calculations considers data vectors, which are constructed on the basis of the shifting time windows. The calculated variables (i.e. residua) are window's data instead of the raw measured diagnostic signals. The proposed solutions of algorithms consider two configurations of time windows: with different steps of their shifting defined by the determined volume of signal samples. While building both window configurations, not only the speed of leak detection was considered, but also the need of computing power. The detailed solutions of all algorithms are discussed in the following part of this subchapter.

At the beginning, measured diagnostic signals x_n (suitably: q_n – flow rate signals, p_n – pressure signals; where: $n = 1, \dots, j$ – point number, j – amount of measuring points) being selected for the analysis are transformed into variables Δx_n .

Variables Δx_n represent deviations (residua) and are calculated as the differences between the signal current values x_n^k and their reference values \bar{x}_n^k , according to (1). The reference values are calculated by applying a low pass recursive filtering such as recursive averaging with fading memory (exponential smoothing), according to the formula (2).

$$\Delta x_n^k = x_n^k - \bar{x}_n^k \quad (1)$$

where: x_n^k – the value of the measured signal in the moment k , \bar{x}_n^k – the reference value in the moment k ,

$$\bar{x}_n^k = (\alpha \cdot \bar{x}_n^{k-1}) + ((1 - \alpha) \cdot x_n^k) \quad (2)$$

where: \bar{x}_n^{k-1} – the reference value in the moment $k-1$ resulting from the applied sampling time T_p , x_n^k – the value of the measured signal in the moment k , α – filter correction factor $0 < \alpha < 1$.

The use of the variables Δx_n instead of x_n allows to avoid the necessary adjustment of relatively large changes of the alarm thresholds, resulting from the inherent fluid dynamics changes, which for example relate to changes of the pipeline operating point. It is quite easy to calculate them considering that the reference values are obtained using the described low pass filtering. According to the practice [10], such approach is efficient with regards to steady states (normal operation). Potentially it might be also applied to some inconsiderable transient states. The used filtering also, to some extent, enables eliminating noise effects and slow drift effects (drifting measurements), what is mentioned about in [10]. For comparison, the algorithm presented in paper [1], which uses the residua defined on the basis of flow rate signals measured at the pipeline's inlet and outlet, requires far more complex calculations as reference values are estimated using a mathematical model of flow dynamics. Adopting such approach for leak diagnosis in steady states is not required. It is also worth mentioning that the residua are also used in leakage diagnosis methods for pipeline's networks, especially for water distribution networks [8]. The way of their calculations is different, because these are the differences between the measured values and reference values but the other ones concern the approximated states without leakages.

Next, the pairs of the variables, defined according to the formula (3), are created. The individual pairs correspond to consecutive measuring points Δx_n located along the pipeline, together with the neighboring point Δx_{n+1} , counting towards the end of the pipeline:

$$U_{xs=1,\dots,j-1} = \{\Delta x_{n=s}, \Delta x_{n+1=s+1}\} \quad (3)$$

where: s – variable pairs number, j – total amount of measuring points z_n (analyzed signals x_n).

For individual pairs of the variables U_{xs} cross-correlation functions are determined. There are taken into account here functions with variable delay time, i.e. *cross-correlograms* (4), additionally estimated. These functions, which are vectors of about $2N-1$ elements, are calculated for N sample long data vectors (time windows) of variables Δx_n and Δx_{n+1} . Number of samples N in the window includes period $\langle k-\tau, k \rangle$. The shift value τ is determined knowing the dynamics of leak phenomenon (the velocity of the pressure wave propagation in given section of the pipeline, which included analyzed measuring points, is taken into account) and distances between measuring points which are related to analyzed variables Δx_n and Δx_{n+1} . In case of flow rate signals, due to more slow character of their changes, the shift value τ should be greater then for pressure signals.

Time windows with different moving mode may be used, what is presented in Figure 3. In case of both types of windows, current leak detection assessment, i.e. in moments k and $k+1$ relates to the last sample in window:

$$R_{\Delta x_n \Delta x_{n+1}}(m)_s = \frac{1}{N} \hat{R}_{\Delta x_n \Delta x_{n+1}}(m-N)_s \quad (4)$$

where: $m = 1, 2, \dots, 2N-1$.

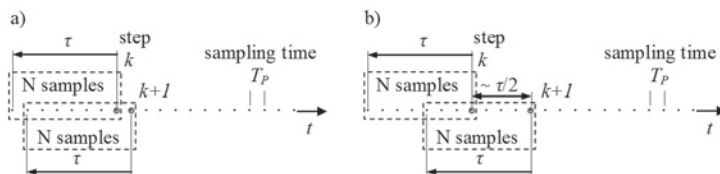


Fig. 3. Schemes of used time windows

Next, for the obtained functions (4), if flow rate signals are analyzed then average value (5a) is calculated and if pressure signals are analyzed then maximum value (5b) is calculated:

$$\hat{R}_{qs}^k = \frac{1}{2N+1} \sum_{m=k-\tau}^{m=k+\tau} R_{\Delta q_n \Delta q_{n+1}}(m)_s \quad (5a)$$

$$\hat{R}_{ps}^k = \max \{R_{\Delta p_n \Delta p_{n+1}}(m)_s\} \quad (5b)$$

To eliminate disturbances the calculated value \hat{R}_{xs}^k is filtered, by applying a low pass recursive filtering, according to the formula (6):

$$\hat{R}_{xs}^k = (\beta \cdot \hat{R}_{xs}^{k-1}) + ((1-\beta) \cdot \hat{R}_{xs}^k) \quad (6)$$

where: \hat{R}_{xs}^{k-1} – the reference value in the moment $k-1$ resulting from the applied sampling period T_p , β – filter correction factor $0 < \beta < 1$.

In states without leakage values of the individual functions \hat{R}_{xs} are close to zero.

If the analysis concerns only two flow rate signals $q_{n(in)}$ and $q_{n+1(out)}$ ($s=1$), as result of the occurrence of the leakage a value of the function \hat{R}_q decreases and becomes negative, because of $+\Delta q_{n(in)}$ and $-\Delta q_{n+1(out)}$. A leak alarm is generated, when the function \hat{R}_q exceeds its alarm threshold Pal_q , according to the condition (7):

$$\hat{R}_q < Pal_q \quad (7)$$

If the analysis concerns only two pressure signals $p_{n(in)}$ and $p_{n+1(out)}$ ($s=1$), as result of the occurrence of the leakage a value of the function \hat{R}_p is increasing and becomes positive, because of $-\Delta p_{n(in)}$ and $-\Delta p_{n+1(out)}$. A leak alarm is generated, when the function \hat{R}_p exceeds its alarm threshold Pal_p , according to the condition (8):

$$\hat{R}_p > Pal_p \quad (8)$$

However, if the analysis concerns larger number of pressure signals p_n ($s > 1$), the average value (9) is calculated on the basis of the set of individual calculated variables \hat{R}_{ps} :

$$\hat{R}_{pall} = \frac{1}{j-1} \sum_{s=1}^{s=j-1} \hat{R}_{ps} \quad (9)$$

Next, the condition (10) which defines the possibility of the occurrence of a leakage, is checked:

$$\hat{R}_{pall} > Pal_{pall} \quad (10)$$

Below there is another algorithm presented, which considers slightly different way of processing the same flow rate variables. In general, it is aimed at improving the leak detection level by resolving some problems we might be faced with, which are discussed in chapter 8.

The novelty of the proposed solution consist in using new variables dq and $d\bar{q}$, calculated according to (11) and (12), instead of a pair of variables U_q (3) as residua $\Delta q_{in(1)}$ and $\Delta q_{out(2)}$ (1):

$$dq^k = q_{1(in)}^k - q_{2(out)}^k \quad (11)$$

$$d\bar{q}^k = \bar{q}_{1(in)}^k - \bar{q}_{2(out)}^k \quad (12)$$

where: dq^k – difference between the flow rate signals measured at the inlet and outlet of a pipeline, $d\bar{q}^k$ – difference between the reference values calculated according to (2).

The next calculation's steps correspond to previous dependencies (4), (5a) and (6), which may be expressed as (13), (14) and (15):

$$R_{dq\bar{q}}(m) = \frac{1}{N} \hat{R}_{dq\bar{q}}(m - N) \quad (13)$$

where: $m = 1, 2, \dots, 2N - 1$.

$$\hat{R}'_q{}^k = \frac{1}{2N+1} \sum_{m=k-\tau}^{m=k+\tau} R_{dq\bar{q}}(m) \quad (14)$$

$$\hat{R}''_q{}^k = (\beta \cdot \hat{R}'_q{}^{k-1}) + ((1-\beta) \cdot \hat{R}'_q{}^k) \quad (15)$$

The proposed algorithm assumes that two functions might be responsible for leak detection: a \hat{R}'_q function, obtained on the basis of the relation (15) or the result of its median filtration, i.e. a function \hat{R}''_q , which corresponds to the relation (16):

$$\hat{R}''_q{}^k = \text{med}[\hat{R}'_q{}^{k-i}, \hat{R}'_q{}^{k-i+1}, \dots, \hat{R}'_q{}^k, \dots, \hat{R}'_q{}^{k+i-1}, \hat{R}'_q{}^{k+i}] \quad (16)$$

where: $N_A = 2i + 1$ – number of samples.

In no leakage situation values of the both functions \hat{R}'_q and \hat{R}''_q are close to zero. A leak alarm is generated, when the particular functions \hat{R}'_q and \hat{R}''_q exceed their alarm thresholds Pal'_q and Pal''_q , according to the conditions (17) and (18):

$$\hat{R}'_q > Pal'_q \quad (17)$$

$$\hat{R}''_q > Pal''_q \quad (18)$$

Initially we can state that the proposed algorithm might not require any change in alarm thresholds for slow changes in pipeline's flow conditions. An alternation of alarm thresholds might not be necessary as well in case of a change in pipeline's operating point. However, it is important to alert such a situation in order to avoid false alarms being generated by the algorithm in transition states. Once the pipeline achieves the new operating point, i.e. new steady state conditions, residua function should be calculated again. If \hat{R}'_q and \hat{R}''_q functions are still close to zero, it will mean the lack of leakage. On the contrary, respectively higher values of both functions might indicate a leak occurrence.

The implementation of the \hat{R}'_q function may consider two time window options, which are presented in the Figure 3. In case of \hat{R}''_q

function, which uses median filtering, the best solution is obtained for time windows showed in Figure 3a.

5.2. Method II and III

In practice, the algorithms presented in the previous subchapter, based on the correlative analysis, require determined sampling frequency. The applied sampling should ensure the visibility of signal dynamics (i.e. change trend) related to the leak occurrence, which improves the effectiveness of such analysis. It is also necessary to use wide time windows, with the right shifting (e.g. overlapping windows). The simplified detection algorithms presented in this subchapter don't require such conditions, in particular in respect to sampling of measured signals.

In the first algorithm it is assumed that pressure p_n is measured at several points along the pipeline, where $n = 1, \dots, j$ (j – the number of pressure sensors). This algorithm recalls the idea of Pressure Point Analysis [6], which was modified by altering the method's structure and adopting a new approach towards all the pressure measurements.

Instead analyzing a single measurement point, data gathered at all sensors is simultaneously taken into account. Such a solution should ensure the ability to detect a leak, which is no longer significantly dependent on a leak location.

The second algorithm is based on the traditional *volume balance approach* [13], where it is assumed that flow rates $q_{1(in)}$, $q_{2(out)}$ are measured on the inlet and outlet of a pipe. The proposed solutions of both algorithms are characterized by the use of indicator functions IF , which create the basis for alarm generation.

The approach adopted in the first index function IF_P , which recalls in searching for a pressure drop produced by a leak, focuses on the comparison of the pressure over a fixed period of time.

At the start, diagnostic parameters p_n are being transformed into variables \bar{p}_n by averaging within a time window of N sample long:

$$\bar{p}_n(t_i) = \frac{1}{N} \sum_{k=0}^{N-1} p_n(t_{i-k}), \quad (19)$$

where: t_i – a time of the succeeding measurement sample.

The next step is to calculate the deviations $\Delta\bar{x}_n$ between \bar{p}_n boundary values of the reference window T_r long (Fig. 4), which is being moved over the time to follow measurement samples:

$$\Delta\bar{x}_n(t_i) = \bar{p}_n(t_i) - \bar{p}_n(t_i - T_r) \quad (20)$$

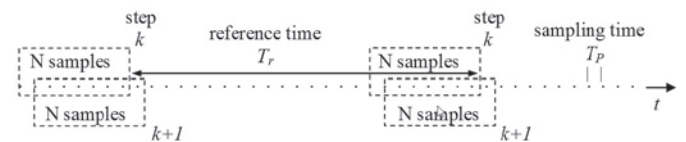


Fig. 4. Scheme of IF_P time windows

The function IF_P is defined as the minimum value of deviations $\Delta\bar{x}_n$, according to the formula:

$$IF_P(t_i) = \min \{ \Delta\bar{x}_n(t_i); n = 1, \dots, j \}. \quad (21)$$

The second index function IF_Q utilizes the principle of mass conservation. This approach, in the simplified form of volume balance without compensation [13], is expressed with the following relationship:

$$IF_Q(t_i) = \sum_{i=0}^{N-1} q_{2(out)}(t_i) - \sum_{i=0}^{N-1} q_{1(in)}(t_i). \quad (22)$$

In non-leakage states functions IF are close to zero. As a result of leakage occurrence, the index function decreases and has negative values. Its drop depends on the size of the leakage. Taking into account the calculation method of both functions IF with data averaging, associated with specified time windows, their width should be enough large to obtain satisfactory calculation precision and limit the measurement errors and noise impact. Once the P threshold limit is reached, the alarm is generated according to the below condition:

$$IF < P. \quad (23)$$

6. Test stand overview and experimental test scenarios

The above presented solutions have been put through experimental tests. They were conducted on the test stand with a physical model of the pipeline (Fig. 5). The medium pumped through the pipeline was water.

The pipeline is 380 meters long and is made of polyethylene (PEHD) pipes which are 34 mm in internal and 40 mm in external diameter. It consists of three sections each of which is over one hundred meter long. The sections: 0÷140 m, 140÷280 m and 280÷380 m, are joined with the use of special connectors of the same diameter as the pipeline.

The pipeline is equipped with standard measuring devices: two electromagnetic flow meters (located at the inlet and outlet), six pressure transducers (at the inlet and outlet, and also in several points along the pipeline) and two thermometers. Sensors are connected to a PC provided with the 16 bit A/D converter NI PCI 6259. More information about the location and metrological characteristics of the sensors and the measurement system is shown in Table 1.

In order to simulate leakages, proportional solenoid valves automatically controlled were used.

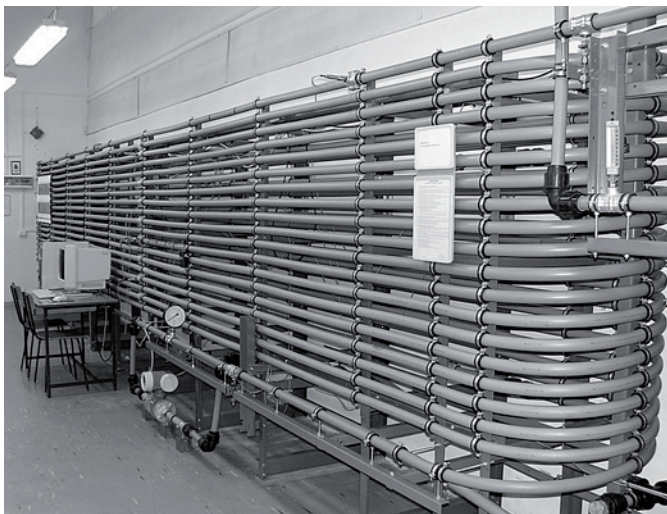


Fig. 5. View of the pipeline

Leakage simulations were performed under steady-state conditions of the pipeline. The results of the carried out experiments, which are presented in next chapters, were obtained for the following scenarios:

- the operating point settings of the pipeline: inlet pressure $p_{in} \approx 7.50$ bar, outlet pressure $p_{out} \approx 1.35$ bar, nominal flow rate $q_{nom(in=out)} \approx 140$ l/min, temperature of pumped water ranging from 15 °C to 25 °C;
- sudden leakages with the size range between 0.1 and 10.0 % of the nominal flow rate $q_{nom(in=out)}$, simulated at the selected points whose distance from the pipeline's inlet was about 75, 155 and 235 m;
- two experiments were performed for each leakage value.

The PC-based data acquisition system was used to acquire pressure and flow sensors' signals with sampling frequency of $f_p = 100$ Hz.

Table 1. Characteristics of the measurement system

devices	pressure sensors	flow rate sensors
location [m]	p1(in)=1 p3=141 p5=281 p2=61 p4=201 p6(out)=341	q1(in)=6.5 q2(out)=382.2
range	0÷10 [bar]	0÷200 [l/min]
accuracy	0.1 % of range	0.2 % of range
uncertainty of measurement*	±0.012 [bar]	±0.44 [l/min]

* uncertainty of measurement = sensor + 16-bit converter

7. Aspects of using compared solutions during experimental tests

7.1. General assumption

Comparison and assessment of three solutions, presented in the chapter 5, was performed based on the basis of practical diagnostic effectiveness for detection of simulated leakages.

For each solution the following performance indexes were determined: *leakage detection level* and *detection response time*. The principal behind the evaluation was the ability to detect the smallest possible leakage in the shortest possible time, even under unfavorable conditions, i.e. with the substantial level of disturbance affecting the measured signals.

In performed experiments the source of false alarms could be found in fluctuations and noises from the pumping (flow) of water through the pipe and measurement transducers. Other additional disturbances were not simulated.

When determining leakage detection level for compared methods one should be aware that, among others, it depends on the obtained form of a diagnostic function (respectively: $\hat{R}f_q$, $\hat{R}f'_q$, $\hat{R}f''_q$, $\hat{R}f_p$, $\hat{R}f_{pall}$, IF_P , IF_Q). The form of diagnostic functions should be characterized by suitably large change of their values in a state with leakage in comparison to a state without leakage.

Moreover, the question of appropriate choice of the alarm thresholds is one of crucial elements for proper operation of each solution. Alarm threshold values had to be chosen in such a way that they ensure the absence of alarms for states without leakage. To meet the accepted criterion, on the one hand, the alarm thresholds values should have had sufficiently large margins to prevent generating accidental

alarms in states without leakage. On the other hand, too large margins would make small leaks impossible to detect.

In order to compare the methods, each experiment was analyzed according to the scheme presented in Figure 6. Diagnosing simulated leakages concerns period T_{test} . Period T_0 was explored only to determine alarm thresholds.

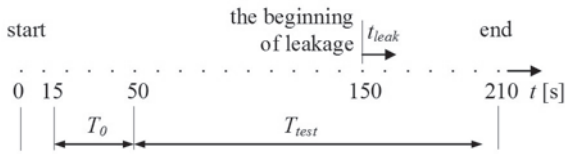


Fig. 6. Time scenario of experiments, where: T_0 - period for the selection of alarm thresholds margins, T_{test} - period for the detection of simulated leakages

7.2. Method I

The method's investigation considered different signal configurations, various settings of essential parameters and modes of data processing, i.e.:

- all configurations of diagnostic signals (labeled as “ q ”, “ p ”, “ $pall$ ”) discussed in chapter 5.1;
- calculation of the variables Δx_n (respectively: Δq_n – for flow rate signals, Δp_n – for pressure signals) in a period corresponding to the sample time T_p ;
- two types of time windows shown in Figure 3a and 3b. Standard time windows (labeled as “A”) were moved with every single signal sample. No-standard time windows (labeled as “B”) were moved every $N/2$ signal samples, where N denotes the number of samples in a window;
- different window lengths for particular configurations of diagnostic signals: $N_q = 500$, $N_p = 200$, $N_{pall} = 50$;
- finding of *cross-correlogram* (4) for variables Δx_n and Δx_{n+1} in Matlab with the procedure “`xcorr(Δxn, Δxn+1, 'biased')`”;
- the following filter parameters: $\alpha = 0.995$, $\beta = 0.900$.

In the proposed algorithm, the $\hat{R}f'_q$ and $\hat{R}f''_q$ functions, based on flow rate signals, are determined on the same set of N_q , α , β parameters. The same approach was followed as well during time steps calculation of dq and $d\bar{q}$ variables and procedures for cross-correlogram calculations (13) in Matlab program. Whereas the median filtering (16) was achieved by using $N_A = 3001$ data samples.

A selection of alarm thresholds Pal_q , Pal'_q , Pal''_q , Pal_p , Pal_{pall} was based on the statistical analysis of individual functions $\hat{R}f_q$, $\hat{R}f'_q$, $\hat{R}f''_q$, $\hat{R}f_p$, $\hat{R}f_{pall}$ in a state without leakage, i.e. in period T_0 shown in Figure 6. Furthermore, a constraint, which assumes selecting thresholds to ensure inexistence of false alarms in period T_{test} , i.e. before occurrence of leakage, was imposed.

The alarm thresholds were set as the average value of the standard deviations calculated for all experiments at different leakage points, according to the following relationship:

$$\begin{aligned} Pal_q &= -b_q \cdot std \{ \hat{R}f_q \} \\ Pal'_q &= b'_q \cdot std \{ \hat{R}f'_q \} \\ Pal''_q &= b''_q \cdot std \{ \hat{R}f''_q \} \\ Pal_p &= b_p \cdot std \{ \hat{R}f_p \} \\ Pal_{pall} &= b_{pall} \cdot std \{ \hat{R}f_{pall} \} \end{aligned} \quad (24)$$

where: b_q , b'_q , b''_q , b_p , b_{pall} – coefficients determined experimentally.

7.3. Method II and III

Calculations were performed for both index functions, marked as IF_p and IF_Q . IF_p function considers all available 6 pressure points of an experiment. To average any pressure p_n , 100 measurement samples within 1 second window ($N = 100$) were used, while T_r , time between the comparative data, was set to 10 seconds.

IF_Q function takes only supply and delivery flows into consideration and also is based on 1 second time window ($N = 100$).

The threshold limits were proposed on the basis of the statistic analysis of index functions in pre-leak period T_0 (Fig. 6). This period defines populations IF_p^0 and IF_Q^0 of observed values with 1 second interval. On the basis of these populations the threshold limits were made as follows:

$$P = E \{ IF^0 \} - b \cdot std \{ IF^0 \} \quad (25)$$

It should be mentioned, that the same value of coefficient b was established for both functions and every leak experiment.

8. The results

The Table 2 shows *detection response times* of the simulated leakages, obtained for the compared methods. The time is given in seconds and represent the average value of results gained in two experiments.

Non-detection of leakage in both experiments is marked with “–” sign. If only one leakage detection succeeded, then it has been marked with “–/+”.

Moreover, the Table 2 presents localization's results of simulated leakages (in the shape of localization errors), which were gained by using a method based on pressure wave detection method (NPWM) and a gradient method (GM).

To have leak point estimated with a NPWM method, a procedure presented in [15] was applied. The first part of this procedure consists of the leak occurrence detection algorithm based on the functions

$\hat{R}f_p$ or $\hat{R}f_{pall}$ already discussed, while the second part is aimed at detecting the transition of pressure waves through each pressure sensor points z_n . After detection of a leak occurrence and having given the times $t_{wav}(z_n)$, determined by the second algorithm, it is possible to locate the leak with the below formula (26):

$$z_{leak} = \frac{a_k}{a_p + a_k} \cdot l + \frac{t_{wav}(z_{in}) - t_{wav}(z_{out})}{a_p + a_k} \quad (26)$$

where: $a_p = 1/c_p$, $a_k = 1/c_k$ – coefficients; c_p , c_k – average pressure wave velocities along the sections: $0 < z < z_{leak}$, $z_{leak} < z < l$; l – the length of the pipeline, i.e. the distance between the extreme measurement points z_{in} and z_{out} ; $t_{wav}(z_{in})$, $t_{wav}(z_{out})$ – time when the pressure wave front reaches the points $z_{in} = 0$, $z_{out} = l$.

In case of GM method, upon detection of a leak, a localization procedure is carried out with the formula (27). For this purpose the pressure measurement data, corresponding to the identified steady state of the pipeline both with and without a leak, are used. These data sets were acquired from four sensors installed on the pipeline, i.e. $p_{1(in)}$, p_2 located before a leak point, p_5 behind a leak, and $p_{6(out)}$:

$$z_{leak} = \frac{l \cdot dg_{out}}{dg_{out} - dg_{in}} + \frac{dp_{in} - dp_{out}}{dg_{out} - dg_{in}} \quad (27)$$

where: l – the length of the pipeline; dg_{in} , dg_{out} – average increments of pressure gradients in the section between the beginning of the pipeline and the leak point and in the section between the leak point and the end of the pipeline; dp_{in} , dp_{out} – average pressure increments at the inlet and outlet of the pipeline.

Analyzing the results, one can observe that:

- *leakage detection level* varies in the compared solutions. Depending on the method and the leak point, it was possible to detect leakages, which values were equal to 0.1–1.3 % of the nominal flow rate $q_{nom(in=out)}$. From the type of diagnostic signals perspective, the best results were achieved when complete set of pressure signals was used (the methods I – \hat{Rf}_{pall} and II – IF_p). Even better detection level was achieved with the proposed algorithm, based on two flow rate signals and data transformation performed with median filtering (the method I – \hat{Rf}''_q). If we were to compare this algorithm with other solutions, it is worth pointing out that only this one took advantage of median filtering. Such filter lengthens considerably the time needed to detect a leak. On the other hand, median filtering enabled elimination of flow disturbance impacts, which in case of other solutions enforced applying enough wide margins of an alarm threshold. Although wide margins prevented false alarm generation, they resulted in a deterioration of the leak detection level. Quite good results were also obtained when two flow rate signals were used and analyzed with the proposed algorithm without median filtering (the method I – \hat{Rf}'_q). Then, slightly worse results were obtained for the solutions based on flow rate signals measured at the inlet and outlet of the pipeline (the methods I – \hat{Rf}_q and III – IF_Q). The least confident and satisfactory results were achieved using only two pressure signals measured at the inlet and outlet of the pipeline (the method I – \hat{Rf}_p). It has to be underlined here that leakage detection level depends on location of a leak. It is especially noticeable while pressure signals are used. Considering this as a criterion, the best results were achieved for leakages in the middle section of the pipeline. Getting closer to the ends of the pipeline, detection level is getting worse (the size of detectable

leaks becomes greater). The obtained results correspond to the leak detection distribution in relation to its location, which is presented in [7]. In case of using flow rate signals, such relation is not so evident. Moreover, in the method I with different window times, no significant differences were noticed for windows type A and B. Besides, B type time windows located unfavorable with respect to the time period, which includes changes of signals caused by the leakage occurrence, may result in a deterioration of the leakage detection level;

- *detection response time* of simulated leakages significantly differs in the compared solutions. Observed discrepancies relate to the use of different type of diagnostic signals. The shorter time was obtained in case of pressure signals (the methods I and II) and the longer one for flow rate signals (the methods I and III). This is conditioned by the course of leak phenomenon, with different dynamics of pressure and flow rate change. If more than only two pressure signals, i.e. at the inlet and outlet of the pipeline, are measured, significant improvement of detection response time can be obtained. Comparing the obtained results of the presented algorithm based on flow rate signals, the detection time in the proposed option without median filtering (the method I – \hat{Rf}_q) was slightly longer, than in case of other known solutions (the methods: I – \hat{Rf}'_q and III – IF_Q). The longest detection time was observed however in case of the proposed solution with median filtering (the method I – \hat{Rf}''_q). This is due to the application of a median filter. Obtaining a filter estimator for a given time involves considering the additional time, which corresponds to the length of the half of a data vector N_A . In case of the method I, with variable time windows, the detection response time did not exceed behind values resulting from accepted moving mode of implemented time windows;
- *localization errors* of simulated leakages were greater for the smallest leakages and they reduced for larger leakages. In both methods, errors were significantly smaller when a gradient technique was used. The precision of leak localization could be improved further by considering other configurations of sensors, i.e. including sensors placed closer to a leak location. In case of the method based on pressure wave detection, leak position errors were greater and for a few leakages it was even not possible to determine the leak point. The reason behind that is related to issues with a detection and identification of pressure wave forehead. It might be worth noticing that experiments considered only simulations of sudden leaks. If there are slowly increasing leakages, results of localization could be even worse.

Besides, Figures 7e-h show an example of a comparison of \hat{Rf}_q functions, derived from the known algorithm, with \hat{Rf}'_q and \hat{Rf}''_q functions calculated with the algorithm proposed in this paper. This comparison is performed for two different leak simulation experiments. In addition, Figures 7a-d captured flow rate signals q_{in} and q_{out} as well as reference variables \bar{q}_{in} and \bar{q}_{out} , on the basis of which the functions \hat{Rf}_q , \hat{Rf}'_q , \hat{Rf}''_q were obtained.

In Figure 7e we might notice that the previous solutions didn't ensure a successful leak detection. This is a result of unfavorable shape of \hat{Rf}_q function. However, a leak detection was possible with a use of the proposed solution (Fig. 7g), both in case of \hat{Rf}'_q and \hat{Rf}''_q functions, whose shapes are far more satisfactory.

In Figure 7b a distortion of flow rate q_{in} is visible. It provokes a noticeable change in \hat{Rf}_q function, which however does not result in

Table 2. Detection response times and localization errors of simulated leakages obtained in compared solutions

task		detection [s]										localization [m]	
method		I								II	III	NPWM	GM
used signals		q_{in}, q_{out}				P_{in}, P_{out}		P_{all}		P_{all}	P_{in}, P_{out}	P_{all}	
simulated leakages		diagnostic functions (used windows)								diagnostic functions		errors $ER = \hat{L} - L$	
[m]	[% q_{nom}]	$\hat{R}f_{q^A}$	$\hat{R}f'_{q^A}$	$\hat{R}f''_{q^A}$	$\hat{R}f_{q^B}$	$\hat{R}f_{p^A}$	$\hat{R}f_{p^B}$	$\hat{R}f_{pall^A}$	$\hat{R}f_{pall^B}$	IF_p	IF_Q		
75	0.09	–	–	–	–	–	–	–	–	–	–	–	–
	0.29	–	37.34	37.77	–	–	–	–/+	–/+	0.97	–	–	10.0
	0.55	–	7.77	19.35	–	1.96	–/+	0.34	0.49	0.91	4.88	190.7	-12.0
	0.84	4.08	5.90	17.89	6.24	0.98	1.49	0.30	0.49	0.61	2.64	0.3	-2.7
	1.17	2.98	4.82	19.22	4.99	0.90	0.99	0.27	0.49	0.63	2.77	-4.0	-0.5
	1.30	3.05	3.92	18.18	4.99	0.83	0.99	0.25	0.36	0.53	2.28	-5.7	-2.3
	1.94	2.73	3.71	17.05	4.99	0.82	0.99	0.26	0.36	0.39	2.00	-0.6	-4.7
155	0.06	–	–	–	–	–	–	0.34	–/+	–	–	–	-92.7
	0.25	–	14.05	–/+	–	–	–	0.32	1.12	2.30	–	–	-3.9
	0.45	5.59	6.55	20.57	–/+	–/+	–	0.24	0.61	0.70	–/+	-62.6	1.9
	0.78	3.46	4.68	18.94	6.24	0.74	1.99	0.20	0.49	0.68	4.12	25.7	-4.3
	1.19	2.42	4.45	17.54	3.74	0.66	0.99	0.20	0.36	0.52	2.56	0.4	-0.1
	1.43	2.62	4.09	18.69	4.99	0.67	0.99	0.21	0.36	0.56	2.43	-3.7	-2.4
	1.99	2.63	4.13	18.74	4.99	0.64	0.99	0.19	0.36	0.42	2.44	0.4	-0.8
235	0.17	–	–	–/+	–	–	–	–	–	–	–	–	–
	0.37	–	–	17.39	–	–	–	–	–	–	–	–	-14.9
	0.54	–/+	–	21.17	–/+	–	–	–/+	–	1.20	–	45.4	11.1
	0.88	3.67	9.35	19.33	6.24	–	–	0.58	0.86	1.84	4.47	-14.9	-3.4
	1.28	2.36	5.67	17.05	3.74	0.95	1.99	0.38	0.61	0.91	2.06	-0.4	-3.9
	1.41	3.79	6.35	17.98	4.99	0.97	1.99	0.41	0.61	0.91	2.67	-1.6	-4.2
	1.86	1.97	5.13	16.45	2.49	0.94	0.99	0.34	0.49	0.73	2.00	3.3	0.2

false alarm generation and also does not require any change in alarm threshold margins (Fig. 7f). We might notice as well that function's impulse $\hat{R}f_q$, alerting a leak occurrence, does not always take a favorable shape or amplitude's value. Considering the proposed algorithm, the mentioned above disturbances could provoke a false alarm in case of $\hat{R}f'_q$ function (Fig. 7h). In order to avoid it, it was indispensable to enlarge considerably the alarm threshold margin. Such an issue didn't occur in case of $\hat{R}f''_q$ function because the disturbance impact was eliminated by applying median filtering.

In general, we also could notice that $\hat{R}f'_q$ and $\hat{R}f''_q$ functions have a considerable change in their amplitude as a result of a leak occurrence. It significantly facilitates a leak detection.

Summarizing, in comparison to the results of the leakage detection levels mentioned in [5], the obtained results can be assessed as highly satisfactory. However, it should be noticed, that they refer to the model installation. For real pipelines, one should expect slightly worse results using proposed solutions. Due to the greater length of real pipelines, *detection response time* will be also longer.

It should also be noted that the discussed results relate to sudden leakages. In case of diagnosing slow leakages, *leakage detection level* would be worse and *detection response time* longer.

Moreover, the research was focused on detection of the smallest possible leak, assuming no alarms for non-leak states. An important

issue was the course of the analyzed diagnostic functions and alarm thresholds selection. The proposed solution to this problem is quite simple and effective. However, it can be assumed that the use of even more sophisticated solution may create opportunities for further improvement of *leakage detection level*.

9. Conclusion

This paper presents the comparison of several improved (modified) SLDA (simplified leakage detection algorithms). The compared methods were parameterized and considered for different configurations of diagnostic signals. On the basis of the leakage diagnosis results, obtained during simulations of leaks on the laboratory pipeline, the assessment of these solutions has been performed.

The obtained results prove that, with the simple leak detection methods, it is possible to detect leakages with highly satisfactory diagnosing efficiency (considered as the ability to detect very small leakages in a short time).

The proposed detection algorithm, with two diagnostic functions, improves also a leak detection level. Both diagnostic functions are reliable shape and amplitude indicators.

The discussed methods can be used for building leak detection systems (LDS) in parallel to more sophisticated solutions based on transient models of pipeline installations.

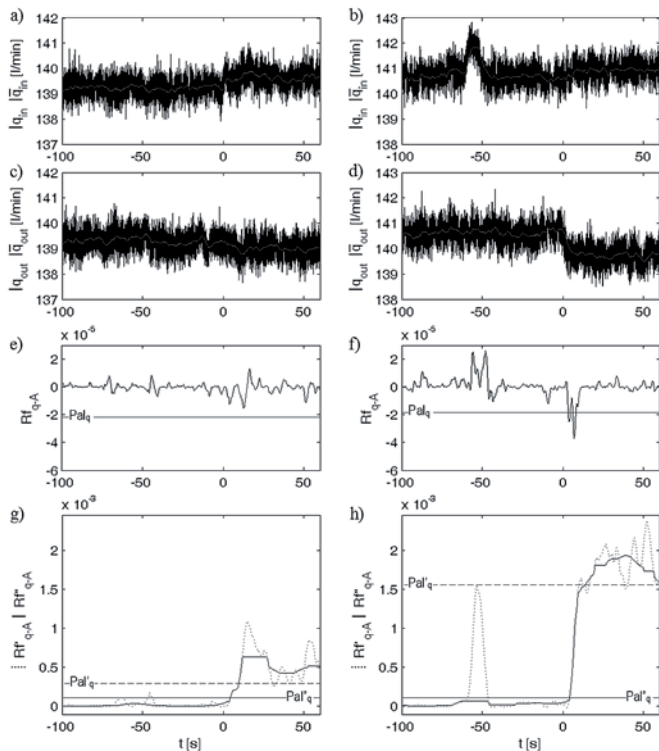


Fig. 7. Flow rate signals and diagnostic functions obtained for the experiments with simulated sudden single leakages with the size of 0,55% $q_{in=out}$ at the point 75 m (left side) and the size of 0,88% $q_{in=out}$ at the point 235 m (right side), where: a), b), c), d) - flow rate and reference variables, e), f) - functions generated by the previous algorithm, g), h) - functions generated by the newly proposed algorithm; "0" means the beginning of leakage

It was pointed out that the requirement to perform further investigations of simple leak detection methods is crucial to achieve even better leak detection efficiency.

Acknowledgement

The research work financed with the means of the Ministry of Science and Higher Education (Poland) in the years 2010-2015 as the research project Nr N N504 494439.

References

1. Begovich O, Navarro A, Sanchez E N, Besancon G. Comparison of two detection algorithms for pipeline leaks. Proceedings of 16th IEEE International Conference on Control Applications, 1-3 October 2007. Singapore; 777-782, <http://dx.doi.org/10.1109/CCA.2007.4389327>
2. Billman L, Isermann R. Leak detection methods for pipelines. Automatica 1987; 23: 381-385, [http://dx.doi.org/10.1016/0005-1098\(87\)90011-2](http://dx.doi.org/10.1016/0005-1098(87)90011-2)
3. Brunone B, Ferrante M. Detecting leaks in pressurised pipes by means of transients. Journal of Hydraulic Research 2001; 39(5): 539-547, <http://dx.doi.org/10.1080/00221686.2001.9628278>
4. Colombo A F, Lee P, Karney B W. A selective literature review of transient-based leak detection methods. Journal of Hydroenvironment Research 2009; 2(4): 212-227, <http://dx.doi.org/10.1016/j.jher.2009.02.003>
5. da Silva H V, et al. Leak detection in petroleum pipelines using a fuzzy system. Journal of Petroleum Science and Engineering 2005; 49(3): 223-238, <http://dx.doi.org/10.1016/j.petrol.2005.05.004>
6. Farmer E. System for monitoring pipelines. US Patent 4,796,466, 1989.
7. Ge Ch, Wang G, Ye H. Analysis of the smallest detectable leakage flow rate of negative pressure wave-based leak detection systems for liquid pipelines. Computers and Chemical Engineering 2008; 32: 1669-1680, <http://dx.doi.org/10.1016/j.compchemeng.2007.08.011>
8. Gertler J, Romera J, Puig V, Quevedo J. Leak detection and isolation in water distribution networks using principal component analysis and structured residuals. Proceedings of Conference on Control and Fault Tolerant Systems, 6-8 October 2010. France Nice; 191-196, <http://dx.doi.org/10.1109/SYSTOL.2010.5676043>
9. Haghighi A, Covas D, Ramos H. Direct backward transient analysis for leak detection in pressurized pipelines: from theory to real application. Journal of Water Supply: Research and Technology – AQUA 2012; 63(3): 189-200, <http://dx.doi.org/10.2166/aqua.2012.032>
10. Isermann R. Leak detection of pipelines, in.: Fault-Diagnosis Applications: Model-Based Condition Monitoring: Actuators, Drives, Machinery, Plants, Sensors and Fault-tolerant Systems. Berlin: Springer-Verlag, 2011, http://dx.doi.org/10.1007/978-3-642-12767-0_7
11. Kowalczyk Z, Gunawickrama K. Detecting and locating leaks in transmission pipelines, in.: Korbicz K J, Koscielny J M, Kowalczyk Z, Cholewa W (Eds.). Fault Diagnosis: Models, Artificial Intelligence, Applications. Berlin: Springer-Verlag, 2004, http://dx.doi.org/10.1007/978-3-642-18615-8_21
12. Li Y, Sun L. Leakage detection and d for long range oil pipeline using negative pressure wave technique. Proceedings of 4th IEEE Conference on Industrial Electronics and Applications, May 25-27 2009. China Xi'an; 3220-3224, <http://dx.doi.org/10.1109/ICIEA.2009.5138796>
13. Liou C. Pipeline leak detection based on mass balance. Proceedings of the International Conference on Pipeline Infrastructure II, ASCE, 1993.
14. Ostapkowicz P. Improving the efficiency of diagnosing of leaks from liquid transmission pipelines by using the new diagnostic information -

- the signals of weak interactions between objects. Solid State Phenomena 2009; 147-149: 492-497, <http://dx.doi.org/10.4028/www.scientific.net/SSP.147-149.492>
15. Ostapkowicz P. Leakage detection from liquid transmission pipelines using improved pressure wave technique. Eksploatacja i Niezawodność – Maintenance and Reliability 2014; 16(1): 9-16.
 16. Siebert H, Isermann R. Leckererkennung und Lokalisierung bei Pipelines durch on-line Korrelation mit einem Prozesrechnen. Regelungstechnik 1977; 25: 69-74, <http://dx.doi.org/10.1524/auto.1977.25.112.69>
 17. Turkowski M, Bratek A, Slowikowski M. Methods and systems of leak detection in long range pipelines. Journal of Automation, Mobile Robotics & Intelligent Systems 2007; 1: 39-46. ISSN 1897-8649
 18. Verde C, Molina L, Carrera R. Practical issues of leaks diagnosis in pipelines. Proceedings of 18th IFAC World Congress, 28 August - 2 September 2011. Italy Milano; 12337-12342, <http://dx.doi.org/10.3182/20110828-6-IT-1002.01688>
 19. Wang X J, Simpson A R, Lambert M F, Vitkovsky J P. Leak detection in pipeline systems using hydraulic methods: a review. Proceedings of the Conference on Hydraulics in Civil Engineering, The Institution of Engineers, 23-30 November 2001. Australia Hobart; 391-400.
 20. Zhang J. Statistical pipeline leak detection for all operating conditions. Pipeline & Gas Journal 2001; 228(2): 42-45.

Paweł OSTAPKOWICZ

Faculty of Mechanical Engineering
Białystok University of Technology
ul. Wiejska 45C, 15-351 Białystok, Poland

Andrzej BRATEK

Industrial Research Institute for Automation and Measurements
Al. Jerozolimskie 202, 02-486 Warsaw, Poland

E-mails: p.ostapkowicz@pb.edu.pl, abrateg@piap.pl

INFORMATION FOR AUTHORS

Eksploracja i Niezawodność – Maintenance and Reliability – the journal of the Polish Maintenance Society, under the scientific supervision of the Polish Academy of Sciences (Branch in Lublin), published four times a year.

The scope of the Quarterly

The quarterly *Eksploracja i Niezawodność – Maintenance and Reliability* publishes articles containing original results of experimental research on the durability and reliability of technical objects. We also accept papers presenting theoretical analyses supported by physical interpretation of causes or ones that have been verified empirically. *Eksploracja i Niezawodność – Maintenance and Reliability* also publishes articles on innovative modeling approaches and research methods regarding the durability and reliability of objects.

The following research areas are particularly relevant to the journal:

1. degradation processes of mechanical and biomechanical systems,
2. diagnosis and prognosis of operational malfunctions and failures.
3. analysis of failure risk/wear,
4. reliability-and-environmental-safety engineering in the design, manufacturing and maintenance of objects,
5. management and rationalization of object maintenance,
6. risk management in the processes of operation and maintenance,
7. the human factor and human reliability in operation and maintenance systems.

Terms and Conditions of Publication

The quarterly *Eksploracja i Niezawodność – Maintenance and Reliability* publishes only original papers written in English or in Polish with an English translation. Translation into English is done by the Authors after they have received information from the Editorial Office about the outcome of the review process and have introduced the necessary modifications in accordance with the suggestions of the referees! Acceptance of papers for publication is based on two independent reviews commissioned by the Editor.

The quarterly *Eksploracja i Niezawodność – Maintenance and Reliability* proceeds entirely online at submission.ein.org.pl

Technical requirements

- After receiving positive reviews and after acceptance of the paper for publication, the text must be submitted in a Microsoft Word document format.
- Drawings and photos should be additionally submitted in the form of high resolution separate graphical files in the TIFF, SVG, AI or JPG formats.
- A manuscript should include: names of authors, title, abstract, and key words that should complement the title and abstract (in Polish and in English), the text in Polish and in English with a clear division into sections (please, do not divide words in the text); tables, drawings, graphs, and photos included in the text should have descriptive two-language captions, if this can be avoided, no formulae and symbols should be inserted into text paragraphs by means of a formula editor; references (written in accordance with the required reference format); author data – first names and surnames along with scientific titles, affiliation, address, phone number, fax, and e-mail address.

The Editor reserves the right to abridge and adjust the manuscripts. All submissions should be accompanied by a submission form.

Detailed instructions to Authors, including evaluation criteria can be found on the journal's website: www.ein.org.pl

Editor contact info

Editorial Office of „Eksploracja i Niezawodność - Maintenance and Reliability”
Nadbystrzycka 36, 20-618 Lublin, Poland
e-mail: office@ein.org.pl

INFORMATION FOR SUBSCRIBERS

Fees

Yearly subscription fee (four issues) is 100 zloty and includes delivery costs. Subscribers receive any additional special issues published during their year of subscription free of charge.

Orders

Subscription orders along with authorization to issue a VAT invoice without receiver's signature should be sent to the Editor's address.

Note

In accordance with the requirements of citation databases, proper citation of publications appearing in our Quarterly should include the full name of the journal in Polish and English without Polish diacritical marks, i.e.,

Eksploracja i Niezawodność – Maintenance and Reliability.

No text or photograph published in „Maintenance and Reliability” can be reproduced without the Editor's written consent.

Wydawca:
Polskie Naukowo Techniczne
Towarzystwo Eksploatacyjne
Warszawa



Publisher:
Polish Maintenance Society
Warsaw

Członek:
Europejskiej Federacji
Narodowych Towarzystw
Eksploatacyjnych



Member of:
European Federation of National
Maintenance Societies

Patronat naukowy:
Polska Akademia Nauk
Oddział Lublin



Scientific Supervision:
Polish Academy of Sciences
Branch in Lublin

